



Forschungszentrum Karlsruhe
in der Helmholtz-Gemeinschaft

Wissenschaftliche Berichte
FZKA 6759

Proceedings of the German-Japanese Workshop on Multi-Phase Flow

Compiled by
T. Schulenberg, M. Ozawa, G. Grötzbach
Institut für Kern- und Energietechnik
Programm Nukleare Sicherheitsforschung

März 2003

Forschungszentrum Karlsruhe

in der Helmholtz-Gemeinschaft

Wissenschaftliche Berichte

FZKA 6759

**Proceedings of the German-Japanese Workshop
on Multi-Phase Flow**

Karlsruhe, Germany, August 25-27, 2002

Compiled by

T. Schulenberg, M. Ozawa*, G. Grötzbach

Institut für Kern- und Energietechnik
Programm Nukleare Sicherheitsforschung

*Kansai University, Osaka, Japan

Forschungszentrum Karlsruhe GmbH, Karlsruhe

2003

Für diesen Bericht behalten wir uns alle Rechte vor

Forschungszentrum Karlsruhe GmbH
Postfach 3640, 76021 Karlsruhe

Mitglied der Hermann von Helmholtz-Gemeinschaft
Deutscher Forschungszentren (HGF)

ISSN 0947-8620

Preface

The German-Japanese Workshop on Multi-Phase Flow was held on August 25 to 27, 2002 at Forschungszentrum Karlsruhe, Germany. It was the third meeting of a series of formerly bilateral Symposia on Two-, Three-, or Multi-Phase Flows held in 1994 at Karlsruhe and in 1997 at Tokyo.

The purpose of the workshop was to provide a forum for specialists from Japan, Germany, and also for partners from neighbouring countries in order to consolidate recent advances in various basic and applied areas of multi-phase flow in science and technology. Thus, it brought together scientists and engineers working on experimental, theoretical and numerical investigations of multi-phase flows, and those working on related engineering applications.

The announcement of the German-Japanese Workshop had been warmly accepted in both countries, as well as in some other countries. In total 24 papers were submitted which were focussed on

the measurements and predictions of
three-dimensional flow phenomena in multi-phase flow.

In detail, the presentations cover of the following topics:

- Phase distribution and separation
- Flow patterns in macro and micro channels
- Interfacial phenomena and instabilities
- Instrumentation and measurement techniques
- Flow visualizations
- 3D-modeling and computational methods
- Numerical simulation of flows with interfaces

The proceedings include all these contributions and are arranged accordingly.

Dr. Günther Grötzbach and Prof. Mamoru Ozawa took the responsibility for the technical organization of the meeting and the handling of the papers to produce the proceedings. Prof. G. Schnerr and Prof. M. Shoji helped to select the papers to focus the workshop on the intended subject. I like to thank all of them for their excellent organization to make this workshop a great success.

Great thanks also to Günther Grötzbach and Heide Hofmann for arrangement of the accommodation and transportation and for the wonderful evening in the Palace of Heidelberg.

Karlsruhe, October 2002

Mamoru Ozawa

**Participants of the
German-Japanese Workshop on Multi-Phase Flow
Karlsruhe Aug. 25 – 27, 2002**

On the occasion of the conference dinner at the Palace of Heidelberg



From lower front to upper back, each from left to right:

Row 1:

Suzuki, Shoji, Shirakawa, Graf, Ozawa, Schulenberg, Schulenberg, Abe

Row 2:

Shiomi, Hirayama, Wang, Auracher, Auracher, Fukano, Hara, Ilic, Asano, Buchholz

Row 3:

Artemyev, Grötzbach, Kunugi, Müller, Suryawijaya, Giese, Pilz, Lucas, Schütz

Row 4:

Grötzbach, Ito, Morita, Cheng, Saptoadi, Gharaibah, Seeger, Wörner, Schnerr, Schäfer, Ghidersa

Missing on the picture are the following participants:

Brücker, Goldbrunner, Wilhelm, Meyer, Uchiyama, Matsumoto

LIST OF CONTENTS

A. Local Phenomena and Data

<i>K. Suzuki, M. Suzuki, S. Takahashi, H. Kawamura, Yo. Abe</i>	A-1
Observation of Contact Area of Bubbles with Heating Surface in Pool Boiling of Water under Microgravity	
<i>Yu. Abe, H. Nariai</i>	A-9
Study on the Gas-Liquid Interfacial Behavior during Trigger Process of Vapor Explosion	
<i>Ch. Brücker, W. Schröder</i>	A-17
Statistical Investigation of Particle-Interaction in Multiphase Flows	
<i>T. Fukano, T. Inatomi, Y. Matsuzawa, T. Yoshida, N. Uchimichi</i>	A-18
Generation of Entrained Droplets from an Imitated Disturbance Wave and their Deposition on the Wall	
<i>M. Goldbrunner, J. Karl, D. Hein</i>	A-28
Local Phenomena in Case of Condensation at Stratified Flow with Non Condensable Gases	

B. Measurement Techniques

<i>M. Buchholz, H. Auracher</i>	B-1
Improved Optical Probes and their Validation for Local Measurements in Two Phase Flows	
<i>A. Seeger, K. Affeld, U. Kertzscher, L. Goubergrits, E. Wellenhofer</i>	B-11
Measurements of Three-Dimensional Flow Phenomena in Multi-Phase Flow by X-Ray Particle Tracking Velocimetry	
<i>H. Asano, N. Takenaka, T. Fujii, K. Takeshima</i>	B-17
Visualization and Void Fraction Measurement of Gas-Liquid Two-Phase Flow in Heat Exchangers by Neutron Radiography	
<i>R. Pilz, E. U. Mahnke, D. C. Hempel</i>	B-29
The Measurement of Shear Stresses in Bubble Columns and Airlift Loop-Reactors	

C. Flow Regime Phenomena and Data

<i>D. Lucas, E. Krepper, H.-M. Prasser</i>	C-1
Experimental Investigations and Modelling on the Transition from Bubble to Slug Flow in Vertical Pipes	
<i>M. Hirayama, H. Umekawa, M. Okano, M. Ozawa</i>	C-13
Flow Pattern and Void Fraction Fluctuation in Oscillatory Two-Phase Flow	
<i>S. F. Wang, M. Shoji</i>	C-26
Dynamic Behavior of Gas-Liquid Two-Phase Flow Splitting at an Impact T-junction	

D. Applied Flow Phenomena and Data

- Y. Shiomi, S. Nakanishi, K. Yamagami*.....D-1
Experimental Study of Bubble Noise at Orifice
- P. Suryawijaya, G. Kosyna*.....D-9
Unsteady Measurement of the Static Pressure on the Impeller Blade Surfaces and
Optical Observation on Centrifugal Pumps under Varying Liquid/Gas Two-Phase
Flow Conditions

E. Methods for CFD

- E. Gharaibah, M. Brandt, W. Polifke*.....E-1
A Numerical Model of Dispersed Two Phase Flow in Aerated Stirred Vessels
based on Presumed Shape Number Density Functions
- N. Shirakawa, H. Horie, Y. Yamamoto*..... E-11
Analysis of the Forced Convection Boiling with the Particle Interaction Method
- E. Laurien, T. Giese, D. Saptoadi, J. Schütz*.....E-24
Multidimensional Modeling and Simulation of Subcooled Pool Boiling

F. Physical Models for CFD

- V. Artemyev, Y. Kornienko*..... F-1
Numerical Method for Modeling of Turbulent Two-Phase Bubble Flow
Anomalous Shear Stress and Heat Transfer Behavior
- W. Basuki, G. H. Schnerr, W. Yuan*.....F-14
Single-Phase and Modified Turbulence Models for Simulation of Unsteady
Cavitating Flows
- K. Morita, K. Fukuda, Y. Tobita, Sa. Kondo, T. Suzuki, W. Maschek*.....F-30
Generalized Modeling of Multi-Component Vaporization/Condensation
Phenomena for Multi-Phase-Flow Analysis

G. Physical Interpretation by Numerical Simulation

- B. Ghidersa, M. Wörner, D. G. Cacuci*.....G-1
Numerical Simulation of Bubble-Train Flow in a Small Channel of Square Cross-
Section
- M. Wörner*..... G-10
Invariance of the Velocity Field Induced by a Bubble Rising Steadily Through
Liquid under Variation of the Gas-Liquid Density Ratio
- T. Uchiyama, T. Honda*..... G-22
Vortex Simulation of Bubble Dispersion in an Excited Round Jet
- T. Kunugi, C. Kino, A. Serizawa*..... G-34
Surface Wave Structure and Heat Transfer of Vertical Liquid Film Flow

A. Local Phenomena and Data

OBSERVATION OF CONTACT AREA OF BUBBLES WITH HEATING SURFACE IN POOL BOILING OF WATER UNDER MICROGRAVITY

Koichi SUZUKI¹⁾, Motohiro SUZUKI²⁾, Saika TAKAHASHI²⁾,
Hiroshi KAWAMURA¹⁾ and Yoshiyuki ABE³⁾

¹⁾Department of Mechanical Engineering, Faculty of Science and Technology,
Tokyo University of Science
Yamasaki 2641, Noda, Chiba, 278-8510 Japan
Phone: +81 4 7124 1501, Fax: +81 4 7123 9814
E-mail: suzuki@rs.noda.tus.ac.jp

²⁾Graduate School of Science and Technology, Tokyo University of Science

³⁾The National Institute of Advanced Industrial Science and Technology

ABSTRACT

Burnout heat flux was measured in subcooled pool boiling of water under attached boiling bubbles on heating surface with bubble holding plate in ground experiment. A thin stainless flat plate was employed for heating surface. The experimental setup and the heating procedures were same as used in reduced gravity experiment performed by a parabolic flight of jet aircraft. Same burnout heat flux as in the reduced gravity was obtained by adjusting the clearance between the bubble holder and the heating surface. They were 100 ~ 400 percent higher than the widely accepted existing theories.

As extending heating time longer than the reduced gravity duration until burnout occurred, burnout heat flux decreased gradually and became a constant value calculated from the existing theories. In a result of observing contact area of boiling bubbles with transparent heating surface, the contact area was smaller in quick heating time than that in long time heating at same heat flux. The experimental results suggest in microgravity that liquid layer is remained between rapidly expanded bubbles and heating surface.

In microgravity experiment by a drop shaft facility, contact area of bubbles with heating surface increased considerably at starting of microgravity.

1. INTRODUCTION

In the widely accepted theories on critical heat flux, it has been decreased in proportion to the one-quarter power of gravity in microgravity [1][2]. But the critical heat flux observed in microgravity experiments obtained by a parabolic flight of aircraft and a drop tower has been 100~300 percent higher than the existing theories [3]. It has been reported in some previous experiments, boiling bubbles detach from a heating surface in microgravity [4]. Recently, boiling bubbles are considered to detach from a heating surface by Marangoni flow or thermo-capillary flow activated on the boundary surface of liquid and vapor, then the liquid is supplied into the heating surface. This is considered to be acceptable reason why the higher critical heat flux is obtained in microgravity. However, it is difficult to understand the mechanism of boiling in microgravity because a lot of factors such as wettability of liquid and solid surface, inertia of bubble growth and g-jitter are strongly related to the bubble detachment and bubble behavior. In fact, critical heat flux is very difficult to be obtained in microgravity, because the heating surface is easy to dry out and

high-powered electric current is needed. Therefore, no or few data on the bubble behavior near the critical heat flux and the burnout of heating surface have been found in the many experiments on boiling in the very high heat flux region under microgravity condition. Then the details of boiling in microgravity are still unknown.

The present paper introduces authors' previous works on boiling experiment in reduced gravity and discusses a mechanism of boiling and bubble behavior.

2. BURNOUT HEAT FLUX OBTAINED UNDER REDUCED GRAVITY

In the experiment on subcooled pool boiling of water under reduced gravity realized by a parabolic flight of aircraft, a thin stainless steel plate of 20 mm length, 5 mm width and 0.1 mm thickness, was physically burned out by an alternate electric current and the bubble behavior was observed until the heating surface was burned [5]. The level of g was $0.01 \sim 0.04g$ and it lasted 25 seconds. An alternative electric current supplied by the aircraft was applied into the heating surface at 10 seconds before the reduced gravity started and was increased at constant rate of power until the burnout. The burnout heat flux (critical heat flux) was 100 ~ 400 percent higher than the existing theories [1][2] as shown in Figure 1. No bubble detachment was observed at any liquid subcooling until the burnout under the microgravity.

According to the bubble behavior in the reduced gravity, the ground experiment on subcooled pool boiling water was performed and the burnout heat flux was obtained by the attaching boiling bubbles on the heating surface over a flat plate with a small clearance [6]. The heating surface and the experimental conditions were used same as in the reduced gravity. Same heat burnout flux as in the reduced gravity was obtained by adjusting the clearance between the heating surface and the cover plate as shown in Figure 1 [6].

In the ground experiment, heating time until burnout was extended to 400 seconds. The burnout heat flux decreased rapidly until about 80 seconds over 20 seconds (reduced gravity period), then it became constant as shown in Figure 2.

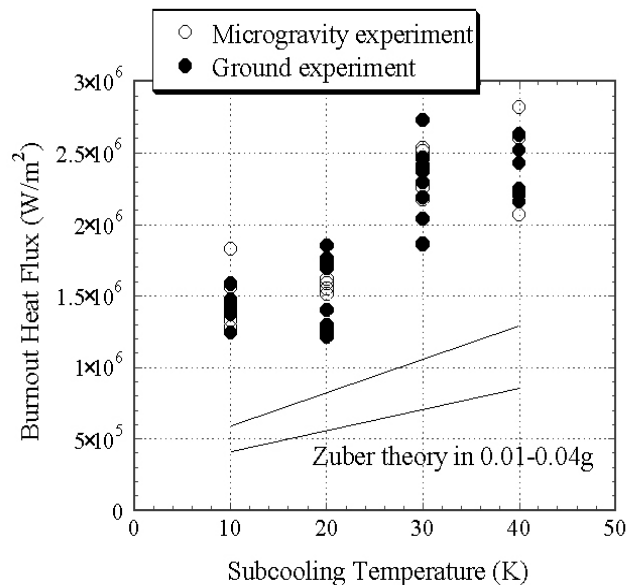


Figure 1: Burnout heat flux obtained in reduced gravity and ground experiment in subcooled pool boiling of water.

The constant heat flux is coincident with a value calculated from the existence theory [7]. No remarkable effect of heating time on the burnout heat flux was observed for the boiling experiment without bubble holder (cover plate) as shown in Figure 2. As a result of dependence of heating time on the burnout heat flux, we consider that microlayer of liquid or liquid layer remained between the heating surface and boiling bubbles expanded rapidly is closely related to the higher burnout heat flux in quick heating conducted under the reduced gravity as illustrated in Figure 3.

3. EXPERIMENTAL SETUP FOR OBSERVING CONTACT AREA OF BUBBLES WITH HEATING SURFACE

As mentioned above, the higher burnout heat flux in microgravity is closely associated with the remained liquid layer on the heating surface. Thus, the visual observation of contact area of boiling bubbles with heating surface was tried experimentally by using an experimental setup as shown in Figure 4. The experimental setup consists of three sections, which are a power supply section, a control section and a boiling section.

The heating surface is ITO film coated on a transparent soda lime glass with 1.8 mm of thickness and placed horizontally in a transparent boiling vessel shown in Figure 5. The thickness of ITO film is 0.4 μm and the dimension of heating surface is 20 mm in length and 5 mm in width. Heat flux is calculated by an electric power applied into the ITO surface. Temperature of heating surface is calculated from an electric resistance of ITO film. A bubble holding plate is placed over the heating surface with a suitable clearance.

Contact area of boiling bubbles with heating surface was visually observed from backside of the heating surface by CCD video camera as shown in Figure 5. In the video pictures, a dry surface is the lightest part by a complete reflection of light beam and a liquid contact surface is dark by a penetration of the beam. A microlayer and a thin liquid film were not visualized in the present experiment.

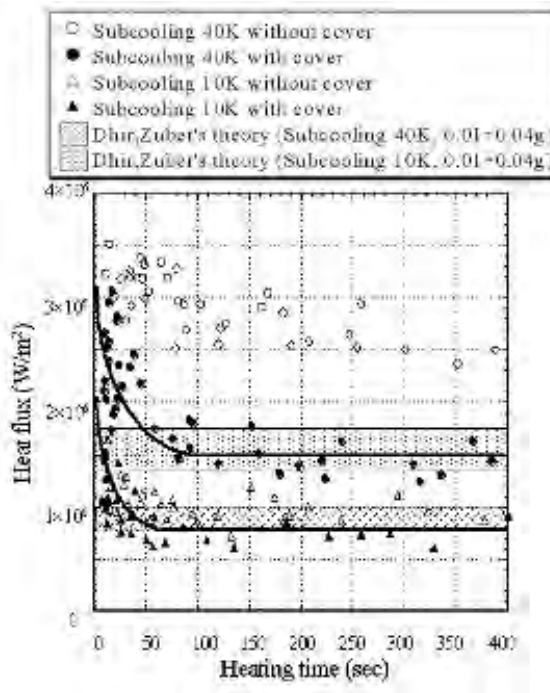


Figure 2: Change of burnout heat fluxes with heating time in subcooled pool boiling of water at 10 K and 40 K of liquid subcooling.

Tested subcoolings of water were 10 K and 40 K. Subcooled pool boiling of water was conducted according to the same heating procedure as employed in the reduced gravity and the long time heating until the heater surface was burned out.

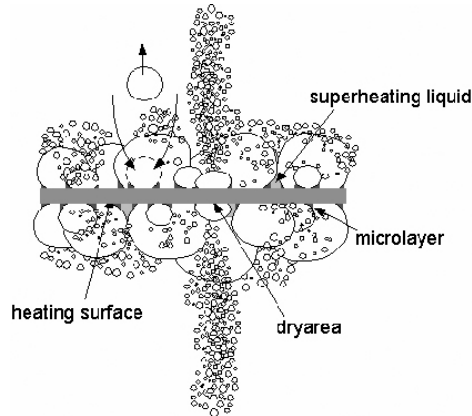


Figure 3: Illustration of imagined boiling bubbles on heating surface in microgravity.

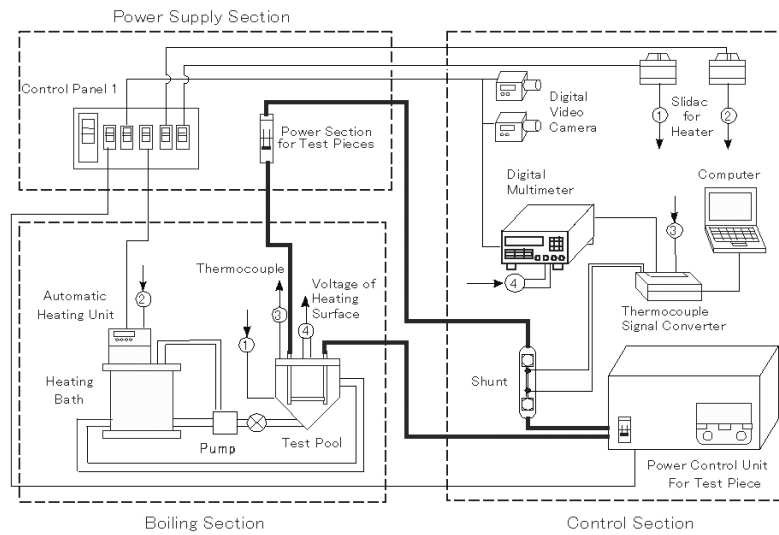


Figure 4: Experimental setup for observing contact area of boiling bubbles with ITO coated heating surface in subcooled pool boiling of water.

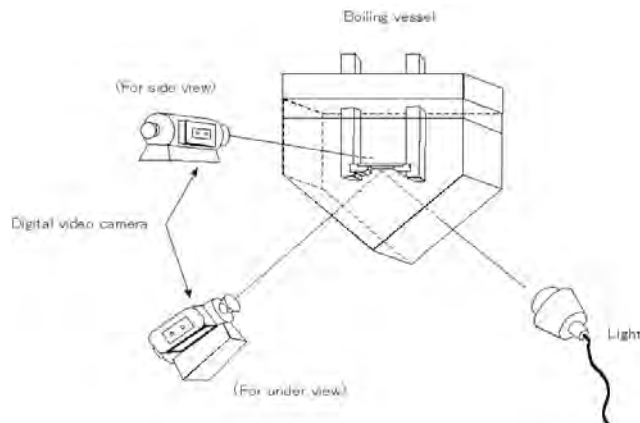


Figure 5: Test section of observing boiling bubbles with heating surface in subcooled pool boiling of water and recording system.

4. EFFECT OF HEATING TIME ON CONTACT AREA OF BOILING BUBBLES WITH HEATING SURFACE: GROUND EXPERIMENT

A contact angle of water droplet was measured for temperature of the ITO surface, stainless surface and rough stainless surface. The stainless surface was a same one used in the reduced gravity experiment. The contact angle of the droplet increases with temperature rise for the stainless surface but it is not so changed for the ITO surface as shown in Figure 6. The contact angle of the stainless surface closes to the one of the ITO surface. The result means that the wetting condition of the droplet is nearly the same for both surfaces.

An effect of heating time on the contact area of boiling bubbles with heating surface is shown in Figure 7 for 10 K of liquid subcooling and Figure 8 for 40 K of liquid subcooling. As seen from both experimental results, the ratio of contact area of boiling bubbles to the area of heating surface in quick heating is smaller than that in longtime heating. According to the results, the quick heating suggests liquid layer remained between the boiling bubbles and the heating surface by the rapid expansion of boiling bubbles.

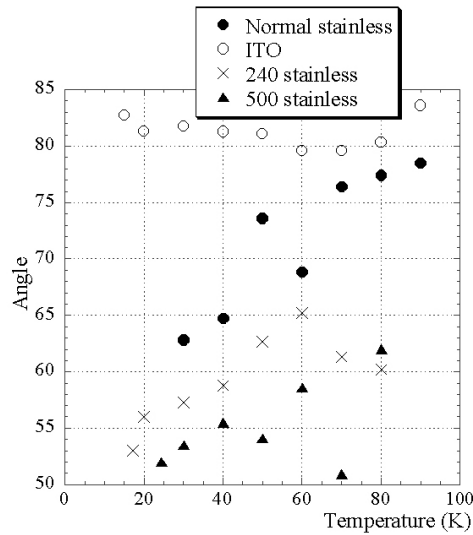


Figure 6: Contact angle of water droplet to heating surfaces with temperature.

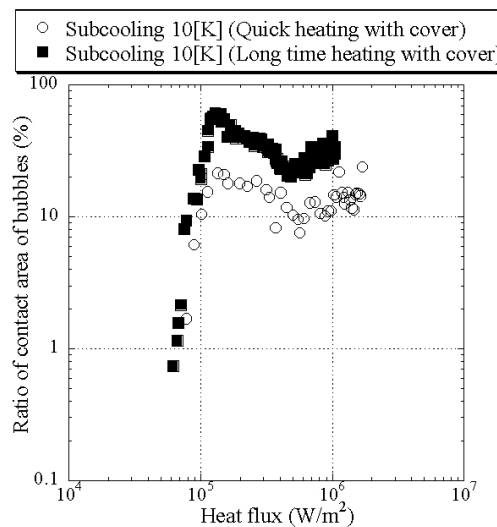


Figure 7: Effect of heating time on contact area of boiling bubbles with heating surface in subcooled pool boiling of water with bubble holder at 10 K of liquid subcooling.

5. CONTACT AREA OF BUBBLES WITH HEATING SURFACE IN SUBCOOLED POOL BOILING OF WATER UNDER MICROGRAVITY: DROP SHAFT EXPERIMENT

An experiment on subcooled pool boiling of water was performed in microgravity practiced by a drop shaft facility in JAMIC (Japan Microgravity Center). Same experimental set up shown in Figures 4 and 5 employed in ground experiment was used but DC power for heating was supplied by integrated solid batteries.

$10^{-5}g$ of gravity was obtained for 10 seconds in JAMIC. The heating was started at 10 seconds before the starting drop. Subcooled pool boiling of water was performed in the five drops. Tested liquid subcooling was 38 K and heating power was applied into the heating surface at constant voltage of 72 V, 96 V, 108 V, 132 V and 144 V for the each drop.

Change of contact area of boiling bubbles with dropping time is shown in Figure 9 for an example. Only the case of 108 V was succeeded in the experimental observation. As shown in Figure 9, contact area of bubbles increases instantaneously just starting microgravity. This result means that many bubbles do not detach from the heating surface.

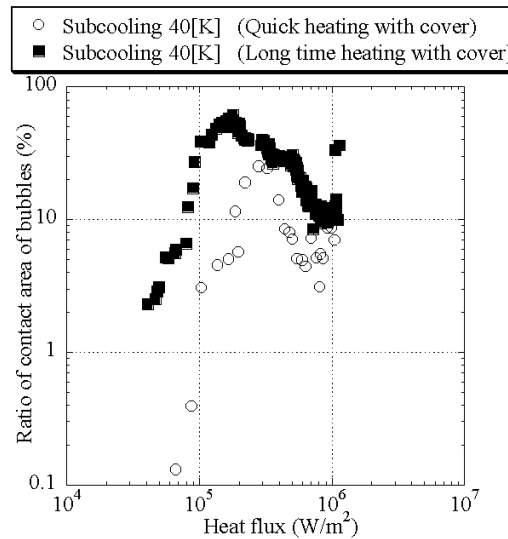


Figure 8: Effect of heating time on contact area of boiling bubbles with heating surface in subcooled pool boiling of water with bubble holder at 40 K of liquid subcooling.

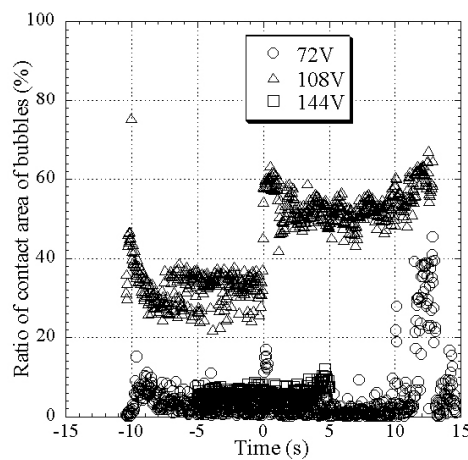


Figure 9: Contact area of boiling bubbles with heating surface in subcooled pool boiling of water in microgravity practiced by drop shaft.

Contact area of bubbles with heating surface in the microgravity is displayed in the ground experimental result on contact area and heat flux at 40 K of liquid subcooling as shown in Figure 11.

The microgravity data are well agreed with the contact area of bubbles with heating surface in quick heating. Accordingly, in case of quick heating such as short time microgravity duration, boiling bubbles expand rapidly on the heating surface and larger liquid layer is remained between the expanding bubbles and the heating surface.

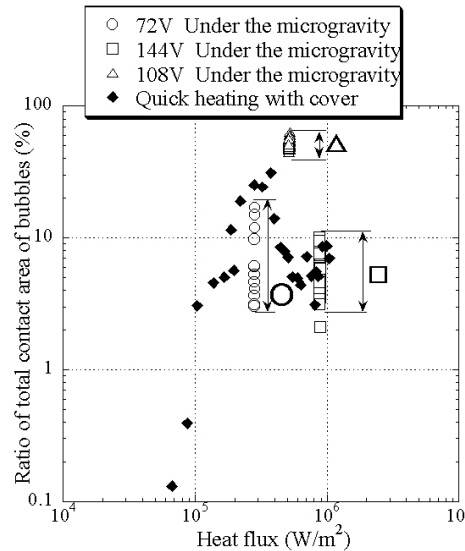


Figure 10: Contact area of boiling bubbles in subcooled pool boiling water in quick heating at 40 K of liquid subcooling including microgravity data.

6. CONCLUSION

In the simulated experiment on the bubble behavior in subcooled pool boiling of water observed under the reduced gravity, same burnout heat flux was obtained. It was 100 – 400 percent higher than widely accepted existing theories. As the heating time was extended until the burnout the heat flux gradually decreased over reduced gravity duration and became constant at longer than 100 seconds. In the simulated experiment of bubble behavior, contact area of bubbles with heating surface was observed using transparent heating surface for quick heating and long time heating. The contact area was smaller in quick heating than long time heating at same heat flux. In the drop shaft experiment, observed contact area of bubbles increased considerably in microgravity.

According to the series of authors' experiments, it is suggested the following conclusion.

In short time microgravity condition performed by a drop shaft and a parabolic flight of aircraft, boiling bubbles expand rapidly and liquid layer is remained between boiling bubbles and heating surface. The rapid evaporation of liquid layer near burnout is one of the reasons for the higher critical heat flux in microgravity.

ACKNOWLEDGEMENT

Authors greatly appreciate the help of JAMIC (Japan Microgravity Center) for the drop shaft experiment.

REFERENCES

- [1] Kutateladze, S.S., Heat transfer in condensation and boiling, USAEC Rep., AEC-tr-3770, 1952.
- [2] Zuber, N., On stability of boiling heat transfer, Trans.ASME J. Heat Transfer 80, pp. 711-720, 1958.
- [3] Straub. J., Zell, M. and Vogel, B., Boiling under microgravity conditions, Proceedings of the 1st European Symposium on Fluid in Space, Ajaccio, France, ESA SP-353, pp. 269-297, 1991.
- [4] Oka, T., Abe, Y., Mori and Nagashima, A., Pool boiling heat transfer in microgravity - Experiments with CFC-113 and water utilizing drop shaft facility, Trans. JSME, Vol. 60, No. 77, pp. 3093-3100, 1994.
- [5] Suzuki, K., Kawamura, H., Aoyama, Y., Koyama, M., Kawasaki, H. and Imai, R., Subcooled pool boiling of water in microgravity – Observation of bubble behavior and burnout, J. the Japan Society of Microgravity Application, Vol. 15, No.4, pp. 206-212, 1998.
- [6] Suzuki, K., Kawamura, H., Koyama, Y. and Aoyama, Y., Experiments on subcooled pool boiling of water on microgravity, 5th ASME/JSME Joint Thermal Engineering Conference, San Diego, CA, pp. 6420-CD, 1999.
- [7] Suzuki, K., Koyama, Y. and Ka, H., Burnout heat flux in microgravity, United Engineering Foundation, The International Conference on Microgravity Fluid Physics and Heat Transfer, Oahu, Hawaii, pp. 144-150, 1999.

STUDY ON THE GAS-LIQUID INTERFACIAL BEHAVIOR DURING TRIGGER PROCESS OF VAPOR EXPLOSION

Yutaka Abe¹⁾ and Hideki Nariai¹⁾

¹⁾Institute of Engineering Mechanics and Systems, University of Tsukuba,
1-1-1 Tennoudai, Tsukuba, Ibaraki, 305-8573, Japan
TEL&FAX: 0298-53-5266
E-mail: abe@kz.tsukuba.ac.jp

ABSTRACT

In the present study, the vapor film collapse behavior around high temperature solid particle submerged into water was experimentally investigated by applying a pressure pulse to the vapor film on a high temperature solid particle. Microscopic interfacial phenomena between vapor and water were visually observed by using a high-speed video camera. The visual data obtained were processed by visual data processing techniques. Furthermore, the transients of the temperature and pressure were simultaneously measured. The interfacial temperature was estimated by solving the heat conduction equation with the data obtained at the boundary conditions.

It is clarified that vapor collapse by pressure pulse occurs homogeneously around the vapor film surface on a high temperature particle. Microscopic information is obtained from the visual data by using visual data processing technique, PIV technique and digital auto-correlation technique. At the time the vapor film surface changes to white, the saturation temperature exceeds the interfacial temperature. The microscopic vapor film collapse behavior indicates the possibility of the phase change at the vapor film collapse.

1. INTRODUCTION

During severe accident of a light water reactor, various thermal hydraulic phenomena including vapor explosion could threaten the integrity of the containment vessel. The occurrence of the severe accident is extremely unlikely since LWRs are designed based on the defence-in depth concept. However, it is important to investigate the thermal hydraulic phenomena including vapor explosion in order to evaluate the safety margin and potential risks of the accident management measures to prevent and mitigate the severe accident.

In order to achieve the vapor explosion, several processes should be sequentially satisfied. The process is called "trigger process". The most important processes for the trigger process for the vapor explosion are the vapor film collapse around high temperature molten material droplets and the following atomization. If the trigger process is not satisfied, the vapor explosion does not occur but violent boiling occurs. The model proposed by Board and Hall is based on the categorization of the break up mechanism of liquid droplet by flow as shown in this Fig. 1. The mechanism of the fragmentation in the previously proposed model is based on the instability due to flow.

On the other hand, Koshizuka conducted the calculation with MPS method that the water column comes homogeneously from the surrounding water to the molten material droplet. The middle figures are the shadow images of the calculation and the lower figures are the experimental X-ray pictures taken by Ciccarelli and Frost. It is indicated that the calculation results are quite similar to the experimental results observing homogeneous filaments generation around the molten Tin material. The result indicates that the violent boiling of the water homogeneously immersed

into the molten material causes the fine fragmentation. One of the biggest questions is what is the driving force of such a homogeneous liquid-liquid contact? Can differential acceleration by relative flow velocity between molten material and surrounded liquid cause the homogeneous liquid-liquid contact?

The objective of the present study is to investigate what is the driving force of such a homogeneous liquid-liquid contact. Since the fragmentation follows the vapor film collapse, the driving force of the water surrounding the molten droplet could be caused by the vapor film collapse behavior. In order to achieve the present objective, it is necessary to investigate only the vapor film collapse behavior separately from the following fragmentation.

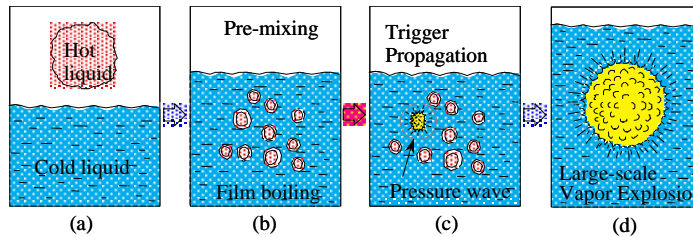


Figure 1: Schematic diagram of thermal detonation model.

2. EXPERIMENTAL APPARATUS AND PROCEDURE

2.1. Experimental apparatus

Figure 2 shows the schematic diagram of the experimental apparatus. Test section is composed of the stainless steel square vessel. Its inner dimension is 54 mm, thickness is 3 mm, and length is 316 mm. Polycarbonate plates for the visual observation are installed on three sides of the test vessel. Strain-gauge type pressure transducers are installed on the center of a rest side in order to measure the pressure and to obtain the trigger signal for high-speed video camera. The sheathed thermocouple to measure the water temperature is in the test vessel 30 mm above the center. The pressure pulse generator is located at the bottom of the test vessel. The pressure pulse is generated by hitting the piston at the bottom of the test section with a bullet driven by nitrogen gas. The nitrogen gas flow is operated with electromagnetic valve to obtain good repeatability. Experimental data are recorded as voltage data into analyzing recorder through amplifier. Those data are transferred to the computer through GP-IB. Visual data are obtained by the high-speed video camera with the maximum speed of 40,500 fps. The high-speed video camera starts with trigger signal from the pressure transducer through analyzing recorder.

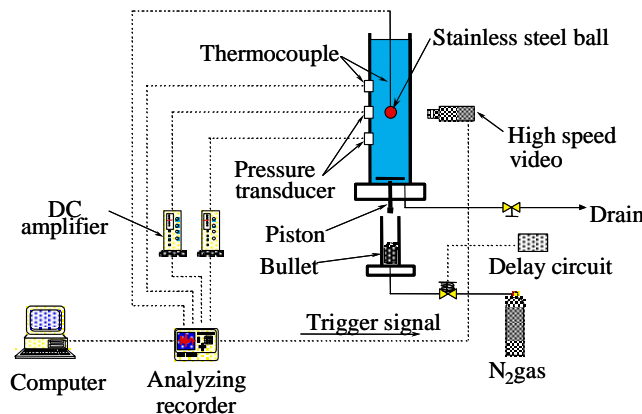


Figure 2: Schematic diagram of the experimental apparatus.

2.2. Experimental procedure

This figure shows the experimental procedure. At first, steel ball was heated up to the specified temperature by a burner. Next, the steel ball was submerged into the water to generate the film boiling on the high temperature ball surface. Finally, pressure pulse was generated at the bottom of the test vessel to attack the film boiling on the high temperature ball surface. The vapor film collapse behavior is observed with high-speed video camera. The maximum recording speed of the video camera is 40,500 fps. The graphic data are stored in the memory unit as 8-bits digital data.

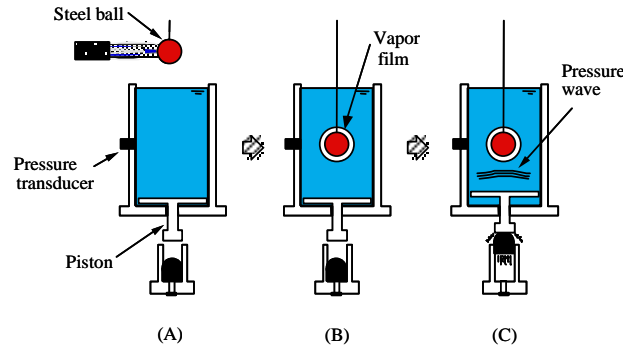


Figure 3: Schematic diagram of the experimental procedure.

3. EXPERIMENTAL RESULTS

3.1. Experimental results

This is one of the direct measurement results in the experiment, Fig. 4. At first you can see transparent and smooth vapor film around a high temperature particle surface. At the moment when the pressure pulse arrives at the particle, you can see homogeneous vapor generation around the high temperature particle. Although the pressure pulse comes from bottom to top, it is clearly observed that vapor is generated homogeneously around the high temperature particle.

Besides with the visual data, pressure around the particle and the particle surface temperature are simultaneously measured as shown in this figure. The figure shows the experimental results of pressure and surface temperature with the pictures of the visual data. Horizontal axis shows time in ms. The surface temperature started to decrease when the pressure pulse arrived. Symbols of A to F correspond to the pictures right. A clear and smooth vapor film was observed at time A before pressure pulse arrived. The peak of the pressure pulse arrived at time B. At the time, vapor film surface changed white. After the pressure pulse passed away, vapor generation occurred homogeneously all over the surface as shown in C through F.

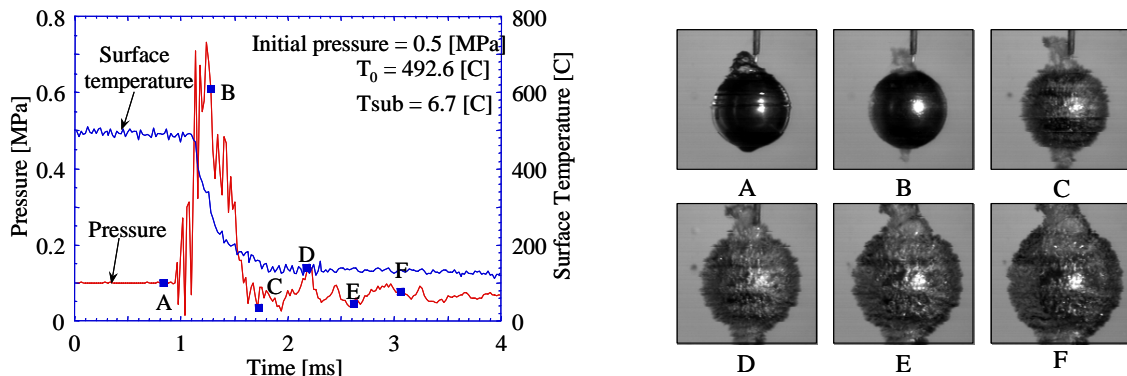


Figure 4: Surface temperature and pressure in forced collapse experiment.

3.2. Estimation of mean film thickness

The digital graphic data are processed to estimate vapor film thickness on the steel particle surface by using the graphical image data processing technique. The schematic diagram of the determination procedure of vapor film thickness is shown in Fig. 5.

The procedure is

1. Capture graphic data of steel particle without vapor film before experiment.
2. Capture graphic data of vapor film collapse on steel particle.
3. Change the 8-bits digital graphic data into binary information. Turn over the binary information of the graphic data with vapor film.
4. Superimpose two graphic binary data.
5. Count the number of pixels of vapor film.

Divide the number of pixels of vapor film by the length of the particle outer surface to estimate the vapor film thickness. The minimum spatial resolution is estimated as 0.02 mm.

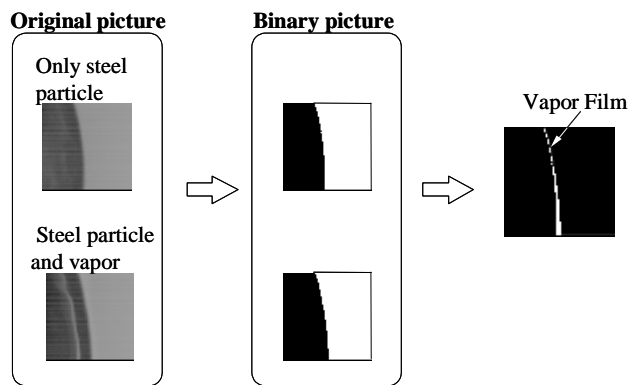


Figure 5: Determination procedure of vapor film thickness.

3.3. Two dimensional velocity field of interface movement

In order to obtain microscopic vapor film collapse behavior, it is very important to estimate the two dimensional velocity field of the interface movement, as well as the above mentioned mean vapor film thickness. PIV technique is tried to apply to estimate the interface movement. In usual PIV technique, visual pattern of the tracer particles are correlated to reproduce the velocity field. In the present study, the pattern of the binary line data of the interface obtained from the visual observation is used to correlate the interfacial movement. That is, the outlines of the vapor film in following two times are converted into binary data as shown in Figure 6. Then the 64 pixels by 64 pixels full picture is divided into 4 by 4 equal 16 elements. When the two patterns of the lines in different time is matched, the distance and the angle between two elements is estimated to reproduce the velocity vector field of the interface movement.

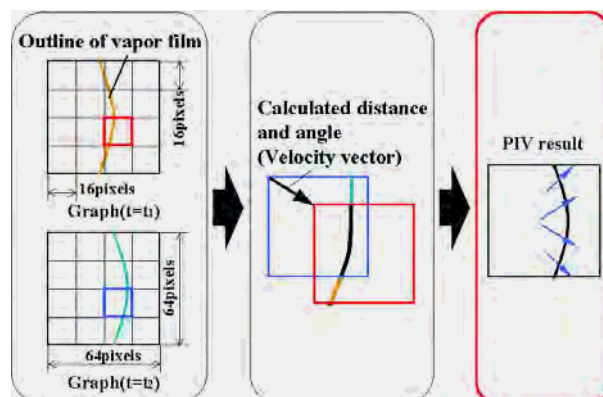


Figure 6: PIV procedure to determine the interface movement.

3.4. Interface movement by digital auto-correlation

Although the velocity field of the interface obtained with the PIV technique is useful to grasp the two dimensional interfacial movement, the results include some error since PIV technique traces the image of the binary visual data pattern. In order to precisely determine the location of the interface at each time, digital auto-correlation technique is applied as shown in Figure 7. At first, the visual data is changed into a matrix of the brightness information. The matrix of the brightness information and a reference matrix function are cross-correlated with the equation to yield the cross-correlation function as shown in the Fig. 7. The reference function is chosen to make the cross-correlation function highest at the gas liquid interface.

Once the locations of the interface at different times are obtained, it is possible to estimate the interfacial velocity. This figure shows the estimated location of the interface with the Gaussian fitting function. The difference of the locations at two different times make it possible to estimate the interfacial velocity in x direction.

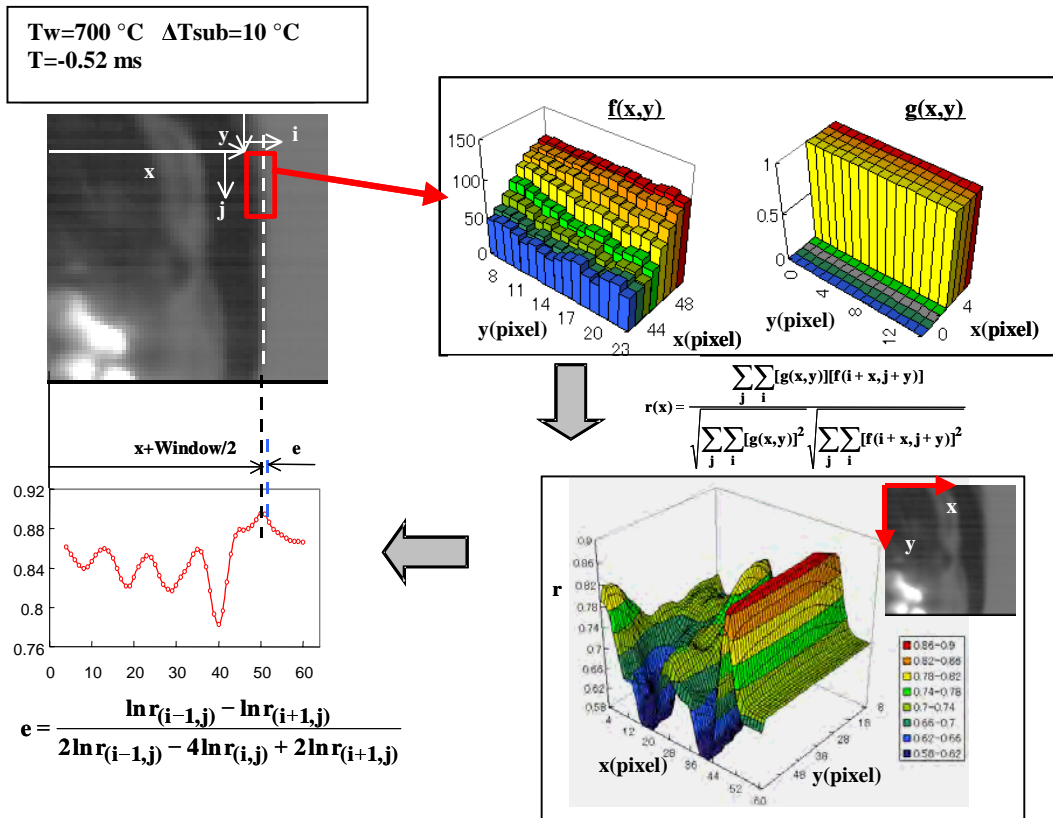


Figure 7: Auto-correlation function and determination of the interface location.

3.5. Heat conduction analysis

From the above visual data processing technique, the mean vapor film thickness can be estimated. By using the mean film thickness as a boundary condition, it is possible to estimate the vapor-liquid interfacial temperature with the following heat conduction equation. The Following heat conduction equation (1) is numerically solved to yield the temperature distribution as shown in Fig. 8. Once the temperature distributions were obtained, the vapor-liquid interface temperature is estimated.

$$\frac{\partial T}{\partial t} = \frac{1}{r^2} \frac{\partial}{\partial r} \left(r^2 \frac{\partial T}{\partial r} \right) \quad (1)$$

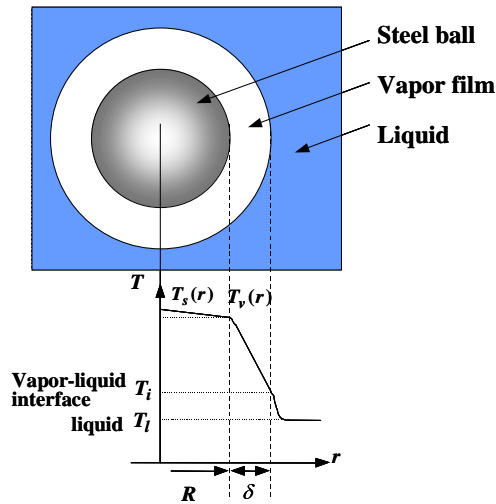


Figure 8: Schematics of heat conduction analysis

3.6. Summary of the data estimation

Figure 9 shows the summary of the estimated results from the visual observation data and pressure measurement results simultaneously obtained in the experiment.

The upper graph shows the estimated mean film thickness and the measurement result of the pressure. The middle graph shows the measured particle surface temperature, saturation temperature from the pressure measurement, and the interfacial temperature calculated by solving the heat conduction equation. The lower graphs show the visual data, the velocity distribution estimated with the PIV technique, and the x-direction velocity estimated by the digital auto-correlation technique.

The symbols A through E are corresponding to the pictures on the right hand side. At first vapor film is smooth and transparent as shown at time A. At the time B, pressure pulse arrived at the particle. And the vapor film surface changes to white and the saturation temperature estimated from the pressure exceeds the interfacial temperature. The interfacial velocity toward the horizontal direction is very small at the moment. After time B, vapor generation starts from time C. The interface movement changes its direction at time D. Finally, violent vapor generation occurs from time E when the saturation temperature decreases below the interfacial temperature.

Considering the present results, the vapor film collapse occurs homogeneously in all directions and the vapor surface turns white when the pressure pulse arrives. Furthermore, it is estimated that the saturation temperature exceeds the interfacial temperature. These results of the microscopic vapor film collapse behavior indicate the possibility that the phase change occurs at the time when the vapor film changes white.

4. CONCLUSIONS

- It is clarified that vapor collapse by pressure pulse occurs homogeneously around the vapor film surface on a high temperature particle.
- Microscopic information are obtained from the visual data by using visual data processing technique, PIV technique and digital auto-correlation technique.
- At the time the vapor film surface changes to white, the saturation temperature exceeds the interfacial temperature.

The microscopic vapor film collapse behavior indicates the possibility that experimentally obtained homogeneous vapor film collapse behavior is caused not by differential acceleration due to relative flow difference but by pressure force due to phase change within vapor film.

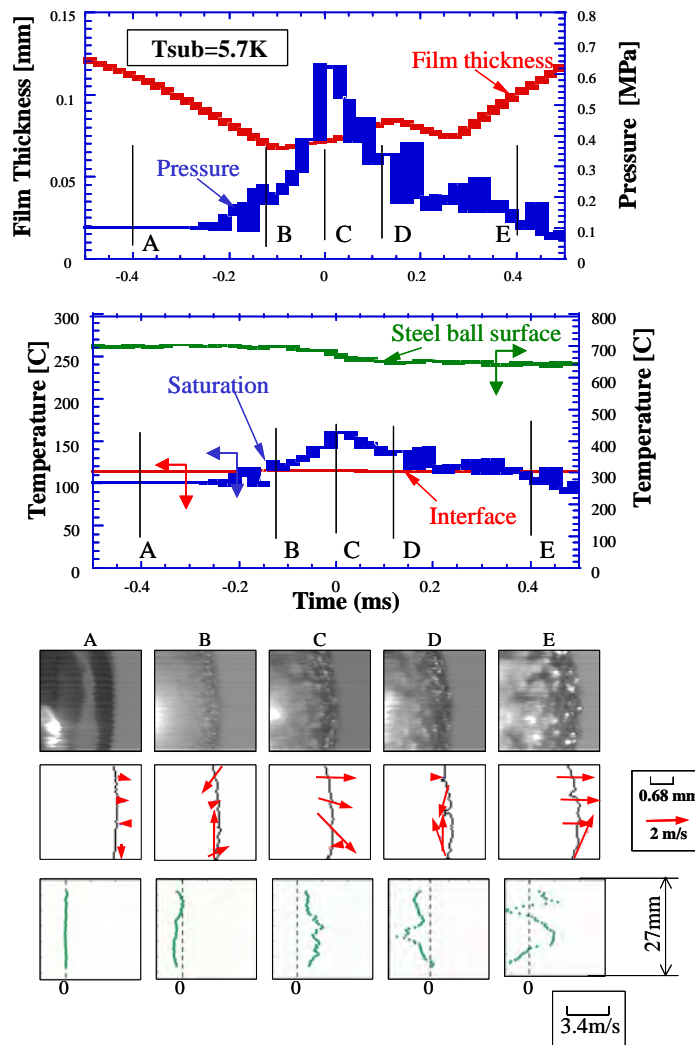


Figure 9: Summary of microscopic vapor film collapse behavior

ACKNOWLEDGMENTS

Authors are acknowledged to Mrs. Daisuke Tochio, and Hiroshi Yanagida for their help to the present research.

REFERENCES

- [1] Board, S. J., Hall, R. W. and Hall, R. S., Detonation of Fuel Coolant Explosion, Nature 254, pp. 319, 1975.
- [2] Board, S. J., Farmwe, C. L. and Poolel, D. H., Fragmentation in Thermal Explosion, Int. J. Heat Mass Transfer, Vol. 17, pp. 331-339, 1974.
- [3] Nelson, L. S. and Guay, K. P., Suppression of Steam Explosion in Tin and Fe-Al₂O₃ Melts by Increasing the Viscosity of the Coolant, High Temp. High Pressures, 18, pp. 107-111, 1986.
- [4] Nelson, L. S. et al., Thermal- and Ignition- Type Steam Explosions of Single Drops of Molten Aluminum, Trans. ANS, 63, pp. 378-379, 1991.

- [5] Nelson, L. S. et al., The Triggering of Steam Explosions of Single Drops of Pure and Alloyed Molten Aluminum, *Trans. ANS*, 61, pp. 458-459, 1991.
- [6] Shoji, M. and Takagi, N., An Experimental Study of Small-Scale Vapor Explosions for Molten Tin Dropped into Water, *Bulletin of JSME*, Vol. 26, No. 215, pp. 791-765, 1983.
- [7] Shoji, M. and Takagi, N., Thermal Interaction When a Cold Volatile Liquid Droplet Impinges on a Hot Liquid Surface, *Bulletin of JSME*, Vol. 29, No. 250, pp. 1183-1187, 1986.
- [8] Iida, Y., Takashima, T. and Akiyoshi, R., A Study of the Vapor Explosion Mechanism with Single Drops of High Temperature Liquid and Volatile Liquids (1st Report, Experiments with a single Drop), *J. JSME Ser. B*, Vol. 52, No. 476, pp. 1777-1783, 1986.
- [9] Iida, Y., Takashima, T. and Akiyoshi, R., A Study of the Vapor Explosion Mechanism with Single Drops of High Temperature Liquid and Volatile Liquids (2nd Report, Temperature Effect of Cold Liquid and Experiments with Plural Drops), *J. JSME Ser. B*, Vol. 53, No. 485, pp. 222-230, 1987.
- [10] Matsumura, K. and Nariai, H., Thermal interaction zone of vapor explosion with tin-water drop experiment, *The 4th International Topical Meeting on Nuclear Thermal Hydraulics, Operation and Safety*, Taipei, Taiwan, 1994.
- [11] Inoue, A. and Bankoff, S. G., Destabilization of Film Boiling due to Arrival of a Pressure, *Trans. ASME, J. of Heat Transfer*, Vol. 103, pp. 459-471, 1981.
- [12] Ciccarelli, G. and Frost, D. L., *Nuclear engineering and Design*, 146, pp.109-132, 1994.
- [13] Koshizuka, S., Ikeda, H. and Oka, Y., Fundamental Process of Thermal-Hydraulic Phenomena in Severe Accident (6) Three Dimensional Numerical Analysis of Melt Drop Fragmentation in Vapor Explosion, *2000 Annual Meeting of the Atomic Energy Society of Japan*, E12, p. 483., 2000.
- [14] Yagi, M., Abe, Y. et al., Study on Film Collapse Behavior during Vapor Explosion, *J. JSME Ser. B*, Vol. 65, No. 636, pp.2799-2805, 1999.
- [15] Abe, Y., Kobayashi, T., Study on Film Collapse Behavior on High Temperature Particle Surface (1st Report, Measurement of Vapor film Collapse Pressure), *J. JSME Ser. B*, Vol. 66, No. 642, pp. 627-632, 2000.
- [16] Abe, Y. and Tochio, D., Study on Film Collapse Behavior on High Temperature Particle Surface (2nd Report, Effect of Subcooling on Micro-Mechanism), *J. JSME Ser. B*, Vol. 66, No. 642, pp. 633-639, 2000.

NOMENCLATURE

$f(x,y)$:	Brightness function	Greek
$g(x,y)$:	Reference function	δ : Vapor film thickness
$r(x)$:	Correlation function	α : Thermal diffusivity
r :	Distance from the center of the particle,	
t :	Time	
T :	Temperature distribution	
$T_l(r)$:	Temperature distribution in liquid	
$T_s(r)$:	Temperature distribution in steel	
$T_v(r)$:	Temperature distribution in vapor film	
T_l :	Bulk liquid temperature	
T_w :	Particle surface temperature	

STATISTICAL INVESTIGATION OF PARTICLE-INTERACTION IN MULTIPHASE FLOWS

Ch. Brücker, W. Schröder

Aerodynamisches Institut der RWTH Aachen,
D-52062 Aachen, Germany
Tel.: +49.241.809-5429
Fax.:+49.241.809-2257
E-Mail: bruecker@aia.rwth-aachen.de

ABSTRACT

This study was carried out to understand the bubble or particle interaction in multiphase flows. We used light polystyrol particles (density 0.05 g/cm³) which were colored to detect the particles at higher void fractions. To investigate the influence of the shape on the particle interaction spherical as well as ellipsoidal particles were used. The polystyrol particles behave similar as air bubbles in water because of their relative low density. This was documented by several experiments of the motion and wake structure with single rising bubbles and particles [1]. The particles were studied in a water tank in counter-flow. A stereoscopic three-dimensional PTV systems was built up to record the particle motion. By using different concentration of water/glycerine mixture we are able to simulate different Reynolds-numbers. The results demonstrates that the shape of the particles plays a dominant role on the interaction, see the particle pair distribution shown in Fig. 1. In case of the spherical particles, most of the particle pairs are horizontally aligned which is a clear trend of bubble pairing. This agrees with the observations made by Fortes et al. (1987). In contrast, the prolate spheroids show a different distribution which can only be attributed to the different shape. It is likely, that the additional degree of freedom of the prolate spheroids to tilt or to align with the flow is the main reason which has also great influence on the drag and lift-forces.

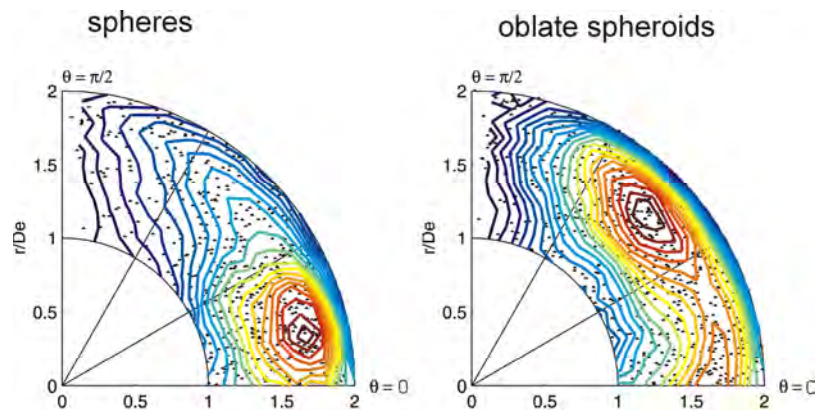


Figure 1: Radial profiles of the temperature variance at three different axial positions. Comparison between measurements and calculation.

REFERERENCES

- [1] Bruecker, Ch.: Structure and dynamics of the wake of bubbles and its relevance for bubble interaction. *Physics of Fluids* 11 (7), 1781-1796, 1999.
- [2] Fortes, A.; Joseph, D. D.; Lundgren, T.: Nonlinear mechanics of fluidization of beds of spherical particles. *J. Fluid Mech.* 177, 467-483, 1987.

GENERATION OF ENTRAINED DROPLETS FROM AN IMITATED DISTURBANCE WAVE AND THEIR DEPOSITION ON THE WALL

T. Fukano, T. Inatomi,
Y. Matsuzawa, T. Yoshida and N. Uchimichi

Graduate School of Engineering, Kyushu University,
6-10-1 Hakozaki, Higasi-ku, Fukuoka, 812-8581 Japan
Phone: +81 92 642 3392, Fax: +81 92 642 3392
E-mail: fukanot@mech.kyushu-u.ac.jp

ABSTRACT

In the present experiment, an isokinetic sampling probe technique was used for the measurement of the local droplet flow rate generated from an imitated disturbance wave, which was constructed by injecting liquid through a slit mounted on the bottom wall of a horizontal rectangular duct. The experimental data on the distribution of entrained droplets and their deposition on the duct wall are presented. As a result, it is clarified that the droplet generation is periodic and the distribution of the droplet flow rate is not uniform in both axial and height directions. And accordingly the droplet flow is fundamentally unsteady. Furthermore, the correlation of the entrainment fraction proposed by Paleev-Filippovich is superior to that by others.

1. INTRODUCTION

Gas-liquid annular two-phase flow is an important flow pattern in terms of the liquid film dry out in the high quality region in various kinds of heat exchangers. In the past, many investigations on an annular-dispersed flow in horizontal pipelines were conducted, and the behaviors of entrained droplets have been discussed. They, however, focused only on spatially averaged values of the droplet parameters. On the other hand the disturbance waves are not uniform in the height and scale even under the same flow condition of both phases. Therefore, we measure entrainments as well as crests of disturbance waves together at the location near the wave height if we use an isokinetic sampling method. If we use the suction method in which liquid film is subtracted from the bottom of the duct, the accuracy of the measurement is not satisfactory [1]~[4] because the disturbances run fast. These facts give us the common understanding that nobody has got entrainment data with high accuracy and detailed information.

In the present experiment we tried to measure entrainment parameter from the relative frame of reference fixed to the disturbance wave. For this purpose an imitated disturbance wave is constructed by injecting liquid through a slit mounted on the bottom of a horizontal rectangular duct. This enabled us to measure the distribution of the entrainment flow rate in the height direction at the axially different distance from the imitated disturbance wave. From the measured data we also discussed the droplets deposition rate and compared the measured droplet flow rate with the correlations which have been proposed previously by the other investigators.

2. EXPERIMENTAL APPARATUS AND MEASUREMENT

Figure 1 shows the schematic view of the experimental apparatus. The horizontal test section with a square cross section of 40×40 mm and 7 m in axial length was made of transparent acrylic resin so as to observe the flow phenomena. Air was introduced from a compressor and water from a pump was introduced into the horizontal duct from the bottom of the test section. Figure 2 shows the detail of the water injection part of the test section where the imitated disturbance wave was created. Fig. 3 shows the isokinetic probe which was axially moved in the range of $z=20 \sim 90$ mm at the interval of 10 mm as well as $z=200$ mm and 350 mm from the slit for introducing water. The isokinetic probe was also traversed in the height direction.

The time averaged wave height and the maximum height were measured by a needle contacting probe which could be traversed in the height direction. From the on-off signal from the needle contacting probe we defined the maximum wave height as the 1 % of the contacting liquid phase. We observed the behavior of the imitated disturbance wave which was fixed on the water introducing slit by a high speed video camera.

We used air and water of 20~30 degree C. The superficial velocities of air and water were 10~40 m/s and 0.001~0.10 m/s, respectively.

3. EXPERIMENTAL RESULTS AND DISCUSSION

3.1 Range of Experiment and Behavior of the Disturbance Wave Crest at Droplet Generation

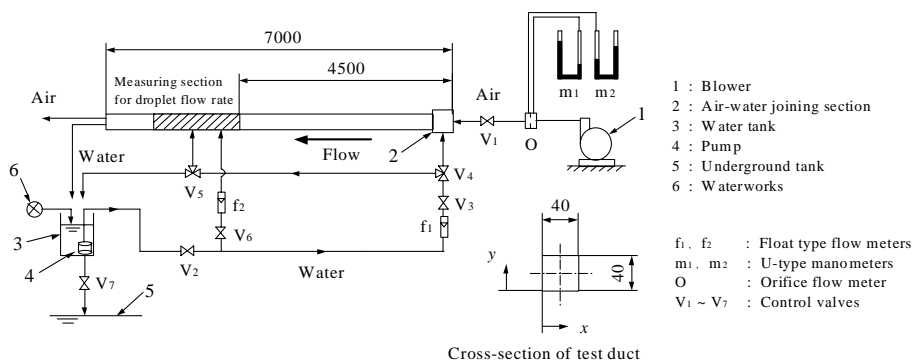


Figure 1 : Experimental apparatus

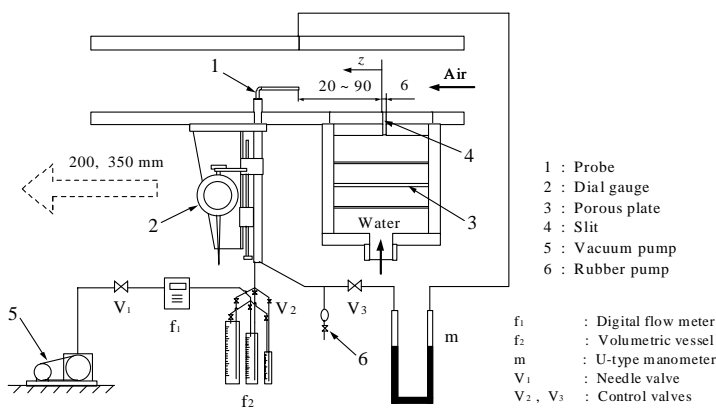


Figure 2: Isokinetic sampling probe

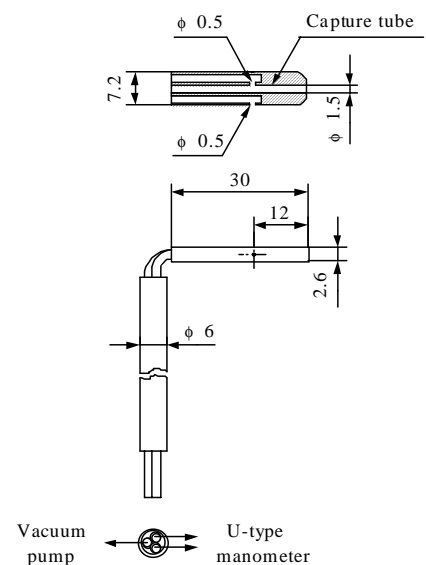


Figure 3: Detail of the sampling probe

Figure 4 shows the experimental points by marks and the area map for droplet onset pattern. The broken line shows the boundary of droplet onset, above of which droplets generated from the crest of the imitated wave. It is generally understood that the droplets are generated from the disturbance wave, but the mechanism of generation has not been clarified. In the present experiment we observed droplet generation in detail because the disturbance wave was fixed on the water supplying slit. Fundamentally the droplets generated periodically. Typical patterns are shown in Fig. 5. The arrows show the phenomena repeats this direction.

In the pattern (a): droplets generated periodically when the wave crest is accelerated with undulation by the action of gas flow. In the pattern (b): Due to the high velocity of gas flow the wave crest is accelerated more strongly by the gas flow and the wave crest was sliced off then generated droplets became very fine instantaneously. The change of the shape of the wave was large. In the pattern (d): the wave crest was stretched and droplets generated. The wave crest fluctuated violently and periodically. The amount of generation of droplets was large because of the larger liquid flow rate into the imitated disturbance wave. Small air bubbles were involved in the downstream side of the disturbance wave due to the separation of air flow. In the pattern (e): the generation of droplet was also intermittent and periodic, but the frequency was so high that it was seen to be continuous from the whole body of the disturbance wave. From the observation discussed above it is concluded that the droplets are generated periodically from the wave crest by the action of gas flow.

3.2 The wave height of the disturbance wave

In Figure 6 shown is the maximum and the mean height of the disturbance wave, h_m and h_{max} . Both of them increase with increasing liquid flow rate and decrease with increasing gas flow rate. The larger difference in value between h_m and h_{max} show the violent change of the wave crest due to the generation of droplets.

3.3 Frequency of the droplet generation

Figure 7 shows the frequency of the droplet generation, n , from the crest of the disturbance wave. The value of n was 30~100 1/s and increases with increasing both air and liquid phases. In the case of lower air flow rate its dependence on the liquid flow rate is small.

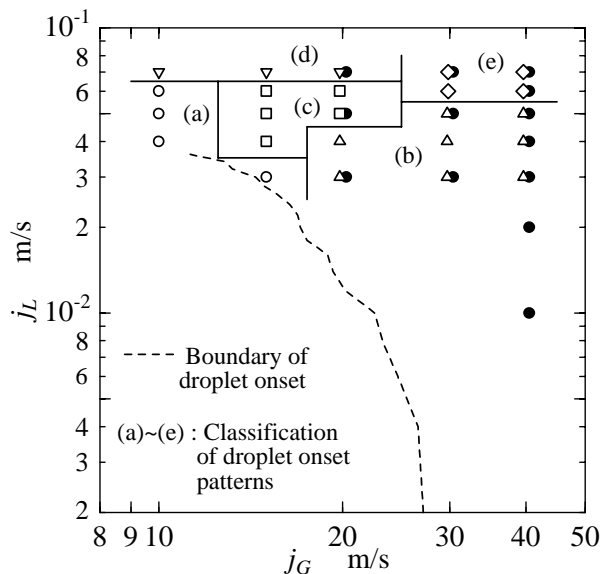


Fig. 4: Classification of droplet onset patterns

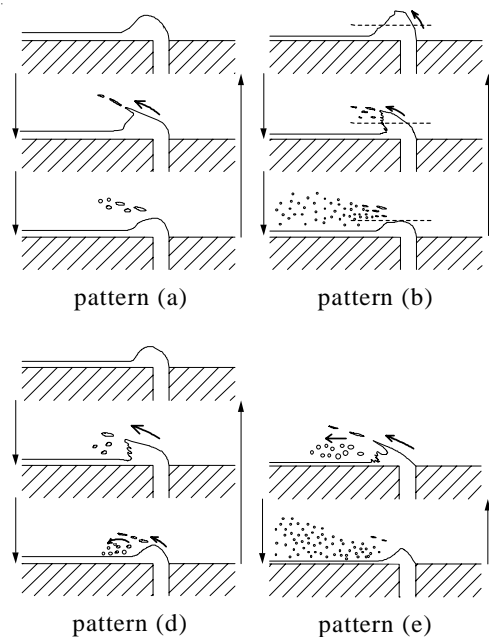


Fig. 5: Frequency of droplet generation

3.4 Distribution of local droplet flow rate and the total droplet flow rate

Figs. 8(a) and (b) show the distributions of local droplet mass flow rate G_{Ey} in the duct height direction, (a) being for the high air flow rate case and (b) for $j_L=0.05\text{m/s}$. In the case of $j_L=0.01\text{m/s}$ droplets flow rate was zero in the range of $y/H < 0.6$, which means that in this case droplets did not diffuse up to the top of the duct even at the location of $z=350\text{mm}$ while in the cases of $j_L=0.04$ and 0.07m/s the droplets diffused almost whole cross section of the duct even at $z=90\text{mm}$. Figure 8(b) shows that the upward diffusion is stronger in the case of larger j_G under the same flow rate of j_L .

The total droplet flow rate passing through each cross section is defined as,

$$G_E = \int_{h_m}^H G_{Ey} dy \times B \quad (1)$$

Figure 9 shows the change of G_E in the axial direction. It sharply decreases with the axial distance in the case of large j_L and reaches the asymptotic value which differs depending on the magnitude of j_L . This shows the distribution has reached to the equilibrium state at $z \cong 150\text{mm}$. On the other hand in the case of smaller j_L the change is slow because the droplet generation rate is small due to the low wave height and the upward velocity component given by the interaction between the air flow and the geometry of disturbance wave is small.

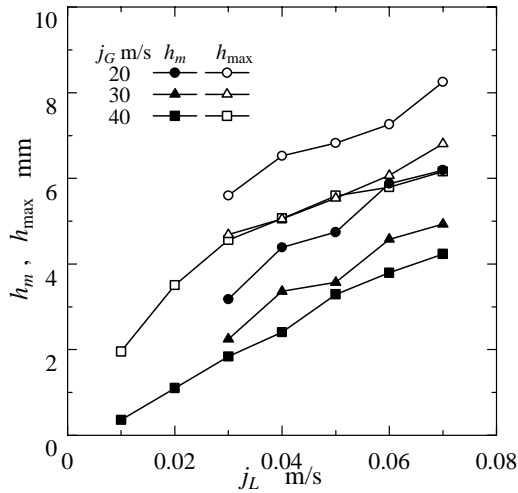


Fig. 6: Maximum and mean wave height

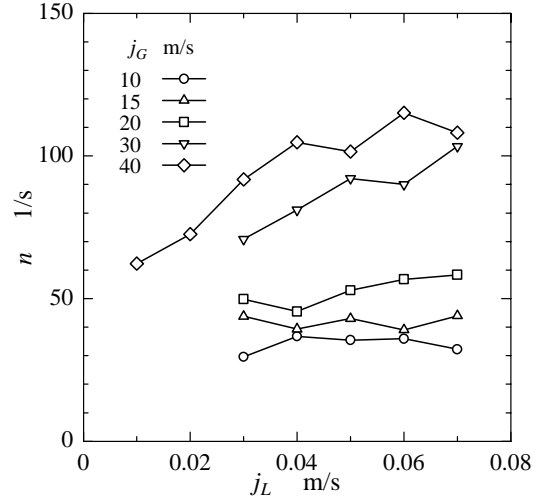
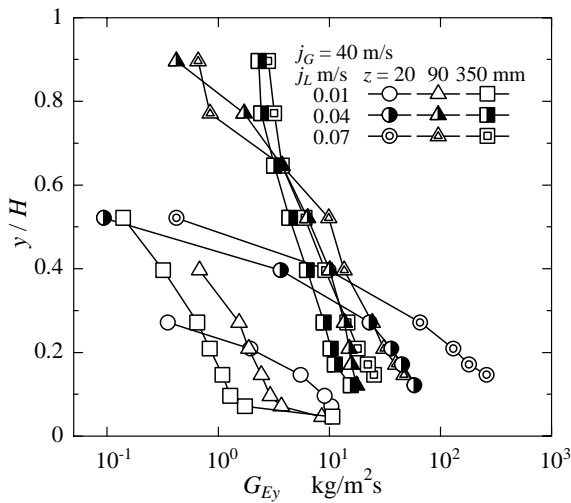
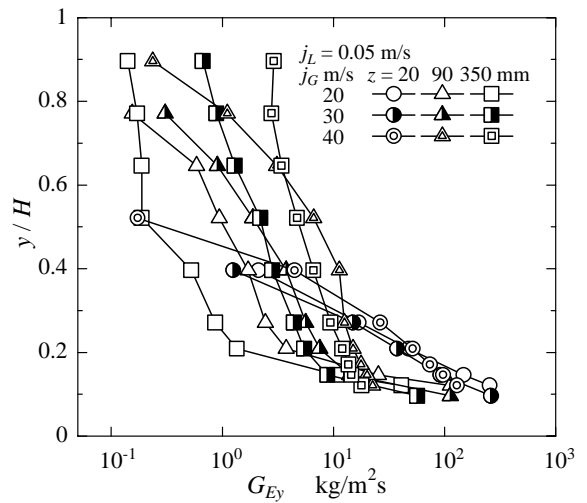


Fig. 7: Frequency of droplet generation



(a) $j_G = 40\text{m/s}$



(b) $j_L = 0.05\text{m/s}$

Figure 8: Local droplet mass flow rate

In the present experiment the effect of the base film flow which exist upstream of the disturbance wave on the droplet generation was examined. The result shows that the effect of the existence of the base film is negligibly small. In the actual disturbance wave flow base film does not flow into the disturbance wave from the rear side of the disturbance wave because the velocity of the disturbance wave is much faster than that of base film, the situation of which corresponds to the case without the upstream base film in the present experiment. Then the data shown in the present paper are taken under the condition without upstream base film.

3.5 Droplet generation rate

We assumed that the total droplet flow rate measured at $z = 20$ mm is equal to the total droplets generation rate. And we defined the droplets generation rate in one shot of the generation $W_{E0} (\equiv G_{Ez=20}/n)$. W_{E0} is plotted against wave height h_m in Fig. 10, which shows clearly that the droplets generation rate depends more strongly on the wave height than on j_G .

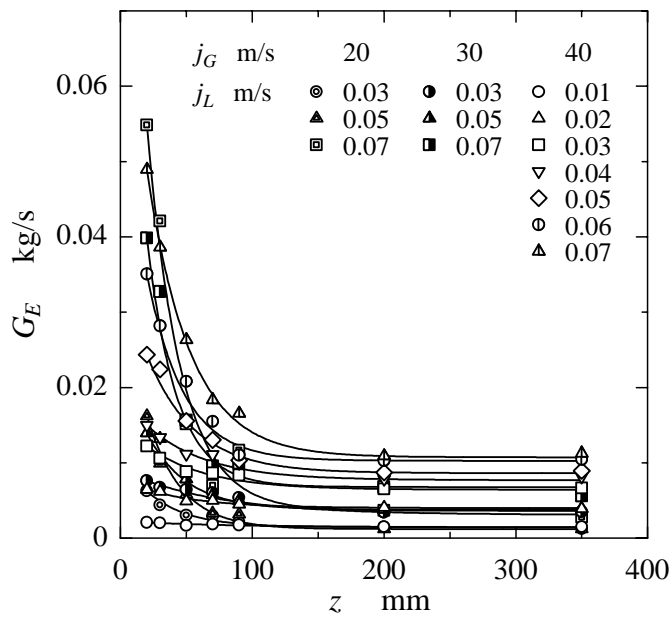


Figure 9: Total droplet mass flow rate

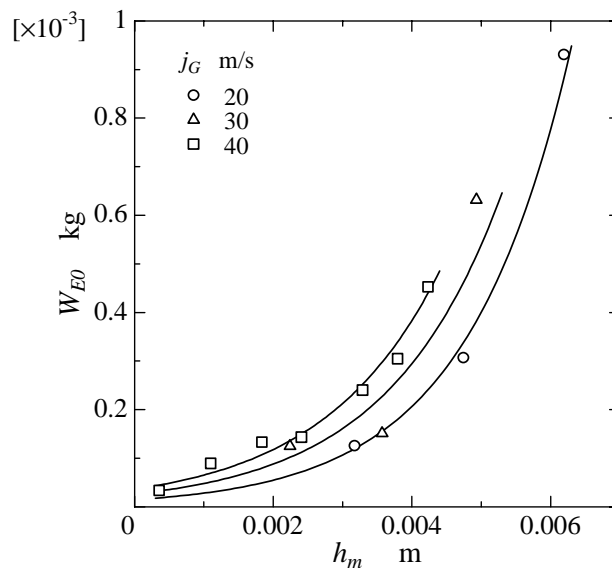


Figure 10: Mass of one shot of droplet generation

3.6 Droplet deposition coefficient

By using G_E the droplet deposition coefficient by the turbulent air flow on to the walls is defined as [8],

$$K = -H_m \frac{V_G}{s} \frac{d(\ln G_E)}{dz} \quad (2)$$

here $H_m=A/S$ is the hydraulic mean depth m , $s = V_G/V_d$ the velocity ratio between air flow and droplet, which was assumed to be unity in the present paper. Many researchers discussed the droplet deposition coefficient K . It, however, is time averaged value, in other words, space averaged value while in the present paper the local value is discussed.

Figure 11 shows the changes of K plotted against the distance from the disturbance wave. It is shown that there are two regions in the process of droplet deposition, i. e., Region 1: K decreases sharply along the duct axis and Region 2: K asymptotically decreases in the downstream region of $z = 150$ mm, the trend of which is similar to one described in Fig. 9. This fact means an important thing that the distribution of the droplets along the duct axis is not uniform, i. e., the droplet flow rate repeatedly changes every times the disturbance wave passes by the measurement station fixed to the absolute frame of reference.

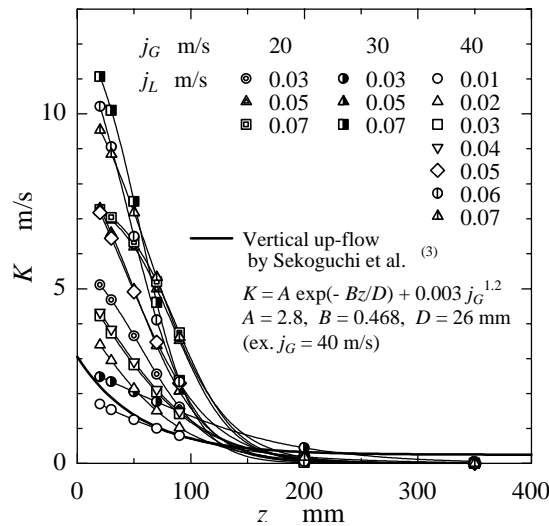


Figure 11: Droplet deposition coefficient

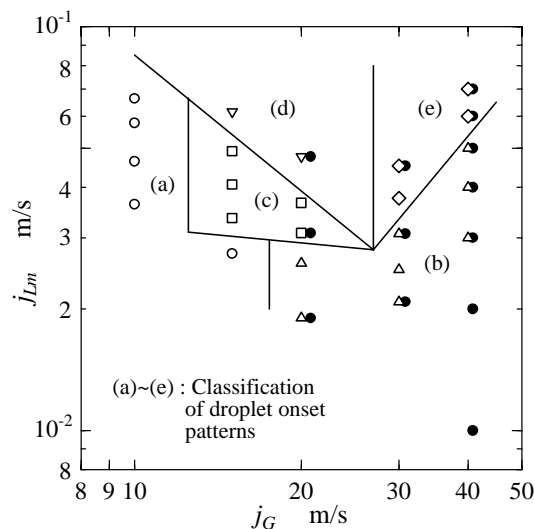


Figure 12: Classification of droplet onset patterns by j_{Lm}

3.7 Correction of the liquid flow rate

The imitated disturbance wave formed by injecting water flow from the bottom of the duct is possibly different from one generated naturally in actual annular flow. The droplet flow rate is strongly dependent on the wave height as discussed in section 3.5. Taking this fact into consideration the water flow rate is experimentally corrected so as to agree the maximum wave height of the imitated disturbance wave with that of actual disturbance. It must be noticed that, however, the disturbance wave in actual annular flow is large and small, so the above correction is not enough and still has problem. The area map of the classification of droplet onset pattern changes if we use the corrected water flow rate as shown in Fig. 12. Where we did not correct in case of $j_G = 40$ m/s because the maximum wave height in both cases is approximately equal with each other.

3.8 Droplet flow rate ratio

Droplet flow rate ratio is defined as the rate of local droplet flow rate to the total droplet flow rate in the region where the droplet generation rate is balanced with the droplet deposition rate and therefore both the droplet flow rate and the liquid film flow rate do not change along the duct axis.

(1) Mean local droplet flow rate: We calculated the mean local droplet flow rate at the height of y by the next equation.

$$W_{Ey} = \frac{1}{z_2 - z_1} \int_{z_1}^{z_2} G_{Ey} dz \quad (3)$$

W_{Ey} is shown in Fig. 13. Generally the distance between two disturbance waves is 200~500 mm, and we considered that $z_2 - z_1$ corresponds to the disturbance distance and took $z_1 = 20$ mm and $z_2 = 350$ mm. The shape of each curve in Fig. 13 is similar to that of the droplet flow rate at $z = 350$ mm as already shown in Fig. 8 while the amount is one or two order smaller. It is clearly shown that droplets did not diffuse up to the top wall in the case of $j_{Lm} = 0.01$ m/s and $j_G = 40$ m/s.

In the actual annular flow many droplets flow into the region between two disturbance waves from upstream side of the disturbance wave then the distribution must be more uniform. We can not estimate its flow rate so far, the following discussion is based on the data shown in Fig. 13.

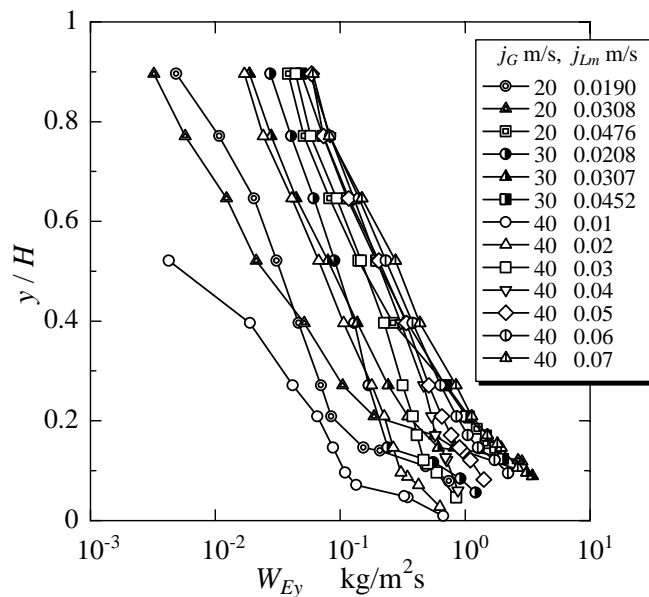


Figure 13: Axially mean droplet mass flow rate

(2) Correlation of droplet flow rate: Integrating W_{Ey} in the height direction from h_m to H and assuming that the droplet distribution is uniform in the width direction of the duct we calculated the total droplet flow rate between two disturbance wave by the next equation

$$W_E = B \times \int_{h_m}^H W_{Ey} dy \quad (4)$$

The relation between W_E and h_m is shown in Fig. 14. This shows again the close relation between those parameters and the data with same air flow rate are on one straight line independent of liquid flow rate. This relation is correlated by the next equation

$$W_E = 1.01 \times 10^{-6} j_G^{2.08} h_m^{0.89} \rho_L \quad (5)$$

where the unit of h_m is mm. The straight lines in Fig. 14 mean Eq. 5. As a whole the agreement of the data points with Eq. (5) is satisfactory.

(3) Comparison between the proposed correlations with the present data: The ratio of the droplet flow rate to the total liquid flow rate is calculated for the present experimental data by the following equation, where $W_{Lm} (\equiv \rho A j_{Lm})$. And j_{Lm} is the corrected water flow rate.

$$E_{\text{exp}} = \frac{W_E}{W_{Lm}} \quad (6)$$

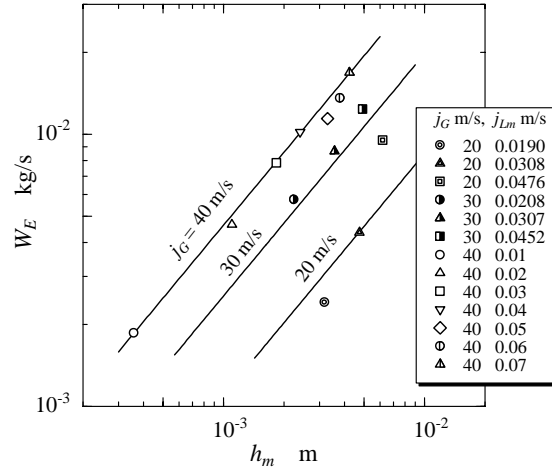


Figure 14: Relation between W_E and h_m

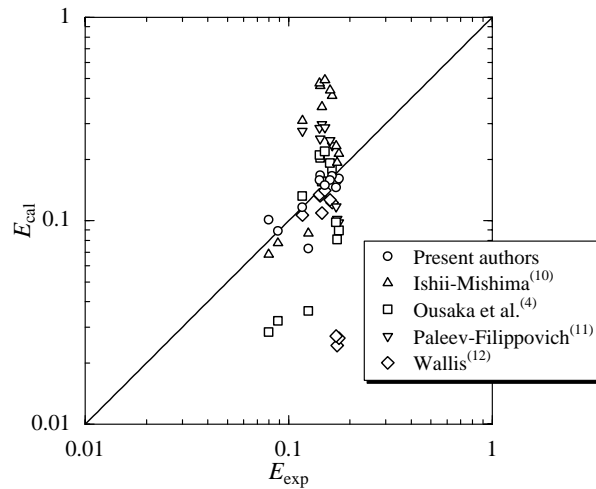


Figure 15: Comparison of correlations with present experimental data against droplet fraction

Figure 15 shows the comparison of the present data with the proposed correlations. Ousaka correlation [4] was obtained by modifying Ishii-Mishima correlation so as to be useful for the annular flow in an inclined pipe line. Ishii-Mishima correlation gives larger values than the experimental values while Ousaka correlation gives smaller values in the case of $j_G = 20\text{m/s}$. These two correlation have been obtained in the case of circular pipes, and therefore the experimental condition is different to the present one. On the other hand Paleev-Filppovich correlation [11] has been obtained for the horizontal rectangular duct and gives more accurate estimations. Wallis correlation [12] gives accurate estimation in case of $j_G = 40\text{m/s}$. But it has a problem that it gives negative values in the case where j_G is smaller than 28 m/s. It is noticed that the droplet flow rate flowing into the region between the disturbance waves is neglected in the experimental values.

The wave height is one of the controlling factors for the generation of droplets as discussed above. But no correlations proposed so far do explicitly include this parameter, while the correlation proposed by the present authors has this parameter. The wave height, however, changes depending on the flow rate of both phases, the geometry of the test section and properties of the fluids. Further there exist disturbance waves with various dimensions even under the identical flow condition. Therefore it is noticed that the present correlation which includes the wave height must be investigated further in the future.

4. CONCLUSIONS

Detailed experimental examination is made into the generation and the deposition of droplets generated from an imitated disturbance wave which is fixed to the absolute frame of reference. The results are summarized as follows.

- (1) Droplets are generated by the action of the shear force of air flow mainly from the crest of the disturbance wave periodically with the frequency of 20~120 Hz depending on the flow condition. The generation patterns are classified into five.
- (2) Deposition of droplets on the bottom wall is large in the region just downside of the disturbance wave due to the gravity force acting on larger droplets and the separated air flow and diffuse uniformly by the turbulence of the air flow in the region far downstream of the disturbance wave.
- (3) Droplet flow rate is large just downstream of the disturbance wave and decreases with the distance from the disturbance wave. And accordingly the axial distribution of droplet is not uniform, which means that the droplet flow rate measured at a fixed point is unsteady.
- (4) Compared with the actual and the present situations, the droplet flow rate measured in the present experiment has a problem that it does not include the droplets flowing from the upstream of the disturbance wave. The present data, however, agree comparatively well with the Paleev-Filippovich correlation.

ACKNOWLEDGEMENT

Authors are grateful to Professor Akiharu Ousaka (Tokushima University) for his useful advise on the measurement of droplet.

REFERENCES

- [1] Namie, S. and Ueda, T., Transportation of Droplets in Annular Dispersed Flow, Part 1, Trans. of JSME, 38-308, B, pp. 821- 831. 1972.

- [2] Akagawa, K., Fujii, T., Ito, J., Hamano, I., and Horiuchi, T., Annular Dispersed Flow, Part 2, Trans. of JSME, 50-454, B, pp. 1585-1593, 1984.
- [3] Sekoguchi, K., Tanaka, S., and Ueno, T., Measurement of Entrainment Flow Rate in Annular Mist Flow, Trans. of JSME 50-458, B, pp. 2343-2351, 1984.
- [4] Ousaka, A., Nagashima, T., Kariyasaki, A., Morioka, I., Kiyota, M., and Mamoto, E., Effect of Inclination on Distribution of Entrainment Flow Rate in an Inclined Upward Annular Flow, Trans. of JSME, 62-600, B, pp. 2950-2956, 1996.
- [5] Nakazatomi, M., Sekoguchi, K., and Nishikawa, K., Generation of Entrainment in Gas-Liquid Annular Flow by Imitated Disturbance Wave and Deposition on the Wall, Trans. of JSME, 41-342, B, pp. 615-623, 1975.
- [6] Sekoguchi, K., Fukui, H., Matsuoka, T., and Nishikawa, K., Statistical Characteristics of Bubbly Flow, by a Needle Contact probe, Part 1, Fundamentals of the, Trans. of JSME 40-336, B, pp. 2295-2301, 1974.
- [7] Sekoguchi, K., Ousaka, A., Fukano, T., and Morimoto, T., Gas-Liquid Two-Phase Annular Flow, Part 1, Circumferencial Distribution of Film Thickness, Trans. of JSME 48-426, B, pp. 346-354, 1982.
- [8] Ueda, T., Gas –Liquid Two-Phase Flow and Heat Transfere, Yokendo, pp. 137-174, 1981.
- [9] Cousins, L. B. and Hewitt, G. F., Liquid mass transfer in annular two-phase flow: droplet deposition and liquid entrainment, AERE-R5657, 1968.
- [10] Ishii, M. and Mishima, K., Droplet entrainment correlation in annular two-phase flow, Int. J. Heat Mass Transfer 32-10, pp. 1835-1846, 1989.
- [11] Paleev, I. I. and Filippovich, B. S., Phenomena of liquid transfer in two-phase dispersed annular flow, Int. J. Heat Mass Transfer 9, pp. 1089-1093, 1966.
- [12] Wallis, G. B., Phenomena of liquid transfer in two-phase dispersed annular flow, Int. J. Heat Mass Transfer 11, pp. 783-785, 1968.

LOCAL PHENOMENA IN CASE OF CONDENSATION AT STRATIFIED FLOW WITH NON CONDENSABLE GASES

M. Goldbrunner, J. Karl, D. Hein

Technische Universität München
Lehrstuhl für Thermische Kraftanlagen mit Heizkraftwerk
Boltzmannstr. 15
85748 Garching, GERMANY

ABSTRACT

Condensation in the presence of non condensable gases is a security relevant process during a postulated loss of coolant accident in a nuclear pressurised water reactor. In the framework of a research project supported by the Bundesministerium für Wirtschaft experiments have been performed at the LAOKOON test facility at the Technische Universität München, to study the effect of non condensable gases on direct contact condensation at stratified steam/water flow. Also experiments on a test facility with a vertical cooled wall were made. The paper presents the measurement techniques, the experimental setup, the theoretical description and a selection of the experimental results. The used laser measurement technique called linear Raman spectroscopy allows the local investigation of concentration profiles in the vapour phase. With the concentration profiles it is possible to determine local heat and mass transfers by using theoretical descriptions. Experimental results with different system parameters and the occurred phenomena are presented.

1. INTRODUCTION

If pure steam condenses at a cold surface, the heat and mass transfer resistances in the vapour phase can be neglected. If a non condensable gas is present, it can accumulate at the phase interface and reduce the heat and mass transfer in the vapour phase observable.

In many applications the condensation with non condensable gas plays an important role (e.g. design of condensers, distillation columns). Safety relevant is it in particular in the nuclear technology.

In a nuclear pressurized water reactor the vessels for the Emergency Core Cooling water (ECC) are normally pressurized with nitrogen. Therefore the water is saturated with the nitrogen. In case of a loss of coolant accident the injection of the ECC-water releases the nitrogen as a result of the increasing temperature and the decreasing pressure. A high concentration of nitrogen is brought into the system, especially if no more water is remaining in the ECC-vessels.

In particular with low steam velocities the condensation rates at the cold Emergency Core Cooling water can be reduced strongly due to the non condensable gas accumulation at the phase interface. This leads to an insufficient heating of the Emergency Core Cooling water and an increase of the structure stress at the hot wall of the reactor pressure vessel.

For the development and validation of computer codes for numerical simulations of the thermohydraulic processes, a detailed knowledge of the transport processes between the two phases is essential. For this it is necessary, to perform experiments with defined boundary conditions and measurements with a high local resolution.

For measurements with high local resolutions optical techniques are the method of choice, because the flow field remains undisturbed. The optical measurement of the nitrogen concentrations, outlined in this paper, bases on the linear or spontaneous Raman effect. The main advantage of the

LRS is a comparative simple setup and evaluation of the measured signals. But the intensities are very weak. Therefore a very sensitive camera system combined with a high power laser is necessary.

The measured concentration profile can be described with suitable theories, like film theory, in order to calculate local heat and mass-transfer coefficient.

In many experiments with non condensable gas fog occurs above the phase interface because of homogeneous condensation. The droplets of the fog produce a liquid water Raman signal in the vapour phase and therefore it is possible to estimate the fog density using the intensity of the water signal.

In addition to the laser measuring technique conventional measuring techniques, like thermocouples and flow meters, are used.

To be able to evaluate the influence of many parameters on the heat transfer, numerous experiments with different boundary conditions were executed and analysed. Changeable parameters are the non condensable gas concentration, the steam velocity and the direction as well as system pressure.

2. THEORY

2.1. Condensation with non condensable gases

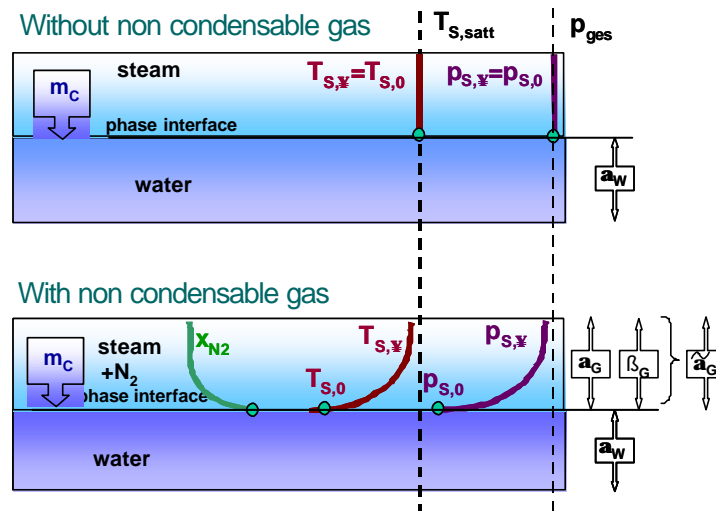


Fig. 1: Condensation with and without non condensable gas.

If saturated steam condenses at a cold water layer, there is no partial pressure or temperature gradient (Figure 1) in the vapour phase. The steam partial pressure corresponds to the total pressure of the system. The temperature is the saturation temperature of the steam at this pressure. On the assumption of thermal equilibrium at the phase interface the interface temperature is equal to the steam temperature. The heat transfer resistance in the vapour phase can be neglected. There is only a heat transfer resistance in the water layer.

If non condensable gas is present in the vapour phase, the condensation process changes fundamentally. The non condensable gas is transported to the phase interface by the condensing steam mass flow. Since the phase interface is impermeable for the non condensable gas, it accumulates

there and reduces the steam partial pressure. On the assumption of thermodynamic equilibrium also the temperature at the phase interface decreases with the steam partial pressure.

Because of this accumulation, there is an additional heat and mass transfer resistance in the vapour. For simplification the two transfer resistances can be combined to a hypothetical heat transfer resistance. A steady state status is achieved, if the quantity of the non condensable gas, which is transported from the condensing steam to the boundary layer, corresponds to the contrary diffusion flow.

2.2. 'Classical' film theory

For a better distinction the correlations in the literature, so called film theory, are named in this work 'classical' film theory. The 'classical' film theory is described by numerous authors (e.g. [1]). It is still used for the design of technical components, like condensers (e.g. [2]).

The model assumes a laminar gaseous film. The molar concentrations as driving potential for the mass transfer change only within this film. Changing of the concentration, the pressure and the velocity in the direction x parallel to the phase interface are neglected. Thermal equilibrium is assumed at the phase interface. The following equations were deduced for a mixture of steam and nitrogen.

The molar flux of condensing steam can be written as:

$$\dot{n}_D = -c_G \cdot D_G \cdot \frac{\partial x_D}{\partial y} + x_D(y) \cdot (\dot{n}_D + \dot{n}_{N_2}) \quad (1)$$

$-c_G \cdot D_G \cdot \frac{\partial x_D}{\partial y}$ is the diffusive part und $x_D \cdot (\dot{n}_D + \dot{n}_{N_2})$ the convective part of the molar flux. In the case of a phase interface, which is impermeable for nitrogen, the molar flux of nitrogen to the interface is zero ($\dot{n}_{N_2} = 0$). Integration of Eq. (1) with the boundary conditions $\frac{\partial \dot{n}_D}{\partial y} = 0$ und $x_D|_{y=0} = x_{D,0}$ provides the known correlation for the molar flux of condensing steam:

$$\dot{n}_D = \frac{c_G \cdot D_G}{y} \cdot \ln \left(\frac{x_{N_2}(y)}{x_{N_2,0}} \right) \quad (2)$$

This correlation is valid for $y \leq s_x$. At the position $y = s_x$ is $x = x_x$.

If the convective part is neglected, the concentration profile over the boundary layer thickness s_x is linear.

2.3. 'Generalised' film theory

The following described correlations are simplified called 'generalised' film theory.

The conservation equation of continuity for steam reads as follows:

$$\frac{\partial c_D}{\partial t} + \left((\dot{n}_{D,x} + \dot{n}_{N_2,x}) \frac{\partial x_D}{\partial x} + (\dot{n}_{D,y} + \dot{n}_{N_2,y}) \frac{\partial x_D}{\partial y} + (\dot{n}_{D,z} + \dot{n}_{N_2,z}) \frac{\partial x_D}{\partial z} \right) = D_G \cdot c \cdot \left(\frac{\partial^2 x_D}{\partial x^2} + \frac{\partial^2 x_D}{\partial y^2} + \frac{\partial^2 x_D}{\partial z^2} \right) \quad (3)$$

Assuming a steady state and 1-dimensional problem and integration with the boundary conditions $x_D|_{y=0} = x_{D,0}$, $x_D|_{y \rightarrow \infty} = x_{D,\infty}$, $\frac{\partial x_D}{\partial y}|_{y \rightarrow \infty} = 0$ and $\frac{\partial \dot{n}_D}{\partial y} = 0$ leads to the correlation for the molar flux of condensing steam:

$$\dot{n}_D = \frac{c_G \cdot D_G}{y} \cdot \ln \left(\frac{x_{N_2}(y) - x_{N_2,\infty}}{x_{N_2,0} - x_{N_2,\infty}} \right) \quad (4)$$

Equation (4) merges to Eq. (2), if the bulk concentration of nitrogen is zero. Figure 2 shows the different distributions of the concentration profiles calculated with ‘classical’ and ‘generalised’ film theory.

The experiments show, that the ‘generalised’ film theory provides a much better description of the measured concentration profiles than the ‘classical’ film theory, in particular with a high bulk concentration of nitrogen.

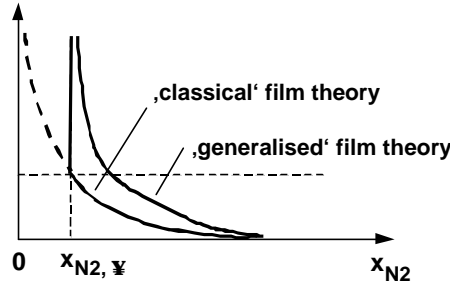


Fig. 2: Concentration profiles calculated with ‘classical’ and ‘generalised’ film theory.

3. LASER MEASUREMENT

3.1. Raman scattering

If laser light hits a molecule, it comes to an elastic scattering (Rayleigh scattering) and an inelastic scattering (Raman scattering) of the incident light. During the inelastic scattering a part of the laser energy remains in the molecule. Therefore the energy of the scattered light is reduced and the wavelength of the scattered light is larger than the laser wavelength. The energy and thus the wave number $\nu_R = 1/\lambda_R$ of the scattered light can be calculated from the energy difference of the laser light with the remaining energy in the molecule $E_{J,v}$

$$h \cdot c \cdot \nu_R = h \cdot c \cdot \nu - E_{J,v} \quad (6)$$

with the Planck’s constant h and the speed of light c . The linear Raman spectroscopy allows both stretching oscillations (vibration oscillations) and rotational oscillations with defined transitions [5]. In this work we only use the spectra of the stretching oscillations because the large wavelength allows a simpler separation.

A further advantage of the Raman effect is the independence from the incident wavelength.

3.2. Raman spectra of the vapour phase

Main aim of the laser measurements in the vapour phase was the determination of concentration profiles of nitrogen. The intensity of the scattered light of one component can be written as:

$$I_j = \text{const.} \cdot P_L \cdot c_j \cdot L \cdot \left(\frac{\partial s}{\partial W} \right)_j \quad (7)$$

The constant coefficient includes effects from the experimental setup. P_L is the power of the laser, c is the molar density of the component, L is the length of the laser area and $\frac{\partial s}{\partial W}$ is the differential scattering cross section. With the Definition of an relative Raman cross section of nitrogen $S_{H_2O} = \left(\frac{\partial s}{\partial W}\right)_{H_2O} / \left(\frac{\partial s}{\partial W}\right)_{N_2}$ (e.g. [5]) the molar concentration x_{N_2} of nitrogen in the nitrogen / steam mixture can be calculated from

$$x_{N_2} = \frac{c_{N_2}}{c_{H_2O} + c_{N_2}} \quad (8)$$

and from Eq. (7) as:

$$x_{N_2} = \frac{I_{N_2}}{I_{N_2} + \frac{I_{H_2O}}{S_{H_2O}}} \quad (9)$$

If the relative Raman cross section is known, it is possible to calculate the concentration profiles from the measured intensity profiles with Eq. (9).

The relative Raman cross section depends on the experimental setup, in particular on the angle between laser light and scattered light. Literature values exist for the used 90° -setup in these experiments ([6], [7], [8]), but the variation is partially very large. Therefore the relative Raman cross section was determined for the used experimental setup according to the procedure described in [9]. A experiment specific average value of $S_{H_2O}=2.34$ results, with a standard deviation of 0.19.

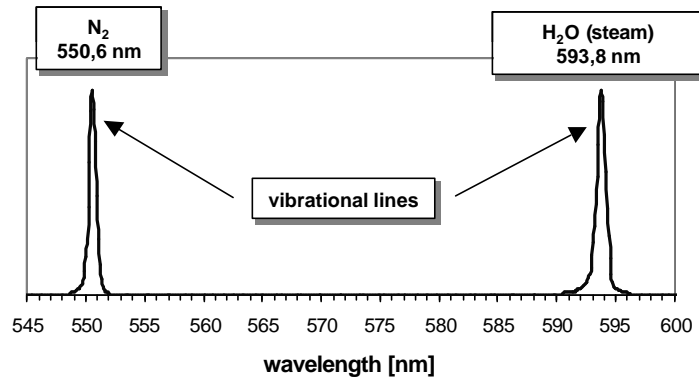


Fig. 3: Raman signal of water steam and nitrogen with a laser wavelength of 488 nm.

As shown in Figure 3, the vibrational oscillation of the N_2 -molecule and the vaporous H_2O -molecule causes two narrow-band peaks with 550.6 (N_2) and 593.8 Nm (H_2O) with the used Argon ion laser (wavelength 488 nm).

If the concentration profiles are known, the molar flux of condensing steam and hence the heat and mass transfers can be calculated with Eq. (4).

3.3. Evaluation of the laser measurements

The heat transfer coefficient can be generally written as

$$\tilde{\alpha}_G = \frac{\dot{q}_0 + \dot{q}_K}{(T_{D,\infty} - T_{D,0})} \quad (10)$$

with the sensible heat \dot{q}_o and the latent heat \dot{q}_K from the condensation of the steam. Therefore the heat transfer coefficient for the ‘classical’ film theory can be calculated from

$$\bar{\alpha}_G = \frac{\dot{n}_D \cdot M_D \cdot \left(\frac{c_{p,D} \cdot (T_{D,\infty} - T_{D,0})}{1 - e^{-\frac{\dot{m}_D c_{p,D} \frac{ST}{I}}}} + Dh_V \right)}{(T_{D,\infty} - T_{D,0})} \quad (11)$$

and for the ‘generalised’ film theory from

$$\bar{\alpha}_G = \frac{\dot{n}_D \cdot M_D \cdot (c_{p,D} \cdot (T_{D,\infty} - T_{D,0}) + Dh_V)}{(T_{D,\infty} - T_{D,0})} \quad (12)$$

with the calculation of errors by Gauß.

3.4. Experimental setup

For the experiments an Argon ion laser with a wavelength of 488 nm and a power of 1.7 W is used. The 90° -scattered light is focused on the entrance slit of a spectrograph by means of a 50 mm objective for horizontal and a 105 mm objective for vertical experiments. Before the objective a filter is installed, which fades out the scattered light below 530 Nm (Rayleigh scattering). The spectrograph with a focal length of 250 mm divides the wavelengths of the scattered light and produces two-dimensional pictures of the scattered light. The wavelength and the height are the coordinate axes (Figure 4).

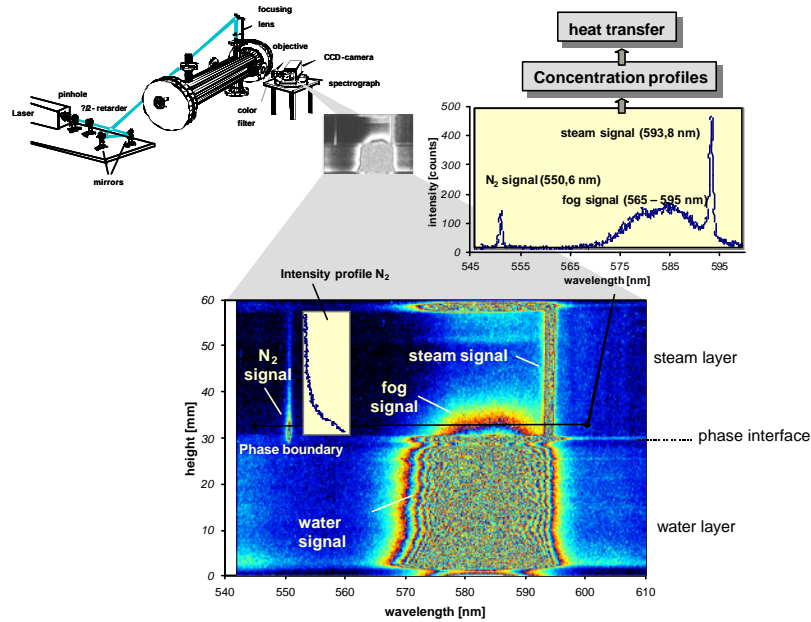


Fig. 4: Raman spectra of a horizontal stratified flow.

A height calibration provides a local resolution of 0.1584 mm per pixel for the horizontal setup and 0.01465 mm per pixel for the vertical setup. In the spectrograph a grating with 300 lines and a blaze at 500 nm was installed. The two-dimensional picture at the output of the spectrograph is captured by an intensified CCD camera. Although this camera has a single photon sensitivity, a capture time of 2 seconds per picture proved as appropriate. In case of stationary experiments 30 pictures are averaged for a better signal to noise ratio and the averaged picture is stored. In case of transient experiments every 2 seconds a picture is captured and stored individually.

4. TEST FACILITIES

4.1. Cooled, vertical wall

The test facility consists of two sections, an integrated steam generator and the actual measuring volume with the cooled wall and the optical accesses. The steam, which is generated in the electrical steam generator, condenses at the cooled wall and drops again into the water trap (Figure 5). Therefore condensing and boiling is a closed cycle, which does not need a peripheral device up to the electrical links and the cooling water. Thermocouples are installed in the wall to measure local temperature gradients. With these local temperature gradients it is possible to calculate local heat transfers. These values can be used for validating the laser measurement.

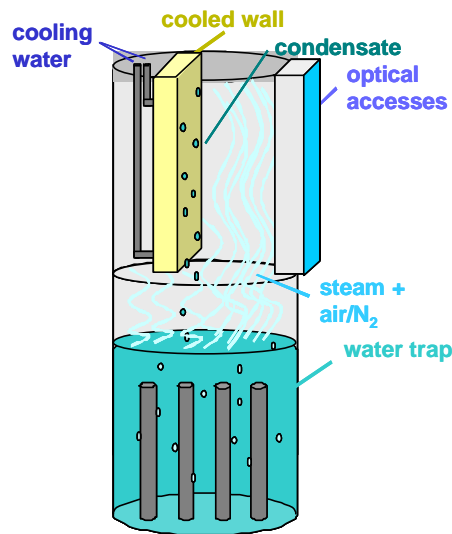


Fig. 5: Test facility with cooled vertical wall.

4.2. Horizontal stratified flow

Main part of the test facility is the pressure vessel with an upward opened, horizontal, rectangular duct (Figure 6). At the position where the thermocouples are installed optical accesses are implemented at the vessel and in the duct. Saturated steam from the steam generator is dried and following temperature as well as mass flow are determined. After the measuring section for the steam the nitrogen feeding is installed. The steam/nitrogen mixture flows co-current or counter-current to the water flow in the duct into the test vessel.

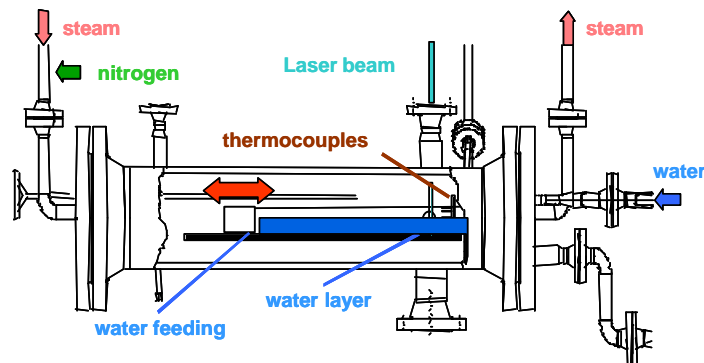


Fig. 6: Test vessel with horizontal water duct.

After leaving the vessel and before condensing, the temperature and the mass flow of the steam is measured again. The pressure control valve was attached directly at the output of the steam generator. Before the condenser a additional valve is used for the regulation of the steam mass flow.

The water feeding into the duct can be shifted axially. Therefore it is possible to get the average water temperature and the concentration profiles at different locations of the water layer. With the average water temperature at different locations it is possible to draw energy and mass balances.

The nitrogen feeding was realised by pressure bottles and a manually operated valve. The nitrogen could be preheated over an electrical heating on the system temperature. Subsequently, nitrogen mass flow, pressure and temperature were determined and the nitrogen was fed into the steam pipe.

Figure 7 shows the flow sheet of the test facility. Several measurement equipments were installed to measure all parameters, which are important for analysing the experiments, like system pressure, mass flow and temperature of steam, water and nitrogen etc. To determine global heat transfers along the water layer by energy balances it is necessary to determine the temperature profile of the water layer over the height. This is made by thermocouples, which are mounted on a kind of sword at one measurement position in the water layer (Figure 8). With the axially shifted water feeding it is possible to realise different energy balance areas with one measurement position.

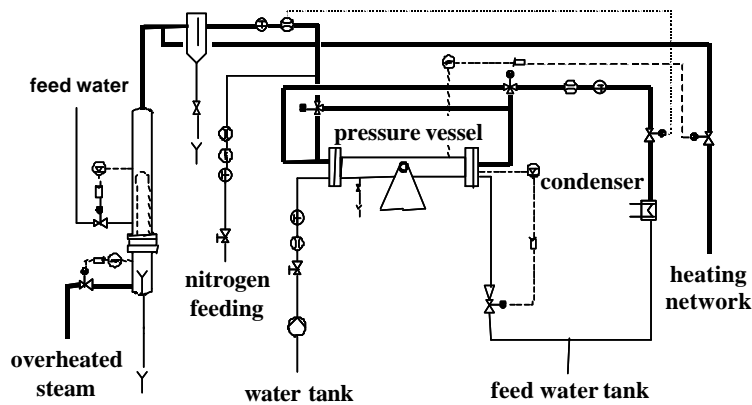


Fig. 7: Flow sheet of the test facility.

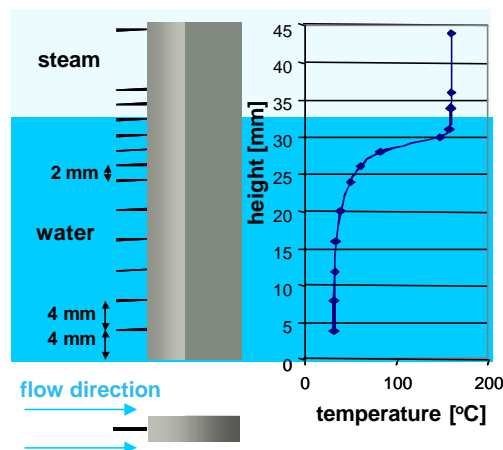


Fig. 8: Thermocouples in the water layer.

5. RESULTS OF THE STEADY STATE EXPERIMENTS

5.1. Vertical cooled wall

Figure 9 shows the measured concentration profile and the concentration profiles approximated with ‘generalised’ and ‘classical’ film theory of one exemplary experiment. Besides the calculated heat transfers from both film theories the heat transfer from the thermocouple measurement are pictured, as well as the phase interface and bulk concentrations. It can be clearly seen, that the ‘generalised’ film theory provides a better approximation as the ‘classical’ film theory. The heat flow calculated from the ‘generalised’ film theory corresponds very good with the thermocouple measurements. The heat flow calculated from the ‘classical’ film theory is clearly too small.

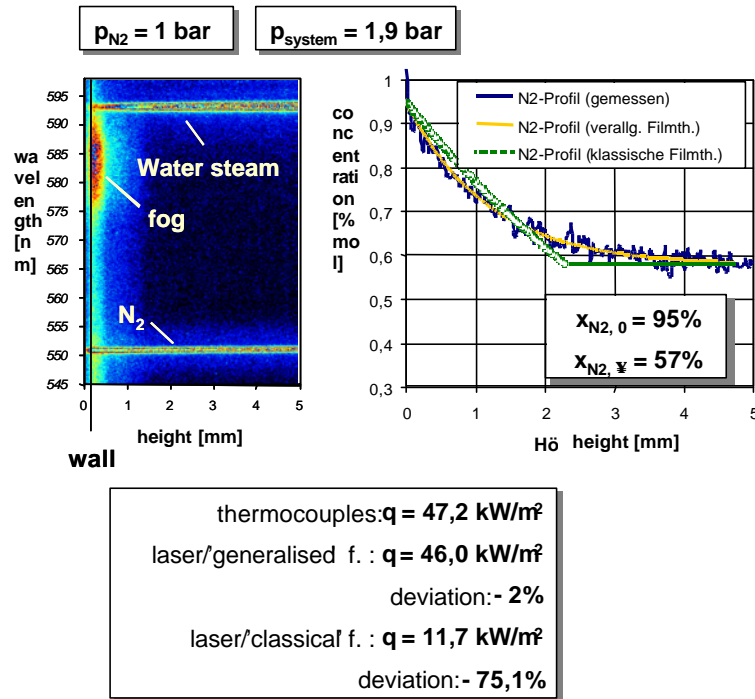


Fig. 9: Raman spectra and concentration profile at the vertical cooled wall.

5.2 Horizontal stratified flow

Figure 10 shows the nitrogen accumulation at the phase interface and the heat transfer with different steam velocities. The other experimental parameters are identical. The steam velocities and Reynolds' numbers are specified for the measuring point.

The strong increase of the nitrogen accumulation at the phase interface within a small range of Reynolds' numbers is remarkable. Already the change of the steam Reynolds' number of 6800 to 5200 (23,5% change) causes a doubling of the nitrogen concentration at the boundary layer (10 mol% to 19 mol %) and a reduction of the heat transfer on an eighth of the original value (20744 W/m²K to 2528 W/m²K). A reduction of the steam Reynolds' number around further 42,3 % (5200 to 3000) causes an increase of the nitrogen concentration at the boundary layer from 19 mol % to 81 mol %. The heat transfer decreases thereby on approximately a twelfth (2528 W/m²K to 204 W/m²K).

During detailed view of the last concentration profile in Figure 10 it is noticeable that the measured and the calculated concentration profile deviate from each other. These deviations occur mainly at the end of the duct with low steam velocities. The analysis of the concentration profile

resulted in the fact that there is a linear profile several millimeters above the phase interface. After this linear layer the profile is still logarithmic. Because of the missing convective part, the condensation rates in the layer with a linear concentration profile are substantially smaller than in the logarithmic layer. This would mean that a large part of steam already condenses as fog droplets above the phase interface.

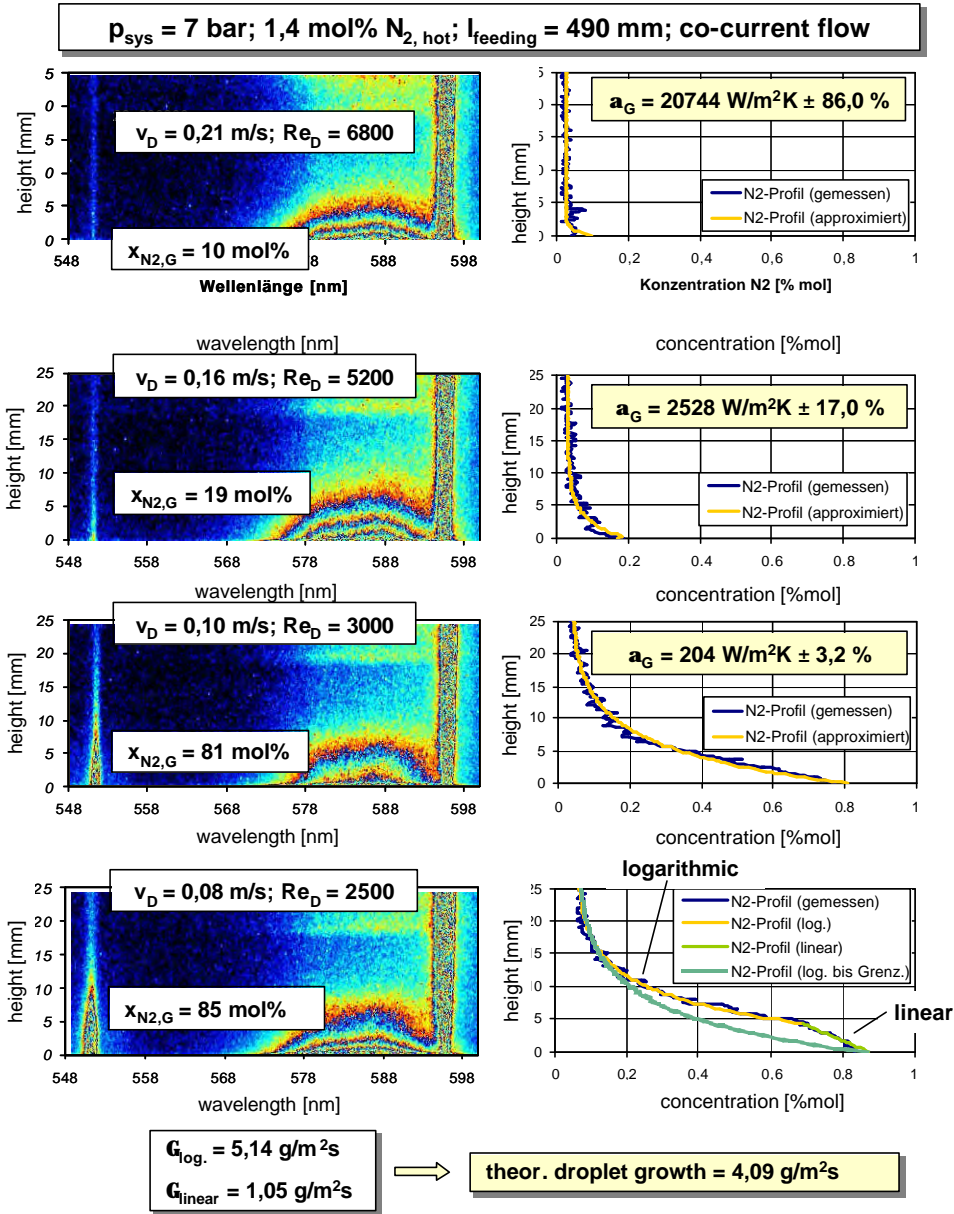


Fig. 10: Nitrogen concentration profiles and heat transfers with different steam Reynolds' numbers.

6. RESULTS OF THE TRANSIENT EXPERIMENTS WITH NATURAL CONVECTION

The transient experiments were performed with outlet valve to the condenser closed. Therefore the steam is flowing in natural convection co-current or counter-current to the water flow. The convection is only influenced by the condensation rates. In order to be able to investigate transient processes at the boundary layer, every two seconds a Raman spectrum was captured with the CCD camera and stored. Because of the short recording time the signal-to-noise ratio is clearly worse

than with the steady state experiments, but sufficient for a qualitative analysis. For a quantitative analysis several pictures must be averaged, in order to improve the signal-to-noise ratio.

Figure 11 shows a typical run of the average water temperature with co- and counter-current flow over the time. The feeding of the constant nitrogen mass flow (4 kg/h) begins with 0 s and ends with 180 s. The system pressure is 7 bar, the distance between the water feeding and the measurement position is 490 mm.

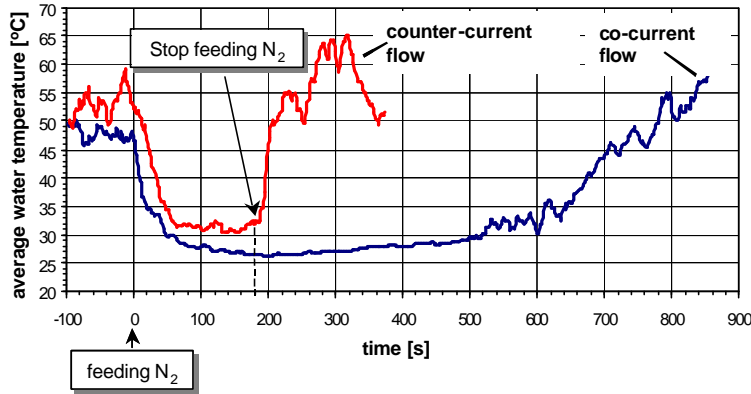


Fig. 11: Run of the average temperature of the water layer over time with co-current and counter-current convection.

Immediately after the start of the nitrogen feeding the average water temperature and therefore the heat transfer decreases strongly with both directions of flow. After a short time both water temperatures have nearly a constant value at a low stage. The average water temperature of the co-current flow is slightly higher than with counter-current flow. After stopping the feeding of nitrogen a remarkable phenomenon occurs. In case of counter-current flow the average water temperature and thus the heat transfer increases immediately and after 40 seconds it reaches nearly the value before the nitrogen feeding. In contrast to it, the average water temperature in the co-current flow rises after the stop of nitrogen feeding only around approximately 2 K within 300 seconds. Only further 250 seconds later the water temperature reaches the value before the nitrogen feeding.

The following analysis of the laser spectra gives more information on the processes in the boundary layer.

6.1. Co-current flow

Figure 12 shows the spectra at different points in time from the start of the nitrogen feeding. The accumulation of nitrogen is already strong 60 seconds after start of feeding. At 180 seconds (stop of the nitrogen feeding) a formation of a boundary layer with nearly constant nitrogen concentration can be observed. 20 seconds after stopping the nitrogen feeding (point in time 200 seconds) a change in the nitrogen concentration cannot be recognised. After further 180 seconds (point in time 400 seconds) a reduction of the thickness of the layer with constant nitrogen concentration took place. At 460 seconds this layer is completely resolved. In the further process also the exponential concentration profile continues to resolve, until it disappears at approximately 700 seconds. The formation of a boundary layer with almost constant nitrogen concentration is remarkable with these experiments. This means, that almost no steam is transported through this layer.

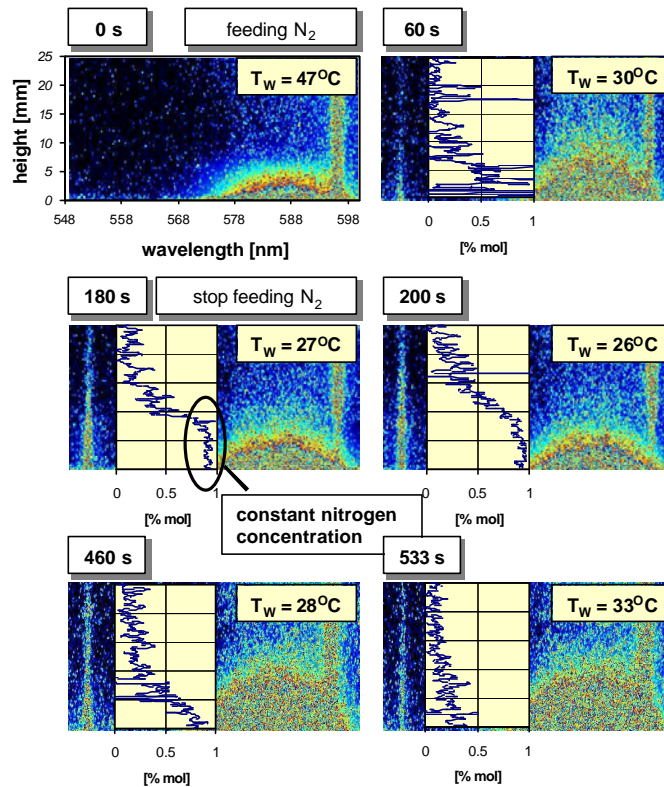


Fig. 12: Raman spectra and concentration profiles with co-current flow at different times.

6.2. Counter-current flow

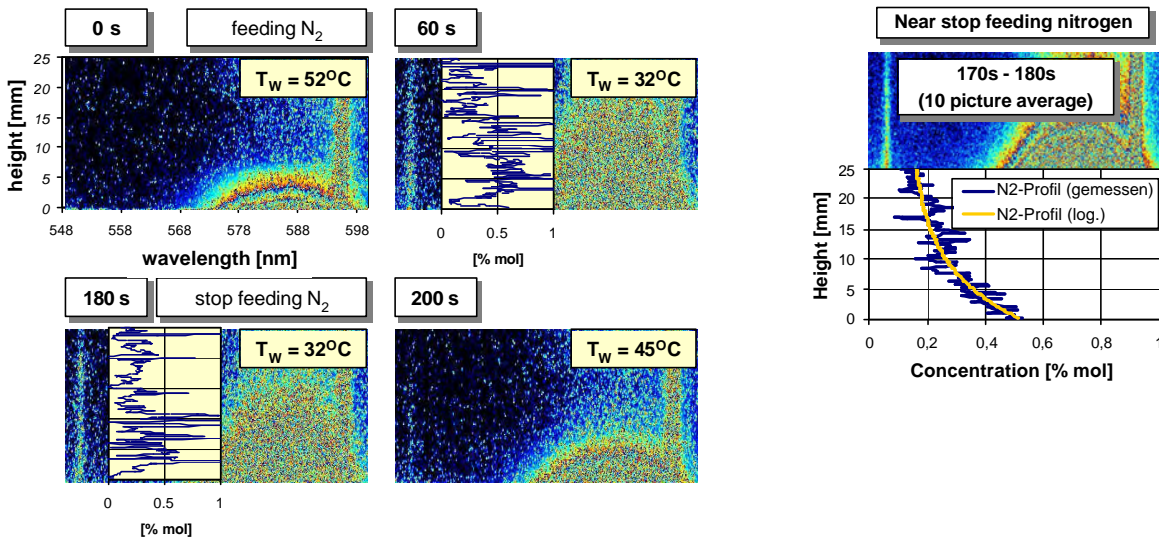


Fig. 13: Raman spectra and concentration profiles with counter-current flow at different times and a 10-picture average at the end of the nitrogen feeding

The Raman spectra of the counter-current flow (Figure 13) shows a clearly different process of the nitrogen accumulation than with co-current flow. Due to the strong formation of fog the signal to noise ratio is worse than with co-current flow. But it can be seen that also with counter current

flow nitrogen accumulates immediately at the phase boundary layer after the start of the nitrogen injection. Therefore the average water temperature decreases strongly. Up to the stopping of the nitrogen feeding no formation of a layer with constant nitrogen concentration can be observed (Figure 13). The second remarkable difference to the co-current flow is the immediate dissolution of the nitrogen profile after stopping the nitrogen feeding. Thus the average water temperature increases immediately.

7. CONCLUSION

The combination of conventional measurement techniques like thermocouples with a optical measurement technique allows to investigate heat transfer phenomena in a wide range. The laser measurement allows to visualise the processes in the boundary layer of a stratified flow. Experiments on a horizontal stratified flow show several interesting phenomena, like the accumulation of nitrogen in a small range of the steam Reynolds' number and the formation of a boundary layer with a linear nitrogen concentration profile. The transient experiments show, that the processes under natural convection are different between co-current flow and counter-current flow. This is caused by the different formation of the nitrogen concentration profile with co-current and counter-current flow.

The experiments, in particular those with vertical setup and high nitrogen bulk concentrations indicate, that the 'generalised' film theory deduced from the equation of continuity delivers a better description of the measured concentration profiles than the often used 'classical' film theory.

NOMENCLATURE

c	kmol/m ³	molar density
c_p	kJ/kg K	specific heat capacity
D	m ² /s	binary diffusion coefficient
I	counts	intensity
\dot{n}	kmol/m ² s	specific molar flux
v	m/s	velocity
x, y, z	m	coordinates
x	kmol/kmol	molar concentration
s	m	thickness of boundary layer

greek symbols

$\frac{\partial \sigma}{\partial \Omega}$	cm ⁶ /sr	differential cross section
α	W/m ² K	heat transfer coefficient

indices

D	steam	∞	bulk
W	water	t	turbulent
G	gas(-mixture)	T	temperature
0	phase interface		

constants

c	$2,9979 \cdot 10^8$ m/s	light velocity
h	$6,62618 \cdot 10^{-34}$ J/s	Plank's constant

REFERENCES

- [1] Bird, R. B., Stewart, W. E., Lightfoot, E. N., Transport Phenomena, John Wiley & Sons, New York, 1960.
- [2] VDI-Wärmeatlas, VDI-Verlag, Düsseldorf, 7.Auflage, 1994.
- [3] Ruile Herbert, Direktkondensation in geschichteten Zweiphasenströmungen, VDI-Fortschrittsbericht Reihe 19, Nr. 88, VDI-Verlag, Düsseldorf, 1996.
- [4] Hobbhahn, W., Beschreibung der Direktkontaktkondensation von Dampf an unterkühltem Wasser mit Anwendung in der Störfallberechnung von Druckwasserreaktoren, Dissertation, Uni Bochum, 1990.
- [5] Atkins, P. W., Physikalische Chemie, VCH, Weinheim, 1988.
- [6] Schrötter, H. W., Klöckner, H. W., Raman Scattering Cross-Sections in Gases and Liquids, in Weber, A. (Ed.), Raman Spectroscopy of Gases and Liquids, p. 123-166, Springer, Berlin, 1979
- [7] Penney, C., Lapp, M., Raman cross sections for water vapour, J. Opt. Soc. Am., Vol. 66, No. 5, S. 422-425, 1976.
- [8] Ahmad, S., Application of Raman scattering in remote sensing, in Sixty Years on Raman Spectroscopy, Elsevier Science Publishers B.V. Amsterdam, Vol. 17B, S. 391-422, 1989.
- [9] Karl Jürgen, Untersuchung des Wärmeübergangs bei der Partialkondensation mittels linearer Ramanspektroskopie, Dissertation, TU-München, 1997.

B. Measurement Techniques

IMPROVED OPTICAL PROBES AND THEIR VALIDATION FOR LOCAL MEASUREMENTS IN TWO PHASE FLOWS

M. Buchholz, H. Auracher

Technische Universität Berlin

Institut für Energietechnik

Marchstr. 18, 10587 Berlin, GERMANY

Phone: +49 30 314-22170, Fax: +49 30 314 21779,

E-mail: auracher@iet.tu-berlin.de

ABSTRACT

An improved optical probe system has been developed for measurements in boiling two-phase flows. The probe has a tip diameter less than 1.5 μm and improved electrical characteristics. The performance of the probe system is determined by combined analysis of high-speed video images and the probe signal during impingement of small liquid droplets on the probe tip. Exemplary probe signals measured in steady-state transition boiling of Isopropanol are also presented.

1. INTRODUCTION

For better understanding and modeling of boiling processes precise knowledge of the two-phase flow characteristics is crucial. The understanding of the boiling process still remains not satisfactory, especially in the high heat flux regions of the boiling curve and in the transition boiling region. Various intrusive and non-intrusive measurement techniques have been proposed and used to gain better insights into boiling and multiphase flow, for example high speed video [1, 2] and X-ray tomography [3, 4] as well as optical [4-9] and electrical probes [9-11]. As long as non-intrusive methods for precise, time resolved and local measurements in boiling between intermediate and high heat fluxes with the corresponding high void fractions and short time scales are not available, probe techniques are needed for these measurements. This is especially true for measurements very close to the heater surface. Close to the heater surface, the size of the probe tip is a crucial parameter for precise measurements because the flow structure and therefore the probe signal may be significantly altered if the probe tip is too large.

In all probe techniques the size of the probes should be as small as possible to minimize flow disturbances caused by the presence of the probes. The importance of probe miniaturisation is even higher for multi-sensor arrangements which should be used to measure parameters such as interfacial area concentration, interfacial velocity etc. in addition to standard parameters such as averaged void fraction and mean contact frequency, for example. Towards this goal an improved optical probe system with a very small tip diameter ($< 1.5 \mu\text{m}$) has been developed. The probe characteristics are identified by analysis of both high speed video frames and the probe signal during impingement of small droplets on the probe tip.

2. THE OPTICAL PROBE SYSTEM

The probe uses different refractive indices of vapor and liquid phase to generate an electrical signal. Light from the probe unit is reflected back into the fiber if vapor (or air) is present at the probe tip whereas with a liquid it leaves the probe tip. The optical signal traveling back to the probe

electronic system is directed to a photodiode and then amplified. An analog electrical signal is acquired by a data acquisition board and the phase indicator function PIF (liquid or vapor) is calculated from the analog signal. The set-up of the optical probe system is based on earlier developments by Hohl et al. [5].

2.1. Preparation of the probe

The improved optical probe system utilizes a singlemode-glassfiber with a cladding diameter of 125 μm and a core diameter of 8 μm . A scheme of the glass fiber is depicted in Fig. 1. The laser light used to operate the probe travels along the core only. The tip of the probe is formed by etching in hydrofluoric acid. This method allows the preparation of very small probe tips. Two SEM photographs of the probe tip with different magnification are depicted in Fig. 2. After preparation of the tip, the glass fiber is sealed into small Kovar tubes with a high temperature adhesive to make the probe sufficiently stiff. A photograph of a 2-probe arrangement is depicted in Fig. 3. Next to the probes a thin copper wire with a bend is also installed for distance calibration purposes. The distances between the two probes and between the lower probe and the wire tip along the probe axis were measured with a microscope prior to measurements. The distance between the probe axes is 125 μm , given by the diameter of the fibers.

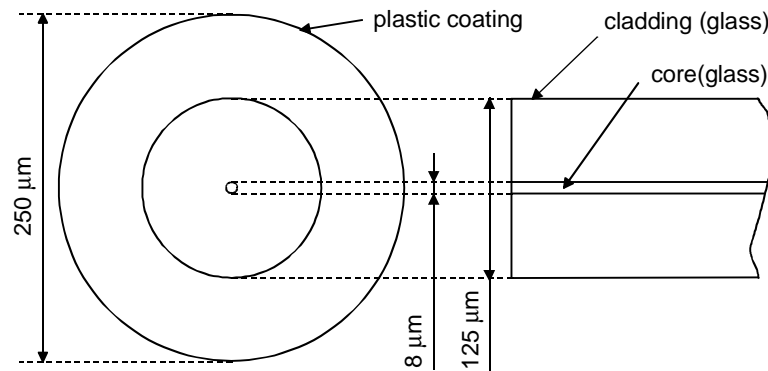


Figure 1: Dimensions of monomode glass fiber for 1300 nm wavelength light

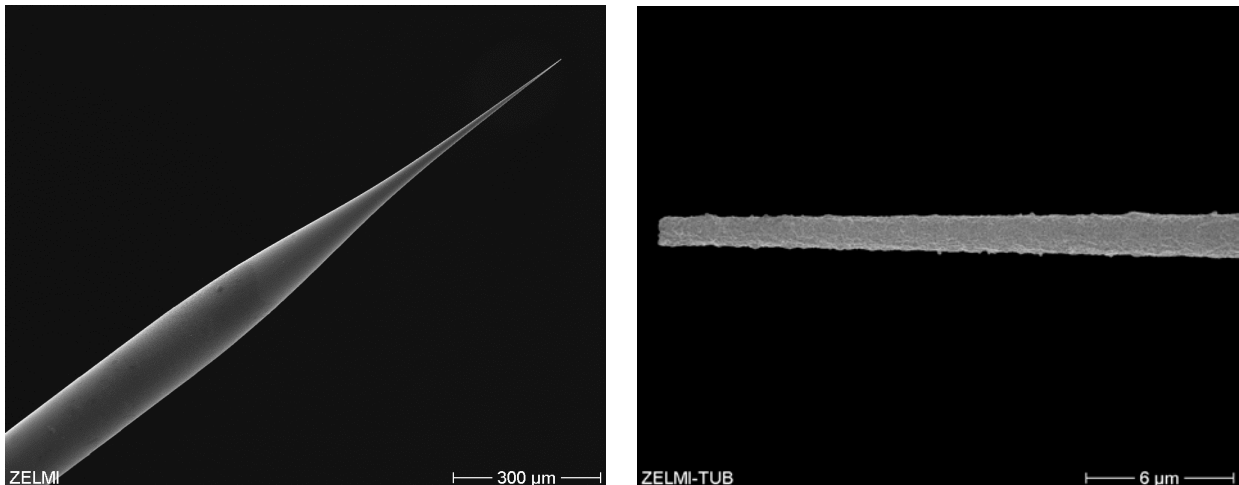


Figure 2: SEM-photographs of the probe tip

The double probe depicted in Fig. 3 was used for all measurements presented in the present paper. Using the double probe to study the probe performance offers the additional chance to examine possible influences of the lower probe (for measurements in boiling; for the droplet impingement test the geometry is inverted so that it becomes the upper probe) on the measurements

taken by the upper probe as well as visual analysis of the droplet motion along the double probe. This is important when using multiple probe tip arrangements.

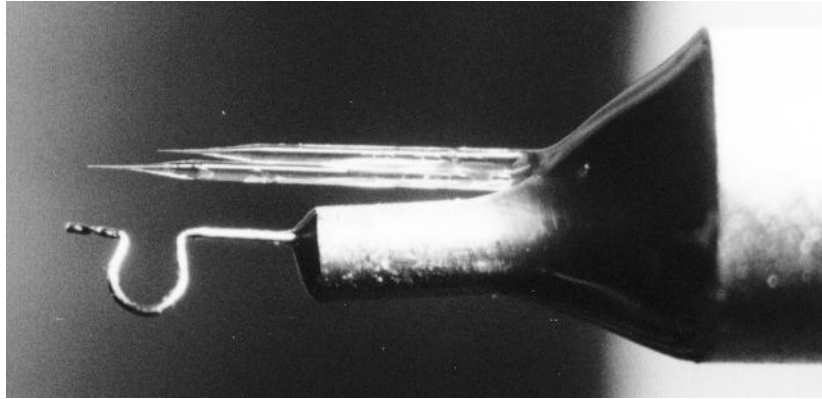


Figure 3: Photograph of the double optical probe

2.2. Probe electronics and data acquisition

The probe is operated by an electronic detection unit. The main part is a bidirectional optical unit Bidi[®] (Infineon AG) which contains all the necessary optical parts: a Laser diode, a beam splitter and a PIN photodiode in a single device. The laserlight to operate the probe has a wavelength of 1300 nm. The electronic detection unit contains also devices for safe operation of the laser diode and for amplification of the photodiode output signal as well as level detection circuits. The amplified electrical signal is acquired with a ADC-64 (Innovative Integration) data acquisition card for PC. The card has an onboard DSP-Processor and 8 A/D converters (each A/D: 16-Bit, max. sampling rate 200 kHz). It supports simultaneous sampling of 8 channels at 200 kHz each channel. The bandwidth (-3 dB point) of the entire PIN-Diode amplifier was measured with the PIN-Diode replaced with an HF source with similar electrical properties. The large signal bandwidth measured was 1.5 MHz, well above the needed bandwidth for a 200 kHz data acquisition. However, the large signal bandwidth may be easily increased to 6.5 MHz by slightly changing the electronics.

3. EXPERIMENTS AND RESULTS

3.1 Probe performance validation

To determine the probe performance, precisely known test conditions are necessary. For these requirements, a vapor-liquid (or gas-liquid) upstream flow was found not to be the best choice, because optical access to single bubbles with magnifying camera lenses is limited and turbulence may effect the bubble shape and hence the accuracy of contact time calculation, using the video frames. To overcome these limitations, we used an inverted geometry with small falling droplets for the tests. Advantages are also the relatively easy setup. A scheme of the test setup is depicted in Figure 4.

The principle of the test is as follows: a small droplet is produced by a droplet generator. The falling droplet crosses a light barrier above the probe tip. The receiver of the light barrier detects the droplet and generates a trigger pulse for both the data acquisition for the probe signal and a high speed video camera. Synchronisation pulses of each video frame are used to fire a high speed LED-stroboscope for back light illumination. The synchronisation pulses are also acquired with the fast data acquisition for later analysis. The video camera used was a Weinberger Speed Cam Pro with a Weinberger Speed Flash and a microscope lens. The test liquid for the droplets was Isopropanol. The lower probe of the upside placed dual probe was used for the tests in order to quantify the influence of the upper probe on the results measured by the lower probe. Video frames were taken at 2000 frames per second, optical probe data was sampled at 200 kHz.

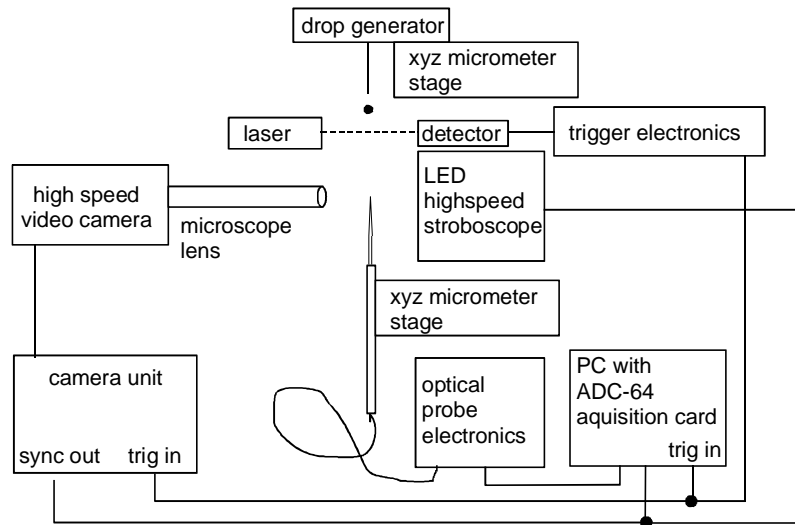


Figure 4: Setup of probe validation experiment

The output voltage of the optical probe system during a drop passage is plotted in Fig. 5, details of both edges of the signal in Fig. 6. The diamond markers in Fig. 6. represent the sampled data points. High signal level represents vapor (or air) at the probe tip, low signal level represents liquid isopropanol at the tip.

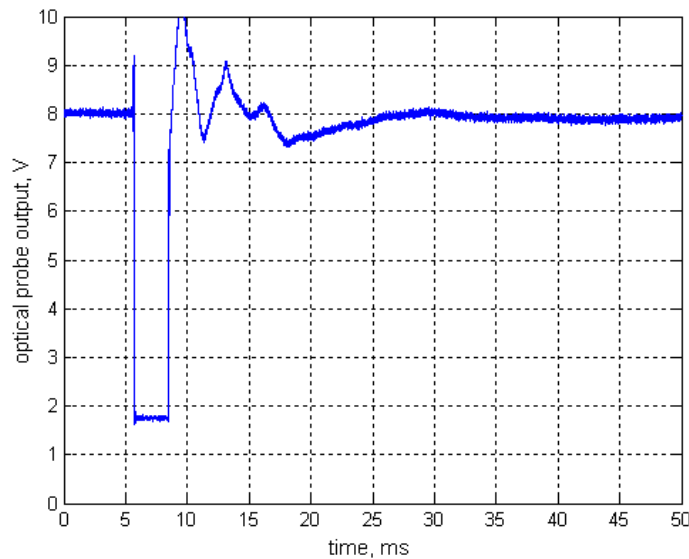


Figure 5: Optical probe signal during contact to a falling droplet

The drop passage can clearly be seen in the signal plotted in Fig. 5. A very sharp decrease of the signal occurs at the contact between optical probe and the isopropanol droplet. After contact to the air again, the signal rises first very fast to the voltage previous to droplet contact. Then some overshoot occurs and also some slow fluctuations at high signal level. These fluctuations vanish after about 18 ms. Looking at the falling edge more closely (see Fig. 6, left) a weak increase of the signal can be found very shortly before the falling edge. At the falling edge, the signal drops during one sampling period ($5 \mu\text{s}$) almost completely to the steady state voltage for liquid phase. It is quite obvious that the entire wetting process of the probe takes place in this short period even though some additional time after the optical detection of the probe wetting is consumed by the probe electronics and data acquisition (fall time). This means that probe wetting takes place very rapidly.

The slight increase before the falling edge may be explained as follows: Some laser light is being emitted by the probe even with a dry probe tip. A fraction of this emitted light is being reflected at the approaching interphase of the droplet back into the probe tip and causes subsequently the signal increase. The probe signal during liquid contact is very stable, there are only weak fluctuations. At the rising edge the signal voltage reaches about 70 % of the total signal rise after three sampling periods (15 μ s) (see Fig. 6, right). Then the signal gradient (regardless of fluctuations) decreases and the signal level rises beyond the steady-state signal voltage for vapor/gas. During a short interval it rises higher than 10 Volts (see Fig. 5), which represents the maximum input voltage of the data acquisition and therefore cannot be measured. Afterwards, some decaying fluctuations occur until they vanish completely about 18 ms after the rising edge. Our measurement equipment does not allow to precisely resolve the processes occurring at the probe tip after the passage of the interface (at 8.5 ms in Fig. 6). It is certainly due to complex processes like film runoff, film rupture and evaporation of the liquid at the probe tip. The experiments needed to study these processes are expected to be extremely difficult. However, this clarification of the process is neither necessary nor helpful to determine the interface passage which can obviously be detected very precisely with the micro-optic probes of this type.

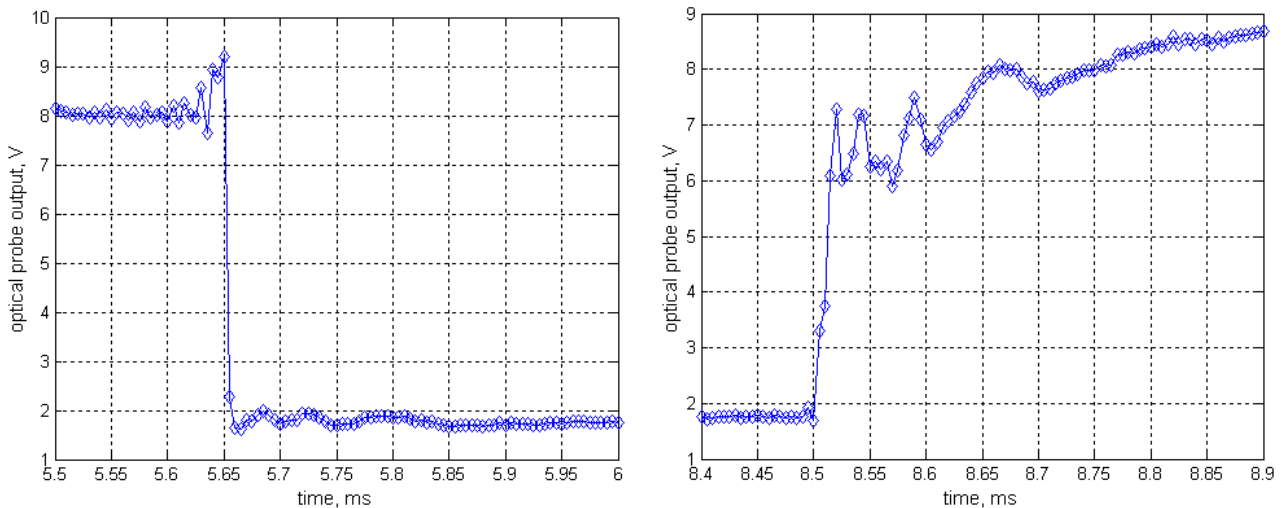


Figure 6: Optical probe signal, left: contact air to liquid, right: liquid to air

Signal noise is low, about 150 mV_{pp} during vapor contact and a little less (about 100 mV_{pp}) during liquid contact. The higher noise level during vapor contact is most likely the result of additional optical noise, which originates from the laser diode and the laser diode drive circuits. During liquid contact, most laser light is not being reflected back into the fiber and therefore contributes to the overall noise to a smaller extent than during a vapor contact.

Measurements with acquisition of both the probe signal and of the high speed video camera were performed at different frame rates. The camera allows up to 1000 frames per second fps with full resolution (512 x 512 pixel) and up to 4000 fps with reduced horizontal resolution. The best compromise between resolution and frame rate for the probe analysis was found to be 2000 fps. At 3000 and 4000 fps the horizontal resolution is too poor for the small probe size and the frame rate should be as high as possible. The measurements at 2000 fps allow calculation of the droplet passage time and therefore comparison with the probe-detected liquid contact time. The calculated passage time (camera) is 2,8 ms, the measured passage time (optical probe) 2,86 ms. The average droplet size of many runs was 1,7 mm diameter. The accuracy of the measurements is mainly limited by optical resolution and optical distance measurement calibration. The overall accuracy is estimated to be better than 5%. Even the high frame rate of 2000 fps is not sufficient for a precise analysis of the behaviour of the droplet bottom and top interfaces at probe piercing and probe dryout, respectively. This analysis requires frame rates well beyond 10,000 fps with good optical

resolution. However, the video frames contain some information on the behaviour of the interfaces. This influence is discussed in the next paragraph with the help of some high speed video images. In these tests the active optical probe is the lower probe because we want to examine the influence of the upper probe on the lower probe (probe test inverted geometry).

At the contact between the probe with the lower interface, a deformation of the interface is not visible, see Fig. 7. Note, that the probe in this frame is located directly under the center of the droplet and the active tip pierced already the interface.

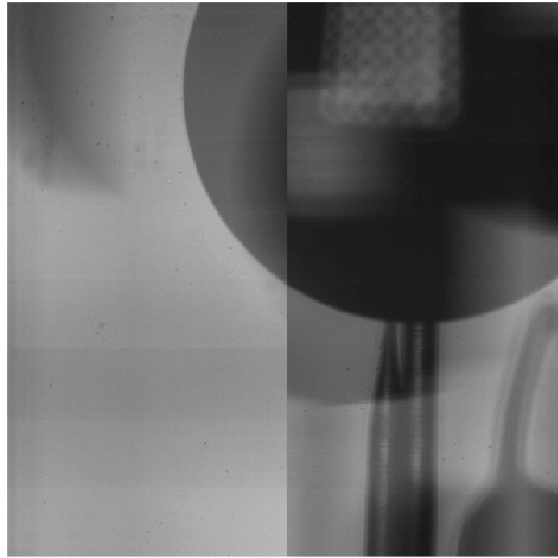


Figure 7: Droplet during first contact to the probe tip (at 1000 fps)

At the upper interface of the droplet, a deformation can be seen; see subsequential images in Fig. 8. In the first frame of Fig. 8, the upper probe tip has already pierced the interface but the lower probe remains inside the droplet. In the next frame the lower probe tip has also pierced the interface. The penetration of the interface must have taken place in the period between the first and the second image (see Fig. 6). Beginning in the second frame, a deformation of increasing magnitude with progressing time can be seen. As mentioned before, even a frame rate of 2000 fps is not sufficient to resolve the piercing process of the probe tip. The measurements of the probe signal indicate, that the phase change occurs very short after the first frame. This fact is a strong support for the conclusion, that – at least – the greatest part of the deformation does occur *after* the probe tip has passed the interface. Therefore the deformation is not relevant as long as phase velocities or droplet / bubble diameters etc. are to be determined. Moreover, the deformation shown in the frames 2 to 4 of Fig. 8 is in a later stage of the droplet passage where both probes indicate vapor. The surprising result that the observed deformation does not cause large errors for the detection of the unaffected phase change (without probe presence) is most likely caused by the very small probe tip and the slender geometry below the tip. The tip seems to pass the interface before the deformation develops. Besides, the deformation seems to be caused mainly by capillary forces between both optical fibers and the flow restriction at the connection of the fibers. This finding is expected to be also true for multi-probe arrangements with similar axial distances of the probes. In such probe arrangements with reduced axial distances the effect of the interface disturbance on measurement accuracy is expected to be negligible. Such probe arrangements with reduced axial tip distance are needed for measurements in pool boiling as explained in the following chapter. However, the deformation of the interface might affect the measurement accuracy for multi probe arrangements with large axial distances between the probes. For such probe arrangements with large axial distances additional verification experiments are advisable. This is even more important with liquids of higher surface tension like water for example.

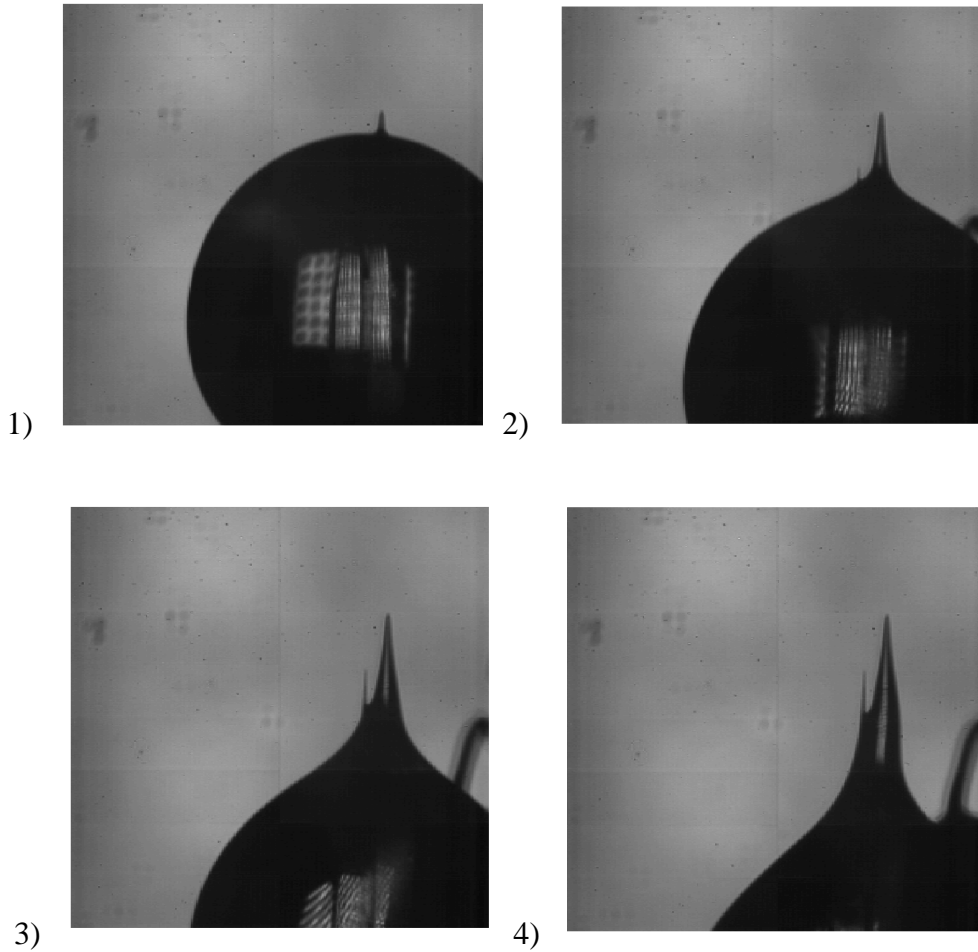


Figure 8: Droplet during last stages of second contact to the probe (at 2000 fps)

3.2 Optical probe measurements under boiling conditions

Measurements under real boiling conditions were also realized. The boiling liquid was Isopropanol boiling on a horizontally positioned flat disc heater with 35 mm diameter. The heater temperature was controlled by a discrete PI controller on a DSP-processor PC card. The system pressure was also controlled by a PI controller. The latter has been implemented in LabView on a PC with installed data acquisition cards. Both controllers maintain stable conditions of both heater temperature and test liquid and enable steady-state measurements along the entire boiling curve. The schemes of the boiling facility and the test heater are depicted in Fig. 9. The double optical probe was installed at the top of the boiling vessel perpendicular to the heater surface. It is moveable in x-, y-, and z- direction with micrometer stages. The distance between heater and lower probe was calibrated at the point of electrical contact between the heater and the copper wire next to the probe (see Fig. 3) with the known distance between the wire and the lower probe. The probe position was measured with a LVDT-displacement sensor with $\pm 1.1 \mu\text{m}$ accuracy. For more details of the boiling facility and measurement setup see [6, 12].

Measurements were taken during steady-state transition boiling of saturated Isopropanol. Saturation pressure was 0.104 MPa which corresponds to $p^*=0.022$. Heater wall superheat was $\Delta T=29.6 \text{ K}$ (which is in between CHF and the Leidenfrost point), the average heat flux for all probe distances studied was 21.2 W/cm^2 . Probe data was measured at each probe distance at a sampling rate of 16.67 kHz each probe for 60 seconds. Both probe signals were sampled simultaneously. The distance between the lower probe and the heater surface was in the range between 120 μm and 20.2 mm, the vertical distance between both probe tips was 425 μm .

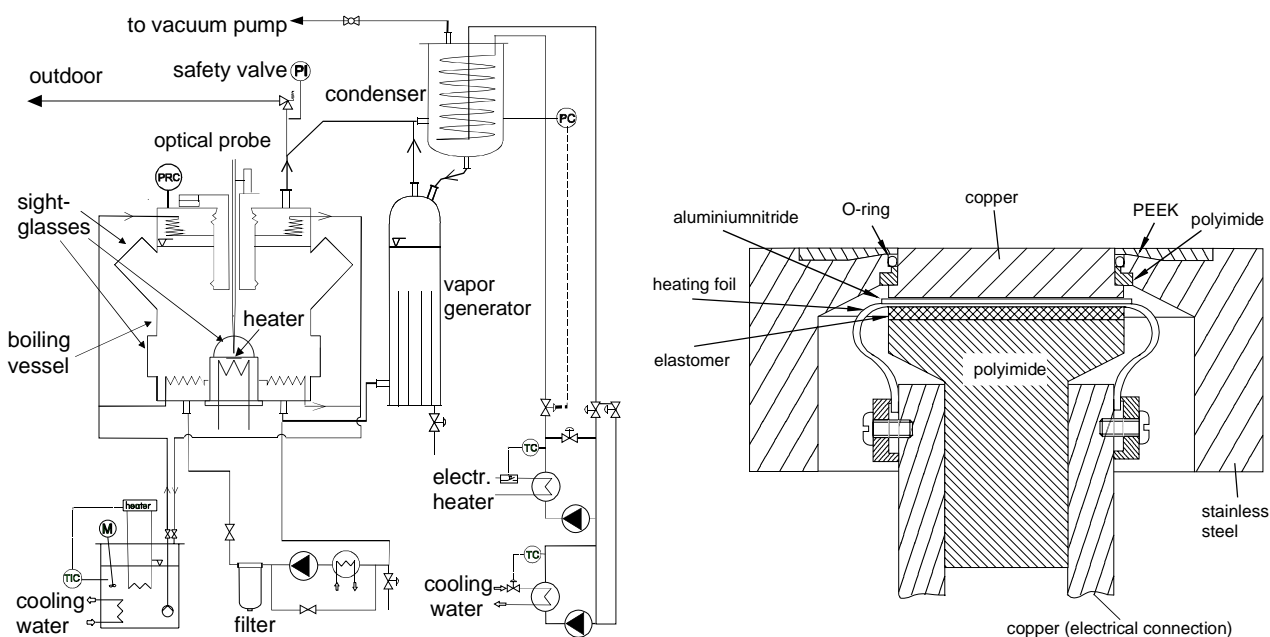


Figure 9: Schemes of boiling facility and test heater

A short sequence of measured signal is depicted in Fig. 10 for a position of the lower probe $120\ \mu\text{m}$ above the heater surface. Like the signals shown in chapter 3.1, high signal level represents vapor, low signal level liquid phase at the probe tip. Compared to the acquired signal voltage of Figs. 5 and 6, the signal amplitudes are smaller and the noise levels are higher. These different results originate from the previous version of the electronic detection unit with inferior electrical characteristics. The signal quality is still well beyond what is needed for an accurate calculation of the PIF. The differences between the voltages representing vapor and liquid between both probes are caused by different settings of offset and gain. They do not contain any physically meaningful information. The signals at a distance of $120\ \mu\text{m}$ (lower probe) and $545\ \mu\text{m}$ (upper probe) are very different. The upper probe detects relatively few phase changes and some longer liquid contacts. The lower probe is located only $425\ \mu\text{m}$ below the upper probe but the signal characteristics are very different. The probe detects more vapor-liquid fluctuations and only short liquid contacts. The mean void fraction at the lower probe position is therefore far higher as the one at the upper probe. The plotted sequence is a good example for the high complexity of the two phase flow very close to the heated surface in transition boiling. Obviously the two phase characteristics change significantly between the distance of both probe tips ($425\ \mu\text{m}$), so that there is – if any – only a poor correlation between the signals. Hohl [5] found a similar behaviour with a single optical probe (tip diameter $10\ \mu\text{m}$) and a similar heater for distances down to $10\ \mu\text{m}$ with FC-72 as test liquid. If cross correlation in multi probe arrangements is required to determine two phase parameter above the heater (as e.g. interfacial velocities), better correlated signals as plotted in Fig. 10 are needed. This may be achieved only with a reduced axial distance between the probe tips.

For the determination of two phase parameters such as void fraction, vapor contact frequency, interfacial velocities and interfacial area concentration the PIF must be determined. This can be done using an algorithm developed by Hohl [5] which must be optimized for the new probe system.

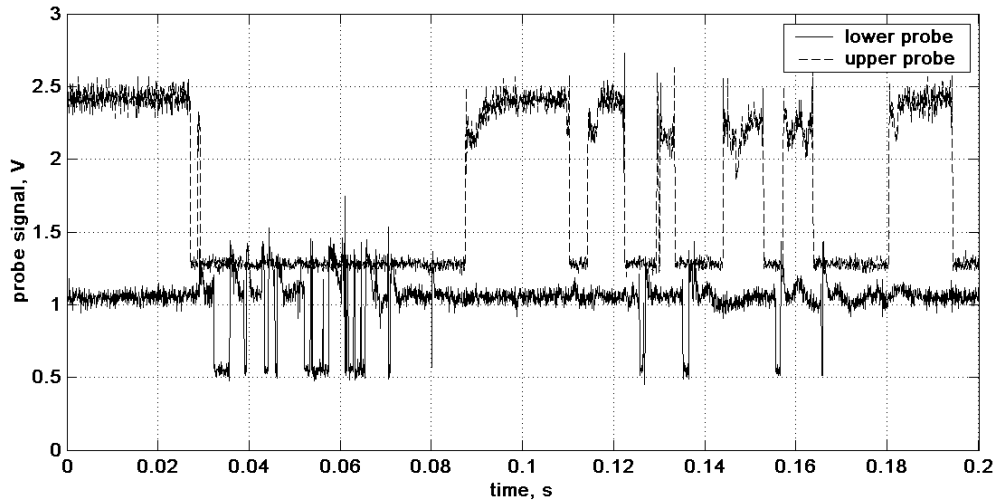


Figure 10: Double probe signal sequence; distance between heater and lower probe 120 μm

4. CONCLUSIONS

An improved optical probe with a tip diameter below 1.5 μm was developed. The characteristics were investigated with measurements of the probe signals and high speed videos during impingement of small free falling isopropanol droplets on the probe tip. The test results prove very good characteristics of the probe – the detection of a vapor to liquid phase change can be detected within 5 μs , the phase change liquid to vapor in less than 15 μs . The latter is most likely caused by the time needed for sufficient dryout of the probe tip. After the liquid to vapor phase change, some fluctuations as well as some overshoot does occur, but these effects do not affect the measurement accuracy. The contact time to the droplet detected by the probe is – within the measurement accuracy – identical to the contact time calculated from high speed video images. The overall accuracy for the determination of interface passages in two phase flows including interface deformation and errors caused by the probe electronics and the data acquisition is well above 95 %. Test measurements with a double probe in steady-state transition pool boiling on a horizontal disc heater have also been carried out. The experiments confirm the applicability of multi-probe arrangements for measurements in complex boiling two phase flows as in transition boiling pool boiling in a zone very close to the heater. Multi-probe measurements allow better insights into the two phase flow dynamics with advanced parameters such as interfacial area concentration and interfacial velocity.

ACKNOWLEDGEMENTS

The authors highly appreciate financial support of Deutsche Forschungsgemeinschaft (DFG) in the frame of a Joint Research Project on fundamentals of boiling heat transfer. The project was supported with bidirectional optical fiber units Bidi[®] by Infineon AG, Germany.

NOMENCLATURE

CHF	critical heat flux
FC-72	C_6F_{14} liquid, 3M-Company
fps	frames per second
LVDT	linear variable differential transformer
p^*	reduced pressure, p/p_{crit}
PIF	phase indicator function

SEM scanning electron microscope
 V_{pp} peak-to-peak voltage

REFERENCES

- [1] Luke, A. & Danger, E., Size Distribution of Active and Potential Nucleation Sites on Horizontal Evaporator Tubes, IIR Int. Conf. Thermophysical Properties and Transfer Processes of New Refrigerants, Paderborn, Germany, pp. 396-403, October 2001.
- [2] Kuwahara, K., Koyama, S. & Hashimoto, Y., Heat Transfer and Flow Pattern of Pure Refrigerant HFC143a Evaporating in a Horizontal Capillary Tube, International Workshop on Current Status and Future Directions in Boiling Heat Transfer and Two-Phase Flow, Univ. Kansai, pp.165-170, October 2000.
- [3] Hori, K., Kawanishi, K. & Tsuge, A., Overview of Studies on Flow Boiling Heat Transfer in PWR Fuel Assembly, International Workshop on Current Status and Future Directions in Boiling Heat Transfer and Two-Phase Flow, Univ. Kansai, pp. 95-102, October 2000.
- [4] Hervieu, E., Joudet, E. & Desbat, L., Development and Validation of a X-Ray tomograph for two-phase flows, Int. Conf. Multiphase Flow, New Orleans, paper No. 429, 2001.
- [5] Hohl, R., Auracher, H., Blum, J. & Marquardt, W., Characteristics of Liquid-Vapor Fluctuations in Pool Boiling at small Distances from the heater, 11th Int. Heat Transfer Conference, Kyongju, Korea, Vol.2, pp. 383-388, 1998.
- [6] Lüttich, T., Buchholz, M., Hertel, C., Marquardt, W. & Auracher, H., Pool Boiling at High Heat Fluxes (Part II): Modeling and Identification of Two Phase Flow Characteristics Close to the Heater Surface, IIR Int. Conf. Thermophysical Properties and Transfer Processes of New Refrigerants, Paderborn, Germany, pp 430-439, 2001.
- [7] Garnier, C., Lance, M. & Marié, J. L., Measurement of local flow characteristics in buoyancy-driven bubbly flow at high void fraction, Exp. Thermal Fluid Sci., in print, 2002.
- [8] Stutz, B. & Reboud, J. L., Experiments on unsteady cavitation, Experiments in Fluids, 22, pp. 191-198, 1997.
- [9] Arosio, S., Bertola, V. & Fossa, M., Comparative Analysis of Intermittent Air-Water Flow Structure by means of Different Measurement Techniques, Two-Phase Flow and Experimentation, pp. 1359-1364, 1999.
- [10] Kim, S., Fu, X. Y., Wang, X. & Ishii, M., Development of the miniaturized four-sensor conductivity probe and the signal processing scheme, Int. J. Heat and Mass Transfer, Vol 43, Iss 22, pp. 4101-4118, 2000.
- [11] Huang, Z. L., Yoyoka, S. & Shoji, M., Experiment on Steady Pool Transition Boiling of Water on a Horizontal Copper Heated Surface, JSME Int. Journal, pp. 896-903, 1994.
- [12] Buchholz, M., Lüttich, T., Mhamdi, A., Auracher, H. & Marquardt, W., Pool Boiling at High Heat Fluxes (Part I): Local Temperature and Heat Flux Fluctuations at the Heater Surface, IIR Int. Conf. Thermophysical Properties and Transfer Processes of New Refrigerants, Paderborn, Germany, pp. 420-429, 2001.

MEASUREMENTS OF THREE-DIMENSIONAL FLOW PHENOMENA IN MULTI-PHASE FLOW BY X-RAY PARTICLE TRACKING VELOCIMETRY

A. Seeger, K. Affeld, U. Kertzsch, L. Goubergrits¹⁾, and E. Wellnhofer²⁾

¹⁾ Biofluidmechanics Laboratory, Charité,
Spandauer Damm 130, D-14050 Berlin, Germany
Phone: +49 30 450 553 808, Fax: +49 30 450 553 938,
E-mail: axel.seeger@charite.de

²⁾ German Heart Institute Berlin,
Augustenburger Platz 1, 13353 Berlin, Germany

ABSTRACT

Multi-phase reactors are widely used in biotechnology and chemical engineering. Despite their widespread use, the fluid mechanics in these apparatuses is not yet fully understood. Therefore, the investigation of the fluid mechanics is necessary. This investigation with standard methods - optical methods - is yet difficult and, for high void fractions, impossible. This is caused by the fact that reflection and refraction of light occur on the gas-liquid boundaries. Moreover, a high solid hold-up yields additional problems, because the solid makes the multi-phase system either opaque or leads to further refraction and reflection. These effects do not occur applying X-rays instead of light. X-rays penetrate a multi-phase flow in straight lines.

We developed a new velocimetry method based on X-rays. The multi-phase flow in question is seeded with X-ray absorbing tracer particles. These particles have the same density and size as the solid. Therefore, the solid motion is measured by the knowledge of the X-ray absorbing particle motion. The particle motion is observed from two directions using X-rays to allow a three-dimensional particle tracking. Velocity fields are calculated from the trajectories. The method was already successfully applied to bubble columns to measure the liquid velocity.

The method proved to be suitable to measure the velocity of the solid phase in a multi-phase flow. It is a 3-dimensional, 3-component method. The main advantages, compared to optical methods, is that no reflection and refraction problems arise at phase boundaries. Therefore, a large void fraction or solids do not limit the application of the method. Like optical methods, the technique is non-intrusive. The time for the assessment of a 3-dimensional velocity field is short (less than 20 seconds). Further developments will allow measuring the liquid and the solid motion simultaneously.

1. INTRODUCTION

Multi-phase reactors are widely used in biomedical and chemical engineering [1]. Despite their widespread use, the fluid mechanics in these apparatuses is not yet fully understood. Many investigators try to model the flow within multi-phase reactors by computational fluid dynamics (CFD) [2]. However, the experimental validation of the results of these simulations is still needed to be done due to the complexity of the system [1]. This experimental validation is yet difficult due to a lack of adequate measurement techniques [3].

In this paper, we are dealing with the flow in multi-phase reactors (three phases: gas/liquid/solid). The fluid mechanics in these devices can be investigated by optical techniques [1] [3] [4]. However, all these methods are based on visible light (Laser Doppler Velocimetry, Particle

Image Velocimetry, Particle Tracking Velocimetry) and face the problem of reflection and refraction of light on the gas-liquid boundaries. Therefore, these methods can only be applied when no bubbles obscure the path of light. Moreover, solids obscure the path of light, too and, in the case of opaque particles, do not allow the light to be transmitted. That means that these methods are only applicable for small void fraction and small solid hold-up.

Another measurement method is the Computer Aided Radioactive Particle Tracking (CARPT, [5]). This method works independently from solid hold-up and/or void fraction. However, this method is a single point measurement method and it takes up to 24 hours to assess a velocity field.

The only multi-point measurement method, which works independently from the void fraction and solid hold-up, is X-ray based Particle Tracking Velocimetry (XPTV). X-rays penetrate a multi-phase flow in straight lines. The method is a 3D-3C (three-dimensional / three component) method and allows to obtain a mean velocity field of the investigated area within 20 seconds. So far, this method was only applied to measure the liquid velocity in a multi-phase flow [3]. However, the method can also be applied to measure the solid velocity in a multi-phase flow. Results obtained by this method are subject of this paper. Other X-ray based methods applicable to multi-phase flows are described in [6].

2. METHOD

2.1. Measurement principle

The multi-phase flow is seeded with X-ray absorbing tracer particles. These particles have the same density and size as the solid. It is assumed that the tracer particles move as the solid. Therefore, by the knowledge of the tracer particle motion, the solid motion is measured. X-rays penetrate a gas-liquid interface in straight lines. Thus the above-described problems of the observation using visible light - refraction and reflection on phase boundaries - do not appear.

A typical experimental set-up is shown in Figure 1. Two X-ray-sources S1 and S2 generate X-rays, which are directed through the multi-phase reactor onto the image intensifiers. The image intensifiers convert X-rays into visible light and intensify it. Digital cameras behind the image intensifier record the images. An X-ray absorbing particle, represented by point P, is mapped on the two image intensifiers I1 and I2 generating the points P1 and P2. The point P is reconstructed from P1 and P2. By recording image series, the motion of a particle can be observed. The velocity of the particle can be obtained by its displacement and the time difference between the images. By the observation of many tracer particles, a vector field can be calculated. The method is closely related to 3D optical PTV.

2.2. Measurement device

A medical X-ray device (Philips Integris BH 3000) was used for the investigations. It is clinically used for flow visualization in human coronary blood vessels and heart ventricles. The German Heart Institute in Berlin generously provided access to the X-ray device during off hours. The input screen of the image intensifier had a size of 23 cm x 23 cm. The image intensifier had a resolution of about 1024x1024 Pixel. Image intensifiers, CCD-camera, and frame grabbers transformed the X-ray intensities into digital 8 bit grayscale images. The CCD-camera had a resolution of 512x512 pixels. 25 image pairs per second were taken. An image series of up to 1000 images (500 image pairs) could be acquired. The investigated area had a size of about 104 mm x 104 mm x 104 mm.

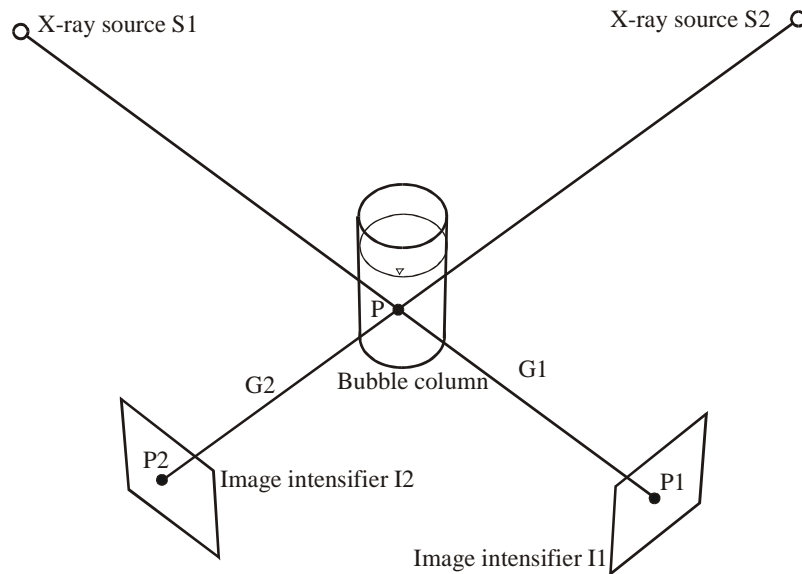


Fig. 1: Experimental set-up.

2.3. Tracer particles

The solid phase consisted of particles made of polymethylmethacrylate. The cubic particles had a side length of 2 mm and a density of about 1.19 g/cm^3 . The X-ray absorbing tracer particles also had a cubic shape with a side length of 2.1 mm. They were made of polyurethane foam having a density of 0.6 g/cm^3 with a cylindrical insert of a tin alloy (60 % tin, 38 % lead, and 2 % copper). The alloy absorbs X-rays, while the foam makes the cubes buoyant. The cylindrical insert had a diameter of 0.5 mm. The integral density of the particle was about 1.15 g/cm^3 .

2.4. Software

The particle recognition, the particle tracking, the distortion correction, the isocenter correction as well as the three-dimensional reconstruction are described in detail in [3]. However, the isocenter correction was improved since that time and the number of reconstructed tracer particles was increased by up to 50 % compared to the algorithm described in [3]. Therefore, this is described in more detail. The straight lines connecting the centers of the image intensifiers and the corresponding X-ray sources ideally touch each other at the so-called isocenter. However, in reality they do not. The isocenter correction corrects an inaccurate positioning of the two "X-ray source - image intensifier" units. Therefore, images of about 300 randomly distributed points in space were taken. One needs to know, which point on image intensifier I1 corresponds to which point on image intensifier I2. Straight lines between the mapped points on the image intensifiers and the X-ray sources were calculated. The distance between the corresponding lines was determined. A virtual change of the positions of the image intensifiers and of the X-ray sources minimized this distance. However, it has to be considered that: (1) The virtual position change of the X-ray sources and the image intensifiers needs to be small. (2) It is necessary to maintain a true scale. This was possible since the distances among the randomly distributed points in space were known. The algorithm yielded the new co-ordinates of the X-ray sources and the image intensifiers. The mean initial distance between the straight lines was 16 mm. After the isocenter correction the mean distance was 1.8 mm. One has to consider that the points in space are recognized by a particle recognition algorithm, which has, as well as the distortion correction, an influence on the preciseness of the algorithm. The whole algorithm reconstructed between 59 % and 76 % of the recognized tracer particles.

2.5. Multi-phase reactor

A cylindrical multi-phase reactor was designed, Figure 2. It had an inner diameter of 104 mm and a filling height of 100 mm. 91 hypodermic needles with inner diameter of 0.34 mm were used as gas dispersers. The use of the needles guarantees a uniform gas distribution. A disc was mounted at the tip of the needles to prevent any flow between them.

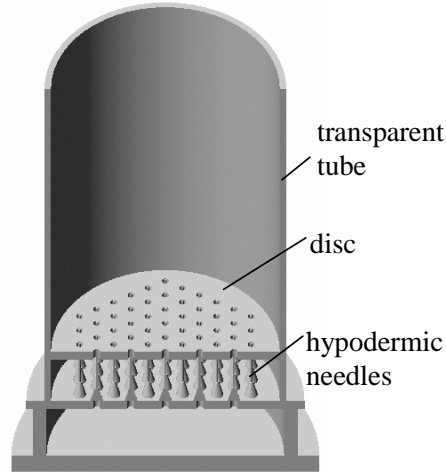


Fig. 2: Multi-phase reactor.

3. RESULTS

One liter Glycerin with a viscosity of $8.50 \cdot 10^{-4} \text{ m}^2/\text{s}$ was used as liquid. The use of glycerin resulted in a slower flow and thus an easier particle tracking. A small velocity in the multi-phase reactor is necessary, because the used system takes only 25 image pairs per second. 100 g particles of polymethylmethacrylate were used as solid phase. The superficial gas velocity was set to 1 mm/s. The resulting integral void fraction was 2 %. The integral solid hold-up was 7.5 %. 460 image pairs were taken. This corresponds to a measurement time of about 18.4 s. 80 X-ray absorbing tracer particles were added to the flow.

The evaluation of the measurement yielded 29749 trajectory vector counts (75.9 % of the recognized tracer particles). The evaluation with the old isocenter correction of [3] found only 20239 trajectory vector counts. A photo of the flow was taken during the measurement. It is shown in Figure 3 (left-hand side). Behind the experiment, a black and white grid (mesh width: 1 cm) was placed in the middle of the reactor to show the distortion and that optical methods would encounter big problems. Figure 3 shows a photo of the grid (right-hand side).

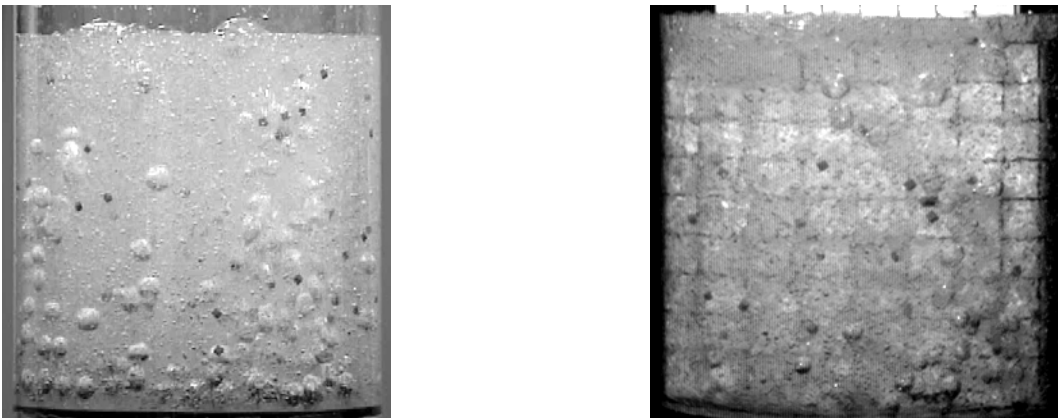


Fig. 3: Photo of the flow and photo of the flow in front of a paper grid.

Some of the obtained particle trajectories are shown in Figure 4 (left-hand side). A velocity field averaged over the measurement time was calculated. It is also shown in Figure 4 (right-hand side). Both images are color-coded. In [7] it was shown that the assumption of a constant flow field of 18.6 seconds in a similar flow is true.

Figure 5 shows the standard deviation of the absolute value of the velocity. The areas where the standard deviation is a special limit is shown as an isosurface. The standard deviation exceeds the limit in the volume inside the isosurface. Figure 5 shows the area, where the standard deviation exceeds 0.012 m/s. The time and space averaged standard deviation is 0.0104 m/s.

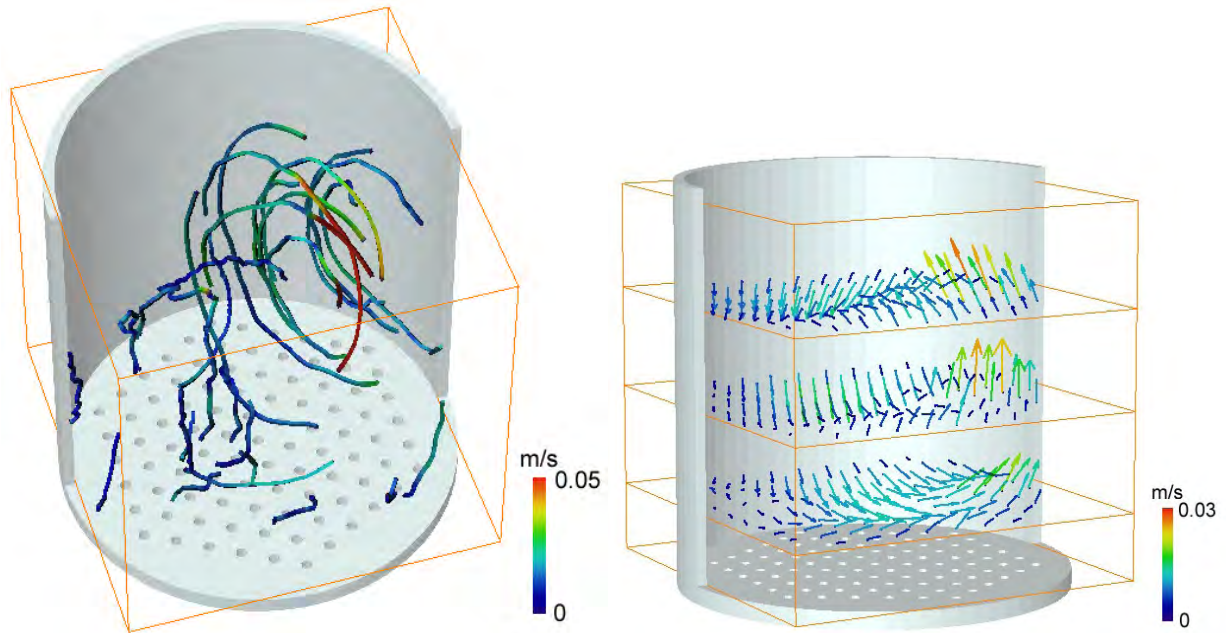


Fig. 4: Particle trajectories (left) and velocity field (right) for the solid phase.

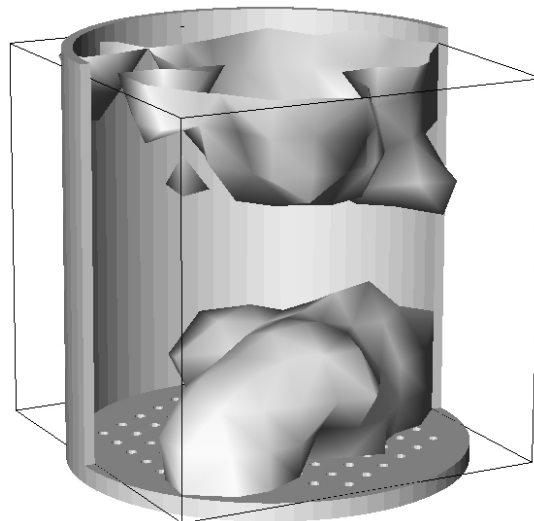


Fig. 5: Isosurface of a standard deviation of 0.012 m/s.

4. CONCLUSIONS

X-ray Particle Tracking Velocimetry was successfully applied to a multi-phase flow. The method is suitable to measure the velocity of the liquid phase and of the solid phase. It is a 3-dimensional, 3-component method. The main advantages, compared to optical methods, is that no reflection and refraction problems arise at phase boundaries. Therefore, a large void fraction or opaque fluids do not limit the application of the method. Like optical methods, the technique is non-intrusive. The time for the acquirement of a 3-dimensional velocity field is short.

Further developments will include a simultaneous velocity measurement of the liquid and the solid phase. To do this, tracer particles with different X-ray absorbing elements (size, shape) have to be designed and manufactured in order to identify the tracer particles properly. The method is also applicable to flows without optical access.

REFERENCES

- [1] Dudukovic, M. P., Larachi, F., & Mills, P. L., Multiphase reactors - revisited, *Chemical Engineering Science*, 54, pp. 1975-1995, 1999.
- [2] Jakobsen, H. A., Sannæs, B. H., Grevskott, S. & Svendsen, H. F., Modeling of Vertical Bubble-Driven Flows, *Industrial & Engineering Chemistry Research*, 36, pp. 4052-4074, 1997.
- [3] Seeger, A., Affeld, K., Goubergrits, L., Kertzscher, U., & Wellnhofer, E., X-ray-based assessment of the three-dimensional velocity of the liquid phase in a bubble column, *Experiments in Fluids*, 31, pp. 193-201, 2001.
- [4] Chen, R.C., Reese, J., & Fan, L. S., Flow structures in a three-dimensional bubble column and three-phase fluidized bed, *AIChE Journal*, 40, pp. 1093-1104, 1994.
- [5] Larachi, F., Chaouki, J., & Kennedy, G., 3D-Mapping of solids flow fields in multiphase reactors with RPT, *AIChE Journal*, 41(2), pp. 439-443, 1995.
- [6] Seeger A., Affeld K., Goubergrits L., Kertzscher U., Wellnhofer E. & Delfos R., X-ray based flow visualization and measurement: Application in multi-phase flows. *Annals of the New York Academy of Science*, 972, in press, 2002.
- [7] Seeger, A., Affeld, K., Kertzscher, U., Goubergrits, L., & Wellnhofer E., X-ray based velocimetry measurements in multi-phase flows - an alternative to optical methods?, 11th International Symposium on Applications of Laser Techniques to Fluid Mechanics, 8th - 11th July 2002, Lisbon.

VISUALIZATION AND VOID FRACTION MEASUREMENT OF GAS-LIQUID TWO-PHASE FLOW IN HEAT EXCHANGERS BY NEUTRON RADIOGRAPHY

H. Asano¹⁾, N. Takenaka¹⁾, T. Fujii¹⁾ and K. Takeshima²⁾

¹⁾ Department of Mechanical Engineering
Kobe University

Rokkodai-cho 1-1, Nada, Kobe

Hyogo 657-8501, Japan

Phone: +81 78 803 6122, Fax: +81 78 803 6122,

E-mail: asano@mech.kobe-u.ac.jp

²⁾ Department of Mechanical Engineering
Kochi National College of Technology

Monobe 200-1, Nankoku

Kochi 783-8508, JAPAN

ABSTRACT

Gas-liquid two-phase flows in a plate heat exchanger and a vertical tube with a wire coil were visualized by a neutron radiography method to clarify the effect of configurations on phase distribution. For plate heat exchangers, adiabatic air-water flows and boiling R141b two-phase flows in a simulated test section with a single channel were visualized. From the results, it was shown that the effect of inlet configuration on the phase distribution was strongly dependent on the inlet configuration and inlet flow conditions. Especially, in the case where the incoming flow was a gas-liquid two-phase flow, liquid stagnation in an enlarged inlet section caused unsymmetrical phase distribution. Liquid mixing in the ribbed channel was weak. On the other hand, for a vertical tube with a wire coil, adiabatic air-water flows were visualized and cross-sectional void fraction distributions were calculated by a CT method from projection images from only one direction. The effect of a wire on the liquid distribution was clearly shown. Under the high gas velocity condition, liquid fraction on the wall at the upstream of the wire was lower than that at the downstream.

1. INTRODUCTION

Recently, conduit configurations of heat exchangers become more complicated and smaller for the compactness and the higher heat transfer performance. On the other hand, obstacles are often placed in a conduit for heat transfer enhancement or as fixing tool in tube banks. In the case where working fluids flow in a heat exchanger as a gas-liquid two-phase flow, the flow and the heat transfer characteristics strongly depend on the flow pattern and the liquid distribution. Since flow pattern is influenced by conduit configurations, it is important to check the flow patterns of gas-liquid two-phase flows in order to develop and improve heat exchangers, and it is necessary to clarify the effect of a conduit configuration on the flow patterns. Flow visualization is very efficient tool to understand flow characteristics. However, since heat exchangers are usually made by metallic material, it is difficult to simulate by a transparent system.

Radiography is a visualization technique by using the difference in attenuation rate of a radio ray to irradiated materials. X-ray, γ -ray, and thermal and fast neutron rays can be used as a radio ray. Radiography using each ray have been applied to three-dimensional measurements of gas-liquid two-phase flows [1-4].

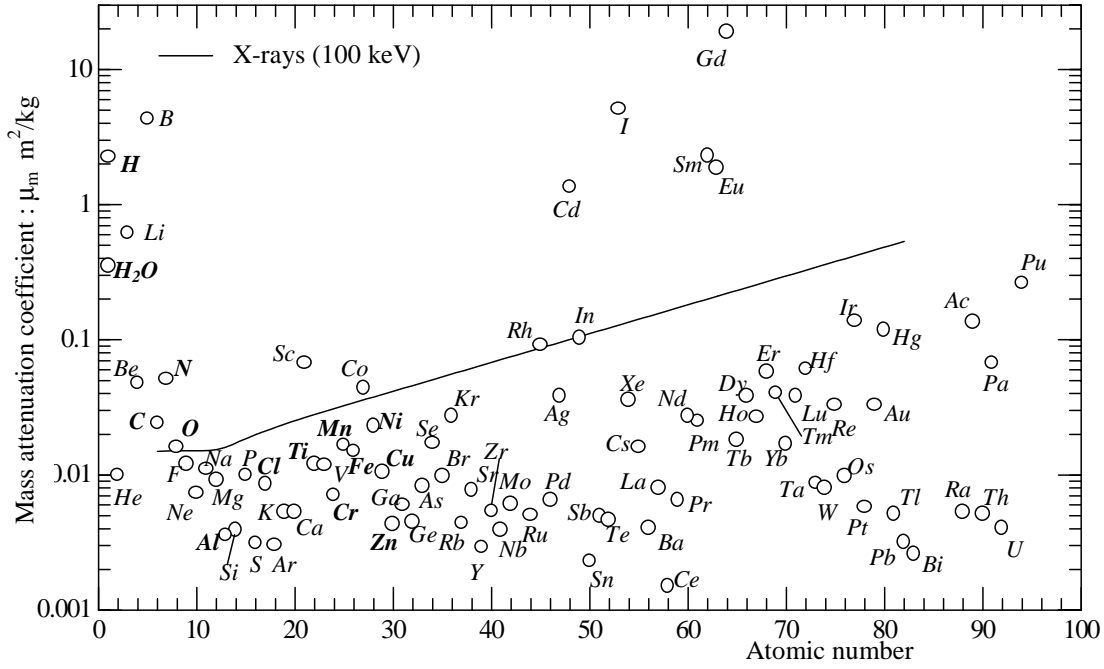


Figure 1: Mass attenuation coefficients of thermal neutron and X-ray.

This study deals with the visualization of gas-liquid two-phase flows by a thermal neutron radiography method. The results on flow visualizations and void fraction measurements of gas-liquid two-phase flows in a plate heat exchanger and a vertical tube with a wire coil are presented. For a plate heat exchanger, adiabatic air-water and boiling R141b two-phase flows in simulated test section with a single channel were visualized, and the effects of the inlet configuration and the inlet conditions on void fraction distributions are considered. On the other hand, for a vertical tube with a wire coil, cross-sectional void fraction distributions of adiabatic air-water two-phase flows were calculated by a CT method, and the effect of a wire coil was considered.

2. NEUTRON RADIOGRAPHY

Radiography is a technique to visualize the structure of an object by the difference of attenuation rates of radio rays to the materials of object. A radio ray is attenuated exponentially in an object depending on the characteristics of the radio ray and the materials of object. The radio ray intensity through an object is expressed as

$$I = I_0 \exp(-\rho\mu_m t) \quad (1)$$

where I_0 is the irradiated intensity of a ray, and t is the thickness of the object. ρ and μ_m are the density and the mass attenuation coefficient, respectively, and are physical properties of the object. The mass attenuation coefficient of object is determined by both the radio ray and the materials. The mass attenuation coefficients of thermal neutron rays for various elements are plotted in Fig. 1 against the atomic number. Those of a X-ray of 100 keV are also plotted by a solid line. The mass attenuation coefficients of X-ray increase with atomic number. On the other hand, those of neutron rays depend strongly on each element. They are large for small atomic number elements of H, B and Li and for some special elements, such as Cd, Gd, but they are small for metal materials used usually as piping element, such as Fe, Al, Cu, Ni. Therefore, it can be stated that the neutron radiography method is suitable for visualizing liquid behavior in a metallic vessel.

The neutron ray intensity through two-phase flow and wall of vessel is expressed as

$$I(x, y) = I_0(x, y) \exp(-\rho_w \mu_w t_w(x, y) - (1 - \alpha(x, y)) \rho_L \mu_L t_c(x, y)) + O_{ns}(x, y) \quad (2)$$

where $\alpha(x, y)$ and $t(x, y)$ are the void fraction and the thickness along the passage of neutron beam. The subscripts of w , L , and c denote wall, liquid phase and conduit, respectively. $O_{ns}(x, y)$ is the offset value due to neutron scattering in object. The offset values depend on a liquid phase distribution and a conduit configuration. In this equation, the attenuation of neutron beam in gas is neglected, because gas density is relatively small compared to liquid density. In a real-time neutron radiography system, the profile of neutron beam intensity through the object is converted to a visible image by a scintillation converter and was recorded by a camera. Since brightness of visualized image is in proportion to the neutron ray intensity on the scintillation converter, two-dimensional distribution of brightness in a two-phase flow image is expressed as

$$S_{TP}(x, y) = G(x, y) \exp(-\rho_w \mu_w t_w(x, y) - (1 - \alpha(x, y)) \rho_L \mu_L t_c(x, y)) + O_{TP}(x, y) \quad (3)$$

where $G(x, y)$ is the gain that is dependent on irradiated neutron beam intensity $I_0(x, y)$ and performance of camera system. $O_{TP}(x, y)$ is the offset value in brightness due to the neutron scattering in a object, the scattering of visible ray in a camera obscure, and a dark current of a camera system. In the case where a test section is filled with liquid, i.e., $\alpha(x, y) = 0$,

$$S_0(x, y) = G(x, y) \exp(-\rho_w \mu_w t_w(x, y) - \rho_L \mu_L t_c(x, y)) + O_0(x, y) \quad (4)$$

On the other hand, for $\alpha(x, y) = 1$,

$$S_1(x, y) = G(x, y) \exp(-\rho_w \mu_w t_w(x, y)) + O_1(x, y) \quad (5)$$

If the irradiated neutron beam intensity and the condition of a camera system are stable enough, the gain can be stated constant. Therefore, void fraction distribution can be calculated by using the following equation obtained from the above three equations, Eq. (2) to (4), without the knowing of the configuration and the material of test section, the properties of working fluids, the irradiated neutron beam intensity, and the characteristics of a camera system.

$$\alpha(x, y) = \frac{\ln[(S_{TP}(x, y) - O_{TP}(x, y)) / (S_0(x, y) - O_0(x, y))]}{\ln[(S_1(x, y) - O_1(x, y)) / (S_0(x, y) - O_0(x, y))]} \quad (6)$$

However, the neutrons scattering in the object and the optical rays scattering in the camera obscure depend on the object. The offsets due to these effects are different in three images. Moreover, the offset at the point (x, y) is affected by the other points over the image. Therefore, it is necessary to measure the offset value $O(x, y)$ under the each condition as well as the brightness $S(x, y)$ simultaneously in one image for the quantitative measurement of void fraction. In this study, the umbra method developed by Takenaka, et al. [5] was applied to measure the offset value for the quantitative measurement.

Flow visualization experiments were carried out by utilizing the real-time thermal neutron radiography facility [6] in Japan Atomic Energy Research Institute shown in Fig. 2. This system uses the reactor core of the research reactor JRR-3M as a neutron source. This system can provide the high quality thermal neutron beam, that is, high neutron fluxes of 1.5×10^8 neutron/(cm²·s), high parallelism of $L/D = 170$, and stable intensity. Neutron beam was irradiated to an object horizontally, and the radiograph was obtained on a scintillation converter \underline{Z} as a visible image. The irradiated area is 255 mm \times 305 mm. Two types of camera were used, that is, a SIT-tube camera for visualization of dynamic behaviors and a cooled CCD camera for quantitative measurement with high resolution in both space and brightness. By the SIT-tube camera, continuous images of 30 frames per second were photographed and each frame was digitized with 8 bit intensity levels (256 gradations). On the other hand, by the cooled CCD camera, still images consisting of 1000 \times 1018 image elements were photographed with an exposure time of 4 seconds, and were digitized with 14

bit intensity levels (16384 gradations). The size of visual field in the present visualization was 180 mm × 180 mm, so the spatial resolution of void fraction distribution was estimated about 180 μm as the size of visual field per image element. The spatial resolution of scintillation converter is about 100 μm. There are many distributed white spot noises in the original image by a cooled CCD camera. These noises were removed by a morphological filter [7].

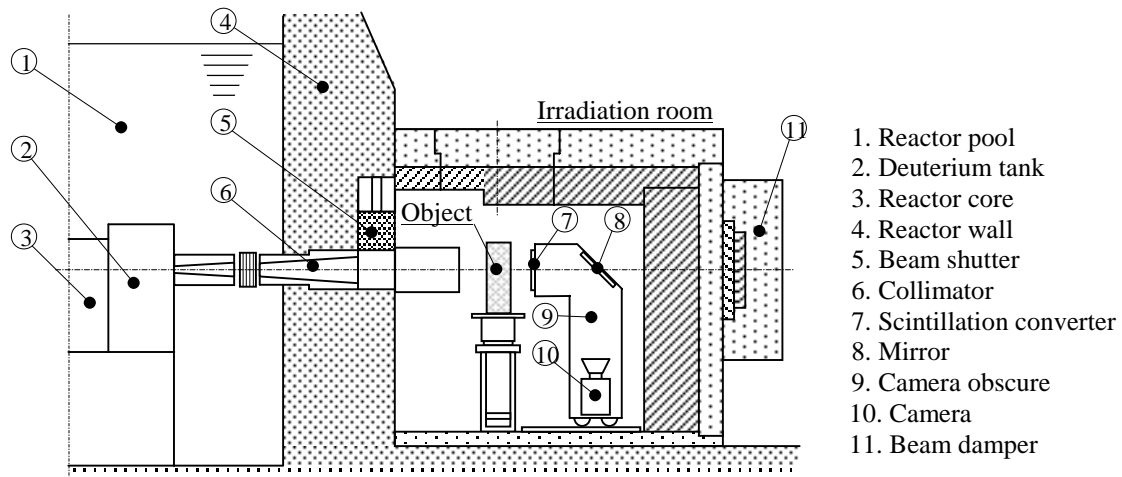


Figure 2: Real-time thermal neutron radiography facility in JRR-3M.

3. PLATE HEAT EXCHANGER

3.1. Background and subjects

Compact plate heat exchangers are often used in refrigerating cycle for the compactness and the improvement of heat transfer performance. The heat exchangers are made from 20 to 280 sheets of wavy thin stainless steel sheets. Working fluids flow through the gaps between these sheets. The channels of each fluid are arrayed alternately, that is, a plate heat exchanger has many parallel channels. Each channel has netlike conduits formed by wave configuration. The configuration leads to larger heat transfer area and higher heat transfer coefficient, but also induces larger pressure loss. Therefore, it is necessary for an increase in heat transfer rate to increase the parallel channels. In order to develop and improve a plate heat exchanger for gas-liquid mixtures, it is important to understand phase distribution characteristics of working fluid not only into parallel channels but also in each channel, and to clarify the effect of configurations and flow conditions on the phase distribution.

Flow characteristics of gas-liquid two-phase flows in simulated plate heat exchangers with a single channel were investigated. Dynamic flow behaviors of adiabatic air-water two-phase flows and boiling two-phase flows were visualized, and two-dimensional void fraction distributions were calculated via some image processing techniques. For adiabatic air-water two-phase flows, average void fraction in the ribbed channel were measured and correlated. From the measured results, the effects of the inlet configuration and the flow condition on the flow characteristics such as phase distribution are shown.

3.2. Experimental apparatus and methods

A schematic diagram of the experimental apparatus for adiabatic two-phase flows is shown in Fig. 3 (a). Water and air were used as the working fluids. Air was fed to a mixing section **4** from an air compressor through a pressure regulating valve **3** and a gas flow meter. Water in a tank **1**, was fed by a pump **2** to the mixing section **4** through a water flow meter. Two-phase flows formed in the mixing section **4** flew into the lower part of a test section placed vertically in an irradiation room for

a neutron radiography. The test section was made of aluminum plates. The configuration is also shown in Fig. 3 (a). Ribs of 8 mm in width, of 2.5 mm in height, and of 30° in chevron angle, were cut on the aluminum plates. The ribs patterns on the two plates are upside-down, i. e., Λ-shape and V-shape. These ribs shape netlike conduits. The average hydraulic diameter of the ribbed channel is 4.65 mm, and the depth of the inlet section is 5.0 mm. Two-phase mixtures flow into the test section from the lower and discharged from the upper.

The experimental conditions were the liquid volumetric fluxes, j_L , of 0.02 and 0.04 m/s and the gas volumetric fluxes, j_G , of 0.9 to 8 m/s. Volumetric fluxes are defined by the following equations.

$$j_L = Q_L/A, \quad j_G = Q_G/A \quad (7)$$

where Q is volumetric flow rate [m³/s], and A is the average cross-sectional area [m²] of the ribbed channel.

The schematic diagram of experimental apparatus for boiling two-phase flows is shown in Fig. 3 (b). Hydro-chloro-fluoro-carbon R141b (CFCl₂-CH₃) was used as the working fluid under the atmospheric pressure. R141b stored in a tank 1 was fed by a gear pump 2 to the test section through a liquid flow meter 3 after setting an inlet condition by a heater 4. The test section was made of copper plates with ribs shown in Fig. 3 (b). The test section was heated by rubber heaters 7 put on the both outsides of the copper plate with a constant wall temperature of about 50°C. The two-phase flow exhausted from the test section was condensed in a condenser 8, and returned to a tank 1.

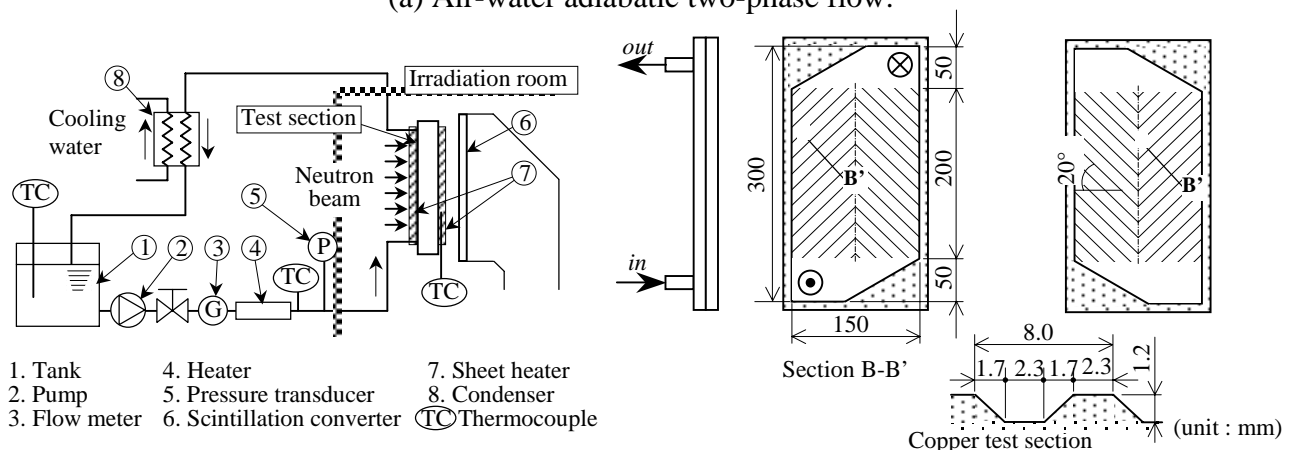
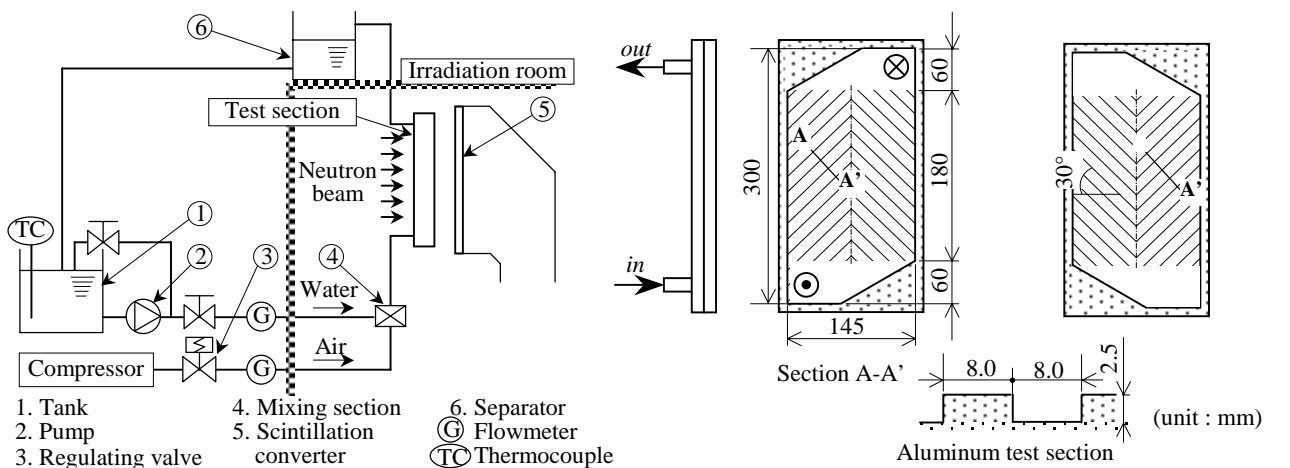


Figure 3: Schematic diagram of experimental apparatus of plate heat exchanger.

3.3. Results and discussion

Adiabatic air-water two-phase flow Figure 4 shows the original image by the SIT-tube camera. Liquid flow was clearly visualized. Continuous images of calculated void fraction distributions are shown in Figs. 5 at intervals of 1/30 second. Void fraction distributions are shown on a grayscale, that is, void fraction is 0 at black part and increase with an increase in brightness. These figures show qualitative distributions calculated by using Eq. (6) with a dark current as offset value. A gas volumetric flux j_G and a liquid volumetric flux j_L were 0.9 m/s and 0.04 m/s, respectively. It can be seen in these images that air was flowing up like as a large bubble in water intermittently.

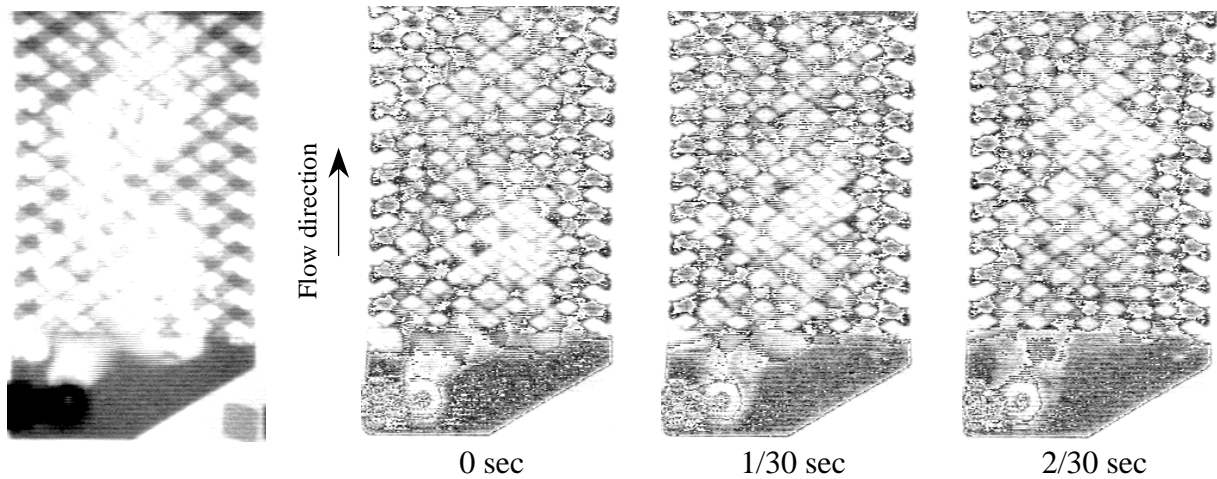


Figure 4: Original image by SIT-tube camera (30 fps, $j_G = 0.9$ m/s, $j_L = 0.04$ m/s). Figure 5: Continuous image of calculated void fraction distribution ($j_G = 0.9$ m/s, $j_L = 0.04$ m/s).

Figures 6 (a) to (h) show time averaged void fraction distributions in 4 seconds for a constant j_L of 0.04 m/s and varied j_G of 0.9 to 8.0 m/s. Flow patterns of gas-liquid two-phase flow were classified into two cases based on visualized images of dynamic behaviors. At low gas volumetric flux ($j_G = 0.9$ m/s, Fig. 6 (a)), gas flows in continuous liquid phase intermittently as shown in Figs. 5. On the other hand, at high gas volumetric flux ($j_G = 8.0$ m/s, Fig. 6 (h)), gas and liquid phases tended to flow straight upward separately, and the most of liquid phase flew along both sides and the center of the test section. The transition boundary of flow patterns was around the j_G of 3 m/s.

Under every condition, the liquid distribution was unsymmetrical being inclined toward the left side. It can be said that the liquid stagnation at the test section inlet caused the unsymmetrical distributions. The unsymmetrical distributions were kept to the test section outlet because of the weak liquid mixing in the ribbed channel. In design of heat exchangers for single-phase flow, inlet sections are usually enlarged for homogenous distributions in flow rate. However, for gas-liquid flows, especially in high gas velocity condition, channel enlargement leads to decrease the momentum of two-phase mixture, and gas and liquid phases are liable to separate by gravity and make a liquid stagnation. If working fluids flow into a heat exchanger as a gas-liquid mixture, an inlet configuration without enlargement will be desirable for the homogenous distribution.

Flow direction distributions of cross-sectional average void fraction, $\bar{\alpha}$, are plotted in Fig. 7 against the distance y indicated in Fig. 6 (a). Plotted values show the quantitatively measured results by the umbra method. The void fraction was high just upstream of $y = 0$, because the cross-sectional area became smaller at $y = 0$ and the gas phase stagnated. In the ribbed channel ($y > 0$), the void fraction periodically fluctuated in a constant range. These fluctuations might be due to the stagnant liquid or gas at the cul-de-sac on the both sides of the test section and the change in cross-sectional area.

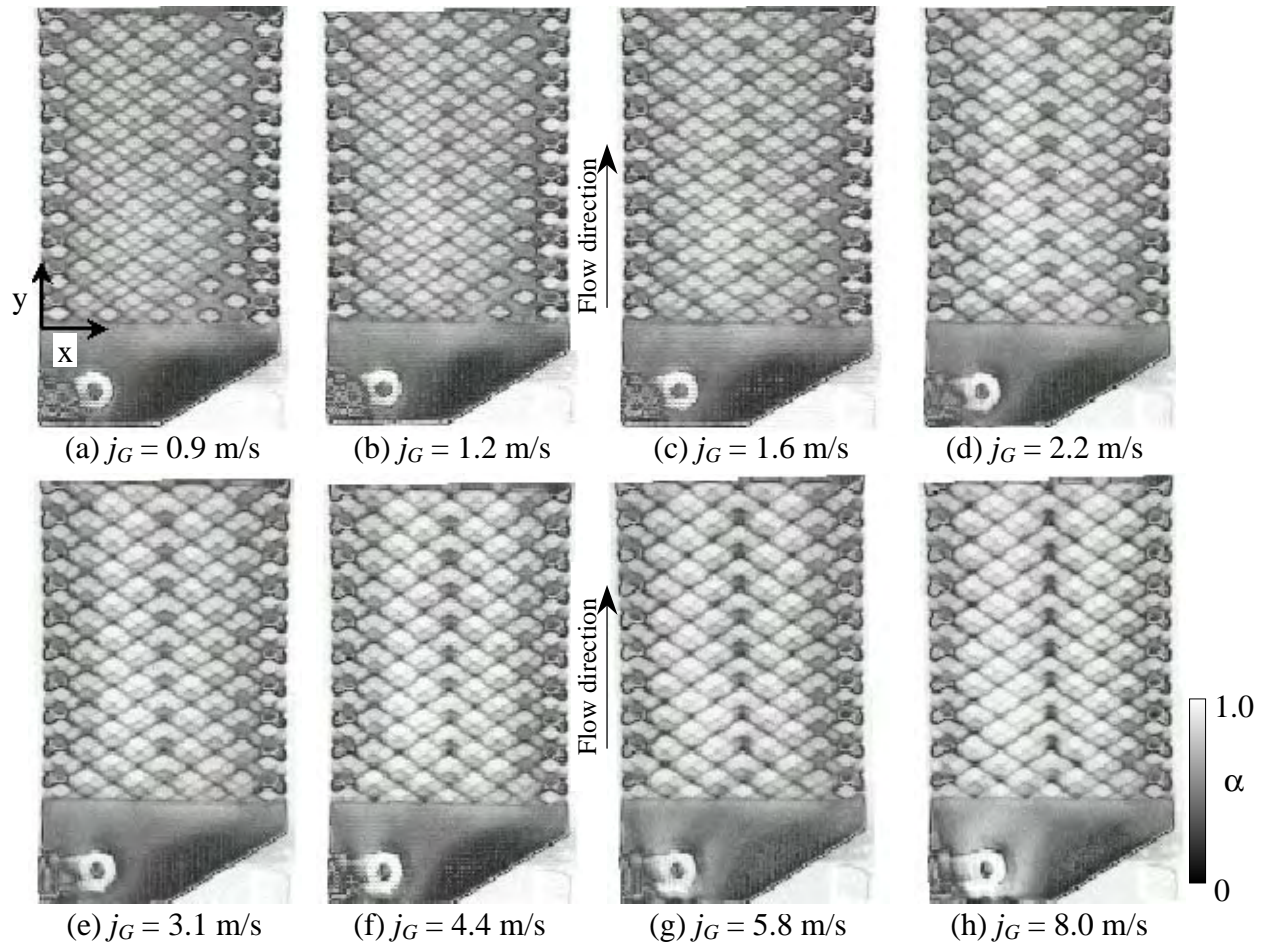


Figure 6: Two-dimensional distributions of time-averaged void fraction ($j_L = 0.04$ m/s).

Averaged void fractions in the ribbed channel, α_{ave} , were correlated based upon the drift flux model as shown in Fig. 8. In the drift flux model, the relation between mean gas velocity $Q_G/(\alpha_{ave}A) = j_G/\alpha_{ave}$ and total volumetric flux $j_G + j_L$ is shown by the following equation.

$$j_G/\alpha_{ave} = C_0(j_L + j_G) + V_{Gj} \quad (8)$$

where C_0 is a distribution parameter which depends on phase distribution and volumetric flux, and V_{Gj} is a average drift velocity. The semi-empirical correlations for vertical upward flows in a circular pipe by M. Ishii [7] and the correlation on the homogenous model were plotted as bold lines and a broken line, respectively. Generally, the values V_{Gj} for the experimental results were larger than those by Ishii's equation. The netlike complicated conduits might cause the increase. Considering the dependency of flow patterns, at the lower gas volumetric flux of $j_G \leq 3.0$ m/s with gas intermittent flows, the effect of j_L on the average void fraction was little. The tendency was the same with that for a slug flow shown in Ishii's model qualitatively. On the other hand, at the higher gas volumetric flux of $j_G > 3.0$ m/s, the effect of j_L appeared just as the correlation curve for an annular flow in Ishii's model, because both phases flow continuously.

Boiling two-phase flow The measured void fraction distributions of boiling two-phase flows are shown in Figs. 9 (a) and (b). In Fig. 9 (a), the incoming flow was a two-phase mixture with the quality of 0.3. Fig. 9 (b) shows the case where the incoming flow was a subcooled liquid with the subcooling of 17 K. In Fig. 9 (a), the liquid fraction distribution was unsymmetrical, i. e., the liquid fraction on the right side was higher than that on the left side in the whole test section. Most of liquid phase tend to flow along the right side due to the existence of liquid stagnation. It can be said

that such phase distribution was induced by the liquid stagnation at the inlet and that may reduce the performance. On the other hand, the tendency in Fig. 9 (b) was different from that in Fig. 9 (a). The black area where the liquid fraction might be high was larger at the center. This means that the liquid flow rate must be larger at the center than at both sides.

That is to say, it is necessary to design the inlet configuration according to the inlet condition. For liquid single-phase flow at the inlet, the design for homogenous velocity profile at the ribbed channel inlet will be effective in a manner like for single-phase flow heat exchanger. On the other hand, for gas-liquid mixture at the inlet, the design without liquid stagnation formation, such as without enlarging of conduit, will be needed.

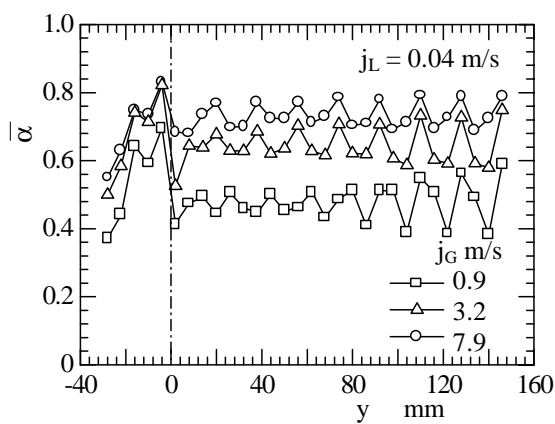


Figure 7: Flow direction distribution of cross-sectional average void fraction.

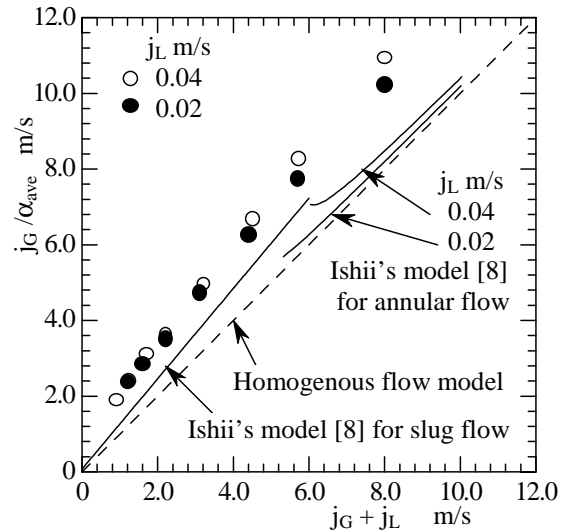
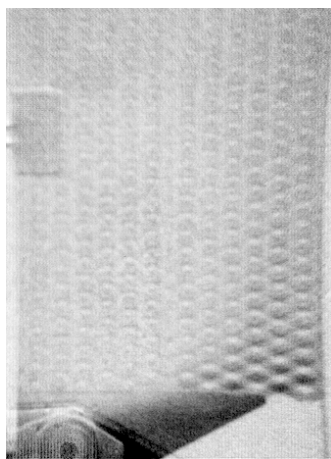
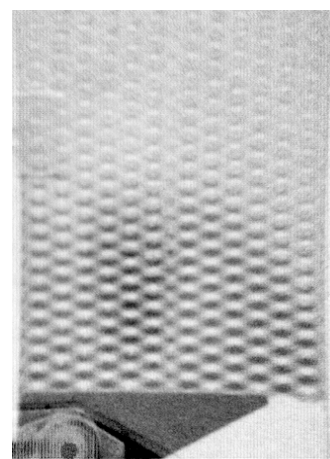


Figure 8: Average void fraction in the ribbed channel correlated based upon drift-flux model.



(a) Inflow of two-phase flow
(Mass flow rate: 0.0042 kg/s,
Inlet vapor quality: 0.3)



(b) Inflow of subcooled liquid flow
(Mass flow rate: 0.0042 kg/s,
Inlet subcooling: 17 K)

Figure 9: Two-dimensional distributions of void fraction in boiling two-phase flow.

4. VERTICAL TUBE WITH A WIRE COIL

4.1. Background and subjects

The heat transfer enhancement in a circular tube is important for compactness of heat exchangers. Several methods have been proposed and investigated such as a wire coil and a twist tape, and grooving on a wall. These configurations are usually spiral to generate swirl flows and to reduce an increase in the pressure loss. It is important to understand the flow structure in these tubes for developments and improvements. Gas-liquid two-phase flows in a vertical tube with a wire coil were visualized in this study.

From the previous experimental results [9] on boiling heat transfer characteristics in a vertical tube with a wire coil, it was shown that the wall temperature at the upstream of a wire coil was lower than that at the downstream in heating under a homogenous heat flux condition, and the temperature difference became greater with the vapor quality. Moreover, the critical heat flux was improved by about 30 % at the maximum by inserting a wire coil. Adiabatic air-water flows were visualized under the high gas volumetric flux region, and cross-sectional void fraction distributions were calculated via some image processing methods.

4.2. Experimental apparatus and methods

Water and air were used as the working fluids under atmospheric pressure and room temperature. The experimental apparatus was the same as that of a plate heat exchanger shown in Fig. 3 (a), and only the test section was replaced. Figure 10 shows an aluminum circular tube of 16 mm inner diameter and 1 mm thickness with a stainless steel wire coil of 2 mm on the inner wall. The pitch of the coil was 32 mm and the helix angle was 56.9 degree. The experimental conditions were the liquid volumetric fluxes j_L of 0.051 and 0.102 m/s, and the gas volumetric fluxes j_G of 2.0 to 61.8 m/s.

4.3. Results and discussion

Figures 11 (a) and (b) show the visualized results of the tube with the wire coil photographed by the cooled CCD camera with exposure time of 4 seconds. In the image of only the test section (Fig. 11(a)), the stainless wire coil was clearly visualized. Visualized results of gas-liquid two-phase flows are also shown in Figs. 11(b). Gas volumetric flux was varied 2.0, 10.3, and 61.8 m/s with a constant j_L of 0.102 m/s. Image become darker with thicker liquid thickness. The brightness of image in flow region increased with the increase of j_G . This means that void fraction becomes higher with j_G . Liquid thickness just downstream of the wire looks larger than that upstream of the wire. However, the effect of the wire on the cross-sectional phase distribution was not clearly shown in these images. Cross-sectional distribution is needed to evaluate the effect of a wire.

To obtain the cross-sectional distribution by radiography, other information such as projections from various directions or an assumption on phase distribution is necessary. In this case, since the conduit configuration rotates about the tube central axis periodically, a CT method can be applied to projection images from one direction on the assumption that relative cross-sectional liquid distributions to a wire coil also rotate and are kept along flow direction in fully developed flow region.

One-dimensional distributions of the cross-sectional averaged void fraction are plotted in Fig. 12 against the distance from the gas-liquid mixing section. That in a circular tube with the same inner diameter of 16 mm is also plotted. The values of j_G and j_L were the highest in this experimental range. It can be seen that void fractions are almost constant in the visualized area in each tube. The gas-liquid two-phase flow was fully developed in the visualized range. It can be assumed that relative cross-sectional liquid distributions to a wire coil are kept. Two-dimensional liquid distributions can be directly used as sinograms in a CT method. An example of liquid

thickness distribution, that is a sinogram, is shown in Fig. 13. The length of the object is equal to the half of the pitch of the wire coil, i. e., 16 mm, and the image consists of 78 pixels. That is to say, this image is equivalent to 78 projections rotating half rotation with an interval of 2.34 degrees.

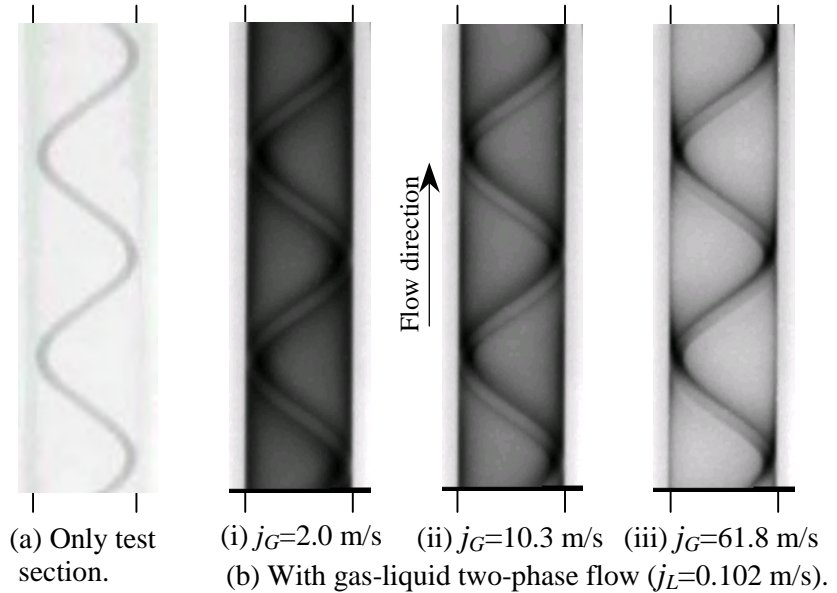
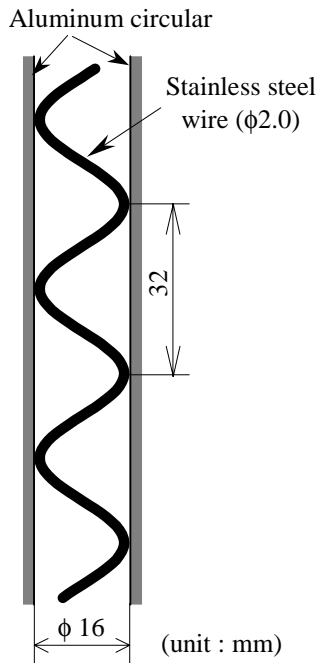


Figure 10: Configuration of circular-tube with a wire coil.

Figure 11: Visualized image of a circular-tube with a wire coil photographed by the cooled CCD camera.

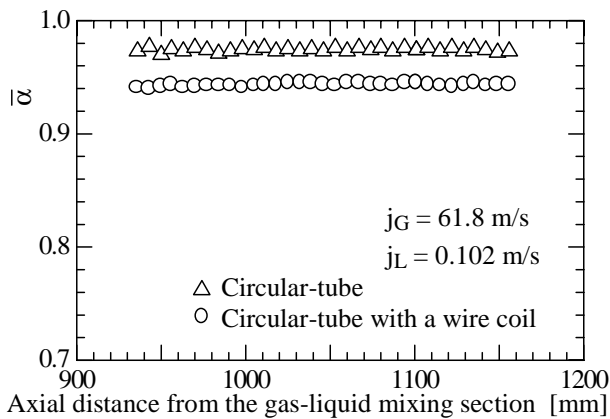


Figure 12: Axial distribution of cross-sectional average void fraction.

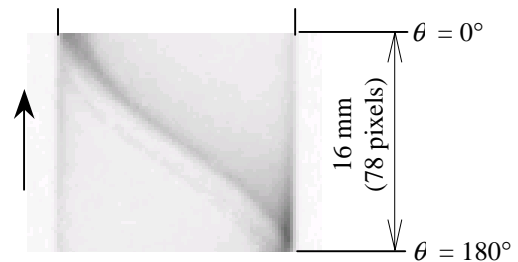


Figure 13: Example of sinogram for CT reconstruction (Profile of liquid thickness)

Calculated results of cross-sectional distribution of void fraction are shown in Fig. 14. The values were shown by a gray scale in arbitrary unit. Black rings show liquid on the inner wall. The small white oval at the left side in the black ring shows the wire. The area upside and downside of the white oval is equivalent to the upstream and downstream of the wire, respectively. That is to say, counter clockwise rotation is equivalent to the flow direction. At low gas velocity with $j_G = 2.0$ m/s, the black area near the wall was large, and the difference between the upstream and the downstream of the wire coil was small. The reason is estimated that the flow pattern was an intermittent or a churn flow, and the liquid thickness on the wall was larger than the wire diameter.

On the other hand, increasing j_G , liquid fraction became lower and the difference across the wire became larger. The liquid fraction at the upstream of the wire was lower than that at the downstream. The liquid phase may be stagnant in a wake of the wire due to gravity and weak gas velocity. The higher liquid fraction might lead to the improvement of critical heat flux. The same tendency is seen in Fig. 14(b) under lower liquid volumetric flux, $j_L = 0.051$ m/s.

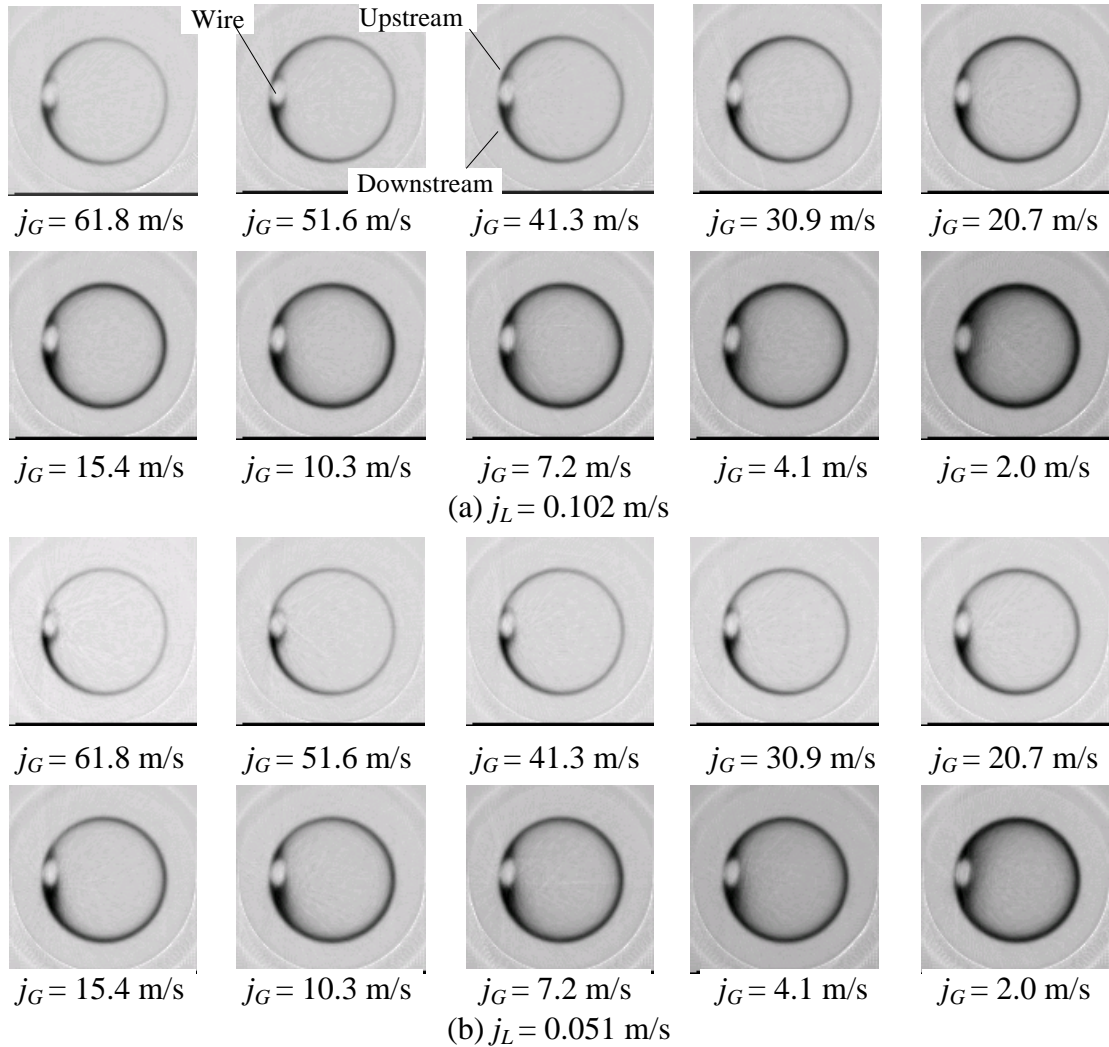


Figure 14: Cross-sectional distribution of void fraction in a vertical tube with a wire coil in arbitrary unit.

5. CONCLUSIONS

To make clear the effect of conduit configurations on phase distributions, adiabatic air-water two-phase flows and R141b boiling two-phase flows in a simulated plate heat exchanger with a single channel and adiabatic air-water two-phase flows in a vertical tube with a wire coil were visualized by a neutron radiography method, and two-dimensional distributions and average values of void fraction were measured via some image processing methods. Moreover, for a tube with a wire coil, cross-sectional distributions were calculated by a CT method. The obtained results are summarized as follows.

For plate heat exchangers, in the case where incoming flow was a gas-liquid two-phase flow, the phase distributions were strongly affected by the liquid stagnation at the enlarged test section inlet. It will be necessary to design the inlet configuration without liquid stagnation formation, such

as without enlarging of conduit. On the other hand, for liquid single-phase flow at the inlet, the design for homogenous velocity profile at the ribbed channel inlet will be as effective like in a single-phase flow heat exchanger. Liquid mixing in the ribbed channel was weak, and the unsymmetrical distribution was kept to the test section exit.

For a vertical tube with a wire coil, cross-sectional void fraction distributions could be calculated by a CT-method directly using projection image from only one direction. Under the high gas velocity condition, there was the large difference in the liquid fraction on the wall between up- and downstream of a wire. The liquid fraction at the just downstream of a wire was high. This method can be applicable to vertical heat transfer enhanced tubes whose conduit configuration rotates about the central axis, such as a tube with a twist tape and a grooved tube.

NOMENCLATURE

A : Cross-sectional area of conduit	$[m^2]$	t : Thickness	$[m]$
G : Gain	$[-]$	α : Void fraction along neutron beam	$[-]$
j : Volumetric flux	$[m/s]$	$\bar{\alpha}$: Cross-sectional averaged void fraction	$[-]$
O : Offset	$[-]$	α_{ave} : Averaged void fraction in ribbed conduit	$[-]$
Q : Volumetric flow rate	$[m^3/s]$	μ_m : Mass attenuation coefficient	$[m^2/kg]$
S : Brightness	$[-]$	ρ : Density	$[kg/m^3]$

Subscripts

0 : $\alpha = 0$	L : Liquid
1 : $\alpha = 1$	TP : Two-phase mixture
c : Conduit	w : Wall
G : Gas	

REFERENCES

- [1] K. Hori, K. Miyazaki, T. Kurosu, S. Sugiyama, J. Matsumoto, & Y. Akiyama, Proc. of ASME/JSME Nuclear Engineering Conference, **1**, p. 69, 1993.
- [2] A. Inoue, T. Kurosu, M. Yagi, S. Morooka, A. Hoshibe, T. Ishizuka, & K. Yoshimura, Proc. of ASME/JSME Nuclear Engineering Conference, **1**, p. 39, 1993.
- [3] N. Takekenaka, H. Asano, T. Fujii, M. Matsubayashi, Nuclear Engineering and Design, **184**, pp. 203-212, 1998.
- [4] N. Takenaka, H. Asano, T. Fujii, K. Yoshii, & M. Matsubayashi, Proc. of the 1st European - Japanese Two-phase Flow Group Meeting and 36th European Two-phase Flow Group Meeting, pp. 1-9, 1998.
- [5] N. Takenaka, H. Asano, T. Fujii, & M. Matsubayashi, Nondestructive Testing and Evaluation, **16**, pp. 345-354, 2001.
- [6] M. Matsubayashi, & A. Tsuruno, Neutron Radiography (4), Gordon and Breach Science Publishers, pp. 415-422, 1992.
- [7] Y. Motomura, A. Ono, & K. Sonoda, Proc. of 5th World Conference on Neutron Radiography, pp. 229-236, 1997.
- [8] M. Ishii, ANL-77-47, 1977.
- [9] K. Takeshima, T. Fujii, N. Takenaka, H. Asano, & T. Kondo, Proc. of the 4th JSME-KSME Thermal Engineering Conference, **1**, pp. 439-444, 2000.

THE MEASUREMENT OF SHEAR STRESSES IN BUBBLE COLUMNS AND AIRLIFT LOOP-REACTORS

R. Pilz¹⁾, E. U. Mahnke²⁾, D. C. Hempel¹⁾

¹⁾Institute of Biochemical Engineering
Gaußstrasse 17, D-38106 Braunschweig, GERMANY
Phone: +49 531 3917650, Fax: +49 531 3917652,
E-mail: ibvt@tu-bs.de

²⁾Cognis Deutschland GmbH & Co. KG
Henkelstraße 67, D-40589 Düsseldorf, Germany
Phone: +49 211 7940 8774, Fax +49 211 798 8955

ABSTRACT

This report presents a method for measuring shear stresses in multiphase reactors by observing the disintegration of a clay-floc system and its time dependence. For this purpose floc sizes are measured in-line by means of a laser scanning microscope probe. The characterisation of the floc system by approaches of fractal geometry and description of the turbulent flow-field by means of a multifractal approach permit a comparison between mechanical stresses in reactors and in the reference system, a turbulent single-phase Couette flow. Shear stresses measured in two- and three-phase systems in bubble columns and airlift loop-reactors are presented.

1. INTRODUCTION

Multiphase reactors are used in diverse processes of chemical and biochemical conversions. The input of energy by gas sparging into these systems leads to improved mixing, heat and mass transfer but although to turbulent eddies and consequently to shear stresses. Particularly for biochemical processes shear stresses can lead to changes in cell morphology or detachment of biofilms. For optimisation of these processes the knowledge and control of shear stresses are essential.

The determination of mechanical stresses by observing the interactions between eddies and a particle system sensitive to shear stresses has already been presented previously [1]. A clay floc suspension first mentioned by Hoffmann et al. [2, 5] has been used for this purpose in different reactors. Henzler et al. [3, 6] as well as Hoffmann et al. [2] determined shear stresses in stirred vessels of different reactor and stirrer geometries. Büscher et al. [4], Mahnke et al. [9] and Henzler [3] examined shear stresses in bubble columns.

The studies presented in this paper are based on the analysis of floc disintegration kinetics in multiphase reactors and in a turbulent reference flow. Analysis of floc break-up processes permits a comparison of measured shear stresses in both systems and leads to a quantitative description of mechanical stresses in the investigated reactor.

2. THEORY

The description of turbulent flows is often based on the theory of energy cascade defined by Taylor. This theory characterises turbulent flows as a superposition of eddies of different sizes. Energy is transferred from larger to smaller eddies and dissipated as heat by the smallest eddies.

The size of the terminating eddies can be described by the Kolmogorov length scale λ_K :

$$\lambda_K = (v_L^3 / \varepsilon)^{0.25} \quad (1)$$

v_L being the kinematic viscosity of the liquid and ε the rate of specific energy dissipation, $\varepsilon = P / (\rho_L)$.

The fluctuations of fluid velocity induced by turbulent eddies cause the observed mechanical stresses. Particularly eddies of equal size as the particles cause significant mechanical stresses. Neeße et al. [7] determined an expression for the stresses induced by turbulent eddies smaller than eddies of three times the Kolmogorov length scale ($3\lambda_K$):

$$\tau = \rho_L \cdot (\varepsilon \cdot v_L)^{0.5} \quad (2)$$

These turbulent eddies are approximately of the same size as the used mineral flocs. Equation (2) emphasises the dominant role of the mean rate of specific energy dissipation on the induced shear stresses. One important aspect of turbulent flows is the intermittency of energy dissipation in time and space. It has to be taken into account for a precise determination of shear stresses. Meneveau and Sreenivasan [8] defined the probability density function $P(\alpha)$ for occurrence of eddies of size α :

$$P(\alpha) \sim (\lambda_{K,i} / L)^{D_S - f_d(\alpha)}, \quad \lambda_{K,i} / L \ll 1 \quad (3)$$

where L is a typical large scale of turbulence imposed on the flow by external boundary conditions, D_S is the dimension of embedding space and $f_d(\alpha)$ is the multifractal spectrum of turbulence. The replacement of $\lambda_{K,i}$ by the floc size d_F leads to the probability density of occurrence of eddies of about the same size as the flocs.

3. EXPERIMENTAL PROCEDURE

3.1. The Floc System

The floc system consists of clay particles suspended in water. After adding CaCl_2 to reduce the repulsion forces between primary clay particles, a solution of a cationic polymer as a flocculant (Praestol 650 BC) is added. At the beginning of the flocculation process the suspension is agitated at a low shear rate. The bridging polymer causes the clay particles to aggregate to flocs with a length distribution median of about $d_{F,50} = 140 - 150 \mu\text{m}$. This standardised procedure of floc generation guarantees a reproducible measuring system.

An important step for measurement of shear stresses by observing floc degradation processes is the adequate description of floc structure and properties. The floc system can be described by means of fractal geometry. This method was already used earlier [4] and enables a transformation of measured floc sizes $d_{F,50}$ to floc densities ρ_F .

$$\rho_F \sim d_{F,50}^{D_f - 3} \quad (4)$$

Considering the primary clay particle size d_{clay} Eq. (5) is obtained for the dimension-less floc density $\rho_{F,rel}$ with the fractal dimension D_f :

$$\rho_{F,rel} = \left(\frac{d_{F,50}}{d_{clay}} \right)^{D_f - 3} \quad (5)$$

3.2. Floc Size Measurement and Reactors

Floc size distribution and its time-dependence was measured with an in-line Particle System Analyser (PSyA 020, Messtechnik Schwartz GmbH, Düsseldorf, Germany). The measurements showed an almost logarithmic normal floc size distribution. The median value of length distribution $d_{F,50}$ was taken as the characteristic floc size for monitoring the floc disintegration process.

Two different bubble columns (BC) with diameters of 292 and 390 mm, and heights of 3000 and 2400 mm, respectively were used in this report. By assembling an inner downcomer tube with an inner diameter of $D_D = 80$ mm the smaller column could be converted to an airlift loop-reactor (ALR). Both columns were equipped with exchangeable perforated plate spargers. The number of orifices n_o was varied between 4 and 288, while the diameter d_o was chosen from 0.5 up to 3 mm. The geometric details of the columns and sparger plates are listed in Tables I and II.

Table I: Data of the bubble columns and the airlift-loop-reactor (BC: bubble column; ALR: airlift loop-reactor).

	BC 1	BC 2	ALR
Inner Diameter of Reactor D [m]	0.292	0.390	0.292
Height of Column H [m]	0.6 to 3	0.8 to 2.4	1.8
Diameter of Downcomer D_D [m]	-	-	0.08
Length of Downcomer H_D [m]	-	-	1.65
Solids Loading Φ_S [% (v/v)]	0 to 4	0 to 4	0 to 10
Volumetric Power Input P/V [W/m^3]	50 to 400	50 to 400	50 to 400
Superficial Gas Velocity u_G [m/s]	0.005 to 0.04	0.005 to 0.04	0.005 to 0.045

The volumetric power input ranged from 50 to 400 Wm^{-3} . Particles for the measurements in three-phase systems consisted of polystyrene with a density of 1050 $kg\ m^{-3}$ and a particle size d_p between 1.0 and 2.8 mm. The solids loading ϕ_S was varied between 0.5 and 10 % (v/v).

The Couette shear system used for determination of floc strength τ_F in dependence on floc density at infinite time (cp. chapter 4.2) consisted of two coaxial cylinders with an inner diameter D_i of 116 mm and a diameter ratio of cylinders $D_o/D_i = 1.068$. Cylinder height was 141 mm and the outer cylinder rotation frequency was varied between of 1000 and 3000 min^{-1} , granting a turbulent flow with turbulence quantities comparable to the flow conditions in the reactors.

Table II: Data of the perforated plates used as spargers in the bubble columns and the airlift loop-reactor (BC: bubble column; ALR: airlift-loop-reactor; d_o : diameter of orifices; n_o : number of orifices, A_o : total area of orifices).

Perforated plate	Reactor	d_o [m]	n_o	$A_o \cdot 10^{-6}$ [m ²]
P0.5/288	BC1 / ALR	0.0005	288	56.5
P0.5/144	BC1 / ALR	0.0005	144	28.3
P1/72	BC1 / ALR	0.001	72	56.5
P1/128	BC2	0.001	128	100.9
P1/36	BC1 / ALR	0.001	36	28.3
P1/64	BC2	0.001	64	50.4
P2/18	BC1 / ALR	0.002	18	56.5
P2/9	BC1 / ALR	0.002	9	28.3
P3/8	BS1 / ALR	0.003	8	56.5
P3/14	BC2	0.003	14	100.9
P3/4	BC1 / ALR	0.003	4	28.3
P3/7	BC2	0.003	7	50.4

4. EXPERIMENTAL RESULTS

4.1. Characterization of Floc System

The floc structure can be described by means of the flocs fractal dimension D_f . The fractal dimension of the floc system was determined by settling experiments with simultaneous recording of floc diameter $d_{F,50}$ and settling velocity. Figure 1 represents the change of floc density in dependence of floc size. The fractal dimension of $D_f = 1.72$ was calculated from these measurements by linear regression according to Eq. (4).

Floc strength τ_F was determined by measuring both the floc degradation in the flow field of the Couette shear gap device and the torque on the inner cylinder. An empirical correlation between the dimensionless floc density at infinite time $\rho_{F,rel,\infty}$ and the floc strength τ_F could be derived:

$$\tau_F = 7.1 + 5.6 \cdot \rho_{F,rel,\infty}^{2.03} \quad (6)$$

The determination of $\rho_{F,rel,\infty}$ and the underlying theory are described in chapter 4.2.

4.2. Analysis of Floc Disintegration Experiments

The floc disintegration process can be divided into three sections (cp. Fig. 2). The first phase is characterised by a significant reduction of floc size caused by the degradation of unstable large flocs. The second section shows an equilibrium between floc disintegration and reaggregation resulting in an approximately constant floc diameter $d_{F,50}$. Starting at the marked time t_0 the third phase shows a slow erosion of flocs not accompanied by growth processes. Monitoring the disintegration process for a long time revealed a slowdown of degradation process without reaching

a constant end-size in finite time. Since a measured floc size at infinite time will only depend on the intensity but not the frequency of turbulent eddies this phenomenon suggests an extrapolation of floc degradation kinetics to infinite time.

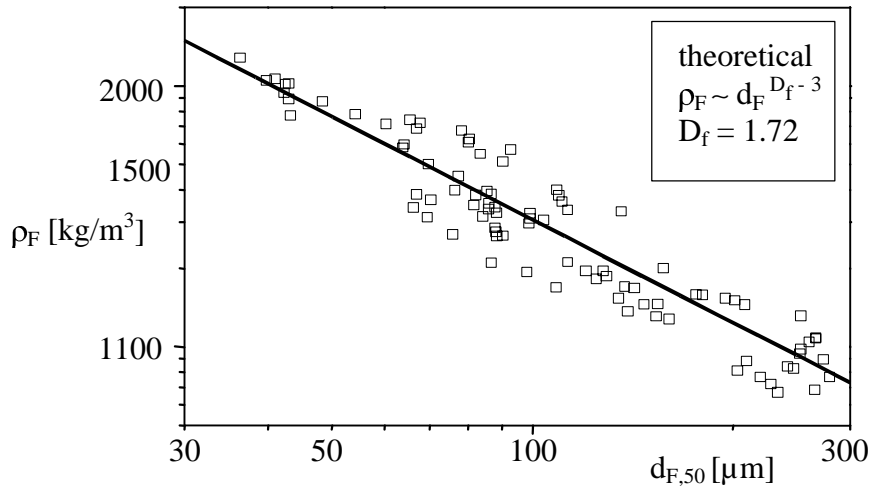


Figure 1: Determination of the fractal dimension D_f of the flocs by correlating floc densities to corresponding floc diameters.

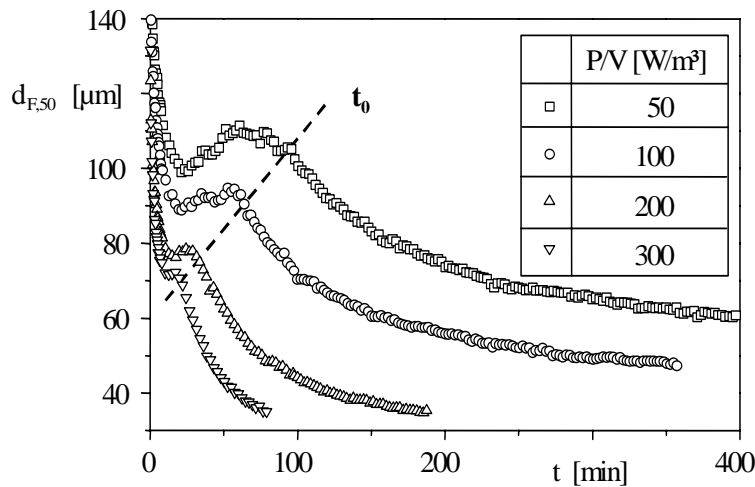


Figure 2: Floc-disintegration kinetics measured in the bubble columns with perforated plate P1/72 and aspect ratio $H/D = 4$ at different volumetric power inputs P/V (t_0 -line indicates the starting point of the disintegration period without any growth).

Because of the non-linearity of degradation kinetics a transformation has to be applied to the disintegration graphs first. This transformation is based on the description of floc characteristics by means of fractal geometry and of turbulent flow by multifractal theory. Since the continuous degradation of a floc requires an increasing rate of energy input but is associated with a decreasing probability of eddy occurrence as well, more time is needed to detect smaller eddies. Taking these aspects into consideration leads to the following correlation:

$$P(\alpha) \cdot \frac{t}{t_0} = \text{constant} \quad (7)$$

The product of probability density $P(\alpha)$ and experimental time scale is constant over the floc degradation process. Combining Eqs. (3), (5) and (7) leads to:

$$\rho_{F,rel} \sim \left(\frac{t_0}{t} \right)^{\frac{D_f-3}{3-f_d(\alpha)}} \quad (8)$$

As can be seen from Eq. (8) plotting the dimensionless floc density $\rho_{F,rel}$ as a function of the modified dimensionless time $(t_0/t)^a$ should show a linear behaviour. The exponent a was fitted to be 0.1, empirically. This value cannot solely be obtained from mentioned theory. The deviation results from the constricted definition of the multifractal spectrum of turbulence $f_d(\alpha)$. The multifractal spectrum of turbulence $f_d(\alpha)$ neither regards the probability for a collision between a turbulent eddy and a floc nor the fact that not every collision inevitably results in a floc breakup. To comprise these probabilities a parameter u has to be introduced into the exponent.

$$\rho_{F,rel} \sim \left(\frac{t_0}{t} \right)^{\frac{D_f-3}{3-u-f_d(\alpha)}} \quad (9)$$

Neither the determination of u nor that of $f_d(\alpha)$ by the current experiments is possible, but there is no necessity for evaluation of these parameters to describe the disintegration kinetics.

Extrapolation of the disintegration kinetics linearised according to Eq. (9) with the exponent 0.1 to infinite time $((t_0/t)^{0.1} \rightarrow 0, \text{ cp. Fig. 3})$ leads to the hypothetical final dimensionless density of flocs $\rho_{F,rel,\infty}$ which can be correlated to shear stresses according to Eq. (6) since the floc strength τ_F was taken as the characteristic parameter describing the effective shear stresses in the reactor.

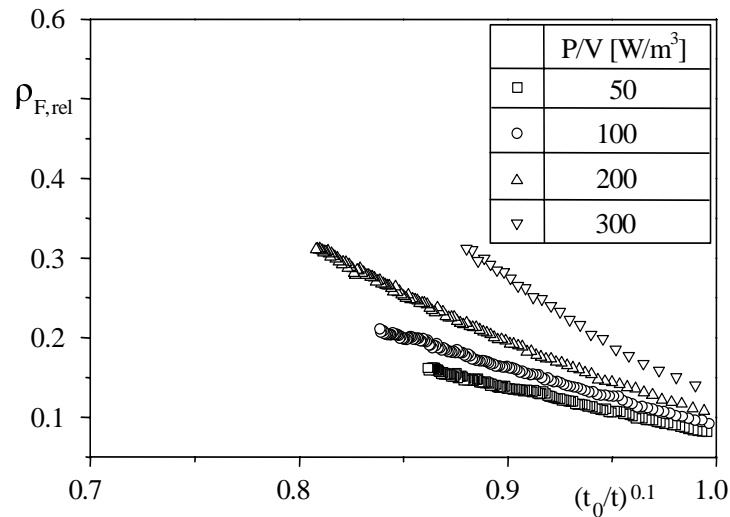


Figure 3: Linearisation of floc disintegration kinetics from experiments in the bubble column (shown in Fig. 2) with perforated plate P1/72 and aspect ratio $H/D = 4$ at different volumetric power inputs P/V .

4.3. Shear Intensity in Bubble Columns and Airlift Loop-Reactors

The installation of an inner downcomer tube to a bubble column leads to a drastic change of flow pattern since it separates up-flow and down-flow region. While stochastic motion dominates the flow field in a bubble column a constant circulation is generated in an airlift loop-reactor. Comparison between both reactor types will give an answer about the effect of circulations on shear stresses.

As can be seen in Fig. 4 it turned out that over a wide range of volumetric power input the shear stresses in airlift loop-reactors and in bubble columns with low solids loadings are apparently the same. The slight deviation of shear stresses between both reactors results from the increase in wall section in the airlift loop-reactor compared to the bubble column accompanied with an increase of energy dissipation in the laminar boundary layer. An increasing wall area will lead to a decreasing amount of energy powering the circulation.

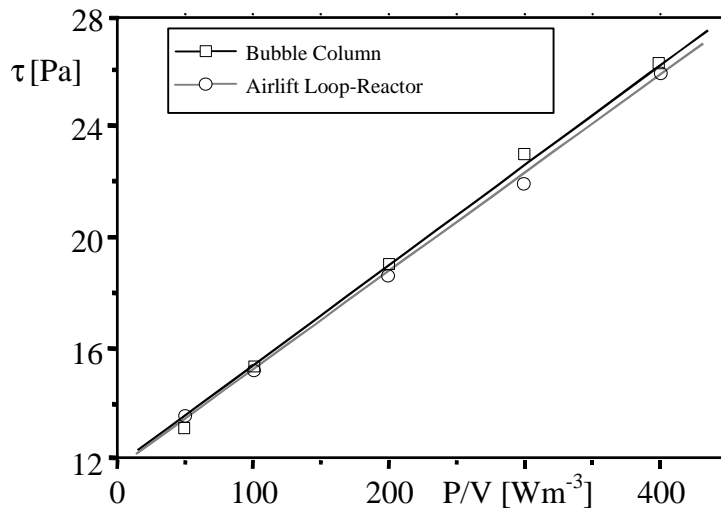


Figure 4: Shear stresses in the bubble column BC 1 and the airlift loop-reactor ALR at varying different power inputs (perforated Plate: P3/4; $D = 292\text{mm}$; $D_D = 80\text{mm}$; $H/D = 6$; $d_p = 2.8\text{mm}$; $\Phi_S = 1\%$ (v/v)).

4.4. Shear Stresses in Three-Phase Flows

According to the results in chapter 4.3 the experiments in three phase flows were carried out in the airlift loop-reactor because of the improved fluidisation of the solids. Adding a solid phase to a two-phase flow causes a decrease in shear stresses if solids loading is low ($\Phi_S = 1\%$ (v/v)) while shear stresses increase at significantly higher loadings of $\Phi_S = 4\%$ (v/v) (cp. curves with filled symbols in Fig. 5).

The linear dependence of shear stresses on volumetric power input as depicted in Fig. 5 could only be verified for coarse dispersed sparging. Aerating by means of a sparger plate with an orifice diameter $d_o = 1\text{mm}$ showed a nonlinear increase of shear stresses in dependence on volumetric power input, pointing out a drastic change of turbulent flow pattern. Furthermore at a power input above 325 W/m^3 shear stresses in a system with low solids loading $\Phi_S = 1\%$ (v/v) exceeds shear stresses in a system with high solids loading $\Phi_S = 4\%$ (v/v) using a fine dispersing sparger.

As can be seen from Fig. 5 the change in turbulent flow pattern not only depends on volumetric power input and solids loading Φ_S . Figure 6 points out changes of shear stresses in dependence on solids loading for different volumetric power inputs. Shear stresses decline for solids loadings of up to $\Phi_S = 2\%$ (v/v) and rises with a higher loading. After reaching a maximum value for shear stresses in Fig. 5 at solid loadings between 4 and 10% (v/v) depending on the power input, the shear stresses finally decrease again.

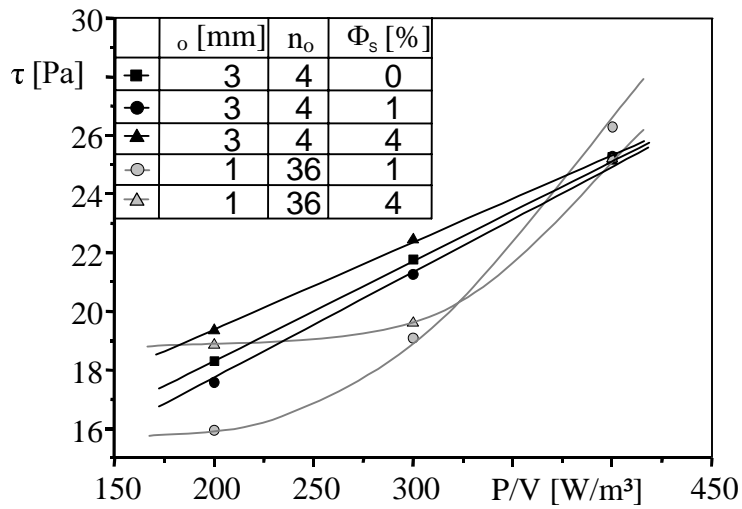


Figure 5: Comparison of shear stresses in the airlift loop-reactor equipped with different spargers (perforated Plate: P3/4 and P1/36; $D = 292\text{mm}$; $H/D = 6$; $d_p = 2.8\text{mm}$).

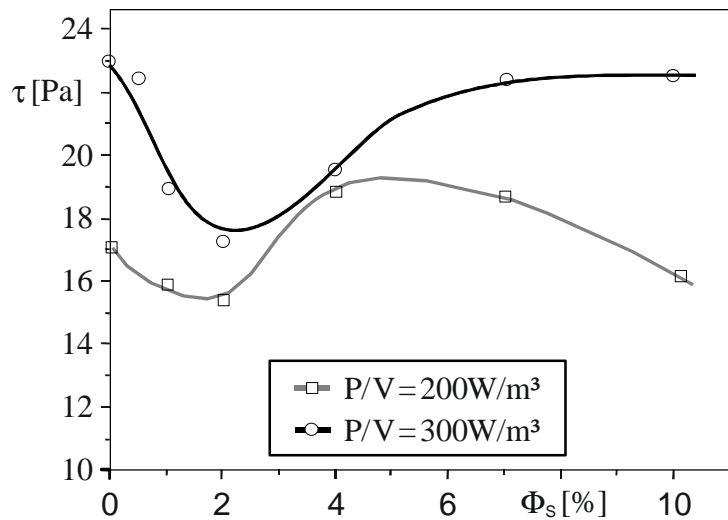


Figure 6: Comparison of shear stresses in the airlift loop-reactor at different solids loadings (perforated Plate: P1/36; $D = 292\text{mm}$; $D_D = 80\text{mm}$; $H/D = 6$; $d_p = 2.8\text{mm}$).

5. CONCLUSIONS

It was shown that the floc system presented and the described transformation of disintegration graphs is suitable for determination of shear stresses induced by turbulent flow in two- and three-phase systems. Marginally deviations in shear stresses between bubble columns and airlift loop-reactors were recorded due to the extended wall area in the airlift loop-reactor. Examinations of interactions between dispersed gas and solids phase in three phase systems showed a complex interrelation. Further investigations have to be undertaken to point out exact correlations.

ACKNOWLEDGEMENT

The authors gratefully acknowledge financial support of this project by the Deutsche Forschungsgemeinschaft.

NOMENCLATURE

A_0	Total area of orifices
a	Exponent of time scale
d_{clay}	Diameter of clay particles
d_0	Diameter of orifices
d_F	Floc diameter
$d_{F,50}$	Median of floc length distribution
d_p	Diameter of particles
D	Diameter of bubble column
D_D	Diameter of downcomer
D_f	Fractal dimension
D_i	Inner diameter of Couette shear system
D_o	Outer diameter of Couette shear system
$f_d(\alpha)$	Multifractal spectrum for scale α
H	Height of bubble column
L	Integral length-scale
n_0	Number of orifices
P	Power input
$P(\alpha)$	Probability of occurrence of eddies with scale α
t	Time
t_0	Starting time of floc disintegration without floc growth
V	Volume
α	Fractal scaling exponent
ε	Specific rate of energy dissipation
Φ_S	Solids loading
λ_k	Kolmogorov length-scale
ν_L	Liquid kinematic viscosity
ρ_F	Floc density
$\rho_{F,rel}$	Dimensionless floc density
$\rho_{F,rel,\infty}$	Dimensionless floc density extrapolated for infinite time
ρ_L	Liquid density
τ	Shear stress
τ_F	Floc strength

REFERENCES

- [1] Yoshida, F., Yamada, T., Average Size of Oil Drops in Hydrocarbon Fermentors, J. Ferment. Technol., 49, pp. 235-244, 1971.
- [2] Hoffmann, J., Tralles, S., Hempel, D. C., Testsystem zur Untersuchung der mechanischen Beanspruchung von Partikeln in Bioreaktoren, Chem. Ing. Tech. 64, pp. 953-956, 1992.
- [3] Henzler, H.-J., Particle Stress in Bioreactors, Adv. Biochm. Eng., 67, pp.35-82, 2000.

- [4] Büscher, K., Hempel, D. C., Bestimmung der Schubspannung durch mechanische Beanspruchung eines Flockensystems in einer zweiphasig betriebenen Blasensäule, Chem. Ing. Tech., 68, pp. 1452-1455, 1996.
- [5] Hoffmann, J., Büscher, K., Hempel, D. C., Ermittlung von maximalen Scherspannungen in Rührbehältern, Chem. Ing. Tech., 67, pp. 210-214, 1995.
- [6] Biedermann, A., Henzler, H.-J., Beanspruchung von Partikeln in Rührreaktoren, Chem. Ing. Tech., 66, pp. 209-211, 1994.
- [7] Neeße, T., Ivanauskas, A., Mühle, K., Zur physikalisch begründeten Modellierung von Flockungsprozessen, Chem. Techn., pp. 292-295, 39, 1987.
- [8] Meneveau, C., Sreenivasan, K. R., The Multifractal Spectrum of the Dissipation Field in Turbulent Flows, in: Nuclear Physics B (Proc. Suppl.) (Duong-Van, M., Ed.), pp. 49-76, North-Holland, Amsterdam, 1987.
- [9] Mahnke, E. U., Büscher, K., Hempel, D. C., A Novel Approach for the Determination of Mechanical Stresses in Gas-Liquid Reactors, Chem. Eng. Technol., 23, pp. 509-513, 2000.

C. Flow Regime Phenomena and Data

EXPERIMENTAL INVESTIGATIONS AND MODELLING ON THE TRANSITION FROM BUBBLE TO SLUG FLOW IN VERTICAL PIPES

D. Lucas, E. Krepper and H.-M. Prasser

Forschungszentrum Rossendorf e.V.
Institute of Safety Research
P.O.Box 510 119, 01314 Dresden, GERMANY
Phone: +49 351 260-2047, Fax: +49 351 260-2383,
E-mail: lucas@fz-rossendorf.de

ABSTRACT

To qualify CFD codes for two-phase flows, they have to be equipped with constitutive laws describing the interaction between the gaseous and the liquid phases. In the case of bubble flow this particularly concerns the forces acting on the bubbles and bubble coalescence and break-up. To obtain detailed experimental data, an electrode wire-mesh sensor was used, which enables the measurement of the phase distribution with a very high resolution in space and in time. Air-water flow at ambient conditions in a vertical pipe (51.2 mm inner diameter) is investigated to have well defined boundary conditions. Local bubble size distributions are calculated from the data. The measurements were done in different distances from the gas injection device. As a result the development of bubble size distributions as well as the development of the radial gas fraction profiles can be studied. It was found, that the bubble size distribution as well as local effects determine the transition from bubble flow to slug flow. The data are used for the development of a model, which predicts the development of the bubble size distribution and the transition from bubble flow to slug flow in case of stationary flow in a vertical pipe.

1. INTRODUCTION

World-wide great efforts are made to develop CFD codes for two-phase flows in complicated three-dimensional geometries. In case of bubble flow, and especially for the correct prediction of the flow pattern transition from bubble to slug flow, the codes must be equipped with constitutive laws describing the interaction between the gaseous and the liquid phases in a more detailed way than this is done by the wide-spread assumption of mono-disperse bubble flow. Recently attempts were made to solve this problem by the introduction of additional equations for the bubble density or similar parameters like bubble diameter, bubble volume or interfacial area. Rates for bubble coalescence and frequencies for bubble break-up, which form the source terms in these equations, are determined as local quantities. That means, they depend on local parameters of turbulence as well as on the local bubble size distribution. In order to reflect the fact that bubbles of different sizes develop different spatial distributions, it is necessary to introduce multi-bubble-size models. The main challenge is to find model equations quantifying the interaction between these bubble-size classes.

Gas-liquid flow in vertical pipes is a very suitable object for studying the corresponding phenomena. Here, the bubbles move under clear boundary conditions, resulting in a shear field of nearly constant structure where the bubbles rise for a comparatively long time. This allows to study the lateral motion of the bubbles in a shear flow by comparing distributions measured at different heights. It was shown, that the radial distribution of bubbles strongly depends on their diameter. For a vertical upflow smaller bubbles tend to move towards the wall, while large bubbles are preferably

found in the centre. This was initially observed for single bubbles [1]. In an air-water system at ambient conditions the change of the direction of the lift force in the shear field occurred at a bubble diameter of about 5 - 6 mm. We could confirm this also for multi-disperse flow [2] (Fig. 2). This is very important for the evolution of the flow because the local bubble size distributions may differ significantly from those averaged over the cross section.

For this reason detailed investigations of gas-liquid flows in vertical tubes including the transition from bubble flow to slug flow along the flow path were made. The change of the bubble size distribution along the pipe as well as the changing radial profiles of the gas fraction represented by bubbles of different size were measured by fast wire-mesh sensors developed by the Research Centre Rossendorf. A model was developed to simulate the development of the flow along the flow path for the special case of vertical pipe flow. This allows to test the models for the forces acting on a bubble perpendicular to the flow path as well as models for bubble coalescence and break-up and to adjust them according to the experimental data.

2. EXPERIMENTS

2.1. Experimental setup and instrumentation

The evolution of the bubble size distribution was studied in a vertical tube of 51.2 mm inner diameter supplied with air-water mixture at 30°C. Different gas injection devices were used. The distance between sensor and air injection was varied from 0.03 m to 3.03 m (inlet lengths 0.6 - 60 L/D). Gas and liquid superficial velocities were varied in a wide range. Stationary flow rates of air and water were used. About 150 combinations of the superficial velocities were considered. They include stable bubble flow, finely dispersed bubble flow, slug flow and annular at the upper end of the pipe. Transitions between the flow regimes were observed within the pipe.

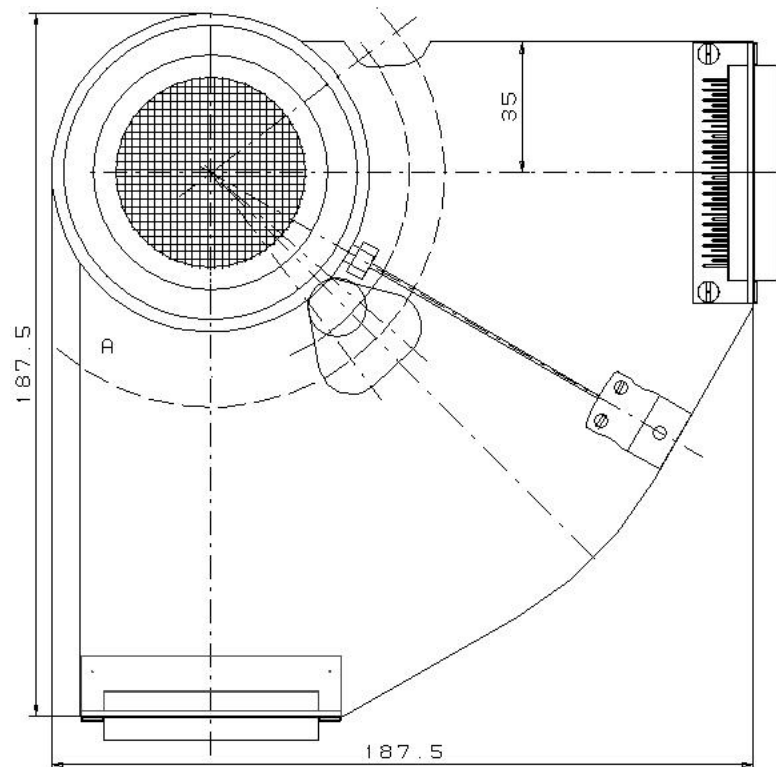


Figure 1: Scheme of the wire-mesh sensor.

Data were obtained by an electrode wire-mesh sensor (Fig. 1) performing measurement of the instantaneous conductivity distribution [3]. Two electrode grids with 24 electrode wires each (diameter 120 μm) are placed at an axial distance of 1.5 mm behind each other. During signal acquisition, the electrodes of the first grid (transmitter wires) are supplied with short voltage pulses in a successive order. The currents arriving at the second grid (receiver wires) are digitalized by ADCs and stored in a data acquisition computer. Two sensors were put in a distance of 36 mm behind each other to measure velocities, too. For this sensor assembly, a time resolution of 2500 frames per second was achieved. The spatial resolution is given by the pitch of the electrodes and equals 2 mm.

The sensor delivers a sequence of two-dimensional distributions of the local instantaneous conductivity, measured in each mesh formed by two crossing wires i and j . Local instantaneous gas fractions are calculated assuming a linear dependence between gas fraction and conductivity. The result is a three-dimensional data array i,j,k where k is the number of the instantaneous gas fraction distribution in the time sequence. A special procedure, described in [4] allows the identification of single bubbles and the determination of their volume and the equivalent bubble diameter. Using this procedure, bubble size distributions as well as gas fraction profiles for bubbles within a predefined interval of bubble sizes can be calculated, the latter by using the method described in [2].

2.2. Test matrix for the investigations on the transition from bubble to slug flow

A detailed experimental database concerning the development of the flow along the flow path, including the transition from bubble to slug flow was obtained. A description of the database and selected results can be found in [5]. The gas injection device used, consists of 19 capillaries, which are equally distributed over the cross section of the pipe. 89 combinations of gas and liquid volume flow rates and 10 different gas flow rates in case of stagnant liquid were investigated. The measurements were conducted for up to 10 different distances from the gas injection ($L/D = 0.6, 1.6, 2.5, 4.5, 8.4, 16.2, 29.9, 39.6, 49.4, 59.2$). The measuring time was always 10 s, what results in a matrix of raw data with the dimension of $24*24*25.000$ for each sensor. From these data total and local bubble size distributions as well as radial gas fraction profiles decomposed according to the bubble size were calculated.

2.3. Experimental results

Tomiyama found a correlation for the bubble lift force by investigations of the behaviour of single bubbles within a well defined shear field [1]. It changes sign at a bubble diameter of about 5.5 mm in air-water flow at ambient conditions. This was confirmed by our own experiments in a multi-dispersed flow (Figs. 2c-2f).

Stable bubble flow was only observed for high water superficial velocities and low air superficial velocities. In this case a stable sharp wall peak of the gas fraction was found. In all cases with a core peak, the development of the bubble size distributions along the pipe indicates, that the coalescence rate exceeds the break-up rate. Although at $L/D \cong 60$ the transition to slug flow is not yet completed in many cases, it can be expected at larger distances. This is also evident by the comparison of experiments for the same superficial velocities, but different gas injection devices. If the initially generated bubbles are larger than the critical bubble diameter of about 5.5 mm, slug flow is established for many combinations of superficial velocities, for which we still found bubble flow in case of an initial bubble diameter less than 5.5 mm. The experiments clearly show, that the transition from wall to core peak leads to a transition to slug flow somewhere upwards in the pipe, if the length is sufficient. In pipes of a larger diameter the effects have still to be investigated, since there is a maximum pipe diameter for the establishment of slug flow [6].

The transition from wall to core peaking is demonstrated at Fig. 2. Figure 2a shows the gas fraction profiles for different distances from the gas inlet. Very close to the gas injection device

(30 mm) still the individual injection nozzles (19 nozzles, equally distributed over the cross section) determine the radial profile. The small bubbles migrate quickly to the wall and form a wall peak of the gas fraction (830 mm – 1530 mm). With a further increase of the distance from the gas inlet a transition to core peaking is observed (3030 mm). Figure 2b shows the corresponding bubble size distributions. More and more larger bubbles are generated by coalescence.

The Figs. 2c to 2f show again gas fraction profiles for different distances from the inlet, but here they are subdivided according to the bubble diameter. Only few bubbles exceeding 5.5 mm are generated by the air injector. They appear due to coalescence at higher positions and migrate to the core of the pipe. These bubbles form a clear core peak at 3030 mm.

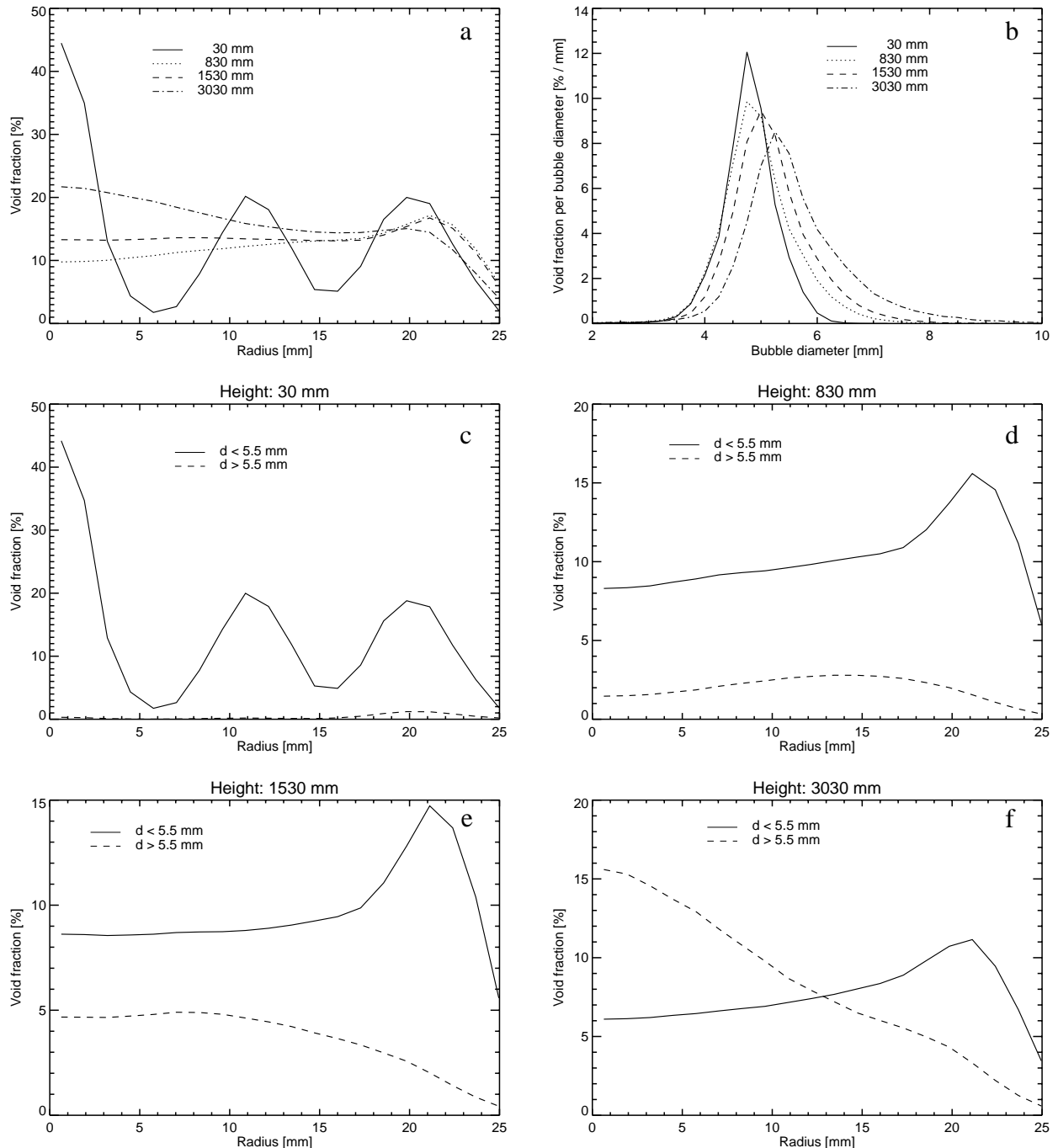


Figure 2: Radial gas fraction profiles and bubble size distributions for different distances from the gas inlet, superficial velocities: $j_1 = 1.0$ m/s, $j_g = 0.14$ m/s.

For other combinations of superficial velocities the transition from bubble to slug flow was observed. The process of transition is very fast, if a sufficient fraction of bubbles with a diameter between 10 mm and 15 mm is generated by coalescence. Figure 3 shows a typical evolution of the bubble size distribution in case of the transition. Bubbles larger than 10 mm in diameter coalesce with an high rate and form slugs. Consequently, a transition to a bi-modal bubble size distribution is observed.

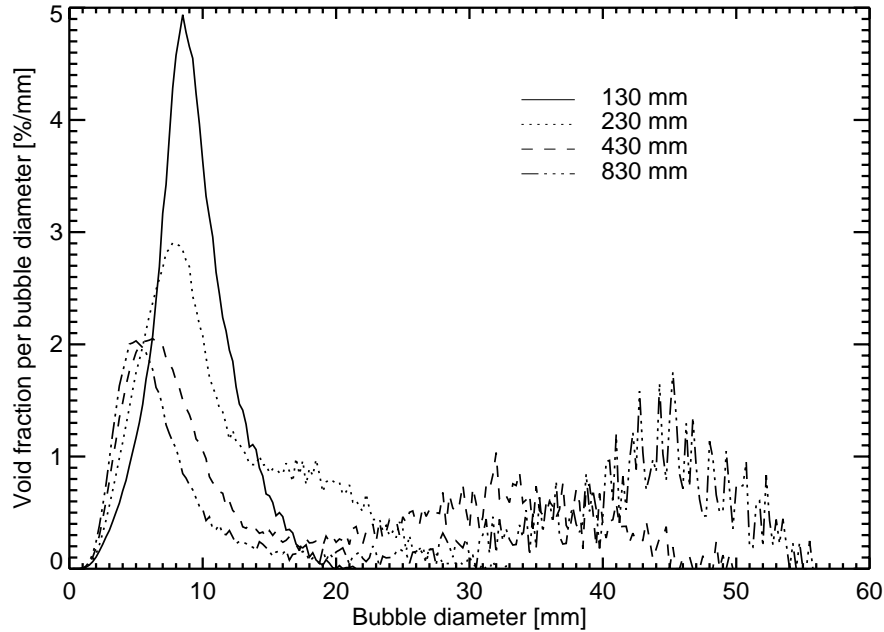


Figure 3: Development of the bubble size distribution during the transition from bubble to slug flow, superficial velocities: $j_l = 0.4$ m/s, $j_g = 0.34$ m/s.

3. THE TRANSITION FROM BUBBLE TO SLUG FLOW

As the experimental data advice, the transition from bubble to slug flow along the flow path in case of an co-current flow within a pipe is influenced by local effects depending on the bubble size. Bubble coalescence and bubble break-up, which cause the transition, depend on the local bubble densities n as well as on the dissipation rate of the turbulent kinetic energy ε :

$$\text{Coalescence rate:} \quad \Gamma_{i,j} = f(d_i, d_j, \varepsilon) * n_i * n_j$$

$$\text{Break-up rate:} \quad \Omega_i = f(d_i, d_j, \varepsilon) * n_i$$

i and j indicate the bubble class. The lift force found by Tomiyama [1] causes, that small bubbles (diameter < ca. 5.5 mm in case of air-water flow) can be found preferably in the wall region, while larger bubbles are accumulated in the core region.

Another important fact is, that the dissipation rate of turbulent energy is larger in the near wall region than in the core flow in most cases. The consequences for the transition to slug flow can be explained by help of Fig. 4. An upward air-water flow is considered. In both considered cases small bubbles (diameter < 5.5 mm) are injected. In the left side of the figure a low superficial gas velocity was assumed. The small bubbles tend to move towards the wall. The local gas fraction in the wall region is larger than the averaged gas fraction, but it is still low. In this case bubble coalescence and break-up are in equilibrium and an stable bubble flow is established.

If the gas superficial velocity is increased (Fig. 4, right side), the equilibrium between bubble coalescence and break-up is shifted towards a larger bubble diameter, because the coalescence rate increases with the square of the bubble density, while the break-up rate is only proportional to the bubble density. The bubble break-up rate strongly increases with the bubble diameter.

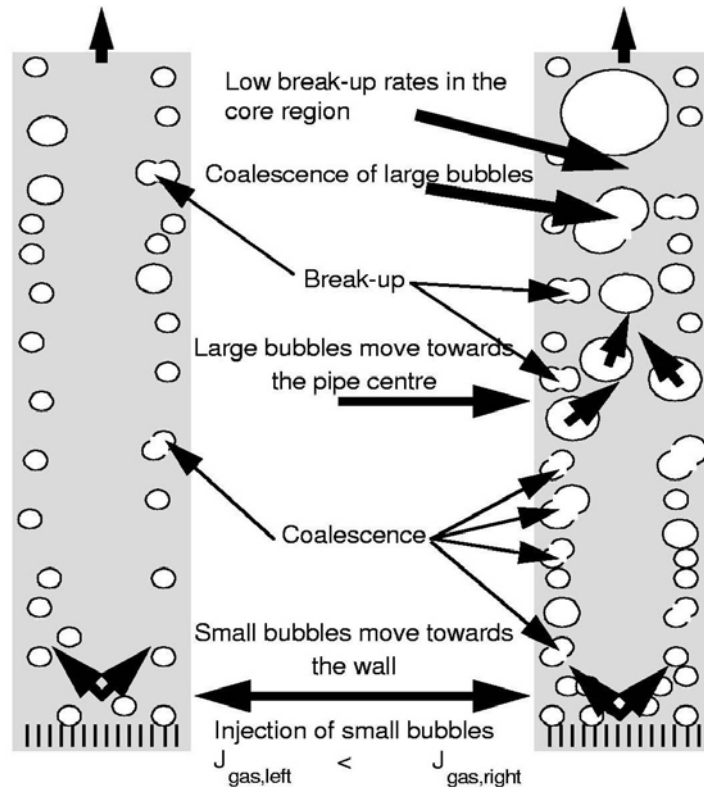


Figure 4: Stable bubble flow (left) and transition to slug flow (right).

By a further increase of the gas superficial velocity, more and more large bubbles (diameter > 5.5 mm) are generated. They start to migrate towards the pipe centre. If enough large bubbles are generated by coalescence in the wall region, some of them can reach the core region without break-up. Because of the lower dissipation rate of turbulent energy they can then growth up by further coalescence at much lower break-up rates, typical for the low shear in the centre. This mechanism is the key for the transition from bubble to slug flow. That means, for an appropriate modelling of the transition a number of bubble classes as well as radial gas fraction profiles for each bubble class have to be considered.

4. MODELLING

4.1. Basic idea of the model

According to the importance of the local bubble size distributions and the dependence of the parameter on the radial position, a model was developed, which considers a large number of bubble classes and resolves the parameter on the radial position. Because this model is explained in detail in [7], only the basic idea of the model is presented here.

The radial profiles of the bubble density are the result of the non drag forces, acting perpendicularly to the flow direction. They are caused by the liquid shear flow, turbulence and no-slip boundary at the tube wall. The radial profiles of the liquid velocity, of the turbulent energy and of the dissipation rate of turbulent energy are calculated on basis of the model from Sato [8] and the

balance equation for the turbulent energy [9]. Using these data, the model calculates the radial gas fraction profiles for each bubble class on the basis of a balance of the non drag forces. In the result local bubble size distributions for all radial positions are available. Simple models for bubble coalescence and break-up calculate from these data rates for bubble coalescence and break-up for each bubble class and each radial position.

The model does not resolve the parameters over the height of the pipe. Instead a bubble velocity, which is equal for all bubble sizes and radial positions is assumed. This allows the approximate evaluation of the flow pattern over the height of the pipe in case of stationary flows by introducing a dependence on time. Because of the assumed uniform bubble velocity the time corresponds to a height position within the pipe. Starting from an initial bubble size distribution for each time step radial profiles and new bubble size distributions are calculated.

For the non drag forces the model assumes an equilibrium. The transient behaviour of the radial gas fraction profiles is modelled by a relaxation. For situations with stable flow conditions a good agreement between predicted and measured radial gas fraction profiles is observed, but deviations occur especially in the region of the transition from bubble to slug flow. The model is up to now not able to simulate the shift of the large bubbles, generated by coalescence in the near wall region, to the centre of the pipe. For this reason it is planned to consider the velocity of the bubble migration in future versions of the model.

First calculations were made using simplified assumptions for coalescence and break-up rates. Starting with the bubble size distribution and the radial profile of the gas fraction measured at the inlet of the test pipe the development of the bubble size distribution was calculated. After adjusting the model parameters a good agreement with the experimental data at the upper end of the pipe was achieved [7]. The transition from bubble to slug flow was reproduced by the model. It has to be remarked that the model adjustment is independent from the flow rates, i.e. the model has a generalising capability. The models for the non-drag bubble forces and the rates for coalescence and break-up can be applied in one-dimensional codes as well as in CFD-codes.

4.2. Comparison with experimental results

The new database, shortly characterised in 2.2, will be used for further improvement of the model. As a first step the model described above was applied on the new experimental data. The only extension of the model is, that it now also considers the decreasing pressure along the flow path, which is connected with an increase of the total gas fraction.

Measured total bubble size distributions and radial gas fraction profiles close to the gas injection device ($L/D = 0.6$) were taken as an input of the model. Starting from these data, the model calculates the radial gas fraction profiles and the bubble size distributions along the flow path. Figures 5 to 7 compare the measured and calculated bubble size distributions at the upper end of the pipe ($L/D = 60$) for different combinations of gas liquid superficial velocities. From Fig. 5 to Fig. 7 the liquid superficial velocity is increased from 0.40 m/s to 0.64 m/s and 1.0 m/s. The gas superficial velocities were chosen in a way, that cases with bubble flow as well as with slug flow at the upper end of the pipe are included.

In general the flow pattern for $L/D = 60$ is well predicted by the model. However, there are deviations in the radial gas fraction profiles as well in the bubble size for other distances from the gas inlet. For this reason it is necessary to include the transient radial migration of the bubbles and more sophisticated models for bubble coalescence and break-up into the model. This will be done on basis of the new experimental database.

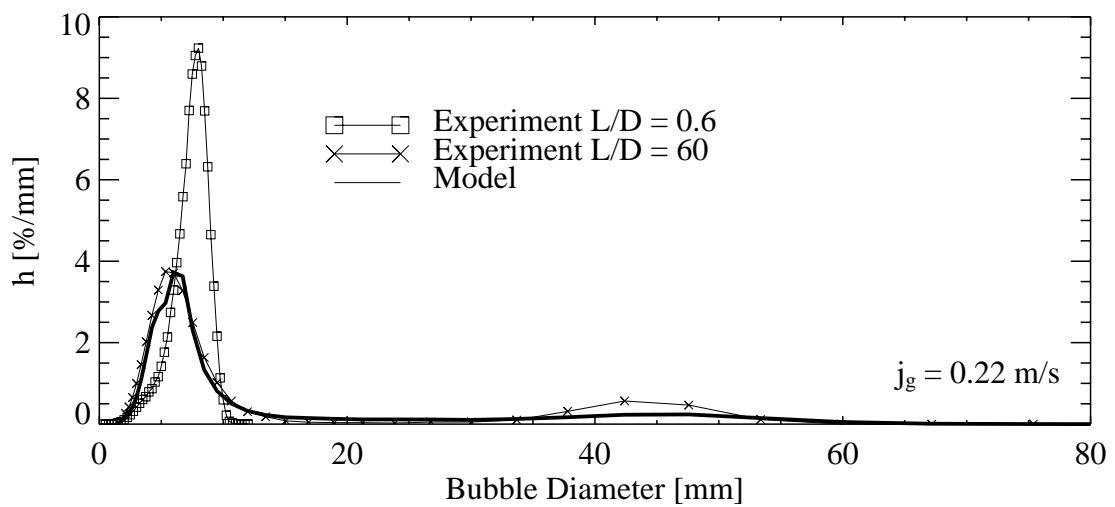
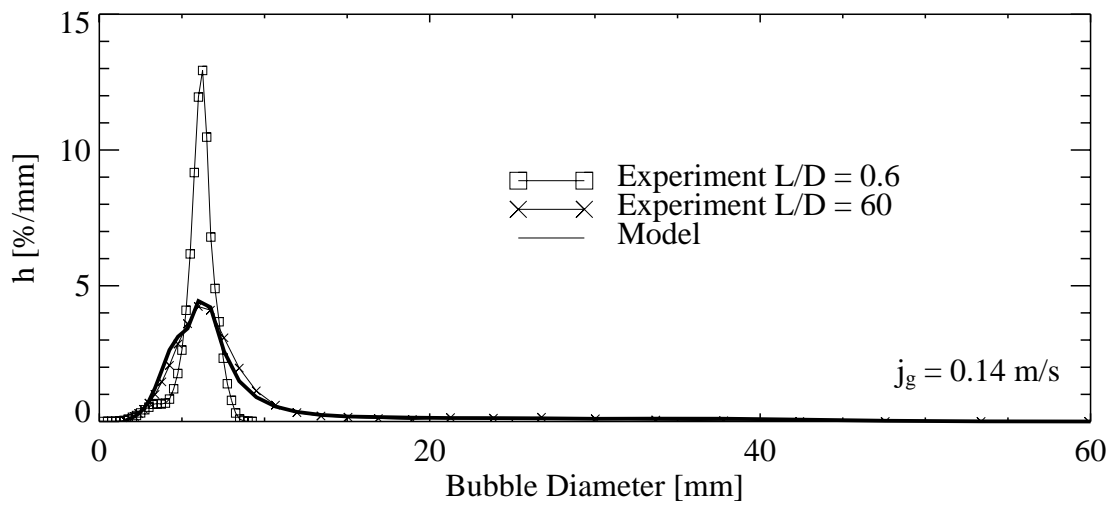
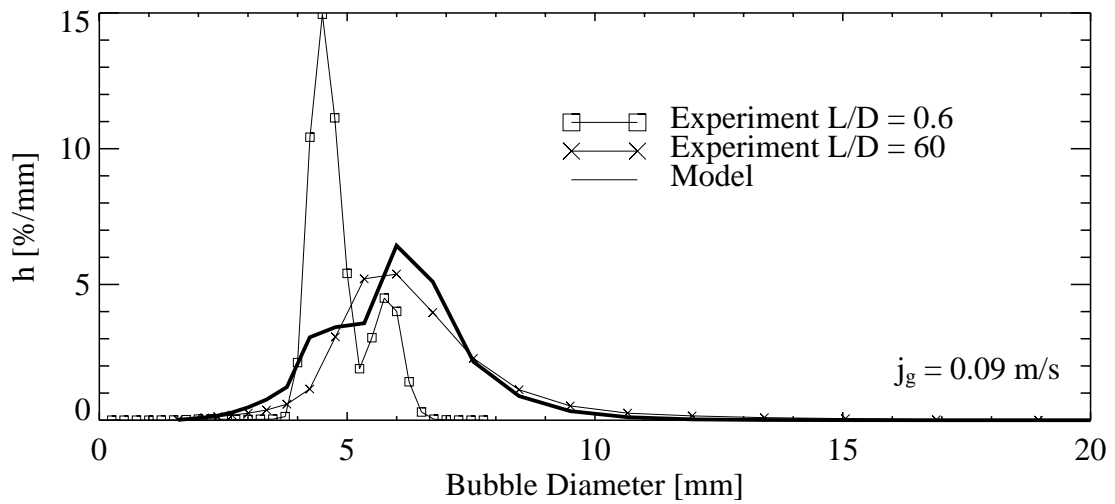


Figure 5: Experimental and calculated bubble size distributions at the upper end of the test section (3030 mm from the gas inlet), liquid superficial velocity: $j_l = 0.40 \text{ m/s}$.

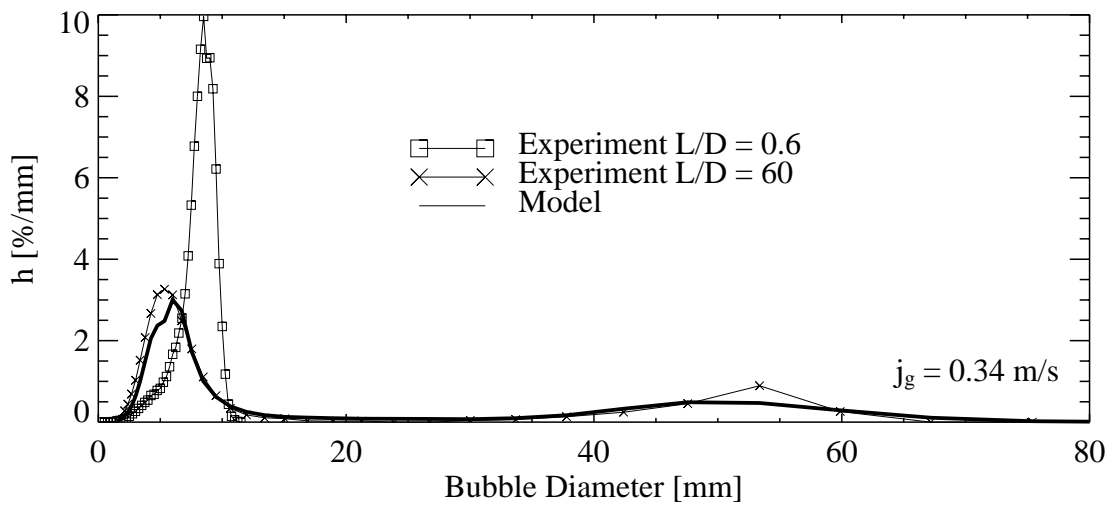
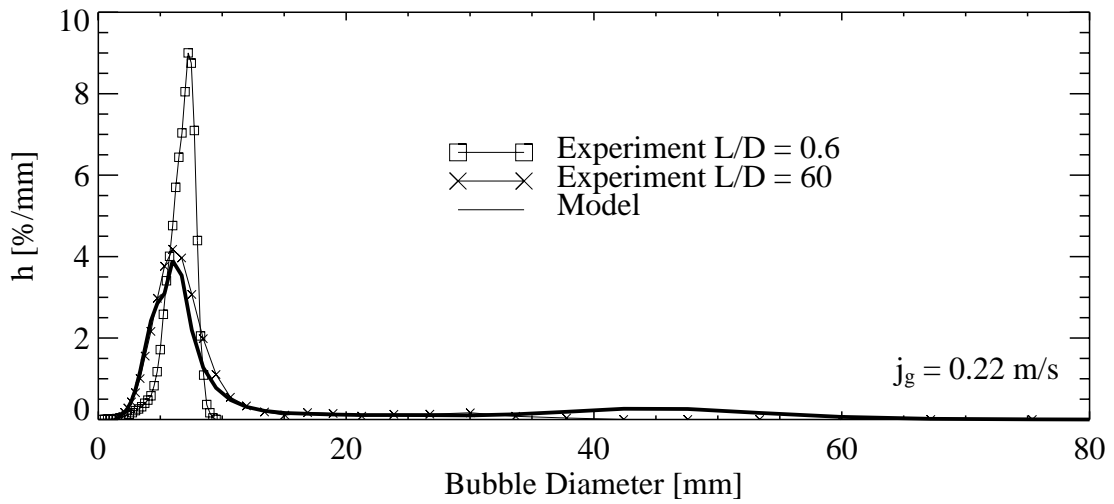
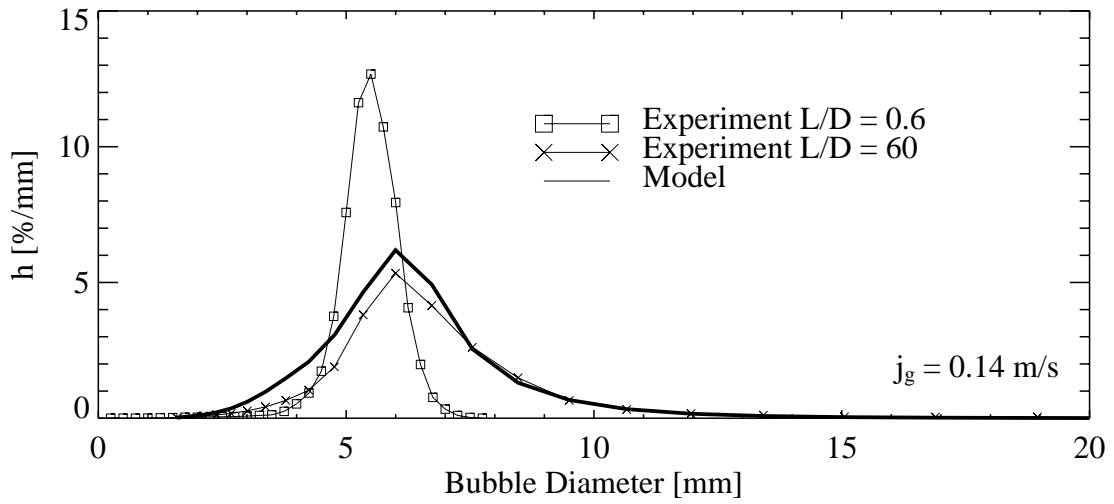


Figure 6: Experimental and calculated bubble size distributions at the upper end of the test section (3030 mm from the gas inlet), liquid superficial velocity: $j_l = 0.64 \text{ m/s}$.

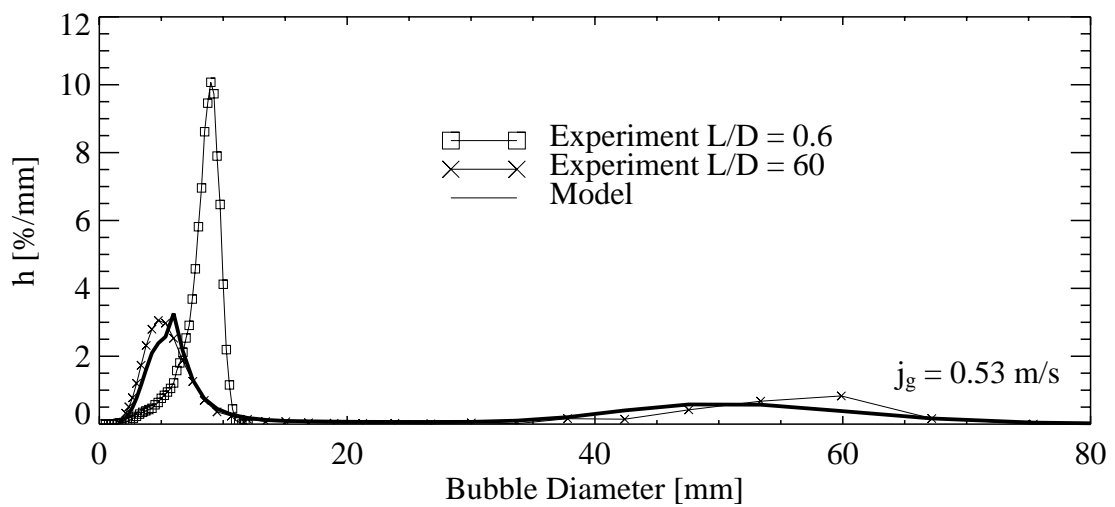
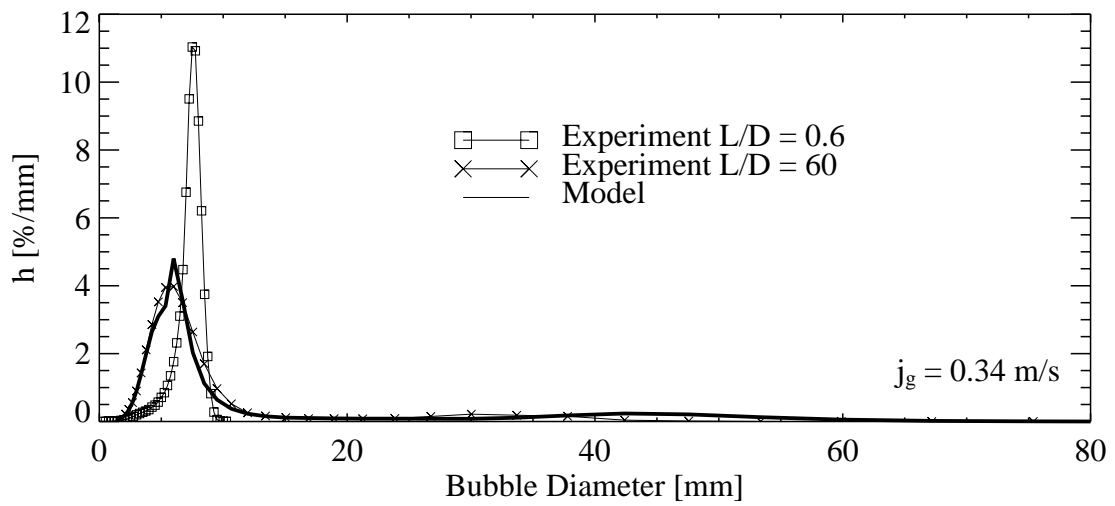
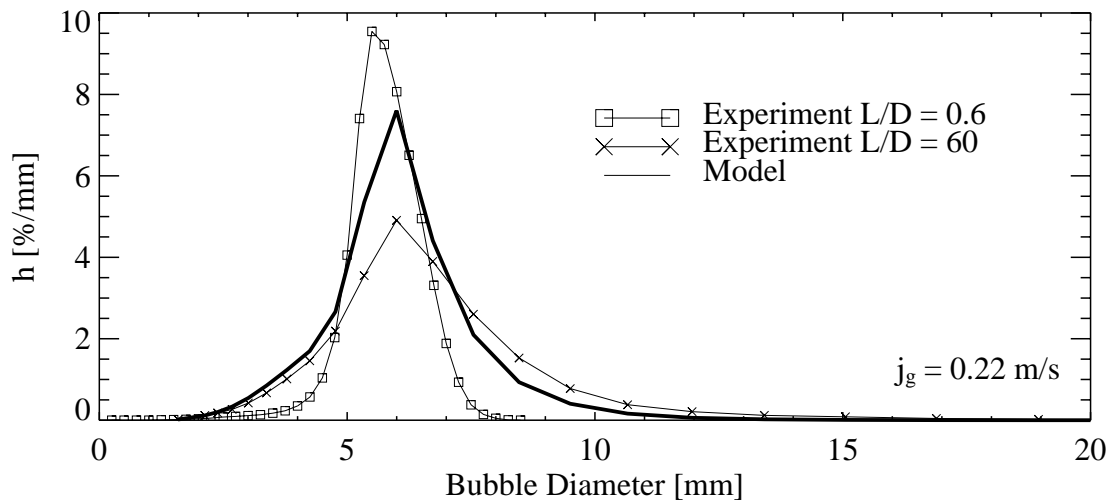


Figure 7: Experimental and calculated bubble size distributions at the upper end of the test section (3030 mm from the gas inlet), liquid superficial velocity: $j_l = 1.0$ m/s.

5. CONCLUSIONS

The experimental data clearly show, that the transition from bubble to slug flow is determined by effects depending on the bubbles sizes as well as on local effects. For an adequate modelling a large number of bubble classes (e.g. 25) has to be considered. There are very different conditions for bubble coalescence and break-up in the core region of the pipe compared to the near wall region. This fact has also to be considered by the models for the simulation of the development of the flow pattern along the pipe. The experimental data obtained in vertical pipes are useful for the development of generalised models for the non-drag bubble forces as well as for local bubble coalescence and break-up. These models can be used by one-dimensional codes as well as 2- or 3-dimensional CFD-codes. The simplified approach is a powerful tool for the model development for CFD codes, since it allows to test model correlations in a very efficient manner.

NOMENCLATURE

d_i	Bubble diameter of the bubble class i
D	Inner diameter of the pipe
j_g	Gas superficial velocity
j_l	Liquid superficial velocity
n_i	Bubble density of the bubble class i
$\Gamma_{i,j}$	Rate of coalescence of bubbles from the bubble class i with bubbles from the bubble class j
ε	Dissipation rate of turbulent energy
Ω_i	Break-up rate for bubbles of the bubble class i

REFERENCES

- [1] Tomiyama A., Struggle with computational bubble dynamics, Third International Conference on Multiphase Flow, ICMF'98, Lyon, France, June 8-12, 1998.
- [2] Prasser, H.-M., Krepper, E., Lucas, D., Evolution of the two-phase flow in a vertical tube - decomposition of gas fraction profiles according to bubble size classes using wire-mesh sensors, International Journal of Thermal Sciences, 41, pp. 17-28, 2002.
- [3] Prasser H.-M., Böttger A., Zschau J., A new electrode-mesh tomograph for gas-liquid flows, Flow Measurement and Instrumentation, 9, pp. 111-119, 1998.
- [4] Prasser, H.-M., Scholz, D., Zippe, C., Bubble Size Measurement using Wire-Mesh Sensors, Flow Measurement and Instrumentation, Flow Measurement and Instrumentation, 12, pp. 299-312, 2001.
- [5] Lucas, D., Krepper, E., Prasser, H.-M., Experimental high-resolution database for co-current air-water flow in a vertical pipe, 40th European Two-Phase Flow Group meeting, Stockholm, Sweden, paper C4, June 10-13, 2002.
- [6] Taitel, Y., Bornea D., Dukler A.E., Modelling Flow Pattern Transitions for Steady Upward Gas-Liquid Flow in Vertical Tubes, AIChE Journal, 26, pp. 345-354, 1980.
- [7] Lucas, D., Krepper, E., Prasser, H.-M., Development of bubble size distributions in vertical pipe flow by consideration of radial gas fraction profiles, 4th International Conference on Multiphase Flow, New Orleans, Conference-CD, Paper 378, May 27 - June 1, 2001.

- [8] Sato, Y., Sadatomi, M., Sekoguchi, K., Momentum and heat transfer in two-phase bubble flow, *International Journal on Multiphase Flow*, 7, pp.167-177, 1981.
- [9] Lucas, D., Krepper, E., Prasser, H.-M., Prediction of radial gas profiles in vertical pipe flow on basis of the bubble size distribution. *International Journal of Thermal Sciences*, 40, pp. 217-225, 2001.

FLOW PATTERN AND VOID FRACTION FLUCTUATION IN OSCILLATORY TWO-PHASE FLOW

M. Hirayama, H. Umekawa, M. Okano and M. Ozawa

Department of Mechanical Engineering
Kansai University
3-3-35 Yamate-cho, Suita,
Osaka 564-8680, JAPAN
Phone and Fax: +81 6 6368 0804
E-mail: ga1m043@kansai-u.ac.jp

ABSTRACT

Safety of large-capacity boiling channel systems were highly advanced in these three decades. But low-mass flux and low-pressure operation of recent advanced compact boilers brought about high possibility of unstable flow condition. Many existing works focused mainly on the stable flow, and therefore discussions on the effect of the flow oscillation on the safety issues, e.g., CHF are essential as was pointed out by Ozawa et al.^[1]. Aiming at the fundamental understanding of the possible mechanisms of these CHF problems, this paper focuses the discussion on the experimental and analytical investigations about the effect of oscillatory flow on the flow pattern and void fraction behavior. Then, the results are summarized as follows: (1) The flow pattern transition at local point was different under oscillatory flow condition from the steady condition, and a large bubble and thus slug flow is temporarily formed in the gas injection area during the flow reversal state. (2) Void fraction fluctuation and void propagation velocity were well predicted by the simulation based on the drift flux model.

1. INTRODUCTION

In these three decades, many researches on critical heat flux (CHF) have been conducted and many correlations have been proposed. Therefore, the safety of boiling system was extensively advanced, and the efficiency has been highly improved than predate typically in large-capacity boilers and nuclear reactors. On the other hand, in recent small capacity boiler technologies considerable efforts were directly toward downsizing and high efficiency of the boiling systems, which have brought about low-mass flux and low-pressure operation, leading easily to unstable flow condition. Most of the existing researches on critical heat flux have focused on the stable flows, while the researches on the effect of flow oscillation on the CHF are very few. In actual boiling systems, parallel evaporating tubes are normally installed and start-up or load-changes are usual events, which may cause flow instability. Ozawa et al.^[1] and Umekawa et al.^[2] pointed out that the CHF is significantly deteriorated by flow instability. When the tube wall is thin, i.e. the heat capacity of tube wall is small, and the mass flux is relatively high, the CHF is dominated by two-phase flow dynamics and is well predicted by a simple lumped-parameter model. On the other hand, when the mass flux is low, as in compact water-tube boilers, the lumped-parameter model does not work well. This may be due to the following reasons: First, the flow structure under flow oscillation has not been well understood, and second, constitutive relationships are based on stable flow condition. In such boiling channels, retrieval tubes are usually installed but the example mentioned below demonstrates the importance of the present investigation.

Suppose a horizontal boiling channel operated at relatively low mass flux. In a certain operating

region, the phase stratification takes place, and thus the upper wall of the tube suffers easily from the dryout even at low quality. When the flow pattern transition takes place from such stratified flow to wavy or intermittent flow, the liquid replenishment to the upper wall is enhanced, leading to cool down the upper wall. Such a liquid replenishment may be greatly, but periodically, enhanced by the flow oscillation, i.e. flow instability, while the wall may, on the contrary, suffer from the severe dryout owing to the drastic reduction during the oscillation cycle. For full understanding the phenomena, it is indispensable to evaluate the influence of flow oscillation on the flow structure, including void fraction behavior, and flow pattern transition.

Aiming at this subject, experimental and analytical investigation was conducted into upward and downward two-phase flows, as a first step, by imposing flow oscillation of the liquid phase.

2. EXPERIMENTAL APPARATUS

Experiments were conducted using upward and downward flow systems. Experimental apparatuses of the upward and downward flows have the same basic structure. The upward-flow system is shown in Fig. 1. Experimental setup mainly consists of a reserve tank, a constant-discharge pump, a mechanical oscillator, a test section, and a gas-liquid separation tank. Water at room temperature was used as working fluid. Water from the reserve tank was supplied at a constant flow rate, measured by rotameter, into the test section. The mechanical oscillator was installed just upstream of the test section, and imposed flow oscillation of a predetermined amplitude on the constant flow from the pump. The volumetric liquid flux in the test section was estimated as the sum of the flow supplied from the pump and the fluctuating component induced by the oscillator, and is given by

$$j = j_0 + \Delta j \sin(2\pi t/\tau) \quad (1)$$

where j_0 is mean volumetric flux supplied from the pump, Δj and τ are the fluctuation amplitude and the period respectively. Oscillatory inflow was monitored by an orifice located near the entrance of the test section.

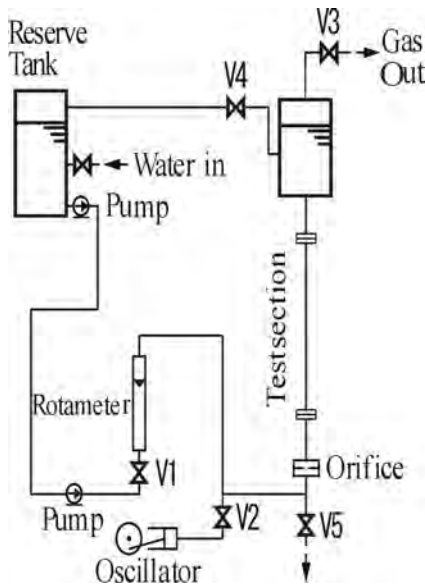


Figure 1: Experimental apparatus.

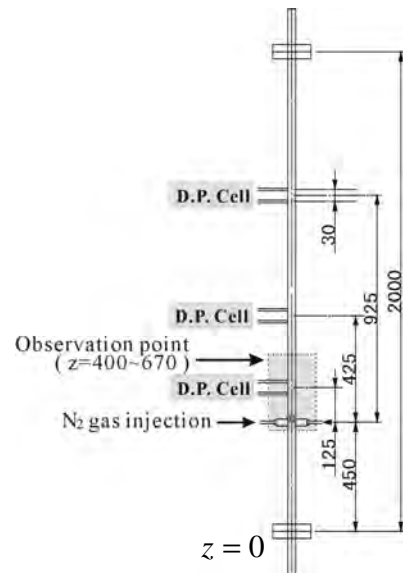


Figure 2: Test section.

The test section consists of a plexiglass tube with dimensions of 2000 mm length, 15 mm I.D. and 19 mm O.D. Three differential-pressure gauges were connected to the test section for measuring the pressure drop in 30 mm distance. As the frictional pressure drop was estimated to be rather small

in magnitude, the measured pressure drop was assumed to be equal to the gravitation at pressure drop, and thus directly converted to the local space-averaged void fraction in 30mm distance. Nitrogen gas (N₂ gas) injection port is located at 450 mm from the inlet of the test tube. N₂ gas was injected at the constant flow rate through a critical flow nozzle. Water and N₂ gas flowed through the test section were separated by gas-liquid separation tank. Then, water was fed back to the reserve tank, and N₂ gas was discharged to the atmosphere.

Experimental condition is listed in Table I. Experiment was conducted under atmospheric pressure. The volumetric liquid flux was set in the range of 0.02-0.16 m/s, the volumetric gas flux, 0.02-4.5 m/s, aiming to observe flow-pattern transition at low mass flux. The oscillation period was set either at 2, 4 or 6 sec, being consistent to the previous CHF experiment^[1,2]. As the flow oscillation was generated by using a cylinder-piston unit of constant stroke, discharged volume during a half cycle was constant, being independent of the oscillation period. This means that the amplitude of volumetric liquid flux is a function of the oscillation period, and thus the amplitude becomes maximum at short period, 2 sec, while it becomes minimum at longer period, 6 sec.

Table I: Experimental condition

Flow direction	Pressure	j_L	j_G	τ	Δj_L
	MPa	m/s	m/s	s	m/s
Upward Flow	0.1	0.02-0.9	0.02-4.5	2	0.327
Downward Flow				4	0.164
		6	0.109		

3. EXPERIMENTAL RESULTS AND DISCUSSIONS

3.1 Flow pattern

Flow pattern identification was conducted by direct visual observation and using high-speed video camera, and observation zone for flow pattern maps are located from $z = 400$ mm to $z = 670$ mm (-50 mm to 220 mm from the gas injection port) in Fig. 2.



Figure 3: Flow pattern transition in upward flow ($j_L = 0.1$ m/s, $j_G = 0.03$ m/s, $\tau = 2$ s, $\Delta j_L = 0.327$ m/s, vertical upward flow, successive photo period 0.2s).

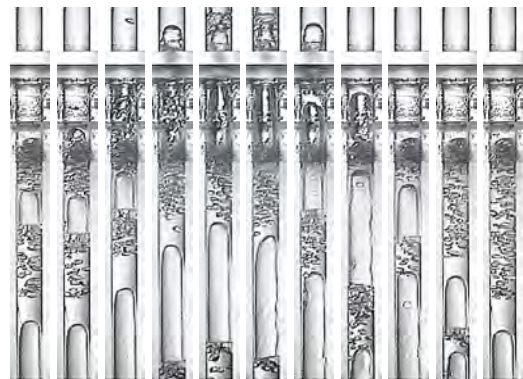


Figure 8: Flow pattern transition in downward flow ($j_L = 0.04$ m/s, $j_G = 0.15$ m/s, $\tau = 4$ s, $\Delta j_L = 0.164$ m/s, vertical downward flow, successive photo period 0.4s).

Upward flow Observed flow pattern under oscillatory upward flow is shown in Fig. 3. The time-averaged volumetric flux of gas phase corresponds to the bubbly flow region.

During the states (2)-(7) in Fig. 3, flow is stagnant or flow reversal state. Flow is bubbly flow at the state (1). But during flow reversal, small bubbles agglomerate to form a large bubble. Then, the large bubble grown up and moved upward gradually. Then during the states (8)-(11), two-phase mixture is pushed upward with an increase in the liquid flow rate. Such a movement of large bubble depended on the liquid phase behavior.

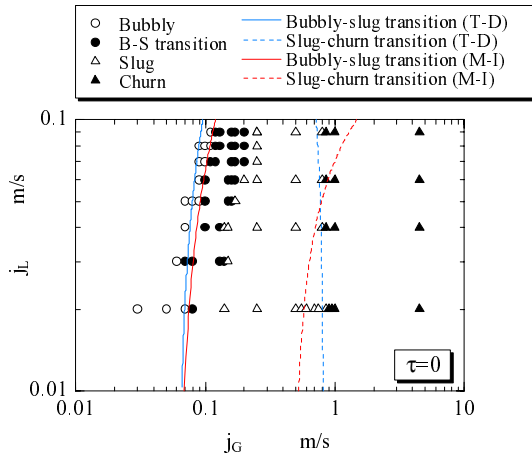


Figure 4: Flow pattern map in upward flow ($\tau = 0$ s, $\Delta j_L = 0$ m/s).

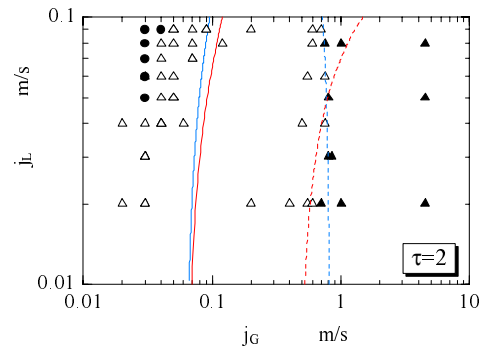


Figure 5: Flow pattern map in upward flow ($\tau = 2$ s, $\Delta j_L = 0.327$ m/s).

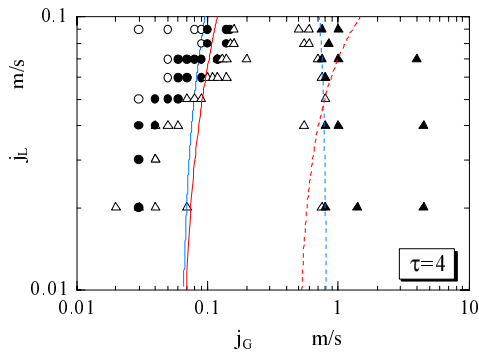


Figure 6: Flow pattern map in upward flow ($\tau = 4$ s, $\Delta j_L = 0.164$ m/s).

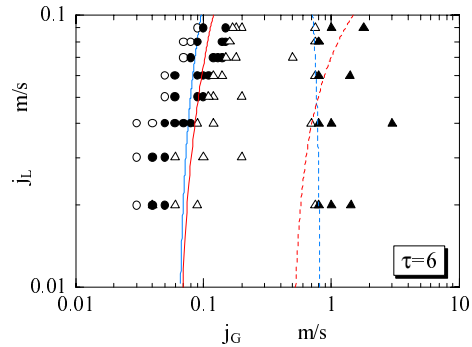


Figure 7: Flow pattern map in upward flow ($\tau = 6$ s, $\Delta j_L = 0.109$ m/s).

Flow pattern maps for stable flow and oscillatory flow at the oscillation period 2 s, 4 s and 6 s are shown in Fig. 4 - Fig. 7, where j_L and j_G represent the volumetric liquid and gas fluxes, respectively. The flow pattern boundaries by Taitel-Dukler (T-D) and Mishima-Ishii (M-I) are drawn as well. The predicted boundaries are in good agreement with the experimental observation for stable flow, even in such a developing region near the gas injection point. In the present range of experiment, flow pattern transition is mainly controlled by the volumetric gas flux.

The flow pattern map under oscillatory flow condition at the period $\tau = 2$ s is shown in Fig. 5. As the volumetric liquid flux oscillates with relatively large amplitude, it may be claimed the time-averaged value is not suitable for the flow pattern map. Provided the quasi-steady state, the instantaneous value of the volumetric flux might be useful as the coordinate system. On the other

hand, the oscillation period, in the present experiment, is the same order of magnitude as the bubble residence time in the test section. Then the volumetric liquid flux changes before the bubble, formed at the injection point at a certain instant, flows out from the test tube. Then the quasi-steady state assumption is not suitable here. Thus, the time-averaged volumetric flux is used for the coordinate as the representative value.

Comparing Figs. 5 with 4, the region of slug flow becomes rather wide, i.e. the bubbly-slug boundary sifts toward the lower j_G region. On the other hand, the slug flow-churn flow boundary is hardly affected by the flow oscillation. The flow pattern map under oscillatory flow condition at the period $\tau = 4$ s is shown in Fig. 6. Comparing with Fig. 5 for $\tau = 2$ s, the bubbly flow region extends, i.e. bubbly-slug boundary shifts toward the higher j_G region. This may be not due to the difference in the period but due to the fact that the amplitude Δj_L in Fig.6 is a half of that at $\tau = 2$ s in Fig. 5. This means that the effect of flow oscillation becomes less significant than the case at $\tau = 2$ s. Figure 7 is the flow pattern map for $\tau = 6$ s. Similarly to Fig. 5, an increase in the oscillation period results in the expansion of bubble flow region. At higher j_G , the effect of flow oscillation on the boundary is rather weak and the slug-churn boundary retains almost the same j_G -values as in the steady flow.

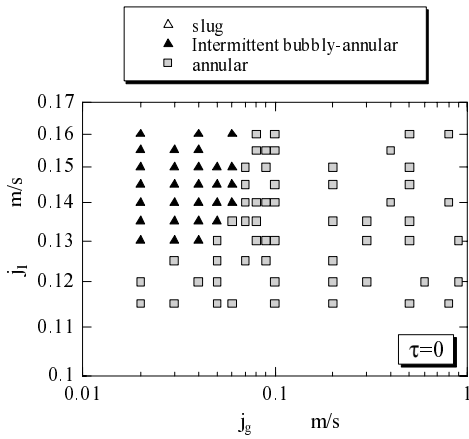


Figure 9: Flow pattern map in downward flow ($\tau = 0$ s, $\Delta j_L = 0$ m/s).

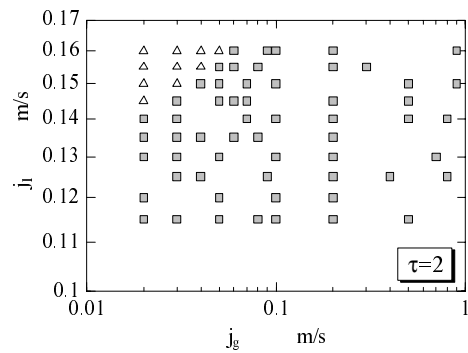


Figure 10: Flow pattern map in downward flow ($\tau = 2$ s, $\Delta j_L = 0.327$ m/s).

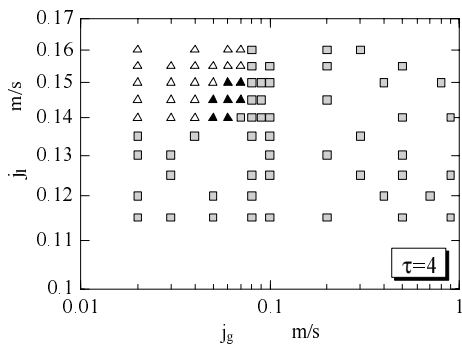


Figure 11: Flow pattern map in downward flow ($\tau = 4$ s, $\Delta j_L = 0.164$ m/s).

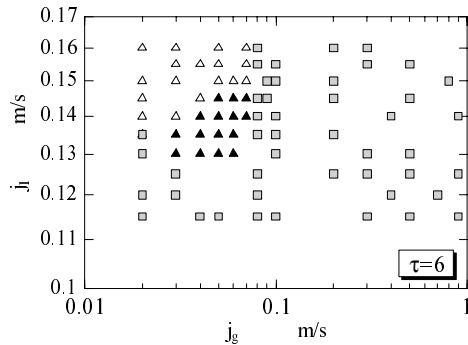


Figure 12: Flow pattern map in downward flow ($\tau = 6$ s, $\Delta j_L = 0.109$ m/s).

Downward flow Figure 8 shows successive photos of two-phase flow under oscillatory downward flow. The flow pattern was identified at 125 mm below the injection point. Under stable

flow condition, intermittent bubbly-annular flow and annular flow were dominant.

During the states (2)-(5) in Fig. 8, flow is stagnant or reversal flow state. During reversal flow or stagnant state, large and small bubbles moves upstream, and the large bubble that passed through the gas injection point becomes large moreover or new large bubble is formed. Then during the state (6)-(11), the temporarily formed large bubble and small bubbles are pushed downstream with an increase in the liquid flow rate. Comparing with upward flow, the large bubble is stagnant at the same point over a long period. In a real boiling system, this is very dangerous because the bubble stagnation brings about the CHF.

Figure 9 - Figure 12 show flow pattern map for stable flow and oscillatory flow at the oscillatory period 2 s, 4 s and 6 s. Oscillatory downward flow showed very irregular flow pattern. Then, annular flow was strictly identified, i.e., the departure from annular flow was determined by appearance of churn or slug even in a short period during a cycle.

The flow pattern map at the stable flow is shown in Fig. 9. As mentioned above, intermittent bubbly-annular flow and annular flow are observed, and annular flow is dominant under lower liquid flux but higher gas flux.

The flow pattern map under oscillatory flow state at a period $\tau = 2$ s is shown in Fig. 10. In the higher j_L and lower j_G region, transition from intermittent bubbly-annular flow to slug flow is observed, and intermittent bubbly-annular flow is disappeared. The flow pattern under the oscillatory flow condition at the period $\tau = 4$ s is shown in Fig. 11, and at $\tau = 6$ in Fig. 12. Comparing with the Fig. 10 for $\tau = 2$, the slug flow region extends, and intermittent bubbly-annular flow is observed again in the higher j_L and the lower j_G region. As in the case of upward flow, fluctuation amplitude has a dominant effect on the formation of the large bubble at $\tau = 2$. On the other hand, the large bubble is not formed in cases of $\tau = 4$ and $\tau = 6$ because of the amplitude being relatively small.

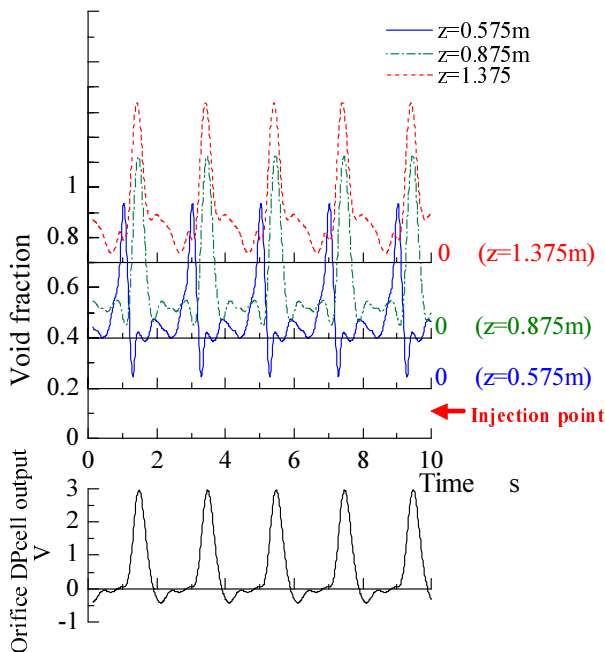


Figure 13: Void fraction fluctuation ($j_L = 0.1$ m/s, $j_G = 0.03$ m/s, $\tau = 2$ s, $\Delta j_L = 0.327$ m/s, vertical upward flow).

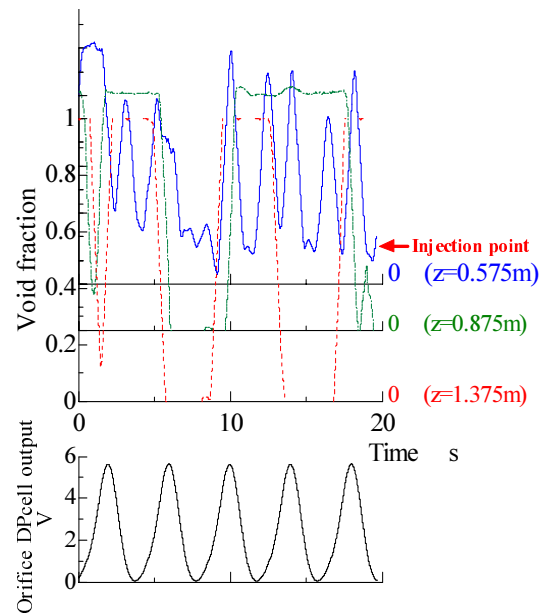


Figure 14: Void fraction fluctuation ($j_L = 0.15$ m/s, $j_G = 0.04$ m/s, $\tau = 4$ s, $\Delta j_L = 0.164$ m/s, vertical downward flow).

3.2 Void fraction fluctuation

Local void fraction was measured at 125 mm, 425 mm and 925 mm away from the gas injection point. Measured void fraction data includes noise, therefore the data was smoothed by successive averaging over 1/8 periods, and sharp pulse-like fluctuations were successfully suppressed.

Upward flow The void fraction fluctuation is shown in Fig. 13 together with the pressure difference in orifice indicating the oscillation amplitude and period in the liquid inflow. During the flow reversal state and stagnation, the void fraction increases rapidly at $z=0.575$ m point. This abrupt increase corresponds to the large bubble formation. Then, with an increase in the inflow, a peak in the void fraction moves downstream, i. e. the large bubble formed there moves downstream.

In the case of the steady flow, flow pattern is almost consistent throughout the observed zone. However under the oscillatory flow, the flow pattern is different, or principle, at every local point and instant. Accordingly, the void fraction fluctuation becomes considerable under the oscillatory condition.

Downward flow The void fraction fluctuation is shown in Fig. 14. In the downward flow, a large bubble, formed at the gas injection point, grows up rapidly, and the large bubble tends to stagnate under low volumetric liquid flux. Small bubbles agglomerate in the vicinity of $z = 0.575$ m. This large bubble grows up in its scale, and then stagnates downstream the injection point. Formation and growth of the large bubble is irregular, and may be hardly predicted. This may be a reason of a wide dispersion of the downward-flow CHF in the boiling system ^[1].

4. VOID PROPAGATION SIMULATION

As is well known, the density wave oscillation is caused by the propagation delay of the void wave. The bubble agglomeration and bubble stagnation phenomena can be described with reference to the void wave propagation and the interaction with the flow field. Thus in this section, the numerical simulation is conducted on the basis of the drift-flux modeling originally proposed by Zuber et al. ^[3,4,5].

4.1 Void propagation equation

The following mass conservation equations are used in the analysis.

$$\frac{\partial}{\partial t}(\alpha \rho_G) + \frac{\partial}{\partial z}(\alpha \rho_G u_G) = 0 \quad (2)$$

$$\frac{\partial}{\partial t}[(1-\alpha)\rho_L] + \frac{\partial}{\partial z}[(1-\alpha)\rho_L u_L] = 0 \quad (3)$$

Provided incompressible flow of gas, the mass conservation equation of gas phase becomes

$$\frac{\partial \alpha}{\partial t} + \frac{\partial}{\partial z}(\alpha u_G) = 0 \quad (4)$$

This equation is referred to as void propagation equation.

Here the drift-flux model is introduced to express the gas phase velocity.

$$u_G = j + v_{Gj} \quad (5)$$

Then this relationship is substituted into Eq. (4).

$$\frac{\partial \alpha}{\partial t} + \frac{\partial}{\partial z}(\alpha j + \alpha v_{Gj}) = 0 \quad (6)$$

Cross-sectional averaging is introduced

$$\langle f \rangle = \frac{1}{A} \int_A f da \quad (7)$$

Then the void propagation equation is given by

$$\frac{\partial}{\partial t} \langle \alpha \rangle + \frac{\partial}{\partial z} [\langle \alpha j \rangle + \langle \alpha v_{Gj} \rangle] = 0 \quad (8)$$

Now, the following distribution parameter defined by Eq. (9)

$$\langle \alpha j \rangle = \frac{\langle \alpha j \rangle}{\langle \alpha \rangle \langle j \rangle} \langle \alpha \rangle \langle j \rangle = C_0 \langle \alpha \rangle \langle j \rangle \quad (9)$$

and the weighted mean drift velocity defined by Eq. (10)

$$\langle \alpha v_{Gj} \rangle = \frac{\langle \alpha v_{Gj} \rangle}{\langle \alpha \rangle} \langle \alpha \rangle = \overline{v_{Gj}} \langle \alpha \rangle \quad (10)$$

are substituted into Eq. (8), then

$$\frac{\partial}{\partial t} \langle \alpha \rangle + \frac{\partial}{\partial z} [C_0 \langle \alpha \rangle \langle j \rangle + \overline{v_{Gj}} \langle \alpha \rangle] = 0 \quad (11)$$

This equation is rewritten in the next form for convenience.

$$\frac{\partial}{\partial t} \langle \alpha \rangle + \frac{\partial}{\partial z} [\langle \alpha \rangle \langle u_G \rangle] = 0 \quad (12)$$

where

$$\langle u_G \rangle = C_0 \langle j \rangle + \overline{v_{Gj}} \quad (13)$$

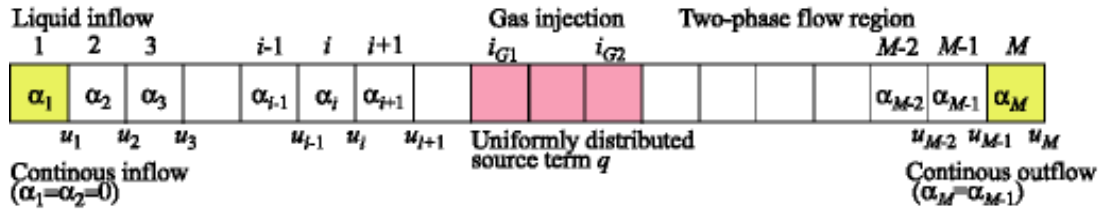


Figure 15: Flow model.

4.2 Model description

The flow model is shown in Fig. 15. The flow model consists of three regions, following along the channel. The first region is a single-phase flow of liquid until N_2 gas is injected. The second region is a mixing region, and the gas injection is conducted uniformly along a length L_G . The last region is a two-phase flow region. The liquid inflow, $\langle j_{L0} \rangle$, is imposed by the sinusoidal fluctuation component, $\langle j_{LA} \rangle \sin(\omega t)$, where $\langle j_{LA} \rangle$ denotes an amplitude of imposed oscillation, ω the angular frequency. On the other hand, the volumetric gas flux, i.e. volumetric gas flow rate injected in the channel, is constant even during the flow oscillation.

Now provided steady state, the following relationship holds based on the mass conservation of gas phase, where gas injection is considered as a source term.

$$\frac{\partial \alpha u_G}{\partial z} = \frac{\partial j_G}{\partial z} = q \quad (14)$$

where $q = j_{G0}/L_G$, and this source term of gas phase means an increase in the volumetric gas flux along a unit length of the channel.

In the present flow model, this source term is constant, but limited in the gas injection region. This source term disappears upstream and downstream the gas injection regions. Then the velocity distribution along the channel is given by the next equations.

In the single-phase flow region of liquid, the velocity $\langle u_G \rangle$ in Eq. (12) must be replaced by

$$\langle j_L \rangle = \langle j_{L0} \rangle + \langle j_{LA} \rangle \sin(\omega t) \quad (15)$$

The flow is incompressible in the corresponding region and the velocity there is determined at the inlet of the channel. This, however, does not mean the void fraction is always zero, i.e. the void may propagate upstream the gas injection region during the flow reversal.

In the gas injection region, the velocity is given by

$$\langle u_G \rangle_{MIX} = C_0 [\langle j_L \rangle + q(z - z_{Gini})] + \overline{v_{Gj}} \quad (16)$$

where z denotes the coordinate measured from the inlet of the channel, and z_{Gini} the coordinate of the inlet of the gas injection region.

Finally, the two-phase region is expressed by

$$\langle u_G \rangle_{TP} = C_0 [\langle j_L \rangle + \langle j_{G0} \rangle] + \overline{v_{Gj}} \quad (17)$$

Then the void propagation equation in each region along the channel is expressed by;

in the single phase flow region of liquid,

$$\frac{\partial}{\partial t} \langle \alpha \rangle + \frac{\partial}{\partial z} [\langle \alpha \rangle \langle j_L \rangle] = 0 \quad (18)$$

in the gas injection region,

$$\frac{\partial}{\partial t} \langle \alpha \rangle + \frac{\partial}{\partial z} [\langle \alpha \rangle \langle u_G \rangle_{MIX}] = q \quad (19)$$

and in the two-phase flow region,

$$\frac{\partial}{\partial t} \langle \alpha \rangle + \frac{\partial}{\partial z} [\langle \alpha \rangle \langle u_G \rangle_{TP}] = 0 \quad (20)$$

These void propagation equations are solved numerically.

The differential equation is solved by a finite-difference method based on the staggered mesh system. Then the velocity is defined at the node, and the void fraction in the middle of the cell. The time-derivative is expressed by the forward-difference scheme, and the convective term by the upwind scheme.

5. SIMULATION RESULTS AND DISCUSSIONS

Distribution parameter and drift velocity for the slug flow was used in this analysis, since there was no difference between the results for the parameters in bubbly flow and slug flow, and moreover in almost all cases in this experiment, the flow pattern was slug flow under the oscillatory flow condition. Then the following relationship was used.

Distribution parameter:

$$C_0 = 1.2 \quad (21)$$

Drift velocity:

$$\overline{v_{Gj}} = 0.35 \left[\frac{g(\rho_L - \rho_G)D}{\rho_L} \right]^{0.5} \quad (22)$$

where ρ_L and ρ_G are the densities of liquid and gas, respectively, D is the diameter of the test section, g is the gravitational acceleration. Then, in the simulation, mesh length was set at 5 mm, and time interval at 0.002 s.

5.1 Void fraction fluctuation

The simulation result is shown in Fig. 16 and Fig. 17. Void fraction fluctuations upstream the gas injection point and in the exit area of test section are added as well as those at measured points in the experiment.

The calculation condition of Fig. 16 is the same as in Fig. 13. During the state of flow reversal, bubbles flow upstream with a liquid reversal flow, and the void fraction upstream the gas injection point increases rapidly. Then with an increase in the inlet liquid flow, the peak of void fraction is pushed downstream. But, as oscillation period is short compared with the residence time of void peak, the void peak moves in the vicinity of 925 mm downstream the gas injection point. Before the void peak moves further downstream, the liquid inflow start to reverse, and the void peak stagnates. And again, with an increase in the liquid inflow, the void peak moves downstream.

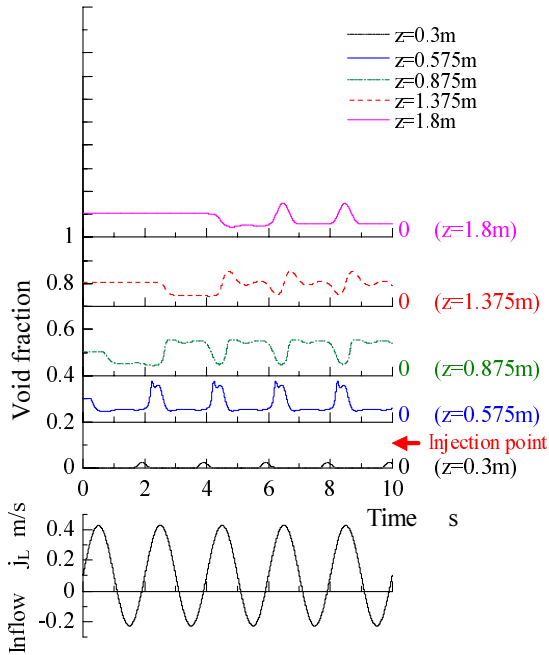


Figure 16: Void fraction fluctuation ($j_L = 0.1$ m/s, $j_G = 0.03$ m/s, $\tau = 2$ s, $\Delta j_L = 0.327$ m/s, vertical upward flow).

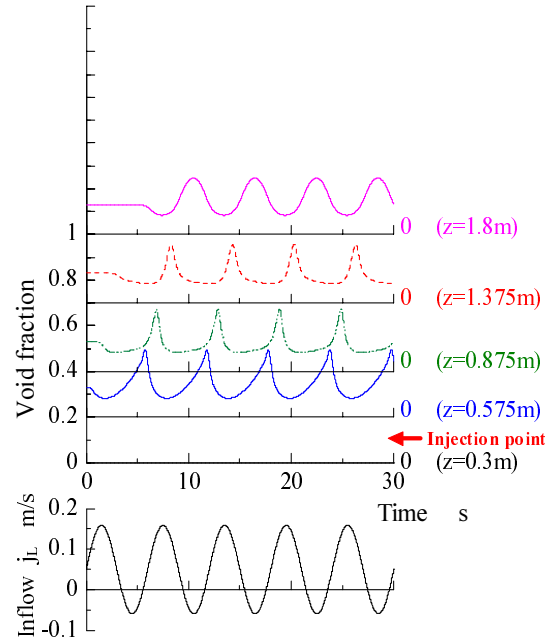


Figure 17: Void fraction fluctuation ($j_L = 0.05$ m/s, $j_G = 0.03$ m/s, $\tau = 6$ s, $\Delta j_L = 0.109$ m/s, vertical upward flow).

The oscillation period in Fig. 17 is longer than that in Fig. 16, $\tau = 6$ s. Similarly to the previous condition, the void fraction-increases rapidly during the state of reversal flow. Then, the void peak

moves with an increase in the liquid inflow along the channel. Comparing with Fig. 16, the void peak does not move in reverse at the point of $z=0.3$ m in Fig. 17. This is because of difference in fluctuation amplitude, and therefore no void is observed at $z=0.3$ m in Fig. 17. In Fig. 16 and Fig. 17, the local void fraction retains almost constant value under the flow reversal of liquid, except for the point that large bubbles are formed. The same tendencies are observed in the experimental results shown in Fig. 13. This suggests the validity of the present simulation in predicting void propagation phenomena.

5.2 Void propagation velocity

Void propagation velocity is determined as a velocity at which the void fraction fluctuation moves along the channel. Phase difference between void fraction fluctuations of two points is found by cross-correlation function, and void propagation velocity between the two points is found with dividing the distance by the phase.

Relationship between void propagation velocity v_{void} and time-averaged total volumetric flux j_T in upward flow is shown in Fig. 18. Comparing the velocities in the upstream and downstream, the velocity in the downstream region seems to be slightly higher than that in the upstream region, while it does not make much difference in the general tendencies. Therefore, mean velocities along the channel are plotted in Fig. 18.

Void propagation velocity increases with an increase in the time-averaged total volumetric flux. The oscillation period has only a little influence on the void propagation velocity. This means that oscillation amplitude has also a little influence, as the amplitude differs by each period in the present case. Then, the following relationships are obtained with the least-squares method, and are drawn in Fig. 18 as well.

From the simulation results,

$$v_{void} = 1.10j_T + 0.17 \quad (23)$$

and from the experiment,

$$v_{void} = 1.59j_T + 0.13 \quad (24)$$

These relationships have actually the same order in magnitude, and moreover mean gas velocity given by the drift-flux model for the time-averaged volumetric fluxes is almost the same order as the value given by Eq. (23). Taking into account the dispersion in the experimental data, it can be said that the void propagation velocity can be predicted with the distribution parameter, the weighted mean drift velocity and the time-averaged total volumetric flux, even in the case of large amplitude of oscillation.

It is clear that the void propagation is brought out with the mean gas velocity, but it is not well established whether the present results can be applied to boiling channel systems. As an example, experimental result obtained in the horizontal boiling channel of liquid nitrogen is shown in Fig. 21. These data was obtained from the wall temperature fluctuations at the upper wall. The tendency, that the void propagation velocity increases with an increase in the total volumetric flux, can be observed, but the void propagation velocity is very small compared with the total volumetric flux. The drift velocity in this horizontal flow was estimated about 0.06 m/s, and the distribution parameter was in the range $1.25 \sim 1.3^{[5]}$. Predicted data based on these parameters is about twice of the data as shown in Fig. 19. This fact suggests that the void propagation effective to the liquid replenishment to the upper wall is quite different from that estimated based on a one-dimensional flow model. Three-dimensional effect may be important in discussing such phenomena, especially in the horizontal flows.

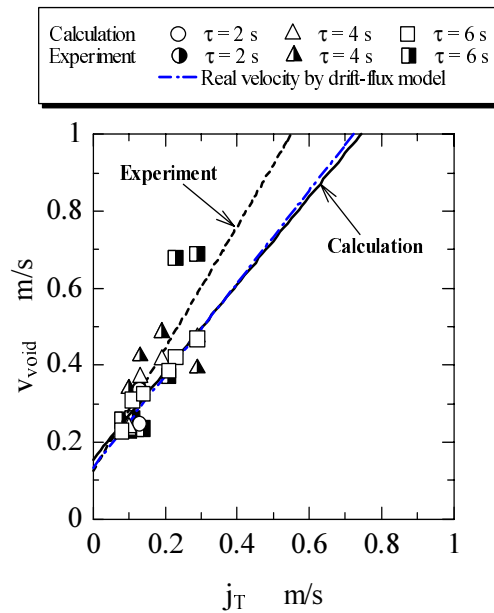


Figure 18: Relationship between void propagation velocity and average total volumetric flux (calculation).

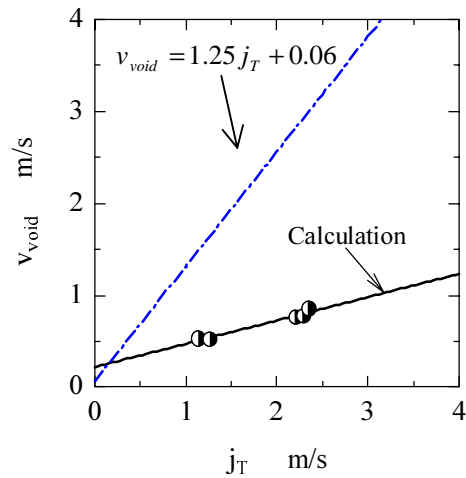


Figure 19: Relationship between void propagation velocity and average total volumetric flux (horizontal boiling flow of liquid nitrogen).

6. CONCLUSION

In order to evaluate the influence of flow oscillation on the flow structure and flow pattern transition including void fraction behavior, experiment and simulation were conducted. The results are summarized as follows:

1. The flow pattern transition at local point was observed under oscillatory flow condition. The large bubble formed there was significantly affected by the oscillatory flow. During the state of flow reversal or stagnant, a large bubble was formed in the gas injection area even in the low quality region originally dominated by bubbly flow. This may lead to the low-quality CHF in boiling channels.
2. Void fraction fluctuation was predicted well by the simulation. At present this is limited only for vertical upward flow.
3. Void propagation velocity was also predicted well by the simulation, and agreed with the experimental data obtained in the vertical flow. Further investigation is, of course, necessary in applying to the actual boiling system.

NOMENCLATURE

A	Cross-sectional area	u	Actual velocity
C_0	Distribution parameter	v_{Gj}	Drift velocity
D	Tube diameter	$\overline{v_{Gj}}$	Weighted mean drift velocity
g	Gravitational acceleration	Greek	
j	Volumetric flux	α	Void fraction
j_0	Mean volumetric flux	ρ	Density
L_G	Gas injection length	τ	Fluctuation period
q	Source term ($= j_{G0}/L_G$)		

Subscripts

<i>G</i>	Gas phase	<i>L</i>	Liquid phase
<i>Gini</i>	Initial point of gas injection	<i>MIX</i>	Mixing of gas and liquid
		<i>TP</i>	Gas-liquid two-phase

REFERENCES

- [1] Ozawa, M., Umekawa, H., Mishima, K., Hibiki, T. and Saito, Y., CHF in oscillatory flow boiling channels, *Ichem E*, vol. 79, Part A, pp. 389-401, 2001.
- [2] Umekawa, H., Ozawa, M., Mitsunaga, T., Critical heat flux and flow pattern under flow oscillation, *Proceedings of The Japan-U.S. Seminar on Two-Phase Flow Dynamics*, pp. 265-271, July 1996.
- [3] Zuber, N. & Findlay, J., Average volumetric concentration in two-phase flow systems, *Trans. ASME J. Heat Transfer* vol. 87, pp. 453-468, November 1965.
- [4] Zuber, N., Staub, F. W., Bijwaard, G., and Koeger, P. G., Steady state and transient void fraction in two-phase systems, *GEAP* 5417.
- [5] Ishii, M., One dimensional drift-flux model and constitutive equations for relative motion between phases in various two-phase flow regimes, *Argonne Nat. Lab. ANL-77-47*, October 1977.

DYNAMIC BEHAVIOR OF GAS-LIQUID TWO-PHASE FLOW SPLITTING AT AN IMPACTING T-JUNCTION

S. F. Wang¹⁾ and M. Shoji²⁾

¹⁾ Department of Mechanical Engineering, school
of Engineering, The University of Tokyo
7-3-1 Hongo, Bunkyo-ku, Tokyo 113-8656, JAPAN
Tel. & Fax: +81-3-5841-6408
E-mail: wang@photon.t.u-tokyo.ac.jp

²⁾ Department of Mechanical Engineering, school
of Engineering, The University of Tokyo
7-3-1 Hongo, Bunkyo-ku, Tokyo 113-8656, JAPAN
Tel. & Fax: +81-3-5800-6987
E-mail: shoji@photon.t.u-tokyo.ac.jp

ABSTRACT

An experimental investigation was carried out on the fluctuation characteristics of two-phase flow splitting at an impacting vertical T-junction (15mm i.d.) to interpret its dynamic behaviour. The statistical analytical method, Root Mean Square (RMS) was employed to exhibit the intensity of the fluctuation, and Power Spectral Density (PSD) was applied to reveal its frequency feature. The main reason for intensifying the fluctuation is considered to be the flow reversal. Thus the critical condition with inception and termination of flow reversal was made clear experimentally. Furthermore, the effect of the flow pattern in inlet tube was discussed in detail.

1. INTRODUCTION

As far as known, piping networks are commonly used in the petroleum industry, chemical process plants, power plants and water-cooled nuclear reactors. Impacting T-junctions are often encountered in these piping networks to distribute two-phase flow.

Several investigations have been undertaken in both horizontal and vertical impacting T-junctions during the past 20 years. Hong (1978) [1] reported experiment results on phase distribution at a horizontal impacting T-junction (9.525 mm i. d.). He concluded that equal phase distribution over a wider range of extraction ratios ($0.15 \leq \frac{W_3}{W_1} \leq 0.85$), where W_1 and W_3 are the mass flow rates through inlet 1 and outlet 3, respectively. Azzopardi et al. (1987) [2] exhibited experimental results on vertical annular two-phase flow entering an equal-sided impacting T-junction (31.8 mm i. d.). They reported that the qualities in each of outlets are only equal when half of the fluids pass into each outlets, i. e. when $W_3/W_1 = 0.5$. They also proposed a model to predict flow split. Azzopardi et al. (1988) [3] conducted experiments on churn flow splitting at a vertical impacting T-junction. They reported that the results show similar trends to data for annular flow obtained by Azzopardi et al. [2] and that the flow split is insensitive to inlet gas and liquid superficial velocity. Hwang et al. (1989) [4] performed an experimental and analytical study of phase separation for two-phase at horizontal impacting tees (38 mm i. d.) and wyes (38 mm i. d. and 45°). They proposed a model based on a dividing-streamline concept and obtained good agreement between model predictions and experimental results. Chien et al. (1992) [5] presented the results of

an experimental investigation conducted on phase splitting of wet steam during annular flow through a horizontal impacting T-junction (2-in. i. d.). They addressed that the extraction ratio and the inlet steam quality have the most significant effects on phase splitting, and that no phase splitting occurs at extraction ratio 0.5. Fujii et al. (1995) [6] proposed a gas-liquid phase separation technique under micro-gravity by using the different inertial force of gas phase and liquid phase through a horizontal impacting T-junction. Hong et al. (1995) [7] described laboratory air/water and field steam flow-splitting tests conducted to develop a method for predicting flow splitting and to find several devices that can be inserted into an impacting T-junction to improve quality distribution in steam lines. Hong et al. (1997) [8] recommended that the best practice for optimising the flow distribution is using impacting T-junctions, with or without insert devices, to maintain uniform steam quality throughout a piping network. Asano et al. (2001) [9] investigated the effect of geometry of impacting T- and Y- (60° , 30°) junctions on phase separation, and stressed that decreasing the angle between the inlet and the side branch could improve the phase separation performance of the Y-junction. However, few of them in the literature deal with time-dependent parameters. Although the idealized case of the true steady state will probably have to be well understood before the more complicated case including fluctuation can be considered, the neglect of the fluctuation of these parameters is acknowledged to be a departure from the physical reality. On the other hand, fluctuation of two-phase flow splitting at T-junctions may cause tube vibration, which will lead to tube failures by fatigue and fretting-wear. So it is vital important to understand fluctuation characteristics of two-phase flow passing through a T-junction.

2. EXPERIMENTAL APPARATUS AND MEASUREMENT

A schematic diagram of the two-phase flow through T-junction loop is shown in Figure 1. The air, before entering the mixing room, was passed through a filter, pressure controller, whilst the water was supplied from the faucet passed through a filter and a rotameter. The mixing room consisted of an annular section surrounding a porous wall section. Water enters it from the periphery whilst the air passes up the middle. The vertical inlet tube of the tee was 1.5 m high, which provided a length/hydraulic diameter ratio of 100. This length was sufficient to ensure that relatively developed air-water two-phase flow entered the T-junction. Two of the horizontal side branches were 1.7 m long, and the inner diameters of all the connecting tubes were 15mm.

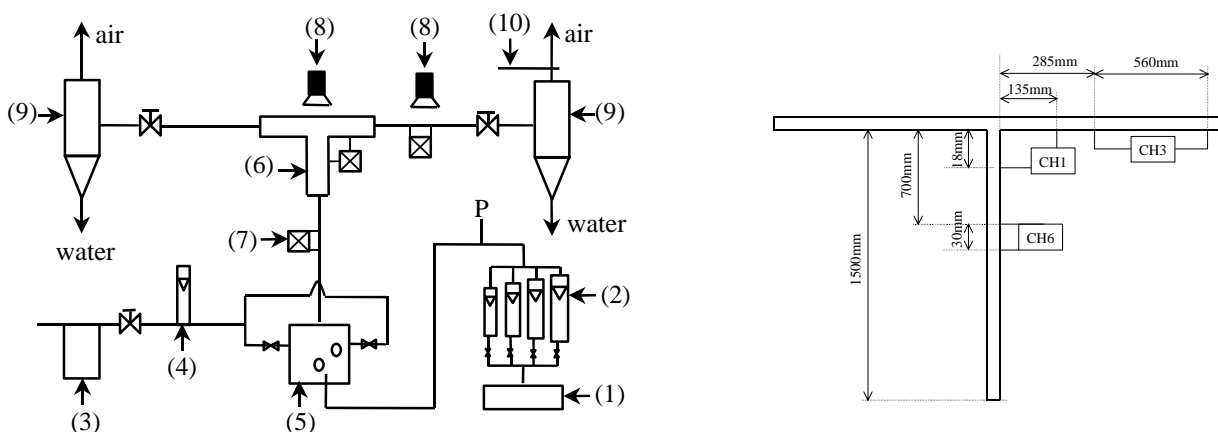


Fig. 1: Schematic diagram of experimental apparatus and test section

(1) Compressor, (2) Air flowmeters, (3) Filter, (4) Water flowmeter, (5) Mixingroom, (6) T-junction, (7) Differential pressure sensor, (8) High speed video, (9) Separator, (10) Hot wire nanometer. CH6: differential pressure at inlet tube; CH3: differential pressure at branch tube; CH1: differential pressure at dividing area.

The apparatus was operated under the following conditions: inlet superficial gas velocities, J_{G1} , ranging between 0.094 and 14m/s, inlet superficial liquid velocities, J_{L1} , ranging between 0.09 and 0.19m/s, and mass extraction rates, $W_3/W_1=0.5$, where W_1 and W_3 are the inlet and branch mass flow rates. All tests were carried out at nominally ambient pressure and room temperature.

Three differential pressure transducers were put into use. One called CH6 was set at the inlet tube. The second one called CH1 was set at the dividing area. The third one, CH3, was at the outlet tube. Gas flow rate at the branch outlet was measured by a hot-wire anemometer sampled simultaneously with differential pressure waveform. All the differential pressure signals and gas flow rate signal were obtained from samples taken over 60 seconds at a rate of 200 samples/s. Water flow rate at the branch outlet was measured by weighting timed efflux. Two high-speed video cameras were employed for visual observation. One was set to record the behaviour of the splitting flow at centre area of the T-junction. The other was set to get the behaviour of two-phase flow in branch tube. Both of the videos were recorded simultaneously with differential pressure signal and gas flow rate signal. About 30 minutes should be waited before each test run to reach the steady state. A steady interface in the separator was maintained while measurement was executed.

3. RESULTS AND DISCUSSIONS

3.1 Classification of the Fluctuation

The fluctuations were classified into four types depending upon the characteristics (intensity and period) of the fluctuation and the observation of the flow reversal from the horizontal outlet tube to the vertical inlet tube:

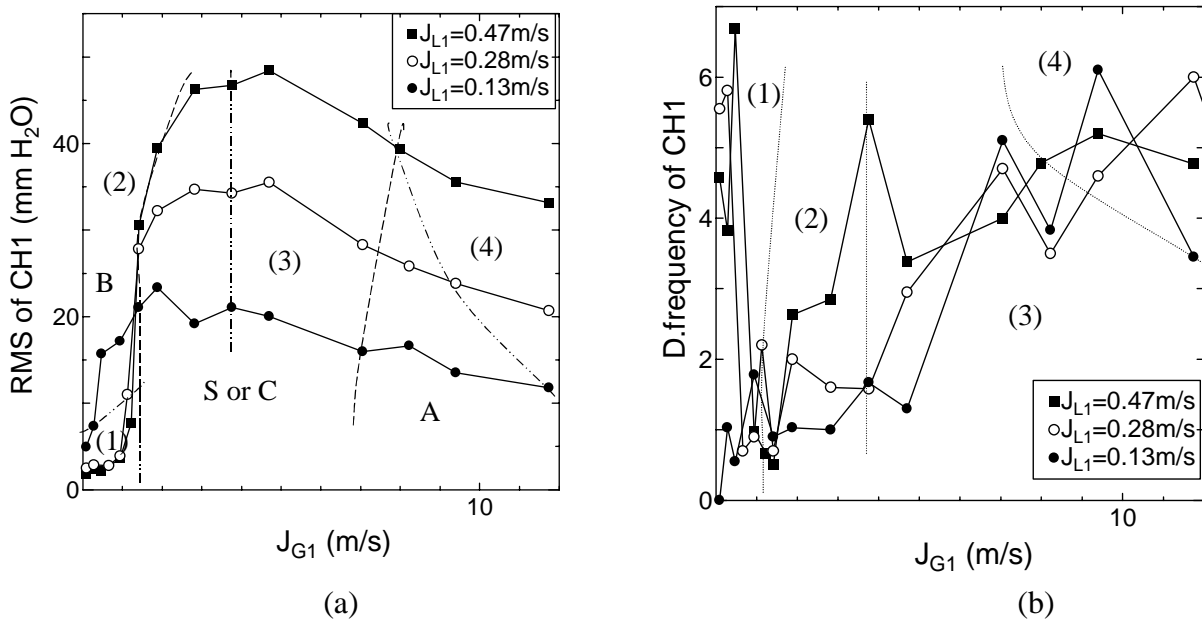


Fig. 2: Fluctuation feature of the differential pressure at the T-junction

(a) Intensity of the fluctuation; (b) Dominant frequency with inlet gas superficial velocity the dash line: flow pattern transition zone; the dot line: flow fluctuation transition zone. CH1: differential pressure at dividing area (see Fig. 1).

Type (1): No reverse flow is observed. The flow pattern inlet is bubbly flow (See Fig. 2 and Fig. 3(a)), the flow fluctuates slightly in T-junction just as in a straight tube, and the fluctuation has very small amplitude and large frequency.

Type (2): Flow Reversal is observed, and the lasting time of the reverse flow is relatively long. The fluctuation is approximately periodic. The amplitude is large but the frequency is very low (Fig. 2). The flow pattern in inlet tube is dispersed-bubbly (Fig. 3 (b)), bubbly-slug and slug.

Type (3): Reverse flow always existed and the last time of it becomes shorter and shorter while the gas superficial velocity increases. The periodicity of the fluctuation is obscure. Both of the amplitude and the frequency are large (Fig. 2). The flow pattern in inlet tube is slug, churn and annular flow.

Type (4): Random fluctuation with no reverse flow observed. The amplitude is relatively small but the frequency is very high (Fig. 2). The flow pattern in inlet is annular or mist flow (Fig. 3(c)).

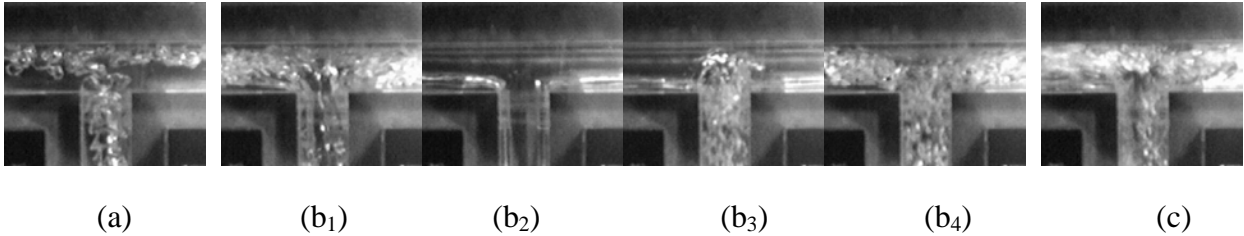


Fig. 3: Fluctuation without flow reversal (a) type (1) and (c) type (4);with flow reversal (b₁₋₄) type (2)

Figure 3 shows a set of photos taken by the high-speed video camera at the center area of the T-junction. The liquid superficial velocity upstream is 0.282(m/s) and the gas superficial velocity is: (a) 0.094(m/s), (b₁₋₄) 1.41(m/s), and (c) 9.4(m/s), respectively. Fig. 3 (b) exhibits a period of the fluctuation with flow reversal initiated as in Fig. (b₁), descended to the vertical main-tube at a distance from the upper stagnation surface of the T-junction as in Fig. (b₂), ascended again as in Fig. (b₃), and finished a whole period as in Fig. (b₄).

3.2 The Fluctuation Feature of the Flow in Inlet tube and Outlet tube

(1) Intensity of the flow fluctuation Root Mean Square (RMS) was chosen to evaluate the intensity of the differential pressure fluctuation at each test run. The RMS amplitude of a signal fluctuation, Y_{rms} , can be calculated from the following equation:

$$Y_{rms} = \sqrt{\frac{1}{N} \sum_{i=1}^N (y_i - \bar{y})^2}$$

Where y_i is the instantaneous value, \bar{y} is the time-averaged value and N is the number of instantaneous data for each test run.

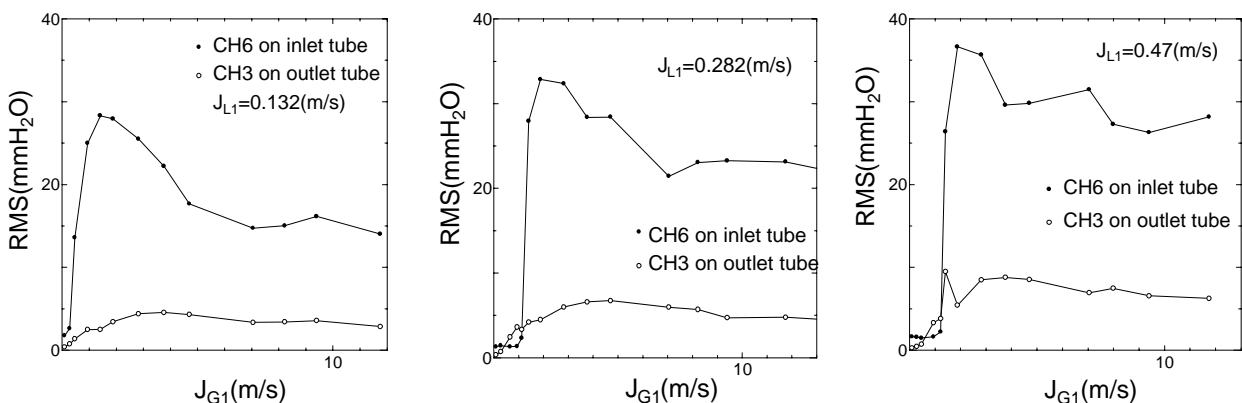


Fig. 4: Intensity of the fluctuation with inlet gas superficial velocity

Figure 4 shows the RMS of the differential pressure on inlet tube (CH6) and outlet tube (CH3) with inlet gas superficial velocity. It is obvious that the situation in downstream is quite different from in upstream even though both of the signals were obtained simultaneously. The main reason is

the variety of the flow pattern. After divided by the T-junction, the flow becomes horizontal and the velocity drops to approximately half of the flow in the vertical inlet. Thus the flow pattern, for example, changes from bubbly flow upstream to plug flow downstream. The curve with black dots demonstrates that the intensity of the fluctuation on upstream is strongest in bubbly-slug flow, which designated as fluctuation type (2). The intensity of the fluctuation on downstream does not necessarily reach maximum because the flow pattern is still long-plug. However, increasing the inlet gas velocity further, the long-plug changes to be slug flow and the intensity of the fluctuation on downstream gets its highest level. It can also be seen in Fig.4 that increasing the liquid superficial velocity upstream gives rise to more intensive fluctuation in both inlet tube and outlet tube.

(2) Frequency of the flow fluctuation The Power spectral density (PSD) is usually employed to extract the periodic feature of a signal. In this work, the PSD of the differential pressure fluctuation on upstream and down stream were computed by the Fast Fourier Transform (FFT) technique. The dominant frequency (D.F) corresponding to the maximum power is applied to evaluate the periodicity of the fluctuation of the system. The correlations of the dominant frequency with inlet gas superficial velocity (J_{G1}) at each constant liquid superficial velocity (J_{L1}) are shown in Figure 5.

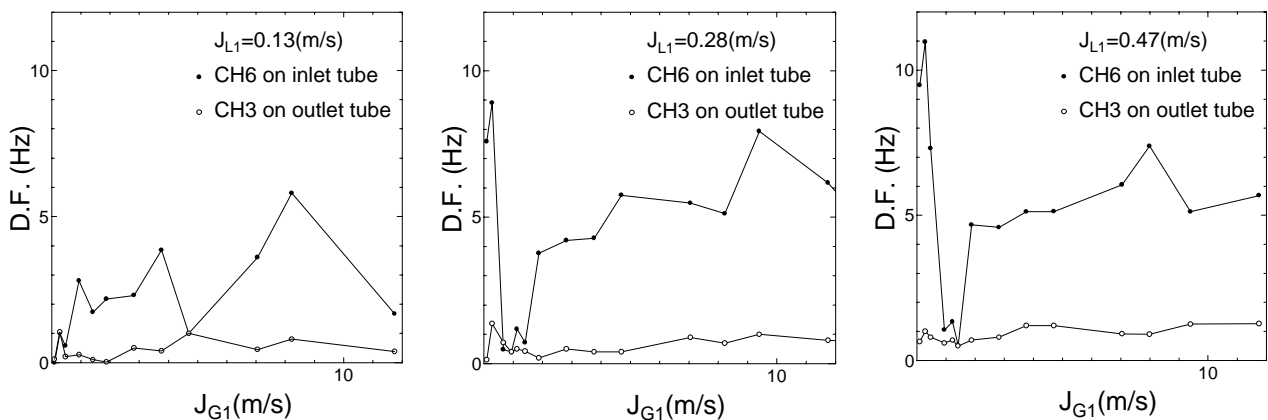


Fig. 5: Dominant frequency of the fluctuation with gas superficial velocity upstream

As can be seen, the lowest frequency of all test runs exists in bubbly-slug transition area where the power of the fluctuation has its maximum (Fig. 6) and the RMS of the fluctuation on main-tube is the largest (Fig. 4) as well. It is reasonable since resonance takes place while the frequency of the upstream and downstream is approximately equal. It is very dangerous in industrial application. While increasing the inlet gas velocity, the dominant frequency increases as a whole. Except for bubbly flow, the curve of the dominant frequency on both upstream and down stream has the similar tendency. It can be deduced that the effect of the fluctuation upstream on downstream is significant in frequency domain.

3.3 Mechanism of the Fluctuation

Azzopardi et al. [2,3] and Hwang et al. [4], and Wang et al. (2002)[10] presented that the qualities in each of the outlet tubes are equal when half of the fluids pass into each outlet. In present work, the extraction ratio W_3/W_1 is always kept at 0.5, so the effect of phase separation on the fluctuation is not necessarily considered. It has been investigated in Wang et al. [10] while inlet flow pattern is churn flow.

Discussion on the mechanism of fluctuation at the T-junction is given according to the classification in 3.1 herein.

For type (1): by the observation, the bubbles in branch come from the same segment. (See Fig. 3 (a)) i.e. the bubbles enter into the right outlet tube are from the right side of the inlet tube.

The fluctuation is so weak that it can be neglected to consider bubbly two-phase flow as single-phase flow in some cases.

For type (4), the flow pattern in the inlet tube is annular or mist flow (Fig. 3 (c)). While the flow pattern in branch is the same as in main tube, the fluctuating situation in the T-junction is like in straight tube as well.

Since the type (1) and type (4) of the fluctuation at the T-junction are very similar to that in a straight tube, particular attention is paid on type (2) and (3) in which flow reversal is always observed.

For type (2), the flow pattern in inlet tube is dispersed-bubbly, bubbly-slug and slug. The fluctuation is mainly caused by two factors: one is the inertia difference of the gas phase and the liquid phase. While the flow in inlet tube reach the stagnation area in the T-junction, the gas slug turn into horizontal branch rapidly for its smaller inertia but a part of the liquid slug descend down due to the larger inertia and the resistance of the system. As a result, flow reversal occurs. The interaction of the flow reversal and the compressibility of the gas phase enhance the periodic fluctuation. This phenomenon is so distinct that it can be observed by naked eye.

For type (3), the flow pattern in inlet tube is churn and annular flow. While the incoming flow is churn, the fluctuation of the inlet tube is very complicated. The second flow and third flow are observed. Thus, the interaction of the reverse flow and the arising flow in the main tube becomes more complicated comparing to type (2). The periodicity becomes obscure. While the flow pattern in inlet is annular, but the flow pattern in branch is slug or churn, the fluctuation is random or chaotic. The difference of the fluctuations in branch and in main tube causes the complexity. If the flow pattern in branch is also annular, the fluctuation changes to type (4).

From the analysis above, it is the flow reversal that enhances the fluctuation. So it is very significant to reveal out the inception and termination of flow reversal with variation in flow rates of the phases to avoid or control the flow fluctuation. Figure 7 shows the range of the gas and liquid superficial velocity upstream in which flow reversal occurs.

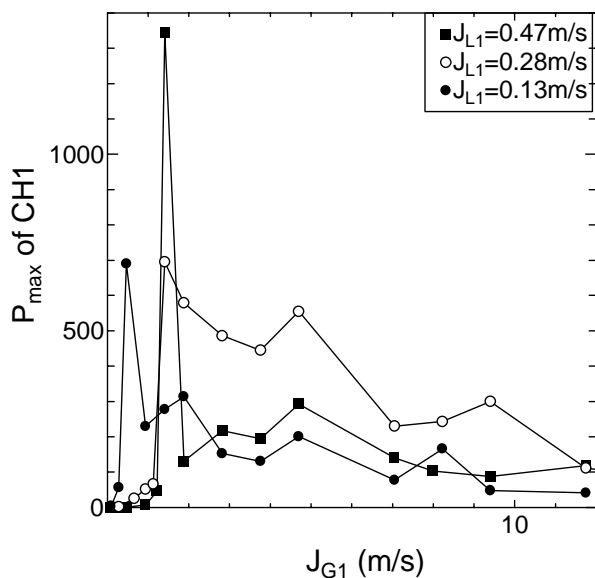


Fig. 6: The largest power with inlet gas superficial velocity. CH1: differential pressure at dividing area.

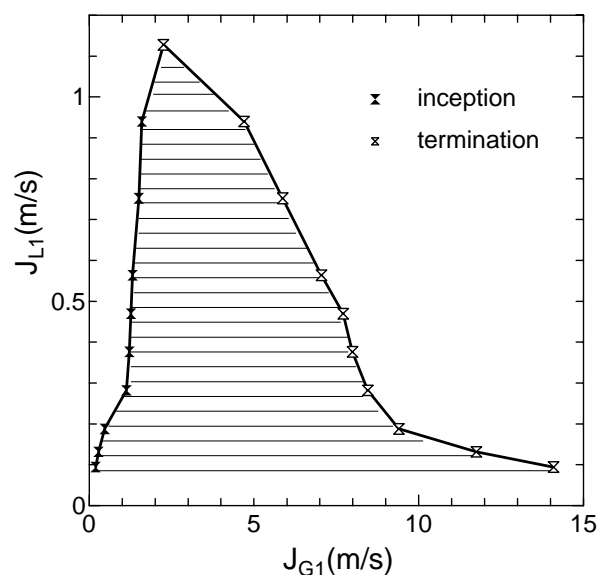


Fig.7: Inception and termination of flow reversal

4. CONCLUSIONS

In order to understand the dynamic behaviour of two-phase flow splitting at an impacting T-junction, particular attention was paid on the fluctuation features. The main reason for intensifying the fluctuation is considered to be the flow reversal. Thus the critical flow rate for inception and termination of flow reversal was disclosed. The effect of the flow pattern in inlet tube on the fluctuation was made clear.

NOMENCLATURE

A	Cross-sectional flow area, [m ²]
D	Inlet diameter, [m]
J _G	Superficial gas velocity [m/s]
J _L	Superficial liquid velocity [m/s]
ΔP ₁₃	Pressure drop from inlet 1 to outlet 3 of the junction [mmH ₂ O]
W	Mass flow rate, [kg/s]
W _G	Gas mass flow rate, [kg/s]
W _L	Liquid mass flow rate, [kg/s]
X	Quality (=W _G /W)
RMS	Root mean square
D.F.	Dominant frequency (Hz)
i.d.	inner diameter of the T-junction [mm]

Subscripts

1,2,3 Inlet 1, outlet 2, and outlet 3 of the T-junction, respectively

ACKNOWLEDGEMENT

The work (partly) was financially supported by the Sasakawa Scientific Research Grant from the Japan Science Society. The authors also would like to express their gratitude to Prof. M. Ozawa of Kansei University, who has provided many suggestions to the present research.

REFERENCES

- [1] Hong, K. C., Two-phase Flow Splitting at a Pipe Tee. *J. Petrol. Technology*, 30, pp. 290-296, 1978.
- [2] Azzopardi, B. J., Purvis, A. & Govan, A.H., Annular Two-phase Flow split at an Impacting T. *Int. J. Multiphase Flow* 13, pp. 605-614, 1987.
- [3] Azzopardi, B. J., Purvis, A. & Govan, A. H., Flow Split of Churn Flow at a Vertical Impacting T. *Int. J. of Engineering Fluid Mechanics*, 1(3), pp. 320-329, 1988.
- [4] Hwang, S. T., Soliman, H. M., Lahey, R. T., Phase Separation in Impacting Wyes and Tees. *Int. J. Multiphase Flow* 15, pp. 965-975, 1989.
- [5] Chien, S.-F., Rubel, M. T., Phase Splitting of Wet Steam in Annular Flow through a Horizontal Impacting Tee. *SPE Production Engineering* 7, pp. 368-374, 1992.
- [6] Fujii, T., Takenaka, N., and Asano, H., The Phase Separation Characteristics of a Gas-Liquid Two-phase Flow in the Impacting T-junction. *Proceeding of the 2th International conference on Multiphase Flow, Kyoto, Japan, 6, pp. 27-32, 1995.*

- [7] Hong, K. C., Griston, S., Two-phase Flow Splitting at an Impacting Tee. *SPE Production & Facilities* 10, pp. 184-190, 1995.
- [8] Hong, K. C., Griston, S., Best Practice for the Distribution and Metering of Two-phase Steam. *SPE Production & Facilities* 12, pp.173-180, 1997.
- [9] Asano, H., Fujii, T., Takenaka, N. & Sakada, K., A Study of the Phase Separation Characteristics in Gas-liquid Two-Phase Flow by an Impacting Y-junction. *Japan Society of Mechanical Engineers* 67, pp. 46-51, 2001.
- [10] Wang, S. F., Shoji, M. Fluctuation Characteristics of Two-Phase Flow Splitting at a Vertical Impacting T-junction. *Int. J. Multiphase Flow* (submitted), 2002.

D. Applied Flow Phenomena and Data

EXPERIMENTAL STUDY OF BUBBLE NOISE AT ORIFICE

Y. SHIOMI, S. NAKANISHI and K. YAMAGAMI

Department of Mechanical and Systems Engineering

Ryukoku University

Seta, Otsu 520-2194, JAPAN

Phone : +81-77-543-7458, Fax : +81-77-543-7457

E-mail : shiomi@rins.ryukoku.ac.jp

ABSTRACT

Noise reduction is strongly required from the viewpoint of comfort in air conditioning. Noise problems caused by two-phase flows in air conditioning units have become more serious, since the level of air conditioner fan noise has decreased. In this study, a large air bubble, water flow and an orifice were used for the purpose of modeling noise problems. The sound occurrence mechanism when the bubble is passing through the orifice was investigated experimentally. A single large bubble in liquid flow was used as the first step and the two-phase slug flow was used as the second step of this study. The pressure behaviors were related to images obtained by the high-speed video. The influence of liquid flux, gas flux and orifice length in two-phase slug flow are discussed.

1. INTRODUCTION

Noises emitted by air conditioners are (a) mechanical vibration sound generated by compressors, (b) air flow noises with fans and heat exchangers, and (c) refrigerant flow noises. The advances in the aerodynamics design reduce the categories (a) and (b) to extremely low level. Consequently, the category (c) becomes more remarkably. Especially, unpleasant sound occurs when vapor bubbles pass through an expansion valve. This problem has been investigated on the basis of trial and error by many engineers concerning to the air conditioner [1] [2] [3]. They suggested that the noise shall be reduced by changing the flow pattern in two-phase flow. Though it is useful for practical application, it is not enough to make clear the fundamental mechanism of an occurrence of this sound. Therefore, it is important to clarify the mechanism of an occurrence of this sound and to grasp a factor of the occurrence of the sound.

In this study, an air bubble, water flow and an orifice were used for the purpose of modeling this problem. The pulse sound and pressure change that occurs when the bubble passes the orifice were measured with a condenser microphone placed close to the orifice and with hydrophones in upstream and downstream of the orifice. The bubble behavior was visualized by a high-speed video camera and was related to pressure behaviors and sound. Experiments were carried out in the case of a single large bubble in liquid flow and two-phase slug flow.

2. EXPERIMENT

Schematic diagram of the test section of two-phase slug flow is shown in Fig. 1. In the case of a single large bubble in liquid flow, the large bubble is injected into water flow using a bypass section instead of the mixing section of two-phase flow. The test section is placed horizontally. It consisted of an acrylic pipe, 7.0 mm I.D., an orifice with 2.0 mm diameter and 5, 10 and 20 mm length, and fittings as shown in Fig. 2. The orifice and fittings were made of acryl or copper and experiments were carried out in these combinations. An outside condenser microphone was installed very close

to the orifice and two hydrophones were upstream and downstream of the orifice, 300 mm apart from the orifice.

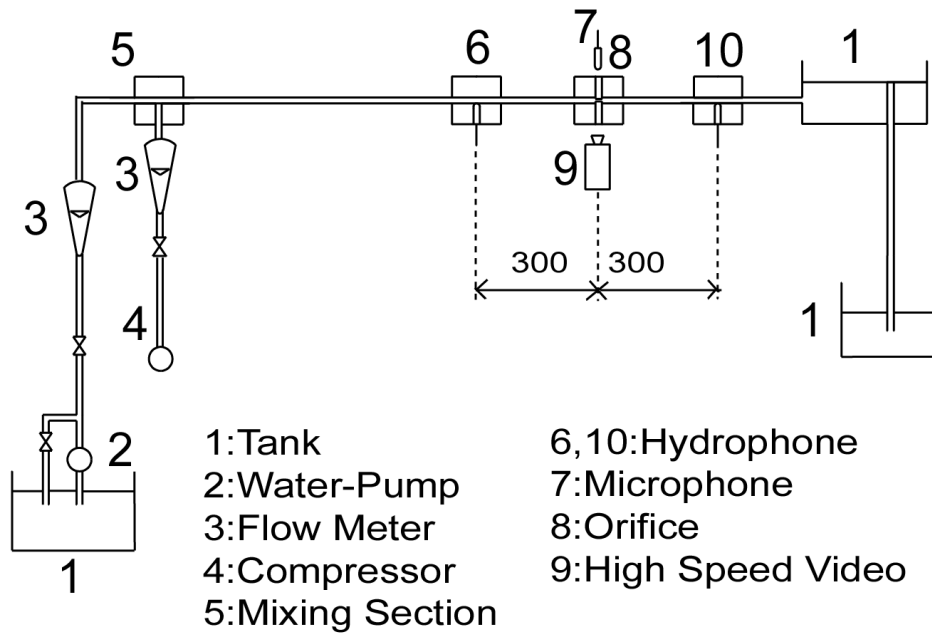


Figure 1: Experimental setup.

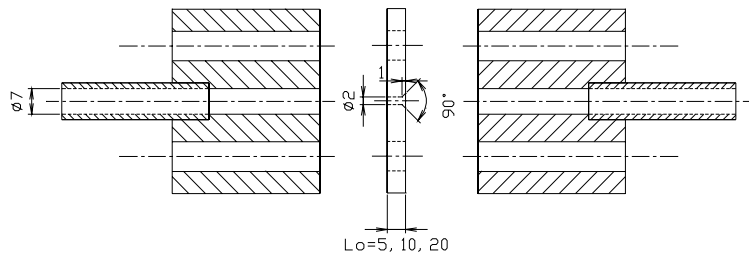


Figure 2: Orifice and fittings.

In the case of a single large bubble in liquid flow, the bubble length was set 30 mm and liquid flux, $j_L=0.4\sim 1.4$ m/s. Experimental range of two-phase flow were $j_G=0.28\sim 0.83$ m/s, $j_L=0.28\sim 0.83$ m/s. Flow patterns in this experimental range correspond to the plug or slug flow in the horizontal pipe without the orifice.

Bubble state was taken by the high-speed video camera at 18000 frames per second. The pressure fluctuations were taken at 100 kHz sampling and related to images obtained by the high-speed video.

3. RESULTS

3.1. Single large bubble in liquid flow

The images of the single large bubble in liquid flow into the orifice are shown in Fig. 3. The time when the bubble tip enters the orifice is set to $t=0$. The bubble tip begins to sharpen, when the

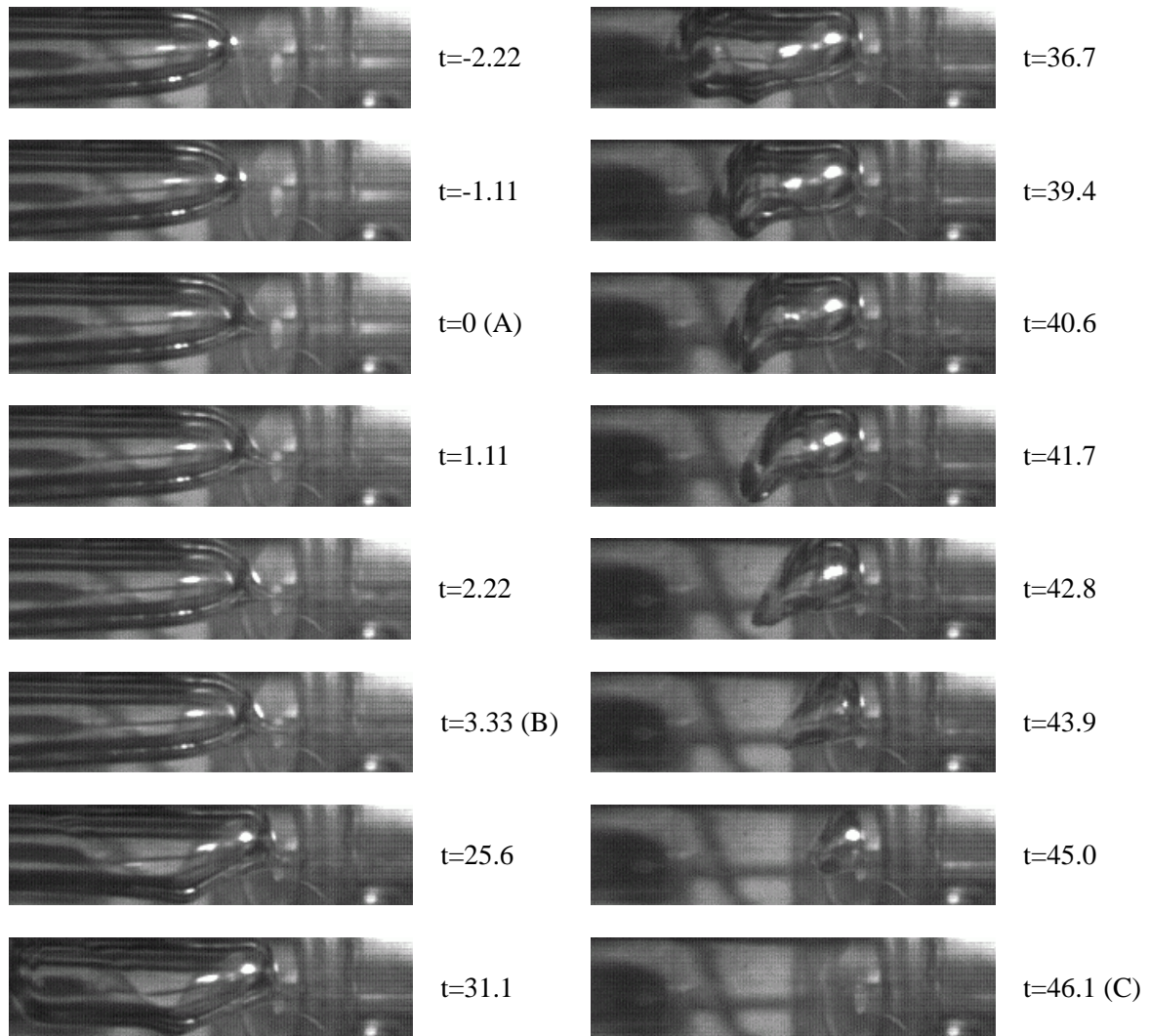


Figure 3: Bubble behavior at orifice entrance (t : msec).

bubble approaches the orifice, and it is drawn in the orifice. In the orifice, the bubble flows as a small plug or small bubble. When the tail of bubble approaches to the orifice, the bubble tip shows wavy. Its tail is not flat, and the central of the tail becomes concave. At the orifice exit, the mixture flows as a jet with the small bubbles.

Figures 4 and 5 show the outputs of hydrophones installed at the upstream and downstream of the orifice and output of the outside microphone in the case of bubble length 30 mm, orifice length, $L_o=5$ mm, liquid flux, $j_L=0.9$ and 1.10 m/s, where A, B, C, D corresponds to the time when the tip of the bubble enters the orifice, the tip of the bubble flows out from the orifice exit, the tail of the bubble enters the orifice, and the tail of the bubble flows out from the orifice exit. When the bubble enters the orifice, the pressure of the upstream begins to increase gradually and that of the downstream decreases and it has the minimum value. Then it increases again. When the tail of bubble enters the orifice, the pressure of the upstream suddenly decreases and large pressure fluctuation of the outside microphone is obtained. The pressure of the upstream damps with the oscillation after the bubble passes the orifice. The sound occurrence through the orifice could be classified into two kinds; a) the projection sound occurred at the instance when the tip of the bubble projects from the orifice, and b) the injection sound occurred when the tail of the bubble sucked into

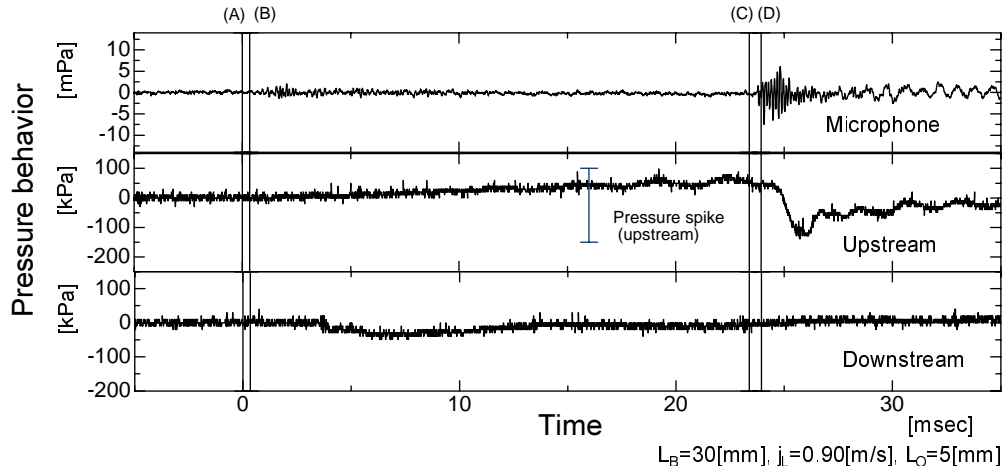


Figure 4: Pressure behavior with injection sound.

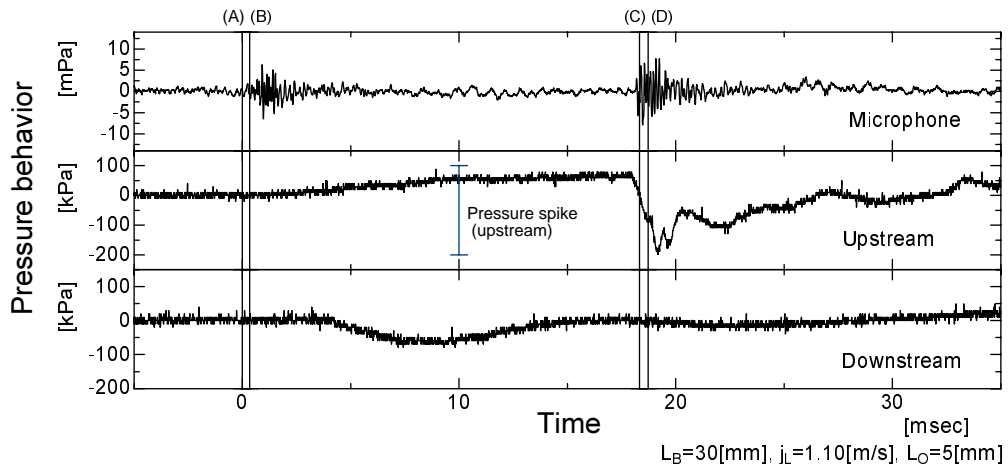


Figure 5: Pressure behavior with injection sound and projection sound.

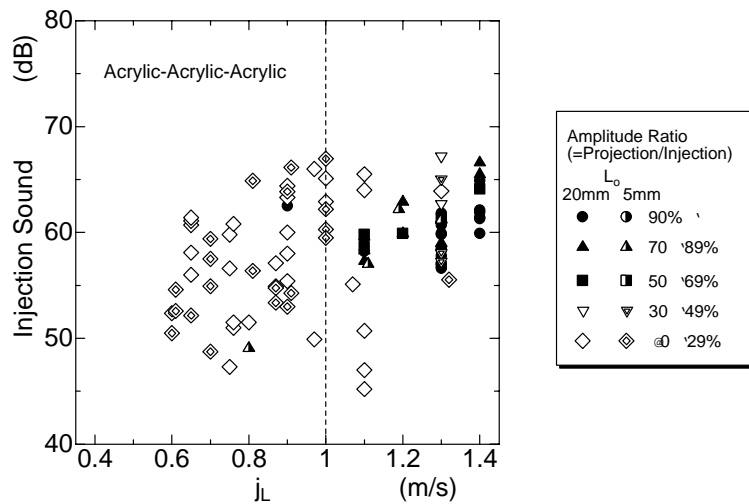


Figure 6: Injection sound vs liquid flux.

the orifice. The former observed in the range of $j_L > 1$ m/s, the later observed in all the experimental range, $j_L = 0.4 \sim 1.4$ m/s. To make clear mentioned above, the injection sounds are plotted against the liquid flux in Fig. 6 using an amplitude ratio that defines as projection sound divided by injection sound. The projection sound is remarkable which means the high amplitude ratio in the range of $j_L > 1$ m/s. This tendency was observed in other combinations of the orifice and fittings.

Pressure spikes at upstream of the orifice are plotted against the liquid flux in several combinations of materials for the orifice and fittings in Figs. 7-10. Pressure spike increases with increasing liquid flux without reference to the orifice length and combinations of materials.

The orifice length does not influence on the condition about two kinds of sound occurrence and sound pressure level. The combination of materials using for the orifice and the fittings does not influence the pressure behavior measured by the microphone, but effects the sound pressure level. The sound pressure levels are small according to the following order; acrylic fittings and orifice, acrylic fittings and copper orifice, copper fittings and acrylic orifice, copper fittings and orifice.

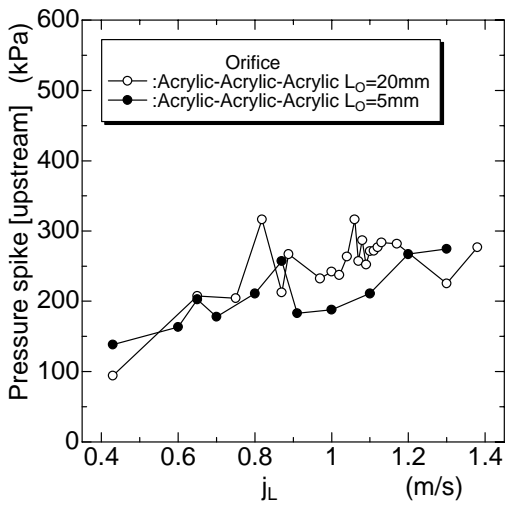


Figure 7: Pressure spike vs liquid flux.

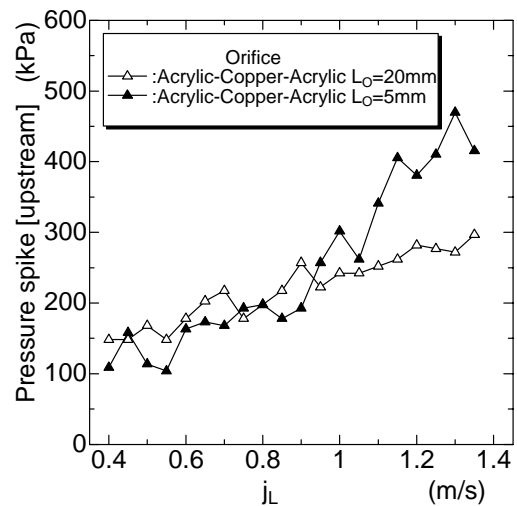


Figure 8: Pressure spike vs liquid flux.

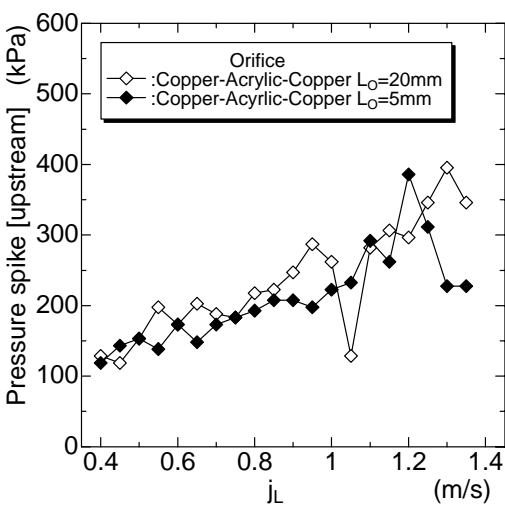


Figure 9: Pressure spike vs liquid flux.

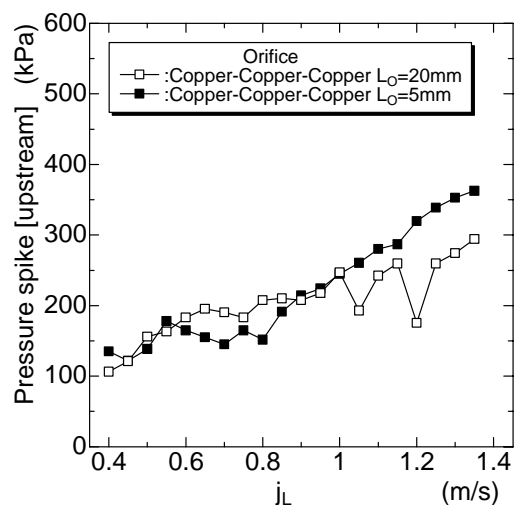


Figure 10: Pressure spike vs liquid flux.

3.2. Two-phase slug flow

Images obtained by the high-speed video in two-phase slug flow are shown in Figs. 11 and 12. At $j_G=0.28$ m/s and $j_L=0.28$ m/s, a shape of large bubble in upstream of the orifice is smooth as same as in the single large bubble in liquid flow and its length is approximately 40 mm. The behavior of large bubble at the orifice is almost same as in the single large bubble in liquid flow. As bubbles flow continuously, large bubble stagnates at the orifice exit. If the test section is set in vertically, this stagnant bubble might not be observed. At the orifice exit, the bubble flows out as a jet with small bubbles into stagnant bubble. At $j_G=0.56$ m/s and $j_L=0.56$ m/s, a shape of large bubble upstream of the orifice is wavy and bubble flows out as a stronger jet. Therefore, the flow seems milky. This consists of many smaller bubbles and they circulate at the orifice exit. After the large bubble passes through the orifice, the flow oscillation was observed upstream of the orifice.

Figure 13 shows the sound spectra obtained by the outside microphone at the orifice. Sound level increases with the increase in liquid flux and shows the same peak of the frequency. On the other hand, the sound level also increases with the increase in gas flux and the peak of the frequency shifts toward higher as the gas flux increases as shown in Fig. 14. In respect of the orifice length, the peak of the frequency in $L_o=10$ mm moves to about 1 kHz smaller one in $L_o=5$ mm as shown in Fig. 15. The difference of sound level of a different liquid flux is larger than that of gas flux because the momentum of liquid phase is larger than that of gas phase. Therefore, the sound level is deeply concerned with the momentum of the two-phase flow.



Figure 11: Bubble behavior at orifice (msec)
 $j_G=0.28$ m/s, $j_L=0.28$ m/s.

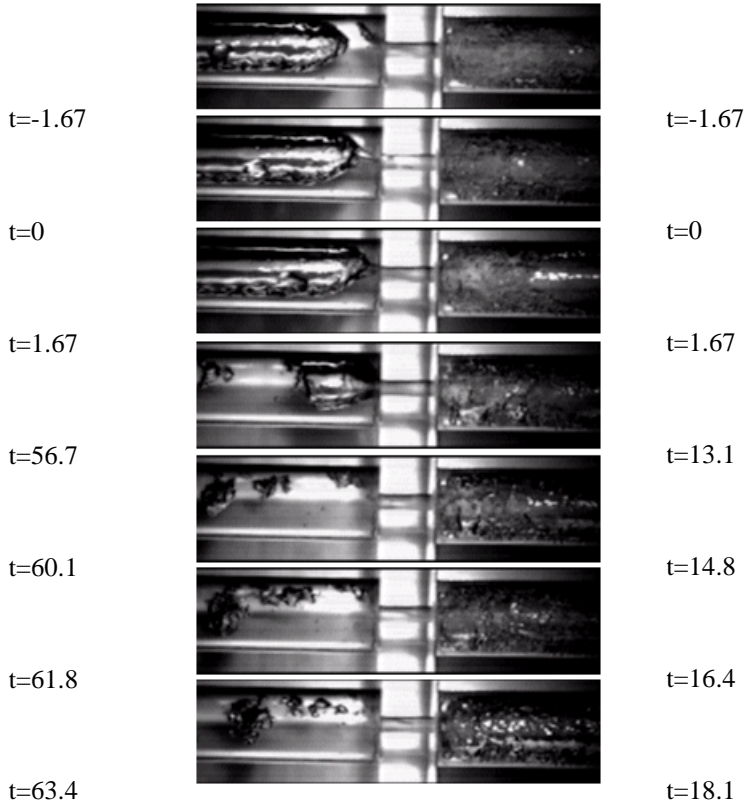


Figure 12: Bubble behavior at orifice (msec)
 $j_G=0.56$ m/s, $j_L=0.56$ m/s.

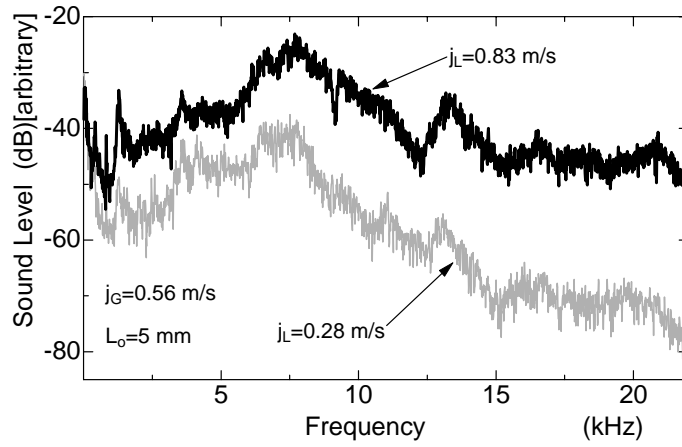


Figure 13: Sound spectra.

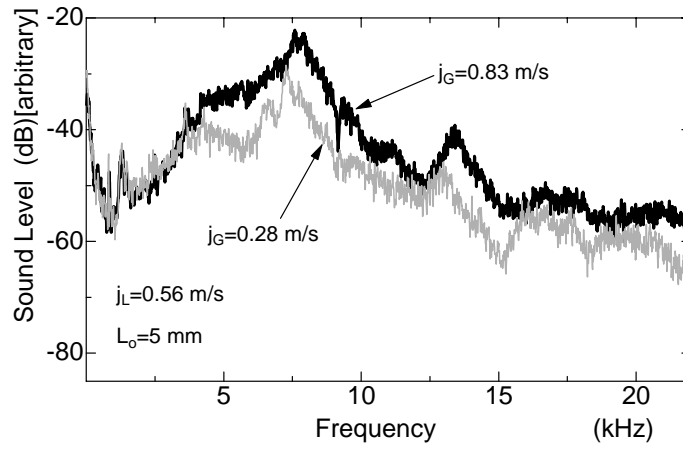


Figure 14: Sound spectra.

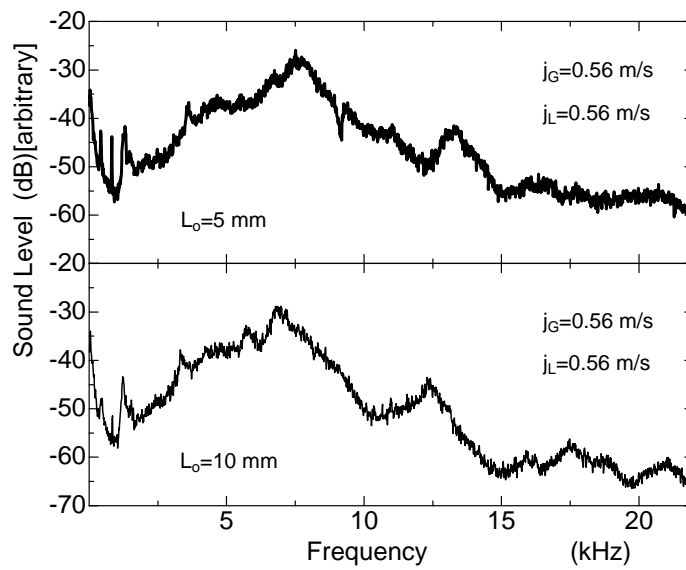


Figure 15: Sound spectra.

4. CONCLUSION

The sound occurrence mechanism when the bubble passed through the orifice was investigated experimentally. The pressures of the upstream and downstream obtained by the hydrophone and of the outside microphone were related to the images using the high-speed video. When the bubble was drawn in the orifice, its tip sharpened. When the bubble entered the orifice, the pressure of the upstream increased gradually. When the tail of the bubble reached the entrance of orifice, the pressure of the upstream decreased drastically and the large pressure oscillation was obtained from the outside microphone. After the large bubble passes through the orifice, the flow oscillation was observed upstream of the orifice. These phenomena were observed in both cases of the single large bubble in liquid flow and the two-phase slug flow. The component of high frequency in the sound becomes remarkable as the orifice length decreases in two-phase slug flow. The difference of sound level of a different liquid flux is larger than that of gas flux because the momentum of liquid phase is larger than that of gas phase. Therefore the sound level is deeply concerned with the momentum of the two-phase flow.

NOMENCLATURE

j_G	Volumetric gas flux
j_L	Volumetric liquid flux
L_B	Large Bubble length
L_o	Orifice length
t	Time

REFERENCES

- [1] Kannon, T., & Tomimasu, K., Study on Noise by Two-Phase Flow in Air Conditioner, Proc. The 2nd International Conference on Multiphase Flow '95-Kyoto, P8-121-127, 1995.
- [2] Umeda, T. et al., Reduction of Noise Caused by Gas-Liquid Two-Phase Refrigerant Flow through an Expansion Valve, Trans. Jpn. Soc. Mech. Eng.(B), 59-557, pp.243-248, 1993 (in Japanese).
- [3] Warjito, Mochizuki, O., & Ishikawa, H., Breakup of a single bubble and its sound, J. Jpn. Soc. Fluid Mech. [nagare], 21, pp.165-172, 2002 (in Japanese).

UNSTEADY MEASUREMENT OF THE STATIC PRESSURE ON THE IMPELLER BLADE SURFACES AND OPTICAL OBSERVATION ON CENTRIFUGAL PUMPS UNDER VARYING LIQUID/GAS TWO-PHASE FLOW CONDITIONS

P. Suryawijaya, G. Kosyna

Pfleiderer-Institute für Strömungsmaschinen, Technische Universität Braunschweig
Langer Kamp 6, D-38106 Braunschweig, Germany
Phone: +49.531.391-2918 Fax: +49.531.391-5769
Internet: www.pfi.ing.tu-bs.de

ABSTRACT

A liquid/gas two-phase flow (liquid contains undissolved gas) can be found in a wide range of pump applications, especially in chemical industries, off-shore oil production and nuclear reactors.

It is well known that the performance of single stage centrifugal pumps decreases rapidly under liquid/gas two-phase flow conditions. The consequences of entrained gas depend on the relative amount of gas and liquid present, and vary from a slight deterioration on performance up to complete blockage known as "gas locking". Before gas locking occurs, other phenomena such as pump head degradation, surging and "gas blocking" take place.

For two-phase flow applications of centrifugal pump the influence of the entrained gas on pump behaviour must be predictable. This is a hard task due to the complexity involved in modelling multiphase flow inside turbomachines. An accurate prediction of the performance for any pump handling liquid/gas mixture is still a problem today.

This paper reports on a research project, carried out at the Pfleiderer-Institute for Turbomachinery, Technical University of Braunschweig, Germany. The purpose of this project is to get a better understanding of the physical background of the two-phase flow behaviour of the centrifugal pumps by measuring the static pressure on the impeller blade surfaces and by optical observation under varying two-phase flow conditions. The results will also be used to validate a numerical code, which is developed in a related research project.

The project is focused on two centrifugal pumps, one scaled down from the other, having the same low specific speed number $n_s = 27$. The pumps are operating under variable two-phase flow conditions. Air and water were used as working fluids. Flow structures within the pump impeller and the overall pump performance are investigated by numerical simulation and experiments. One impeller blade of the pump is equipped with eight KULITE® sub-miniature pressure transducers. The pressure signals either from blade suction or blade pressure side are transmitted by a telemetric system - this measurement technique is implemented the first time for a gas/liquid two-phase pumping project.

1. INTRODUCTION

Many investigations are executed about the change of pump performance due gas/liquid two-phase conditions. Most of the information about this phenomenon in the available literature is concerned with measuring of the integral operating data. Murakami and Minemura [4] investigated the effects of entrained air of the performance of the centrifugal pump at low specific speed $n_s=23$ by measuring the total head of the pump and by photographical observations. Sato et. al. [6] observed the performance of the centrifugal pump impeller with various blade angles. Tillack and

Hellmann [8] presented their experimental results about the behaviour of centrifugal pumps under oil/gas two-phase flow conditions.

The Experiments have shown that the total breakdown of the pumping is caused by the flow structure of the mixtures at the pump impeller due to the air accumulation on the impeller passage. The flow structure and the static pressure at the impeller show in general temporal and local fluctuations. Nevertheless, unsteady measurements in rotating systems were executed only rarely due to the complexity of the measuring technique.

Murakami and Minemura [5] measured the distribution of velocities and gas void fraction in the rotating impeller handling air/water two phase mixtures using 27 special electric resistance probes, which were mounted in the impeller. The signal is transferred by a multi channel slip-ring system from the rotating system to the stationary side. The distribution of the static pressure [3] over the blade surfaces was determined by pressure measuring at the front casing in the stationary system.

Blade pressure measurements in a rotating system [2,7] allow a more in-depth look at the mechanism of energy transfer at the pump impeller for a two-phase flow. The results of the experiments will be used to validate numerical codes, which are developed at the universities of Munich and Dresden. To achieve this, the measurements of the unsteady blade pressure in a rotational system were taken using eight sub-miniature pressure transducers. They serve the purpose to allow measurements along the blade contour and on the suction and pressure sides.

2. EXPERIMENTAL APPARATUS

The general arrangement of the test rig is shown in Figure 1. The test rig is designed as an open circuit. The static pump suction pressure is controlled by a booster pump (1). Air is injected into the suction pipe at a distance of about 1.5 m from the pump inlet. The air supply is controlled by an electro-pneumatically valve in order to achieve constant test parameters.

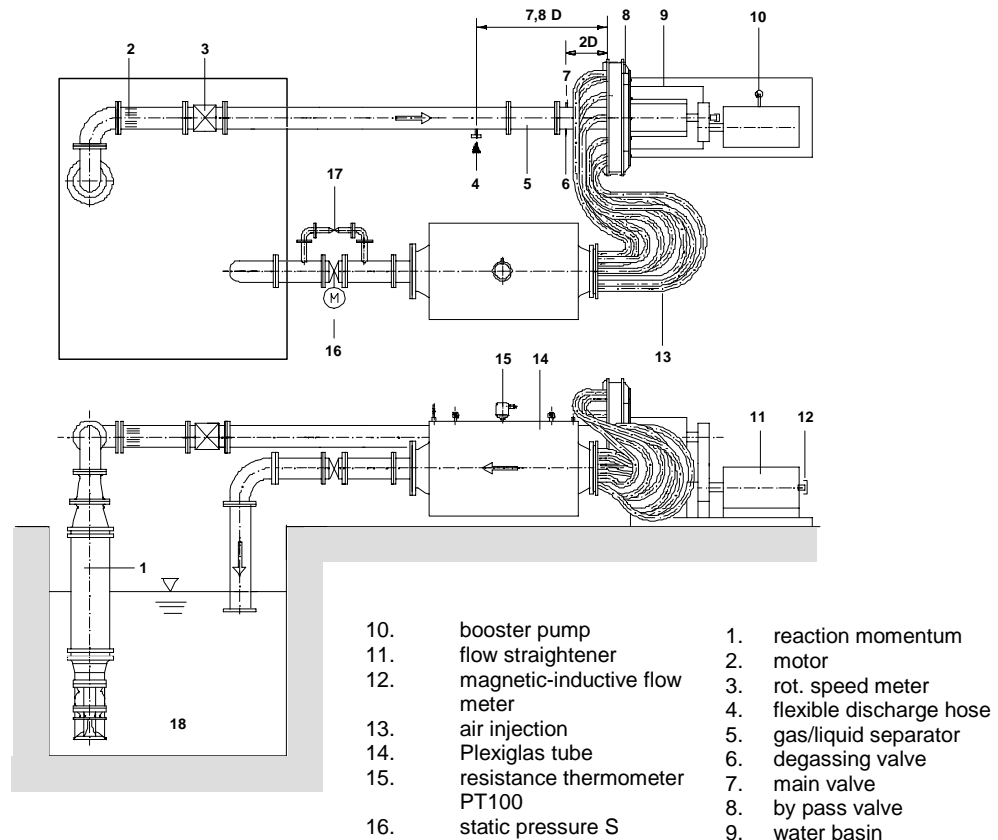


Figure 1: Schematic view of the test rig.

Two identical but scaled radial flow pumps with a specific speed of approximately $ns=27$ are investigated. In order to generate a circumferentially uniform pressure distribution at the impeller outlet, a vane less radial diffuser was used for recollecting the fluid. The diffuser itself was connected to the piping circuit by twelve 2.5" flexible tubes. The impeller consists of five blades, each of them being composed of two circular arcs, one with a smaller radius from inlet to nearly half of the chord and one with a larger radius up to the impeller outlet. The dimensions and specifications of the two scaled test impellers are shown in Figure 3 and Table I.

3. MEASUREMENT TECHNIQUE

For the unsteady measurement of the blade pressure eight piezo-resistive sub-miniature pressure transducers - type XTM-XX-190 M KULITE®- are used. The transducers are fitted along the camber line of the middle span between hub and shroud in axial orientation. These transducers are used for measuring the static pressure on the surface of either the blade suction or the blade pressure side in the relative system.

The unsteady pressure signals of the eight transducers are transmitted from the relative to the stationary frame using a telemetric system, which allows to transmit frequencies up to 2500 Hz. A telemetric system - type dt 204/301/612 from DATATEL® TELEMETRIE ELEKTRONIK - has been chosen for this set-up. The system is able to transmit up to eight unsteady signals simultaneously. For detecting rotating effects relative to the impeller, four additional transducers were mounted on the impeller hub near the middle of the passage (see Figure 2). The first investigation using this technique was completed by Dreiß, 1997 [1].

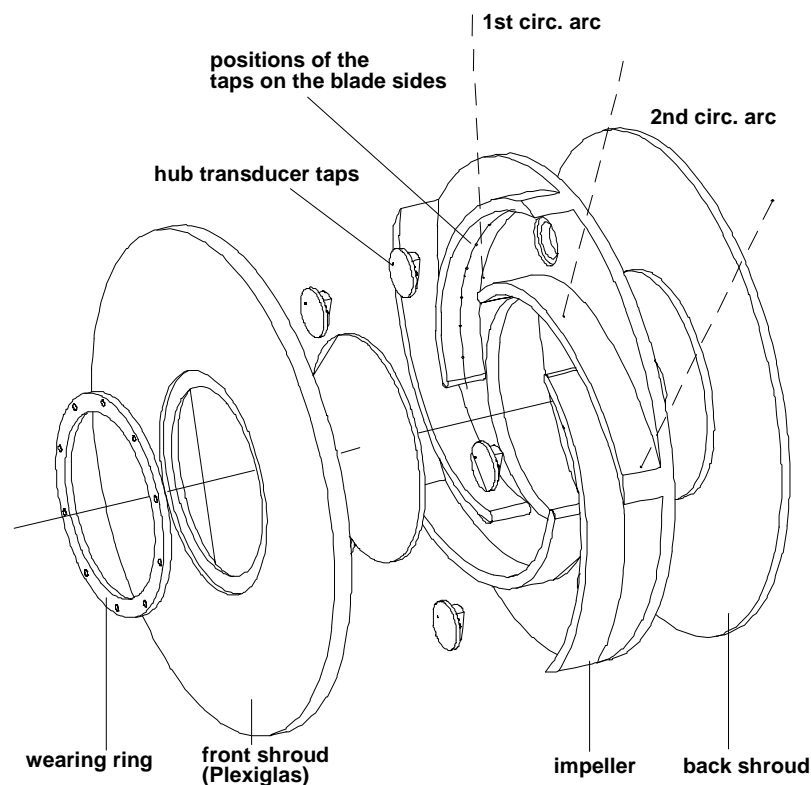


Figure 2: Test impeller.

To investigate the flow structure in the pump impeller visually, a digital high speed camera with a sampling rate of up to 4500 fps was used. These recordings are made using the scaled pump in Magdeburg (2KB-19235-MD). The sequences make it possible to analyse the development of unsteady processes during one or more revolutions.

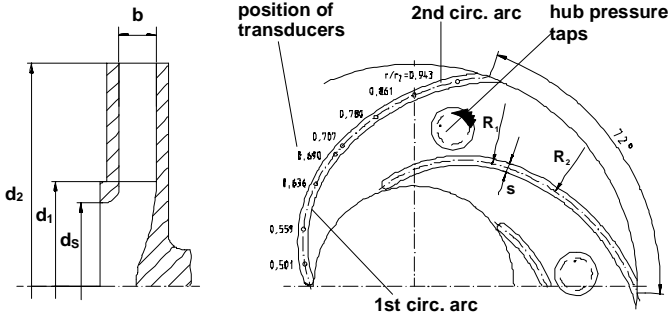


Figure 3: Design parameters of the test impellers.

impeller	2KB-19235-BS	2KB-19235-MD
$b_1; b_2$	19°; 23°	19°; 23°
$b; s$	46 mm; 13 mm	23 mm; 6 mm
$d_1; d_2$	260 mm; 556 mm	130 mm; 278 mm
$R_1; R_2$	169 mm; 270 mm	84.5 mm; 135
z	5	5
$n; n_s$	9 Hz; 27	10 Hz; 27
\dot{V}_{design}	400 m ³ /h	55.5 m ³ /h

Table I: Design parameters of the test impellers.

4. EXPERIMENTAL RESULTS AND DISCUSSION

The performance of the centrifugal pump is influenced by the amount of gas appearing at the suction pipe, which can be described by the gas volumetric fraction:

$$\dot{\epsilon}_s = \frac{Q_{\text{gas}}}{Q} = \frac{Q_{\text{gas}}}{Q_{\text{gas}} + Q_{\text{liquid}}} \quad (1)$$

Since in this case the two-phase-flow is a semi-compressible one, the compressibility dependency of the gas fraction has to be considered. It can then be seen as an isothermal change of state. The flow velocity in the measurement position D (s. Figure 1) shows a high radial component, which is determined by a five-hole yaw probe. The term considering the geodetic energy of the fluid taken into account when calculating the specific work of the pump, since pressure and suction side are located at the same geodetic level. The specific pumping work of the pump can be determined as follows:

$$Y = \frac{1 - \dot{\mu}}{\rho} (p_d - p_s) + \dot{\mu} RT \ln \frac{p_d}{p_s} + \frac{c_d^2 - c_s^2}{2} \quad (2)$$

4.1. Change of pump head due to air loading

The pump head drops when the gas void fraction is increased as can be seen in Figure 4. The curves are constructed by keeping the total flow rate, the static pressure in the suction pipe and the rotational speed of the impeller constant while the amount of gas is gradually increased. The decrease in pump head depends on the operating point. The curves can be split into 3 areas:

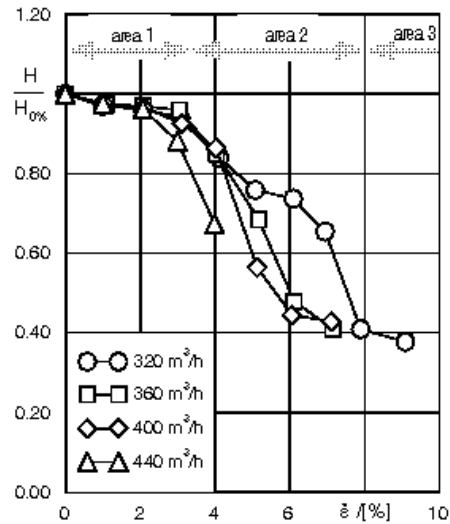


Figure 4: Change of pump head due to air loading.

When the gas fraction is increased from the state without gas loading state the pump alters its delivery continuously in area 1. However, at a certain gas fraction the pump shows an abrupt change (area 2). Depending on the operating point, the pump can possibly deliver in area 3.

4.2. Influence of flow pattern, size of bubbles in the suction pipe and the rotational speed of the impeller

At different experimental set-ups depending on the volumetric flow rates of the mixture and the gas fraction in the suction pipe, different flow patterns of the mixture (bubbles-, wavy- or slug-flow) occur in the suction pipe. A variety of bubble sizes are achieved by the exchange of the air admitting pipe with various orifices ($d_B=0,5 \dots 2 \text{ mm}$). The second curve at Fig. 5 is the pump-head drop depending on the gas fraction for the bubble size of $d_B=2.0 \text{ mm}$, and the third curve for the bubble size of $d_B=0.5 \text{ mm}$. The experiment result shows that neither the location of air injection, nor the flow pattern, nor the bubble size in the suction pipe has any substantial effects on the operating behaviour of the pump. A possible explanation is that the gaseous phase is dispersed into fine bubbles by the pump impeller when entering the rotating system. Subsequently the bubbles are scattered uniformly in the fluid.

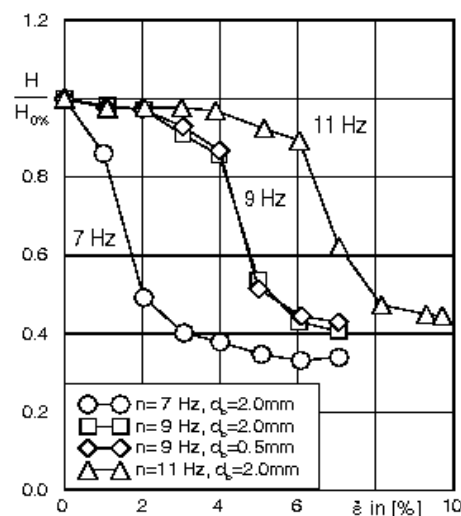


Figure 5: Influence of bubble size in the suction pipe and rotational speed.

Fig. 5 also shows the drops of the pump heads with various rotating speeds, the first curve for $n=7$ Hz, the second curve for $n=9$ Hz and the fourth curve for $n=11$ Hz. At higher rotational speed the critical gas void fraction, at which the performance drops suddenly, increases. This effect is achieved from the fine dispersion of the gaseous phase at the blade entrance and leads to a homogenized mixture. Higher capacities of air loading attained at higher rotational speed is probably due to the fact that the air is dispersed into finer bubbles when entering the pump impeller.

4.3. Pump performance curves handling gas/liquid two-phase mixtures

Figure 6 shows the performance of both pumps found by experiment. The graph plots the pressure rise coefficient ψ versus the flow coefficient ϕ .

Although there are some small differences in the absolute performance, both curves match very well. The numerical results show good consistence with the experiments. Appropriate to the capacity of CFX-TASCflow®, the flow was calculated for steady state and unsteady conditions. The quality of the results increases with the increase in numerical effort. The unsteady simulation with the disc losses yields the best results.

The experiments on pumping liquid/gas mixtures have shown that the drop of pump head essentially depends on the operating point (volumetric flow rate of the mixture). Figure 7 shows the typical performance of a pump handling gas-fluid mixtures. The curves drop with increasing gas fraction. The effect of the gas fraction, however, is different at each operating point. The respective efficiency curves also show that the efficiency optimum moves to smaller volumetric flow rates when increasing the gas fraction. Between the flow coefficients of 0.06 and 0.10 and the gas void fraction being smaller than 4%, the performance curves are nearly parallel to the performance curve without air loading.

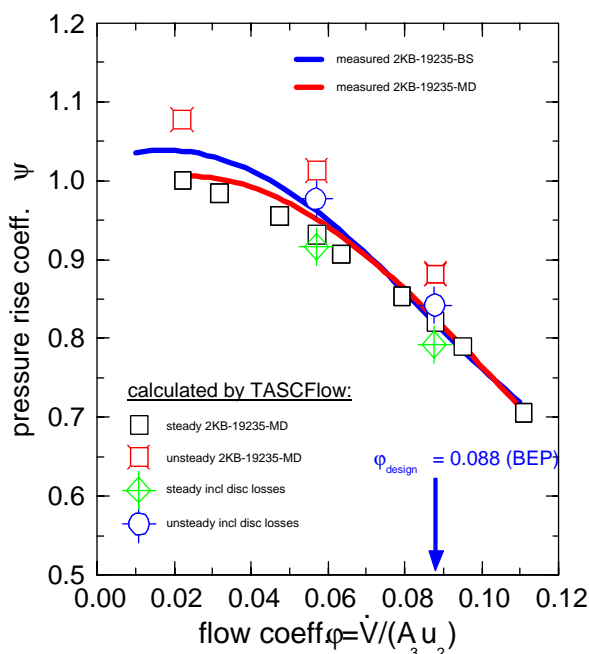


Figure 6: Characteristic curves measured and calculated by CFX-TASCFlow Code.

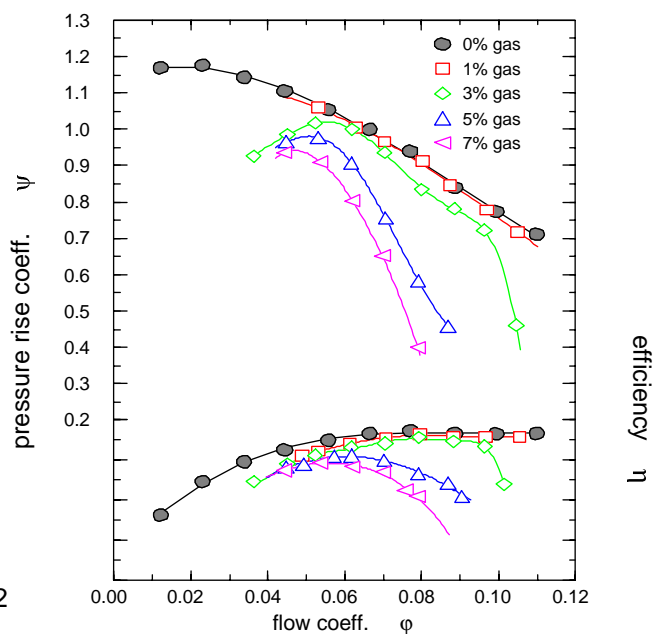


Figure 7: Pump performance curves handling gas/liquid two phase mixtures.

4.4. Blade Pressure

Figure 8 shows the unsteady pressure which was measured by the miniature pressure transducer tr- 8 ($r_{tr8}/r_2 = 0.943$) near the impeller outlet on the suction side. In the case of single-phase flow (100 % water) the pressure oscillates with the pump operating frequency of $n_{pu} = 9$ Hz. Whereas, the existence of gas bubbles in the fluid causes pressure fluctuations and leads to a decrease in the overall pressure level. When the gas fraction reaches 5 %, the fluctuations become chaotic.

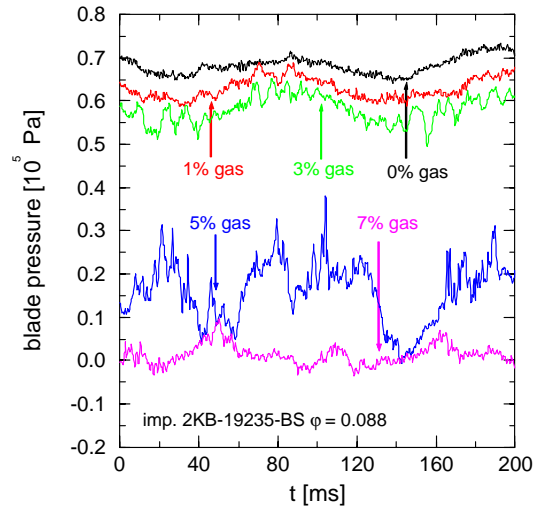


Figure 8: Unsteady pressure signal.

Figure 9 plots the blade pressure distribution versus the impeller radius from inlet to outlet at the optimal operating point of $\phi = 0.088$, $n = 9$ 1/s for gas loadings of 0, 1, 5 and 7 %. When increasing the gas fraction up to 3 % (not shown), the pressure distribution at the blade pressure side drops uniformly. The energy transfer from the impeller into the fluid is disturbed due to the existence of the gaseous phase. Pressure is built up as long as a homogeneous flow exists. With further increase of the gas loading, the gas bubbles merge to a gas zone, where no pressure can be built up. The zone where the pressure cannot rise enlarges with increasing gas loading. Looking at the measurements with a gas loading of 7 %, the pressure does not increase along the entire blade. Consequently the energy transfer stops.

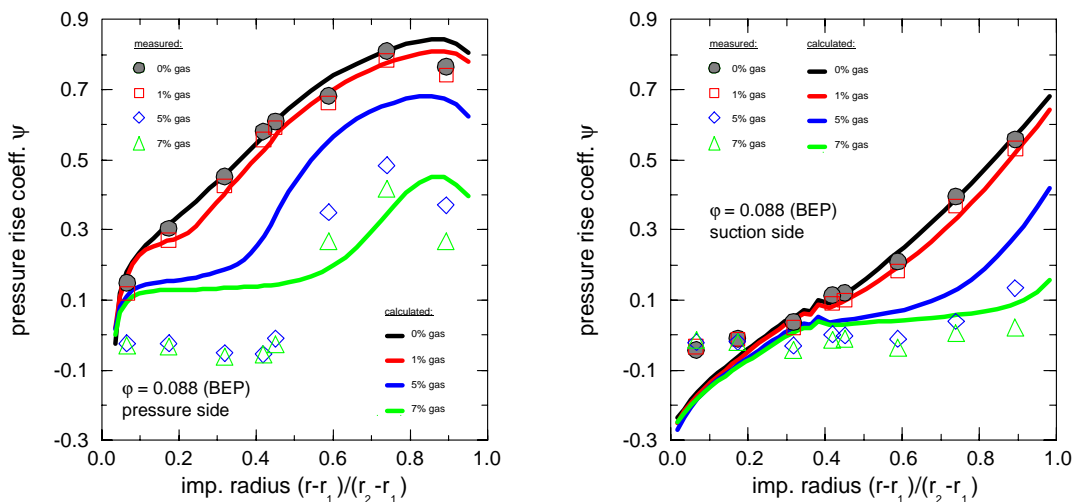


Figure 9: Change of pressure distribution on the blade pressure side due to air loading, experimentally obtained and calculated by PHOENICS.

The numerical simulation performed by means of PHOENICS® determines the pressure distribution qualitatively well. Discrepancies at the rotor inlet may partly arise from the geometric simplification of the blade inlet edge as used for the numerical simulation.

4.5. Blade Momentum and Pump Efficiency

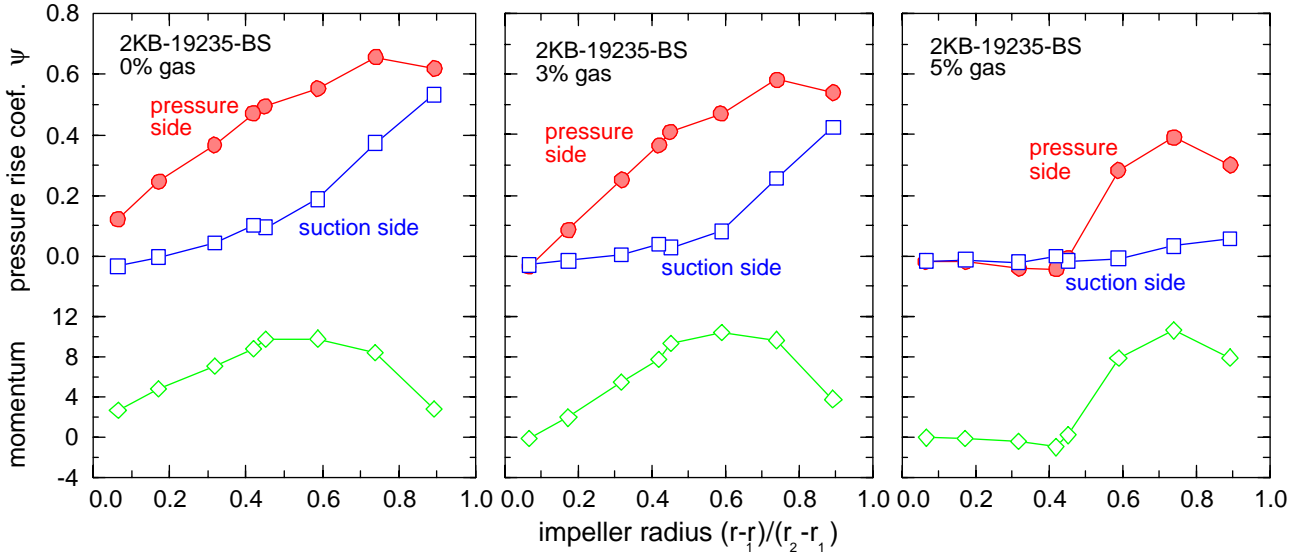


Figure 10: Distribution of static pressure and resulting momentum of the pressure forces.

Figure 10 shows the pressure distribution along suction and pressure side of the blade under two-phase flow conditions with gas fractions of 0, 3 and 5 %, as well as the distribution of momentum from inlet to outlet of the impeller.

The pressure difference Δp_{bld} between pressure and suction side of a blade acts on a small surface element ΔA of the impeller blade at radius r . The blade momentum ΔM_{bld} can be calculated by multiplying the pressure difference Δp_{bld} with the surface element ΔA and the radius r . However, this can only be done when assuming that Δp_{bld} remains constant along the blade width b . The distribution of local blade momentum has nearly symmetrical shape while operating without gas. Its maximum lies in the middle of the blade contour. At a gas loading of 3 %, there is only minimal change in the distribution of blade.

4.6. Observation of Gas Bubbles in the Impeller

A large number of experiments on the flow conditions with two-phase flow were carried out using a high speed-camera. The influence of the gas fraction, the gas distribution at the inlet and the different operating points of the pump were examined. Figure 11 shows a photography of such a distribution of gas in comparison to the numeric calculation. The accumulation of gas on the pressure side of the blade is qualitatively reproduced by the simulation. However, the two-phase flow in a centrifugal pump is unsteady. Shape and size of the gaseous zone in the impeller channel are not constant. The implemented steady state calculation can only yield an average value.

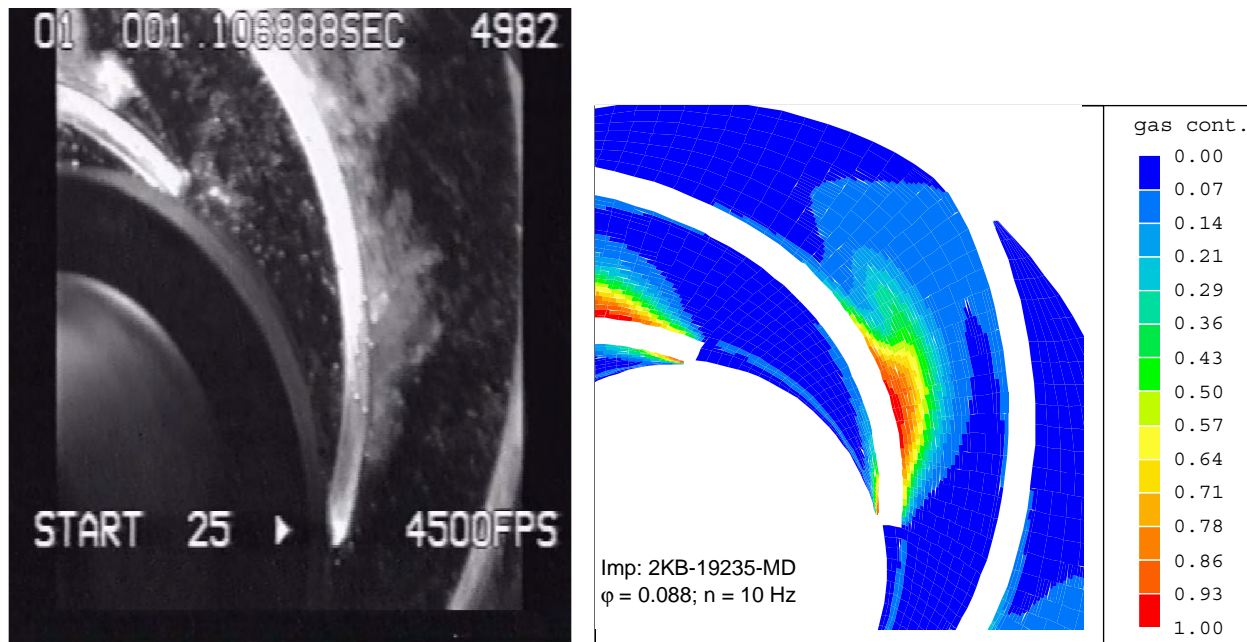


Figure 11: Distribution of gas bubbles (a) obtained from a high speed camera and (b) calculated by PHOENICS at $\phi=0,088$ and 1% gas fraction.

5. CONCLUSION

The measurements of the blade pressure provide further insight into the energy transfer process at the pump impeller handling a two-phase mixture. The pressure along the blade suction and pressure side depends on the amount and distribution of the gas loading.

Assuming a two-dimensional flow in the impeller passage, it is possible to calculate the momentum transferred by the blade. The total impeller momentum describes the energy transfer of the impeller blade into the fluid and the hydraulic work of the impeller.

This additional information allows to divide the total losses into hydraulic loss, disc friction and mechanical loss. Therefore, it supplies an extensive amount of data for the validation of numerical codes.

Numerical calculations by means of CFX-TASCflow® and PHOENICS® were carried out in parallel to the experiments. They show good agreement, although some substantial simplifications were made. Nevertheless, the movement of gas bubbles due to the surrounding pressure field and a crucial dependency of the result on the bubble diameter could be confirmed. The CFD-Codes at present allow the impeller flow relatively accurate for single phase and for two-phase flow also.

REFERENCES

- [1] Dreiß, A.; Kosyna, G. Experimental Investigations of Cavitation-States in a Radial Pump Impeller. Proceedings of the JSME International Conference on Fluid Engineering, 1997.
- [2] Kosyna, G.; Suryawijaya, P.; Friedrich, J., Improved understanding of two phase flow phenomena based on instationary blade pressure measurement, Fluid and Heat Engineering Scientific Conference on the 70th birthday of Prof. Tibor Czibere, Miskolc, October 20th, 2000.
- [3] Murakami, Minemura, Effects of Entrained Air on the performance of a centrifugal pump. Bulletin of the JSME, Vol. 17, No. 110, August 1974 (1st Report) and No 112, Oct 1974 (2nd Report), 1974.

- [4] Minemura, Murakami, PWMressure Distribution in a centrifugal pump. Bulletin of JSME, Vol. 26, No. 220, Oct. 1983.
- [5] Minemura, Murakami, Distributions of Velocities and Void Fractions in a Radial-Flow Pump Impeller Handling Air/Water Two-Phase Mixtures. International Journal of Turbo and Jet Engines, 1991.
- [6] Sato, Furukawa, Takamatsu, Air Water Two-Phase Flow Performance of Centrifugal Pump Impellers with Varios Blade Angles. JSME International Journal, Series B (Fluids and Thermal Engineering), Bd. 39, No. 2, 1996.
- [7] Suryawijaya, P.; Kosyna, G., Schaufeldruckmessungen im rotierenden System an einer Radialpumpe bei Gas/Flüssigkeitsgemischförderung, Chemie Ingenieur Technik, 72, Nov. 2000, p. 1366-1371, WILEY-VCH GmbH, Weinheim, 2000.
- [8] Tillack, Hellmann, Description of the Behavior of Centrifugal Pumps, Dealing with Gas-Loaded Liquids. Proceedings of the JSME International Conference on Fluid Engineering, 1997.

E. Methods for CFD

A NUMERICAL MODEL OF DISPERSED TWO PHASE FLOW IN AERATED STIRRED VESSELS BASED ON PRESUMED SHAPE NUMBER DENSITY FUNCTIONS

Emad Gharaibah, Martin Brandt and Wolfgang Polifke

Lehrstuhl für Thermodynamik
Technische Universität München
85747 Garching, GERMANY
Phone: +49 289 16241, Fax: +49 289 16218

ABSTRACT

Based on the two fluid model and the population balance equation for bubble size, a novel approach to simulate disperse two phase flow, e.g. in aerated stirred vessels, is proposed. The bubble size distribution is represented with a number density function of presumed shape, which makes the solution of the population balance equation in a pre-processing step possible. The pre-processing is not computationally expensive, so the number of bubble size groups may be chosen sufficiently large to represent the evolution of the size distribution due to break-up and coalescence of bubbles very accurately. In the CFD simulation, it is not necessary to solve a set of transport equations for each size group. Instead, the size distribution is represented by its first two moments, i.e. the mean and variance of bubble size. Transport equations for mean and variance are solved by the CFD code, with source terms taken from a look-up table generated during pre-processing.

In the present paper, the overall formulation and solution algorithm of the proposed model is outlined. It is demonstrated that number density functions of presumed shape can indeed represent the evolution of a bubble size distribution under the action of bubble break-up and coalescence with good accuracy. Furthermore, it is shown that quite large numbers of bubble size groups are required to reach discretization independence for the population balance equation. The generation of the unstructured, adaptive lookup-table for mean and variance of bubble size in the pre-processor as well as details of the look-up procedure in the CFD simulation are also discussed. The proposed model has been implemented in a multi-dimensional CFD code, and employed in the simulation of turbulent two-phase (gas-liquid) dispersed flow in an aerated stirred vessel.

1. INTRODUCTION

In multiphase flows, for example in an aerated stirred vessel, the transfer of momentum, mass, and energy across the phase interface is of crucial importance. In general, the transfer processes depend in a sensitive manner on the available interface area, which can only be computed if the bubble (or particle) size distribution is known. The transient evolution of the bubble size distribution resulting from the break-up and coalescence of bubbles can be reproduced by means of a population balance, formulated in terms of a number density function, which depends in general on both temporal and spatial co-ordinates.

Within the last few years, a variety of models for the numerical simulation of two-phase flows including the dispersion and coalescence of gas bubbles have been proposed.

In an Euler-Euler multi-fluid model, one set of transport equations has to be solved for each phase. (Non-linear) coupling between the transport equations due to the transfer processes mentioned above can be strong, which makes the numerical treatment of the equations difficult and

time-consuming. In the simplest mono-disperse models, it is assumed that the bubble diameter is locally single-valued. Of course, this is for many applications an inadmissible over-simplification.

More advanced models represent the bubble size distribution by several size groups. Each size group represents particles from a certain range of diameters and is treated as a separate phase in the multi-phase flow calculation. This formulation requires the solution of $5N+1$ coupled equations to be solved for a dispersed gas-liquid flow with N size groups. In practice, the number of the size groups is limited to rather low values, say $N=4$, due to the extensive numerical effort. Therefore, the evolution of the bubble size distribution due to break-up and coalescence can be represented only in a rudimentary manner.

The MUSIG (MUltiple-SIze-Group) model [15] represents a further development of this type of model. Again a continuity equation for each size group is solved, but it is assumed that all bubble velocities can be related to the average value in an algebraic manner, so that only one set of momentum equations for the gas phase has to be solved. With this simplification, up to 20 classes can be taken into account. Lo, employing a maximum of 10 groups, applied the model to analyse the flow and size distribution of air bubbles in a stirred reactor containing silicone oil [16]. An alternative approach [8] is to assume a certain (self-similar) shape for the number density function, which is determined completely by the mean bubble diameter.

We propose a novel approach to simulate disperse two phase flow (gas bubbles – fluid). This model is based on the two-fluid model [6] and a number density function (NDF) of presumed shape for the bubble size. By the representation of the bubble size distribution (BSD) via a presumed shape NDF, it is possible to solve the population balance equation (PBE) in a pre-processing step separate from the CFD simulation. The pre-processing is not computationally expensive, so the number of bubble size groups may be chosen sufficiently large to represent the temporal evolution of the size distribution due to break-up and coalescence of bubbles very accurately.

In the CFD simulation, it is with the proposed formulation not necessary to solve a set of transport equations for each size group. Instead, the size distribution is represented by its first two moments (therefore “moments model”), i.e. the mean and variance of bubble size. Besides one set of transport equations for each phase, two transport equations for mean and variance of the bubble size distribution are solved by the CFD code, with source terms taken from a look-up table generated during pre-processing.

This novel formulation offers several advantages: a) the bubble size distribution can be represented in great detail due to the possibility to consider a large number of bubble size groups efficiently. b) numerical stability problems are small, as it is not necessary to solve strongly coupled transport equations for numerous size groups. c) arbitrary break-up and coalescence kernel functions can be implemented, appropriate for the respective disperse flow regimes in turbulent or laminar, stirred vessel or bubble column two-phase flow. d) significant computing time reduction can be expected from the tabulation of the population balance dynamics in a pre-processing step. e) the benefits of the tabulation system and the look-up algorithm developed here – as the automatic adaptive refinement and the arbitrary dimensioning of the table to adapt it to the number of independent variables of the kernel functions used, etc. – are further advantages.

In this paper, the formulation of the moments model is outlined and the possibility to replace the NDF by a function of presumed shape, which is the basis of this model, is demonstrated. The generation of the look-up-table and the table-lookup procedure are also discussed. The proposed model has been implemented in a multi-dimensional CFD code, and employed in the simulation of the two-phase (gas-liquid) dispersed flow in an aerated stirred vessel.

2. THE MOMENTS MODEL

2.1. The population balance

The PBE, which describes the temporal evolution of the bubble number density n due to break-up and coalescence - no change in the bubble diameter due to mass transfer and no change in the bubble concentration due to the convection transport - in a unit volume can be simplified in the following form [4], [11]:

$$\frac{\partial n}{\partial t} = B_B - D_C + B_C - D_C \quad (1)$$

where the bubble number density $n=N/\Delta DV$ is the number N of bubbles in the control volume V with the size $D \pm \Delta D/2$ at time t . ΔD is the bubble size class width. B_B , B_C are birth rates in a certain bubble size class due to a break-up of bigger bubbles and coalescence of smaller bubbles and D_B , D_C are death rates in this class resulting from break-up into smaller bubbles and coalescence with other bubbles, respectively. The rate functions are referred to as *kernel functions* and formed with the break-up frequency, the number and size distribution of daughter bubbles in the break-up case as well as collision frequency and efficiency for the determination of the coalescence rate. The detailed descriptions of the PBE and the kernel functions are found in our earlier work [14].

2.2. The principle of the moments model

In CFD simulation of multiphase flows the computational domain is usually divided into tens or hundreds of thousands of control volumes. A complete CFD model with PBE calculated in each cell with a number of size groups sufficient to obtain a realistic particle size distribution will typically exceed presently available computational resources. The MUSIG [15] model solves the PBE with limited size groups, while others [8] simplified the PBE, see the Introduction.

In the moments model suggested here, the size distribution of the bubbles is represented by a number density function (NDF) of presumed shape – i.e. presumed functional form – per which the size distribution is determined by the first two moments – i.e. mean μ and variance σ^2 – of the bubble diameter. These functional distributions satisfy the condition:

$$\int_0^1 f(D; \mu, \sigma^2) dD = 1.$$

The bubble number density n_f resulting from this functional distribution must be scaled to represent the actual gas volume fraction. The evolution of the population balance over a short time interval dt – a time step in the numerical simulation – proceeds then as follows: Given certain values for the mean and variance, the kernel functions for bubble break-up and coalescence act in the usual manner on the presumed shape NDF to generate new values for mean and variance. Fig. 1 illustrates the principle of the proposed model in a flow chart.

In the CFD model, the usual equations of mass and momentum transport for the gaseous and the liquid phase are solved. Additionally, two transport equations are solved for the first two moments of the bubble diameter. Bubble break-up and coalescence appear in these equations as source terms. These source terms, which depend on the local values of mean and variance as well as flow parameters (dissipation rate, velocity gradients, etc.) are computed in the manner outlined in the previous paragraph. It is advantageous to generate a look-up-table with source terms S_μ and S_{σ^2} in a pre-processing step.

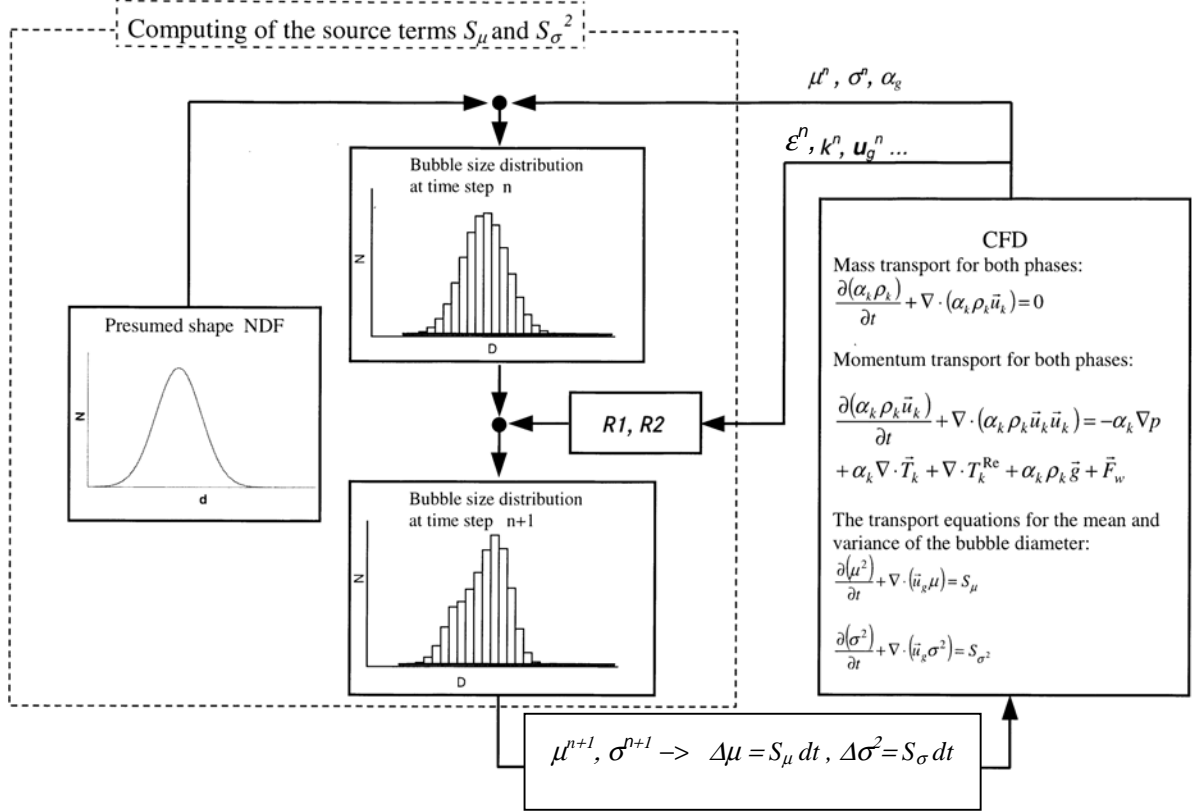


Figure 1: The functionality of the proposed moments model and the links to the CFD.

2.3. Representation of the size distribution by a presumed shape number density function

The source terms S_μ and S_{σ^2} – i.e. the left part of the flow chart illustrated in Fig. 1 – are computed from a solution of the PBE, which represents the transient evolution of the bubble size distribution resulting from break-up and coalescence of bubbles. By the representation of the size distribution via a function of *presumed shape*, the population balance can be solved in a pre-processing step of the CFD simulation. Only in this manner can the PBE be solved with a number of bubble size groups (nc) sufficient to obtain satisfactory accuracy, since, as mentioned above, a complete solution of the transport equations which govern a disperse two phase flow and the PBE with a desired nc is not possible under the presently available computational resources.

The source terms generated during pre-processing are stored in a look-up table, which is accessed during the CFD computation to obtain the source terms corresponding to local flow parameters to solve the transport equations of the mean and variance of the bubbles diameter, which are sufficient to represent the size distribution in our model. In an earlier work [14], the influence of the size group number nc on the evolution of the population has been investigated. This has been carried out by solving the full PBE directly with various bubble size group numbers. The possibility to represent the BSD by a NDF of a presumed shape has also been verified by solving the full PBE in which the size distribution of the bubbles is represented by a NDF of presumed shape after the break-up and the coalescence of the bubbles occurred at each time step. Three functional forms have been tested: the β -function [2], the clipped Gaussian [7] and the uniform distribution [12].

In our earlier work [14], the 1D integro-differential PBE of bubble number density (1) has been solved by dividing the bubble population density into several discrete classes and calculating the integrals in this equation numerically. These investigations were carried out for several initial bubble distributions – i.e. with different μ and σ^2 initial values - and several values for minimum

and maximum bubble diameter. These conditions, the assumed flow parameters and the rate functions – collision frequency [13], collision efficiency [9], droplet break-up frequency [3], distribution for the daughter droplet probability density function [1] – applied in solving the PBE are to take from [14]. It is important to note that arbitrary kernels from the literature can be implement in the moments model suggested in this work without restriction or simplification. Here, the results are discussed.

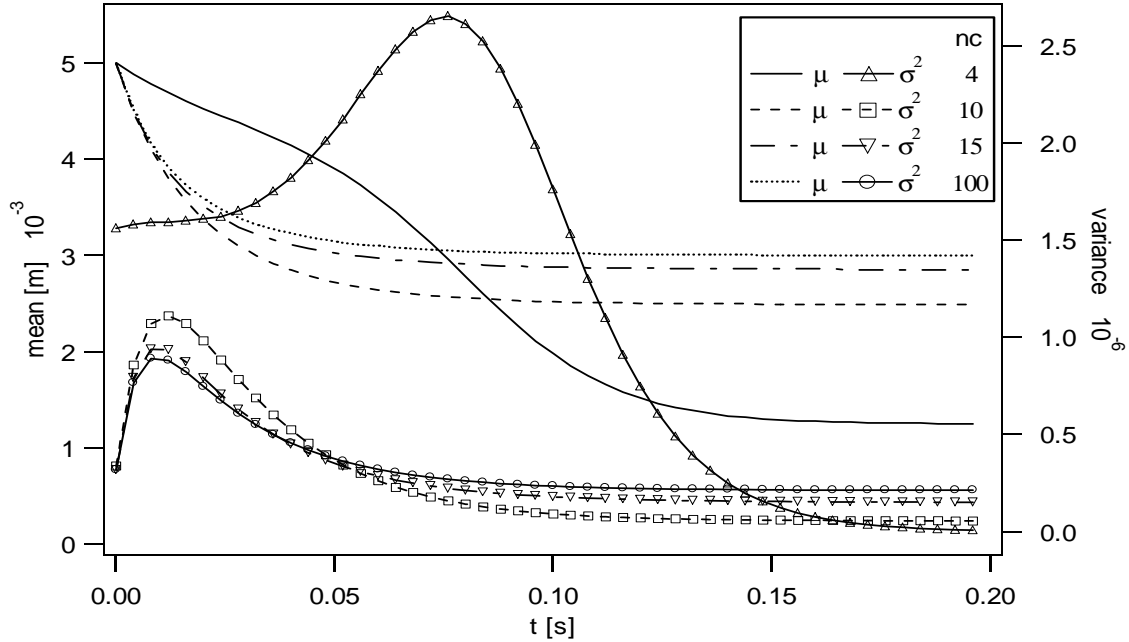


Figure 2: The mean and variance of the bubble diameter resulting from the direct solution of the PBE in its general form with different bubble size group numbers nc .

Figure 2 shows the temporal evolution of μ and σ^2 values resulting from the direct solution of the full PBE with various bubble size group numbers $nc = 4, 10, 15, 100$. Solutions have also been carried out with $nc = 200$, which have been found to agree extremely well with the case $nc = 100$. Since an analytical solution of the PBE is not known, this discretization-independent case $nc = 100$ serves as a reference case for solutions with fewer size classes. It can be observed that at least 10 size classes are required to achieve acceptable agreement with the reference solution. With only 4 size classes – which is often the maximum permissible number of classes in CFD simulations with a discretized PBE – the solution very severely underpredicts the mean bubble diameter obtained in quasi-steady state.

Results of solving the population balance equation with a presumed shape number density function are compared with the direct solution of the PBE – all with $nc=100$ and the same conditions as above – in Fig. 3. Qualitative as well as quantitative agreement between the direct solution and the solutions with the β - and clipped Gaussian- function is found. The solution with the uniform function is unusable and shall not be discussed further. Comparing with Fig. 2, we note that the direct solution obtained with 15 size classes shows a larger discrepancy with the reference case (direct solution with $nc = 100$) than solutions obtained with the β or clipped Gaussian distributions. It is concluded that with β - or clipped Gaussian functions for the number density of , the evolution of bubble size distribution due to the break-up and coalescence in disperse two phase flow can be well represented.

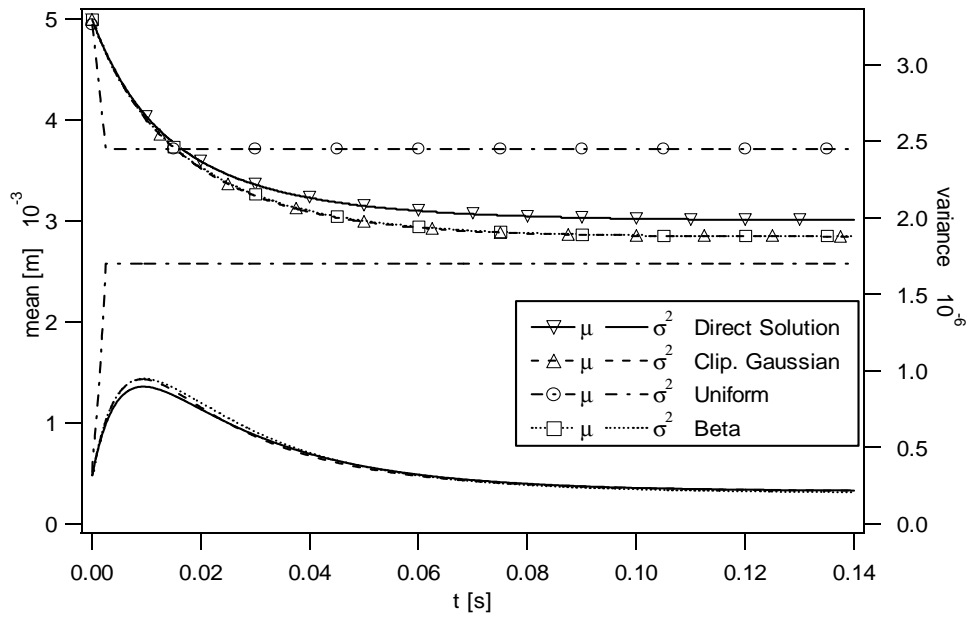


Figure 3: The mean and variance of the bubble diameter resulting from the direct solving of the PBE in its general form compared with the result of PBE solution, in which the bubble size distribution is represented by a number density function of presumed shape (clipped Gaussian, beta, and the uniform distribution).

Figure 4 shows the gas volume fraction conservation resulting by solving the PBE with different number bubble size groups. Note that we have chosen to discretize the size classes in terms of bubble diameter rather than volume. This has the advantage that a wider range of bubble sizes can be represented with a given number of size classes. However, in this formulation, total gas volume fraction will not be conserved if an insufficient number of size classes is chosen. One can see that the volume is conserved very well by the $nc = 100$ reference solution of the PBE. Fig. 4 also shows that the gas volume is also *fully* conserved by the solution of the PBE with the clipped Gaussian function.

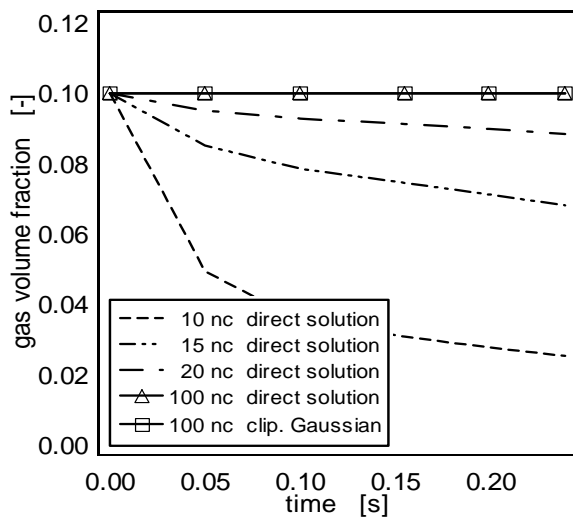


Figure 4: The gas volume fraction conservation resulting by solving the PBE with different number bubble size groups and with presumed shapes of the number density

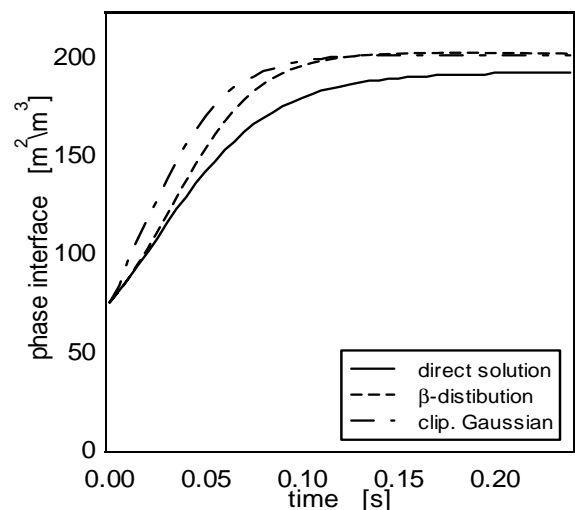


Figure 5: The specific phase interface area resulting by direct solving of PBE and with presumed shapes of the number density function.

One important objective of the simulation of dispersed two phase flows is the determination of the phase interface area, over which mass, heat or chemical species are exchanged between the phases. Figure 5 shows the specific phase interface area obtained with direct solution of PBE and with presumed shape number density functions. The phase interface area increases due to the dispersion of bubbles until it reaches a constant value when the bubble population approaches a steady state with equilibrium between dispersion and coalescence of bubbles. Both simulations with presumed shapes NDF reproduce this behaviour with acceptable quantitative agreement.

Figure 6 shows the evolution of the bubble size distribution for the direct solution of the PBE and the solution obtained with the presumed shapes of the clipped Gaussian distribution.

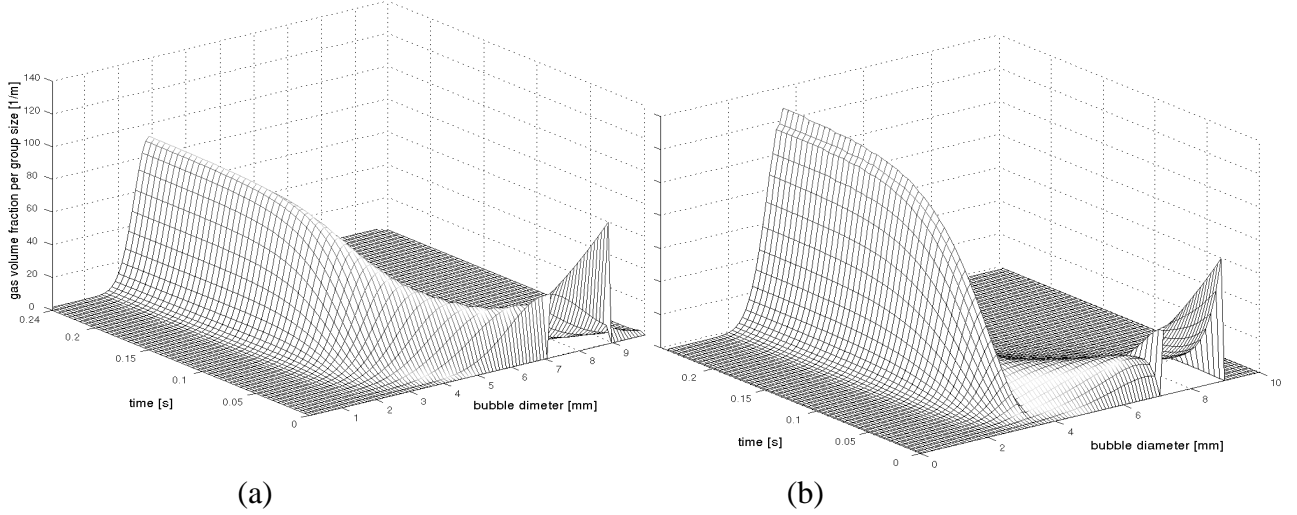


Figure 6: The evolution of the bubble size distribution with the direct solution (a) and the clipped Gaussian distribution (b).

3. THE TABULATION SYSTEM

The algorithm employed in this study to generate adaptive, unstructured look-up tables will be described in this Section. For simplicity, the procedure is explained for function f of two parameters ϕ_1 and ϕ_2 , but it can be extended to cases of higher dimension, – i. e. with a larger number of parameters – in a straightforward manner. The algorithm is restricted to functions in which the parameters can be normalised to values $0 \leq \phi_i \leq 1$. The generated table does not contain the values of the function for certain sets of parameters explicitly, as is often the case in a structured look-up table, but instead the coefficients of certain polynomial fit functions, which are valid in a certain region (a *cell*) of the tabulated domain.

The algorithm is started from a basic level (as illustrated in Fig. 7-a). As all parameters are in the range $0 \leq \phi_i \leq 1$, the region to tabulate is a square (or in general a hypercube). Splitting up the range into two sub-ranges results in the structure shown in Fig. 7-b. This first step is to be done manually and makes it easy to adapt the basic cells, i.e. the topology in the first level, to the shape and slope of the function. For example, the predefined split co-ordinate can be set to a value $\phi_{1.Split}$, where f reaches a maximum or where the change of the slope is at a maximum. Now the automatic algorithm is started by evaluating the function at the corners of the rectangle and determining the coefficients a_i of the fit function which reads for a 2D case:

$$f_{approx}(\phi_1, \phi_2) = a_2 \cdot \phi_2 + a_1 \cdot \phi_1 + a_0. \quad (2)$$

The coefficients can be determined with the Gaussian "*least mean square*" approach. In a next step the accuracy of the fit is tested at the center point of each cell. An error is calculated using the definition:

$$Error = \frac{f_{exact} - f_{fit}}{f_{exact}}. \quad (3)$$

If the error does not exceed a certain limit, the fit represents the exact function well for the current cell, hence this cell is called a *real* cell and is stored in the tables. Otherwise, the cell is a *virtual* cell and has to be refined further by splitting up into two subdivisions. The cell is split in the direction, in which the slope of the function is maximum. To evaluate the slope, the points marked with a star in Fig. 7-b are used.

This procedure of interpolation, error evaluation and refinement is done repeatedly until the whole region is subdivided into cells which fulfill the desired accuracy criterion. Two tables are then generated, the table of polynomial coefficients and the index table – the topology table – in which the split dimension, the indices of the child cells and the split co-ordinates are stored.

The look-up occurs in the following manner: First it has to be determined in which cell of the base level the desired value is located. It is tested whether the cell is a real cell or a virtual cell by determining the split direction. A real cell is indicated by a zero split direction, whereas values greater zero specify the split dimension. For virtual cells, one determines in which of the two cells of the next level the desired point can be found by testing the argument of the dimension, in which the cell has been split against the split co-ordinate. Again this procedure is repeated until a real cell is found. The corresponding index of the coefficients in the second table can be found in corresponding column of the topology table.

The benefits of this tabulation system are:

- the locally adaptive algorithm makes it possible to reduce the table size and makes the tables more flexible,
- the looking-up algorithm is very fast, because the topology is as a binary tree and no interpolation is needed, because the coefficients of the fit function are stored in the table,
- the most important advantage is the arbitrary dimensioning of the generated table so that it can be adapted for the dimensions of the used kernel function of the break-up and coalescence of the bubbles.

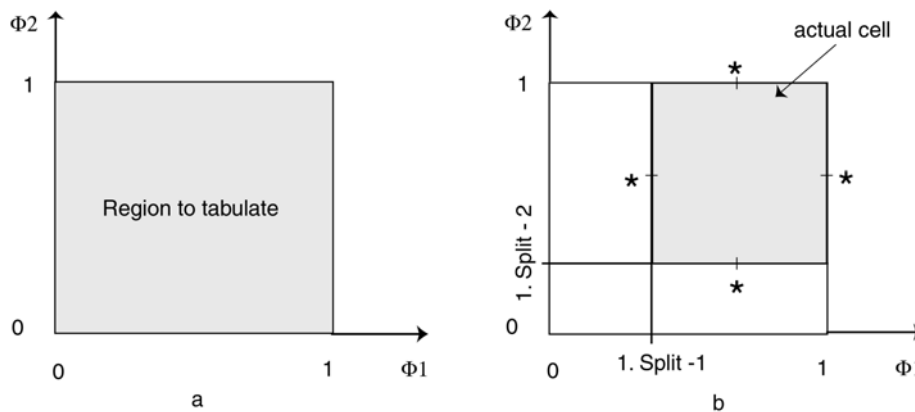


Figure 7: The principle of the generation of adaptive, unstructured look-up table: (a) The region to be tabulated and (b) the manual splitting up to get the basic cells and the automatic splitting up by evaluating the function at the corners of the rectangle and determining the coefficients a_i of the fit function.

4. IMPLEMENTATION OF THE MOMENTS MODEL IN A CFD CODE

The implementation of the moments model in a commercial CFD code has been carried out for a 3D simulation of a dispersed gas-liquid flow in the aerated stirred vessel. The simulation of the gas-liquid two-phase flow in such apparatus, which is widely used in many industrial areas to disperse gases in fluids, is a challenge to existing simulation models. This, due to the complicated nature of the stirred vessel flow pattern including the coalescence and break-up of the gas bubbles caused by the strong collision between the bubbles and the shear forces of the liquid phase. The bubble size distribution can be only accurately simulated by considering a sufficient number of the bubble size groups to cover the wide spectrum of the gas bubble size in the stirred vessel.

The first simulation of the gas-liquid aerated stirred vessel flow with the moments model provided a numerical stability and a computation time reduction, as it is not necessary to solve strongly coupled transport equations for each bubble size groups and due to the tabulation of the population balance dynamics in the pre-processing step. In a next step, the simulation results will be compared to measured data and the moments model will be validated.

5. CONCLUSION AND FUTURE WORK

The population balance equation is in principle a suitable method to represent the size distribution of the dispersed phase in two phase flows (gas bubbles – fluid). A complete CFD model with PBE calculated in each cell for particle size groups sufficient to obtain a reasonable particle size distribution is, however, not affordable with present computational means. In the last few years, several multiphase models have been developed to describe the transient evolution of the bubble size distribution resulting from the break-up and coalescence processes with the help of the simplified PBE or with small bubble size group numbers, which is not able to cover the large bubble size spectrum found in real flows.

In this paper, we proposed a novel approach to simulate disperse two phase flow by solving the PBE to describe the bubble size distribution by a number density function of presumed shape. First, we verified the dependency of the PBE solution accuracy on the particle size classes number. The bubble size distribution can not be represented independent of discretisation with class number <100 , which is far more than the maximal class number in MUSIG model. The direct solution of the full PBE with break-up and coalescence kernels from the literature was compared against the solution of the full PBE in which the size distribution of the bubbles was represented by a NDF of presumed shape. Good agreement has been achieved with the β and clipped Gaussian distribution. Arbitrary break-up and coalescence kernels can be implemented in the moment model and a great number of the bubble size groups may be used.

ACKNOWLEDGMENT

The Authors would like to thank Alexander Maltsev and Johannes Janicka (TU Darmstadt) for the explanation of the table generation principle which is developed by them and further developed from the authors to serve the purpose of generation of a look-up table with arbitrarily dimensions corresponding to the dependent variables of the kernel function used in the solving of the population balance equation.

REFERENCES

Journal article

- [1] Bapat, P. M., Tavlarides, L.L. & Smith, G.W., Monte Carlo Simulation of Mass Transfer in Liquid-Liquid Dispersions, *Chem. Eng. Sc.*, 38, pp. 2003-2013, 1983.
- [2] Girimaji, S. S., Assumed β -pdf Model for Turbulent Mixing: Validation and Extension to Multiple Scalar Mixing, *Combust. Sci. And Tech.*, 78, pp. 177-196, 1991.
- [3] Hesketh, R. P., Etchells A. W. & Russell, T.W., Bubble Breakage in Pipeline Flow; *Chem. Eng. Sc.* 46(1), 1-9, 1991.
- [4] Hsia, M. A. & Tavlarides, L. L., A simulation model for homogeneous dispersion in stirred tanks, *Chemical Engineering Journal*, 20, pp. 225—236, 1980.
- [5] Hulburt H. M. & Katz S., Some Problems in Particle Technology: A Statistical Mechanical Formulation, *Chem. Eng. Sci.*, 19, 555-574, 1964.
- [6] Ishii, M., *Thermo-fluid dynamic theory of two-phase flow*, Eyrolles, Paris, 1975.
- [7] Lockwood, F.C. & Naguib, A. S., The Prediction of the Fluctuations in the Properties of Free, Round-Jet, Turbulent Diffusion Flames, *Combustion and Flame*, 24, pp. 113, 1975.
- [8] Millies, M. und Mewes, D., Phasengrenzflaechen in Blasenstroemungen -- Teil 1: Blasensaeulen, *Chem. Ing. Tech.*, 68, pp. 660-669, 1996.
- [9] Prince, M. J. & Blanch, H.W., Bubble Coalescence and Break-Up in Air-Sparged Bubble Columns, *AIChEJ.*, 36(10), 1485-1499, 1990.
- [10] Randolph, A., A Population Balance for Countable Entities; *Can. J. Chem. Eng.*, 42, 208-281, 1964.
- [11] Valentas, K. J. and Amundson, N. R., Breakage and coalescence in dispersed phase system, *Industrial and Engineering Chemistry Fundamentals*, 5, pp. 533—542, 1996.

Book

- [12] Bronstein, I. N. & Semendjajew, K. A., *Teubner–Taschenbuch der Mathematik*, [Teil 1], B. G. Tubner Stuttgart . Leipzig, 1996.
- [13] Fleicher, C., *Detaillierte Modellierung von Gas-Fluessigkeits-Reaktoren*, Fortschritt-Berichte VDI, Reihe 3, Verfahrenstechnik, Nr. 691, 2001.

Symposium proceedings

- [14] Gharaibah, E. and Polifke, W., A Numerical Model for the Simulation of Dispersed Two Phase Flows based on Presumed Shape Number Density Functions, 10th Workshop on Two-Phase Flow Predictions, Merseburg, Germanys, April 2002. ERCOFTAC.
- [15] Simon Lo, Application of Population Balance to CFD Modelling of Bubbly Flows via the MUSIG Model; 4th Int. Conf. on Gas-Liquid and Gas-Liquid-Solid Reactor Engineering, Delft, August 1999.
- [16] Simon Lo, Some Recent Developments and Applications of CFD to Multiphase Flows in Stirred Reactors, AMIF-ESF Workshop: Computing Methods for Two-Phase Flow, Aussois, France, 12-14 January 2000.

ANALYSIS OF THE FORCED CONVECTION BOILING WITH THE PARTICLE INTERACTION METHOD

Noriyuki SHIRAKAWA¹⁾, Hideki HORIE¹⁾, Yuichi YAMAMOTO²⁾

¹⁾Power & Industrial Systems R&D Center, Toshiba Corporation,
4-1, Ukishima-cho, Kawasaki 210-0862, Japan
E-mail: noriyuki.shirakawa@toshiba.co.jp
Phone: +81 44 288 8035, Fax: +81 44 270 1806
E-mail: hideki.horie@toshiba.co.jp

²⁾Toshiba IT-Solutions Corporation,
1-2-4, Isago, Kawasaki 210-0006, Japan
Phone: +81 6 6368 0807, Fax: +81 6 6388 8785
E-mail: yamamoto.yuuichi@toshiba-it.co.jp

ABSTRACT

A particle interaction method called MPS (the Moving Particle Semi-implicit method), which formulates the differential operators in Navier-Stokes' equation as interactions between particles characterized by a kernel function, has been developed in recent years. We have extended this method to a two-fluid system with a potential-type surface tension in order to analyze the two-phase flow without experimental correlation. This extended method (Two-Fluid MPS: TF_MPS) was successfully applied to a forced convection boiling experiment.

1. INTRODUCTION

In the conventional two-phase flow analysis, the flow regime has characteristics that need to be complemented by experiments. The interfacial areas between two phases and between fluid and structures are evaluated depending on the flow regime. Then, the mass, momentum and energy transfers are evaluated with the interfacial areas, considering the phase change, friction, and heat transfer, to give the source terms of the mass, momentum and energy conservation equations. Finally, mass, momentum and energy conservation equations are solved to evaluate the flow regime for the next time step.

The conventional method [1-5], which determines flow regimes from the hydrodynamic state and evaluates the contact areas, has been improved by taking the transport of interfacial areas into consideration. However, since the experimental correlation is obtained only for macroscopic flow fields under some simple and/or specific conditions, the conventional method cannot be directly extended to general flow simulations. From a calculational point of view, the size of calculation mesh should be consistent with the flow regime. That is, a finer calculation mesh does not always promise more accurate results, which differs from the situation in the single-phase flow calculation.

A number of methods have been developed in recent years to analyze multi-fluid and two-phase flows in a more accurate and general manner. The methods such as Level Set [6,7], improved VOF (Volume of Fluid) [8-10] and generic BFC (Boundary Fitted Coordinate) [11] have been developed to trace accurately the interface between liquid and gas. To ensure its accuracy and applicability to complicated boundaries, the CIVA (Cubic Interpolation with Volume/Area coordinates) method [12, 13], a gridless and high-accuracy method, has been developed.

Each method has its own particular advantageous features for analyzing free surface or two-phase problems. However, these methods have not been applied yet to two-phase flows over a wide range of the void fraction. The Moving Particle Semi-Implicit (MPS) method, a particle interaction method developed in recent years [14,15], formulates the differential operators in Navier-Stokes equations in terms of the interaction between particles characterized by a kernel function. The MPS method adopts a mesh-free algorithm and is particularly suitable for treating liquid breakup. MPS has been widely applied to such problems as the free surface compound with structure deformation [16] and vapor explosion [17].

We extended MPS to an immiscible two-fluid (liquid-liquid and gas-liquid) system and introduced a potential-type surface tension to calculate two-phase flows without experimental correlation. With this extended method which we call Two-Fluid MPS (TF-MPS) method, several two-phase flow experiments were analyzed successfully as reported in our previous papers [18-21].

In this paper, we present the method and algorithm of TF_MPS and the analyses of forced convection boiling.

2. PHYSICAL MODELS AND MPS METHOD

2.1. Basic equations for the one-fluid model

The particle interaction method is a type of representation of differential operators using a weight or a kernel function. This method is applied to Navier-Stokes equations in the following way [14,15]. Mass and momentum conservation equations for a single fluid are

$$\frac{d\rho}{dt} = 0, \text{ and } \frac{D\mathbf{u}}{Dt} = -\frac{1}{\rho}\nabla p + \nu\nabla^2\mathbf{u} + \mathbf{F}, \quad (1), (2)$$

respectively, where $D = \partial / \partial t + (\mathbf{u} \cdot \nabla)$. It should be noted that the mass conservation equation (1) is iteratively solved to conserve the number density as shown in 2.2.

The interaction between particles is specified by a hyperbolic weight function and the initial distance between particles corresponds to the mesh size in the ordinary difference method. The following weight is used in all the calculations except for the interface between different fluids as described later,

$$w(r) = (r_e / r) - 1, \quad (3)$$

where r_e is a cut-off length of the interaction, that is, $w(r) = 0$ outside r_e .

The gradient of physical quantity f is modeled as the slope averaged with the weight between the object particle and the particles within r_e ,

$$\langle \nabla f \rangle_i = \frac{d}{n^0} \sum_{j \neq i} \left[\frac{f_j - f_i}{|\mathbf{r}_j - \mathbf{r}_i|^2} (\mathbf{r}_j - \mathbf{r}_i) w(|\mathbf{r}_j - \mathbf{r}_i|) \right], \quad (4)$$

where \mathbf{r}_i is the position vector of a particle i , d is the spatial dimension, and n^0 is the number density in the initial configuration,

$$n^0 = \sum_{j \neq i} w(|\mathbf{r}_j^0 - \mathbf{r}_i^0|). \quad (5)$$

The Laplacian is interpreted as a diffusion process of f over the particles within r_e ,

$$\langle \nabla^2 f \rangle_i = \frac{2d}{n^0 \lambda} \sum_{j \neq i} [(f_j - f_i) w(|\mathbf{r}_j - \mathbf{r}_i|)], \quad (6)$$

where λ is a coefficient to adjust the variance of f to that of the analytical solution of the diffusion equation, and defined as

$$\lambda = \int_V w(r)r^2 dv \left[\int_V w(r)dv \right]^{-1}. \quad (7)$$

After the calculation of the diffusion and gravity terms, the velocities and positions of particles are updated explicitly. Then, the pressure equation derived by imposing an incompressible condition is solved implicitly with the updated location and velocity of particles.

2.2. Two-fluid model and calculation algorithm

The basic algorithm for the two-fluid model is as follows.

(1) Calculation of the diffusion, gravity and surface tension terms:

$$\begin{aligned} \mathbf{u}_{\xi,i}^* &= \mathbf{u}_{\xi,i} + \left[\nu_{\xi} \nabla_{\xi,i}^2 \mathbf{u} + \mathbf{F}_{\xi,i}^{(g)} + \mathbf{F}_{\xi,i}^{(st)} \right] \Delta t \\ &= \mathbf{u}_{\xi,i} + \left[\nu_{\xi} \frac{2d}{n^0 \lambda} \sum_{j \neq i}^{N_{\xi=1} + N_{\xi=2}} [\mathbf{u}_j - \mathbf{u}_{\xi,i}] w(|\mathbf{r}_j - \mathbf{r}_{\xi,i}|) + \mathbf{F}_{\xi,i}^{(g)} + \mathbf{F}_{\xi,i}^{(st)} \right] \Delta t, \text{ and} \end{aligned} \quad (8)$$

$$\mathbf{r}_{\xi,i}^* = \mathbf{r}_{\xi,i} + \mathbf{u}_{\xi,i}^* \Delta t, \quad (9)$$

where $\xi = 1$ is for the liquid and $\xi = 2$ is for the gas, and $\mathbf{r}_{\xi,i}$ and $\mathbf{u}_{\xi,i}$ are the position and the velocity vector of the particle i of ξ , respectively. $\mathbf{F}_{\xi,i}^{(g)}$ is the gravity force and $\mathbf{F}_{\xi,i}^{(st)}$ is the surface tension only for liquid particles. N_{ξ} is the number of particles of ξ . The kinematic viscosity between liquid and gas particles, ν_{ξ} in Eq.(8), is the averaged one of liquid and gas.

(2) Implicit calculation for the pressure balance with incompressibility condition:

- Calculation of pressure equation;

$$\langle \nabla^2 P \rangle_{\xi,i} = - \frac{\rho_{\xi}}{\Delta t^2} \frac{n_{\xi,i}^* - n^0}{n^0}. \quad (10)$$

The pressure equation is solved for liquid and gas separately to avoid numerical instability due to large difference of density. Firstly, the equation for all the particles is solved assuming they are gas particles. Secondly, the equation for liquid particles is solved by imposing the known gas pressure on the interface liquid particles.

- Correction of velocity and position;

$$\mathbf{u}_{\xi,i}' = - \frac{\Delta t d}{n^0 \rho_{\xi}} \sum_{j \neq i}^{N_{\xi=1} + N_{\xi=2}} \frac{P_j - P_{\xi,i}}{|\mathbf{r}_j^* - \mathbf{r}_{\xi,i}^*|^2} (\mathbf{r}_j^* - \mathbf{r}_{\xi,i}^*) w(|\mathbf{r}_j^* - \mathbf{r}_{\xi,i}^*|), \text{ and} \quad (11)$$

$$\mathbf{r}_{\xi,i}' = \mathbf{u}_{\xi,i}' \Delta t \quad (12)$$

- Update velocity and position;

$$\mathbf{u}_{\xi,i}^* = \mathbf{u}_{\xi,i} + \mathbf{u}_{\xi,i}', \text{ and } \mathbf{r}_{\xi,i}^* = \mathbf{r}_{\xi,i} + \mathbf{r}_{\xi,i}'. \quad (13), (14)$$

(3) Check convergence. If it does not converge, go back to (2).

(4) If convergence is achieved, go to the next time step.

2.3. Surface tension model

The surface tension is formulated as a force between particles as

$$\mathbf{F}_i^{(st)} = \sum_{j \neq i}^N \left[- \frac{\partial \phi(r_{ij})}{\partial r_{ij}} \hat{\mathbf{r}}_{ij} \right], \quad (15)$$

where ϕ is a potential between i - and j -particle and $\hat{\mathbf{r}}_{ij}$ is the unit vector from i - to j -particle. Here,

the parameter in the potential was roughly estimated based on the statistical mechanics and was tuned with the experiment by Peregrine et al. [22]. After trying several types of potentials, a curvilinear function that has a repulsive force in the interval $[0,1]$ and has an attractive force in the interval $[1,2]$ in the unit of dx as shown in Fig. 1, where the value of the differential with r is in the unit of m/s^2 , was selected. Although this model is tuned under the room conditions, the surface tension of saturated water does not depend on temperature strongly enough to influence the droplet behavior fluid-dynamically. To apply this force to the liquid particles in the vicinity of the liquid surface, a factor is multiplied to the force as

$$\mathbf{F}_i^{(sr)} = \sum_{j \neq i}^N \left[-\frac{\partial \phi(r_{ij})}{\partial r_{ij}} \hat{\mathbf{r}}_{ij} \right] \left(\frac{N^0}{N^i} \right)^2, \quad (16)$$

where N^0 and N^i are the number of particles in the region of $2dx$ around the particle i in the initial configuration and in the current one, respectively.

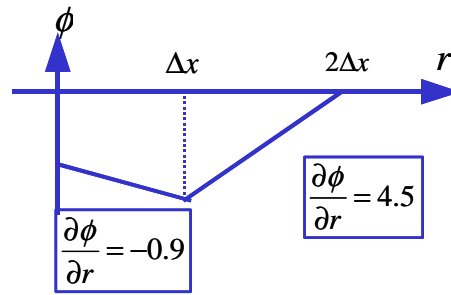


Figure 1: Potential for the surface tension.

2.4. Liquid-gas interaction model

Preliminary experimental analyses of two-phase flows have revealed that the pressure gradient term overestimated the momentum transfer between liquid and gas particles in the higher or lower void fraction regions. Since the interaction between particles is specified by the kernel function in this method, the kernel function *only in* ∇P is modified from the original form of Eq. (11) to

$$w(r) = (r_e / r)^{m_i} - 1. \quad (17)$$

By this modification, local topology of liquid, that is, the shape of interface between gas and liquid is taken into account basically. The force of interaction is reduced if $m_i \leq 1$. m_i is modeled as

$$m_i = \min[\tilde{n}_i / \bar{n}, 1], \quad (18)$$

where $\bar{n}_i = 0.5(n^0 + n_{self})$, and n_{self} is the self-contribution. \bar{n} is known at the beginning of calculation (Fig. 2a). \tilde{n}_i is defined as $\tilde{n}_i = \sum_{j \neq i} w(|\mathbf{r}_j - \mathbf{r}_i|) + n_{self}$, where Σ' indicates that the summation

is taken with respect to the same kind of particles as i . For a solitary particle in another kind of particles, m_i is assumed to be 0.3, which is estimated by analyzing the behavior of a single bubble in a water pool obtained by simple desktop experiments conducted by the authors. By letting $n_{self} = C_{self} n^0$,

$$m_i = \frac{\tilde{n}_i}{\bar{n}} = \frac{C_{self} n^0}{0.5(n^0 + C_{self} n^0)} = \frac{C_{self}}{0.5(1 + C_{self})} = 0.3 \quad (19)$$

holds and C_{self} is evaluated to be 0.176. \tilde{n}_i is calculated every ∇P calculation. Figure 2b sketches the concept of this model. In the cases of Fig. 2(b1) and 2(b2), the particle i is in the inner region in

the identical particles and on the smooth interface, respectively, so that m is calculated to be one and thus the kernel remains original. In the case of Fig. 2(b3), which corresponds to the region of higher or lower void fraction, m is calculated to be smaller than one, resulting in weaker interaction between different kinds of particles.

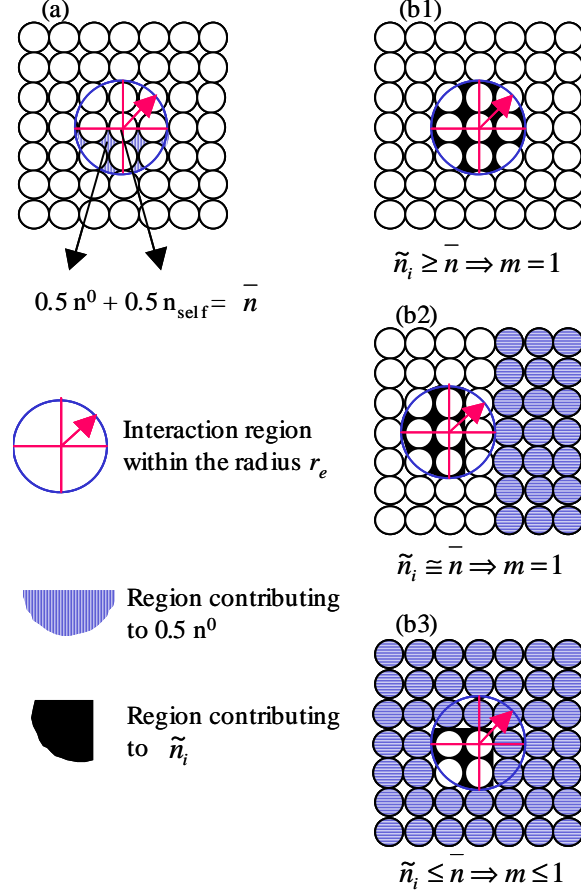


Figure 2: Gas-liquid interaction model.

2.5. Buoyancy Model

The particle interaction method is prone to underestimate buoyancy for a bubble (i. e. a gas particle) because it is difficult for MPS to calculate the pressure head exactly. Therefore, we added a buoyancy term in the pressure gradient term,

$$\mathbf{u}_{\xi,i}^{\dot{}} = -\frac{\Delta t d}{n^0 \rho_{\xi}} \left[\sum_{j \neq i}^{N_{\xi=1} + N_{\xi=2}} \frac{P_j - P_{\xi,i}}{|\mathbf{r}_j^* - \mathbf{r}_{\xi,i}^*|^2} (\mathbf{r}_j^* - \mathbf{r}_{\xi,i}^*) w(|\mathbf{r}_j^* - \mathbf{r}_{\xi,i}^*|) - \sum_{j \neq i}^{N_{\xi=1}} \mathbf{g} (\rho_l - \rho_g) f_B c_B w(|\mathbf{r}_j^* - \mathbf{r}_{\xi,i}^*|) \right] \quad (20)$$

where the second term in the parenthesis represents the buoyancy term, c_B is a parameter to tune the buoyancy, and f_B is formulated as

$$f_B(r) = -\frac{r}{r_e} + 1, \quad (21)$$

which is a function of the distance in the vertical direction between particles i and j . c_B is determined to be 0.003 by analysing the behavior of a single bubble in a water pool obtained by simple desktop experiments conducted by the authors.

2.6. Heat conduction model

The heat conduction equation is simply interpreted into TF-MPS context. The energy conservation equation for the system with heat conduction and phase change can be expressed as

$$\frac{D(\rho e)}{Dt} = k \nabla^2 T + Q_{VC}(\Gamma) + Q_{HT}, \quad (22)$$

where e is the specific internal energy, k is the thermal conductivity, $Q_{VC}(\Gamma)$ is the energy transfer rate due to the mass transfer Γ by vaporization or condensation, and Q_{HT} is the energy transfer rate by the heat transfer process among structure, liquid, and gas. The first term in RHS of Eq. (22) represents the thermal conduction between identical particles, which is modeled in our method as

$$e_i^{n+1} = e_i^n + \frac{k}{\rho n^0 \lambda} \sum_{j \neq i} [(T_j^n - T_i^n) w(|\mathbf{r}_j - \mathbf{r}_i|)] \Delta t, \quad (23)$$

where superscript n denotes the time step. The second and third terms in RHS of Eq. (22) are treated in the phase change model. Thermal conduction and phase change processes are included in the explicit stage.

2.7. Phase change model

Phase change of vaporization and condensation are treated as nonequilibrium heat transfer-limited processes determined by the energy balance at the interface.

(1) Vaporization of liquid particles in contact with a hot wall

The heat transfer rate to the gas phase is expressed as

$$q_{l \rightarrow g} = \frac{a^0}{n^0} \sum_j^{N_s} w(|\mathbf{r}_{s,j} - \mathbf{r}_{l,i}|) [h_s (T_{s,j} - [T]) - h_l ([T] - T_{l,i})], \quad (24)$$

where a^0 is the heat transfer area per unit volume, N_s is the number of wall particles interacting with the particle i , h is the heat transfer coefficient, and $[T]$ is the interface temperature which is the saturated temperature of the liquid particle i . Each term in Eq.(24) is schematically depicted in Fig. 3.

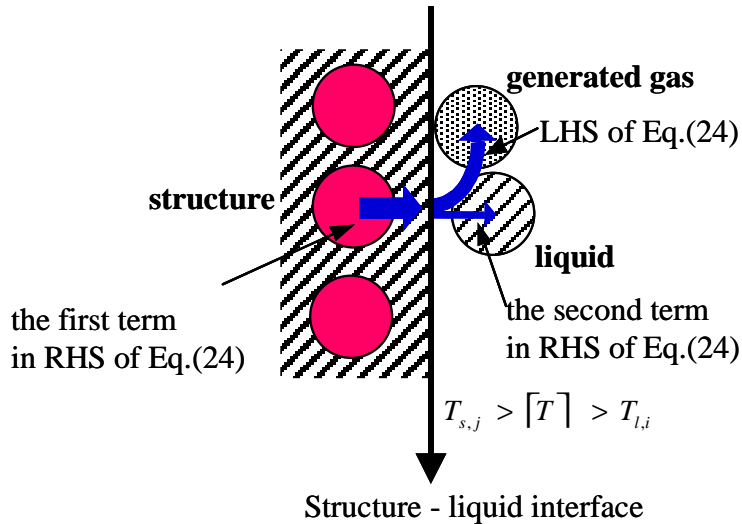


Figure 3: Concept of the heat transfer across the interface.

If $q_{l,i \rightarrow g} > 0$, the mass transfer rate from the liquid phase to the gas phase is given by

$$\Gamma_{l,i \rightarrow g} = \frac{q_{l,i \rightarrow g}}{[\bar{i}]_{\text{vapor}} - i_{l,i}}, \quad (25)$$

where $[\bar{i}]_{\text{vapor}}$ is the specific enthalpy of saturated steam and $i_{l,i}$ is the specific enthalpy of water.

The number of generated gas particles is evaluated by

$$N_{l,i \rightarrow g} = \frac{\Gamma_{l,i \rightarrow g} \Delta t}{\rho_g}, \quad (26)$$

assuming that the gas pressure is the same as the liquid.

If $q_{l,i \rightarrow g} < 0$, phase change does not occur and only heat transfer from structure to liquid is considered with the interface temperature,

$$[T] = \frac{h_s T_{s,j} + h_l T_{l,i}}{h_s + h_l}. \quad (27)$$

If $N_{l,i \rightarrow g}$ is smaller than one, namely a generated bubble is smaller than the initial particle size, the heat transferred to a gas particle is accumulated in a liquid particle i as $\bar{q}_{l,i \rightarrow g}$ until $N_{l,i \rightarrow g}$ exceeds one, that is, $\bar{q}_{l,i \rightarrow g} \leftarrow \bar{q}_{l,i \rightarrow g} + q_{l,i \rightarrow g} \cdot \Delta t$. Then, the transferred mass and the number of generated gas particles are evaluated as

$$\bar{\Gamma}_{l,i \rightarrow g} = \frac{\bar{q}_{l,i \rightarrow g}}{[\bar{i}]_{\text{vapor}} - i_{l,i}}, \text{ and } N_{l,i \rightarrow g} = \frac{\bar{\Gamma}_{l,i \rightarrow g}}{\rho_g}, \quad (28), (29)$$

respectively. When $N_{l,i \rightarrow g}$ is greater than one, the corresponding number of gas particles is generated to be included in the fluid dynamics. At the same time, the corresponding heat is subtracted from the accumulated one, that is, $\bar{q}_{l,i \rightarrow g} \leftarrow \bar{q}_{l,i \rightarrow g} - ([\bar{i}]_{\text{vapor}} - i_{l,i}) \cdot \rho_g$. When $N_{l,i \rightarrow g}$ is smaller than one, any gas particles are not generated and $\bar{q}_{l,i \rightarrow g}$ is continuously accumulated after the current step.

(2) Vaporization/condensation between a liquid particle i and a gas particle j

The heat transfer rate between liquid and gas phases is formulated as

$$q_{l,i \leftrightarrow g,j} = \frac{a^0}{n^0} w(r_{g,j} - r_{l,i}) [h_g ([T] - T_{g,j}) + h_l ([T] - T_{l,i})]. \quad (30)$$

The mass transfer rate is expressed with this $q_{l,i \leftrightarrow g,j}$ as

$$\text{if } q_{l,i \leftrightarrow g,j} < 0, \Gamma_{l,i \rightarrow g} = -\frac{q_{l,i \leftrightarrow g,j}}{[\bar{i}]_{\text{vapor}} - i_{l,i}} \text{ for vaporization, and} \quad (31)$$

$$\text{if } q_{l,i \leftrightarrow g,j} > 0, \Gamma_{g,j \rightarrow l} = \frac{q_{l,i \leftrightarrow g,j}}{i_{g,j} - [\bar{i}]_{\text{liquid}}} \text{ for condensation,} \quad (32)$$

where $i_{g,j}$ is the specific enthalpy of the steam and $[\bar{i}]_{\text{liquid}}$ is the specific enthalpy of the saturated water. In the case of $q_{l,i \leftrightarrow g,j} < 0$, the vaporization heat of Eq.(30) is accumulated in the liquid particle i , $\bar{q}_{l,i \rightarrow g} \leftarrow \bar{q}_{l,i \rightarrow g} + q_{l,i \leftrightarrow g,j} \cdot \Delta t$. In the case of $q_{l,i \leftrightarrow g,j} > 0$, the condensation heat of Eq.(30) is accumulated in the gas particle j , $\bar{q}_{g,j \rightarrow l} \leftarrow \bar{q}_{g,j \rightarrow l} + q_{l,i \leftrightarrow g,j} \cdot \Delta t$. Then, the transferred mass to gas and the number of generated gas particles are evaluated by

$$\bar{\Gamma}_{l,i \rightarrow g} = -\frac{\bar{q}_{l,i \rightarrow g}}{[\bar{i}]_{\text{vapor}} - i_{l,i}}, \text{ and } N_{l,i \rightarrow g} = \frac{\bar{\Gamma}_{l,i \rightarrow g}}{\rho_g}, \quad (33), (34)$$

respectively, where $[i]_{vapor}$ is the specific enthalpy of the saturated steam, and $i_{l,i}$ is the specific enthalpy of the water. The transferred mass to liquid and the number of annihilated gas particles are evaluated as

$$\bar{\Gamma}_{g,j \rightarrow l} = \frac{\bar{q}_{g,j \rightarrow l}}{i_{g,j} - [i]_{liquid}}, \text{ and } N_{g,j \rightarrow l} = \frac{\bar{\Gamma}_{g,j \rightarrow l}}{\rho_g}, \quad (35), (36)$$

respectively, where $[i]_{liquid}$ is the specific enthalpy of the saturated water, and $i_{g,j}$ is the specific enthalpy of the steam. The calculation procedure for the generation or annihilation of gas particles is similar to that described in the subsection (1).

The change of a liquid particle mass due to phase change is expressed by the change of a kernel radius r_e . The kernel radius after gas release r'_e is obtained by solving the equation,

$$\int_0^{r'_e} \rho_l w_{r'_e}(r) dr^3 - \int_0^{r_e} \rho_l w_{r_e}(r) dr^3 = \Delta \bar{\Gamma} \cdot V, \quad (37)$$

where $\Delta \bar{\Gamma}$ is the change of the liquid particle mass, $w_{r_e}(r)$ is the kernel function with a radius r_e , and V is the initial volume of a particle. It is assumed that the macroscopic density, which is defined by

$$\bar{\rho}_l = \int_0^{r'_e} \rho_l w_{r'_e}(r) dr^3 / \int_0^{r_e} w_{r_e}(r) dr^3, \quad (38)$$

is in the range,

$$\frac{1}{2} \bar{\rho}_l^0 \leq \bar{\rho}_l \leq 2 \bar{\rho}_l^0, \quad (39)$$

where $\bar{\rho}_l^0$ is the macroscopic density calculated with the initial kernel radius. If the macroscopic density of a liquid particle is less than $0.5 \bar{\rho}_l^0$, the particle is absorbed into an adjacent particle. On the other hand, if it is greater than $2 \bar{\rho}_l^0$, the particle is divided into two particles. In these two processes, mass and energy are conserved.

3. ANALYSIS OF THE FORCED CONVECTION BOILING

Schrock and Grossman [23, 24] conducted a series of tests on the forced convection boiling in vertical tubes. Figure 4 shows the test loop schematically. The water in the storage tank is kept at 273 K by slow boiling of Monel water heater. The water is circulated by a combination of a booster pump and a bank of eight piston pumps. The flow is metered by a calibrated orifice. Two pre-heaters are used to bring the water temperature to near the saturation temperature before it enters the test section. Heating is accomplished by passing alternating current through the tube. Heat flux is assumed to be uniform. Vapor formed in the test section is condensed in a coil of stainless steel tubing immersed in boiling water, and the condensate is throttled back into the storage tank. Eight-foot mercury manometers are used to measure the pressure drop in short segments of the tube.

We selected the test named series E that was the first integrated test and used a small diameter tube for calculational advantage.

The experimental conditions are:

inner diam.	: 0.003 m,
length	: 0.381 m,
heat flux	: $4.51 \cdot 10^5 \sim 4.57 \cdot 10^6$ W/m ² ,
mass flux	: $9.62 \cdot 10^2 \sim 4.45 \cdot 10^3$ kg/s/m ² and
pressure(Pin/Pout)	: $8.0 \cdot 10^5/4.4 \cdot 10^5 \sim 2.63 \cdot 10^6/ 2.16 \cdot 10^6$ Pa.

The calculational conditions are:

inner diameter	: 0.003 m,
length	: 0.20 m,
initial interval between particles	: 0.0005 m,
number of fluid particles	: 12,704,
number of structure particles	: 11,356,
inlet water velocity	: 2.0 m/s,
inlet water temperature	: 420 K,
pressure	: $5.0 \cdot 10^5$ Pa and
wall temperature (inside)	: 450 K,

where the wall temperature is evaluated by the heat flux.

The heat transfer coefficients (HTC) in Eqs.(24) and (30) are evaluated with the thermal conductivity and the representative length without using flow regime map.

The HTCs between wall and water are evaluated as $h_s = k_s / \Delta$ and $h_l = k_l / \Delta$, where $k_s = 30$ W/m/K, $k_l = 0.68$ W/m/K, and $\Delta = 5.0 \cdot 10^{-4}$ m. The HTCs between water and steam are evaluated as $h_g = k_g / \Delta$ and $h_l = k_l / \Delta$, where $k_s = 0.03$ W/m/K, $k_l = 0.68$ W/m/K, and $\Delta = 1.5 \cdot 10^{-6}$ m. Δ is determined in order that $2 h_l h_g / (h_g + h_l)$ should be about $4 \cdot 10^4$.

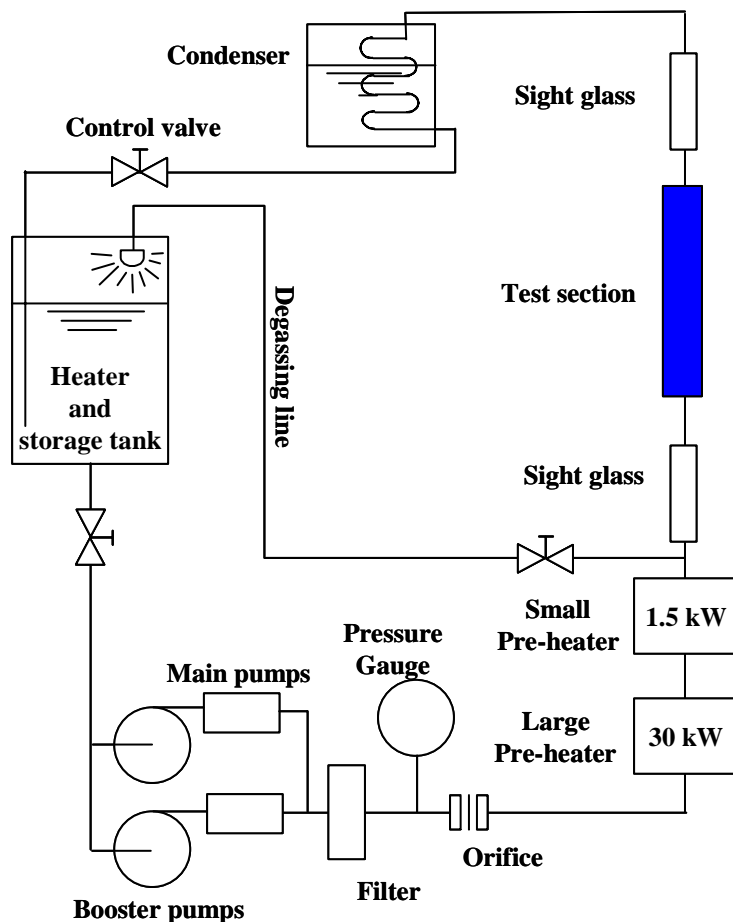


Figure 4: Loop of Schrock and Grossman' forced convection boiling test.

The vertical length 0.20 m is divided into 20 bins to average the velocity, pressure, density, and void fraction in each bin. The flow behavior in the three-dimensional calculation is shown in Fig. 5 at several points of time, where only steam particles are visualized with structure particles unseen.

Figure 6 shows the spatial distribution of the void fraction (left) and axial distribution of the void fraction averaged in the radial direction (right), which are both averaged in the time 0.045-0.050 s after the thermal transient ceased. We can see that the initiation of subcooled boiling develops into bulk boiling.

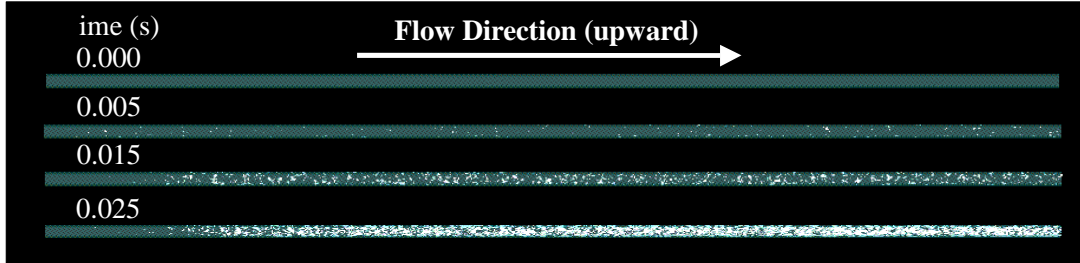


Figure 5: Flow behavior of the forced convection boiling in the calculation.

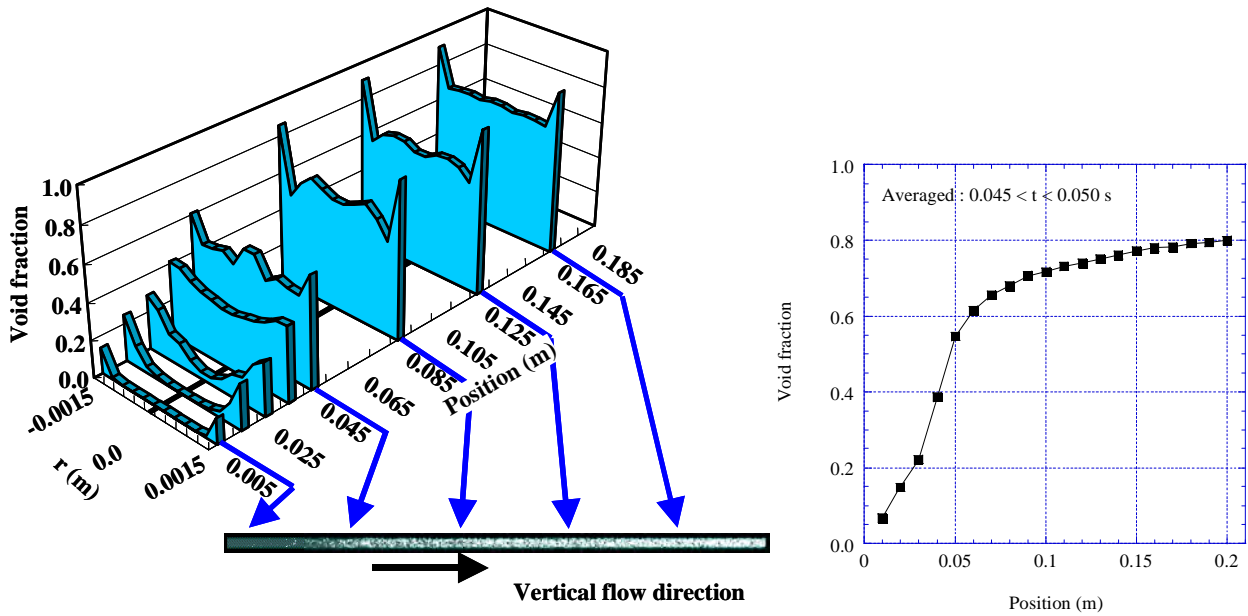


Figure 6: Spatial distribution of the void fraction (left) and axial distribution of the void fraction averaged in the radial direction (right), which are both averaged in the time 0.045-0.050 s.

Schrock and Grossman proposed that for the investigated experimental range the local heat transfer coefficients (defined in terms of the difference between the inner tube wall and local saturation temperature) in forced convection boiling could be expressed as

$$Nu_B = f(Re, Pr, X_{tt}, Bo), \quad (40)$$

where Nusselt, Reynolds, and Prandtl numbers were evaluated using the saturated liquid properties at the local pressure. X_{tt} is the Lockhart-Martinelli parameter defined by

$$X_{tt} = \left(\frac{\mu_f}{\mu_g} \right)^{0.1} \left(\frac{v_f}{v_g} \right)^{0.5} \left(\frac{1}{x} - 1 \right)^{0.9}, \quad (41)$$

while Bo is the boiling number, $Bo = \frac{q/A}{Gh_{fg}}$, where

h_{fg} : heat of vaporization,
 μ_f : liquid viscosity, μ_g : vapor viscosity,
 v_f : liquid velocity, and v_g : vapor velocity.

Consequently, they obtained the correlation where the ratio of the boiling heat transfer coefficient to the non-boiling single-phase heat transfer coefficient was a function of X_{tt} and Bo as

$$\frac{Nu}{Re^{0.8} Pr^{1/3}} = 170 [Bo + 1.50 \times 10^{-4} X_{tt}^{-2/3}]. \quad (42)$$

In the calculation, the Nusselt number is evaluated as

$$Nu = \frac{(q/A)D}{k_l(T_w - T_{sat})} \quad (43)$$

where

D : inner diameter, k_l : heat conductivity of liquid,
 T_w : temperature of the wall inner surface, and T_{sat} : saturation temperature.

Figure 7 shows the experimental and calculated values of LHS of Eq. (42) as a function of X_{tt} with the parameter Bo . At low values of the boiling number, the local heat transfer coefficient is a function of X_{tt} alone, while at large values of the boiling number, the heat transfer becomes independent of X_{tt} and depends solely on Bo over a wide range of exit qualities. The results of calculation are in the appropriate interval between the boiling number curves.

Figure 8 shows the full range of experimental and calculated heat transfer. The best fit for data points in the figure, where test series E, F, and G are involved yields Eq. (42). The results of calculation are sufficiently within the [-35,35]% interval.

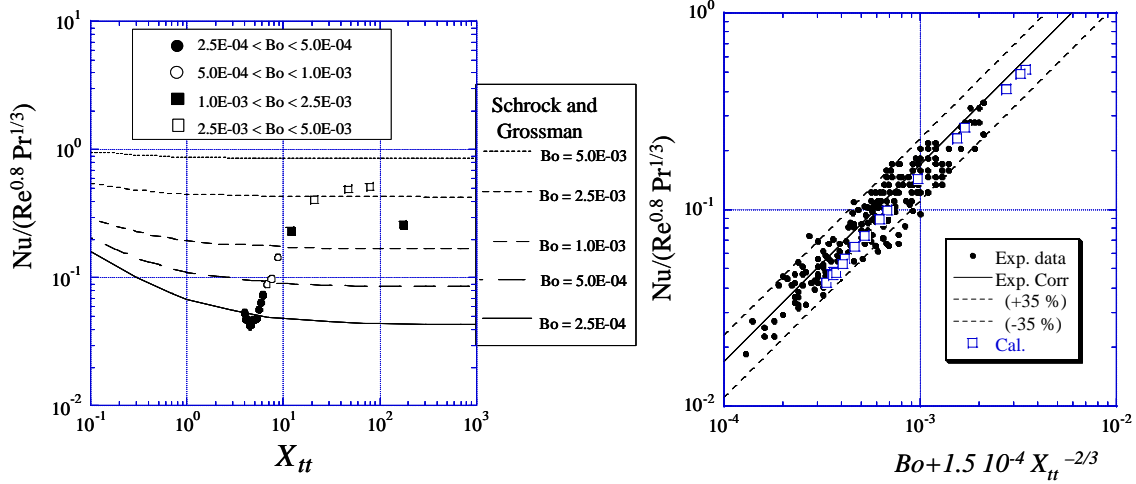


Figure 7: Comparison of the calculation with experiment on the heat transfer ratio vs. X in the parameter Bo .

Figure 8: Comparison of the calculation with experiment on the correlation.

4. CONCLUSION

The proposed TF-MPS method has been shown to be capable of reproducing two-phase flow characteristics through experimental analyses. Herein, we focused on the experimental analysis of forced convection boiling. The results showed reasonable agreement with experiments.

REFERENCES

- [1] Ishii, M. and Mishima, K., Study of Two Fluid Model and Interfacial Area, NUREG/CR-1873, 1980.
- [2] Kocamustafaogullari, G. and Ishii, M., Interfacial Area Nucleation Site Density in Boiling Systems, *Int. J. Heat Mass Transfer*, Vol. 26, No. 9, pp. 1377-1387, 1983.
- [3] Tobita, Y. et al., Interfacial Area Modeling for a Multiphase, Multicomponent Fluid-Dynamics Code, *Int. Conf. on Multiphase Flows '91-Tsukuba*, Tsukuba, Japan, Sept. 24-27, 1991.
- [4] Kondo, Sa. et al., SIMMER-III: An Advanced Computer Program for LMFBR Severe Accident Analysis, Oct.25-29, Tokyo, Japan, ANP'92, vol. 4, pp. 40.5/1-11, 1992.
- [5] Ishii, M. et al., Interfacial Area Transport; Data and Models, OECD-CSNI workshop on Advanced Thermal-Hydraulic and Neutronic Codes, Barcelona, April 2000.
- [6] Sussman, M. et al., An improved level set method for incompressible two-phase flows, *Comput. Fluids*, 27, no. 5-6, pp. 663-680, 1998.
- [7] Sussman, M. et al., An adaptive level set approach for incompressible two-phase flows, *J. Comput. Phys.*, 148, no. 1, pp. 81-124, 1999.
- [8] Margolin, L. et al., Application of the volume-of-fluid method to the advection- condensation problem, *Mon. Weather Rev.*, 125, no. 9, pp. 2265-2273, 1997.
- [9] Jeong, J. H. et al., Finite element analysis of transient fluid flow with free surface using VOF (volume-of-fluid) method and adaptive grid, *Int. J. Numer. Methods Fluids*, 26, no. 10, pp. 1127-1154, 1998.
- [10] Krishna, R. et al., Rise characteristics of gas bubbles in a 2D rectangular column: VOF simulations vs. experiments, *Int. Commun. Heat Mass Transf.*, 26, no. 7, pp. 965-974, 1999.
- [11] Takagi, S. et al., Numerical analysis of a single rising bubble using boundary-fitted coordinate system, *JSME International Journal, Series B*, 40, no. 1, pp. 42-50, 1997.
- [12] Tanaka, N., The CIVA method for mesh-free approaches, Improvement of the CIP method for n-simplex, *Comput. Fluid Dynamics J.*, 8-1, pp. 121-127, 1999.
- [13] Tanaka, N., Development of a highly accurate interpolation method for mesh-free flow simulations, 1. Integration of gridless, particle and CIP methods, *J. Numer. Methods Fluids*, Vol. 30, No. 8, pp. 957-976, 1999.
- [14] Koshizuka, S., Tamako, H. and Oka, Y., A Particle Method for Incompressible Viscous Flow with Fluid Fragmentation, *Comput. Fluid Dynamics J.*, Vol. 4, pp. 29-46, 1995.
- [15] Koshizuka, S. and Oka, Y., Moving-Particle Semi-Implicit Method for Fragmentation of Incompressible Fluid, *Nucl. Sci. and Eng.*, Vol. 123, July, pp. 421-434, 1996.
- [16] Koshizuka, S. et al., Numerical analysis of breaking waves using the moving particle semi-implicit method, *Int. J. Numer. Methods Fluids*, 26, no. 7, pp. 751-769, 1998.
- [17] Koshizuka, S. et al., Numerical analysis of fragmentation mechanisms in vapor explosions, *Nucl. Eng. Des.*, 189, no. 1-3 , pp. 423-433, 1999.
- [18] Shirakawa, N. et al., Development and Verification Study of the Two-Fluid Particle Interaction Method – Two-Phase Flow Analysis Free from Experimental Correlation –, *Comput. Fluid Dynamics J.* vol. 9, No. 4, pp. 348-365, January 2001.

- [19] Shirakawa, N., et al., Analysis of the Void Distribution in a Circular Tube with the Two-Fluid Particle Interaction Method, J. Nucl. Sci. Tech. Vol. 38, No. 6, pp. 392-402, June 2001.
- [20] Shirakawa, N., et al., Analysis of Jet Flows with the Two-Fluid Particle Interaction Method, J. Nucl. Sci. Tech. Vol. 38, No. 9, pp. 729-738, September 2001.
- [21] Shirakawa, N., et al., Analysis of flows around a BWR spacer by the two-fluid particle interaction method, J. Nucl. Sci. Tech., Vol. 39, No. 5, pp. 572-581, May 2002.
- [22] Peregrine, D. H., et al., The bifurcation of liquid bridges, Fluid Mech., 212, pp. 25-39, 1990.
- [23] Schrock, V. E. and Grossman, L.M., Local Pressure Gradients in Forced Convection Vaporization. Nucl. Sci. Eng., 3, 245, 1959.
- [24] Schrock, V. E. and Grossman, L.M., Forced Convection Boiling in Tubes. Nucl. Sci. Eng., 12, 474, 1962.

MULTIDIMENSIONAL MODELING AND SIMULATION OF SUBCOOLED POOL BOILING

E. Laurien, T. Giese, D. Saptoadi and J. Schütz

Institute for Nuclear Technology and Energy Systems (IKE)
University of Stuttgart
Pfaffenwaldring 31, D-70550 Stuttgart, GERMANY
Phone: +49 711 685-2415, Fax: +49 711 685-2010,
E-mail: laurien@ike.uni-stuttgart.de

ABSTRACT

Bubbly flow and boiling in large pools is dominated by the mechanisms of mass, momentum and energy exchange between rising bubbles liquid. In the present work the numerical prediction of such flows is based on a two- or three-dimensional two-fluid formulation [1,2]. The importance of various extensions or simplifications of this model formulation will be demonstrated and discussed in view of a realistic and accurate simulation of subcooled pool boiling of water with the possibility of the system pressure (and thus saturation temperature) increasing in time. If the bubbles are assumed to rise always with their terminal velocity the momentum equation of the gas phase can be omitted. The energy equation is only necessary, when gas superheat has to be taken into account. The bubble size is an important model parameter for the heat and mass exchange as well as for the momentum exchange between bubbles and liquid. In order to take observed bubble-size spectra into account a numerical approach using population classes will be discussed. The aim is to develop a powerful engineering tool for the thermohydraulic design and safety analysis of nuclear reactors [3] and energy systems.

1. INTRODUCTION

The development of nuclear reactors for energy production moves forward to achieve a better, safer and more economic power plant. In competition to other reactor designs, Framatome-ANP develops a new type of boiling water reactor, called SWR 1000 [4]. Similar to other “Generation IV” reactors, the SWR 1000 relies on passive safety reactor features to achieve a higher level of safety. The main objective of the design concept is to avoid a postulated core melt accident by restricting consequences of an accident to the plant and to avoid radioactive release to the environment. The emergency cooling system is deemed to prevent severe accidents by basic laws of physics like gravity and natural convection. This passive safety equipment – where no active or human intervention is required - combined with proven active systems should provide an optimum combination to reduce the probability of core melting.

To achieve these objectives, the reactor is equipped with some passive safety systems. In case of a severe accident, e.g. Loss Of Coolant Accident (LOCA), the decrease of the water level inside the reactor pressure vessel below the normal operating level must be avoided in order to ensure the removal of the decay heat.

In the SWR 1000 concept, four emergency condensers, each with 63 MW capacity, are installed to remove the decay heat generated in the core. At normal water level in the reactor pressure vessel, the emergency condenser tube is filled with water. If the water level drops, steam from the reactor enters the tube. The steam is cooled by the water in the flooding pool and condensates. The

condensed water in the emergency condenser flows back to the reactor pressure vessel due to gravity. All in all, these passive systems should be able to reduce the probability of occurrence of a core melt accident.

In the core flooding pool, boiling occurs even when the bulk water is still at ambient temperature. The reason for this is the different pressure level inside and outside the emergency condenser tube. Therefore, subcooled boiling with re-condensation of the rising vapor occurs. As the water temperature is increased significantly, the bubbles may reach the surface and are released to the reactor containment. The release of vapor from the surface of the flooding pool rises the pressure (in the following referenced as system pressure) in the reactor building. This, in turn, leads to a rising saturation temperature with an increasing ability of the pool to store heat.

The processes in the flooding pool consist of a three-dimensional bubbly flow with boiling, heat transfer, condensation and natural convection. To determine the overall system parameters (pool temperature, system pressure as a function of time), the three dimensional bubbly flow in the flooding pool must be simulated numerically including all the mentioned phenomena. To simulate these phenomena, different approaches made at IKE to simulate multiphase flow were combined. The main phenomena are

- boiling at the condenser tubes
- natural convection of two-phase flow with re-condensation
- rise of system pressure.

This paper is focused on the simulation of natural convection of two phase flow including condensation phenomena.

2. TEST CASE

The analysed test case includes the main phenomena of the emergency cooler in the emergency cooler tank. A heated steel block simulating the tube bundle is submerged in liquid water nearly on saturation temperature. Due to heat sources equivalent to an expected heat output of the emergency coolers, the steel temperature begins to rise. If the wall temperature on the upper side of the block is high enough, nucleate boiling occurs. The production of steam in the closed system is responsible for a rise of pressure in the gas volume beyond the liquid surface. The maximum pressure level in the system for a fixed energy input depends on the re-condensation rate in the liquid area and from a

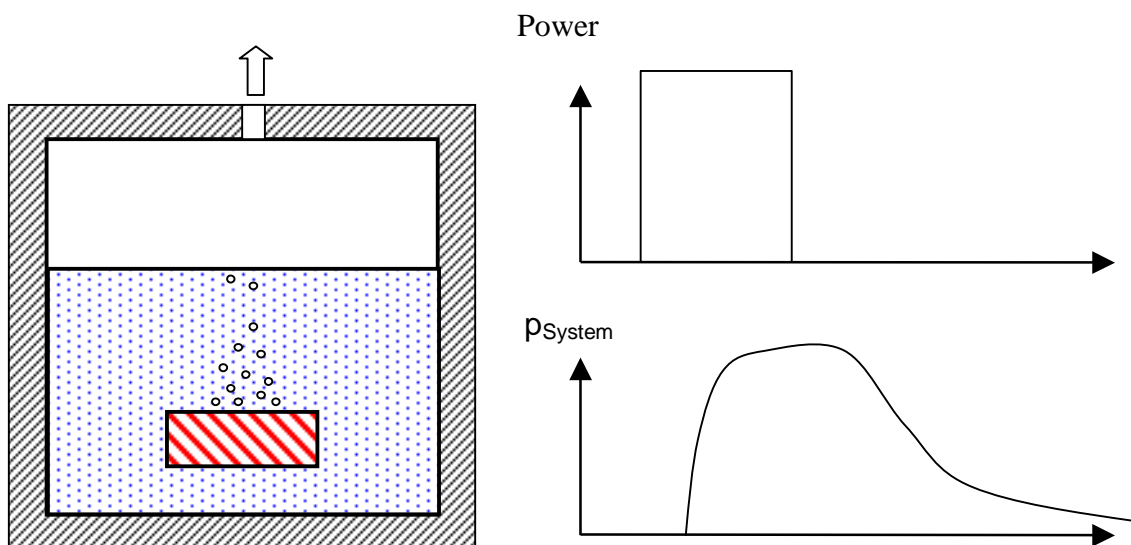


Figure 2.1: Test case description.

loss of steam through a defined opening at the top of the tank. The point of interest is the behaviour of the whole system as a result of boiling at the wall, re-condensation and exhausting steam. These processes depend on the system pressure and vice versa. Using this simple test case, the simulations presented in section 3.5 and 4.2 were performed and showed the ability to take the necessary phenomena into account.

3. SIMULATION WITH CFX-4

3.1. Two Fluid Model

The two-fluid (or “Euler-Euler”-) formulation is chosen to describe the multiphase character of the flow. In this approach both phases, liquid (index L) and air or steam (index G, gas), are regarded as two continua interpenetrating each other. With the help of a phase function ε , defined unity in the liquid phase and zero in the gas phase, and temporal averaging, as described by Drew [5], the basic equations for the average two-phase state quantities can be formulated.

$$\varepsilon(\vec{x}, t) = \begin{cases} 1 \\ 0 \end{cases} \quad (3.1)$$

This leads to a volumetric phase fraction, called volume fraction for the liquid phase

$$\alpha_L = \bar{\varepsilon} = \frac{1}{\Delta t} \int_t^{t+\Delta t} \varepsilon(\vartheta) d\vartheta \quad (3.2)$$

and for the gas phase

$$\alpha_G = 1 - \bar{\varepsilon} = 1 - \frac{1}{\Delta t} \int_t^{t+\Delta t} \varepsilon(\vartheta) d\vartheta = 1 - \alpha_L. \quad (3.3)$$

The “phasic-average” of the instantaneous liquid or gas velocity components u_m , $m = 1, 2, 3$ is defined at any spatial position in the flow

$$\bar{u}_m^L = \frac{1}{\bar{\varepsilon} \cdot \Delta t} \int_t^{t+\Delta t} \varepsilon(\vartheta) \cdot u_m(\vartheta) d\vartheta \quad (3.4)$$

$$\bar{u}_m^G = \frac{1}{(1 - \bar{\varepsilon}) \cdot \Delta t} \int_t^{t+\Delta t} (1 - \varepsilon(\vartheta)) \cdot u_m(\vartheta) d\vartheta. \quad (3.5)$$

This leads to the phase averaged Two-Fluid equations, see Laurien und Saptoadi [2]. The mass conservation equation for the liquid phase is described by

$$\rho_L \frac{\partial \alpha_L}{\partial t} + \rho_L \nabla \cdot (\alpha_L \bar{\mathbf{u}}^L) = \Gamma_L \quad (3.6)$$

and for the gas phase by

$$\rho_G \frac{\partial \alpha_G}{\partial t} + \rho_G \nabla \cdot (\alpha_G \bar{\mathbf{u}}^G) = \Gamma_G, \quad (3.7)$$

the momentum conservation equations for the liquid phase

$$\rho_L \frac{\partial}{\partial t} (\alpha_L \bar{\mathbf{u}}_m^L) + \rho_L \nabla \cdot (\alpha_L \bar{\mathbf{u}}^L \bar{\mathbf{u}}_m^L) = -\alpha_L \frac{\partial \bar{p}}{\partial x_m} + \nabla \cdot (\alpha_L (\underline{\underline{\tau}}^L + \underline{\underline{\tau}}^{ReL})) + M_m^L + f_m^L, \quad (3.8)$$

and for the gas phase

$$\rho_G \frac{\partial}{\partial t} (\alpha_G \bar{\mathbf{u}}_m^G) + \rho_G \nabla \cdot (\alpha_G \bar{\mathbf{u}}^G \bar{\mathbf{u}}_m^G) = -\alpha_G \frac{\partial \bar{p}}{\partial x_m} + \nabla \cdot (\alpha_G \underline{\underline{\tau}}^G) + M_m^G + f_m^G \quad (3.9)$$

and the energy conservation equation for the liquid phase

$$\rho_L \frac{\partial}{\partial t} (\alpha_L \bar{h}^L) + \rho_L \nabla \cdot (\alpha_L \bar{\mathbf{u}}^L \bar{h}^L) = \nabla \cdot (\alpha_L (\bar{\mathbf{q}}^L + \bar{\mathbf{q}}^{\text{ReL}})) + E_L. \quad (3.10)$$

An assumption was made that the gas phase is always on saturation temperature. As a consequence, the energy conservation equation of the gas phase can be omitted.

It is also assumed that both phases are incompressible and that the Boussinesq-approximation with constant densities ρ_L and ρ_G at a reference temperature τ_0 can be used. In the equation for the liquid phase, the additional terms for turbulent fluxes τ^{ReL} and $\bar{\mathbf{q}}^{\text{ReL}}$, describing the Reynolds-stresses and the turbulent heat fluxes, appear. The flow in the liquid phase is modelled as turbulent flow with the Standard-k- ϵ -model. The terms Γ_k , M_m^k and E_k contain the mass, momentum and heat transfer between the phases.

The inter-phase exchange terms in this approach are well known for some of the flow cases, for example for dilute bubbly flow without heat and mass transfer. But for many phenomena like boiling, cavitation and condensation and for different flow regimes the terms

$$\bar{\mathbf{A}}^k = \begin{bmatrix} \Gamma_k \\ M_1^k \\ M_2^k \\ M_3^k \\ E_k \end{bmatrix} \quad (3.11)$$

are a field of current investigation.

3.2. Surface Boiling

At the surface of the steel block in Figure 2.1, boiling may occur. In literature, many boiling correlations, mainly directly derived from experimental data, can be found. However, an accurate and general correlation describing boiling phenomena is still missing [6]. Due to the fact that this study is not focused on boiling phenomena, a simple approach according to Fritz was implemented [7]. The local temperature at the steel surface is used for the derivation of a heat flux between the steel and its liquid surrounding.

3.3. Recondensation

The recondensation of steam occurs in the entire flow field. In this simulation, the dependency of recondensation from the local liquid temperature and the local static pressure is modeled in analogy to a thermal based cavitation model from Giese and Laurien [8]. Attempts to analyse a two phase flow case in pipes led to the development of a cavitation model for water at high temperature and, as a consequence, high saturation pressure. The basic assumption of the developed model is, that phase change is based on thermodynamic processes and not on bubble dynamics. The pressure dependency is very important in a case with increasing system pressure.

The heat transfer between a bubble and surrounding liquid can be used to quantify recondensation phenomena. Assuming that the gas phase is not overheated, the temperature of the gas phase is at saturation temperature T_{sat} . The saturation temperature depends on the local static pressure. The variation of the pressure (assuming same pressure for both phases) or of the temperature of the water leads to a heat transfer, which can be balanced with an interfacial mass transfer. Assuming spherical bubbles with diameter d_B , the heat transfer between the gas phase and

its surrounding can be derived for bubbly flow. The inter-phase heat transfer coefficient α_B of a spherical bubble in motion with a relative velocity to the surrounding fluid can be approximated by

$$\alpha_B = \frac{\lambda_L}{d_B} \cdot (2 + 0,6 \cdot \text{Re}_B^{1/2} \text{Pr}_L^{1/3}). \quad (3.12)$$

In this model, the Reynolds number

$$\text{Re}_B = \frac{d_B \cdot |\bar{u}_G - \bar{u}_L|}{\nu_L} \quad (3.13)$$

and the Prandtl number Pr_L are used to predict the convective heat transfer according to the Ranz-Marshall correlation [9]. In equilibrium the heat flux $\Delta \dot{h}_B$ towards the interfacial area of a bubble can be used to predict the inter-phase mass transfer \dot{m}_B at the bubble which is the basic value for the different source terms in the two-fluid description

$$\Delta \dot{h}_B = \Delta h_{LG} \cdot \dot{m}_B = \alpha_B \cdot (T_L - T_{\text{sat}}) \cdot \pi d_B^2. \quad (3.14)$$

If λ_L is the thermal conductivity of the water and Δh_{LG} the evaporation enthalpy, this leads to the equation

$$\Gamma_B = (T_L - T_{\text{sat}}) \cdot \frac{6 \cdot \alpha_B \cdot \lambda_L}{d_B^2 \cdot \Delta h_{LG}} \cdot (2 + 0,6 \cdot \text{Re}_B^{1/2} \cdot \text{Pr}_L^{1/3}) \quad (3.15)$$

for the mass transfer at the interfacial area per volume. If the liquid is superheated ($T_L > T_{\text{sat}}$), it is assumed that the transported heat (from the liquid to the interfacial area of the bubble) is used for further vaporization of the liquid phase.

3.4. Exhaustion

If phase change phenomena occur in a closed volume, the exchange of mass between the phases leads to a change of the system pressure and vice versa. A similar situation can be found if the tank has a small opening to the surrounding e.g. a check valve. If the system pressure is rising due to boiling phenomena, this leads to a mass flux through the opening. As a consequence, the exhaustion decreases the rise in the system pressure. If the system pressure is rising, the liquid is subcooled in reference to the pressure-dependant saturation temperature. This affects the boiling and condensation rate in the system. Assuming a saturated gas in the volume above the liquid surface, the system pressure p_{System} can be calculated from the equation of a perfect gas

$$p_{\text{System}}(t) = \frac{m_{\text{Gas}}(t)}{V_{\text{Gas}}} R_{\text{H}_2\text{O}} T_{\text{sat}}(p_{\text{System}}). \quad (3.16)$$

V_{Gas} is the volume filled with saturated steam above the liquid and m_{Gas} the mass of steam. The following phenomena influences the system pressure because they affect the amount of steam in the system:

- Boiling at the heated solid \dot{m}_{Boiling}
- Condensation of steam $\dot{m}_{\text{Condensation}}$ in the liquid
- Exhausting steam $\dot{m}_{\text{Exhaustion}}$

The steam production due to boiling and the recondensation have to be monitored during the calculation. The quantity of emanating steam can be calculated with the system pressure of the old time step and the ambient pressure using a simple correlation according to Sigloch [10]. A balance leads to the change of steam mass in the system

$$\dot{m} = \dot{m}_{\text{Boiling}} + \dot{m}_{\text{Condensation}} + \dot{m}_{\text{Exhausting}} \quad (3.17)$$

that can be used in the calculation of the system pressure.

3.5. Simulation Results

The geometry described in section 2 is used for a transient simulation. The power entered into the block of steel is chosen in that way that in a steady state a heat flux of 83000 W/m^2 occurs at the top of the steel block. This heat flux is classified as nucleate boiling.

In the first seconds of power input the temperature in the steel block is rising and only a small convective heat flux is transported to the pool water. If the wall is overheated, nucleate boiling starts and leads to a void fraction on the heater surface. Later, the bubbles start to rise and initiate strong convective movement in the pool. After a certain amount of time, a stable vortex configuration is visible. In Figure 3.1, the void fraction and velocity vectors are shown for simulations with three different bubble diameters (1 mm and 2 mm).

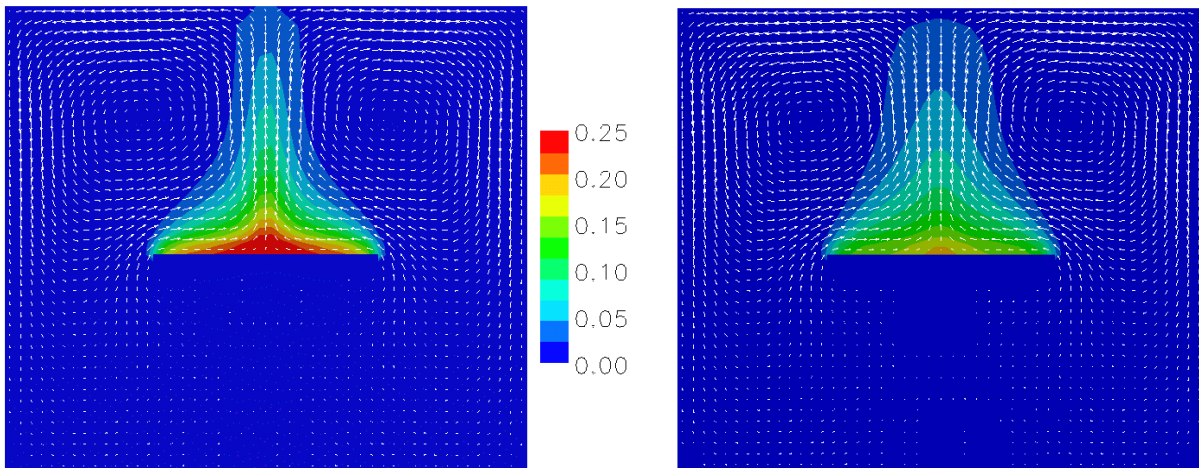


Figure 3.1: Void fraction, bubble diameter 1mm (left) and 2mm (right).

As one can see in Figure 3.1, the assumed bubble diameter affects the formation of steam on the plate and the re-condensation. Small bubbles with a large volumetric interfacial surface allow the formation of large amount of steam (left picture). Additionally, small bubbles have a lower rising velocity, that means the bubbles have a tendency to stay near the plate. If they rise, they quickly recondense. In contrast, bubbles with a large diameter quickly leave the plate. As a consequence, the amount of steam near the plate is lower and the convection stronger. Due to the fact that the volumetric interfacial area of large bubbles is smaller, the recondensation process of large bubbles is slower.

The consequences of this different behaviour in boiling and recondensation can be seen in the progression of the system pressure. If we assume a small opening to the atmosphere (1mm diameter), the pressure in the system rises due to the formation of steam. The rise of the system pressure depends on the bubble diameter, see Figure 3.2. Large bubbles have a lower recondensation rate because their volumetric surface is smaller and they quickly reach the water surface where no further condensation occurs. As a consequence, the pressure in the tank strongly depends on the assumed bubble diameter. However, the existing multiphase codes mainly assume a

constant bubble diameter as a user defined model parameter. It has been shown in Figure 3.2 which difficulties this may cause.

There exist several approaches to overcome the simplification of a constant bubble diameter. One of these approaches is the MUSIG model [11] including fragmentation of bubbles. However, only isothermal flows have been successfully simulated with the MUSIG model and the computational effort is very large. For the future, models based on an additional transport equation for the interfacial surface are proposed but are still a field of basic research. To meet the demands of present applications, a multi-group two-fluid model (MUG2FM) is proposed in the next section.

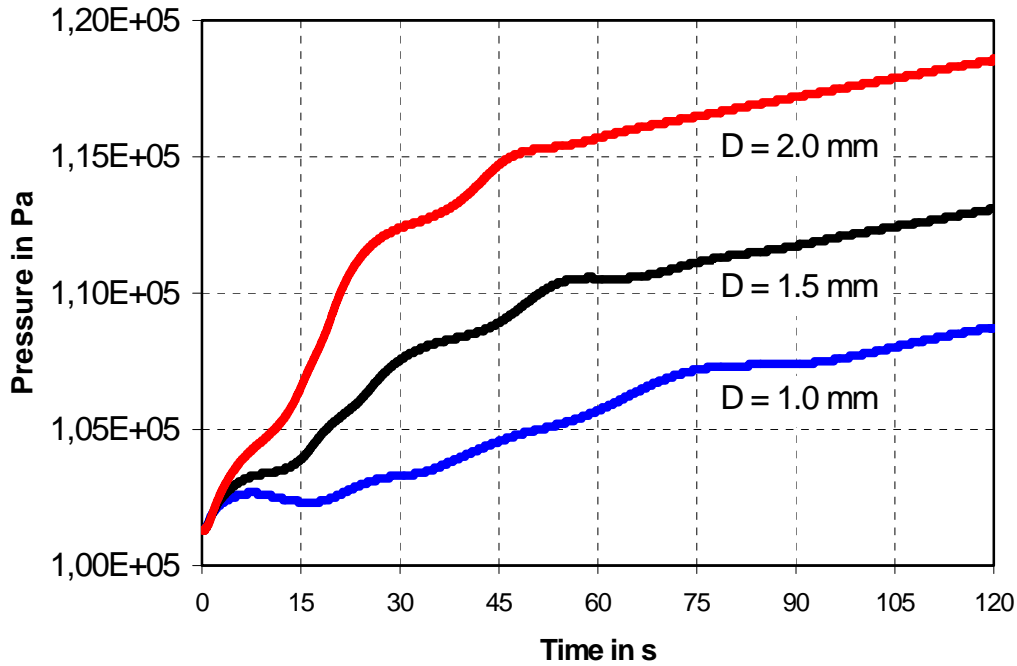


Figure 3.2: System pressure in dependency of the assumed bubble diameter.

4. TWO-FLUID MODEL WITH POPULATION CLASSES

4.1. Mathematical Model

To simulate a bubbly flow where coalescence and fragmentation of bubbles are not important, a simplified two-fluid model can be derived from the incompressible equations of the two-fluid model above. With the assumption that the bubbles move with their terminal rising velocity u_T relative to the liquid, the momentum equation of the gas phase is always satisfied. This simplification allows to extend the two-fluid model towards the simulation of a bubble size spectrum using population classes [12]. The characteristic of each population class or bubble class is the bubble radius R_B .

The governing equations of the two-fluid model with population classes for the liquid phase are as shown in equation (3.6) (3.8) (3.10) before. Whereas, the mass and energy equations of the gas phase have to be solved for each involved bubble class. The following relationship is valid as a consequence of the assumptions,

$$\bar{u}_{G,i} = \bar{u}_L + \bar{u}_{T,i} \quad ; \quad \bar{u}_{T,i} = [0 \quad 0 \quad u_{T,i}]^T \quad (4.1)$$

where the terminal velocity of the bubbles u_T is well known from experiments with bubbles of a given size. The continuity equation of the gas phase is

$$\rho_G \left\{ \frac{\partial \alpha_{G,i}}{\partial t} + \nabla \cdot (\alpha_{G,i} \bar{u}_i^G) \right\} = \Gamma_{G,i} \quad (4.2)$$

and the momentum of the gas phase is

$$\rho_G c_G \left\{ \frac{\partial}{\partial t} (\alpha_{G,i} \bar{T}^G) + \nabla \cdot (\alpha_{G,i} \bar{u}_i^G \bar{T}_i^G) \right\} = \overline{e}_{\text{tot } i}^G \Gamma_{G,i} + E_{G,i} \quad (4.3)$$

where $i=1,2,\dots, l$ is the population class index. The interfacial mass transfer Γ_k , the interfacial momentum transfer M_m^k , the energy transfer due to mass transfer $\overline{e}_{\text{tot } i}^k \Gamma_{k,i}$ and the interfacial energy transfer E_k appear in the equations. They describe the interaction between both phases and have to be modelled to gain a physical result. The phase interaction terms are modelled on the basis of flow and heat transfer around spherical bubbles separately for each population class with a distinct model diameter. In general the interfacial transfer of the liquid phase is a summation of the interfacial transfer for all bubble classes

$$\Gamma_L = \sum_{i=1}^l \Gamma_{G,i}, \quad M_L = \sum_{i=1}^l M_{G,i}, \quad \overline{e}_{\text{tot}}^L \Gamma_L = \sum_{i=1}^l \overline{e}_{\text{tot } i}^G \Gamma_{G,i}, \quad E_L = \sum_{i=1}^l E_{G,i}. \quad (4.4)$$

The models of some of the interfacial transfer terms have been described in section 3, except the interfacial momentum exchange M_m^k . Using the assumption that bubbles move upward with constant terminal velocity, the interfacial momentum exchange is

$$M_{m,G,i} = \frac{3}{8} \frac{\alpha_{G,i} \rho_L C_{D,i}}{R_{B,i}} |\bar{u}_{T,i}| \cdot \bar{u}_{T,i}. \quad (4.5)$$

To satisfy the momentum equation of the gas phase, special care has to be taken in determining terminal $u_{T,i}$ velocity and drag coefficient $C_{D,i}$ to achieve the terminal velocity as in experiments.

4.2. Simulation Results

The simulation is performed with water and steam for the test case shown in Figure 2.1. The radius of the bubbles is between 0.1 mm up to 1.5 mm, divided into 5 bubble population classes. The simulation parameters are summarised in Table 1. The terminal velocity of the bubble depends on the size of the bubbles. In contrast to the simulations in section 3 where a simple boiling model was used, this simulation is performed by injecting the 5-class bubbles at the heat plate with initial void fraction for each class of 2.5 % and temperature of 385 K. The initial liquid temperature is 293 K.

Table 1

Bubble Class	1	2	3	4	5
$R_{B,i}$ [mm]	0.1000	0.3000	0.7000	1.1000	1.5000
α_{G0}	0.0250	0.0250	0.0250	0.0250	0.0250
$U_{T,i}$ [ms^{-1}] (calc.)	0.0156	0.0533	0.3485	0.2819	0.2337

The resulting isolines of the void fraction and the velocity vector of liquid phase for bubble class 2, 3, 5 for $t=10$ seconds are shown in Figure 4.1, whereas the isolines of the water temperature are shown in Figure 4.2. The figures on the left side show the contours of the void fraction without condensation, and on the right side with condensation.

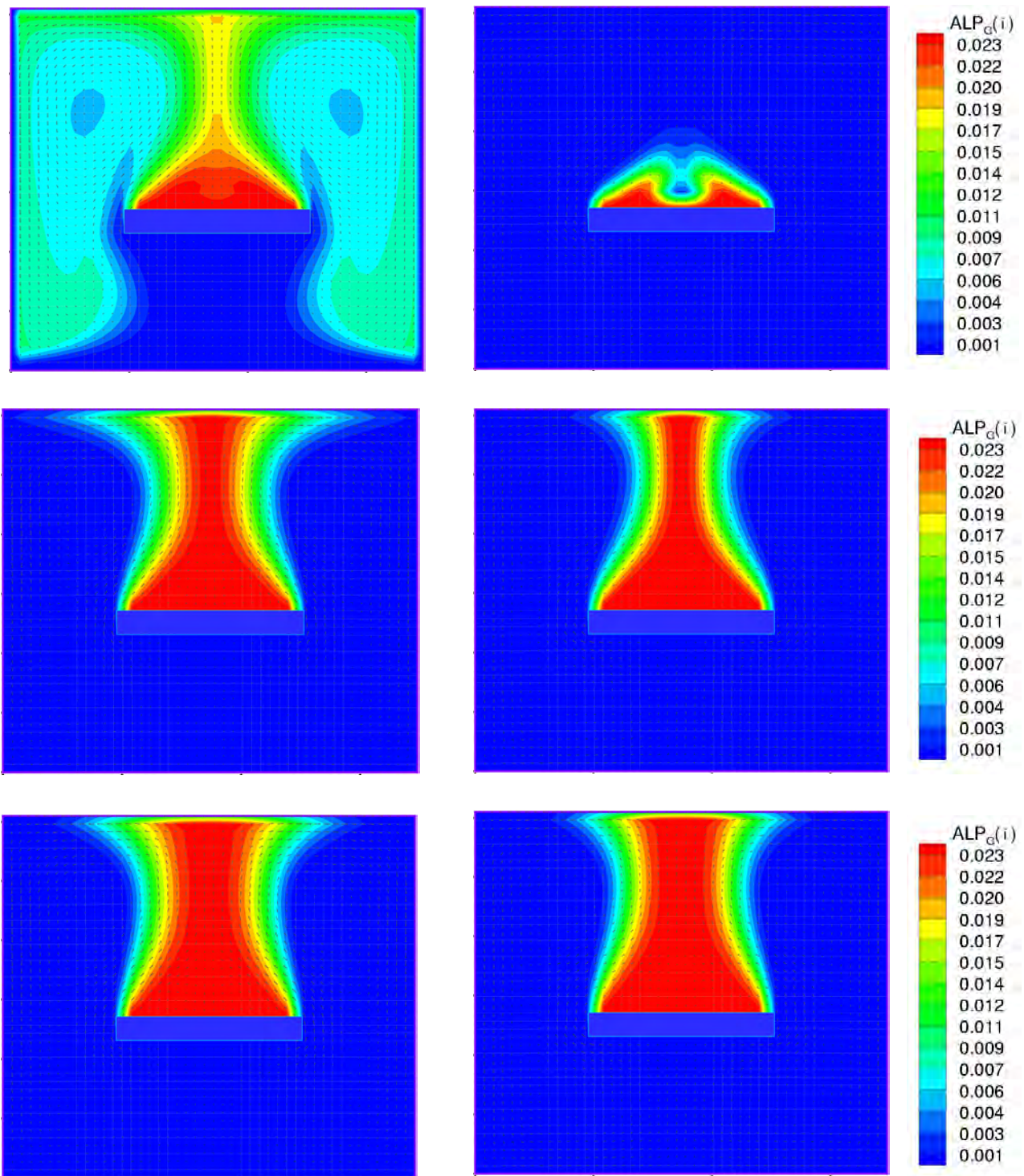


Figure 4.1: Void fraction for bubble class 2, 3, 5 (top, middle, bottom) without (left) or with (right) condensation

As can be observed, different contours of the gas void fraction occur for different bubble classes, because different terminal velocities occur for each bubble class. If condensation is taken into account (as in a 2 component fluid), the lower-class bubbles (class 1 and 2) reach the bottom of the container. The reason is that the terminal velocity of this class is smaller than the liquid velocity. The contour lines of higher-class bubbles (class 3, 4, 5) are very similar to each other. The liquid temperature is shown in Figure 4.2 on the left hand side. The small-class bubbles contribute to the increase in the liquid temperature along the vertical walls. Such results cannot be achieved with a simulation using bubbles with one fixed diameter (for detail, see Saptoadi and Laurien [11]). If condensation occurs, the degree of condensation differs for each class. The first bubble class condenses completely, whereas the bubble of second class condenses almost completely as shown on the right hand side of Figure 4.1 (top). The bubbles of higher classes condense only partly (middle, bottom). If condensation occurs, the sensible heat of the gas phase is transferred to the liquid phase, resulting a higher averaged liquid temperature than without condensation (Figure 4.2, right).

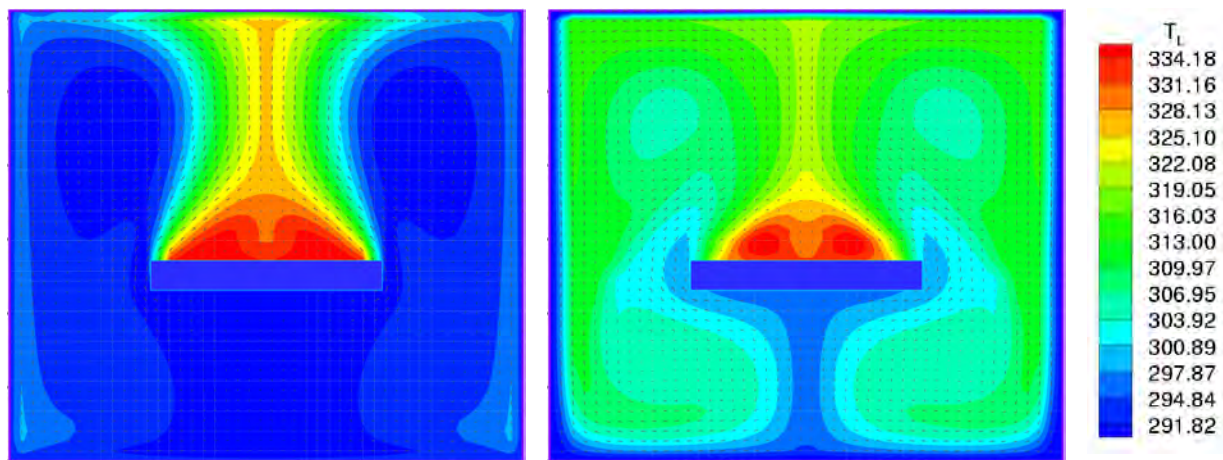


Figure 4.2: Water temperature without (left) and with (right) recondensation

5. CONCLUSIONS AND OUTLOOK

It has been shown that the main phenomena of boiling, recondensation and system pressure calculation can be simulated using an approach with computational fluid dynamics. The simulations showed a strong dependency from certain model parameters – for example the bubble diameter which is extremely important for the recondensation phenomena. To overcome this difficulty, an approach using different bubble classes is proposed.

REFERENCES

- [1] Laurien, E, Becker, S. Saptoadi, D., and Giese, T.: Multidimensional Modelling of Bubbly Flows for Nuclear Reactor Passive Decay Heat Removal, in: (Misale, M. and Mayinger, F. (eds.): Proc. EURO THERM-Seminar No 63, 351-360, 1999.
- [2] Laurien, E and Saptoadi, D.: On the fundamental Two-Fluid Equations to Model Three-Dimensional Bubbly Flows, in: Michaelides E. M. 2001: (ed.) Proceedings of the International Conference on Multiphase Flow, Tulane University, New Orleans, LA, 2001.
- [3] Laurien, E.: The Numerical Simulation of Three-Dimensional Two-Phase Flows as a Tool for Light-Water Reactor Design and Safety Analysis, Annual Meeting on Nuclear Technology, May 16.-18. 2002, Stuttgart, 2002.

- [4] Brettschuh, W. and Wagner, K.: SWR 1000 – das innovative Reaktorkonzept, atw 41, Heft 4, 1996.
- [5] Drew, D.A.: Mathematical Modeling of Two-Phase Flows, Ann. Rev. Fluid Mech. 15, pp. 261-291, 1998.
- [6] Stephan, K.: Wärmeübergang beim Kondensieren und beim Sieden, Springer, Berlin, Heidelberg, 1988.
- [7] Baehr, H. D. and Stephan, K.: Wärme und Stoffübertragung, Springer Verlag, Berlin, 1998.
- [8] Giese, T. and Laurien, E.: Experimental and Numerical Investigation of Gravity-Driven Pipe Flow with Cavitation, 10th International Conference on Nuclear Engineering (ICONE10), Arlington, Virginia, 2002.
- [9] Ranz, W. and Marshall, W.: Evaporation from Drops, Chemical Engineering Progress, Vol. 48, 1952.
- [10] Sigloch, H., Technische Fluidmechanik, Herrmann Schroedel Verlag KG, Hannover, 1980.
- [11] Lo, S. M.: Application of the MUSIG model to bubbly flows, AEAT-1096, AEA Technology.
- [12] Saptoadi, D. and Laurien, E.: Simulation of Two-Phase Bubbly Flow using Population Classes. Proc. of 10th Workshop on Two-Phase Flow Predictions. Merseburg-Germany, April 9-12, 2002.

F. Physical Models for CFD

NUMERICAL METHOD FOR MODELING OF TURBULENT TWO-PHASE BUBBLE FLOW ANOMALOUS SHEAR STRESS AND HEAT TRANSFER BEHAVIOR

V. Artemyev and Y. Kornienko

Institute for Physics and Power Engineering (IPPE), State Scientific Center of Russian Federation
Bondarenko Sq. 1, Obninsk, Kaluga Region, RUSSIA, 249033
Fax: +7 095 230-2326, E-mail: artemyev@ippe.obninsk.ru

ABSTRACT

Implicit numerical method for solving 2D and 3D-dimensional fluid mechanics, heat and mass transfer equations is presented. Special attention is paid to modeling of a void profile form effect and forced flow direction effect on the liquid velocity profile and on the wall shear stress behavior. Discretization of governing equations is carried out on the base of monotonous balance neutral difference schemes, which allow keeping some important integral properties of differential operators. A difference equation for pressure is derived from the difference continuity and momentum equations. Implicit iterative procedure is developed to solve non-linear discrete equations. Explicit incomplete factorization method is employed for solving linearized equations. Results of 2D-numerical studies are presented. The comparison of calculation and experimental results has demonstrated their fairly satisfactory coincidence.

1. INTRODUCTION

Investigation of two-phase flow behavior has great practical value in such different fields as petroleum and chemical industry and heat engineering. Comprehensive understanding of important features of two-phase flows in accident conditions is required for their safety issues [1]. The recent experimental investigations (in a number of world scientific centers) of local characteristics of bubble non-equilibrium two-phase flows have revealed the effects of anomalous wall shear stress [2, 3] increase in the conditions with predominantly wall concentration (void peak) of gas (vapor) phase at low velocities of forced flow.

The current one-dimensional models don't take into account the real multi-dimensional flow structures and fail to predict above-mentioned effects properly [4]. Primarily, it was due to neglecting the bubbles disturbing the effect on the momentum transfer as well as to incompleteness of inherent turbulent two-phase flow motion description. Although, the different versions of multidimensional two-fluid models are in progress, but they are far from "industrial" applications.

The 2-dimensional single-fluid variable density model for bubble flow with known void fraction radial profile is presented. Description of the turbulent viscosity is based on the Prandtl-type model with taking into account the wall turbulence and the "bubble" agitation action [5, 6].

Implicit numerical method for solving 2- and 3-dimensional fluid mechanics, heat and mass transfer equations using in the paper is described in [7, 8]. Discretization of governing equations is carried out on the basis of monotonous balance neutral difference schemes, which allow some important integral properties of differential operators to be kept. A difference equation for pressure is derived from the difference continuity and momentum equations. Implicit iterative procedure is developed to solve non-linear discrete equations. Explicit incomplete factorization method is employed for solving linearized equations.

2. MONOTONOUS BALANCE NEUTRAL (MBN) DISCRETIZATION

In general case, fluid dynamics processes are governed by a system of partial differential equations, which involves continuity, momentum, heat transfer equations, state equation and others. In vector form continuity and momentum equations accounting for the Boussinesq hypothesis Eq. (1) may be written as follows:

$$p^{ij} = \rho g^{ij} + 2\mu \varepsilon^{ij} - 2/3 g^{ij} (\mu \operatorname{div} \bar{U} + \rho K), \quad (1)$$

$$\frac{\partial \rho}{\partial t} + \operatorname{div} \rho \bar{U} = 0, \bar{U} = (u^1, u^2, u^3), \quad (2)$$

$$\rho \left(\frac{\partial \bar{U}}{\partial t} + (\bar{U} \nabla) \bar{U} \right) = \rho \bar{F} - \nabla p + 2 \operatorname{div} \mu Y - \frac{2}{3} \nabla (\mu \operatorname{div} \bar{U} + \rho K) \quad (3)$$

where Y is the tensor of the velocity deformation; g^{ij} are components of the Euclidean metric tensor, p is pressure, ε^{ij} - components of the velocity deformation tensor, $\mu = \mu_m + \mu_t$ - coefficient of molecular and turbulence viscosity. Energy equation is written in form

$$\rho \left(\frac{\partial h}{\partial t} + \bar{U} \nabla h \right) = \frac{d p}{d t} + Q_v - \operatorname{div} \bar{Q}, \quad (4)$$

where h is a enthalpy, Q_v - a volumetric heat generation, \bar{Q} - a heat flux.

A derivation of monotonous balance neutral (MBN) difference scheme is based upon joint consideration of continuity equation and transfer equation. For simplicity, consider the following system in a bounded domain Ω

$$\frac{\partial \rho}{\partial t} + \frac{\partial \rho u^1}{\partial q^1} + \frac{\partial \rho u^2}{\partial q^2} + \frac{\partial \rho u^3}{\partial q^3} = 0, \quad (5)$$

$$\rho \frac{\partial \varphi}{\partial t} + \Lambda(\varphi) = f, \quad \text{where } \Lambda(\varphi) \equiv \rho u^i \frac{\partial \varphi}{\partial q^i} - \frac{\partial}{\partial q^i} \eta^{ii} \frac{\partial \varphi}{\partial q^i}. \quad (6)$$

Here substance φ may be a velocity component, an enthalpy, a concentration, etc. Monotonous schemes simulate important property of a fluid flow as a downstream transfer of some disturbance due to a convection motion. A balance (conservation) property is a discrete analogue of the Ostrogradski-Gauss theorem:

$$\frac{\partial}{\partial t} \int_{\Omega} \rho \varphi d\Omega = \int_{\Omega} f d\Omega - \int_{\partial\Omega} \rho \varphi u^i n_i d\partial\Omega + \int_{\partial\Omega} \eta^{ii} \frac{\partial \varphi}{\partial q^i} n_i d\partial\Omega. \quad (7)$$

Neutral behaviour can be formulated in the form of the integral relationship

$$\int_{\Omega} \frac{\rho \varphi^2}{2} d\Omega \Big|_0^{t_0} + \int_0^{t_0} dt \int_{\partial\Omega} \bar{U} \bar{n} \frac{\rho \varphi^2}{2} d\partial\Omega = \int_0^{t_0} dt \int_{\Omega} f \varphi d\Omega + \int_0^{t_0} dt \int_{\partial\Omega} \eta^{ii} \frac{\partial \varphi}{\partial q^i} \varphi d\partial\Omega - \int_0^{t_0} dt \int_{\partial\Omega} \eta^{ii} \frac{\partial \varphi}{\partial q^i} \frac{\partial \varphi}{\partial q^i} d\partial\Omega. \quad (8)$$

Integral relationship Eq. (8) shows null contribution of the terms describing convection transfer and is called neutral property of Λ operator.

Grid points and grid spacings are defined in a regular region Π ($\Omega \in \Pi$) as:

$$q_b \leq q_{1/2}^i < q_{3/2}^i < \dots < q_{k_i}^i < \dots < q_{N_i}^i \leq q_e, \quad k_i = \overline{1, N_i + 1}, i = \overline{1, n};$$

$$q_{k_i}^i = 0.5(q_{k_i+1/2}^i + q_{k_i-1/2}^i), \quad k_i = \overline{1, N_i}, i = \overline{1, n}; \quad (9)$$

$$\Delta q_{k_i-1/2}^i = q_{k_i}^i - q_{k_i-1}^i, \quad k_i = \overline{1, N_i + 1}, i = \overline{1, n} \quad \text{and} \quad \Delta q_{k_i}^i = q_{k_i+1/2}^i - q_{k_i-1/2}^i, \quad k_i = \overline{1, N_i}, i = \overline{1, n}.$$

In the following formulas the shortened notations of grid function are used:

$$\varphi_{k_1, \dots, k_i, \dots, k_n} \equiv \varphi_k, \quad \varphi_{k_1, \dots, k_i \pm 1, \dots, k_n} \equiv \varphi_{k \pm i}, \quad \varphi_{k_1, \dots, k_i \pm 1/2, \dots, k_n} \equiv \varphi_{k \pm i/2}$$

where $k = (k_1, \dots, k_n)$ is a multi- index; $i = (0, \dots, 1, \dots, 0)$ is a multi- index, having unit in the i -position.

Difference continuity equation is written as

$$\xi_k^{m+1} \equiv \frac{\rho_k^{m+1} - \rho_k^m}{\Delta t_m} + \sum_{j=1}^n \frac{(\rho u^j)_{k+j/2}^{m+1} - (\rho u^j)_{k-j/2}^{m+1}}{h_{k_j}^j} = 0, \quad (10)$$

m - a time step number, Δt_m - a spacing of time discretization. The Eq. (10) is not directly included in the implicit iterative procedure but is a base for derivation of pressure difference equation.

MBN approximation of Eq. (6) has the following form (see for detail the paper [7]):

$$\prod_{\beta=1}^n \Delta q_{k_\beta + \delta^{\beta i/2}}^\beta \rho_{k+i/2}^m \frac{\varphi_{k+i/2}^{m+1} - \varphi_{k+i/2}^m}{\Delta t_m} + A(\varphi_{k+i/2}) = \prod_{\beta=1}^n \Delta q_{k_\beta + \delta^{\beta i/2}}^\beta f_{k+i/2}^{m+1}, \quad (11)$$

where

$$A(\varphi_{k+i/2}) = \prod_{\beta=1}^n \Delta q_{k_\beta + \delta^{\beta i/2}}^\beta \Lambda_h(\varphi_{k+i/2}^{m+1}), \quad (12)$$

$$A(\varphi_{k+i/2}) = c_{k+i/2} \varphi_{k+i/2} - \sum_{j=1}^n a_{k+i/2}^j \varphi_{k-j+i/2} + b_{k+i/2}^j \varphi_{k+j+i/2}, \quad (13)$$

$$a_{k+i/2}^j = (0.5 \rho_{k-j/2+i/2} u_{k-j/2+i/2}^j + (1 + v_{k-j/2+i/2}^j) \eta_{k-j/2+i/2}^j / \Delta q_{k_j + \delta^{j i/2-1/2}}^j) \prod_{\beta \neq j}^n h_{k_\beta + \delta^{\beta i/2}}^\beta, \quad (14)$$

$$b_{k+i/2}^j = (-0.5 \rho_{k+j/2+i/2} u_{k+j/2+i/2}^j + (1 + v_{k+j/2+i/2}^j) \eta_{k+j/2+i/2}^j / \Delta q_{k_j + \delta^{j i/2+1/2}}^j) \prod_{\beta \neq j}^n h_{k_\beta + \delta^{\beta i/2}}^\beta, \quad (15)$$

$$c_{k+i/2}^j = \sum_{j=1}^n a_{k+i/2}^j + b_{k+i/2}^j, \quad (16)$$

$$v_{k+j/2+i/2}^j = \alpha_{k+j/2+i/2} \text{cth}(\alpha_{k+j/2+i/2}) - 1, \quad (17)$$

$$\alpha_{k+j/2k+i/2} = u_{k+j/2+i/2}^j \Delta q_{k_j+\delta^{j/2+1/2}}^j / 2\eta_{k+j/2k+i/2} . \quad (18)$$

In practical calculations function $(\alpha \text{cth} \alpha - 1)$ may be replaced with easily computed expression, $\alpha \text{cth} \alpha - 1 \approx |\alpha|^3 / (1 + |\alpha| + |\alpha|^2)$.

3. IMPLICIT NUMERICAL PROCEDURE

Consider Eq. (6) when φ is a component of velocity:

$$\rho \left(\frac{\partial u^i}{\partial t} + u^j \frac{\partial u^i}{\partial q^j} \right) - \frac{\partial}{\partial q^j} \eta^{jj} \frac{\partial u^i}{\partial q^j} = - \frac{\partial p}{\partial q^i} + f^i . \quad (19)$$

A pressure discrete equation is obtained using momentum difference equations in the form (11)-(18) and Eq. (10). Its general form can be presented as

$$\left(\prod_{\beta=1}^n \Delta q_{k\beta}^\beta \right) \frac{\rho_k^{m+1} - \rho_k^m}{\Delta t_m} + P_h(p_k) = \overline{f_k} , \quad (20)$$

$$P_h(p_k) = \bar{c}_k p_k - \sum_{j=1}^n \bar{a}_k^j p_{k-j} + \bar{b}_k^j p_{k+j} . \quad (21)$$

Pressure, temperature, concentration are computed in the centres of grid cells, components of velocity vector - in the centres of faces. Both the MBN- scheme and a displacement of coordinates of a grid functions enable to obtain physically realistic fields of computed values.

Implicit numerical procedure is developed for solving non-linear system of difference equations (11), (20). Index "L" denotes a number of iterations or a number of stabilization steps. Linearizing

is carried out in such a way that operator A becomes linear relatively to $u_{k+i/2}^{i, m+1, L+1}$, when $u_{k+i/2}^{i, m+1, L}$ is known.

Implicit numerical procedure is written as follows ($1 \leq i \leq n$)

$$\prod_{\beta=1}^n \Delta q_{k\beta}^\beta \delta^{\beta i/2} \rho_{k+i/2}^m \left(\frac{u_{k+i/2}^{i, m+1, L+1} - u_{k+i/2}^{i, m+1, L}}{\tau_L} + \rho_{k+i/2}^m \frac{u_{k+i/2}^{i, m+1, L+1} - u_{k+i/2}^{i, m+1, L}}{\Delta t_m} \right) + A u_{k+i/2}^{i, m+1, L+1} =$$

$$= - \frac{p_{k+i}^{m+1, L+1} - p_k^{m+1, L+1}}{h_{k_i}^i} + f_{k+i/2}^{m+1, L} ,$$

$$\prod_{\beta=1}^n \Delta q_{k\beta}^\beta \left(\frac{p_k^{m+1, L+1} - p_k^{m+1, L}}{\tau_L} + \frac{\rho_k^{m+1, L+1} - \rho_k^m}{\Delta t_m} \right) + P_h p_k^{L+1} = \overline{f_k} ,$$

where τ_L is a step of stabilization. ($1 \leq i \leq n$). The operator P_h is self-adjoint because $\bar{a}_{k+j}^j = \bar{b}_k^j$.

Implicit numerical procedure for prediction of pressure and velocity fields involves the following stages of calculations. Using u^{j^m} , $u^{j^{m+1, L}}$ $1 \leq j \leq n$ from the previous iteration we calculate coefficients of difference equations. Employing incomplete factorization method (see next section) with Chebyshev acceleration we solve pressure equation and using ordinary variant of the method

we calculate velocity components. Iterations on the current time layer are stopped when a given preset accuracy ζ of fulfillment of difference continuity equation is reached:

$$\max_{\Omega_h} \left| \zeta_k^{m+1, L+1} \right| < \zeta . \quad (22)$$

Relationship (22) is the main criterion of convergence. Implicit numerical method allows us to increase stability and to significantly reduce computational expenditures.

4. INCOMPLETE FACTORIZATION METHOD

Successful practical realization of the implicit numerical algorithm depends on a method for solving linear difference equations, first of all ill-conditioned pressure equation. Taking into account self-adjoint property of pressure equation it is suggested to employ incomplete factorization method with Chebyshev acceleration. The subject method is related to a class of explicit incomplete factorization methods developed by Buleev [9]. The method for solving a system

$$A \varphi_k = f_k$$

can be written as follows

$$\Gamma^{-1} B_1 B_2 \varphi_k^m \equiv B \varphi_k^m = f_k + (S + T) \varphi_k^{m-1} .$$

Theoretical analysis [7] has shown that if A is a self-adjoint operator then operator B is also self-adjoint and there are constants $0 < \sigma_0 \leq \sigma_1$ that $(A \varphi, \varphi) / (B \varphi, \varphi) \in [\sigma_0, \sigma_1]$ for $\forall \varphi \neq 0$. Constants σ_0, σ_1 are the bounds of the operator $B^{-1} A$ in the energy space with scalar product $(A \varphi, \varphi)$ or $(B \varphi, \varphi)$; so operators A and B are called energy or spectrum equivalent. Knowledge of estimates σ_0, σ_1 allows us to employ Chebyshev acceleration and to use the following iterative procedure

$$\Gamma^{-1} B_1 B_2 (\varphi^m - \varphi^{m-1}) = \tau_m (F - A \varphi^{m-1}) ,$$

where $\{\tau_m\}$ is the Chebyshev sequence of parameters. Successful employment of Chebyshev acceleration is possible if spectral bounds are known with sufficient precision, that is why a certain variant of the explicit incomplete factorization method is of great practical interest. In this variant of the method constant $\sigma_0 = 1$ is known exactly and the upper bound σ_1 can be easily calculated. This technique enables to adapt Chebyshev acceleration to the real value of spectral bound and essentially increases the efficiency of the method. The use of the incomplete factorization method with Chebyshev acceleration for solving the pressure equation in the implicit method gives good results.

5. MATHEMATICAL MODEL FOR TWO COMPONENT (AIR-WATER) FLUID FLOW

Developed implicit numerical method has been realized as **FLUID2D** code and applied for numerical modelling of two-phase flows, experimentally investigated in the papers [2, 3]. The installation scheme is represented in Fig. 1. Detailed experimental data (void fraction profiles, velocity profiles, shear stresses) have been obtained for upward and downward isothermal flows in the wide range of regime parameters. The purpose of numerical investigations was to obtain velocity, pressure fields, and shear stresses using experimental radial void fraction profiles.

Two-phase flow density is calculated as $\rho=(1-\alpha)\rho_f + \alpha\rho_g$, where α - void fraction, ρ_f and ρ_g - density of fluid and gas correspondingly. For the round pipe of radius R in the $(r-z)$ -geometry we have the following component and coordinate form of Eq. (3)

$$\rho\left(\frac{\partial u_r}{\partial t} + u_r \frac{\partial u_r}{\partial r} + u_z \frac{\partial u_r}{\partial z}\right) = -\frac{\partial p_d}{\partial r} + \frac{1}{r} \frac{\partial}{\partial r} \left(\frac{4}{3} \mu r \frac{\partial u_r}{\partial r} + \frac{\partial}{\partial z} \mu \frac{\partial u_r}{\partial z} + \frac{\partial}{\partial z} \mu \frac{\partial u_z}{\partial r} \right) - \frac{2}{3} \frac{\partial}{\partial r} \mu \frac{\partial u_z}{\partial z} - \frac{4}{3} \mu \frac{u_r}{r^2} \left(1 + 0.5r \frac{\partial \mu}{\partial r} \right), \quad (23)$$

$$\rho\left(\frac{\partial u_z}{\partial t} + u_r \frac{\partial u_z}{\partial r} + u_z \frac{\partial u_z}{\partial z}\right) = -(\rho - \bar{\rho})g - \frac{\partial p_d}{\partial z} + \frac{1}{r} \frac{\partial}{\partial r} \left(\mu r \frac{\partial u_z}{\partial z} + \frac{\partial}{\partial z} \frac{4}{3} \mu \frac{\partial u_z}{\partial z} \right) + \frac{1}{r} \frac{\partial}{\partial r} \mu r \frac{\partial u_r}{\partial z} - \frac{2}{3} \frac{\partial}{\partial z} \frac{\mu}{r} \frac{\partial r u_r}{\partial r}, \quad (24)$$

where p_d - dynamic pressure, $\bar{\rho}$ - cross section average density. Boundary conditions are set as follows: at the symmetry axis $u_r = 0$, $\partial u_z / \partial r = 0$; at the wall $r=R$: $\vec{U}=0$; at the inlet $u_z = U_{in}$, $\partial u_r / \partial z = 0$; at the outlet $u_r = 0$, $\partial u_z / \partial z = 0$.

As in paper [5] we suppose that turbulent viscosity (μ_t) is subdivided into the two components $\mu_t = \mu_1 + \mu_2$, one μ_1 due to inherent liquid turbulence independent of relative motion of bubbles and the other μ_2 due to the additional turbulence caused by bubble agitation. For the μ_1 we used the well-known Reichardt relationship:

$$\mu_1 = \rho_f (1 - \alpha) \mu_f \begin{cases} 0.4 (y^+ - 11 \operatorname{th}(y^+ / 11)), & y^+ \leq 50, \\ 0.133 y^+ (0.5 + (r/R)^2)(1 + r/R), & y^+ > 50, \end{cases} \quad (25)$$

where $y=R-r$, $y^+ = y u_\tau / \nu_m$ - dimensionless coordinate, $u_\tau = \sqrt{\tau_w / \rho}$ - friction velocity; $\tau_w = \mu_m \partial v_z / \partial y$ - wall shear stress; and $u^+ = v_z / u_\tau$ - friction scale velocity.

The additional turbulent viscosity due to relative motion of gas bubbles we used the following relationship:

$$\mu_2 = A_1 \rho_f (1 - \alpha) (1 - \exp(-y^+ / A_2))^2 \alpha u_b d_b, \quad (26)$$

where A_1 - is the value of the order mixing length constant, and A_2 - is the Van Driest type constant.

6. DISCUSSION OF NUMERICAL PREDICTIONS AND COMPARISON WITH EXPERIMENTAL DATA

The grid was $N_r \times N_z = 60 \times 200$. Computational grids are irregular, which results in good precision for the description of thin boundary layers, and calculations can be performed up to solid bounds. For correct shear stress description we used high irregular grid with logarithmic compressibility to the wall, so that the first step near the wall was equal 10^{-5} m.

The input data for the **FLUID2D** code were experimental void fraction profiles and bubble diameters. The bubble drift velocity was equal 0.25 m/s for all of the variants.

Testing of **FLUID2D** code for the single-phase flow is presented in the Figs. 2 and 3. We had good agreement between calculation and experimental results for velocity profiles and for average and local friction factors for different Reynolds number at the inlet.

Principal flow parameters corresponding to each numerical experiment are listed in Table I. It presents the experimental and calculation data for the wall shear stresses and relative wall shear stresses, by which we mean the two-phase wall shear stresses divided by the single-phase wall shear stresses defined by Blasius relationship.

The best agreement between the calculation and experimental data provide constants: $A_1=0.6$, $A_2=32$. The velocity profiles (U – at the outlet cross-section of the pipe (U_c – at the pipe axis)) and friction factors for two-phase flow are presented in Fig. 2 - 6.

The experimental data and calculation results show appreciable enhancement of the wall shear stresses for two-phase up-ward flow and less appreciable enhancement for downward flow. On the whole a rather satisfactory agreement is observed between experimental data and calculations both for velocity profiles and for shear stresses, see Table I.

Table I. Flow parameters for the experiments [2, 3] and calculation results.

№	Up/ Down flow	β	U_f m/s	τ_{Bl} N/m ²	τ_{exp} N/m ²	τ_w^{cal} N/m ²	τ_{exp} / τ_{Bl}	τ_w^{cal} / τ_{Bl}	U_c^{exp} m/s	U_c^{cal} m/s
1	U	0.15	0.221	0.187	1.65	0.78	8.81	4.19	0.29	0.27
2	U	0.25	0.221	0.221	1.54	0.69	6.97	3.12	0.30	0.29
3	U	0.068	0.441	0.617	3.40	3.24	5.51	5.25	0.47	0.48
4	U	0.087	0.442	0.622	3.56	2.30	5.72	3.70	0.52	0.47
5	U	0.15	0.442	0.681	3.36- 4.00	2.54	4.85-5.87	3.74	0.53	0.53
6	U	0.20	0.442	0.733	2.93- 3.75	1.23	4.00-5.12	1.68	0.67	0.49
7	U	0.118	0.785	1.803	7.70- 8.00	7.11	4.27-4.44	3.95	0.90	0.87
8	U	0.127	0.785	1.846	7.50- 8.20	5.79	4.05-4.43	3.14	0.95	0.89
9	U	0.076	1.1	3.082	8.30- 9.20	9.21	2.69-2.99	2.99	1.28	1.27
10	U	0.091	1.17	3.35	9.20	7.79	2.75	2.32	1.35	1.28
11	D	0.084	1	3.20	3.97	4.81	1.24	1.49	-	-
12	D	0.039	1	2.95	3.24	3.53	1.10	1.20	-	-

Precise velocity profile predictions are very important for thermal field for two-component bubble flow. Comparison of fluid temperature profiles obtained by this method show good coincidence with experimental data by Sekoguchi K. et al [10] for different void profiles, see Fig. 7.

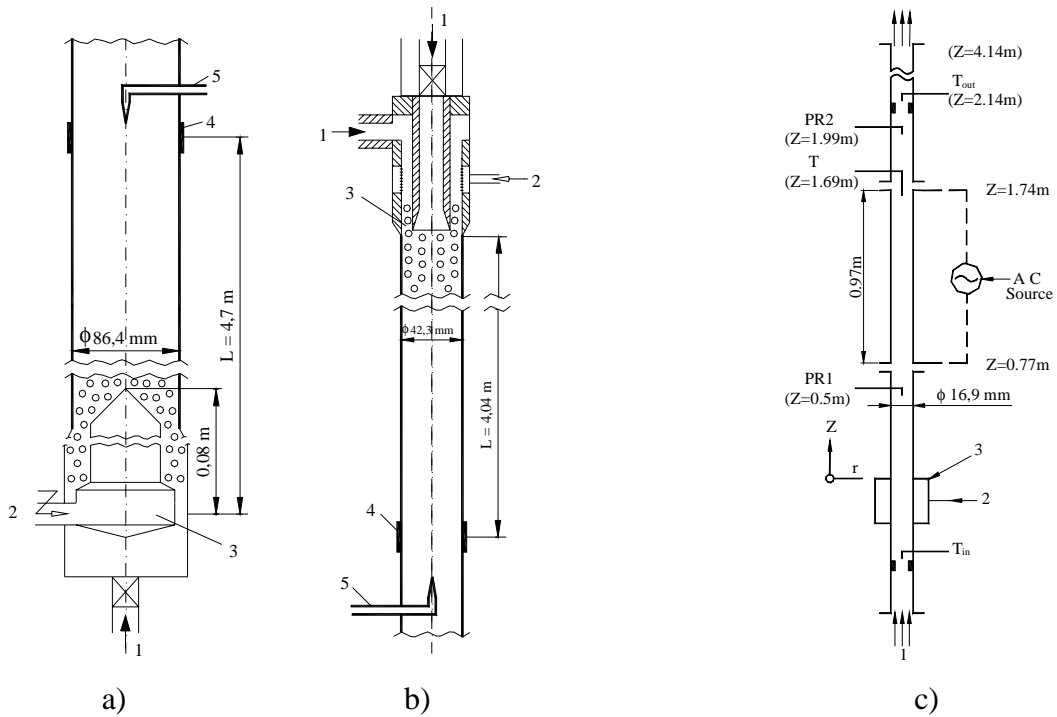


Figure 1: Schematics of the experimental facilities. a) isothermic upward flow [2], b) isothermic downward flow [3], c) test section with heat input [10]. 1 – water input; 2 – air input; 3 – mixer; 4 – wall shear stress measurements; 5 – local velocity and void fraction measurements; PR1, PR2 - local void fraction, T- temperature measurements.

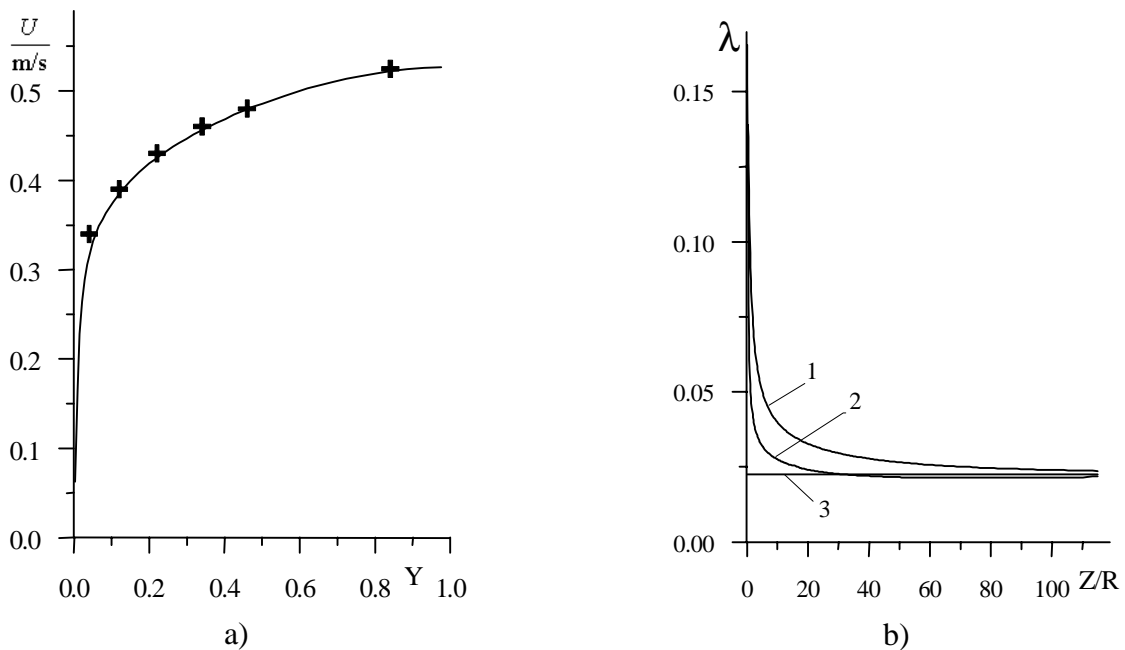


Figure 2: Comparison of the calculated liquid axial velocity profile and experimental data [2]- a); and friction factor- b) for single-phase flow $U=0.442$ m/s, $Re=38188.8$, a) $+$ - experimental data; b) 1 – average friction factor, 2 – local friction factor, 3 - λ_{Bla} -Blasius friction factor, $\lambda_{Bla}=0.0226$.

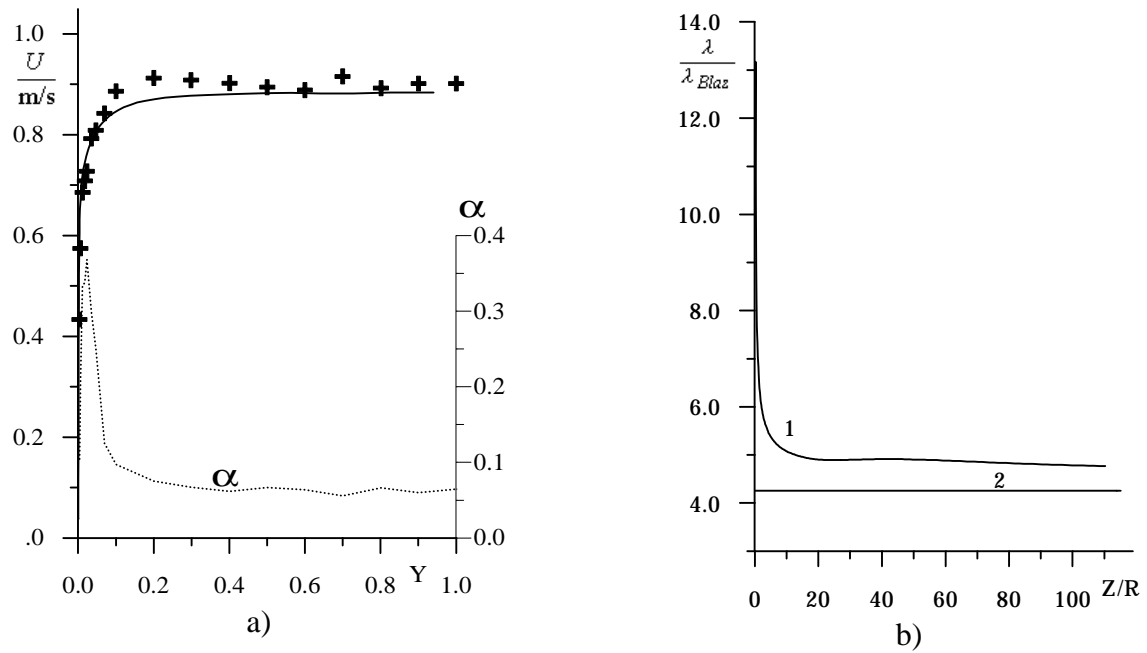


Figure 3: Comparison of the calculated liquid axial velocity profile and experimental data [2]- a); and relative friction factor-b) for two-phase up-ward flow $\beta=0.118$, $U_f = 0.785$ m/s a) $+$ - experimental data; - - - void fraction; b) 1 – calculation, 2- experiment.

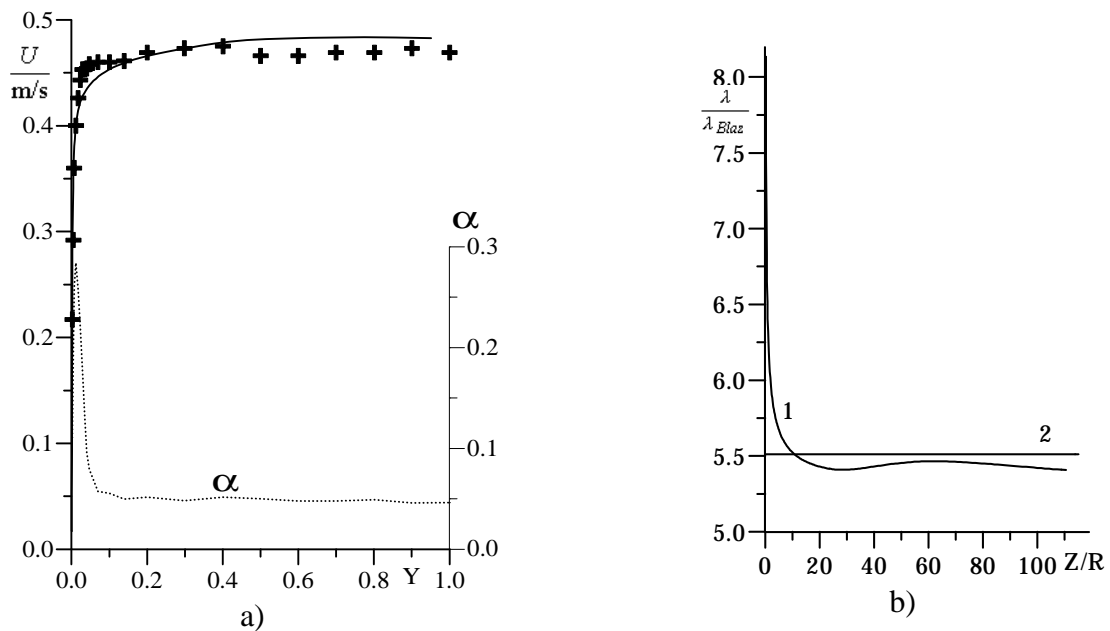


Figure 4: Comparison of the calculated liquid axial velocity profile and experimental data [2]- a); and relative friction factor-b) for two-phase up-ward flow $\beta=0.0685$, $U_f = 0.44$ m/s a) $+$ - experimental data; - - - void fraction; b) 1 – calculation, 2- experiment.

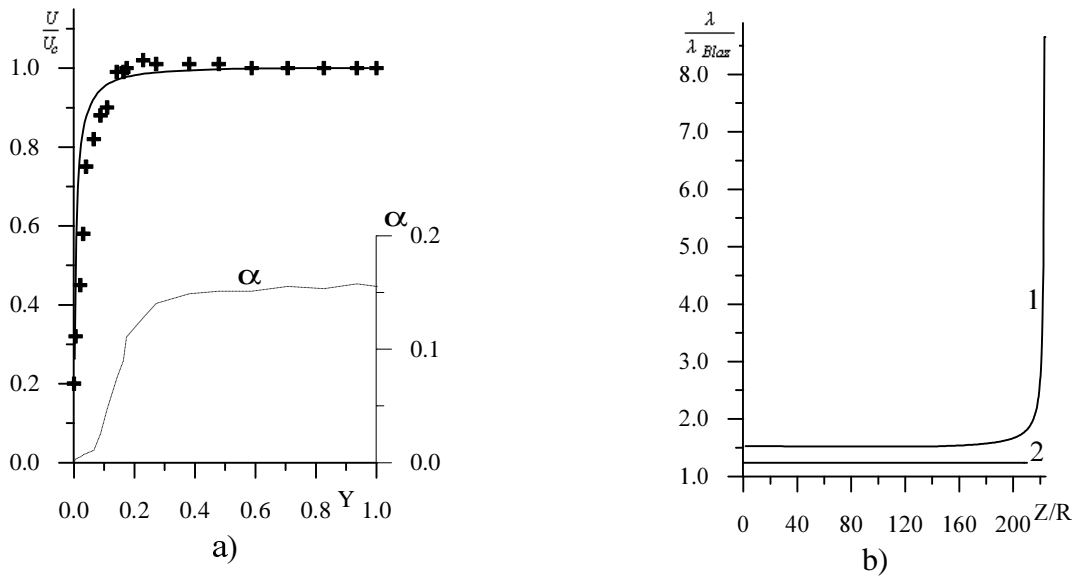


Figure 5: Comparison of the calculated liquid axial velocity profile and experimental data [3]- a); and relative friction factor-b) for two-phase down-ward flow $\beta=0.084$, $U_f = 1$ m/s, a) $+$ - experimental data; - - - void fraction; b) 1 – calculation, 2- experiment.

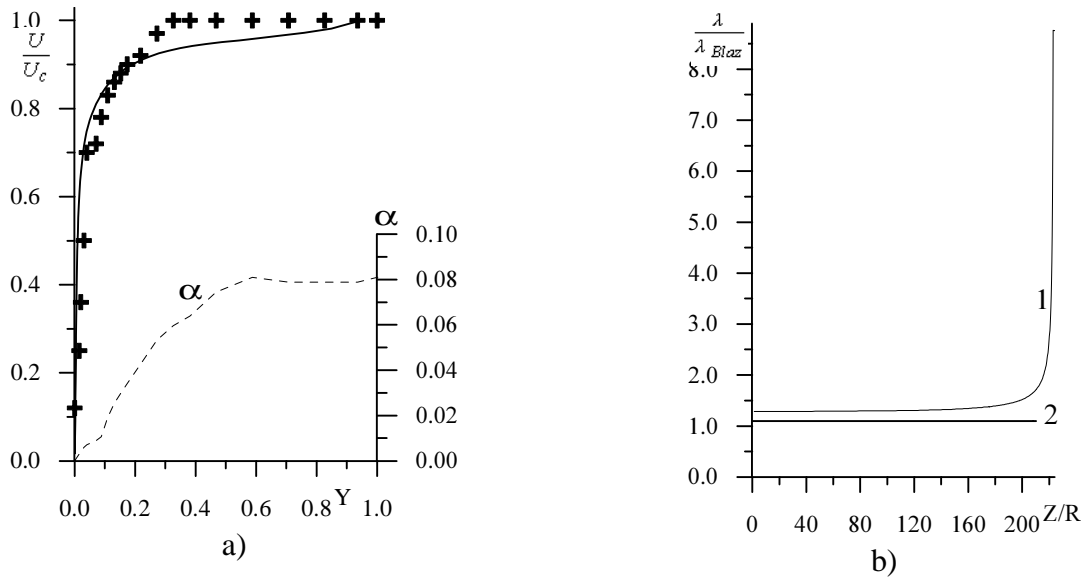


Figure 6: Comparison of the calculated liquid axial velocity profile and experimental data [3]- a); and relative friction factor-b) for two-phase down-ward flow $\beta=0.039$, $U_f = 1$ m/s a) $+$ - experimental data; - - - void fraction; b) 1 – calculation, 2- experiment.

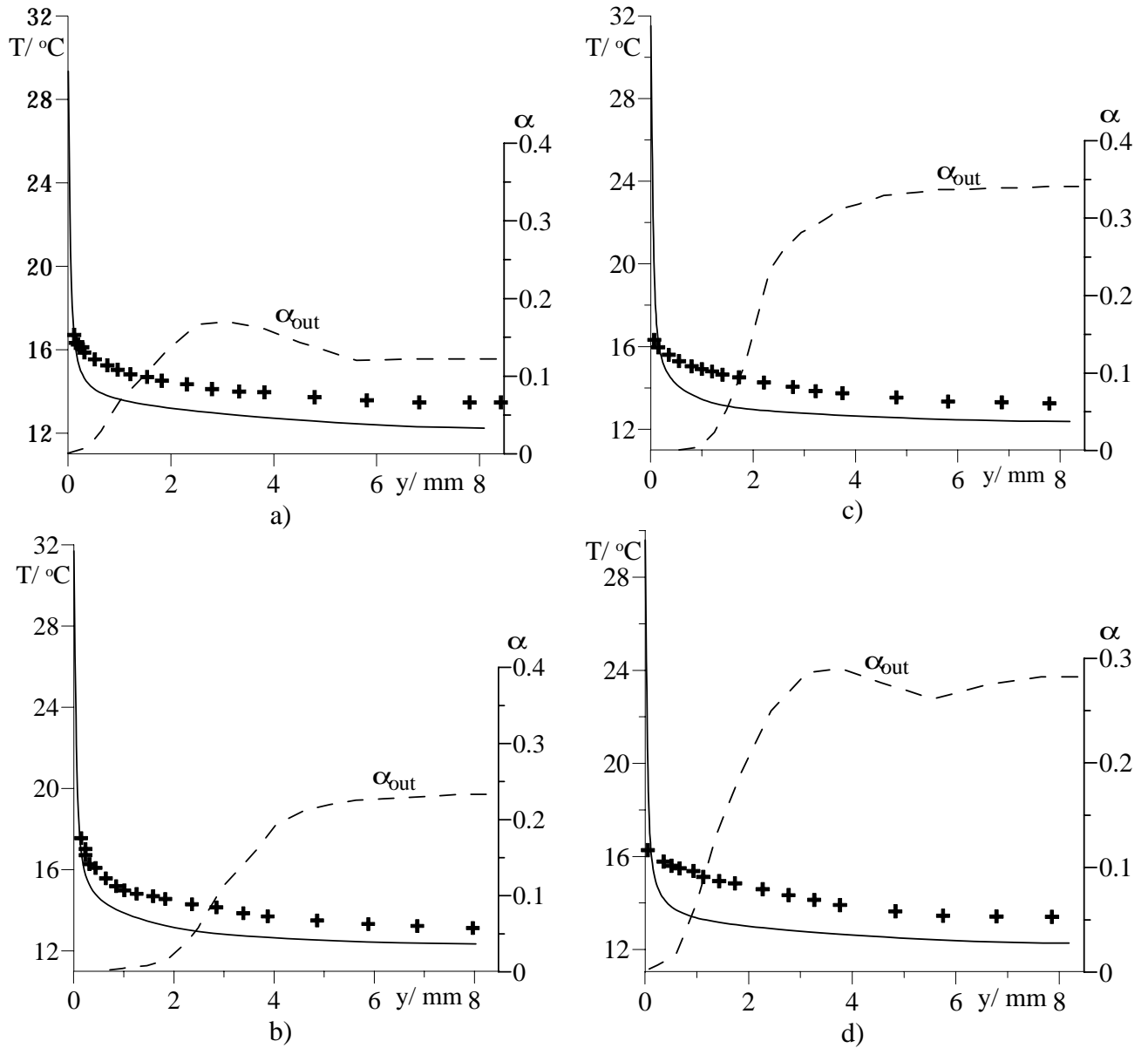


Figure 7: Liquid temperature profiles (corresponding flow parameters are listed in Table II). + - experimental data [10]; — - calculations by present method.

Table II. Flow parameters for the runs shown in Fig. 7 [10].

Case	U_f m/s	U_g m/s	$\bar{\alpha}$	d_b mm	q_w kW/m ²	$T_{w,exp}$ °C	T_{fb} °C
a	0.93	0.13	0.112	2.4	117	32.4	13.6
b	0.93	0.13	0.103	4.0	118	34.6	13.6
c	0.93	0.33	0.191	2.8	119	29.2	13.7
d	0.93	0.32	0.188	4.2	120	31.4	13.8

7. CONCLUSIONS

The general Reynolds-type momentum model which forms the basis for **FLUID2D** code is applied to predict the liquid velocity and temperature profiles and shear stress behaviour for turbulent up-ward and down-ward two-phase flow with known “saddle”-shape void fraction profile and Sato et al [5] hypothesis for gas-liquid phase turbulence. The numerical method makes it possible to conduct calculations up to the rigid wall including laminar layer and to obtain correct values of shear stresses in the frame of the mathematical model considered. Numerical results are in satisfactory agreement with experimental data in a wide range of regime conditions, including anomalous wall shear stress enhancement. This approach may have considerable potentials in improving the models of turbulence and in numerical predictions of specific two-phase flow problems.

NOMENCLATURE

\vec{F}	Body force vector	α	Void fraction
g	Gravitation acceleration	β	Volumetric void fraction
g^{ij}	Components of metrical tensor	ε	Dissipation rate
h	Enthalpy	ε^{ij}	Components of velocity deformation tensor
K	Turbulent kinetic energy	λ	Friction factor
p	Pressure	μ	Dynamic viscosity
p^{ki}	Components of pressure stress tensor	ρ	Density
r	Radial coordinate	τ	Shear stresses
Q	Heat flux		Subscript and Superscript
R	Radius	Bl	By Blasius
T	Temperature	cal	Calculation
t	Time	g	Gas (vapour)
U_{in}	Inlet velocity	f	Fluid
u_τ	Friction velocity	f_b	Fluid bulk
\vec{U}	Velocity vector	exp	Experimental
u	Velocity	t	Turbulent
$y=R-r$	Coordinate from the wall	w	On the wall
Y	Velocity deformation tensor	r	Radial
z	Axial coordinate	z	Axial

REFERENCES

- [1] Delhaye, J. M., Giot, M., Riethmuller, M. L., Thermohydraulics of two-phase systems for industrial design and nuclear engineering, Hemisphere Publ. Corp., New York, 1981.
- [2] Nakoryakov, V. E., et al, Local Characteristics of Upward Gas-Liquid Flows, Int. J. Multiphase Flow, 7, pp. 63-81, 1981.
- [3] Kashinsky, O. N., & Randin, V. V., Downward bubbly gas-liquid flow in a vertical pipe, Int. J. Multiphase Flow, 25, pp. 109-138, 1999.
- [4] Kornienko, Yu. N., Effect of Saddle-Shape Transversal Void Fraction on Low Reynolds Number Wall Friction and Heat Transfer in Bubble Flows, 5th Int. Conf. on Nuclear Engineering (ICONE-5), Nice, France, Paper 2433, Trac 1, May 1997.

- [5] Sato, Y., & Sadatomi, M., & Sekoguchi, K., Momentum and Heat Transfer in Two-Phase Bubble Flow-I Theory, *Int. J. Multiphase Flow*, 7, pp 167-177, 1981.
- [6] Sato, Y., & Sadatomi, M., & Sekoguchi, K., Momentum and Heat Transfer in Two-Phase Bubble Flow-II A Comparison between Experimental Data and Theoretical Calculations, *Int. J. Multiphase Flow*, 7, pp. 179-190, 1981.
- [7] Artemyev, V. K., Development of Numerical Methods for Solving Fluid Dynamics Problems, Thesis, Institute of Physics and Power Engineering, Obninsk, Russia, 1997.
- [8] Artemyev, V. K., Implicit Numerical Method for Solving of Fluid Mechanics, Heat and Mass Transfer Equations, 11th Int. Heat Transfer Conf., Kyongju, Korea, 4, pp. 307-312, 1998.
- [9] Buleev, N. I., A Numerical Method for Solution of Two-Dimensional and Three-Dimensional Equations of Diffusion, *Mat. Sb.*, 51, N 2, pp. 227-238, 1960.
- [10] Sekoguchi, K., Sato, Y., Tanaka, O., Forced convective heat transfer in vertical air-water bubble flow, *Bulletin of the JSME*, 23, N 184, pp. 1625-1631, 1980.

Single-phase and Modified Turbulence Models for Simulation of Unsteady Cavitating Flows

W. Basuki, G.H. Schnerr, W. Yuan
Universität Karlsruhe (TH)
Kaiserstraße 12 D-76128 Karlsruhe GERMANY
email: guenter.schnerr@mach.uni.karlsruhe.de

ABSTRACT

The aim of this research is to provide a physical complete and numerical efficient simulation method to predict developed cavitation in hydrodynamic turbomachinery as well as in micro fluid dynamic applications, e.g. in high pressure injection nozzles of combustion engines. Cavitating two-phase flows are always very unstable, highly unsteady, 3-D and turbulent. To understand cavitation dynamics and its interaction with viscous effects like boundary layers and separation, we introduce the single-phase turbulence $k - \omega$ model of Wilcox [1] without modifications with respect to dispersed structures of bubbly liquids, which overestimates viscous effects in the transitional regime between the vapor and liquid phase and tends to suppress typical cavitation instabilities. Consequently our further approach consists of modifications of the single-phase Wilcox model to account for the strong nonlinear variation of the turbulent viscosity μ_t , depending on the local void fraction α . The key issue of all numerical methods for simulation of cavitating flows is the treatment of the sudden density change of the fluid, in cold water up to 40.000:1, embedded in a global incompressible liquid flow. Here the two-phase fluid is modeled as dispersed mixture of an incompressible liquid and tiny vapor bubbles which grow or collapse, accordingly to the local static pressure and their convective transport. Therefore, the standard VOF method for capturing distinct interfaces without phase transition, e.g. free surface flow or single bubbles, is extended to include phase transition of dispersed mixtures. For simulation of bubble dynamics we apply the Rayleigh equation, which is completed by an energy balance to account for thermal effects, if hot water or if technical fluids others than water, e.g. refrigerants, with high vapor densities are considered. By using our CFD tool CAVKA we present examples of cavitating flow around hydrofoils and through single hole injection nozzles. Comparing Euler and single-phase turbulence simulations, results based on the inviscid approach are closer to experiments, which indicates an interesting option to reduce computational time.

1 Introduction

Cavitation occurs in flows of liquids when the local static pressure falls below the vapor pressure, resulting in regions of vapor. It can occur in a broad variety of technical devices, where it usually degrades their performance, accompanied with intense erosion of structural components and very loud noise, see e.g. the review by Arndt [2]. It is interesting to note that cavitation can also be found in nature, e.g. snapping shrimps produce a loud snapping sound by an extremely fast closure of their snappers, which produce a high speed collapsing jet to kill prey animals ([3]).

Progress in understanding of cavitation phenomena is of great importance and interest for industry. In the past, several models were developed to simulate cavitation ([4], [5]), which do in general not model the complicated and highly transient bubble growth and collapse. This process is responsible for the cavitation damage and therefore, the location where the bubbles collapse is of great interest and the need for a cavitation model rises that also includes effects based on bubble dynamics. Since hydrofoils make up so many different types of machines - pumps, turbines, propellers - the study of as how cavitation affects hydrofoil performance is of special interest.

The type of cavitation most frequently observed at hydrofoils with a well-rounded leading edge is the so-called traveling bubble cavitation. From experiments it can be seen that for such foils the cavitation region is made up of individual bubbles rather than by a large vapor-filled cavity. These bubbles originate from small cavitation nuclei (particles, air bubbles), which are already existing in the bulk flow. The nuclei reach the low pressure region (suction peak) and grow to vapor bubbles while they are convected downstream, supposed the static pressure is sufficiently below the vapor pressure. Then, the bubbles are swept in the region of higher pressure and finally collapse. Many experimental studies, see e.g. [6], [7], [8], point out the importance of the nuclei content of the liquid for the inception and development of cavitation. The nuclei content affects the tensile strength of the liquid and therefore is responsible if or if not cavitation occurs at given conditions.

At the beginning clouds form a dispersed sheet attached to the solid surface, which seems to be steady at first sight. Due to the entrainment of bubbles into the wake the sheet becomes unstable, causing large parts of the cavity to break off. The resulting dynamics forms by interaction between the dynamics of individual bubbles and the motion of the liquid fluid. During collapse single bubbles near solid walls create extremely high pressure pulses which seem to be responsible for erosion and destruction, and global (hydrodynamic) pressure waves, formed during the collapse of bubble clouds ([9]). The aim of the inviscid approach is to improve understanding of the global pressure dynamics, which is not controlled by the viscosity of the fluid.

We reproduce recently performed experiments of Keller and Arndt (Technical University Munich and University of Michigan) [7]. Despite the fact that the present model is not yet complete, comparison of experiment and inviscid flow simulations shows surprisingly good agreement of the global structure of the unsteady cavitation dynamics around an inclined NACA 0015 hydrofoil. The time dependent resolution of the simulation of the unsteady cavitation dynamics allows interesting insight and analysis of the interaction of the surrounding unsteady hydrodynamic pressure field and the dynamics of bubble clouds, and of the strong impact of individual boundary conditions on strength and extension of cavitation regimes.

Due to very high inlet pressures of typically up to 1000-2000 bar in injection nozzles of Diesel engines cavitation cannot be avoided. In addition, the pressure upstream and behind the nozzle fluctuates with high frequencies of the order of 1-100 kHz. From experiments it is well known that spray characteristics changes, if cavitation is present [10]. Advanced partial evaporation and sudden collapse of bubbles within the jet indicate an interesting potential to improve the spray quality by optimization of the interaction of cavitation and the jet flow. Because of the limited access to the micro scale problem of $100\mu m - 1mm$ by experiments, simulations are most important. Therefore, in the second chapter we show systematic tests and parameter variations for identification of the main model parameters and their sensitivity in the operating regime.

It is well known, that single-phase turbulence models tend to suppress natural instabilities of partial cavitating flows with their typical re-entry jets and bubble cloud separation. Several empirical modifications are proposed in the literature ([1],[11], [12]). Here we present first results of modifications of the turbulent viscosity μ_t , dependent on the local vapor content α . These investigations are certainly not yet complete. However, the modified turbulence model provides better agreement with experiments, as compared with single-phase turbulence models.

2 Modeling

2.1 Physical modeling

Our cavitation model bases on the following physical assumptions: Cavitation is modeled as the growth and collapse process of vapor bubbles. The bubbles originate from nuclei, which already exist in the bulk flow and grow or collapse depending on the surrounding conditions (pressure and temperature). It is assumed, that the slip between the vapor bubbles and the liquid can be neglected. The growth of vapor bubbles due to pseudo or gaseous cavitation is not yet taken into account. Cavitation is assumed to be dominated by heterogeneous nucleation, hence a homogeneous nucleation

theory, known e.g. from modeling of condensing flows is not employed. The interested reader may refer to see [13].

The perhaps most important feature of the model is, that it resolves the interior dispersed structure of bubble clouds. From the numerical point of view, the cavitation model simulates the production (bubble growth), destruction (bubble collapse) and convection of the vapor phase. But due to the underlying modeling of the nuclei content, it is possible to reconstruct from the vapor content of the computational cell, the number of bubbles that are currently in the computational cell and their radii. Therefore, a certain value of the vapor fraction α directly corresponds to a certain bubble radius R . Radius and vapor fraction are related by Eq. 5.

2.2 Numerical modeling

The formation of cavitation leads to a two-phase flow with phase transition. Entering or leaving the cavitation region, the mixture density varies from that of the pure liquid to a much smaller value or vice versa.

To overcome problems due to a discontinuous density distribution, a special numerical treatment is required. Front tracking methods (level set, marker particles, surface-fitting) were not found to be suitable, since they require the presence of distinct interfaces to be tracked. In this context, the interface is simply the bubble wall, that separates the vapor from the liquid phase. Because of the huge number of bubbles (typically 1000 per cm^3 liquid) and consequently a huge number of interfaces to be tracked, application of interface tracking methods would result in enormous CPU time and storage requirements. Instead, we prefer the usage of a front capturing method, namely the Volume-of-Fluid technique, proposed by Nichols & Hirt [14]. For a detailed description of our CFD tool CAVKA see [15], [25], [27].

2.3 Modified Volume-of-Fluid method for simulation of developed cavitation

The Volume-of-Fluid (VOF) method tracks the motion of a certain fluid volume through the computational domain, irrespective whether the volume contains pure liquid, pure vapor or a mixture of vapor bubbles and liquid. Within the scope of the VOF approach, the two-phase flow is treated as a homogeneous mixture and hence only one set of equations is used for description. The VOF method requires in addition to the continuity and the momentum equations (which are coupled by a SIMPLE algorithm) the solution of a transport equation for the cell vapor fraction α , which is defined as the ratio of the vapor (gas) volume to the cell volume, see Eq. 5:

$$\frac{\partial \alpha}{\partial t} + \frac{\partial(\alpha u)}{\partial x} + \frac{\partial(\alpha v)}{\partial y} = 0, \quad (1)$$

where u and v are Cartesian components of the velocity vector \mathbf{u} . The equations of motion are closed with the constitutive relations for the density and dynamic viscosity:

$$\varrho = \alpha \varrho_v + (1 - \alpha) \varrho_l, \quad (2)$$

$$\mu = \alpha \mu_v + (1 - \alpha) \mu_l. \quad (3)$$

Here the subscripts l and v stand for the properties of pure liquid and pure vapor which are assumed to be constant. The equations derived are general and describe the motion of two fluids with an interface between them. A more detailed discussion of the governing equations without phase transition can be found for example in the work of Ubbink [16]. For simulation of cavitation in fuel injection nozzles, including simulation of the direct interaction of cavitation dynamics with the external jet flow behind the nozzle exit, this set of constitutive equations is extended by a second fluid component "gas", see chapter 4.2. As suggested by Spalding [17], the continuity equation is used in its non-conservative form:

$$\nabla \cdot \mathbf{u} = -\frac{1}{\varrho} \frac{d\varrho}{dt}. \quad (4)$$

The usage of the volume fluxes rather than mass fluxes (conservative form) accounts for the numerical advantage, that the volume fluxes are continuous at the interfaces and thus simplifies the solution of the pressure correction equation. For standard VOF applications, i.e. both fluids are assumed to be incompressible and no phase transition takes place, the rhs. of Eq. 4 reduces to zero, meaning that the flow field is divergence-free. Care has to be taken for discretization of the transport equation of the volume fraction Eq. 1. In order to avoid smearing of the interface, special methods are used to derive the cell face values for the void fraction α . For that reason, the CICSAM scheme (Compressive Interface Capturing on Arbitrary Meshes) as proposed by Ubbink [16] was implemented and the code was verified by several test cases (convection tests, sloshing, dam breaking). Note that the CICSAM scheme is employed, if there exists a discrete sharp interface to be tracked, e.g. the motion of the free surface, see Sauer [15]. In the case of cavitation, the vapor bubbles and hence the vapor fraction are homogeneously distributed in the computational cell. A schematic sketch of the distribution of the gaseous phase for a standard VOF application and for cavitation is presented in Fig. 1 to explain this difference.

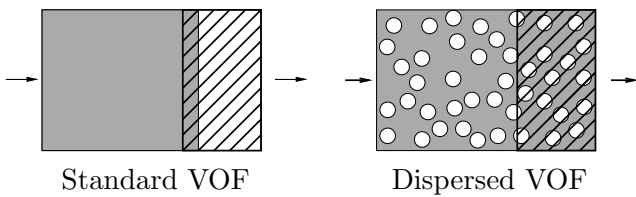


Figure 1: Distribution of the gaseous phase in a computational cell. Left: Standard VOF application, non-homogeneous distribution. Right: Cavitation, homogeneous distribution of the gaseous phase within the liquid. The marked volume leaves the cell due to convection.

In contrast to standard VOF applications, cavitation leads to a polydispersed two-phase flow including phase transition. The bubbles grow and collapse and hence change the vapor fraction in a computational cell, in addition to the convective transport. The standard VOF method does account for convective transport, but not for phase transition. With respect to cavitation, the void fraction α may be reformulated as follows:

$$\alpha = \frac{V_v}{V_{cell}} = \frac{N_{bubbles} \cdot \frac{4}{3}\pi R^3}{V_v + V_l} = \frac{n_0 V_l \cdot \frac{4}{3}\pi R^3}{n_0 V_l \cdot \frac{4}{3}\pi R^3 + V_l} = \frac{n_0 \cdot \frac{4}{3}\pi R^3}{1 + n_0 \cdot \frac{4}{3}\pi R^3}, \quad (5)$$

where V_{cell} is the volume of the computational cell, V_v and V_l are the volumes occupied by vapor and liquid, respectively and $N_{bubbles}$ is the number of bubbles in the computational cell. As a consequence of the bubble growth process, the velocity field is no longer divergence-free (Eq. 6) and the void fraction transport equation has to be extended by a vapor production source term:

$$\nabla \cdot \mathbf{u} = -\frac{\rho_v - \rho_l}{\alpha \rho_v + (1 - \alpha) \rho_l} \frac{d\alpha}{dt}, \quad (6)$$

$$\frac{\partial \alpha}{\partial t} + \frac{\partial(\alpha u)}{\partial x} + \frac{\partial(\alpha v)}{\partial y} = \left(\frac{n_0}{1 + n_0 \cdot \frac{4}{3}\pi R^3} \right) \frac{d}{dt} \left(\frac{4}{3}\pi R^3 \right). \quad (7)$$

The vapor production is taken into account by the source term on the right hand side of Eq. 7. The change of the cell vapor fraction does now depend on the number of bubbles per cell volume (rhs:1st term) times the volume change of a single bubble (rhs:2nd term) and on the convective transport. The parameter n_0 is defined as the bubble concentration per unit volume of pure liquid. Using this definition, the number of nuclei is explicitly coupled to the water volume in a cell. The physical background of this more formal aspect is, that relating the number of bubbles to the water volume (rather than to the volume of the mixture) guarantees the conservation of the number of bubbles. If the nuclei grow, the vapor fraction rises and hence the water fraction decreases. Therefore, the number of bubbles in the cell does also decrease. In Fig. 2 the growth of nuclei in a cell is schematically depicted. For the initial situation, Fig. 2 left, the cell contains a large water fraction and hence a large number of nuclei. If the nuclei grow, Fig. 2 middle, they displace water and at the same time other bubbles. Therefore, the gain of vapor fraction due to nuclei growth is reduced by a loss of vapor fraction due to bubbles that are displaced out of the cell. Further growth, Fig. 2 right, leads to a further reduction

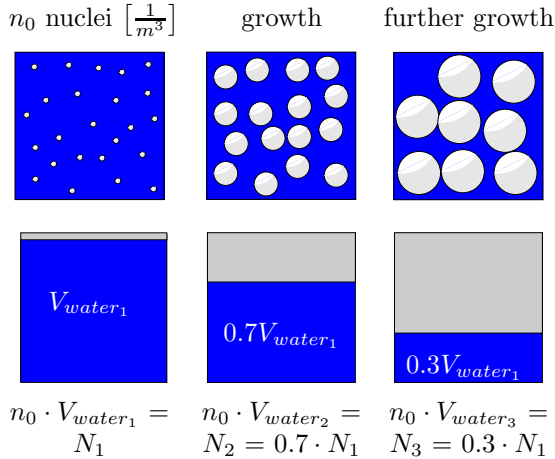


Figure 2: Number of bubbles depending on the water fraction in a computational cell. Left: Initial simulation. Middle: Growth of the nuclei. Right: Further growth of the vapor bubbles.

of the number of bubbles. Since every vapor bubble originates from a nuclei, the definition of n_o also holds for vapor bubbles. A given volume of water V_l always contains $N = n_o \cdot V_l$ bubbles, the bubbles can either be nuclei of radius $R = R_0$ or vapor bubbles with arbitrary larger radius. The interested reader may refer to Sauer [15] for further explanation of modeling the nuclei content of the flow.

Note that for the discretization of the convection terms of Eq. 7 the UPWIND differencing scheme of Ferziger and Perić [18] is employed. This is consistent with the homogeneous assumption. A mixture of liquid and bubbles leaves the cell, as shown in Fig. 1. The composition of the fluid volume that is convected out of the cell has the same composition than the fluid that is currently in that cell. This physical aspect is numerically taken into account by using UPWIND discretization.

To complete the derivation of the numerical method, a relation to model the bubble growth is needed. Under the assumptions that bubble-bubble interactions and bubble coalescence can be neglected and that the bubbles remain spherical, the Rayleigh-Plesset equation, see [19], together with the energy equation is well suited to model the bubble growth and collapse process:

$$R \frac{d^2 R}{dt^2} + \frac{3}{2} \left(\frac{dR}{dt} \right)^2 = \frac{p(R) - p_\infty}{\rho_l} - \frac{2\sigma}{\rho_l R} - 4 \frac{\mu}{\rho_l R} \frac{dR}{dt}. \quad (8)$$

Note that in our model the Rayleigh-Plesset equation can be treated as an ordinary differential equation, even when dealing with 2-D or 3-D flow problems, and can e.g. be solved by a Runge - Kutta method. For details of the solution procedure we refer to the work of Lee et al. [20].

If the system pressure is sufficiently low and the pressure difference $p(R) - p_\infty$ is large, the Rayleigh relation (9) may be considered as an adequate description for the so-called inertia controlled bubble growth:

$$\dot{R} = \sqrt{\frac{2}{3} \frac{p(R) - p_\infty}{\rho_l}}, \quad (9)$$

where $p(R)$ is the pressure in the liquid at the bubble boundary and p_∞ is the pressure in the liquid at a large distance from the bubble. Within the scope of this model, $p(R)$ is set equal to the vapor pressure p_{sat} and p_∞ to the ambient cell pressure. The Rayleigh relation was used to obtain the results presented in the following sections. To simulate cavitation in liquids others than cold water, i.e. if thermal effects are important (organic fluids, hot water), the model is extended by a simplified equation for the mixture enthalpy h , to account for the temperature change of the mixture caused by cavitation. For details and results see [21]. The advantage of the present modeling is the option for simultaneous application of both methods, the standard front capturing method without phase transition and the modified VOF technique to track dispersed voids. Numerical simulations of unsteady cloud cavitation including free surface flow effects are interesting examples for simultaneous application of these two methods.

3 Results for Turbulent Cavitating Flows

3.1 Single-phase $k - \omega$ model of Wilcox without modification

Cavitation in high pressure fuel injection nozzles From experiments it is well known, that cavitation in injection nozzles of Diesel engines has a strong impact on spray angle and momentum of the jet, which are important for control and efficiency of primary break up and atomization of the liquid fuel and the combustion process. Further important details, e.g. dispersion and droplet size, dependent on the cavitation intensity, are not yet known, but of great interest and therefore in focus of many research projects dealing with this subject ([10],[22],[23], [24]). Due to the very short time scale of the flow of $1 - 10\mu s$ and the micro scale of the nozzles of $100\mu m - 1mm$, experiments and detailed quantitative data are very rare. Therefore, accurate physical modeling together with efficient numerical simulation methods are most important and promising to improve understanding of this complex unsteady turbulent two-phase multi-component micro fluid dynamic problem. Here the viscous version of our simulation tool CAVKA is applied. Because the Reynolds number is of the order of 30.000 we make use of the single-phase $k - \omega$ turbulence model of Wilcox [1] with wall functions, but without modification in the two-phase regime.

Here the cavitation model parameters, nuclei concentration n_0 and nuclei size R_0 , are unknown and it is important to realize, that quantitative verification of these submicron data by experiments in the real micro scale flow, including thermodynamic nonequilibrium is not to be expected in future. Therefore, we have performed systematic tests with parameter variations to identify necessary nuclei sizes R_0 and concentrations n_0 , which lead to cavitation structures as observed in injection nozzle experiments. This fact emphasizes an important difference with respect to classical hydraulic cavitation in macro scale, as presented in the previous chapter. There representative data of n_0 and R_0 are known from direct measurements. It is interesting to note, that the required nuclei size is of the order of $10^{-7}m$, but the required concentration is about $10^{14}nuclei/m^3$ water, i.e. 6-7 orders higher as compared with hydraulic cavitation. Such high concentrations are not typical for pre-existing heterogeneous nuclei. In conclusion, the formation of homogeneous vapor nuclei cannot be excluded. This enlightens another difficult but quite interesting physical aspect of this engineering problem.

Due to the high sensitivity of cavitation on the imposed initial and boundary conditions, simulations with restriction to the internal nozzle flow, i.e. without direct interaction with the external jet flow are qualitatively and quantitatively incorrect. Simulation of the external jet flowing into the surrounding air requires inclusion of a second non-condensable fluid component (gas or air), for details see [25]. To close the system of conservation equations for unsteady turbulent flows, for the mixture density ρ and the mixture viscosity μ we introduce the following extended set of constitutive equations:

$$\rho = \alpha_l \rho_l + \alpha_v \rho_v + \alpha_g \rho_g, \quad (10)$$

$$\mu = \alpha_l \mu_l + \alpha_v \mu_v + \alpha_g \mu_g, \quad (11)$$

where the subscripts l , v and g stand for the values of pure liquid, pure vapor and pure gas (air), α_i indicates the volume fraction of the fluid component "i" with the compatibility condition:

$$\alpha_l + \alpha_v + \alpha_g = 1. \quad (12)$$

As before the properties ρ and μ of pure liquid, pure vapor and of pure gas are assumed to be constant. Turbulence modeling is carried out, μ_{eff} is therefore used instead of the molecular viscosity μ :

$$\mu_{eff} = \mu + \mu_t, \quad (13)$$

where μ_t represents the turbulence viscosity which is modeled using the Wilcox $k - \omega$ model. For details of the turbulence modeling see [25].

For the volume fractions α_i we derive the following transport equations:

$$\frac{\partial \alpha_v}{\partial t} + \nabla \cdot (\alpha_v \vec{c}) = \frac{(1 - \alpha_g) \rho_l + \alpha_g \rho_g}{\rho} \frac{d\alpha_v}{dt}, \quad (14)$$

$$\frac{\partial \alpha_l}{\partial t} + \nabla \cdot (\alpha_l \vec{c}) = -\frac{(1 - \alpha_g) \rho_v + \alpha_g \rho_g}{\rho} \frac{d\alpha_v}{dt}, \quad (15)$$

$$\frac{\partial \alpha_g}{\partial t} + \nabla \cdot (\alpha_g \vec{c}) = \alpha_g \frac{\rho_l - \rho_v}{\rho} \frac{d\alpha_v}{dt}. \quad (16)$$

Multiplication of the volume fraction α_i with the density ρ_i yields the mass conservation for each fluid component

$$\frac{\partial(\rho_v \alpha_v)}{\partial t} + \nabla \cdot (\rho_v \alpha_v \vec{c}) = \rho_v \frac{(1 - \alpha_g) \rho_l + \alpha_g \rho_g}{\rho} \frac{d\alpha_v}{dt}, \quad (17)$$

$$\frac{\partial(\rho_l \alpha_l)}{\partial t} + \nabla \cdot (\rho_l \alpha_l \vec{c}) = -\rho_l \frac{(1 - \alpha_g) \rho_v + \alpha_g \rho_g}{\rho} \frac{d\alpha_v}{dt}, \quad (18)$$

$$\frac{\partial(\rho_g \alpha_g)}{\partial t} + \nabla \cdot (\rho_g \alpha_g \vec{c}) = \rho_g \alpha_g \frac{\rho_l - \rho_v}{\rho} \frac{d\alpha_v}{dt}. \quad (19)$$

Summation of Eqs. 17, 18 and 19 represents the continuity equation.

Scaling of model nozzle Here the 2-D plane experimental test cases of Roosen et al. [26] are recalculated, to validate our numerical scheme and to study the physical effects concerning the interaction between the cavitating flow and the external jet of the injection nozzle. The fluid used in the experiments was tap water. The “bore hole” of the nozzle consists of a rectangular-shaped channel of $0.2\text{mm} \times 0.28\text{mm} \times 1\text{mm}$ (*width* \times *height* \times *length*). The calculated flow regime includes simultaneous treatment of internal and external flow. Figure 3 shows the nozzle geometry and boundary conditions. To reduce the computational time, we assume a 2-D flow and symmetry with respect to the nozzle axis. A computational mesh of 95×13 nodes for the nozzle block and 79×49 for the outflow block is used for the spatial discretization. Stationary liquid in the nozzle and a sharp liquid interface with the air behind the nozzle exit are assumed as initial conditions. Both inflow and outflow boundaries are modeled as constant pressure surfaces. At the inlet, the turbulence kinetic energy k is set to be $6 \times 10^{-4} u_{in}^2$. The value of the specific dissipation rate ω is selected using the length scale equation, see Ferziger & Peric [18] and Yuan & Schnerr. [27]. On the wall, the boundary conditions are the impermeability and no-slip for the velocity, and the normal gradient of the pressure is assumed to be zero. Wall functions based on the law of wall are used as boundary conditions for turbulence modeling.

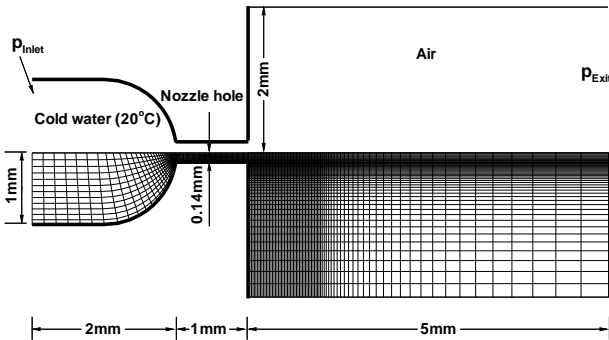


Figure 3: Computational mesh and boundary conditions of the 2-D plane model injection nozzle.

Inception of cavitation in a liquid requires the presence of nuclei. Our parameter tests have shown that the numerical solutions using the nuclei concentration of the order of $n_0 = 1 \times 10^{14} \frac{\text{nuclei}}{\text{m}^3 \text{water}}$ agree very well with experimental observations of Roosen et al. and the nuclei radius $R_0 = 0.3 \mu\text{m}$ is in the insensitive range. In this study these values will be used, which correspond to an initial vapor fraction $\alpha_{v0} = 0.0017\%$.

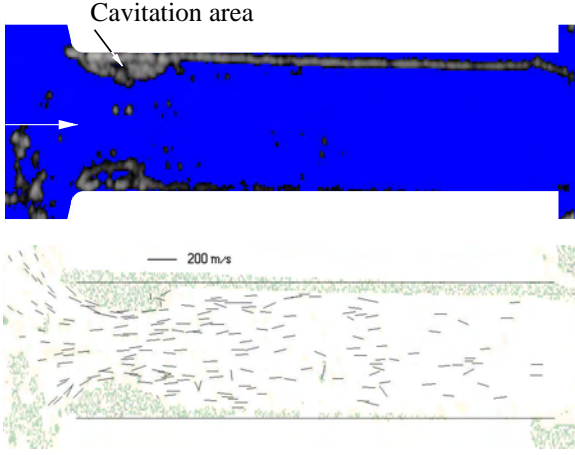


Figure 4: Experimental density gradient and velocity distribution in the nozzle hole for $p_{Injection} = 80\text{bar}$ and $p_{Exit} = 21\text{bar}$, flow from left to right, from Roosen et al. [26].

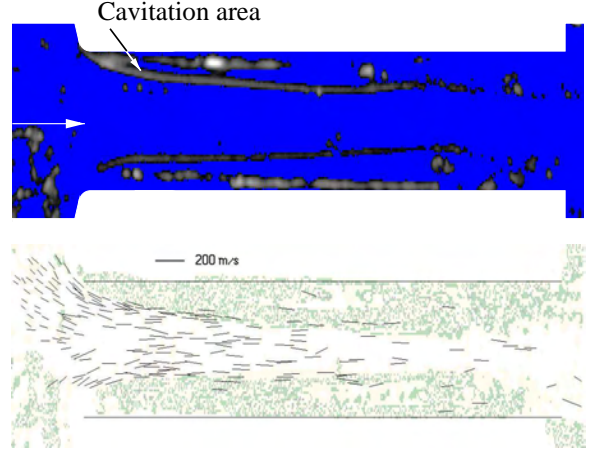


Figure 6: Experimental density gradient and velocity distribution in the nozzle hole for $p_{Injection} = 80\text{bar}$ and $p_{Exit} = 11\text{bar}$, flow from left to right, from Roosen et al. [26].

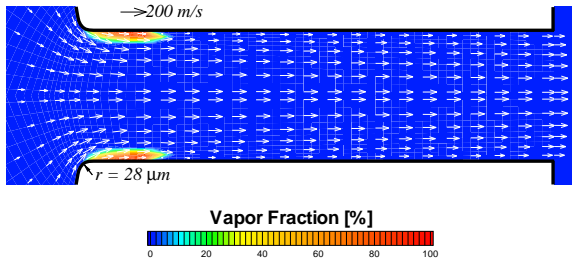


Figure 5: Computed steady vapor fraction distribution in the nozzle hole. $p_{Inlet} = 80\text{bar}$, $p_{Exit} = 21\text{bar} = \text{const.}$, $Re = \frac{\bar{u}_{Inlet} \cdot H}{\nu} \approx 2.78 \times 10^4$.

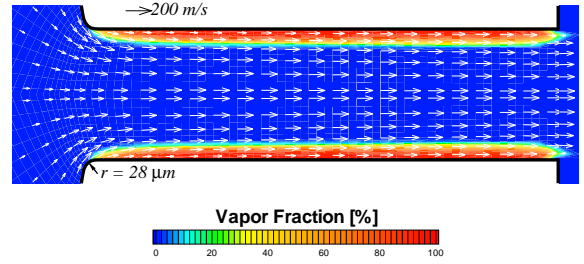


Figure 7: Computed steady vapor fraction distribution in the nozzle hole. $p_{Inlet} = 80\text{bar}$, $p_{Exit} = 11\text{bar} = \text{const.}$, $Re = \frac{\bar{u}_{Inlet} \cdot H}{\nu} \approx 2.78 \times 10^4$.

Moderate and high injection pressure and steady cavitating flow The calculation is first carried out for the case with $p_{Injection} = 80\text{bar}$ and $p_{Exit} = 21\text{bar}$. The computed result yields a length of the cavitation region of about $200\mu\text{m}$, which agrees well with the experimental observation of Roosen et al. [26], see Figs. 4, 5. Chaves et al. [10] have observed, that after a small increase of the injection pressure above the pressure at which cavitation first appears at the nozzle lip, the cavitation regime reaches the nozzle exit. To confirm their observation, another test case with $p_{Injection} = 80\text{bar}$ and $p_{Exit} = 11\text{bar}$ is performed, which demonstrates that under these conditions the cavitation extends toward the nozzle exit, see Figs. 6, 7. It is obvious, that in this supercavitating situation inclusion of the outflow is necessary, because some of the cavitation bubbles collapse outside.

Cavitation has its own length scale which is not possible to be scaled up, see Chaves et al. [10] and Yuan & Schnerr [27]. This length scale is determined by the characteristic collapse time of a given cavity and the flow velocity. If the collapse of a bubble or cavity occurs downstream of the nozzle exit, i.e. in the external jet, this is called supercavitation. Supercavitation occurs, if the collapse time of the vapor cavities is longer than the transit time of the fluid through the nozzle. It can be expected that higher pressure differences cause stronger supercavitation. For demonstration an example with a realistic pressure of $p_{Injection} = 800\text{bar}$ and $p_{Exit} = 11\text{bar}$ is calculated. Figure 8 shows the computed steady vapor distribution.

High frequency periodic inlet pressure excitation Chaves et al. [10] have claimed that supercavitation is an inherent unsteady process that can only occur at high flow velocities. So far, this

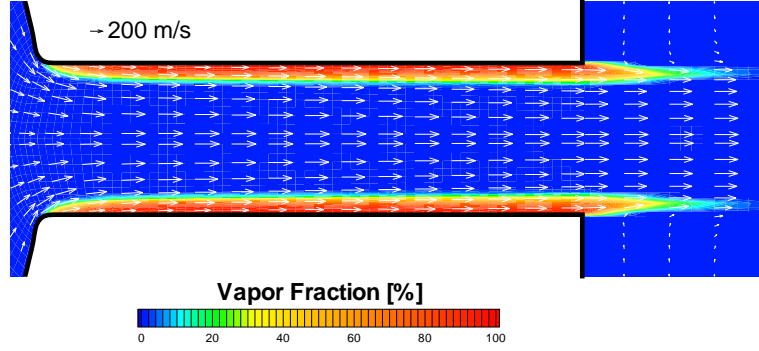


Figure 8: Computed steady vapor fraction distribution. $p_{Inlet} = 800\text{bar}$, $p_{Exit} = 11\text{bar} = \text{const.}$, $Re = \frac{\bar{u}_{Inlet} \cdot H}{\nu} \approx 8.82 \times 10^4$.

unsteadiness has not yet been captured, because of the constant outflow boundary conditions and the single-phase turbulence model. The collapse process is strongly influenced by the boundary conditions, the nozzle geometry and the main axial flow. The single-phase turbulence model overestimates the viscous effects in two-phase regions.

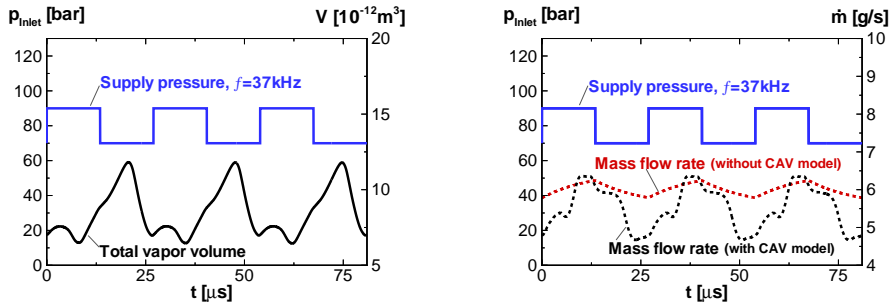


Figure 9: Integrated total vapor volume within and outside the nozzle (left) and mass flow rate at the nozzle exit (right) depending on the rectangular inlet pressure pulse. Back pressure $p_{Exit} = 11\text{bar} = \text{const.}$, $Re = \frac{\bar{u}_{Inlet} \cdot H}{\nu} \approx 2.78 \times 10^4$.

In reality the pressure upstream and behind the nozzle fluctuates with high frequencies. The reason for the upstream pressure fluctuation is the well known “water hammer” effect in the needle chamber. In order to understand the effects caused by the fluctuation of the upstream pressure further, calculations for the case with a rectangular inlet pressure pulse are performed. The pressure pulse and the calculated results are shown in Figs. 9-11.

The integrated total vapor volume in the nozzle shown in Fig. 9 indicates that the cavitation process in the injection nozzle is very complex. As a difference to the unsteady partial cavitation, see Yuan and Schnerr [27], here the total vapor volume reveals two peaks during one inlet pressure period. Also the vapor distribution, shown in Fig. 10 confirms, that the cavitation reaches the nozzle exit two times within the same period. The physical reason is the inflow of air from the nozzle outlet. The velocity field shows that the cavitating flow separates instantaneously in the nozzle. In this situation the external pressure forces the gas (air) to flow into the cavitating region (hydraulic flip), first observed by Bergwerk [28].

The calculated mass flow rates shown in Fig. 9 demonstrate that the discharge of the nozzle strongly depends on the cavitation intensity. The variation of the computed mass flow rate, with and without cavitation model, is of the order of 10% of the averaged mass flow rate, i.e. cavitation reduces the discharge significantly. In addition, it is recognized from Fig. 9 that the cavitation process enhances the mass flow rate fluctuation of $\pm 15\%$, which intensifies jet atomization, see Fig. 11.

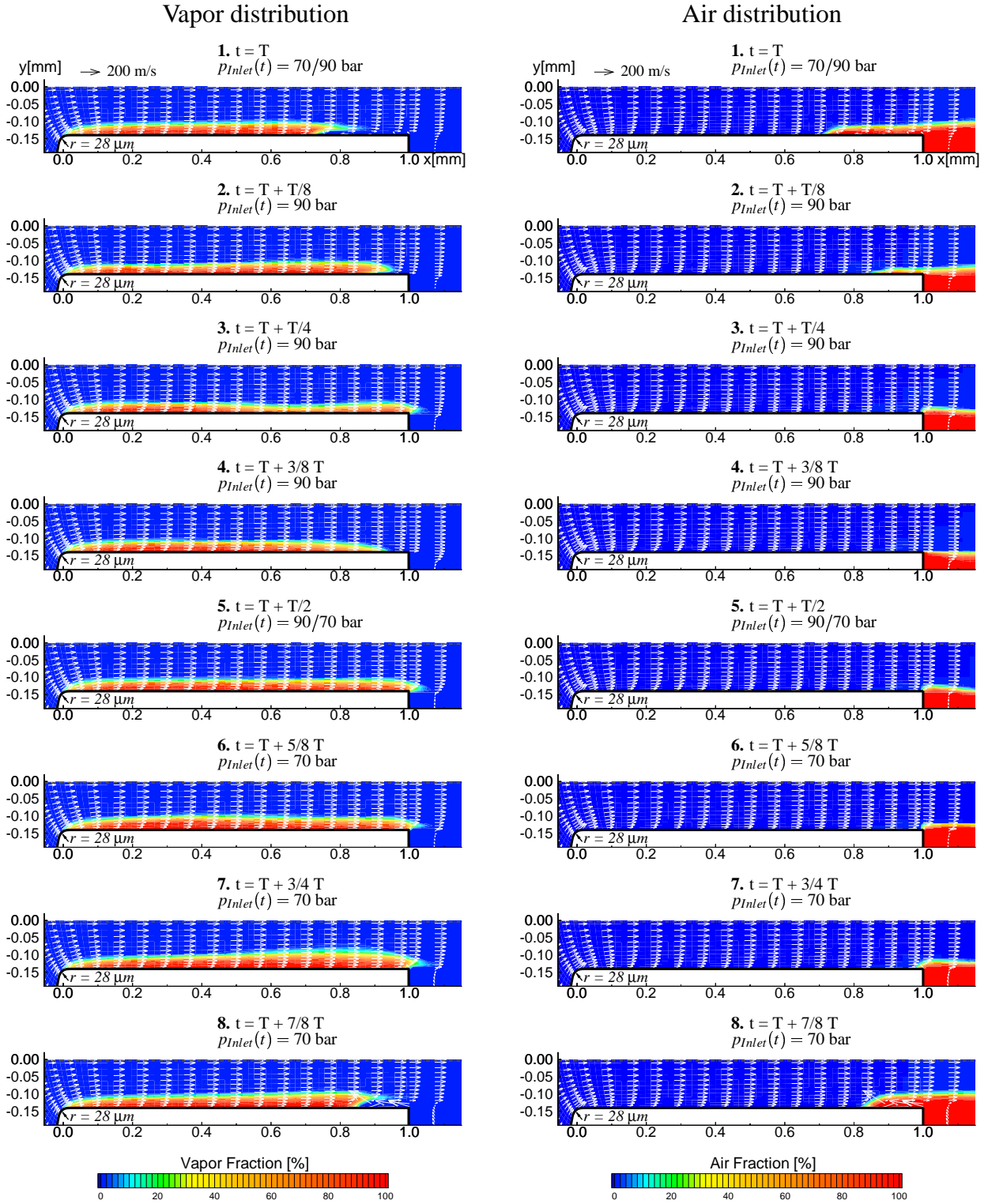


Figure 10: Unsteady supercavitation: vapor and air distribution of one cycle. Periodic unsteady inlet pressure $p_{Inlet} = 80 \pm 10$ bar, $f = 37$ kHz, back pressure $p_{Exit} = 11$ bar = const.; $Re = \frac{\bar{u}_{Inlet} \cdot H}{\nu} \approx 2.78 \times 10^4$.

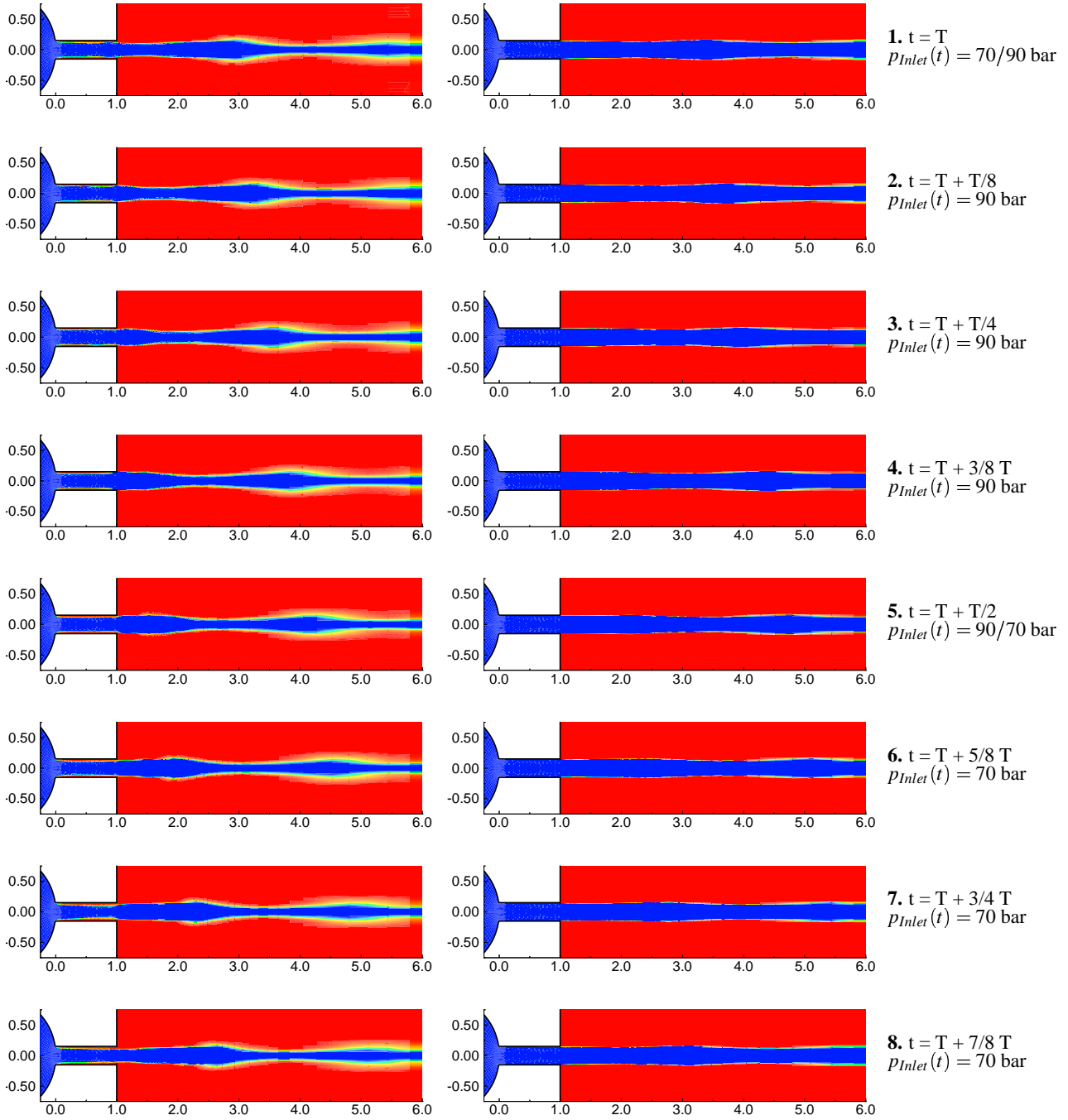


Figure 11: Unsteady jet flow nearby the nozzle exit. Periodic unsteady inlet pressure $p_{Inlet} = 80 \pm 10$ bar, $f=37$ kHz, back pressure $p_{Exit} = 11$ bar. Left: computed with cavitation model, $Re = \frac{\bar{u}_{Inlet} \cdot H}{\nu} \approx 2.78 \times 10^4$; right: without cavitation model, $Re = \frac{\bar{u}_{Inlet} \cdot H}{\nu} \approx 3.0 \times 10^4$.

3.2 Modified $k - \omega$ model for simulation of cavitating flows

The intention is to enhance the single-phase $k - \omega$ model with empirical modifications to provide a two-equation turbulence model for quantitative correct simulation of steady and unsteady partial cavitating flows. From the actual literature modifications are known with respect to

- turbulent viscosity μ_t [11]
- local compressibility [1]
- pressure fluctuations [12].

Due to the lack of experimental data in cavitating microscale flows, as typical for injection nozzles, the effects of turbulence model modifications have been investigated in macroscale flows, having a characteristic length scale of 0.1m and where much more experimental data are available, e.g. from Keller & Arndt [7]. In addition, in external cavitating flow around hydrofoils the structural variation of flow pattern due to the turbulence modelling becomes much more obvious. Therefore, as appropriate test case we investigate the cavitating flow around a slender 2-D hydrofoil at moderate angle of attack. From preliminary tests we found that inclusion of pressure fluctuations has no significant influence on developed or partial cavitation. This is what is to be expected, except if dealing with incipient cavitation. Because the effect of the first two modifications is similar to some extent, results of turbulent viscosity modifications are shown here and compared with Euler and single-phase $k - \omega$ simulations.

Modification of turbulent viscosity μ_t In the two-phase regime all fluid properties vary accordingly to the local void fraction α between the threshold values of the pure liquid and the vapor phase. In the original model the turbulent viscosity μ_t varies explicitly proportional to the fluid density. To account for the typical very large density variation of 40.000 : 1 (water 293.15K), the linear dependence on the mixtures density is replaced by $f(\varrho)$ with the free parameter N:

$$\mu_{turb} = f(\varrho) \cdot \frac{k}{\omega} \quad (20)$$

$$f(\varrho) = \varrho_{vap} + \left(\frac{\varrho_{vap} - \varrho}{\varrho_{vap} - \varrho_{liq}} \right)^N \cdot (\varrho_{liq} - \varrho_{vap}). \quad (21)$$

In the pure liquid and vapor phase μ_t remains unchanged. In the two-phase regime and especially for higher values of N μ_t decreases suddenly and approximates the lower value of the pure vapor phase, see Fig.12. Figures 13, 14 and 15 demonstrate the effect by the vapor fraction α . Figure 13 starts with the inviscid model, we observe the typical instability with formation of a re-entry jet and separating bubbly clouds, $f = 5.2Hz$. If the Euler

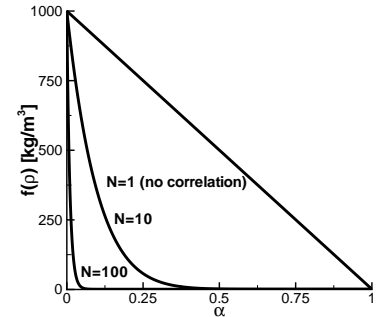


Figure 12: Turbulent viscosity dependence of α

equation is replaced by the Reynolds averaged Navier-Stokes equation, closed by the single-phase $k - \omega$ model, the global instability of the dispersed vapor sheet disappears (Fig. 14). Due to the strong gradients in the collapse region there is still a slight local unsteadiness with $f = 7.7Hz$. However cloud separation does not exist. Modification of the turbulent viscosity μ_t with N=1000 re-establishes the global unsteadiness, similar to the inviscid case with $f = 6.6Hz$. This demonstrates the potential of the method. Experiments are necessary and under preparation to calibrate the parameter N quantitatively. The time dependent development of the total vapor volume $V[dm^3]$ depicts the typical difference between the quasi steady result Fig. 17 with the maximum mean vapor production rate of all three cases and the global unsteady flows of Figs. 16 and 18, with the typical instantaneous disappearance of the vapor production at the beginning of each cycle. Obviously after about 5 cycles periodicity establishes, independent of the model used.

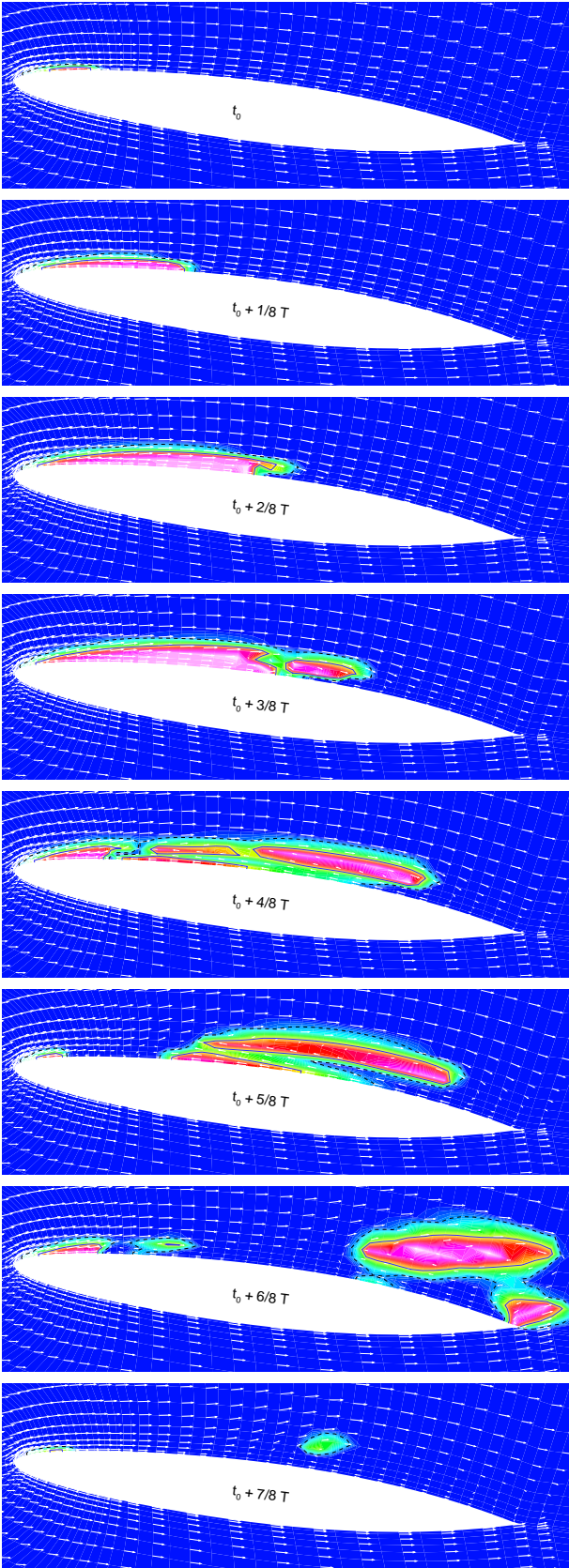


Figure 13: Unsteady cavitating Euler flow. $\sigma_{ref} = 0.8$, $f=5.2$ Hz, $u_{inlet} = 6m/s$, $p_{exit} = 9528.6Pa$, $n_0 = 10^8 nuclei/m^3$, $R_0 = 3 \times 10^{-6}m$, $l_c = 0.1m$, $Re_c = 6 \times 10^5$.

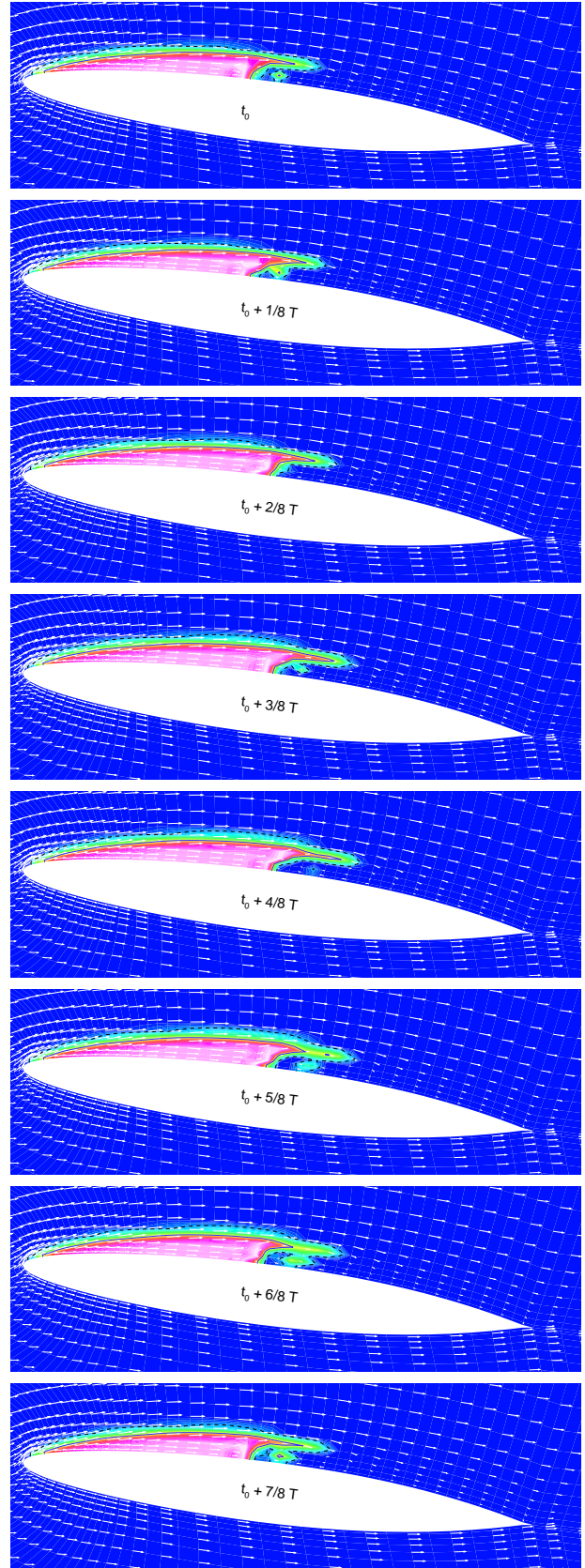


Figure 14: Unsteady cavitating flow with single-phase $k - \omega$ model of Wilcox. $\sigma_{ref} = 0.8$, $f=7.7$ Hz, $u_{inlet} = 6m/s$, $p_{exit} = 9528.6Pa$, $n_0 = 10^8 nuclei/m^3$, $R_0 = 3 \times 10^{-6}m$, $l_c = 0.1m$, $Re_c = 6 \times 10^5$.

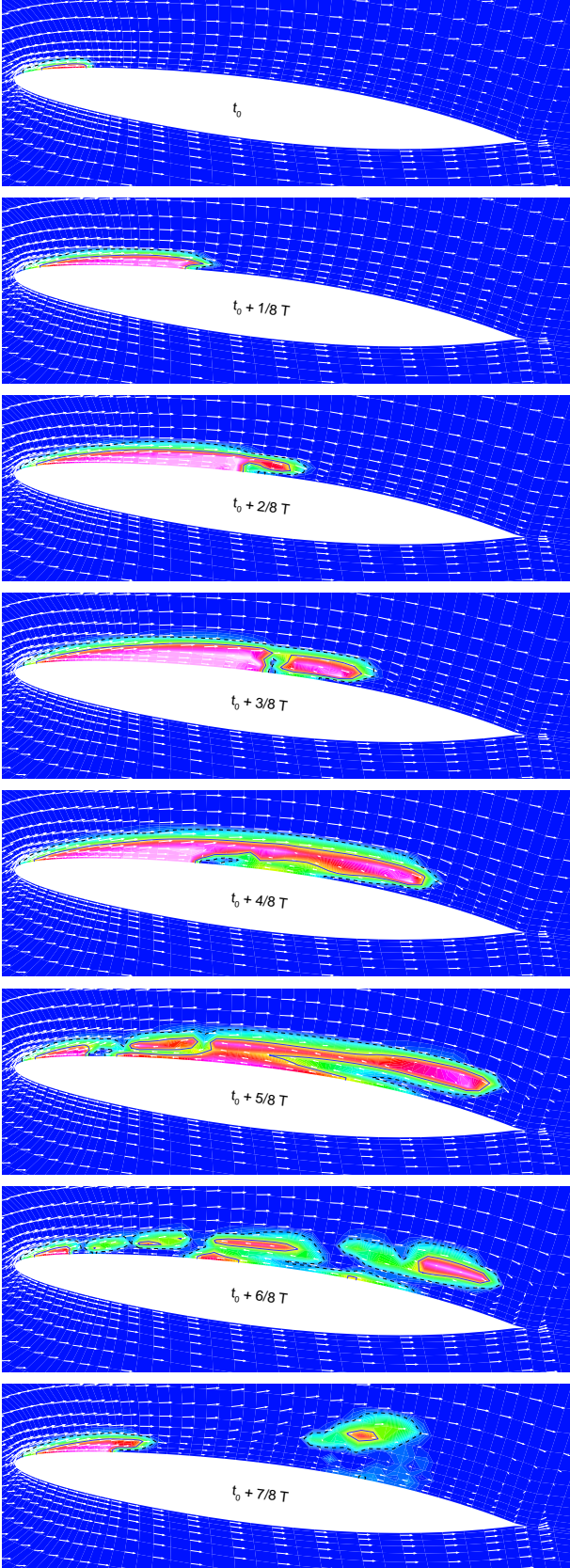


Figure 15: Unsteady cavitating flow with turbulent viscosity modification, $N=1000$. $\sigma_{ref} = 0.8$, $f=6.6$ Hz, $u_{inlet} = 6m/s$, $p_{exit} = 9528.6Pa$, $n_0 = 10^8 nuclei/m^3$, $R_0 = 3 \times 10^{-6}m$, $l_c = 0.1m$, $Re_c = 6 \times 10^5$.

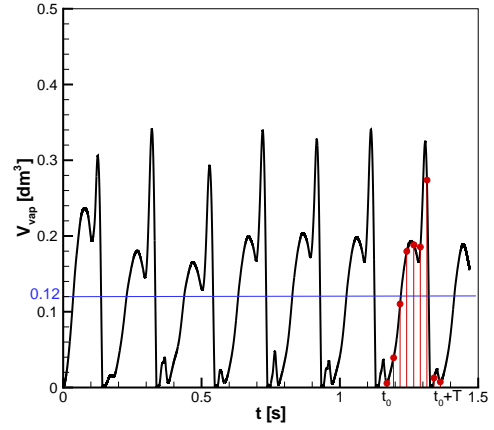


Figure 16: Vapor volume in Euler flow. $\sigma_{ref} = 0.8$, $f=5.2$ Hz, see Fig.13.

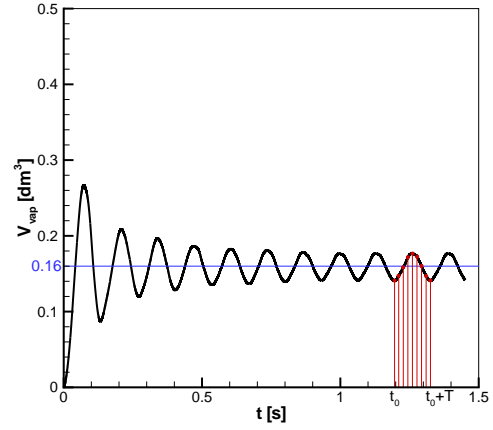


Figure 17: Vapor volume with single-phase $k-\omega$ model of Wilcox. $\sigma_{ref} = 0.8$, $f=7.7$ Hz, see 14.

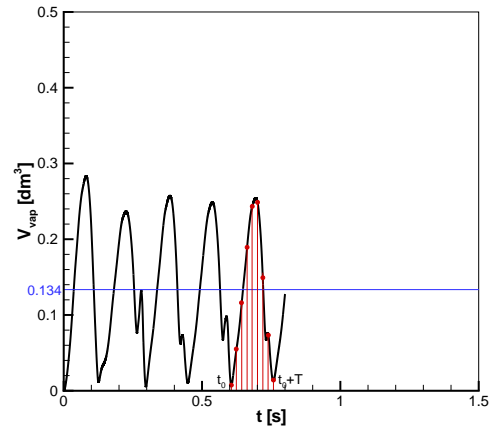


Figure 18: Vapor volume with turbulent viscosity modification, $N=1000$. $\sigma_{ref} = 0.8$, $f=6.6$ Hz, see Fig. 15.

4 Conclusions

Application of our dispersed cavitation model to different test cases with developed cavitation in internal and external flows demonstrates the capability of our CFD tool CAVKA for simulation of cavitating flows, especially in the unsteady regime. Comparison of Euler and Navier-Stokes simulations with experiments emphasizes the necessity of further tests and development of appropriate models. Fortunately the simpler inviscid model is closer to experiments, mainly because the single-phase reference flows are free of separation.

In tendency lift and drag dynamics of cavitating hydrofoils are in good agreement with experiments. Application of our model to the injection nozzle problem demonstrates interesting details and the potential of cavitation as a fluid dynamic tool to control the formation and quality of sprays. Again, despite the fact, that the model assumption are rather coarse, agreement with experiments is surprisingly good and promising for further developments.

Due to the natural stiffness of the two-phase problem appropriate initial and boundary conditions are extremely important. For example, simulation of the injection nozzle problem without appropriate unsteady pressure fluctuations at the inlet are not realistic. At the outlet the same conclusion holds for the linkage of the higher pressure outside with the bubble collapse regime inside the nozzle.

Because simulation of sheet formation, bubble clouds and re-entry jets are natural capabilities of our dispersed cavitation model without any need to define artificial closure conditions, extension to supercavitation for simulation of external hydrodynamic flows around high speed moving bodies is possible without any model change. Due to the fascinating aspect of significant viscous drag reduction, simulation of supercavitation is subject of many research projects around the world. A most comprehensive and most complete documentation of the state of the art in this field can be found in [29].

Acknowledgement

The support of the Deutsche Forschungsgemeinschaft (DFG) Bonn by grant SCHN 352/16-2 during performing this research is greatly acknowledged.

References

- [1] D.C. Wilcox: *Turbulence Modeling for CFD*, 2nd edn. (DCW Industries, California, 1998)
- [2] R.E. Arndt: *Ann. Rev. Fluid Mech.* **13**, 273-328 (1981)
- [3] M. Versluis, B. Schmitz, A. von der Heydt, D. Lohse: *Science* **289**, 2214-2117 (2000)
- [4] G.H. Schnerr, S. Adam, K. Lanzenberger, R. Schulz: 'Multiphase flows: Condensation and cavitation problems'. In: *Computational Fluid Dynamics REVIEW* ed. by M. Hafez and K. Oshima (John Wiley & Sons, Ltd., 1995)
- [5] J.L. Reboud, Y. Delannoy: 'Two-phase flow modeling of unsteady cavitation'. In: *Proc. 2nd Int. Symp. on Cavitation, Tokyo, Japan, 1994*
- [6] B. Gindroz, M.L. Billet: *J. of Fluids Engineering*, 87-97 (1976)
- [7] A. Keller, R.A. Arndt: Private communication (1999)
- [8] C.Y. Li, S.L. Ceccio: *ASME-FED.* **190**, 283-290 (1994)
- [9] C.E. Brennen: *Multiphase Science and Technology.* **10**, 303-321 (1998)
- [10] H. Chaves, M. Knapp, A. Kubitzek, F. Obermeier, T. Schneider: *Journal of engines, SAE 1995 Transactions, Section 3*, **104**, 645-657 (1995)

- [11] O. Coutier-Delgosha, R. Fortes-Patella, J.L. Reboud: 'Evaluation of the turbulence model influence on the simulations of unsteady cavitation'. In: *Proc. of ASME FEDSM'01, New Orleans, Louisiana, 2001*
- [12] M.M. Athavale, H.Y. Li, Y. Jiang, A.K. Singhal: 'Application of the full cavitation model to pumps and inducers'. In: *Proc. of ISROMAC-8, Honolulu, 2000*
- [13] G. Winkler, M. Heiler, G.H. Schnerr: 'Homogeneous/heterogeneous condensation dynamics in turbulent low pressure turbine flows'. In: *Proc. Int. Conf. SYMCOM99, Ciepłne Maszyny Przepływowe, Turbomachinery, No. 115, Lodz, Polen, pp. 445-456, 1999*
- [14] B.D. Nichols, C.W. Hirt: *Journal of Comp. Physics*, **12**, 343-448 (1973)
- [15] J. Sauer: 2000. Instationär kavitierende Strömungen - Ein neues Modell, basierend auf Front Capturing (VoF) und Blasendynamik. Ph.D. thesis, University of Karlsruhe, Germany (2000)
- [16] O. Ubbink: Numerical prediction of two fluid systems with sharp interfaces. Ph.D. thesis, University of London, London (1997)
- [17] D.B. Spalding: CHAM report 910/2 (1974)
- [18] J.H. Ferziger, M. Perić: *Computational methods for fluid dynamics*, (Springer, Berlin Heidelberg, 1996)
- [19] M.S. Plesset, A. Prosperetti: *Annual Review of Fluid Mechanics*. **9**, 145-185 (1977)
- [20] H.S. Lee, H. Merte: *Journal of Heat Mass Transfer*. **39**, 12, 2427-2447 (1996)
- [21] J. Sauer, G.H. Schnerr: 'Unsteady Cavitating Flow - A New Cavitation Model Based on a Modified Front Capturing Method and Bubble Dynamics'. In: *ASMEFEDSM2000-11095, 2000*
- [22] J. Walther, J.K. Schaller, R. Wirth. C. Tropea: 'Characterization of Cavitating Flow Field in Transparent Diesel Injection Nozzles using Fluorescent Particle Image Velocimetry (FPIV)'. In: *Proc. ILASS - 16th Annual Conference on Liquid Atomization and Spray Systems, Darmstadt, Germany, September 11-13, 2000 (eds. Tropea, C., Heukelbach., K.) (2000) I.8 1- I.8.6*
- [23] A. Alajbegovic, D.A. Drew, R.T. Lahey: *Chem. Eng. Comm.* **174**, 85-133 (1999)
- [24] A. Alajbegovic, G. Meister: 'Three-phase Cavitating Flows in High Pressure Swirls Injectors'. In: *Proc. ICMF- 2001 - 4th International Conference on Multiphase Flow, New Orleans, USA, May 27-June 1, 2001 (ed. E.E. Michaelides). Tulane University (2001) CD-ROM*
- [25] W. Yuan, J. Sauer, G.H. Schnerr: *Mécanique & Industries*. **2**, 383-394 (2001)
- [26] P. Roosen, O. Unruh, M. Behmann M.: 'Untersuchung und Modellierung des transienten Verhaltens von Kavitationserscheinungen bei ein- und mehrkomponentigen Kraftstoffen in schnell durchströmten Düsen'. In: *Report of the Institute for Technical Thermodynamics, RWTH Aachen, Germany, March 1996*
- [27] W. Yuan, G.H. Schnerr: 'Cavitation in injection nozzles - Effect of injection pressure fluctuations'. In: *Proc. 4th International Symposium on Cavitation, California Institute of Technology, Pasadena, CA, USA, June 20-23, 2001*
- [28] W. Bergwerk W.: 'Flow pattern in Diesel nozzle spray holes'. In: *Proceedings of the Institute on Mechanical Engineers, Vol. 173, No. 25, pp. 655-660, 1959*
- [29] Proc. HSH 2002 - High Speed Hydrodynamics - Cheboksary Washington, Russia June 16-23, 2002 (eds. Cherny, G.G., Tulin, M.P., Terentiev, A.G., Serebryakov, V.V.). Cortana Corp. USA (2002)

GENERALIZED MODELING OF MULTI-COMPONENT VAPORIZATION/CONDENSATION PHENOMENA FOR MULTI-PHASE-FLOW ANALYSIS

K. Morita¹⁾, K. Fukuda¹⁾, Y. Tobita²⁾, Sa. Kondo²⁾, T. Suzuki³⁾ and W. Maschek³⁾

¹⁾Kyushu University
Institute of Environmental Systems
6-10-1 Hakozaki, Fukuoka 812-8581, JAPAN
Phone/Fax: +81-92-642-3788
E-mail: morita@nucl.kyushu-u.ac.jp

²⁾Japan Nuclear Cycle Development Institute
O-arai Engineering Center
4002 Narita, O-arai, Ibaraki 311-1393, JAPAN
Phone: +81-29-267-4141, Fax: +81-29-267-7834
E-mail: tobita@oec.jnc.go.jp

³⁾Forschungszentrum Karlsruhe GmbH
Institut für Kern- und Energietechnik
Postfach 3640, 76021 Karlsruhe, GERMANY
Phone: +49 7247 82-2490, Fax: +49 7247 82-3824
E-mail: tohru.suzuki@iket.fzk.de

ABSTRACT

A new multi-component vaporization/condensation (V/C) model was developed to provide a generalized model for safety analysis codes of liquid metal cooled reactors (LMRs). These codes simulate thermal-hydraulic phenomena of multi-phase, multi-component flows, which is essential to investigate core disruptive accidents of LMRs such as fast breeder reactors and accelerator driven systems. The developed model characterizes the V/C processes associated with phase transition by employing heat transfer and mass-diffusion limited models for analyses of relatively short-time-scale multi-phase, multi-component hydraulic problems, among which vaporization and condensation, or simultaneous heat and mass transfer, play an important role. The heat transfer limited model describes the non-equilibrium phase transition processes occurring at interfaces, while the mass-diffusion limited model is employed to represent effects of non-condensable gases and multi-component mixture on V/C processes. Verification of the model and method employed in the multi-component V/C model of a multi-phase flow code was performed successfully by analyzing a series of multi-bubble condensation experiments. The applicability of the model to the accident analysis of LMRs is also discussed by comparison between steam and metallic vapor systems.

1. INTRODUCTION

The multi-component vaporization/condensation (V/C) model is one of the key constitutive models of safety analysis codes for liquid metal cooled reactors (LMRs) such as fast breeder reactors and accelerator driven systems. This is because mechanistic simulation of an accident sequence during a postulated core disruptive accident (CDA) in such reactors is only achieved by using a comprehensive computational tool that systematically models multi-phase thermal-hydraulic and neutronic phenomena occurring during the so-called transition and expansion phases

of CDA. In this area, the SIMMER-II code was developed as the first practical tool of its kind [1], and has been used in many experimental and reactor analyses [2]. The code has played a pioneering role especially in advancement of the mechanistic simulation of CDAs, but at the same time extensive worldwide code application revealed many limitations due to the code framework as well as needs for model improvement. For this reason, the development of a totally new series of the SIMMER codes [3,4] has been conducted at the Japan Nuclear Cycle Development Institute (JNC) in collaboration with Forschungszentrum Karlsruhe (FZK), Germany, and Commissariat à l'Energie Atomique (CEA), France. The objective of the present study is to develop a V/C model that reliably describes the multi-component phase transition processes for core materials in sufficient physical details for use in reactor safety analysis. The development is intended to provide a generalized model that is useful for analyzing relatively short-time-scale multi-phase, multi-component thermal-hydraulic problems, among which vaporization and condensation, or simultaneous heat and mass transfer, play an important role. The model characterizes the V/C processes associated with phase transition through heat transfer and mass-diffusion limited models to follow the time evolution of the reactor core under CDA conditions. In this paper, the physical models employed as the multi-component V/C model in the new SIMMER codes are described, and then its validity is demonstrated by analyzing a series of multi-bubble condensation experiments.

2. MODELING OF PHASE TRANSITION PHENOMENA

2.1. Non-equilibrium mass transfer model

The phase transition processes occurring at interfaces are described employing a heat transfer limited model. These are non-equilibrium processes because the bulk temperature does not generally satisfy the phase transition condition when the mass transfer occurs at the interface. The basic concept of this model is illustrated in Fig. 1, where a binary contact interface of the energy components A and B is shown. Each energy component interfaces with the other energy components simultaneously, and each interface has a uniquely defined interfacial area. Energy transfers between components are based on the interfacial area and heat transfer coefficients. A specified temperature is assigned to each possible interface to calculate heat flows from/to each interface into/from the respective bulk materials. These heat flows are summed to give net interfacial energy loss or gain. The net energy transfer rate from the interface is defined as:

$$q_{A,B}^I = a_{A,B} [h_{A,B}(T_{A,B}^I - T_A) + h_{B,A}(T_{A,B}^I - T_B)] \quad (1)$$

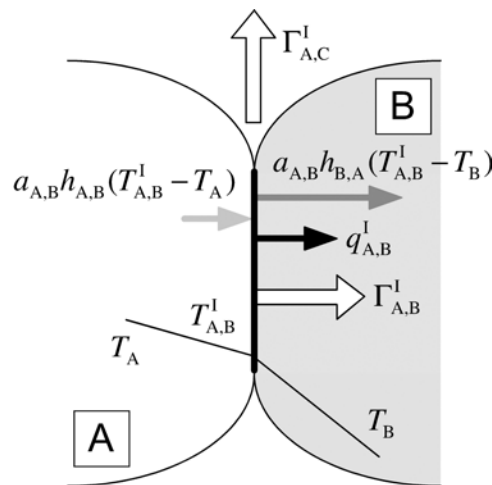


Figure 1: Basis of heat transfer limited process.

An interfacial energy loss is defined as positive and means condensation must occur to conserve (provide) energy. An interfacial energy gain, which is defined as negative, means the energy is going into vaporization. For example, Fig. 1 shows interface (A, B) where the interface is undergoing a net loss energy to component B. This energy is either coming from condensation of component A. The resulting product will be either more of component B, or component C depending on the process involved.

The phase transition rate is determined from energy balance at the interface. If the net heat flow $q_{A,B}^I$ is zero, sensible heat is exchanged without phase transition. If $q_{A,B}^I$ is positive, namely the energy is lost at the interface, a vapor component condenses. Then the mass transfer rate for this case is determined from:

$$\Gamma_{A,B}^I = \frac{q_{A,B}^I}{i_A - i_B^I} \text{ if the component formed by the phase transition is B, or} \quad (2)$$

$$\Gamma_{A,C}^I = \frac{q_{A,B}^I}{i_A - i_C^I} \text{ if component C formed by the phase transition is not B.} \quad (3)$$

If $q_{A,B}^I$ is negative, on the other hand, namely the energy is gained at the interface, a liquid component vaporizes. Then the mass transfer rate for this case is determined from:

$$\Gamma_{B,A}^I = -\frac{q_{A,B}^I}{i_A^I - i_B} \text{ if the component formed by the phase transition is A, or} \quad (4)$$

$$\Gamma_{B,D}^I = -\frac{q_{A,B}^I}{i_D^I - i_B} \text{ if component D formed by the phase transition is not A.} \quad (5)$$

It should be also noted that the latent heat of phase transition is defined here as the difference between the enthalpy at the interface and the bulk enthalpy of a component undergoing a phase transition process. Although more correctly the bulk enthalpy should be replaced with the interfacial one, SIMMER-III does not calculate temperature gradients in liquid and vapors. Besides, the experience from the previous codes suggests that better results are obtained with this definition of effective latent heat [5,6].

When the phase transition is predicted at the vapor/liquid and vapor/solid interfaces, the interface temperatures $T_{A,B}^I$ should be determined so as to take account of the effect of non-condensable gases and multi-component mixtures on vaporization and condensation. Typically, the condensation rate can be reduced significantly when non-condensable gases are present in the vapor mixture due to a buildup of non-condensable gas concentration at which condensation occurs, reducing the condensation saturation temperature below the bulk mixture saturation temperature. The procedure to determine $T_{A,B}^I$ based on the mass diffusion limited process is discussed in the next section. At the liquid/liquid interfaces, $T_{A,B}^I$ is defined as the saturation temperature of a phase transition species. On the other hand, in the case of no mass transfer, the interface energy transfer is zero and hence the equivalent interface temperature should be:

$$T_{A,B}^I = \frac{h_{A,B}T_A + h_{B,A}T_B}{h_{A,B} + h_{B,A}} \quad (6)$$

2.2. Effect of multi-component mixture

The physical model to represent the effect of non-condensable gases and multi-component mixtures on V/C processes is based on a study performed originally for SIMMER-II [1]. The equations for this model were obtained by considering the quasi-steady, stagnant Couette flow

boundary layer, as shown in Fig. 2, to relate the mass and energy fluxes to the overall forces driving heat and mass transfer. This classical Couette flow model has been shown to provide a good engineering model for single-component vapor condensation in the presence of non-condensable gases, thus confirming the adequacy of its theory for incorporation in two-fluid computer codes [7,8,9]. In SIMMER-II, the model extended to multi-component systems was designed to predict not only the suppression of condensation by non-condensable gases such as a fission gas, but also the phase transition rate for a vapor component condensing on the surface of a different material. However, this previous effort was not successful for the practical use of the code because its solution scheme was incompatible with numerical algorithms applied to SIMMER-II multi-phase-flow modeling.

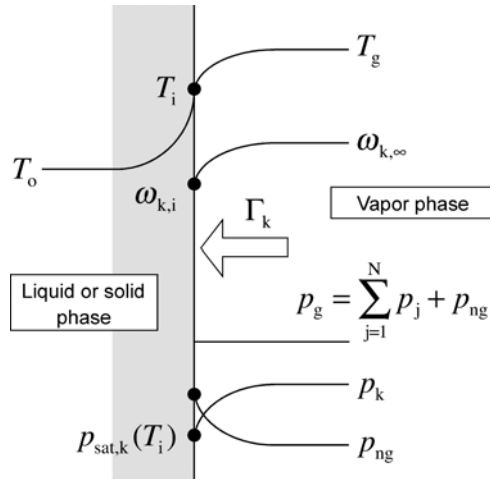


Figure 2: Basis of mass diffusion limited process.

The physical model and coordinate system are shown in Fig. 2. A multi-component vapor mixture at temperature T_g and mass fraction $\omega_{k,\infty}$ ($k = 1 \dots N$) is under the phase transition on a liquid or solid phase, which is maintained at a constant temperature T_o . Here, the conservation of each vapor species can be described based on multi-component diffusion law given, for example, by Bird et al. [10]. Assuming that mass diffusion due to thermal and pressure gradient is negligibly small, the mass transfer rate of vapor component k at the interface i , defined positive for condensation, is governed by:

$$\Gamma_k = a_i \rho_g D_{kg} \left. \frac{d\omega_k}{dy} \right|_i + \omega_{k,i} \sum_{j=1}^N \Gamma_j \quad (7)$$

It is noted that the right side of this equation includes both diffusive and convective contribution.

The heat flow per unit volume at the interface should include contribution of heat conduction, bulk convection and diffusion, that is:

$$q_i = -a_i \kappa \left. \frac{dT}{dy} \right|_i - \sum_{j=1}^N \Gamma_j i_j \quad (8)$$

Thus, approximating the temperature gradients by overall heat transfer coefficients, energy balance applied to the interface yields

$$a_i h_g^* (T_i - T_g) - \sum_{j=1}^N \Gamma_j i_{j,g} = -a_i h_o (T_i - T_o) - \sum_{j=1}^N \Gamma_j i_{j,o}, \quad (9)$$

where h_g^* is the vapor-side heat transfer coefficient in the presence of mass transfer, and then the effect of mass flow through the boundary layer can be accounted for by [10]:

$$h_g^* = - \left(\sum_{j=1}^N \Gamma_j c_{p,j} / a_i \right) / \left[\exp \left(- \sum_{j=1}^N \Gamma_j c_{p,j} / a_i h_g \right) - 1 \right] \quad (10)$$

Equation (9) represents that the heat flow at the interface equals the sum of the latent heat flow and the sensible heat flow through the interface.

The second term on the right side of Eq. (7) is simplified by introducing the mass transfer coefficient in a manner analogous to the heat transfer coefficients, that is

$$\rho_g D_{kg} \left. \frac{d\omega_k}{dy} \right|_i = -k_k^* (\omega_{k,i} - \omega_{k,\infty}), \quad (11)$$

where the mass transfer coefficient k_k^* in the presence of mass transfer is also modeled by [10]:

$$k_k^* = - \left(\sum_{j=1}^N \Gamma_j / a_i \right) / \left[\exp \left(- \sum_{j=1}^N \Gamma_j / a_i k_k \right) - 1 \right] \quad (12)$$

Using the analogy between heat and mass transfer [10], the mass transfer coefficient k_k independent of mass transfer can be evaluated from an experimental correlation developed for sensible heat transfer.

In summary, the interface equations of the mass-diffusion limited model to be solved are described by

$$\Gamma_k = -a_i k_k^* (\omega_{k,i} - \omega_{k,\infty}) + \omega_{k,i} \sum_{j=1}^N \Gamma_j \quad (13)$$

$$\sum_{j=1}^N \Gamma_j i_{lg,j} = a_i \left[h_g^* (T_i - T_g) + h_o (T_i - T_o) \right], \quad (14)$$

where i_{lg} is the latent heat of vaporization as the enthalpy difference between i_g and i_o , but is replaced with the effective latent heat as already discussed. Equations (13) and (14) can be integrated into the following single algebraic equation:

$$\sum_{j=1}^N k_j^* (\omega_{j,i} - \omega_{j,\infty}) i_{lg,j} + \sum_{j=1}^N \omega_{j,i} i_{lg,j} \sum_{j=1}^N k_j^* (\omega_{j,i} - \omega_{j,\infty}) / \omega_{ng} = - \left[h_g^* (T_i - T_g) + h_o (T_i - T_o) \right] \quad (15)$$

The mass fraction $\omega_{k,i}$ of the vapor component k at the interface is determined by the relation between mass and mole fractions:

$$\omega_{k,i} = x_{k,i} W_k / \left(\sum_{j=1}^N x_{j,i} W_j + x_{ng} W_{ng} \right) \quad (16)$$

The mole fractions of vapor component at the interface are obtained by assuming a constant pressure through the boundary layer to the interface. In addition, the condensed phase at the interface is assumed to be in saturated thermodynamic equilibrium with the vapor component, of which saturation pressure in the immiscible system is independent of its concentration in the condensed phase. Treating the vapor components and non-condensable gases as a mixture of ideal gases, the mole fraction $x_{k,i}$ of vapor component k at the interface is related to the interface temperature T_i according to

$$x_{k,i} = \frac{p_{\text{sat},k}(T_i)}{p_g}, \quad (17)$$

where $p_{\text{sat},k}(T_i)$ is the saturation pressure of a phase transition component at the interface and p_g is the total pressure. The total pressure p_g is expressed as the sum of $p_{\text{sat},k}(T_i)$ and the partial pressure of the non-condensable gases at the interface:

$$p_g = \sum_{j=1}^N p_{\text{sat},j}(T_i) + p_{\text{ng},i} \quad (18)$$

In the presence of non-condensable gases, a solution of Eq. (15) in terms of the interface temperature T_i can be obtained iteratively because there are non-linear thermodynamic relationships between T_i and the partial pressures of vapor components. For the case of no non-condensable gas, T_i is evaluated as an iterative solution of Eq. (18) with $p_{\text{ng},i} = 0$.

3. APPLICATION TO MULTI-PHASE FLOW CODES

The new SIMMER codes are multi-dimensional, multi-velocity-field, multi-phase, multi-component, Eulerian, fluid-dynamics codes coupled with a fuel pin model and a space- and energy-dependent neutron kinetics model [3,4]. In the three dimensional code, SIMMER-IV [4], the seven fluid energy components (liquid fuel, steel, sodium; fuel, steel and control particles; and vapor mixture) have 21 binary contact modes, and each fluid component can interact with five kinds of structure surfaces (a fuel pin and four can walls). In this code, 36 paths are treated as the non-equilibrium V/C processes occurring at interfaces. These paths have major effects on key phenomena such as boiling pool dynamics, material expansion (through a channel and into a pool), fuel-coolant interactions, which are directly relevant to accident sequences of a CDA. Typical mass transfer paths are envisioned among a vapor mixture and three liquid components. The liquid vaporization can occur at the liquid/liquid interfaces as well as at the vapor/liquid interfaces. Condensation processes of fuel or steel vapor on other colder liquids can be considered at the vapor/liquid interfaces. The vapor condensation on solid particles and structures is also treated as mass transfer paths. In the new SIMMER codes, the heat transfer coefficients are also determined depending on the flow regime for the binary contacts. The coefficients for solid particles, liquid droplets and gas bubbles are simply based on heat conduction, but the effects of internal circulation and oscillations are also considered for the fluid particles. The convective heat transfer in continuous fluids is formulated by empirical correlations for Nusselt numbers.

The present model was applied to the new SIMMER codes successfully representing these complicated non-equilibrium V/C processes. Employing the heat and mass transfer analogy, the vapor-side mass transfer coefficients independent of mass transfer can be found as a function of the Sherwood number from the empirical correlations developed for sensible heat transfer. For example, correlations for forced convection are generally in the forms:

$$\text{Nu}_g = \frac{h_g L}{\kappa_g} = f(\text{Re}_g, \text{Pr}_g) \quad \text{and} \quad (19)$$

$$\text{Sh}_g = \frac{k_g L}{\rho_g D_{kg}} = f(\text{Re}_g, \text{Sc}_g) \quad (20)$$

The binary contact areas for possible contact interfaces are determined based on the convective interfacial areas and a flow regime, which describes the geometry of the multi-phase flow [11]. By solving Eq. (15) in terms of the interface temperature T_i at each binary interface, both the condensation rate suppressed by non-condensable gases and the condensation rate on the surface of a different material can be considered simultaneously. To recast both heat transfer and mass

diffusion limited models in a mathematical form compatible with the solution algorithm of SIMMER, an advanced numerical method was newly developed in order to make it suitable for implementation in the codes because a simultaneous solution of Eq. (15) and conservation equations used for the V/C calculation would be complex and inefficient numerically [12].

4. MODEL VERIFICATION

A new series of multi-bubble condensation experiments was performed to demonstrate that the new SIMMER codes using the present V/C model are practically applicable to multi-component, multi-phase flow systems with phase transition. In the experiments, a mixture of steam and non-condensable gas was injected into a thin rectangular water pool. Nitrogen or xenon was used as a non-condensable gas in the mixture. A schematic view of the experimental apparatus is illustrated in Fig. 3. Through five narrow nozzles at the bottom of the pool, multi-bubble flow was produced in the pool such that almost no breakup and coalescence of bubbles occur. The pool of 3 cm depth and 30 cm width was filled with slightly subcooled water up to 36 cm from the exits of the injection nozzles. The flow pattern and the bubble distribution in the pool were recorded directly as digital motion pictures. Quantitative information such as bubble diameter and void fraction was obtained from visualized images, as shown in Fig. 4, using an image processing technique, of which accuracy was also confirmed through some calibrations [13]. Concentration of non-condensable gas in the mixture and water subcooling in the pool were taken as experimental parameters as well as a species of non-condensable gas in the mixture. In SIMMER calculations, a 40 cm high rectangular pool with the cover gas region was modeled by a two-dimensional geometry with 37 lateral and 50 axial computational cells. The gas-mixture was injected from discrete computational cells simulating the five narrow nozzles. This condition is different from our previous experimental calculations [14], in which a uniform injection was assumed from bottom cells.

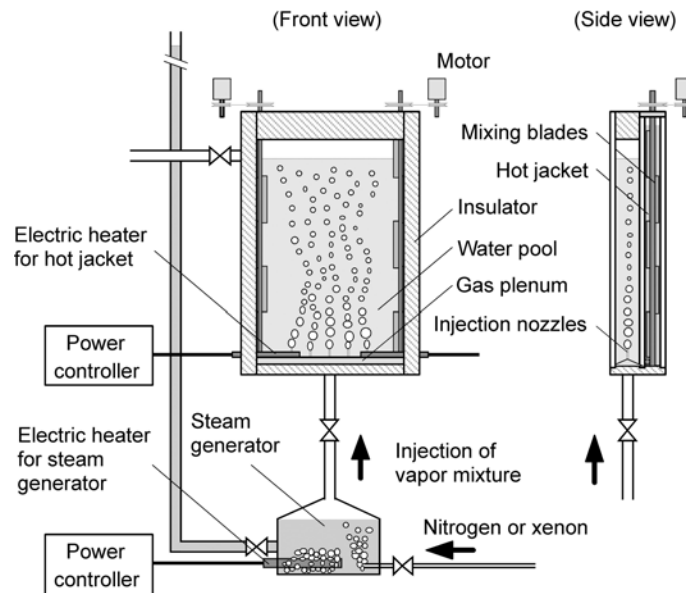


Figure 3: Schematic view of experimental apparatus.

In Fig. 5, vertical distributions of mean bubble diameter above the nozzle exits are compared between observations and SIMMER predictions for various nitrogen concentrations. Here, the experimental data were obtained under the conditions of pool water subcooling of 1.1 ~ 1.9 K and steam flow rate of $6.7 \sim 6.8 \times 10^2$ l/h. The mean bubble diameters were evaluated as lateral- and time-averaged values for 10 sec. For pure steam condensation, where the liquid-side heat transfer dominates the process, multi-bubbles injected from the nozzles condense completely at about

90 mm above the nozzle exit. On the other hand, the size of steam-nitrogen mixture bubbles approaches a non-zero value, which depends on nitrogen concentration, during their condensation. It can be seen from Fig. 5 that the vertical bubble-size distributions are appropriately represented by SIMMER using the present V/C model for variable amounts of nitrogen. SIMMER predicts the definite differences in bubble size depending on the nitrogen concentration. These differences are much larger than experimental uncertainty [13].

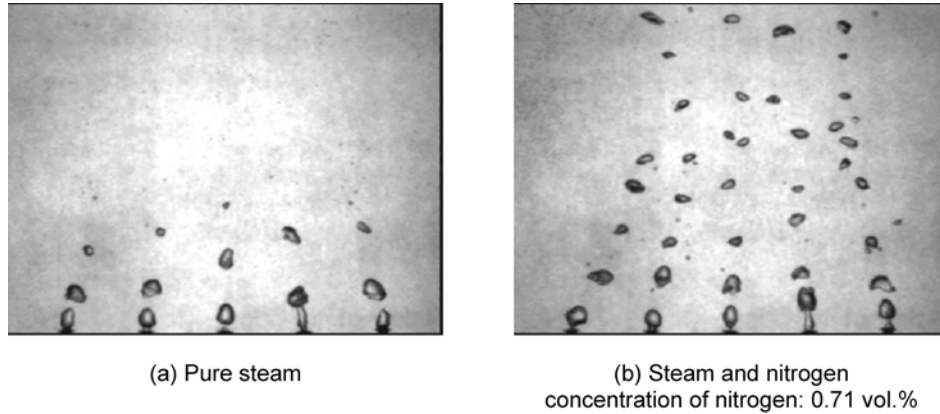


Figure 4: Photographs of multi-bubble flows with condensation.

The effect of thermo-physical properties of non-condensable gas on multi-bubble condensation was also investigated by comparison between steam-nitrogen and steam-xenon mixtures. Figure 6 shows the results for 0.71 vol. % concentration of non-condensable gas. Here, the experimental data were obtained under the conditions of pool water subcooling of 1.6 ~ 1.8 K and steam flow rate of 6.7×10^2 l/h. As shown in Fig. 6, the condensation rate in the steam-xenon system becomes smaller than that in the steam-nitrogen system. This is because the diffusion coefficient in the steam-xenon system is smaller than that in the steam-nitrogen one due to the larger molecular weight of xenon than that of nitrogen. In other words, a mass transfer resistance for the diffusion of steam toward the interface in the steam-xenon system is larger than that in the steam-nitrogen one. SIMMER also reproduces this gas property effect depending on a species of non-condensable gas suitably.

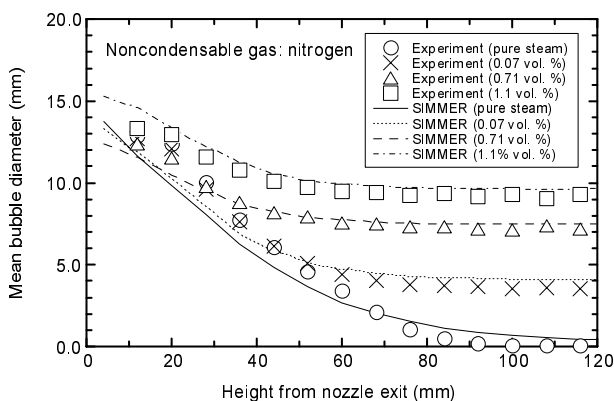


Figure 5: Vertical distributions of mean bubble diameter for variable amount of nitrogen concentration.

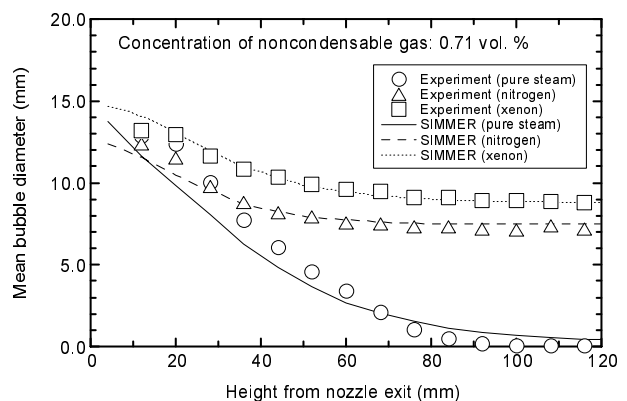


Figure 6: Vertical distributions of mean bubble diameter for different species of non-condensable gas.

As shown in Figs. 5 and 6, in the cases of non-condensable gas presence, the results show that the influence of non-condensable gas on condensation is remarkably large even if the mixture has only a low concentration of non-condensable gas. The process must be affected by the mass

diffusion. In Fig. 7, the vapor-liquid interface temperatures in the case of steam-xenon mixture are compared between the predictions by the present V/C model and only by the heat transfer limited model. In the latter prediction, the interface temperature corresponds to the steam saturation one. It can be seen from this figure that the result with the mass-diffusion process indicates considerable reduction in the interface temperature. This is because the non-condensable gas accumulates at the liquid-vapor interface due to the mass transfer toward the interface. The vertical distribution of average void fraction shown in Fig. 8 indicates that the resultant condensation rate is reduced definitely when compared to the prediction controlled only by the heat transfer.

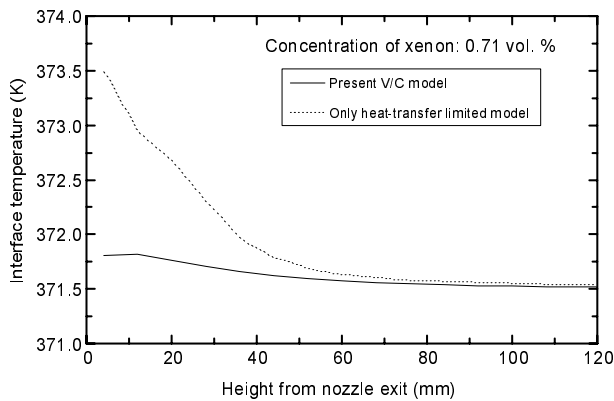


Figure 7: Vertical distributions of vapor-liquid interface temperature (effect of mass-diffusion process).

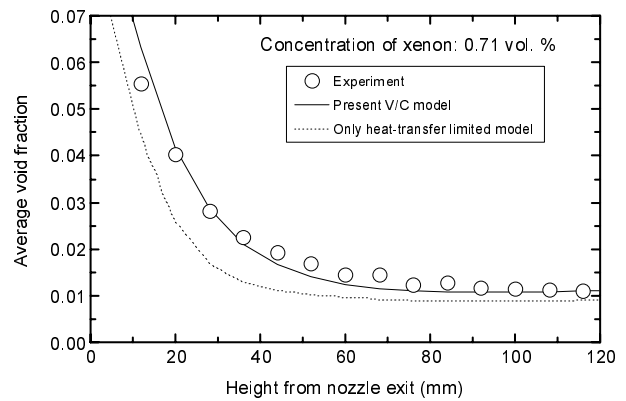


Figure 8: Vertical distributions of average void fraction (effect of mass-diffusion process).

In the experiment, a peculiar oscillatory behavior of multi-bubble motion was observed in the rectangular pool. This is a two-dimensional flow pattern with the bubble condensation as shown in Fig. 9. The observed transient of two-dimensional void distributions is indicated as a series of void-fraction contours in Fig. 9 (a), which was obtained through the image-processing technique. Figure 9 (b) shows the SIMMER result corresponding to the observation. A similar two-dimensional oscillatory motion with about a 20 sec cycle, which is comparable to the observation, is well reproduced by SIMMER. It is encouraged that SIMMER using the present V/C model can represent not only condensation behavior of multi-bubbles, but also their fluid motion in the rectangular pool qualitatively.

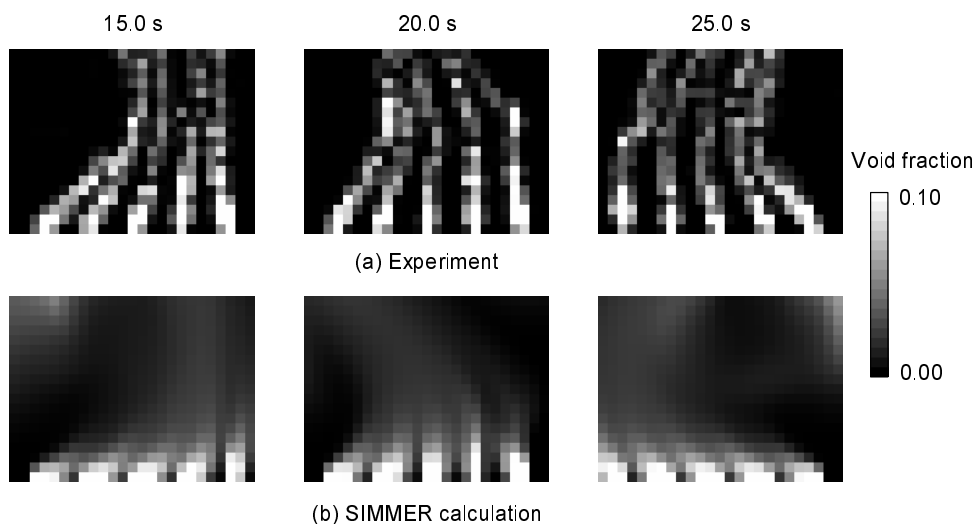


Figure 9: Two-dimensional transient of multi-bubble motion in the rectangular pool near the nozzle exits (concentration of xenon: 0.71%).

5. DISCUSSION

Basic validity of the present multi-component V/C model for different species of non-condensable gas in the mixture has been demonstrated using a series of multi-component phase transition experiments [14]. However, the results suggested that the present model could give rather poor estimation of the non-condensable gas effect if the Lewis number ($= \alpha_g / D_{kg}$) of the mixture is too far from unity. This might be because the present model representing the mass diffusion process employs the heat and mass analogy in evaluating the vapor-side mass transfer coefficients, as described in Chapter 3. For example, the model gave relatively large underestimation of the non-condensable gas effect in the case of steam-helium mixture, of which Lewis number is about 0.18, especially for the high concentrations of non-condensable gas in the mixture. On the other hand, for the steam-air and steam-nitrogen mixtures with the Lewis number of about 0.65, the results showed reasonable solutions for variable amounts of non-condensable gas in the mixture. Under the present experimental conditions of the multi-bubble condensation, the Lewis numbers of steam-nitrogen and steam-xenon mixtures are about 0.84 and 1.2, respectively.

For the accident analysis of LMRs, we have to consider a mixture of liquid metal coolant vapor and fission gas. Typical coolant materials of LMRs are, for example, sodium and lead-bismuth eutectic (LBE). Evaluating their vapor properties using the thermophysical property model of SIMMER [15], the Lewis numbers of sodium-xenon and LBE-xenon mixtures are about 0.68 and 0.73, respectively, at their boiling points. As compared to the experimental results for steam-non-condensable gas mixtures, this suggests that the present model yield reasonable predictions for the typical mixtures of liquid metal coolant vapor and fission gas. Therefore, it is expected that the present model could represent the effect of multi-component mixture on the phase transition in sufficient physical details for use in reactor safety analysis. Experimental verification is highly required to demonstrate the applicability of the model to the metallic vapor systems.

6. CONCLUSIONS

A generalized multi-component V/C model has been developed for analyses of relatively short-time-scale multi-phase, multi-component thermal-hydraulic problems. The model characterizes the V/C processes associated with phase transition by employing heat transfer and mass diffusion limited models to describe the non-equilibrium phase transition processes occurring at interfaces and the effects of non-condensable gases and multi-component mixture on V/C behaviors. It was demonstrated that the model incorporated in multi-phase flow codes represents the condensation process in the vapor and non-condensable gas mixtures appropriately in the case of their Lewis numbers are not far from unity. The applicability of the model to the mixtures of liquid metal coolant vapor and fission gas was discussed, and it is indicated that the present V/C model would be expected to simulate the multi-component phase transition processes reliably in sufficient physical details for use in the accident analysis of LMRs.

ACKNOWLEDGEMENTS

A part of this work was performed as joint researches between JNC, FZK and Kyushu University. The authors wish to thank Tatsuya Matsumoto, Ryo Akasaka, Takashi Uyama and Takashi Ishibashi of Kyushu University for their contributions to this work.

NOMENCLATURE

a	Binary-contact area per unit volume (m^{-1})
$a_{A,B}$	Binary-contact area of the A/B interface per unit volume (m^{-1})

c_p	Specific heat at constant pressure ($\text{J kg}^{-1} \text{K}^{-1}$)
D_{kg}	Binary diffusivity of component k in a multi-component mixture ($\text{m}^2 \text{s}^{-1}$)
h^*, h	Heat transfer coefficient with and without mass transfer, respectively ($\text{W m}^{-2} \text{K}^{-1}$)
$h_{A,B}$	Heat transfer coefficient for side A of the A/B interface ($\text{W m}^{-2} \text{K}$)
i_{lg}	Heat of vaporization (J kg^{-1})
i	Specific enthalpy (J kg^{-1})
i_A^I	Specific enthalpy of the component A at the interface (J kg^{-1})
k^*, k	Mass transfer coefficient with and without mass transfer, respectively ($\text{kg m}^{-2} \text{s}^{-1}$)
L	Characteristic length (m)
N	Number of condensable gases
Nu	Nusselt number
p	Pressure (Pa)
q	Heat transfer rate per unit volume (W m^{-3})
$q_{A,B}^I$	Net Heat transfer rate at the A/B interface per unit volume (W m^{-3})
Pr	Prandtl number
Re	Reynolds number
Sc	Schmidt number
Sh	Sherwood number
T	Temperature (K)
$T_{A,B}^I$	Interface temperature at the A/B interface (W m^{-3})
W	Molecular weight (kg mol^{-1})
x	Mole fraction
y	Coordinate normal to interface (m)
α	Thermal diffusivity ($\text{m}^2 \text{s}^{-1}$)
Γ	Mass transfer rate per unit volume ($\text{kg s}^{-1} \text{m}^{-3}$)
$\Gamma_{A,B}^I$	Mass transfer rate from component A to B ($\text{kg s}^{-1} \text{m}^{-3}$)
κ	Thermal conductivity ($\text{W m}^{-1} \text{K}^{-1}$)
ρ	Density (kg m^{-3})
ω	Mass fraction

Subscripts

A, B, C, D	Species in multi-component systems
g	Vapor mixture
i	Interface quantity
j, k	Species in multi-component systems
ng	Non-condensable gas
o	Condensation site
sat	Saturation quantity
∞	Bulk quantity

REFERENCES

- [1] Bohl, W. R., & Luck, L. B., SIMMER-II: A Computer Program for LMFBR Disrupted Core Analysis, Los Alamos National Laboratory, LA-11415-MS, 1990.
- [2] Smith, L. L., Bell, C. R., Bohl, W. R., Luck, L. B., Wehner, T. R., DeVault, G. P., & Parker, F. R., The SIMMER Program: Its Accomplishment, Proc. Int. Mtg. on Fast Reactor Safety, pp. 977-980, Knoxville, TN, April 1985.

- [3] Kondo, Sa., Yamano, H., Suzuki, T., Tobita, Y., Fujita, S., Cao, X., Kamiyama, K., Motita, K., Fischer, E. A., Brear, D. J., Shirakawa, N., Mizuno, M., Hosono, S., Kondo, T., Maschek, W., Kiefhaber, E., Buckel, G., Rineinski, A., Flad, M., Coste, P., Pigny, S., Louvet, J., & Cadiou, T., SIMMER-III: A Computer Program for LMFR Core Disruptive Accident Analysis, Japan Nuclear Cycle Development Institute, JNC TN9400 2001-002, 2000.
- [4] Kondo, Sa., Yamano, H., Y. Tobita, Y., Fujita, Morita, K., Mizuno, M., Hosono, S., & Kondo, T., SIMMER-IV: A Three Dimensional Computer Program for LMFR Core Disruptive Accident Analysis – Version 1.B Model Summary and Program Description –, Japan Nuclear Cycle Development Institute, JNC TN9400 2001-003, 2000.
- [5] Bohl, W. R., Wilhelm, D., Parker, F. R., Berthier, J., Goutagny, L., & Ninokata, H., AFDM: An Advanced Fluid-dynamics Model, Volume I: Scope, Approach, and Summary, Los Alamos National Laboratory, LA-11692-MS, Vol. I, 1990.
- [6] Bohl, W. R., Investigation of Steam Explosion Loadings using SIMMER-II, U.S. Department of Energy, NUREG-CP-72, Vol. 6, pp. 159-174, 1986.
- [7] Ghiaasiaan, S. M., Kamboj, B. K., & Abdel-Khalik, S. I., Two-fluid Modeling of Condensation in the Presence of Non-condensables in Two-phase Channel Flows, Nucl. Sci. Eng., 119, pp. 1-17, 1995.
- [8] Yao, G. F., Ghiaasiaan, S. M., & Eghbali, D. A., Semi-implicit Modeling of Condensation in the Presence of Non-condensables in the RELAP5/MOD3 Computer Code, Nucl. Eng. and Des., 166, pp. 217-291, 1996.
- [9] Yao, G. F., & Ghiaasiaan, S.M., Numerical Modeling of Condensing Two-phase Flows, Numerical Heat Transf., B, 30, pp. 137-159, 1996.
- [10] Bird, B., Stewart, W. E., & Lightfoot, E. N., Transport Phenomena, John Wiley and Sons, New York, 1960.
- [11] Tobita, Y., Morita, K., Kondo, Sa., Shirakawa, N., Bohl, W. R., Parker, F. R., Brear, D. J., Interfacial Area Modeling for a multi-phase, multi-component Fluid-Dynamics Code, Proc. Int. Conf. on Multi-phase Flows '91-TSUKUBA, Vol. 2, pp. 361-364, Tsukuba, Japan, September 1991.
- [12] Morita, K., Matsumoto, T., Akasaka, R., Fukuda, K., Suzuki, T., Tobita, Y., Yamano, H., & Kondo, Sa., Development of multi-component Vaporization/Condensation Model for a Reactor Safety Analysis Code SIMMER-III – Theoretical modeling and basic verification –, Nucl. Eng. and Des., 2002, in submission.
- [13] Suzuki, T., Tobita, Y., Yamano, H., Kondo, Sa., Morita, K., Matsumoto, T., Akasaka, R., & Fukuda, K., Development of multi-component Vaporization/Condensation Model for a Reactor Safety Analysis Code SIMMER-III – Extended verification using multi-bubble condensation experiment –, Nucl. Eng. and Des., 2002, in submission.
- [14] Morita, K., Matsumoto, T., Akasaka, R., Fukuda, K., Suzuki, T., Tobita, Y., Yamano, H., & Kondo, Sa., Advanced Modeling of multi-component Vaporization/Condensation Phenomena for a Reactor Safety Analysis Code SIMMER-III, Proc. 10th Int. Conf. on Nuclear Engineering, ICONE10-22229, Arlington, VA, April 2002.
- [15] Motita, K., Tobita, Y., Kondo, Sa., & Fischer, E.A., SIMMER-III Analytic Thermophysical Property Model, Japan Nuclear Cycle Development Institute, JNC TN9400 2000-004, 1999.

G. Physical Interpretation by Numerical Simulation

NUMERICAL SIMULATION OF BUBBLE-TRAIN FLOW IN A SMALL CHANNEL OF SQUARE CROSS-SECTION

B. Ghidersa, M. Wörner, D. G. Cacuci

Forschungszentrum Karlsruhe GmbH
Institut für Reaktorsicherheit
Postfach 36 40, 76021 Karlsruhe, GERMANY
Phone: +49 7247 82-3764, Fax: +49 7247 82-3718,
E-mail: ghidersa@irs.fzk.de

ABSTRACT

Bubble-train flows in small channels are widely used in industrial applications due to their good mixing properties and heat transfer enhancement. In this paper, the three-dimensional flow structure of a bubble-train flow in a square capillary is analyzed using direct numerical simulation. For a fixed value of the void fraction ($\varepsilon = 33\%$) the influence of the interface surface tension is studied by considering two different values of the Capillary number. Comparison of the computed global parameters with experimental data reported in the literature for these values of the Capillary number shows good agreement.

1. INTRODUCTION

Flow channels with hydraulic diameters (D_h) of 1mm or below are applied e.g. in compact heat exchangers, microelectronic cooling systems, chemical processing, or small-sized refrigeration systems. In many of these applications frequently gas-liquid two-phase flow occurs. Because the importance of surface tension increases with decreasing channel size, the hydrodynamics of gas-liquid two-phase flow in small channels in principal differ from that in larger channels. For design, optimization and safe operation of devices built from micro-channels the understanding of the basic hydrodynamic phenomena in a single channel is mandatory. This motivates an increasing number of experimental and theoretical studies devoted to this topic. Recently, Triplett et al. ([1],[2]) studied the two-phase flow patterns, void fraction and the pressure drop of air-water two-phase flows in a horizontal circular or triangular channel with diameters of order of 1 mm. Depending on the gas and liquid flow rates, bubbly, slug, churn and annular flow regimes have been identified. For both circular and triangular channels the flow pattern transition is different than the one predicted using large channels correlations.

The present numerical study investigates the slug flow in straight capillaries of square cross-section. This type of flow, also referred as bubble-train flow [3], consists of trains of long bubbles separated by liquid slugs. The bubbles occupy most of the channel cross-section while the liquid slugs are free of smaller bubbles [1]. Breakage and coalescence of bubbles is largely absent. Due to the dominance of the surface tension effects the walls are always wetted and a thin liquid layer separates the gas from the channel walls. Bubble-train flow is very effective to increase heat and mass transfer rates compared to single-phase and therefore is widely used in gas-liquid processing. Thulasidas et al. [3] examined the bubble size and shape, bubble velocity, and volume fraction of gas inside capillaries of circular and square cross-section for slug flow regime. These parameters are of significant interest in predicting the mass transfer rates between the fluid and the wall. Thulasidas et al. [4] uses a particle imaging velocimetry (PIV) to determine the velocity distribution inside the liquid slug. Video images recorded in a reference frame moving with the bubble indicate the

presence of recirculating patterns with a high degree of mixing. Depending on the capillary number of the flow, counter rotating vortices or a complete bypass flow inside the liquid slug were observed.

While these experimental approaches offer the advantage of dealing directly with the physical problem they have limited access to the local characteristics of the flow in small channels, where only non-intrusive methods can be used. Our goal here is to study the local characteristics of the flow by means of direct numerical simulation (DNS). For this we use an extended and improved version of our in-house computer code TURBIT-VOF [5], which was originally developed for investigation of bubbly flow in large channels. To account for the phase-interface evolution the volume fraction of the continuous phase is tracked using a Volume of Fluid method. A short description of the equations and the computer code TURBIT-VOF will be given in section 2 while the numerical set-up will be described in section 3. The structure of the flow inside the bubble and in the liquid phase will be then analyzed for bubble-train flows at two different values of Capillary number. To validate our method the numerical results will be compared with experimental data from the literature. In section 5 we present the conclusions.

2. MATHEMATICAL AND NUMERICAL BACKGROUND

The direct numerical simulations are performed with an extended and improved version of our in-house computer code TURBIT-VOF [5]. The code is based on a single set of equations for the entire domain, which expresses the conservation of mass, momentum and enthalpy for a continuous Newtonian fluid [6]. Starting from the local instant equations, a set of volume-averaged equations for each phase are written. These equations and the local interface jump conditions are used to write a single set of equations for the mean values of the variables. These mean values are defined in terms of volume averaging.

If V is a control volume, which, in our case, is taken to be a computational cell, for incompressible fluids, the dimensionless continuity equation becomes

$$\nabla \cdot \bar{\mathbf{v}}_m = 0 \quad (1)$$

while the momentum equation, in dimensionless form, is

$$\frac{\partial \rho_m \bar{\mathbf{v}}_m}{\partial t} + \nabla \cdot \rho_m \bar{\mathbf{v}}_m \bar{\mathbf{v}}_m = -\nabla P + \frac{1}{Re_{ref}} \nabla \cdot \bar{\boldsymbol{\tau}}_m - (1-f) \frac{E\ddot{\sigma}_{ref}}{We_{ref}} \frac{\bar{\mathbf{g}}^*}{g^*} + \frac{1}{We_{ref}} \kappa \bar{n} a_{int} \quad (2)$$

where, f is the liquid volume fraction within the averaging volume V , and ρ_m is the dimensionless mean density,

$$\rho_m = \frac{f\rho_l^* + (1-f)\rho_g^*}{\rho_l^*}. \quad (3)$$

In (2) we use the reduced pressure P , which is the difference between the pressure p in that point and the liquid hydrostatic pressure in the same point $\left(\frac{\bar{\mathbf{x}}^* \cdot \bar{\mathbf{g}}^*}{L_{ref}^* (v_{ref}^*)^2} \right)$. Due to this, the influence of the gravity in the momentum equation is accounted by a buoyancy term. The last term in (2) expresses the contribution of the surface tension forces in the momentum balance for the volume V . There, κ is the interface curvature, $\bar{\mathbf{n}}$ is the unit normal vector to the interface, pointing from the gas into the liquid, and a_{int} is the interfacial area concentration within the volume V . In the previous equations the superscript (*) denotes dimensional quantities, while the subscript m denotes the mean value of the corresponding quantity. The dimensionless momentum equation has been obtained using the

liquid inertia $\rho_l^*(v_{ref}^*)^2$ as reference scaling quantity. Thus, the definitions of the reference Reynolds number (Re_{ref}), reference Weber number (We_{ref}) and reference Eötvös number ($Eö_{ref}$) appearing in (2) are:

$$Re_{ref} = \frac{\rho_l^* L_{ref}^* v_{ref}^*}{\mu_l^*}; \quad (4)$$

$$We_{ref} = \frac{\rho_l^* L_{ref}^* (v_{ref}^*)^2}{\sigma^*}; \quad (5)$$

$$Eö_{ref} = \frac{(\rho_l^* - \rho_g^*) g (L_{ref}^*)^2}{\sigma^*}. \quad (6)$$

To account for the phase-interface evolution the volume fraction of the continuous phase is tracked using a Volume of Fluid procedure. Thus, the liquid volumetric fraction is advected using the transport equation

$$\frac{\partial f}{\partial t} + \nabla \cdot (\vec{v}_m f) = 0 \quad (7)$$

while the interface inside each volume V is reconstructed using the PLIC (Picewise Linear Interface Calculation) method EPIRA (for details, see[5]).

To numerically integrate the momentum equation (2) while enforcing the continuity condition (1) a projection method is used: first, an intermediate velocity field is computed using the equation (2) in which the pressure gradient is neglected. The time integration is done using a third order Runge-Kutta scheme. A second order central difference scheme is used to approximate the convective and diffusive terms. For the discretization of the surface tension term we refer to [5]. This velocity field is not divergence-free. To obtain a velocity that satisfies the continuity condition (1) a projection step is required, that is, compute the pressure gradient that we have neglected in the previous step and construct the projection operator. This operator is then applied to the intermediate velocity field. Special care is taken when the gradient of the (physically discontinuous) pressure at the phase-interface is computed.

The form of the equations (1), (2) and (7) as given above already implies that within volume V both phases have the same volume-averaged velocity and that there is no source term due to phase transfer across the interface, i.e. the velocity is continuous. The first assumption corresponds to a locally homogenous model [6].

3. NUMERICAL SETUP

In small channels, the channel length is typically much larger than its hydraulic diameter, therefore, one can identify a region where there is no influence of the entrance effects and the bubbles have identical shape, they move with the same velocity and are uniformly distributed along the channel. Thus, one can define a fluid cell consisting of a bubble and the slug in the rear of the bubble that fully characterizes the bubble-train flow in the steady region. Experimentally, the measurements are done by following the fluid cell in its movement along the channel by a moving camera. Numerically, we define the computational domain so that it has the same dimensions as the fluid cell. This domain is fixed while the bubbles move through it (see Figure 1). The presence and influence of the neighboring cell is simulated using periodic boundary conditions in streamwise direction.

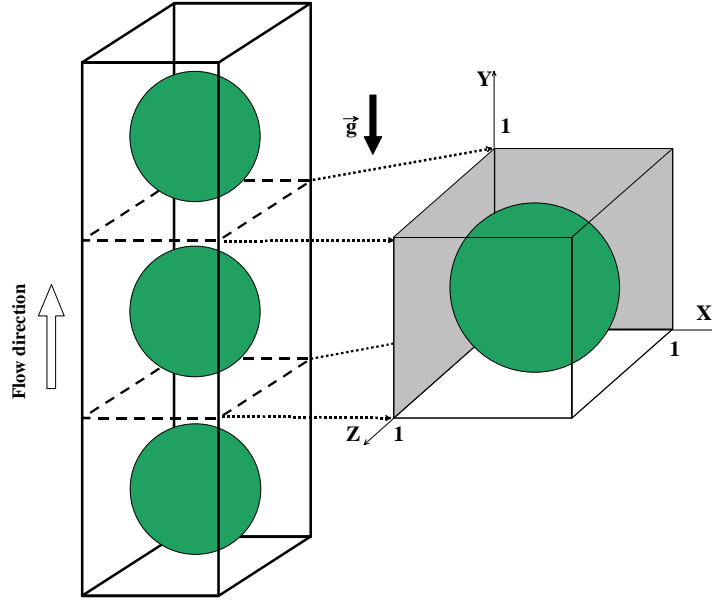


Figure 1: Computational domain and initial condition

For the present study we consider the case where the length L_y^* of the fluid cell is the same as the width of the channel $L_x^* = L_z^* = L_{ref}^*$. In Figure 1 the coordinate system and a sketch of the computational domain is presented. The computational domain in terms of L_{ref}^* is $1 \times 1 \times 1$ and is discretized by 64^3 uniform mesh cells. The flow is in y-direction while in the other two directions walls bound the domain where no-slip boundary conditions are used.

The simulation is started from an initially spherical bubble with diameter $d^* = 0.858 L_{ref}^*$; this corresponds to an overall void fraction of $\varepsilon = 33\%$. To establish a specific overall flow rate a constant pressure drop is imposed in y-direction.

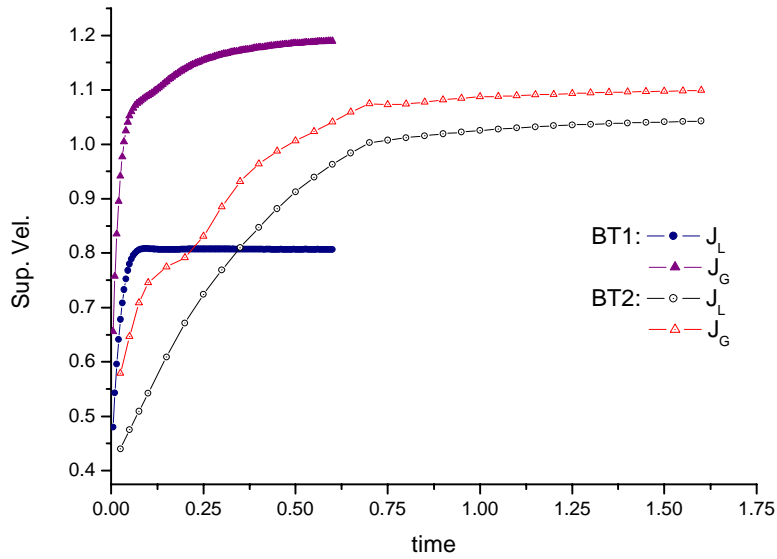


Figure 2: Time evolution of the dimensionless liquid and gas superficial velocities.

4. RESULTS AND DISCUSSIONS

In this section we present the results for two different cases (Table I). Initially the flow is accelerated but, after a transient, the simulation results in a fully developed regime with constant gas and liquid flow rates (Figure 2). In the first case (BT1) we simulate a flow for which the kinematic viscosity of the liquid is three times larger than for the gas. After $t = 0.6$, the bubble shape and velocity are steady. Because of the high value of the liquid viscosity the liquid layer near the wall is thick and the bubble is axisymmetric.

Table I Simulation parameters. The Re and $E\ddot{o}$ numbers are computed using the bubble diameter and bubble velocity as reference length, and velocity, respectively.

	ε	ρ_g / ρ_l	μ_g / μ_l	Re	$E\ddot{o}$	$-\Delta p/L$	J_L	J_G
BT1	33 %	1/81	1/260	1.35	1.065	27	0.806	1.189
BT2	33 %	1/78	1/25	75.88	1.347	0.2	1.04	1.10

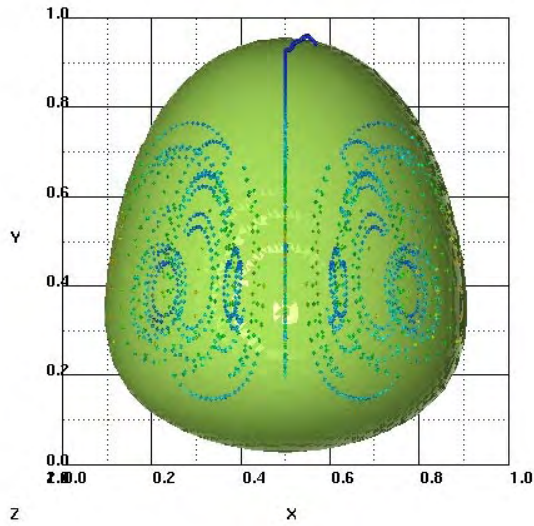
In the second case (BT2) the liquid is taken to be less viscous than in the first case, therefore it takes more time for to have a steady bubble shape and bubble velocity ($t = 1.0$). The bubble diameter becomes larger than in the (BT1) case and almost fills the channel width. Since the liquid film in the axial planes becomes very thin the liquid is pushed to the corners of the channel and it is strongly accelerated. This results in a stronger mixing both in the liquid slug and inside the bubble. The flow inside the bubble for the two cases is compared in Figure 3. For that, we consider the referential linked to the bubble center of mass and insert massless particles into the flow at different position inside the bubble. Since the flow is steady and the bubbles move with constant speed there is no need to take in to account acceleration effects. For (BT1) the gas inside the bubble forms a single annular vortex while in (BT2) a second vortex appears at the rear side of the bubble. The presence of the second vortex can be explained by a more intense recirculation in the liquid slug.

The strong mixing inside the bubble is of great interest in chemical processing where the bubbles are used as micro-reactors in which the precipitation reagents are thoroughly mixed avoiding the heterogeneous reaction conditions in classical large batch reactors. For the heat exchangers, the structure of the flow inside the liquid is more important. In Figure 4 the flow in the liquid layer between the bubble and the walls and in the liquid slug is presented. Again, a referential linked to the bubble is used. The massless particles are inserted in front of the bubble ($y=1$). At the corner of the channel the particles have a rectilinear trajectory and their velocity is almost constant along the channel. Close to the bubble, particles are accelerated as they approach the cross-section where the bubble has the larger diameter, and then decelerate, some of the particles being captured in the vortex behind the bubble. For the BT2 case, the presence of the second vortex inside the bubble generates also two vortices in the liquid slug: one close to the rear side of the bubble that is coupled with the vortex at the bottom of the bubble, and a second one coupled with the vortex at the top of the next bubble.

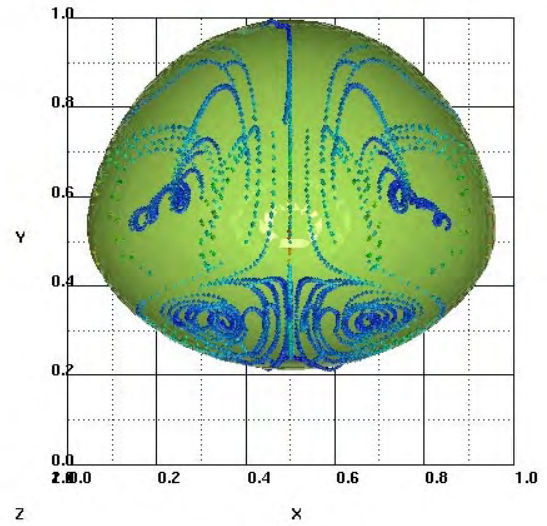
In order to assess our numerical code we compare the results with the experimental data obtained by Thulasidas *et al.* [3] (Figure 5). They measured the bubble diameter and the bubble velocity for a bubble-train flow in a square channel with a hydraulic diameter of 2 mm. From the measured values they compute the dimensionless bubble diameter D_B/D_h , dimensionless bubble velocity $U_B/(J_L + J_G)$, and the relative bubble velocity $W = (U_B - v_{ls})/U_B$, where v_{ls} is the liquid slug velocity. They plot their results as a function of the Capillary number of the flow $Ca = \mu_l U_B / \sigma$. The values of these parameters obtained from the numerical simulations are given in Table II.

Table II Computed Capillary number, dimensionless bubble diameter, bubble velocity and relative bubble velocity.

	Ca	D_B/D_h	$U_B/(J_L + J_G)$	W
BT1	0.205	0.798	1.80	0.445
BT2	0.043	0.919	1.55	0.355

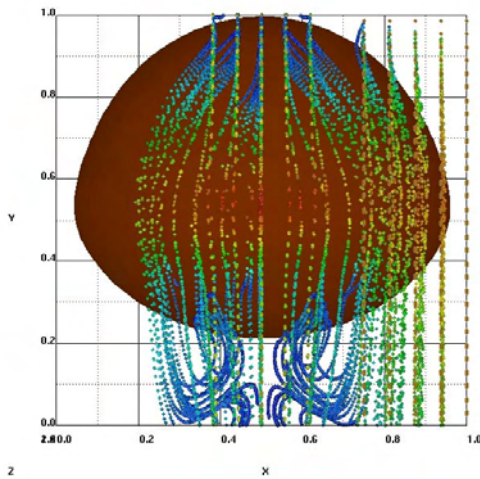


(BT1) $t = 0.6$

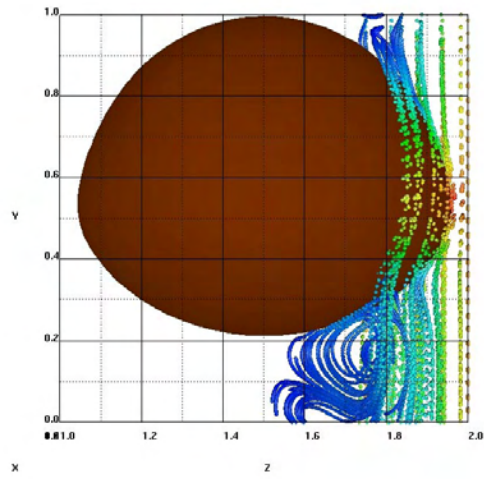


(BT2) $t = 1.4$

Figure 3: Visualization of the flow structure inside the bubble. Massless particles were inserted inside the bubble and advected by the velocity field, in a referential linked to the bubble center of mass.

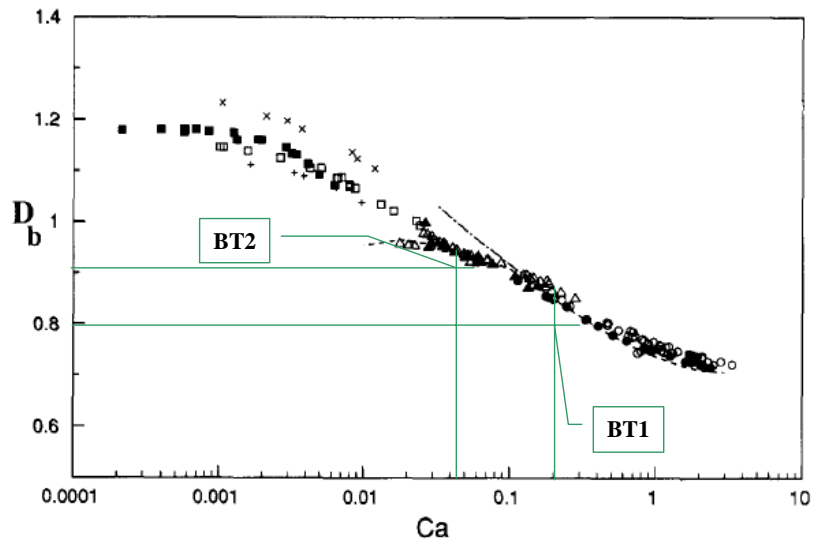


(a)

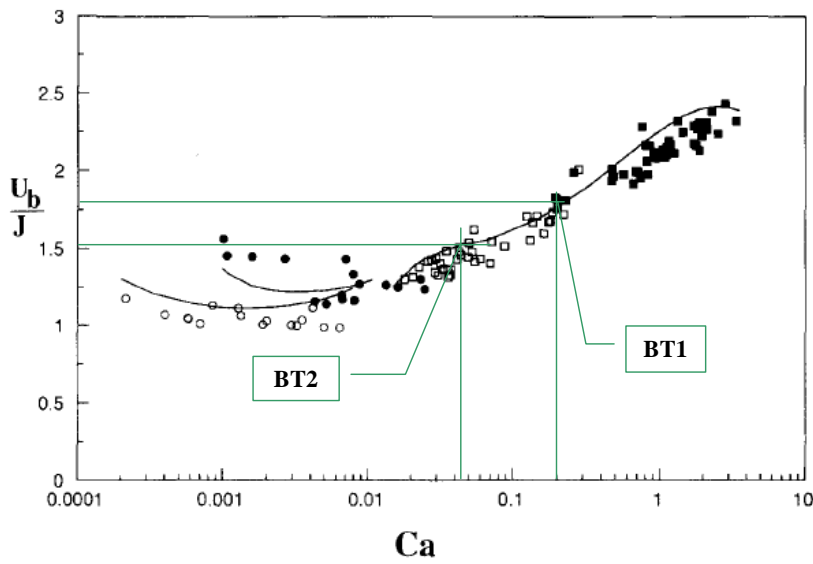


(b)

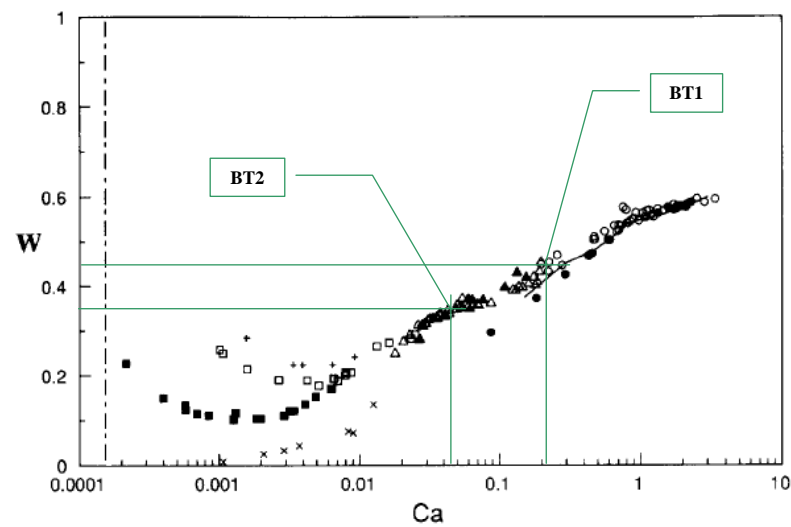
Figure 4: Visualization of the flow structure in the liquid for the BT2 case: front view (a); lateral view (b). A referential linked to the bubble center of mass is used. The massless particles are inserted in the top of the computational domain and they move along the current lines of the flow.



(a)



(b)



(c)

Figure 5: Comparison of the computed values (Table II) with experimental data from Thulasidas *et al.* [3]: (a) dimensionless bubble diameter; (b) dimensionless bubble velocity ($J = J_L + J_G$); (c) relative bubble velocity ($W = (U_B - v_{ls})/U_B$). Reproduced from [3].

For the dimensionless bubble diameter (Figure 5.a) the computed values are slightly smaller than the measured values. This difference can be explained by the fact that in experiments the bubbles have the length several times the channel width and the diameter is measured in the cylindrical part while in our computations the bubbles are much shorter and can not develop in a Taylor bubble. For the bubble velocity and relative bubble velocity we have a better agreement, the computed values being in the range of the measured data (Figure 5.b, c).

5. CONCLUSIONS

In the present paper we use direct numerical simulation to investigate the local characteristics of a bubble-train flow in a channel with square cross-section. Using the computed three dimensional flow field we were able to visualize the structure of the flow inside the bubble and in the liquid. For low Ca flow a second vortex appears both in the liquid slug and inside the bubble increasing the mixing properties of the flow. Also, flow parameters like bubble shape and diameter and bubble velocity, which are of significant interest in predicting the mass transfer rates between the fluid and the wall, have been computed. Comparison of the computed global parameters with experimental data reported in the literature for the same values of the Capillary numbers shows good agreement.

NOMENCLATURE

a_{int}	interfacial area concentration	Greek symbols	
Ca	Capillary number		
D	diameter	ρ	density
$Eö$	Eötvös number	κ	interface curvature
f	liquid volume fraction	τ	stress tensor
g	gravitational acceleration	σ	surface tension coefficient
J	superficial velocity	ε	total void fraction
L	reference length	μ	viscosity
P	pressure	Subscripts	
Re	Reynolds number	G, g	gas phase
U	bubble velocity	L, l	liquid phase
V	control volume	m	volume averaged value
\vec{v}	velocity	ref	reference quantity
v_{ls}	liquid slug velocity		
W	relative bubble velocity		
We	Weber number		

REFERENCES

- [1] Triplett, K. A., Ghiaasiaan, S. M., Abdel-Khalik, S. I., Sadowski, D. L., Gas-liquid two-phase flow in microchannels; Part I: two-phase flow patterns. *Int. J. Multiphase Flow*, Vol. 25, pp. 377, 1999.
- [2] Triplett, K. A., Ghiaasiaan, S. M., Abdel-Khalik, S. I., Sadowski, D. L., Gas-liquid two-phase flow in microchannels; Part II: void fraction and pressure drop. *Int. J. Multiphase Flow*, Vol. 25, pp. 395, 1999.
- [3] Thulasidas, T. C., Abraham, M. A., Cerro, R. L., Bubble-train flow in capillaries of circular and square cross-section. *Chem. Eng. Science*, Vol. 50, No. 2, pp. 183, 1995.
- [4] Thulasidas, T. C., Abraham, M. A., Cerro, R. L., Flow patterns in liquid slugs during bubble-train flow inside capillaries. *Chem. Eng. Science*, Vol. 52, No. 17, pp. 2947, 1997.

- [5] Sabisch, W., Wörner, M., Grötzbach, G., Cacuci, D. G., 3D Volume-of-Fluid simulation of a wobbling bubble in a gas-liquid system of low Morton number. Fourth International Conference on Multiphase Flow, ICMF-2001, New Orleans, Louisiana, USA, June 2001.
- [6] Wörner, M., Sabisch, W., Grötzbach, G., Cacuci, D. G., Volume-averaged conservation equations for volume-of-fluid interface tracking. Fourth International Conference on Multiphase Flow, ICMF-2001, New Orleans, Louisiana, USA, June 2001.

INVARIANCE OF THE VELOCITY FIELD INDUCED BY A BUBBLE RISING STEADILY THROUGH LIQUID UNDER VARIATION OF THE GAS-LIQUID DENSITY RATIO

M. Wörner

Forschungszentrum Karlsruhe GmbH
Institut für Reaktorsicherheit
Postfach 3640, 76021 Karlsruhe, GERMANY
Phone: +49 7247 82-2577, Fax: +49 7247 82-3718,
E-mail: woerner@irs.fzk.de

ABSTRACT

We investigate the influence of the density ratio on the buoyancy driven motion of a single bubble rising through still liquid by two series of volume-of-fluid simulations. In each series the values of the Morton number (Mo) and bubble Eötvös number ($Eö_B$) are fixed while the density ratio is varied, so that the liquid density is two to fifty times the gas density. The runs of series A ($Mo = 3.09 \cdot 10^{-6}$, $Eö_B = 3.06$) result in an ellipsoidal bubble, those of series B ($Mo = 266$, $Eö_B = 243$) in an ellipsoidal-cap bubble. In both cases the bubble rises along a rectilinear path. We find that the density ratio affects the bubble acceleration. Once the bubble rise is steady, the bubble shape, the bubble Reynolds number and the properly scaled bubble driven liquid motion are virtually independent of the density ratio.

1. INTRODUCTION

1.1. Motivation

Despite the enormous amount of research that has been devoted to the buoyancy-driven motion of bubbles and drops in the past, there are still some aspects that are not fully clarified. For example, the influence of the disperse-to-continuous phase density ratio (Γ_ρ) as one of the fundamental similarity parameters determining the shape and rise of fluid particles has attracted rather little attention up to now. Associated with the development of advanced methods for direct numerical simulation (DNS) of interfacial flows and the availability of more and more powerful computers there is, however, an increased interest to quantify the influence of Γ_ρ . This is because in two-phase flow a DNS is often not performed for a density ratio of about 1/1000, as it is typical for air bubbles in water. Instead, in order to avoid numerical problems and to minimize the computational costs, a density ratio of about 1/100 is often chosen. Ye et al. [1], for example note that for very small values of Γ_ρ the disparity of the fluid property across the interface makes the computation stiff and often leads to numerical instability. Bunner & Tryggvason [2] observe that their multi-grid solver fails to converge in the solution of the pressure Poisson equation if the density ratio is very small. They state that a SOR solver is more robust, but its use is impractical because it increases the computational time required to achieve the same accuracy by one to two orders of magnitude. Another drawback of values of Γ_ρ substantially different from unity is the difference in diffusive time scale of both phases. Wörner [3] reports that the maximum time step size allowed for numerical stability of an explicit time integration scheme decreases almost linear with Γ_ρ . For all these reasons it appears favorable to perform simulations with a density ratio of order 1/10 or 1/100 instead of 1/1000. This, however, raises the question to what extent results obtained from such simulations can be transferred to gas-liquid systems of higher density ratio.

1.2. Literature survey

For a fluid particle rising with its terminal velocity through an infinite liquid there are eight physical quantities of influence [4]: ρ_c^* , ρ_d^* , μ_c^* , μ_d^* , σ^* , g^* , d_B^* , V_T^* . Here ρ^* denotes the density, μ^* the dynamic viscosity, σ^* the coefficient of surface tension, g^* the acceleration of gravity, d_B^* the sphere-equivalent diameter of the fluid particle and V_T^* its terminal rise velocity. The subscripts d and c denote the dispersed and continuous phase, respectively, and $*$ is used to indicate a dimensional quantity. These eight quantities obey three basic dimensions (length, time, mass). Dimensional analysis therefore yields that there are five independent dimensionless groups [4], namely the bubble Reynolds number (Re_B), the bubble Eötvös number ($Eö_B$), the Morton number (Mo), and the ratios of disperse-to-continuous phase density (Γ_ρ) and viscosity (Γ_μ):

$$Re_B \equiv \frac{\rho_c^* d_B^* V_T^*}{\mu_c^*}, \quad Eö_B \equiv \frac{g^* (\rho_c^* - \rho_d^*) d_B^{*2}}{\sigma^*}, \quad Mo \equiv \frac{(\rho_c^* - \rho_d^*) g^* \mu_c^{*4}}{\rho_c^{*2} \sigma^{*3}}, \quad \Gamma_\rho \equiv \frac{\rho_d^*}{\rho_c^*}, \quad \Gamma_\mu \equiv \frac{\mu_d^*}{\mu_c^*} \quad (1)$$

Therefore, there exists for example a functional relationship of type $Re_B = f(Mo, Eö_B, \Gamma_\rho, \Gamma_\mu)$. We note that any of the non-dimensional groups Re_B , Mo , $Eö_B$ can be replaced by the Weber number in virtue of the identity $We_B \equiv \rho_c^* d_B^* V_T^{*2} / \sigma^* = Re_B^2 \sqrt{Mo / Eö_B}$. The set of non-dimensional groups according to Eq. (1) has the advantage that there is only one group (Re_B) that incorporates the rise velocity and only one group ($Eö_B$) that incorporates the equivalent diameter.

Experimental studies on the influence of the density ratio as a similarity parameter are rare. The reason is that Γ_ρ is not a parameter which can be easily varied in an experiment, while at the same time all the other parameters are kept constant. In the course of an experimental series, usually one specific continuous phase and various dispersed phases are used, or vice versa. In general, by this approach together with the density ratio also the viscosity ratio and the Morton number are varied. This procedure is therefore unsuited to reveal the specific functional dependence of Re_B from Γ_ρ . Nevertheless, Grace [4] notes that for bubbles rising in liquids Γ_ρ and Γ_μ tend to be very small so that the density and viscosity of the dispersed phase become unimportant causing $Re_B = f(Mo, Eö_B)$.

The specific influence of the density ratio can be investigated more easily by means of numerical simulation. Dandy & Leal [5] study the steady axisymmetric motion and deformation of a fluid particle in a streaming flow by a finite-difference scheme using the stream function-vorticity formulation of the Navier-Stokes equation and a boundary-fitted orthogonal coordinate system. The authors consider both the case of a bubble and a drop. For the bubble the viscosity ratio is 1 and the values of the Reynolds and Weber number are fixed to $Re_B = 100$, $We_B = 4$, while two values of the density ratio are considered: $\Gamma_\rho = 0.1$ and 0.01 . For the drop they use $Re_B = 60$, $We_B = 4$, $\Gamma_\mu = 100$ and the values of the density ratio are $\Gamma_\rho = 10$, 100 , and 1000 . The authors find that the variation of the density ratio produces only a slight change in shape and flow field. They state that “the only surprise is that the effect of variation of the density ratio is so weak”. Recently, Ye et al. [1] developed a combined Eulerian-Lagrangian method where the Navier-Stokes equation is solved on a fixed grid and the interface is explicitly defined by geometric curves in the computational domain. They compute the rise of an axisymmetric bubble for the same constant parameters as Dandy & Leal (i.e. $Re_B = 100$, $We_B = 4$, $\Gamma_\mu = 1$), but consider values of the density ratio that span three orders of magnitude: $\Gamma_\rho = 0.1$, 0.01 , 0.001 . They confirm that the differences are small, but observe that for the higher values of Γ_ρ the bubble is slightly less deformed.

Oka & Ishii [6] performed 3D level-set simulations of a single bubble rising through liquid in a square duct. They introduce the reduced Morton number $Mo^\dagger = Mo / (1 - \Gamma_\rho)$ and reduced Eötvös number $Eö^\dagger = Eö / (1 - \Gamma_\rho)$ and perform simulations for fixed values $Mo^\dagger = 3.125 \cdot 10^{-3}$, $Eö^\dagger = 20$ for the three different density ratios $\Gamma_\rho = 0.02$, 0.01 , 0.001 . They find that the effect of variation of Γ_ρ on the cap-type bubble shape and the flow field is extremely weak when Γ_ρ is smaller than 0.02 . Additionally, they perform a run with $\Gamma_\rho = 0.1$ and $Mo^\dagger = 3.125 \cdot 10^{-3} / (1 - 0.1) = 3.472 \cdot 10^{-3}$ and $Eö^\dagger$

$= 20 / (1 - 0.1) = 22.22$. By this choice of Mo^\dagger and $E\delta^\dagger$ they take into account the effect of the change of the density difference $\Delta\rho^*$ that results from variation of the density ratio and thus ensure that in all four runs the values of Mo and $E\delta_B$ are (almost) identical. Oka & Ishii [6] find that in the run with $\Gamma_\rho = 0.1$ the rise velocity is about 5.5% less than in the run with $\Gamma_\rho = 0.001$.

Bunner & Tryggvason [2] use a front-tracking method to perform simulations of 3D bubbly flow for $E\delta_B = 1$ and $Mo = 1.23 \cdot 10^{-6}$ using $\Gamma_\rho = 0.02$. They justify this choice by the observation that in 2D tests using much smaller density ratios the effect of the density ratio and of the inertia of the fluid inside the bubble is small for these values [7].

Sabisch et al. [8] performed 3D simulations of a single bubble rising through an initially quiescent liquid within a vertical channel by the volume-of-fluid (VOF) method. For the density ratio they used $\Gamma_\rho = 0.5$ and for the viscosity ratio $\Gamma_\mu = 1$. They considered four different combinations of $(Mo, E\delta_B)$ which were chosen so that from the diagram of Cliff, Grace, and Weber (CGW) [9] in which Re_B is displayed as function of $(Mo, E\delta_B)$ a spherical, ellipsoidal, oblate spherical cap, and a wobbling bubble shape should be expected. Despite the density ratio 0.5, the Reynolds number, shape, rising path, and wake type of the bubble agreed qualitatively very well with the regime of CGW for all four combinations of $(Mo, E\delta_B)$. From this result one may conjecture that the dependence of the bubble Reynolds number on the density ratio is weak in general, not only for $\Gamma_\rho < 0.02$. These results motivated a study by Wörner [3] who systematically investigated the influence of the density ratio on the bubble Reynolds number by a series of 3D VOF simulations with the parameters of the ellipsoidal bubble ($Mo = 3.09 \cdot 10^{-6}$, $E\delta_B = 3.06$, $\Gamma_\mu = 1$) but for different values of the density ratio: $\Gamma_\rho = 0.5, 0.2, 0.1, 0.02$. He found that the density ratio affects how fast the bubble accelerates from rest towards its terminal velocity. This can be explained by the added mass force [3]. However, the terminal value of the bubble Reynolds number Re_B was found to be virtually unaffected by the density ratio.

1.3. Objective

The velocity that enters into the bubble Reynolds number is the velocity of the center-of-mass of the bubble. This is an integral quantity. A question that arises is how is the influence of the density ratio on the *local* velocity field, both in the liquid and gas phase. This topic is investigated in the present paper. In section 2 we first give the non-dimensional equations governing the local motion in both phases. In these equations the five non-dimensional groups mentioned above appear. In section 3 we analyze results of direct numerical simulations obtained with the volume of fluid method for the rise of a bubble in a vertical channel. Two different cases are considered. The first corresponds to the ellipsoidal bubble of [3] and thus represents a medium Morton number system. The second case is that of a dimpled ellipsoidal cap bubble in a high Morton number system ($Mo = 266$, $E\delta_B = 243$, $\Gamma_\mu = 1$). For this case a new series of computations has been performed for three different values of the density ratio ($\Gamma_\rho = 0.5, 0.2, 0.1$). In section 4 we present the conclusions.

2. THEORY

2.1. Dimensional equations in fixed frame of reference

We consider the buoyancy driven motion of a single gas bubble rising through an immiscible fluid of infinite extend. The fluids reside in domains $\Omega_c^*(t^*) \subset \mathbb{R}^3, \Omega_d^*(t^*) \subset \mathbb{R}^3$ that change with time. Both fluids are considered to be Newtonian with constant viscosity. Also the density of each phase is assumed to be constant. Then, the motion of each fluid is described by the incompressible conservation equations for mass and momentum:

$$\nabla^* \cdot \mathbf{u}_c^* = 0, \quad \frac{\partial^* \rho_c^* \mathbf{u}_c^*}{\partial t^*} + \nabla^* \cdot \rho_c^* \mathbf{u}_c^* \mathbf{u}_c^* = -\nabla^* p_c^* + \mu_c^* \nabla^{*2} \mathbf{u}_c^* + \rho_c^* \mathbf{g}^*, \quad \mathbf{x}^* \in \Omega_c^*(t^*) \quad (2)$$

$$\nabla^* \cdot \mathbf{u}_d^* = 0, \quad \frac{\partial^* \rho_d^* \mathbf{u}_d^*}{\partial t^*} + \nabla^* \cdot \rho_d^* \mathbf{u}_d^* \mathbf{u}_d^* = -\nabla^* p_d^* + \mu_d^* \nabla^{*2} \mathbf{u}_d^* + \rho_d^* \mathbf{g}^*, \quad \mathbf{x}^* \in \Omega_d^*(t^*) \quad (3)$$

Here, \mathbf{u}_c^* , \mathbf{u}_d^* are the fluid velocities at specified time t^* and position in space \mathbf{x}^* within a fixed coordinate system. For $|\mathbf{x}^*| \rightarrow \infty$ we assume the fluid of the continuous phase to be at rest.

We denote the boundary between both fluid domains by $S_i^*(t^*)$, a point on the interface by \mathbf{x}_i^* , and the unit normal vector pointing into the continuous phase by \mathbf{n}_i . We assume that the interface thickness is zero and the coefficient of surface tension is constant. At the interface we have the conditions of continuity of velocity and the continuity of normal and tangential stresses:

$$\left. \begin{aligned} \mathbf{u}_c^* &= \mathbf{u}_d^* = \mathbf{u}_i^* \\ (p_c^* - p_d^* + \kappa^* \sigma^*) \mathbf{n}_i &= [\mu_c^* (\nabla^* \mathbf{u}_c^* + \nabla^{*\top} \mathbf{u}_c^*) - \mu_d^* (\nabla^* \mathbf{u}_d^* + \nabla^{*\top} \mathbf{u}_d^*)] \cdot \mathbf{n}_i \end{aligned} \right\} \mathbf{x}_i^* \in S_i^*(t^*) \subset \mathbb{R}^2 \quad (4)$$

Here, κ^* is twice the mean interface curvature.

The interface can be specified geometrically by the equation $F(\mathbf{x}_i^*, t^*) = 0$. As the boundary between the two fluids is a material surface, F is a quantity which is invariant for a fluid particle at the interface, so that the interface evolution is described by

$$\frac{DF}{Dt^*} = \frac{\partial F}{\partial t^*} + \mathbf{u}_i^* \cdot \nabla^* F = 0 \quad (5)$$

We now introduce some integral quantities of the bubble and denote these by subscript ‘‘B’’. As the disperse phase is incompressible the volume of the fluid particle is constant in time. The bubble volume, sphere-equivalent diameter, position vector of the center-of-mass, and the translational velocity of the bubble are given by

$$\mathcal{V}_B^* \equiv \iiint_{\Omega_d^*(t^*)} dV^*, \quad d_B^* \equiv \left(\frac{6\mathcal{V}_B^*}{\pi} \right)^{\frac{1}{3}}, \quad \mathbf{Y}_B^*(t^*) \equiv \frac{1}{\mathcal{V}_B^*} \iiint_{\Omega_d^*(t^*)} \mathbf{x}^* dV^*, \quad \mathbf{V}_B^*(t^*) \equiv \frac{d\mathbf{Y}_B^*(t^*)}{dt^*}, \quad V_B^*(t^*) \equiv |\mathbf{V}_B^*(t^*)| \quad (6)$$

For the analysis that will follow it is convenient to introduce a frame of reference moving with the center-of-mass of the bubble. For this purpose we make the following transformation

$$t' = t^*, \quad \mathbf{z}^* = \mathbf{x}^* - \mathbf{Y}_B^*(t^*), \quad \mathbf{w}_c^*(\mathbf{z}^*, t^*) = \mathbf{u}_c^*(\mathbf{x}^*, t^*) - \mathbf{V}_B^*(t^*), \quad \mathbf{w}_d^*(\mathbf{z}^*, t^*) = \mathbf{u}_d^*(\mathbf{x}^*, t^*) - \mathbf{V}_B^*(t^*) \quad (7)$$

The acceleration of the moving coordinate system O' is given by $(-dV_B^*/dt^*)$. As it is well known (see e.g. [10], p. 140) the equation of motion in a moving frame is identical in form with that in an absolute frame provided that the fictitious body force per unit mass is added to the real body forces.

2.2. Non-dimensional equations in moving frame of reference

To make the above equations dimensionless we use the sphere-equivalent bubble diameter d_B^* as reference length and the bubble’s center-of-mass velocity $V_B^* \neq 0$ as reference velocity. The reference time is given by d_B^*/V_B^* . As reference density and viscosity we choose the values of the continuous phase. To distinguish a non-dimensional quantity from its dimensional counterpart we use the same symbol but omit the superscript $*$. The non-dimensional density and viscosity of the continuous phase are then unity $\rho_c = \mu_c = 1$ while the disperse phase values are $\rho_d = \Gamma_\rho$ and $\mu_d = \Gamma_\mu$. The definition of the non-dimensional pressure is different as we incorporate in it the effect of the hydrostatic pressure of the continuous phase:

$$p_c \equiv \frac{p_c^* - \rho_c^* \mathbf{g}^* \cdot \mathbf{x}^*}{\rho_c^* V_B^{*2}}, \quad p_d \equiv \frac{p_d^* - \rho_c^* \mathbf{g}^* \cdot \mathbf{x}^*}{\rho_c^* V_B^{*2}} \quad (8)$$

Introducing the unit vector in the direction of gravity $\mathbf{n}_g \equiv \mathbf{g}^* / g^*$ the non-dimensional equations in the moving frame of reference become

$$\nabla' \cdot \mathbf{w}_c = 0, \quad \frac{\partial \mathbf{w}_c}{\partial t} + \nabla' \cdot \mathbf{w}_c \mathbf{w}_c = -\nabla' p_c + \frac{1}{Re_B} \nabla'^2 \mathbf{w}_c - \frac{d\mathbf{V}_B}{dt}, \quad \mathbf{z} \in \Omega'_c(t) \quad (9)$$

$$\left. \begin{aligned} \nabla' \cdot \mathbf{w}_d &= 0 \\ \Gamma_\rho \left(\frac{\partial \mathbf{w}_d}{\partial t} + \nabla' \cdot \mathbf{w}_d \mathbf{w}_d \right) &= -\nabla' p_d + \frac{\Gamma_\mu}{Re_B} \nabla'^2 \mathbf{w}_d - \sqrt{\frac{E\ddot{\alpha}_B^3}{MoRe_B^4}} \mathbf{n}_g - \Gamma_\rho \frac{d\mathbf{V}_B}{dt} \end{aligned} \right\} \mathbf{z} \in \Omega'_d(t) \quad (10)$$

The conditions for $|\mathbf{z}| \rightarrow \infty$ are $\mathbf{w}_c = -\mathbf{V}_B(t)$ while those at the interface are

$$\left. \begin{aligned} \mathbf{w}_c &= \mathbf{w}_d = \mathbf{w}_i \\ \left(p_c - p_d + \kappa \sqrt{\frac{E\ddot{\alpha}_B}{MoRe_B^4}} \right) \mathbf{n}_i &= \frac{1}{Re_B} \left[(\nabla' \mathbf{w}_c + \nabla' \mathbf{w}_c^T) - \Gamma_\mu (\nabla' \mathbf{w}_d + \nabla' \mathbf{w}_d^T) \right] \cdot \mathbf{n}_i \end{aligned} \right\} \mathbf{z}_i \in S'_i(t) \quad (11)$$

From the Eqs. (9) - (11) we see that the non-dimensional field variables $p_c, p_d, \mathbf{w}_c, \mathbf{w}_d$, respectively $\mathbf{u}_c, \mathbf{u}_d$, and the location of the interface depend on the five independent non-dimensional groups $Re_B, E\ddot{\alpha}_B, Mo, \Gamma_\rho$, and Γ_μ . Unlike in section 1.2 we have received this result not by dimensional analysis but directly from the basic governing equations.

In this paper we are especially interested in the influence of the density ratio. We note that the density ratio does neither appear in the momentum equation of the continuous phase, Eq. (9), nor in the coupling condition at the interface, Eq. (11). Therefore, the influence of the density ratio is restricted to the flow within the bubble. The flow within the bubble is likely to be a circulatory one. When there is no internal flow ($\mathbf{w}_d = 0$) or in the limit $\Gamma_\rho \rightarrow 0$ the density ratio drops from Eq. (10). In this case it is thus without influence and obviously it is $Re_B = f(Mo, E\ddot{\alpha}_B, \Gamma_\mu)$.

2.3. Steady flow in moving frame of reference

In what follows we consider now the special case of steady motion. We assume that the bubble rises with constant velocity $V_B \neq 0$ and in the moving frame of reference the bubble shape and the flow inside and outside the bubble are steady. Then the time derivatives in Eqs. (9) and (10) cancel and the domains Ω'_d and Ω'_c are constant in time. The Navier-Stokes equation for the disperse phase then reduces to the form

$$\Gamma_\rho \nabla' \cdot \mathbf{w}_d \mathbf{w}_d = -\nabla p_d + \frac{\Gamma_\mu}{Re_B} \nabla' \cdot \left[\nabla' \mathbf{w}_d + \nabla' \mathbf{w}_d^T \right] - \sqrt{\frac{E\ddot{\alpha}_B^3}{MoRe_B^4}} \mathbf{n}_g, \quad \mathbf{z} \in \Omega'_d \quad (12)$$

Making use of the generalized Gauss-Ostrogradskii divergence theorem for dyads we can integrate Eq. (12) over the domain Ω'_d and obtain

$$\iint_{S'_i} \mathbf{n}_i \cdot \left\{ -\Gamma_\rho \mathbf{w}_d \mathbf{w}_d - \mathbf{I} p_d + \frac{\Gamma_\mu}{Re_B} \left[\nabla' \mathbf{w}_d + \nabla' \mathbf{w}_d^T \right] \right\} dS = \mathcal{V}'_B \sqrt{\frac{E\ddot{\alpha}_B^3}{MoRe_B^4}} \mathbf{n}_g \quad (13)$$

Equation (13) is equivalent to the momentum theorem ([10], pp. 138) where the control surface is represented by the gas-liquid interface. The first term in Eq. (13) represents the convective flux of momentum out of the region bounded by S'_i . Since there is no flow across the interface it follows that this term is zero. This can readily be shown for the local term. As the terms on the left-hand-side of Eq. (13) have to be evaluated at the interface we have $\mathbf{w}_d = \mathbf{w}_i$ and thus

$$\Gamma_\rho \mathbf{n}'_i \cdot \mathbf{w}_d \mathbf{w}_d = \Gamma_\rho \mathbf{n}'_i \cdot \mathbf{w}_i \mathbf{w}_i = (\mathbf{n}'_i \cdot \mathbf{w}_i) \mathbf{w}_i = \mathcal{W}_{i\perp} \mathbf{w}_i \quad (14)$$

Here, $W_{i\perp}$ is the component of the interface velocity normal to the interface. As we assumed the interface position to be steady in the moving frame of reference it is $W_{i\perp} = 0$ and the momentum theorem expressed by Eq. (13) simplifies to the form

$$\iint_{S_i} \mathbf{n}_i \cdot \left\{ -\mathbf{I}p_d + \frac{\Gamma_\mu}{Re_B} \left[\nabla' \mathbf{w}_d + \nabla' \mathbf{w}_d^T \right] \right\} dS = \mathcal{V}'_B \sqrt{\frac{E\ddot{\sigma}_B^3}{MoRe_B^4}} \mathbf{n}_g \quad (15)$$

Equation (15) states that there is a balance between the drag force and the buoyancy force.

The significance of the momentum theorem is that it shows that the details of the motion within the region enclosed are irrelevant and knowledge of the conditions at the surface are sufficient to describe the problem. As the gas-liquid density ratio Γ_ρ has cancelled from Eq. (15) this suggests that for steady motion and fixed bubble shape the bubble Reynolds number is a function only of Mo , $E\ddot{\sigma}_B$, Γ_μ but not of Γ_ρ . The density ratio may, however, have an influence on the shape of the bubble. This topic is investigated in the next section by means of direct numerical simulation.

3. NUMERICAL SIMULATION RESULTS

3.1. Physical parameters

In this section we present results of direct numerical simulations. Two series of simulations for two different types of bubbles are analyzed. The physical parameters are chosen so that a steady bubble rising along a rectilinear path and an axisymmetric bubble shape should be expected. In simulation series A the value of the Morton number is $Mo = 3.09 \cdot 10^{-6}$, which is a typical value when the liquid phase is of intermediate viscosity. The value chosen for the bubble Eötvös number is $E\ddot{\sigma}_B = 3.06$. From the CGW regime diagram [9] we expect an oblate ellipsoidal bubble. In simulations series B the value of the Morton number is $Mo = 266$ which is characteristic for a very viscous liquid. The value of the bubble Eötvös number is $E\ddot{\sigma}_B = 243$. The parameters of series B are the same as in an experiment by Bhaga & Weber [12] where a dimpled ellipsoidal cap bubble was observed. In all our simulations the value of the viscosity ratio is fixed to unity, while the value of the density ratio is varied to investigate its influence on the simulation results.

3.2. Governing equations and numerical method

We perform the simulations in a fixed frame of reference. For tracking of the gas-liquid interface we use the volume-of-fluid method. The foundation of the method is the definition of a scalar quantity f representing the volumetric fraction of the continuous (liquid) phase within an averaging volume. Here, the averaging volume is taken to be a mesh cell. For $f = 1$ the cell is filled with liquid, for $f = 0$ it is filled with gas, while for $0 < f < 1$ both phases instantaneously coexist in the mesh cell and thus an interface is present. Based on f we define the (non-dimensional) mixture density, mixture viscosity, and center-of-mass velocity within a mesh cell:

$$\rho_m \equiv \frac{f\rho_c^* + (1-f)\rho_d^*}{\rho_c^*} = f + (1-f)\Gamma_\rho, \quad \mu_m \equiv f + (1-f)\Gamma_\mu, \quad \mathbf{u}_m \equiv \frac{1}{U_{ref}^*} \frac{f\rho_c^* \mathbf{u}_c^* + (1-f)\rho_d^* \mathbf{u}_d^*}{f\rho_c^* + (1-f)\rho_d^*} \quad (16)$$

Based on above quantities the equations governing the motion in the continuous phase (Eq. (2)), in the disperse phase (Eq. (3)), and the coupling condition (Eq. (4)) can be combined into one single continuity and momentum equation valid in the entire domain $\Omega = \Omega_c \cup \Omega_d$ (see [11]):

$$\nabla \cdot \mathbf{u}_m = 0 \quad (17)$$

$$\frac{\partial \rho_m \mathbf{u}_m}{\partial t} + \nabla \cdot \rho_m \mathbf{u}_m \mathbf{u}_m = -\nabla p + \frac{1}{Re_{ref}} \nabla \cdot \mu_m \left[\nabla \mathbf{u}_m + \nabla \mathbf{u}_m^T \right] - (1-f) \frac{E\ddot{\sigma}_{ref}}{We_{ref}} \mathbf{n}_g + \frac{\kappa a_i \mathbf{n}_i}{We_{ref}} \quad (18)$$

Here a_i is the non-dimensional interfacial area within the averaging volume. The above equations are made dimensionless by a reference length L_{ref}^* and a reference velocity U_{ref}^* . Based on these scales - equivalent to the definitions of Re_B , $Eö_B$, We_B in section 1.2 - a reference Reynolds number (Re_{ref}), reference Eötvös number ($Eö_{ref}$), and reference Weber number (We_{ref}) can be defined. The set of equations is completed by the transport equation for the liquid volumetric fraction

$$\frac{\partial f}{\partial t} + \nabla \cdot (f \mathbf{u}_m) = 0 \quad (19)$$

For the solution of Eq. (19) by the VOF method we have developed the interface reconstruction algorithm EPIRA which belongs to the class of PLIC (Piecewise Linear Interface Calculation) methods. Equations (17) and (18) are discretized employing a regular staggered grid and second order central differences. The solution strategy is based on a projection method and a third order Runge-Kutta time integration method. Details about the numerical method can be found in [8].

3.3. Computational set up

Figure 1 shows the coordinate system and a sketch of the computational domain. The x -, y - and z -axes are assigned in vertical, transverse, and wall-normal direction, respectively. The gravity vector points in negative x -direction. In x - and y -direction we have periodic boundary conditions; at $z = 0$ and $z = 1$ we have rigid walls and no-slip boundary conditions. The size of the computational domain in terms of L_{ref}^* is $2 \times 1 \times 1$. This domain is discretized by $128 \times 64 \times 64$ uniform mesh cells. A spherical bubble with diameter 0.25 is positioned in the domain with its center located at $(0.5, 0.5, 0.5)$. The overall void fraction is about 0.4 %. Both, liquid and gas are initially at rest.

To perform the simulations we must specify the reference quantities. We use $L_{ref}^* = 4$ m, $U_{ref}^* = 1$ ms⁻¹, $g^* = 9.81$ ms⁻². To determine the values of the reference Eötvös, Weber, and Reynolds number in the Navier-Stokes Eq. (18) we proceed as follows. Choosing a certain value for the density ratio and taking the values for Mo and $Eö_B$ given above we successively compute

$$Eö_{ref} = \left(\frac{L_{ref}^*}{d_B^*} \right)^2 Eö_B, \quad We_{ref} = \frac{Eö_{ref}}{1 - \Gamma_\rho} \frac{U_{ref}^{*2}}{g^* L_{ref}^*}, \quad Re_{ref} = \left(\frac{Eö_{ref} We_{ref}^2}{Mo} \right)^{0.25} \quad (20)$$

In Table I we give these input values for the different density ratios considered in the present study. Additionally, we give the values of We_{ref} and Re_{ref} for the asymptotic case $\Gamma_\rho \rightarrow 0$.

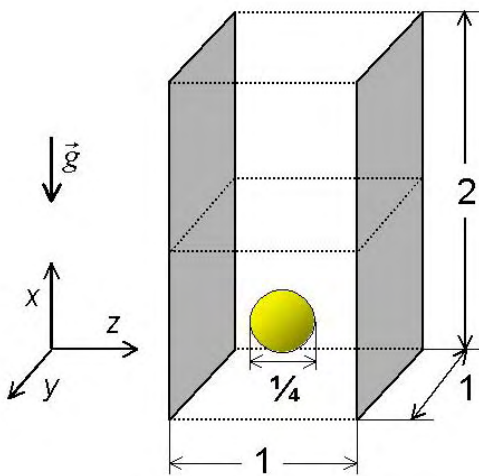


Figure 1: Sketch of coordinate system and computational domain.

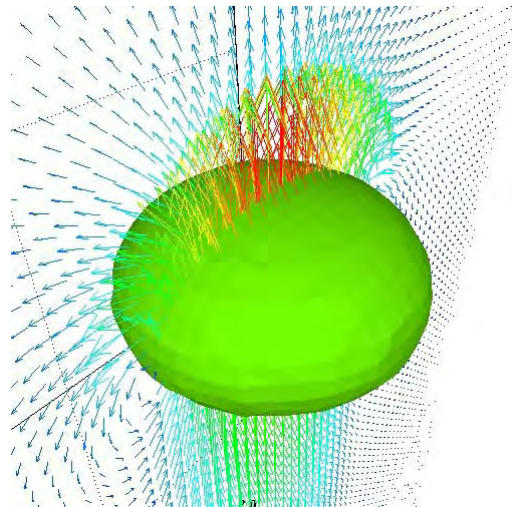


Figure 2: Instantaneous bubble shape and velocity vectors in plane $y = 0.5$ for run A50.

Table I: Simulation parameters (Δt = time step, N_t = number of time steps computed).

Run	Γ_ρ	$1 / \Gamma_\rho$	$E\ddot{o}_{ref}$	We_{ref}	Re_{ref}	Δt	N_T
A2	0.5	2	49.05	2.5	100.00	0.0005	1,100
A5	0.2	5	49.05	1.5625	78.90	0.0003	1,800
A10	0.1	10	49.05	1.3888	74.39	0.00015	3,200
A50	0.02	50	49.05	1.2755	71.29	0.00003	13,000
	0	∞	49.05	1.25	70.57		
B2	0.5	2	3,888	792.7	55.05	0.0005	5,000
B5	0.2	5	3,888	495.4	43.52	0.0001	17,000
B10	0.1	10	3,888	440.4	41.03	0.0001	16,000
	0	∞	3,888	396.3	38.93		

3.4. Bubble Reynolds number

In Fig. 3 the time history of the vertical position of the bubble center-of-mass is shown for all simulations of series A and B. It is apparent that the density ratio affects how fast the bubble accelerates from rest towards its terminal velocity and also affects the specific value of the terminal velocity. This behavior can be explained by the added mass force [3]. Figure 4, however, shows that the terminal value of the bubble Reynolds number Re_B is obviously unaffected by the density ratio. In case A the value of the terminal bubble Reynolds number is about 56. As shown in [3] this value is in good agreement with that of a correlation $Re_B = f(Mo, E\ddot{o})$ obtained from two-phase wave theory [13]. In case B Re_B is about 6.5 and thus is about 16% smaller than in the experiment [12], where $Re_B = 7.77$. We attribute the lower value in the simulation to the influence of the viscosity ratio which is here unity but in the experiment is estimated to be about 10^{-5} .

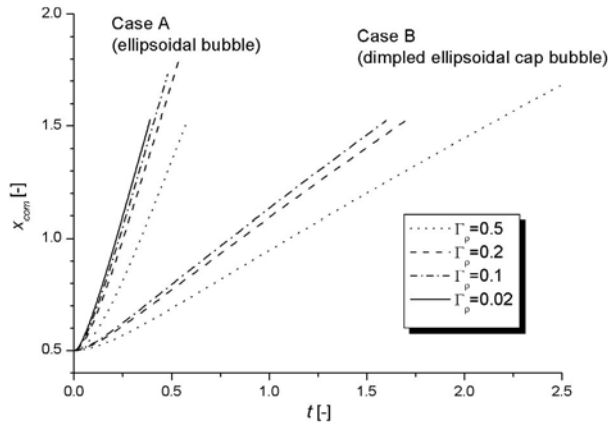


Figure 3: Time history of vertical position of bubble center-of-mass (x_{com}).

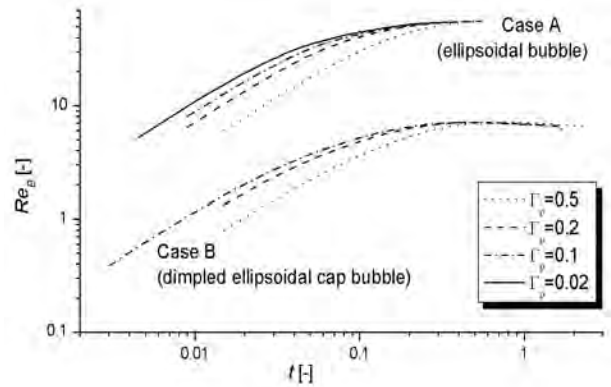


Figure 4: Time history of bubble Reynolds number.

3.5. Bubble shape

Figure 2 shows a snapshot of the bubble shape for run A50. As expected the bubble is of oblate ellipsoidal shape. The steady bubble shape for run B2 is displayed in Figure 5. For a better visualization of the dimpled ellipsoidal shape only the back half of the bubble is shown. Figure 6 shows the experimental bubble shape reproduced from [12]. Though in the simulation the density ratio is $\Gamma_\rho = 0.5$ and in the experiment it is $\Gamma_\rho = 0.0008$ the bubble shapes in Figs. 5 and 6 are quite similar. However, one can identify a small difference in curvature at the bottom of the bubble.

We now make a quantitative comparison of the bubble shape for the runs of case A and B. We consider that instant in time when the vertical position of the bubble center-of-mass is $x_{com} = 1.5$ and thus the bubble has moved four times its initial diameter. Note that this time level differs from run to run (see Fig. 3). In Table II we give the ratios of the bubble dimensions a_x , a_y , a_z for the different runs. We see that the influence of the density ratio on the bubble dimensions is surprisingly small. However, as Γ_ρ decreases the values of a_x/a_y and a_x/a_z slightly increase in case A and thus the bubble is less oblate. This is in agreement with the numerical findings of Ye et al. [1]. For case B the trend is opposite. The ratio of the horizontal dimensions a_x/a_y is always close to unity indicating that the bubble is axisymmetric. Note that in our 3D simulations on a Cartesian grid no assumption regarding axisymmetry is involved. In most cases the ratio a_y/a_z is larger than 1 so that the bubble dimension in span-wise direction is slightly larger than in wall-normal direction. This indicates that the walls are not sufficiently far away to have any influence. Nevertheless, we conclude that neither in case A nor in case B the density ratio has any major influence on the bubble shape.

Table II: Ratios of the bubble dimensions.

Γ_ρ	$1 / \Gamma_\rho$	Case A			Case B		
		a_x / a_y	a_x / a_z	a_y / a_z	a_x / a_y	a_x / a_z	a_y / a_z
0.5	2	0.648	0.659	1.017	0.538	0.556	1.033
0.2	5	0.652	0.665	1.021	0.528	0.544	1.030
0.1	10	0.658	0.669	1.016	0.528	0.543	1.029
0.02	50	0.668	0.666	0.998	-	-	-



Figure 5: Computed bubble shape for run B2 (only the back half of the bubble is shown).

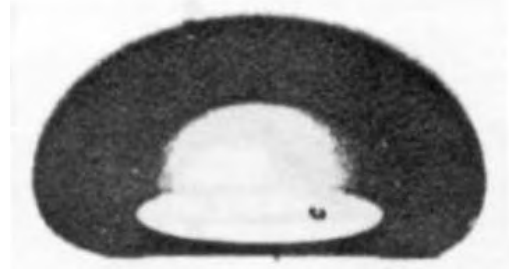


Figure 6: Experimental bubble shape reproduced from [12].

3.6. Local velocity profiles

We now compare local velocity profiles along a certain line within the flow domain. In Fig. 7 the vertical velocity component u is shown as function of the vertical co-ordinate x for fixed span-wise and wall-normal co-ordinates $y = z = 0.492$ for the runs of series A. Additionally, in Fig. 7 the profile of the liquid volumetric fraction is displayed to indicate the bubble position ($f = 0$). While the profiles of f almost collapse to a single curve, the profiles of u are similar, but do not collapse. The latter result is not really surprising since in all runs the velocity is normalized by the same value $U_{ref}^* = 1 \text{ ms}^{-1}$. From the analysis in section 2 we expect similarity of the velocity field when it is scaled by the bubble rise velocity. In Fig. 8 we show the velocity profiles normalized by the bubble rise velocity of the respective run and indeed find that the profiles collapse to a single curve.

In Fig. 9 the profiles of f and the scaled vertical velocity u/V_B are shown along the wall-normal coordinate. This figure illustrates the internal circulation within the bubble. Inside the bubble at $z = 0.5$ we can identify a small effect of the density ratio on the velocity profile. However, within the liquid phase the profiles again collapse to a single curve. This also holds for the wall-normal profile of the scaled wall-normal velocity u/V_B at a position within the bubble wake, see Fig. 10.

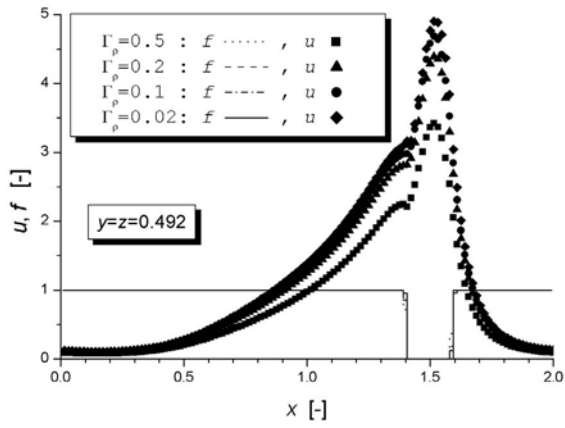


Figure 7: Vertical profile of local instantaneous vertical velocity, u , and liquid volume fraction, f , for case A and $y = z = 0.492$.

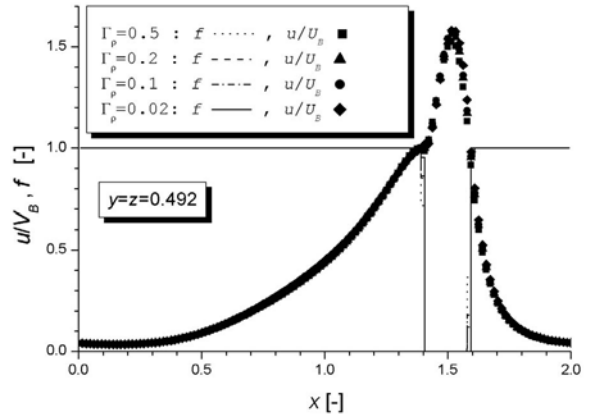


Figure 8: Vertical profile of normalized local instantaneous vertical velocity u/V_B and liquid volume fraction, f , for case A and $y = z = 0.492$.

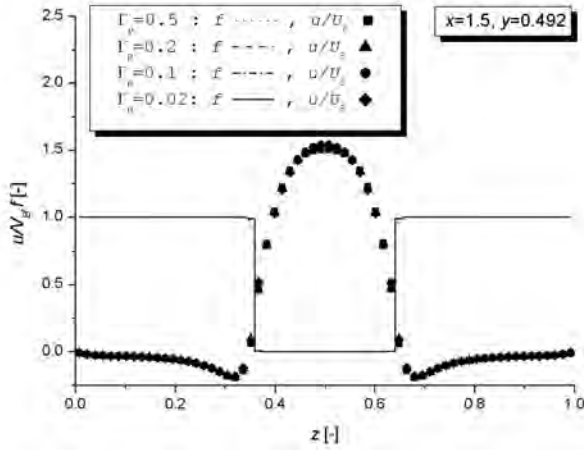


Figure 9: Wall-normal profile of scaled vertical velocity, u/V_B , and liquid volume fraction, f , for case A and $x = 1.5, y = 0.492$.

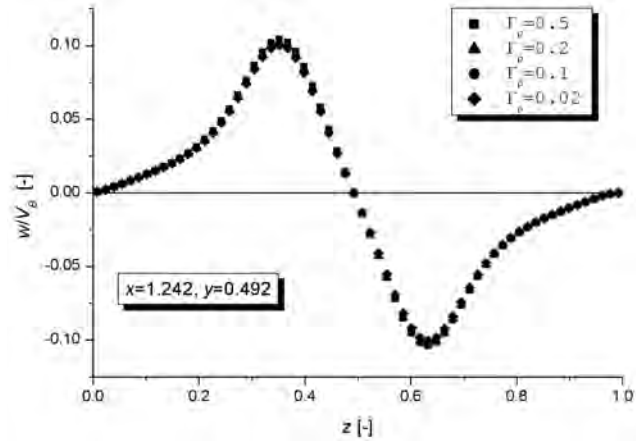


Figure 10: Wall-normal profile of scaled wall-normal velocity w/V_B for case A and $x = 1.242, y = 0.492$ (bubble wake).

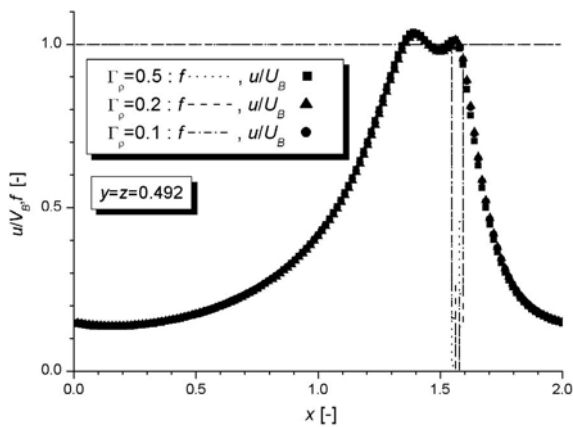


Figure 11: Vertical profile of normalized local vertical velocity u/V_B and liquid volume fraction, f , for case B and $y = z = 0.492$.

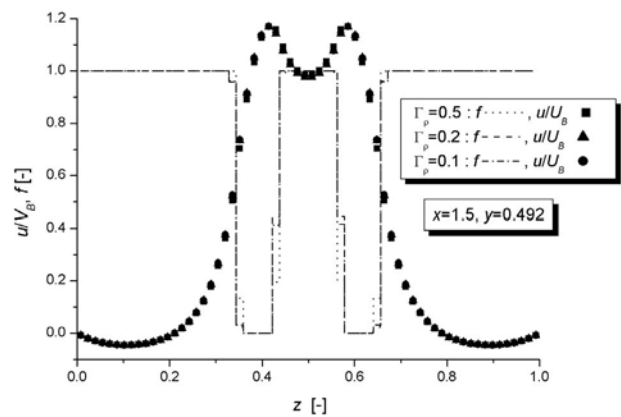


Figure 12: Wall-normal profile of scaled vertical velocity, u/V_B , and liquid volume fraction, f , for case B and $x = 1.5, y = 0.492$.

In Figs. 11 and 12, we show similar graphs as in Figs. 8 and 9 but for case B. Again we find that the scaled velocity profiles are independent of Γ_ρ . However, the profiles for case A and B clearly differ. For case A, the value of u/V_B at $x = 0$ and $x = 2$ in Fig. 8 is about 0.05. For case B this value is about 0.15, see Fig. 11. This value can be considered to give a measure on the influence of the periodic boundary conditions applied in vertical direction. The rather high value in case B indicates that the bubble already may experience the influence of the “leading” bubble. In case B the bubble’s center-of-mass lies - due to the dimpled ellipsoidal shape - within the liquid phase. As a consequence the wall-normal profile of the vertical velocity exhibits a local minimum, see Fig. 12.

4. CONCLUSIONS

In the present paper the influence of the gas-liquid density ratio (Γ_ρ) on the buoyancy driven motion of a single bubble is investigated theoretically and numerically. Using the volume-of-fluid method for tracking the gas-liquid interface, two series of simulation series are performed for fixed values of the Morton number and the bubble Eötvös number and a unity viscosity ratio. Case A ($Mo = 3.09 \cdot 10^{-6}$, $E\ddot{o}_B = 3.06$) corresponds to a liquid phase of intermediate viscosity while case B ($Mo = 266$, $E\ddot{o}_B = 243$) corresponds to a very viscous liquid. In each simulation series various density ratios are considered, namely 0.5, 0.2, 0.1 and (only in case A) 0.02. After an initial transient, all simulations result in steady bubbles rising along a rectilinear path. In case A the bubble shape is oblate ellipsoidal, in case B it is of ellipsoidal-cap type. The results show that the density ratio has a notable influence on the initial acceleration of the bubble. Once the bubble reached its terminal velocity, however, the bubble shape and Reynolds number are virtually independent of the density ratio. This also holds for the local velocity field induced by the rising bubble within the liquid phase, when scaled by the bubble rise velocity. For case A a minor influence of the density ratio on the internal motion within the bubble is identified. We find the computed bubble shape of case B to be in good agreement with an experiment [12] performed for the same values of Mo and $E\ddot{o}_B$ but for a density ratio of 1/1300 and a viscosity ratio of about 10^{-5} .

At present the invariance of the density ratio for steady rising single bubbles is demonstrated only for the specific parameters of $E\ddot{o}_B$, Mo , and Γ_μ given above. However, the simulations cover two orders of magnitude in the bubble Eötvös number, eight orders of magnitude in the Morton number and one order of magnitude in the bubble Reynolds number which is about 56 in case A and 6.5 in case B. We therefore expect that for steady bubbles the influence of the density ratio is marginal in general. For such bubbles then rather universal relations for bubble Reynolds number and drag coefficient in terms of Mo and $E\ddot{o}_B$ should exist. Furthermore, the scaling of the bubble driven liquid motion suggests that rather universal models may be derived in terms of Mo and $E\ddot{o}_B$ also for the pseudo-turbulence induced by bubbles rising almost steadily in dilute gas-liquid flows. Finally, we conclude that for steady bubbles it is possible to perform computationally efficient direct simulations with density ratio of order 0.1 while the results can be transferred to gas-liquid systems with density ratio of order 0.001.

It would be interesting to verify the invariance of the density ratio experimentally. This requires measurements with at least two sets of different gas-liquid or liquid-liquid systems which have the same Morton number but a different density ratio. If the Morton number of both systems is the same, then similarity of the Eötvös number can be ensured by properly setting the bubble diameters.

NOMENCLATURE

a_i	interfacial area concentration	Γ_μ	gas-liquid viscosity ratio
a_x, a_y, a_z	bubble dimensions	Γ_ρ	gas-liquid density ratio
d_B	bubble diameter	κ	interface curvature
$E\ddot{o}$	Eötvös number	μ	dynamic viscosity

f	liquid volumetric fraction	ρ	density
g	gravity	σ	coefficient of surface tension
L_{ref}	reference length	Superscripts	
Mo	Morton number	*	dimensional variable
\mathbf{n}	unit normal vector	'	coordinate system in moving frame of reference
p	pressure	Subscripts	
Re	Reynolds number	B	bubble
t	time	c	continuous phase (liquid)
\mathbf{V}_B, V_B	bubble velocity	com	center-of-mass
U_{ref}	reference velocity	d	disperse phase (gas)
\mathbf{u}, \mathbf{w}	velocity vectors	i	interface
u, v, w	velocity components	m	mixture value
We	Weber number	ref	reference value
\mathbf{x}, \mathbf{z}	position vectors		

REFERENCES

- [1] Ye, T., Shyy, W., & Chung, J.N., A fixed-grid, sharp-interface method for bubble dynamics and phase change, *J. Comput. Phys.*, 174, pp. 781-815, 2001.
- [2] Bunner, B., & Tryggvason, G., Dynamics of homogeneous bubbly flows. Part I: Motion of the bubbles. Submitted to *Journal of Fluid Mechanics*.
- [3] Wörner, M., The influence of gas-liquid density ratio on shape and rise velocity of an ellipsoidal bubble: A numerical study by 3D volume-of-fluid computations, F.-P. Schindler (Hrsg.), *VDI Fortschritt-Berichte, Reihe 3, Nr. 738*, pp. 67-84, VDI Verlag Düsseldorf, ISBN 3-18-373803-1, 2002.
- [4] Grace, J.R., Shapes and velocities of bubbles rising in infinite liquids, *Trans. Instn. Chem. Eng.*, 51, pp. 116-120, 1973.
- [5] Dandy, D.S., & Leal, L.G., Buoyancy-driven motion of a deformable drop through a quiescent liquid at intermediate Reynolds number, *J. Fluid Mech.*, 208, pp. 161-192, 1989.
- [6] Oka, H., & Ishii, K., Numerical analysis on the motion of gas bubbles using level set method, *J. Physical Soc. Japan*, 68, pp. 823-832, 1999.
- [7] Tryggvason, G., Bunner, B., Ebrat, O., & Tauber, W., Computations of multiphase flows by a finite difference/front tracking method. I. Multifluid flows, *Von Karman lecture notes*, the von Karman Institute, 1998.
- [8] Sabisch, W., Wörner, M., Grötzbach, G., & Cacuci, D.G., 3D volume-of-fluid simulation of a wobbling bubble in a gas-liquid system of low Morton number, 4th Int. Conf. on Multiphase Flow, New Orleans, LA, U.S.A., CD-ROM, paper 244, May 27 - June 1, 2001.
- [9] Clift, R., Grace, J.R., & Weber, M.E., *Bubbles, Drops, and Particles*, Academic Press, 1978.
- [10] Batchelor, G.K., *An introduction to fluid dynamics*, Cambridge Univ. Press, Reprint 1970.
- [11] Wörner, M., Sabisch, W., Grötzbach, G., & Cacuci, D.G., Volume-averaged conservation equations for volume-of-fluid interface tracking, 4th Int. Conf. on Multiphase Flow (ICMF), New Orleans, LA, U.S.A., CD-ROM, paper 245, May 27 - June 1, 2001.
- [12] Bhaga, D., & Weber, M.E., Bubbles in viscous liquids: shapes, wakes and velocities, *J. Fluid Mech.*, 105, pp. 61-85, 1981.
- [13] Mendelson, H.D., The prediction of Bubble Terminal Velocities from Wave Theory, *AICHe Journal*, 13, pp. 250-253, 1967.

VORTEX SIMULATION OF BUBBLE DISPERSION IN AN EXCITED ROUND JET

Tomomi Uchiyama¹⁾ and Tsuyoshi Honda²⁾

- ¹⁾ Center for Information Media Studies, Nagoya University
Furo-cho, Chikusa-ku, Nagoya 464-8603, JAPAN
Phone/Fax: +81-52-789-5187
E-mail: uchiyama@info.human.nagoya-u.ac.jp
- ²⁾ Graduate School of Human Informatics, Nagoya University
E-mail: t_honda@info.human.nagoya-u.ac.jp

ABSTRACT

This study is concerned with the three-dimensional numerical simulation of a bubbly jet, injected vertically upward in still water, when axial and helical disturbances are imposed. The water flow is simulated by a vortex method, and the equation of motion for a bubble is solved on the flow by the Lagrangian method. The disturbances markedly change the vortical structure of water in the developing region. Since the bubbles accumulate on the high vortical region, their dispersion remarkably varies owing to the disturbances. The helical and combined two helical disturbances are found to cause the larger dispersion of bubble. The present simulation suggests the possibility of the active control of the bubble dispersion in bubbly jet.

1. INTRODUCTION

Bubbly jets are observed in various engineering applications including chemical reactors, heat exchangers and waste treatment systems. The performance and efficiency of such devices markedly depend on the bubble dispersion. Thus, the void fraction has been thus far measured, and the relation with the velocity and turbulent intensity of the liquid-phase has been investigated [1][2]. On the other hand, the numerical analyses of the bubble motion in an isotropic turbulent flow by using a direct numerical simulation have elucidated that the bubbles preferentially accumulate on the high vorticity region [3][4]. In free shear layers, such as jets, wakes and mixing layers, large-scale organized vortical structures exist. Therefore, the preferential accumulation of bubbles in the large-scale vortices has been studied through the simulation of bubble motion in a plane mixing layer [5]-[7]. Recently, the relation between the bubble motion and the large-scale vortices in the developing region of a round jet attracts much attention, and the effect of bubble diameter on the bubble dispersion is gradually being clarified [8][9].

According to the experiments on a single-phase round jet by Long-Petersen [10][11], the vortical structure drastically changes due to the excitation by helical disturbances. This suggests the possibility of active control of a jet. Since the bubble motion is very sensitive to the vortical structure of fluid, the appropriate excitations promise to be applicable to control the bubble dispersion. But the bubble motion in excited jet has not been studied.

In this study, the possibility to control the bubble dispersion in a round jet by the excitation is discussed through the calculation of bubbly jet, injected vertically upward from a circular nozzle in still water. The bubbly jets excited by the axial, helical, and combined two helical disturbances are calculated. The three-dimensional vortex method is employed for the simulation of water flow, and the Lagrangian method is used for the calculation of bubble motion. The vortex method is based on the Lagrangian method, in which the time variation of the vorticity field is computed by tracing the motion of the vortex elements having vorticity. Thus, the method can directly calculate the

development of vortical structure without employing any turbulence model, and it has been usefully applied to analyse single-phase jet. The present numerical results demonstrate that the vortical structure changes due to the disturbances, and accordingly the bubble dispersion markedly varies. It is also indicated that the bubbles rapidly disperse due to the three-dimensional small-scale vortical structure generated just downstream of the nozzle, when the jet is excited by the single helical disturbance and the combined two helical disturbances.

2. BASIC EQUATIONS

2.1. Vorticity equation and Biot-Savart equation

Air-water bubbly jet is simulated. It is assumed that the diameter and volumetric fraction of the bubble are small and that the water flow is not affected by the bubble. The conservation equations for the water are expressed as follows:

$$\nabla \cdot \mathbf{u}_l = 0 \quad (1)$$

$$\frac{D\mathbf{u}_l}{Dt} = -\frac{1}{\rho_l} \nabla p + \nu \nabla^2 \mathbf{u}_l \quad (2)$$

Taking the curl of Eq. (2) and substituting Eq. (1) into the resulting equation, the transport equation for the vorticity $\boldsymbol{\omega}$ is obtained.

$$\frac{D\boldsymbol{\omega}}{Dt} = (\boldsymbol{\omega} \cdot \nabla) \mathbf{u}_l + \nu \nabla^2 \boldsymbol{\omega} \quad (3)$$

When the distribution of $\boldsymbol{\omega}$ is known, \mathbf{u}_l at \mathbf{x} is given by the Biot-Savart equation [12].

$$\mathbf{u}_l(\mathbf{x}) = -\frac{1}{4\pi} \int \frac{(\mathbf{x} - \mathbf{x}') \times \boldsymbol{\omega}(\mathbf{x}')}{|\mathbf{x} - \mathbf{x}'|^3} d\mathbf{x}' + \mathbf{u}_p \quad (4)$$

where \mathbf{u}_p stands for the potential velocity.

2.2. Vortex element

The vorticity field is discretized by vortex elements. This analysis employs a blob model [13], which is frequently used to solve engineering problems. The vortex element has a cylindrical shape as illustrated in Fig. 1, while the vorticity distribution is spherical. When the vortex element α at \mathbf{x}^α is supposed to have core radius σ_α , the vorticity at \mathbf{x} , $\boldsymbol{\omega}^\alpha(\mathbf{x})$, induced by the element is expressed by the following equation.

$$\boldsymbol{\omega}^\alpha(\mathbf{x}) = \frac{\boldsymbol{\gamma}^\alpha}{\sigma_\alpha^3} f\left(\frac{|\mathbf{x} - \mathbf{x}^\alpha|}{\sigma_\alpha}\right) \quad (5)$$

Here $f(\varepsilon)$ is the core distribution function, and $\boldsymbol{\gamma}^\alpha$ is the strength of vortex element expressed as:

$$\boldsymbol{\gamma}^\alpha = \boldsymbol{\omega}^\alpha \delta v_\alpha = \Gamma_\alpha \mathbf{l}^\alpha \quad (6)$$

where δv_α is the volume, \mathbf{l}^α the length vector, and Γ_α the circulation.

The following equation proposed by Winckelmans-Leonard [13] is used for $f(\varepsilon)$.

$$f(\varepsilon) = \frac{15}{8\pi} \frac{1}{(\varepsilon^2 + 1)^{3.5}} \quad (7)$$

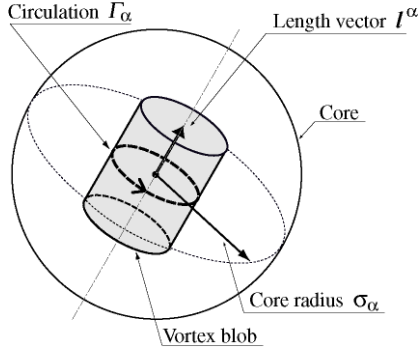


Fig. 1: Vortex element

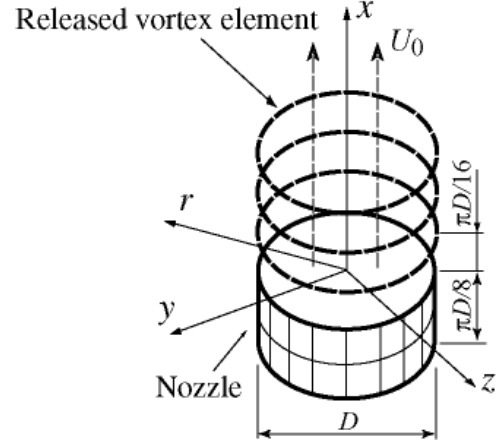


Fig. 2: Nozzle and released vortex element

2.3. Evolution of vortex element

When the vorticity field is discretized into a set of N vortex elements, the velocity $\mathbf{u}_l(\mathbf{x})$ is given by the following equation derived from Eqs. (4) and (5).

$$\mathbf{u}_l(\mathbf{x}) = -\frac{1}{4\pi} \sum_{\alpha=1}^N \frac{(\mathbf{x} - \mathbf{x}^\alpha) \times \boldsymbol{\gamma}^\alpha}{|\mathbf{x} - \mathbf{x}^\alpha|^3} g\left(\frac{|\mathbf{x} - \mathbf{x}^\alpha|}{\sigma_\alpha}\right) + \mathbf{u}_p \quad (8)$$

where the function $g(\varepsilon)$ is determined as:

$$g(\varepsilon) = 4\pi \int_0^\varepsilon f(\zeta) \zeta^2 d\zeta \quad (9)$$

The vortex element α convects with the fluid velocity at its centre.

$$\frac{d\mathbf{x}^\alpha}{dt} = \mathbf{u}_l(\mathbf{x}^\alpha) \quad (10)$$

The vorticity varies with the lapse of time owing to the change in the length of vortex element and the viscous diffusion as found in Eq. (3). The three-dimensional vortex methods separately simulate these variations. To calculate the effect of the viscous diffusion, the core spreading method [12] is employed, which can yield reasonable solution with less vortex elements. The method makes the core radius increase with the lapse of time.

$$\frac{d\sigma_\alpha^2}{dt} = 4\nu \quad (11)$$

The time variation of vorticity owing to the change in the length of vortex element is computed by using the Lagrangian expression of Eq. (3).

$$\frac{d\boldsymbol{\omega}}{dt} = (\boldsymbol{\omega} \cdot \nabla) \mathbf{u}_l \quad (12)$$

where the viscous term is neglected because it is already considered in the core spreading method.

When substituting Eqs. (5) and (8) into Eq. (12), the time rate of change in the strength of vortex element α , $\boldsymbol{\gamma}^\alpha$, is derived.

$$\frac{d\boldsymbol{\gamma}^\alpha}{dt} = \frac{1}{4\pi} \sum_{\beta} \frac{1}{\sigma_{\beta}^3} \left\{ -\frac{g(\zeta)}{\zeta^3} \boldsymbol{\gamma}^\alpha \times \boldsymbol{\gamma}^\beta + \frac{1}{\sigma_{\beta}^2} \left[-\frac{d}{\zeta d\zeta} \left(\frac{g(\zeta)}{\zeta^3} \right) \right] \times \left[\boldsymbol{\gamma}^\alpha \cdot (\mathbf{x}^\alpha - \mathbf{x}^\beta) \right] [(\mathbf{x}^\alpha - \mathbf{x}^\beta) \times \boldsymbol{\gamma}^\beta] \right\} \quad (13)$$

where $\zeta = |\mathbf{x}^\alpha - \mathbf{x}^\beta| / \sigma_{\beta}$.

The vorticity of vortex element generally increases with the passage of time in the downstream region due to the vortex stretching, causing the decrement in the spatial resolution. To maintain the resolution, the vortex element α , of which initial strength is $\boldsymbol{\gamma}^\alpha$, is divided into two vortex elements having the strength $\boldsymbol{\gamma}^\alpha / 2$, when the strength becomes greater than twice its initial value [14].

2.4. Equation of motion for bubble

The equation of motion for a spherical bubble having diameter d is expressed as [15]:

$$\frac{d\mathbf{u}_g}{dt} = \frac{1+C_V}{\beta+C_V} \frac{D\mathbf{u}_l}{Dt} - \frac{1}{\beta+C_V} \frac{3C_D}{4d} \mathbf{u}_r |\mathbf{u}_r| + \frac{\beta-1}{\beta+C_V} \mathbf{g} - \frac{C_L}{\beta+C_V} \mathbf{u}_r \times (\nabla \times \mathbf{u}_r) \quad (14)$$

where $\mathbf{u}_r = \mathbf{u}_g - \mathbf{u}_l$, $\beta = \rho_g / \rho_l$. C_V , C_D and C_L are the virtual mass coefficient, the drag coefficient and the lift coefficient, respectively. The coefficients C_V and C_L are set as 0.5, while the C_D value is determined by the following equation [16].

$$C_D = 24f / \text{Re}_b \quad (15)$$

where $f = 1 + 0.15\text{Re}_b^{0.687}$ and $\text{Re}_b = d|\mathbf{u}_r| / \nu$.

Rewriting Eq. (14) in the nondimensional form by using the velocity at the nozzle exit U_0 and the axial space between the large-scale vortices λ near the nozzle exit, the following equation is obtained.

$$\frac{d\tilde{\mathbf{u}}_g}{d\tilde{t}} = \frac{1+C_V}{\beta+C_V} \frac{D\tilde{\mathbf{u}}_l}{D\tilde{t}} - \frac{f}{\text{St}} \tilde{\mathbf{u}}_r + \frac{\beta-1}{\beta+C_V} \frac{\mathbf{g}}{g\text{Fr}^2} - \frac{C_L}{\beta+C_V} \tilde{\mathbf{u}}_r \times (\tilde{\nabla} \times \tilde{\mathbf{u}}_r) \quad (16)$$

where $\tilde{\mathbf{u}}_g = \mathbf{u}_g / U_0$ and $\tilde{t} = tU_0 / \lambda$. St and Fr are the modified Stokes number and the Froude number, respectively, and they are defined as:

$$\text{St} = (\beta + C_V) \frac{d^2 / 18\nu}{\lambda / U_0} \quad (17)$$

$$\text{Fr} = \frac{U_0}{\sqrt{g\lambda}} \quad (18)$$

St stands for the ratio of the relaxation time of bubble motion τ_g to the characteristic time of large-scale vortices τ_1 , resulting in $\text{St} = (\beta + C_V) (\tau_g / \tau_1)$.

3. CALCULATING CONDITION

3.1. Modelling of cylindrical nozzle

The bubbly jet, injected vertically upward with velocity U_0 from a circular nozzle with diameter $D = 13$ mm in still water, is calculated. The Reynolds number, $U_0 D / \nu$, is 13000. The

flow in the nozzle is simulated through a panel method [14]. The nozzle length is $\pi D/8$ and the wall is divided into square panels as shown in Fig. 2. Vortex elements are fixed on the centre of each panel. The circulation of vortex element is determined so as to satisfy the zero cross-flow velocity at the centre of each panel. The nozzle has a source disk at its bottom. The disk consists of 49 sources arranged on three concentric circles and the centre as shown in Fig. 3. The strength of source is determined so that the uniform velocity distribution is achieved at the nozzle exit.

The velocity shear layer originating from the nozzle edge is represented by releasing vortex elements from the edge at a time interval Δt_v . The panel adjacent to the nozzle edge and the vortex element are illustrated in Fig. 4. The vortex elements are released from a position $\pi D/16$ downstream of the nozzle edge. The core radius of vortex element at the release is set at $0.4D$. The circulation of released vortex element at time t , $I_r(t)$, is given by the following equation.

$$I_r(t) = I_f(t) - I_f(t - \Delta t_v) \quad (19)$$

where $I_f(t)$ stands for the circulation of fixed vortex element, and $I_r(0) = I_f(0)$.

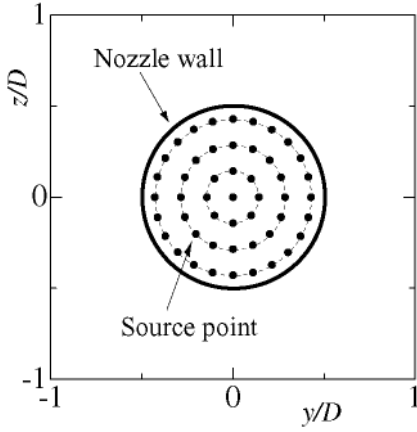


Fig. 3: Source panel at nozzle bottom

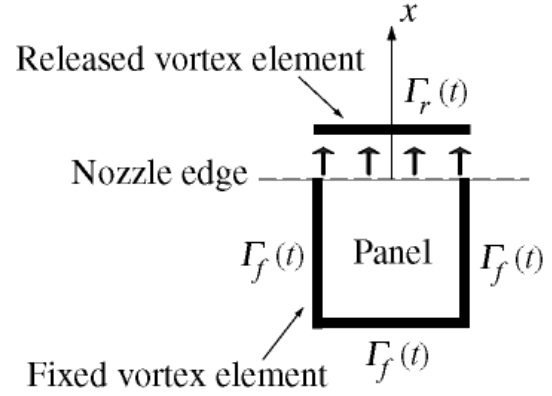


Fig. 4: Panel at nozzle exit

3.2. Convection of vortex element and bubble

The convection of vortex element and the evolution of vortex strength are calculated by the second-order Adams-Bashforth method. The time increment Δt is $0.1D/U_0$, while the time interval to release the vortex element Δt_v is $2\Delta t$.

The second-order Adams-Bashforth method is also employed for the calculation of bubble motion. The calculation is performed for the bubble with diameter $d = 0.5$ mm. Fifteen bubbles are loaded into the water from the nozzle exit at a time interval $5\Delta t$. The initial velocity coincides with the water velocity, and the initial position is determined by using random numbers.

3.3. Excitation

Random disturbance with small amplitude ε_R is superimposed on the uniform velocity U_0 at the nozzle exit to simulate the experimental condition at the exit. The disturbance is given randomly in space and time, where ε_R is set at $0.003U_0$. Periodical disturbance u_x is superimposed on the jet.

$$u_x = \varepsilon_F \sin(m\phi - 2\pi ft) \quad (20)$$

where ε_F is the amplitude, m the mode number, ϕ the azimuthal angle about the x axis, and f the excitation frequency. The condition $m=0$ yields the axial excitation, while $m \neq 0$ produces the helical one. The disturbance is imposed on the outermost two rows of the source disk.

When the fundamental frequency of the flow $2D$ downstream of the nozzle, f_0 , is computed without the periodical disturbance, the Strouhal number $f_0 D / U_0$ indicates 0.35. Therefore, the characteristic time of the large-scale vortices τ_l is 0.037 s, the Stokes number St is 0.19, and the Froude number Fr is 1.66. Four kinds of calculations, listed in Table 1, are performed in this study, where the forcing frequency f is set at f_0 .

Table 1 Calculating condition

	Pattern	ε_F / U_0	m	fD / U_0
Case 1	No disturbance	0	-	-
Case 2	Axial disturbance	5%	0	0.35
Case 3	Helical disturbance	5%	1	0.35
Case 4	Two helical disturbances	5%	± 1	0.35

4. RESULTS AND DISCUSSIONS

4.1. Evolution of vorticity

The evolution of the vorticity ω and the axial component ω_x are shown in Figs. 5 to 8. The iso-surfaces of ω / ω_0 and ω_x / ω_0 are depicted, where ω_0 is the average value of ω at the nozzle exit. The nondimensional time t^* is defined as tU_0 / D .

Figure 5 shows the evolution in Case 1. The iso-surfaces of $\omega / \omega_0 = 3.5$ and $\omega_x / \omega_0 = \pm 0.005$ are depicted. Vortex rings appear at a constant interval downstream of the nozzle owing to the instability of the shear layers. The axisymmetrical distribution of ω decays with increasing the axial distance, and an axial vorticity ω_x appears. But the three-dimensional feature of the flow is not so remarkable, because the magnitude of ω_x is much smaller than that of ω .

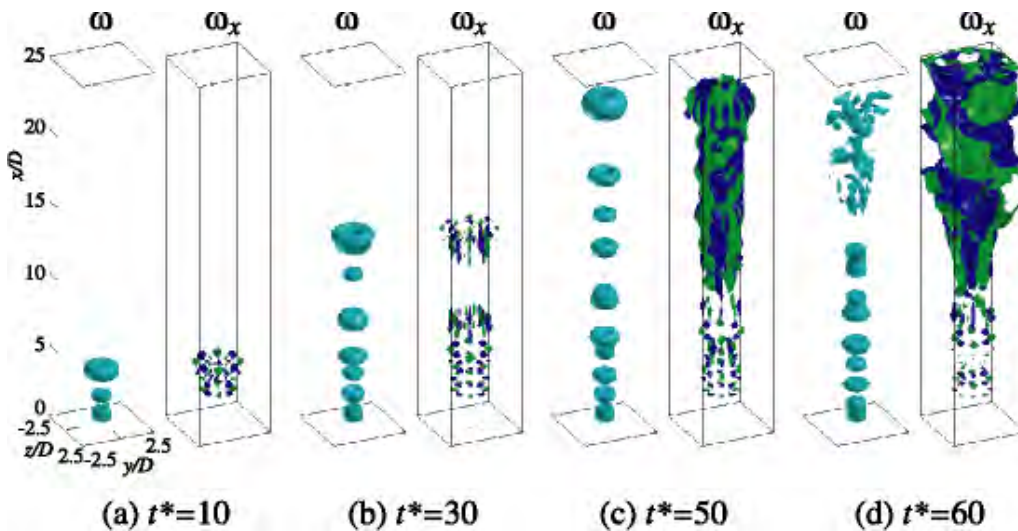


Fig. 5: Evolution of vorticity in Case 1 ($\omega / \omega_0 = 3.5$ and $\omega_x / \omega_0 = \pm 0.005$)

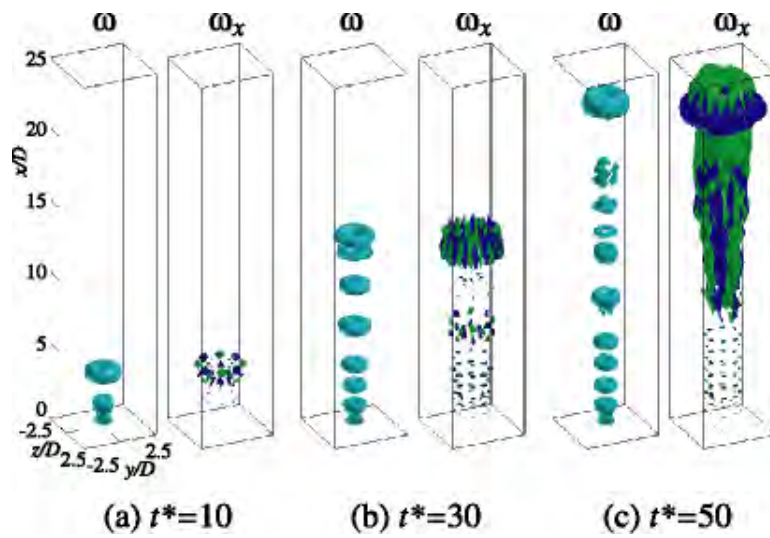


Fig. 6: Evolution of vorticity in Case 2 ($\omega / \omega_0 = 3.5$ and $\omega_x / \omega_0 = \pm 0.005$)

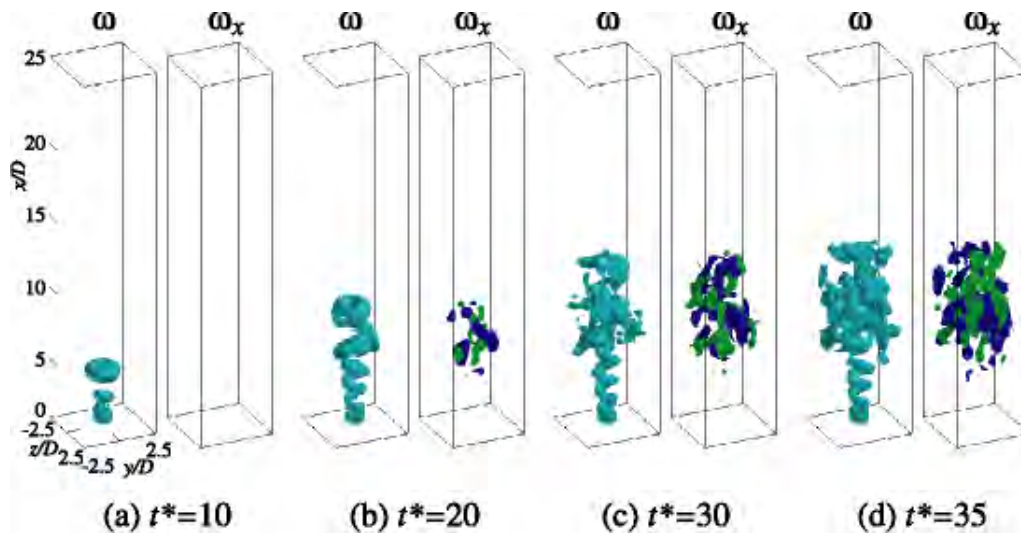


Fig. 7: Evolution of vorticity in Case 3 ($\omega / \omega_0 = 3.5$ and $\omega_x / \omega_0 = \pm 1.5$)

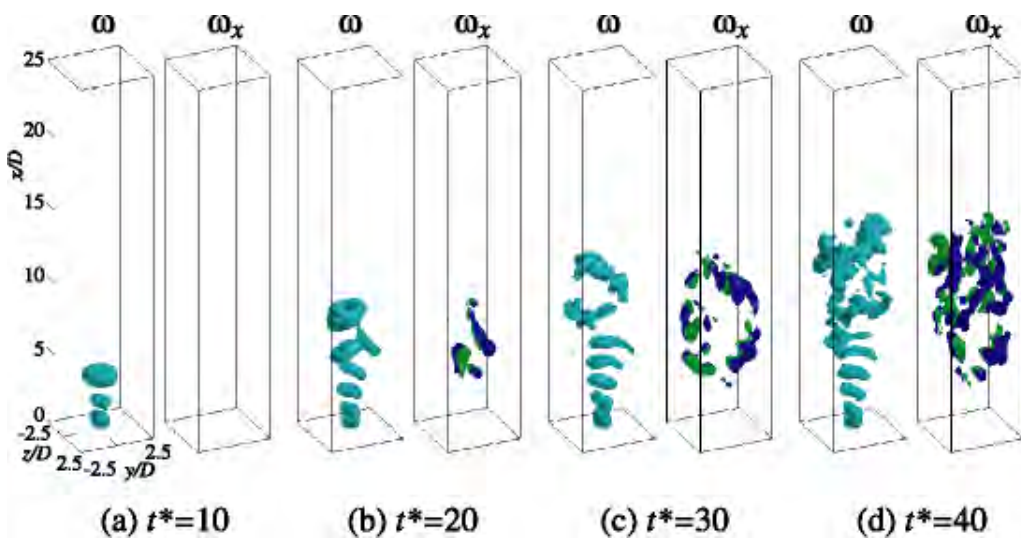


Fig. 8: Evolution of vorticity in Case 4 ($\omega / \omega_0 = 3.5$ and $\omega_x / \omega_0 = \pm 1.5$)

The evolution in Case 2 is shown in Fig. 6. Highly axisymmetrical vortex rings exist. The vortical structure is quite similar to that in Case 1.

The result in Case 3 is shown in Fig. 7, where the iso-surfaces of $\omega/\omega_0=3.5$ and $\omega_x/\omega_0=\pm 1.5$ are depicted. Helical vortex tube is generated just downstream of the nozzle. But the vortical structure rapidly changes into three-dimensional small-scale one at $x/D \geq 4.8$. In this region, the axial vorticity ω_x is observed, and pairs of positive and negative axial vortices are generated. The magnitude of ω_x is much larger than those in Case 1 and Case 2, indicating the remarkable three-dimensional feature of the flow.

Figure 8 shows the evolution of vorticity in Case 4. The maximum amplitude of disturbance exists at $\phi=0$ and π in the $x-y$ plane. The vortex rings are not axisymmetrical just downstream of the nozzle exit. A part of the vortex ring merges with the upstream or downstream ring. In the region of $x/D \geq 6.7$, the axial vortices ω_x with almost the same strength as that in Case 3 appear, and three-dimensional small-scale vortices are rapidly produced.

The distributions of the vorticity in the cross-section of the jet ($y-z$ plane) at $t^*=35$ and 40 in Case 3 and Case 4, respectively, are shown in Fig. 9, where the results on the sections of $x/D=8$ and 9 are plotted. The magnitude of ω_x is as large as that of ω , suggesting that axial vortices with high strength appear in the sections. In Case 3, the distributions are random. But both ω and $|\omega_x|$ distribute symmetrically around the y -axis in Case 4, and they take the maximum values near the y -axis at $x/D=8$.

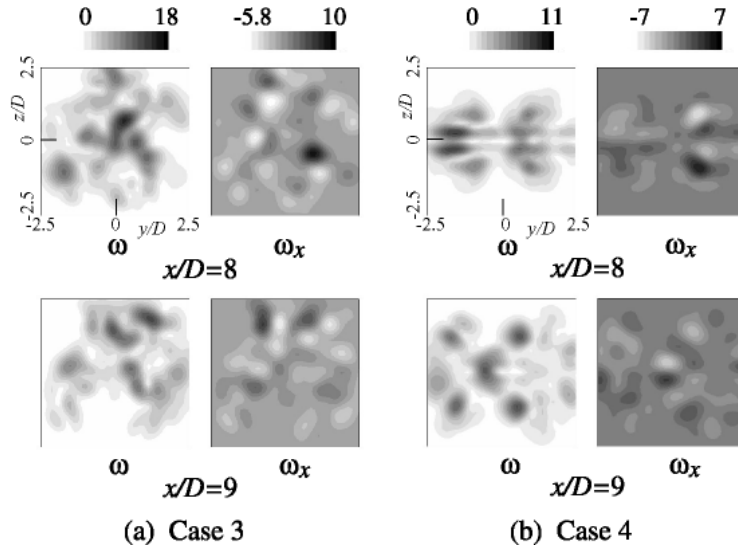


Fig. 9: Distribution of ω and ω_x in cross-sectional area for Case 3 and Case 4

4.2. Time variation of bubble dispersion

The time variation for the bubble dispersion is shown in Figs. 10 to 13. The change in the iso-surface of $\omega/\omega_0=3.5$ is also depicted.

The result in Case 1 is shown in Fig. 10. The bubbles distribute almost uniformly in the region of $x/D \leq 2$, but a number of them accumulate in the vortex rings downstream of the region. This is because the pressure is lower in the vortex ring, and therefore the bubbles move to the vortex ring due to the pressure gradient. Such accumulation on the high vorticity region, which is called preferential accumulation, has been also reported by the direct numerical simulation of the isotropic

turbulent flow [3][4] and by the vortex simulation of the two-dimensional mixing layer [7]. In the region of $x/D \geq 14.8$, where three-dimensional vortical structures appear, the bubbles disperse in the lateral direction.

Figure 11 shows the time variation in Case 2. Since the vortical structure is parallel with that in Case 1, the bubble distribution is almost similar to the result of Case 1 shown in Fig. 10.

The time variation for the bubble distribution in Case 3 is shown in Fig. 12. The bubbles distribute helically at $0 \leq x/D \leq 4.8$ owing to the helical structure of the vorticity. Just downstream of the region, the bubbles markedly disperse in the lateral direction. This is because the three-dimensional small-scale vortical structures are generated there.

In Case 4, the bubbles disperse as shown in Fig. 13. The bubbles distribute around the centerline of the jet near the nozzle exit. But they rapidly disperse due to the generation of the three-dimensional vortical structures in $x/D \geq 2.9$ at $t^* = 30$ and 40.

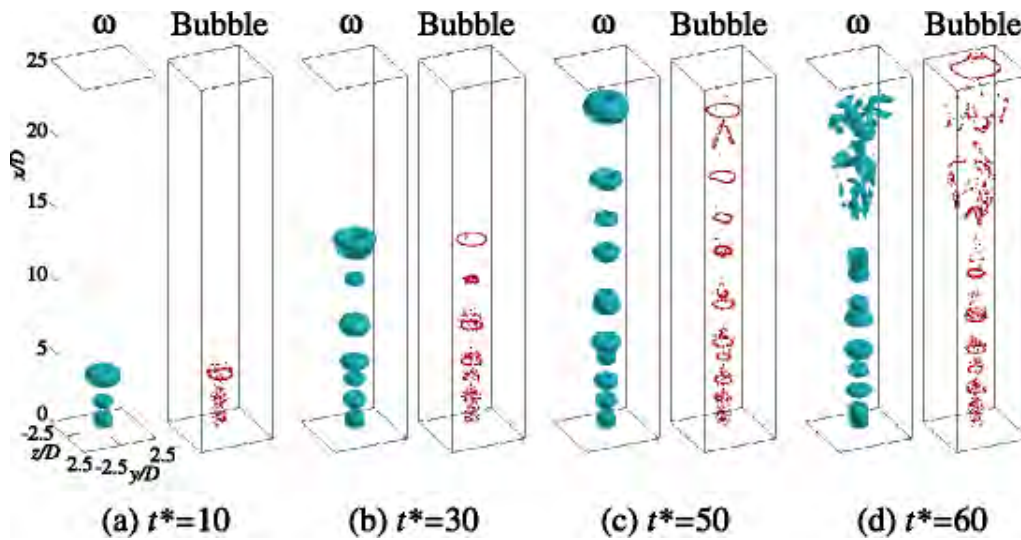


Fig. 10: Time variation of bubble dispersion in Case 1 ($\omega / \omega_0 = 3.5$)

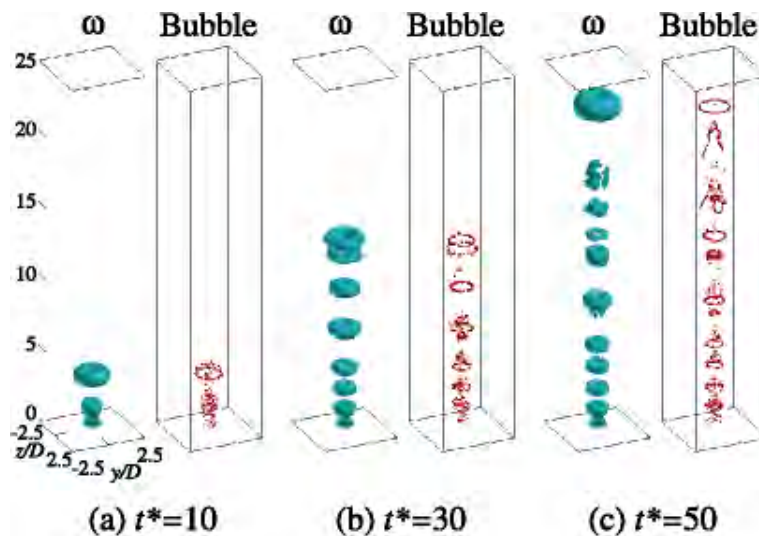


Fig. 11: Time variation of bubble dispersion in Case 2 ($\omega / \omega_0 = 3.5$)

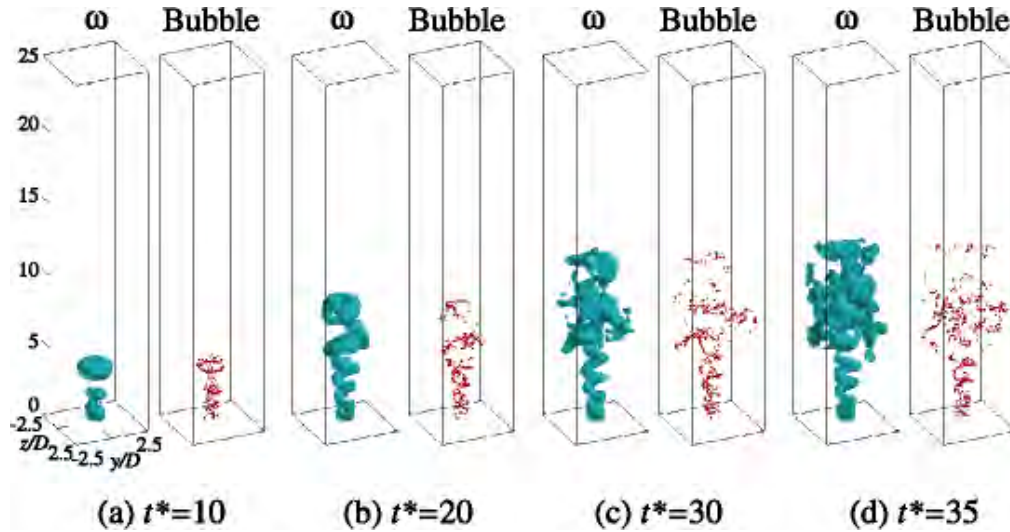


Fig. 12: Time variation of bubble dispersion in Case 3 ($\omega / \omega_0 = 3.5$)

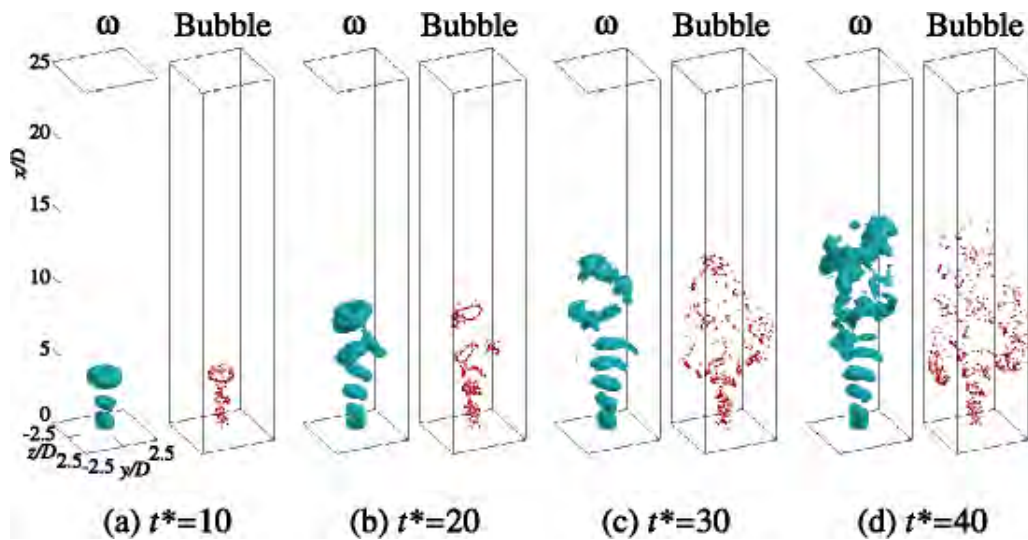


Fig. 13: Time variation of bubble dispersion in Case 4 ($\omega / \omega_0 = 3.5$)

To grasp the bubble distribution in the jet cross-section more definitely, the distributions are plotted in the $y - z$ plane as shown in Fig. 14. In Case 1 and Case 2, the bubbles distribute around the jet centreline and they less disperse in the lateral direction. The bubbles in Case 3 almost uniformly distribute within a circle of diameter $5D$. In Case 4, the bubbles concentrate near the y -axis, distributing along the axis. This is because the vorticity reaches its maximum value near the y -axis as indicated in Fig. 9. From the above-mentioned results, it is found that the bubble dispersion is successfully controlled by changing the vortical structure with the aid of excitations.

4.3. Dispersion of bubble

To estimate the bubble dispersion, the bubble dispersion coefficient D_b is defined as:

$$D_b = \frac{1}{N} \sum_{i=1}^N \frac{(r_i - \bar{r})^2}{\bar{r}^2} \quad (21)$$

where N is the number of bubbles, \bar{r} the average radial position for bubble, and r_i the radial position of bubble. Figure 15 shows the time variation of D_b . In Case 1 and Case 2, D_b takes its minimum value at $t^*=40$. This is due to the bubble accumulation on the vortex rings. In Case 3 and Case 4, it reaches its maximum value at $t^*=30$, while it decreases thereafter. Because the axial vorticity more develops as shown in Figs. 6 and 7, and accordingly the bubbles accumulate on these vortices.

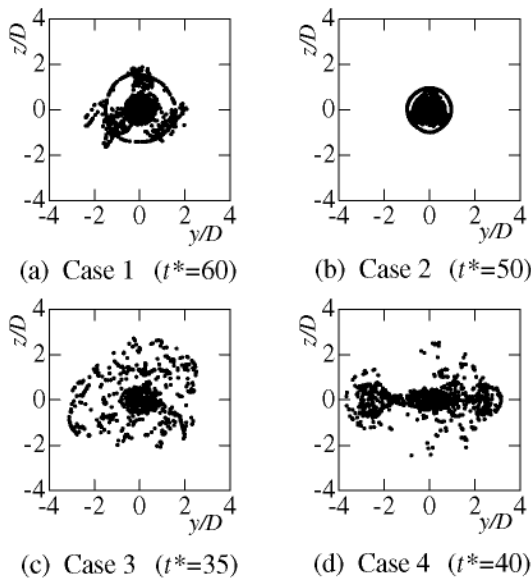


Fig. 14: Bubble distributions in cross-sectional area

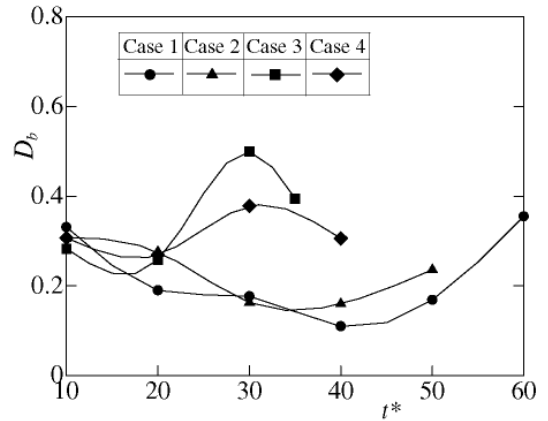


Fig. 15: Time variation of bubble dispersion coefficient

5. CONCLUSIONS

The three-dimensional calculation is performed on a developing round bubbly jet excited by periodical disturbances. The results are summarized as follows.

- (1) The bubbles accumulate on the high vortical region in the jet, being in accordance with the preferential accumulation of bubble.
- (2) The bubble dispersion in the lateral direction is small when the jet is not excited or the axial disturbance is imposed.
- (3) The single helical disturbance and combined two helical disturbances can produce the three-dimensional small-scale vortical structures with high strength, and accordingly they rapidly disperse the bubbles.
- (4) The bubble dispersion is successfully controlled by changing the vortical structure with the aid of excitation.

REFERENCES

- [1] Sun, T-Y. and Faeth, G. M., Structure of turbulent bubbly jets - I. Methods and centerline properties, *Int. J. Multiphase Flow*, Vol. 12, No. 1, pp. 99-114, 1986.
- [2] Kumar, S. et al., Effect of bubbles on the turbulence near the exit of a liquid jet, *Experiments in Fluids*, Vol. 7, pp. 487-494, 1989.
- [3] Wang, L.-P. and Maxey, M. R., The motion of microbubbles in a forced isotropic and homogeneous turbulence, *Appl. Sci. Res.*, Vol. 51, pp. 291-296, 1993.
- [4] Maxey, M. R. et al., Simulation of interactions between microbubbles and turbulent flows, *Appl. Mech. Rev.*, Vol. 4, S70, 1994.
- [5] Sene, K. J. et al., The role of coherent structures in bubble transport by turbulent shear flows, *J. Fluid Mech.*, Vol. 259, pp. 219-240, 1994.
- [6] Druzhinin, O. A. and Elghobashi, S., Direct numerical simulation of a three-dimensional spatially developing bubble-laden mixing layer with two-way coupling, *J. Fluid Mech.*, Vol. 429, pp. 23-61, 2001.
- [7] Yang, X. et al., Two-way coupled bubble laden mixing layer, *Chem. Eng. Sci.*, Vol. 57, pp. 555-564, 2002.
- [8] Stanley, K. N. and Nikitopoulos, D. E., Dispersed, bubbly, axisymmetric jets, *Proc. Int. Conf. Multiphase Flow*, New Orleans, (on CD-ROM), 2001.
- [9] Farish, R. et al., The effect of large-scale structures on the condensation of bubbles in an axisymmetric jet, *Proc. Int. Conf. Multiphase Flow*, New Orleans, (on CD-ROM), 2001.
- [10] Long, T. A. and Petersen, R. A., Controlled interactions in a forced axisymmetric jet, Part 1. The distortion of the mean flow, *J. Fluid Mech.*, Vol. 235, pp. 37-55, 1992.
- [11] Petersen, R. A. and Long, T. A., Controlled interactions in a forced axisymmetric jet, Part 2. The modulation of broadband turbulence, *J. Fluid Mech.*, Vol. 235, pp. 57-72, 1992.
- [12] Leonard, A., Vortex methods for flow simulation, *J. Comput. Phys.*, Vol. 37, pp. 289-335, 1980.
- [13] Winckelmans, G. S. and Leonard, A., Contribution to vortex particle methods for the computation of three-dimensional incompressible unsteady flows, *J. Comput. Phys.*, Vol. 109, pp. 247-273, 1993.
- [14] Izawa, S. and Kiya, M., A turbulent model for the three-dimensional vortex blob method, *JSME Int. J., Ser. B*, Vol. 43, No. 3, pp. 434-442, 2000.
- [15] Thomas, N. H. et al., Entrapment and transport of bubbles by transient large eddies in multiphase turbulent shear flows, *Proc. Int. Conf. Physical Modelling of Multiphase Flows*, Coventry, pp. 169-184, 1983.
- [16] Clift, R. et al., *Bubbles, drops and particles*, Academic Press, New York, 1978.

SURFACE WAVE STRUCTURE AND HEAT TRANSFER OF VERTICAL LIQUID FILM FLOW

T. Kunugi, C. Kino and A. Serizawa
Department of Nuclear Engineering
Kyoto University
Yoshida, Sakyo, Kyoto, 6060-8501, JAPAN
Phone & Fax: +81 75 753 5823
E-mail: kunugi@nucleng.kyoto-u.ac.jp

ABSTRACT

Two- and three-dimensional numerical simulations of falling liquid film on a vertical wall have been performed in order to investigate the relationship between the interfacial wave behavior and heat transfer. Fully developed two-dimensional wave consists of a solitary and a capillary waves. Numerical results indicate that the heat transfer of falling film flow is enhanced by small vortices between the solitary and capillary waves in addition to the well-known flow recirculation in the solitary wave. Three-dimensional simulation results indicate the importance of relationship between the surface wave structure and the wall shear stress.

1. INTRODUCTION

It is very important to grasp and understand the falling film flow behavior along the vertical wall from the heat and mass transport point of view in many engineering fields [1]. According to the stability theory, the vertical falling film flows are always unstable and various types of surface waves appeared due to the non-linear wave interactions such as a solitary wave and a capillary wave, etc. Although the heat and mass transfer are certainly enhanced by these waves, the enhancement mechanism is not well understood until today.

There are many experimental studies for investigating the film flow characteristics. However, most of numerical studies are focused on the two-dimensional laminar liquid film flow because of the limitation of computer power and the difficulty of the free surface treatment numerically [2].

In the present study, the two- and three-dimensional numerical simulations of falling liquid film on a vertical wall have been performed in order to investigate the relationship between the interfacial wave behavior and heat transfer.

2. NOMENCLATURE

C_v :	Specific heat at constant volume	T_{air}, T_b, T_{wall} :	Air, bulk and wall temperatures
F_m :	Volume fraction of m-th fluid	t :	Dimensionless time
F_γ :	Surface tension term	U, U_0 :	Velocity and initial velocity
f :	Frequency	X :	Dimensionless distance from inlet
G :	Gravity	y :	Dimensionless distance from wall
h :	Film thickness	λ :	Thermal conductivity
h_0 :	Initial film thickness (equilibrium height)	ν :	Viscosity
Nu :	Nusselt number	ρ :	Density
P :	Pressure	τ :	Shear stress
Q :	Heat source	$\langle \rangle$:	Linear average
Re :	Reynolds number	$\langle \rangle_M$:	Material average

3. NUMERICAL PROCEDURES

The governing equations are the continuity for multi-phase flows, momentum equation based on the one-filed model and the energy equation as follows:

$$\frac{\partial F_m}{\partial t} + \nabla \cdot (F_m U) - F_m \nabla U = 0 \quad (1)$$

$$\frac{\partial U}{\partial t} + \nabla \cdot (UU) = G - \frac{1}{\langle \rho \rangle} (\nabla P - F_V) - \nabla \cdot \tau \quad (2)$$

$$\frac{\partial \langle \rho C_v \rangle_M T + \nabla \cdot (\langle \rho C_v \rangle_M TU)}{\partial t} = \nabla \cdot (\langle \lambda \rangle_M \nabla T) + Q \quad (3)$$

Here, F is the volume fraction of fluid, λ is the thermal conductivity, C_v is the specific heat at constant volume and the suffix m denotes the m -th fluid or phase, $\langle \rangle$ denotes the material average and the F_V is body force due to the surface tension based on CSF (Continuum Surface Force) model. The interface tracking technique is based on the MARS (Multi-interface Advection and Reconstruction Solver) [3].

As for the two-dimensional simulation, the mesh sizes are $(\Delta x, \Delta y) = (0.4h_0, 0.1h_0)$ and $(\Delta x, \Delta y, \Delta z) = (0.6h_0, 0.2h_0, 1.0h_0)$ for 3D simulation. Here, h_0 is an equilibrium liquid film thickness. The inlet mean velocity U_0 can be controlled by the external forcing as expressed:

$$U = [1 + \varepsilon \sin(2\pi ft)] U_0 \quad (4)$$

Here, the forcing frequency is f . The 0 Hz, 13 Hz, 20 Hz and 45 Hz are considered in the present study. Reynolds number ($Re = U_0 h_0 / \nu$) is set to 75 that is a critical Re [4]. ε is set to 0.03 as same as the reference [2]. The outflow boundary is assumed to be a zero pressure gradient, the airside boundary surrounding the solution domain is assumed to be a constant pressure. At the wall, the non-slip velocity condition is applied. In case of 3D simulation, no disturbance is applied to the inlet velocity, that is, the three-dimensional flow is naturally developed. The periodic boundary condition is applied to the span (z)-direction. Applied heating conditions are as follows:

- (1) Constant temperature at both wall and air
- (2) Constant temperature at air and constant heat flux at the wall

4. RESULTS AND DISCUSSIONS

4.1 Two-dimensional Simulation Results

Figures 1(a), (b) show the film thickness distribution for 0 and 20 Hz, respectively. According to the stability theory, the vertical falling film flows are always unstable [4]. The film thickness shown in Fig. 1(a) is very stable. It might be depending on the computational mesh size. As for (b), the liquid film becomes unstable in the downstream region, and eventually the solitary wave and the capillary waves in front of the solitary one are developed. The numerical results of the relationship between the peak height of solitary wave and the frequency is in very good agreement with the experiments as shown in Figure 2. Figure 3(a) shows the streamlines on the moving coordinate with the wave celerity. A large recirculation flow can be seen in the solitary wave. Figure 3(b) shows the velocity vector and the vortices can be seen between waves. There is no report on these vortices in the previous experimental and numerical studies. Figure 4 shows the distributions of Nusselt

number: $Nu = [(T_{wall} - T) / (T_{air} - T_b)] h / \Delta y$ for heating condition (1), and Figure 5 shows it for heating condition (2). Here, T_{air} is air temperature, T_{wall} is the wall temperature, Δy is the distance from wall and T_b is the bulk temperature. In the no-disturbance case, the Nu value is almost kept constant, but for 20 Hz case it can be seen a large fluctuation of the heat transfer. Figure 6 shows the temperature contours in the liquid film. At the boundary region between the solitary wave and the capillary wave, the heat transfer is enhanced due to the existence of the vortex there. On the other hand, the heat transfer in the solitary wave is deteriorated due to the temperature stratification. The mean Nu is around 0.43 for 0 Hz and 1.1 for 20 Hz in case of heating condition (1), and around 2.8 for 0 Hz and 2.7 for 20 Hz in case of heating condition (2).

4.2 Three-dimensional Simulation Results

Figure 7 shows (a) the mean film thickness and (b) the mean Nu along the streamwise (x)-direction. Many large waves that could not be seen in the 2D simulation are observed. This fact is also confirmed by the flow visualization regarding the free surface shape as shown in Fig. 8. According to the shear stress and the local Nu distributions not shown in the paper, the large shear stress regions appear at the boundary regions between the solitary and capillary waves. Eventually, the heat transfer is enhanced in that region. The overall mean Nu becomes around 1.0 and is greater than that of 2D simulation. Therefore, it can be considered that the liquid film heat transfer is strongly affected by the 3D wave structure.

REFERENCES

- [1] Nosoko, T., Characteristics of Two-Dimensional Waves on A Falling Liquid Film, Chem. Eng. Soc., 51 (1996) 725-732
- [2] Miyara, A., Numerical Simulation of Wavy Liquid Film Flowing Down on a Vertical Wall and an Inclined Wall, Int. J. Therm. Sci. (2000) 39, 1015-1027
- [3] Kunugi, T., MARS for Multiphase Calculation, Computational Fluid Dynamics J., 9, (2001) 563-571
- [4] Alekseenko, S. V., Nakoryakov, V. E. and Pokusaev, B. G., Wave Flow of Liquid Films, Begell House, New York, 1994

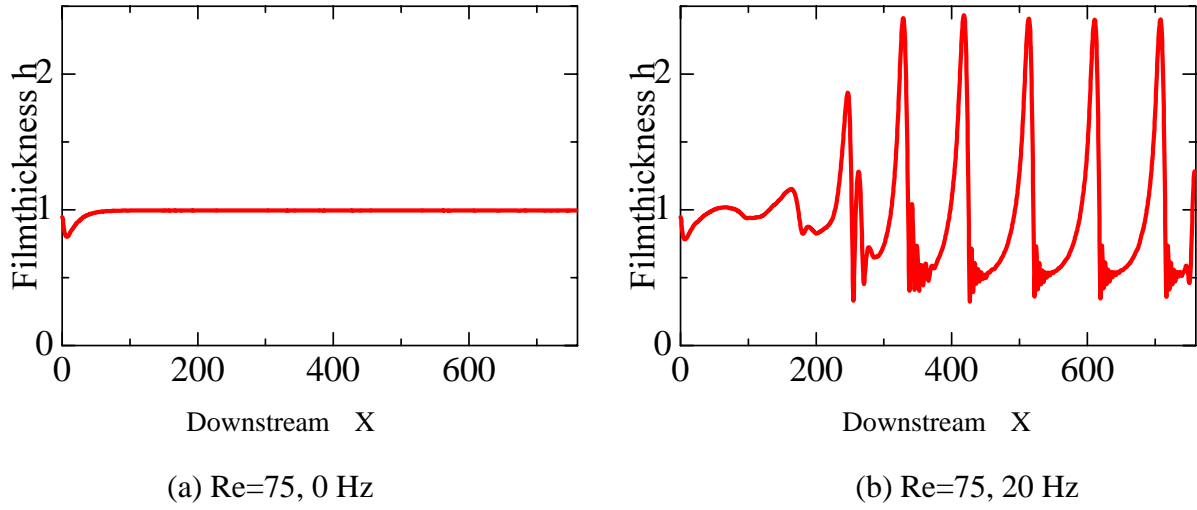


Figure 1: Fully developed film thickness behavior.

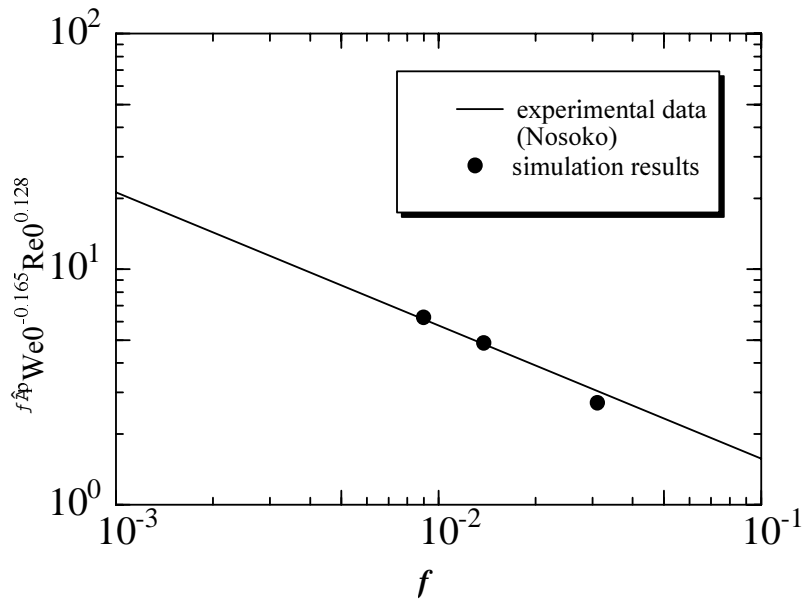


Figure 2: Comparison of wave peak height between simulation and experimental data [1].

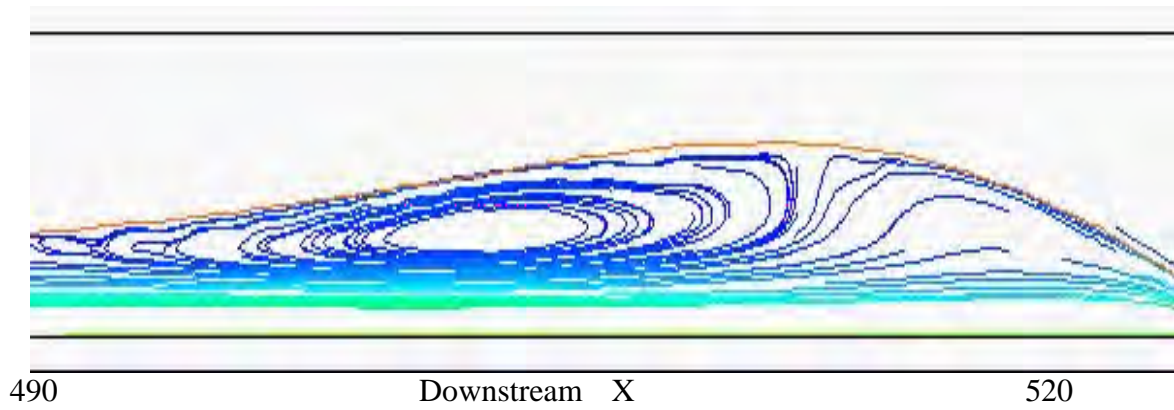


Figure 3(a): Streamlines observed from moving coordinates with wave celerity for $Re = 75$ and 20 Hz.

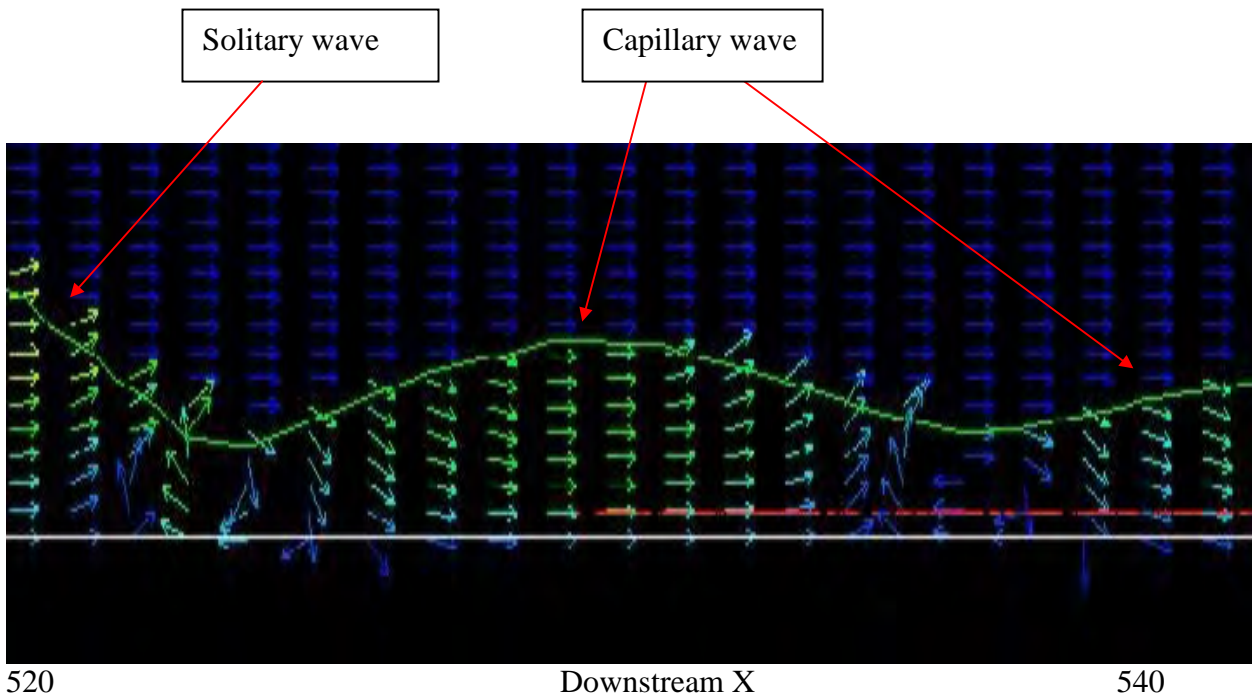


Figure 3(b): Vector of velocity for $Re = 75$ and 20 Hz.

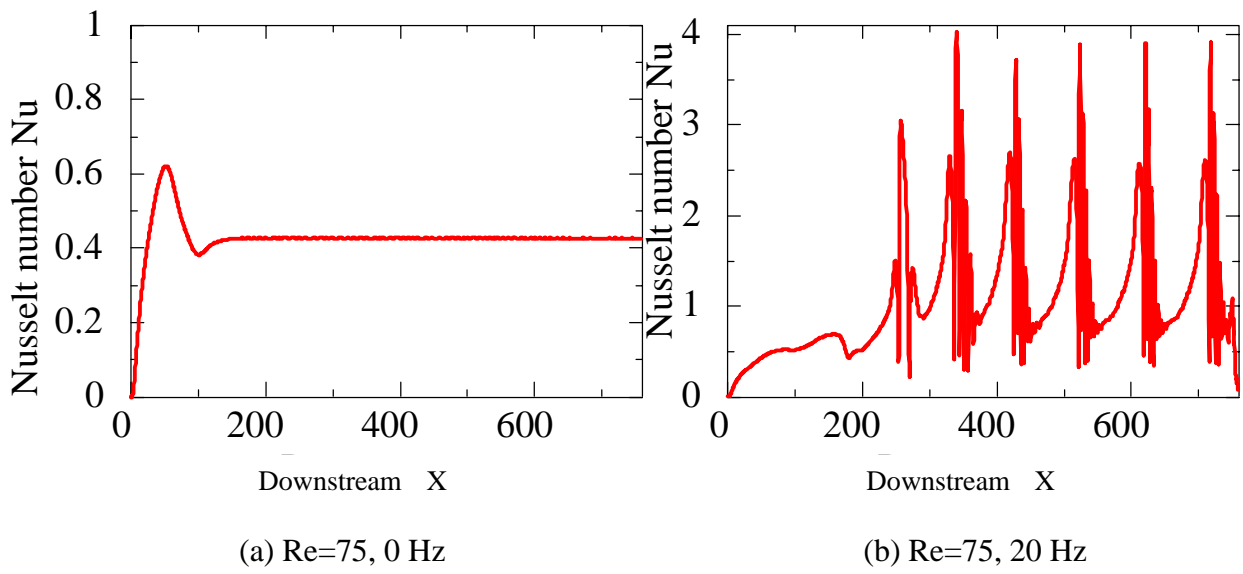


Figure 4: Nusselt number profiles on heating condition (1).

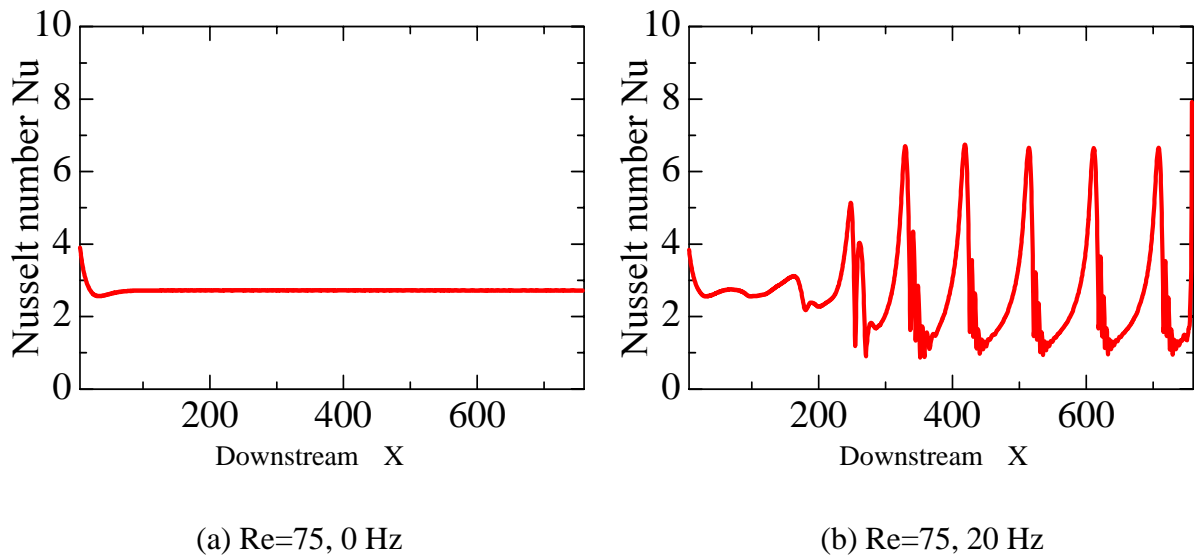
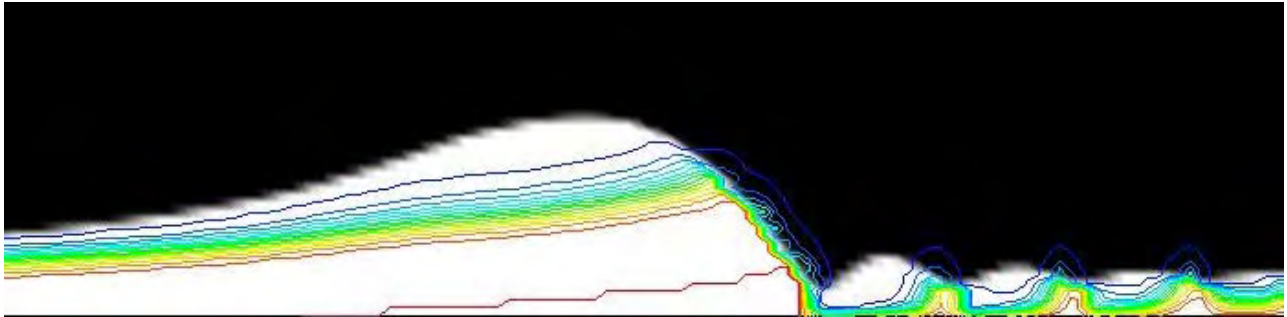
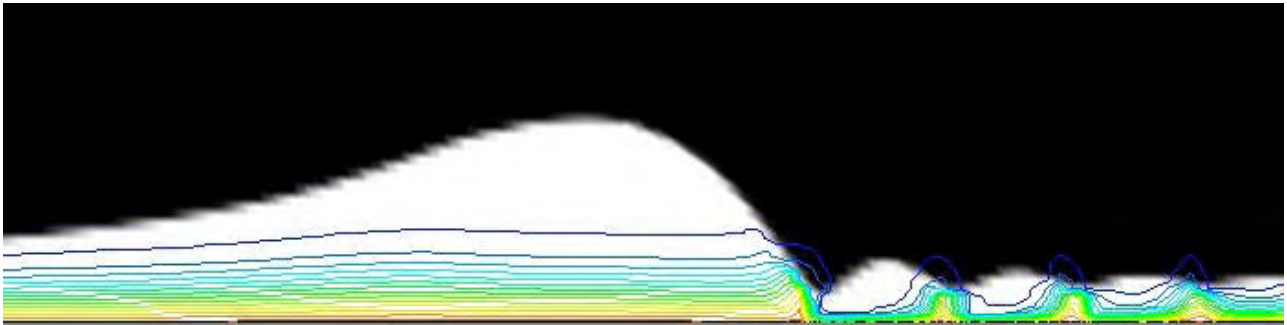


Figure 5: Nusselt number profile for on heating condition (2).

$t = 0.03 \text{ s}$



$t = 0.06 \text{ s}$

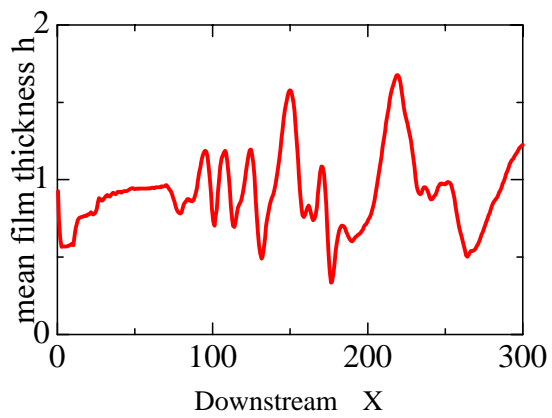


490

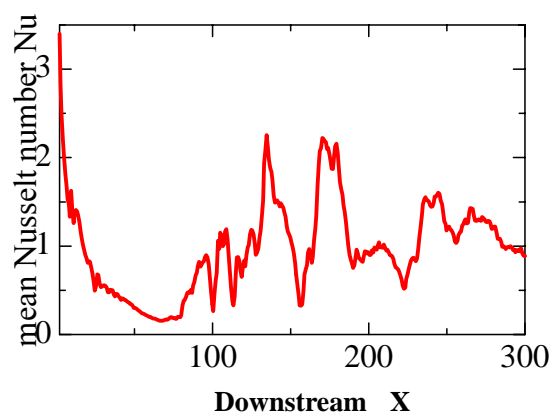
Downstream X

550

Figure 6: Temperature contours for $Re=75$, 20 Hz on heating condition (1).



(a) Mean film thickness



(b) Mean Nu

Figure 7: Mean film thickness and mean Nu for $Re=75$ and 0 Hz.

t=300

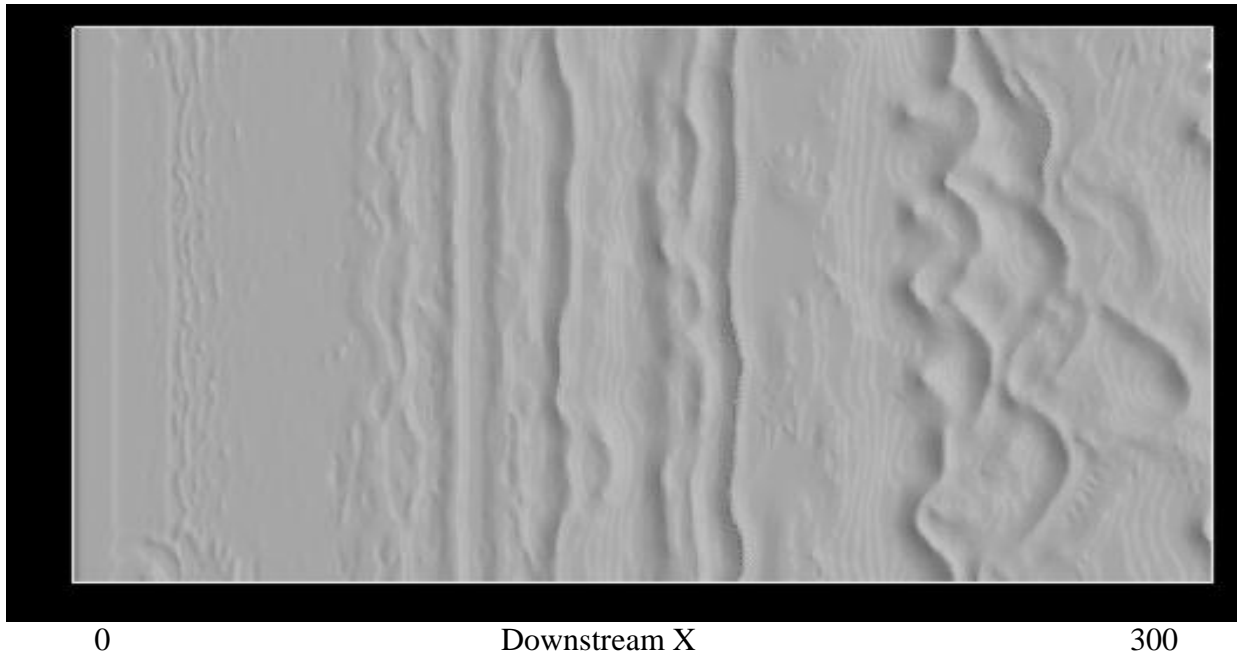


Figure 8: Visualization of free surface for $Re=75$ and 0 Hz (no disturbance case)

AUTHOR INDEX

ABE, Yo.	A-1
ABE, Yu.	A-9
AFFELD, K.	B-11
ARTEMYEV, V.	F-1
ASANO, H.	B-17
AURACHER, H.	B-1
BASUKI, W.	F-14
BRANDT, M.	E-1
BRÜCKER, Ch.	A-17
BUCHHOLZ, M.	B-1
CACUCI, D. G.	G-1
FUJII, T.	B-17
FUKANO, T.	A-18
FUKUDA, K.	F-30
GHARAIBAH, E.	E-1
GHIDERSA, B.	G-1
GIESE, T.	E-24
GOLDBRUNNER, M.	A-28
GOUBERGRITS, L.	B-11
HEIN, D.	A-28
HEMPEL, D. C.	B-29
HIRAYAMA, M.	C-13
HONDA, T.	G-22
HORIE, H.	E-11
INATOMI, T.	A-18
KARL, J.	A-28
KAWAMURA, H.	A-1
KERTZSCHER, U.	B-11
KINO, C.	G-34
KONDO, Sa.	F-30
KORNIENKO, Y.	F-1
KOSYNA, G.	D-9
KREPPER, E.	C-1
KUNUGI, T.	G-34
LAURIEN, E.	E-24
LUCAS, D.	C-1

MAHNKE, E. U.	B-29
MASCHEK, W.	F-30
MATSUZAWA, Y.	A-18
MORITA, K.	F-30
NAKANISHI, S.	D-1
NARIAI, H.	A-9
OKANO, M.	C-13
OZAWA, M.	C-13
PILZ, R.	B-29
POLIFKE, W.	E-1
PRASSER, H.-M.	C-1
SAPTOADI, D.	E-24
SEEGER, A.	B-11
SERIZAWA, A.	G-34
SHIOMI, Y.	D-1
SHIRAKAWA, N.	E-11
SHOJI, M.	C-26
SURYAWIJAYA, P.	D-9
SUZUKI, K.	A-1
SUZUKI, M.	A-1
SUZUKI, T.	F-30
SCHNERR, G. H.	F-14
SCHRÖDER, W.	A-17
SCHÜTZ, J.	E-24
TAKAHASHI, S.	A-1
TAKENAKA, N.	B-17
TAKESHIMA, K.	B-17
TOBITA, Y.	F-30
UCHIMICHI, N.	A-18
UCHIYAMA, T.	G-22
UMEKAWA, H.	C-13
WANG, S. F.	C-26
WELLNHOFER, E.	B-11
WÖRNER, M.	G-1 + G-10
YAMAGAMI, K.	D-1
YAMAMOTO, Y.	E-11
YOSHIDA, T.	A-18
YUAN, W.	F-14